Interaction between Stream Development and Propagating Extensional Faults

Ruth Elisabeth Gilpin

Thesis submitted in fulfilment of
the requirements for the degree of
Doctor of Philosophy
to the University of Edinburgh
2002

EX BIBL. UNIV. EDINBURGH

I declare that this thesis has been composed by myself and that no part of it has been submitted in any previous application for a degree. The work in it is entirely my own, except where the contribution of others has been duly acknowledged.

Ruth ~~Elisabeth~~ Gilpin
Edinburgh, 2002

Abstract

Fault populations are dynamic. Recent studies have highlighted the fundamental control of the interaction and feedback between individual faults in shaping the overall growth of a population. Each time a fault moves, it changes the distribution of stress in the surrounding rock, and hence can trigger, or retard, slip on nearby structures. The distribution of displacement in the population changes constantly through time, as faults interact and link. Although new faults are constantly nucleated, unfavourably-oriented faults may become abandoned, as strain gradually localises onto a few large structures, with high slip rates. Slip is also not uniform along a singe fault, and interaction may lead to grossly asymmetrical displacement profiles. After linkage, the new fault may retain evidence of the slip pattern of its contributing segments for some time, with local displacement lows at palaeo-segment boundaries.

Rivers are extremely sensitive to small changes in local topography. They respond rapidly to perturbations of their profile by changing their pattern, cross sectional morphology or by complete changes in course. Hence the changing mosaics of erosion, incision and deposition provide a high resolution record of the influence of the contemporary fault pattern. However, streams are controlled by a number of different factors, and their ability to record an external change is a delicate balance between their own power, and the magnitude and rate of the trigger. Thus the isolation of the tectonic signal from the fluvial record is not always straightforward, and there remains a desperate need for quantitative information about the rates and scales of the landscape's response to tectonic forcing.

This study explores the development of a series of recently-abandoned stream networks which drain a well-exposed extensional fault array on the Volcanic Tableland, eastern California. Low erosion rates have preserved excellent stream and fault morphologies, and study of their evolution is simplified by a well-constrained recent climatic history, and the single lithology. High resolution GPS surveys of both faults and streams demonstrate that the evolution of the streams has been intimately linked to that of the faults. Dramatic changes in stream course and incision and reorganisations of the stream networks and sediment distribution patterns are directly linked to changing interactions between neighbouring faults. Variations in the jointing and welding of the tuff have also influenced stream patterns and incision styles. The stream cross-sectional aspect ratio is shown to be a sensitive indicator of fault movements.

In situ cosmogenic ^{10}Be and ^{26}Al have been used to date samples from bedrock channels in the overlap between the two largest faults. This has constrained the timing and length of stream occupation, the relative importance of tectonic and climatic forcing, and rates of both surface and tectonic processes. Incision in the footwall of the main fault has been dominated by the upstream migration of knickpoints developed in response to fault movements, and aided by the joint geometry.

The first incorporation of dynamic interacting faults into a surface process model is described. Model results demonstrate that interaction between faults must be specifically considered if the complexity of natural fluvial responses is to be accurately reproduced. However, the initial topography exerts a major influence on the later

evolution of the landscape, and stream development is also affected by the resolution of the tectonic steps applied.

The complexity of the tectonic landscape is a direct results of the mechanism of fault growth, where interaction dominates the distribution of displacement. This variability is exploited by streams, which are very therefore very sensitive markers of the changing patterns of faulting. Major features of the landscape may be determined relatively early in the evolution of the controlling faults.

And I tell you, if you have the desire for knowledge and the power to give it physical expression, go out and explore. If you are a brave man you will do nothing: if you are fearful you may do much, for none but cowards have need to prove their bravery. Some will tell you that you are mad, and nearly all will say, "What is the use?" For we are a nation of shopkeepers, and no shopkeeper will look at research that does not promise him a financial return within a year. And so you will sledge nearly alone, but those with whom you sledge will not be shopkeepers: that is worth a good deal. If you march your Winter Journeys, you will have your reward, so long as all you want is a penguin's egg.

from '*The Worst Journey in the World*' by Apsley Cherry-Garrard

Acknowledgements

I'd like to thank my supervisors for the help they have given me. In particular, Nancye Dawers for her help in the field, and for the loan of her brand new GPS kit - the only way I'll ever be able to test drive something worth $40 000. Patience Cowie introduced me to Peter van der Beek and hence to the wonders of CASCADE, as well as for her contributions particularly with the dynamic fault modelling.

Bill Phillips was never an official supervisor, but has more than filled that role on all things cosmogenic. He has been a constant source of support and encouragement, patiently corrected my theoretical errors and gone out of his way to make life simple for me in Geography. Chris and Jez explained pretty much most of the lab protocols to me, and also put up with the geology interloper in their lab. The fact that I had targets to send at all is largely due to the help of the geography crowd: Chris, Jez, Bill, Allan and Jessica. Bill, Nancye and Patience have all read various drafts of this thesis and helped me improve it substantially. The errors that remain are entirely my own.

The work on CASCADE was begun during a 6 week placement in Grenoble with Peter van der Beek. The steps I have made with the model have been considerably helped by discussions with Peter during a 6-week placement in Grenoble University, and also with Patience, Katie Hardacre, Aileen McLeod and Paul Bishop and others at Glasgow University. I would also like to thank Jean Braun for the initial permission to use the code. Shane, Justin, Katie, Dave and Rog have all helped me in my first tottering steps to master enough computing skills to get the code to run, and to look at the results it produced in more constructive formats than ASCII. Most of the data in this thesis has been analysed, and the figures generated using GMT - many thanks to Paul Wessel and Walter Smith for the free use of their software.

Fieldwork in the Volcanic Tableland would probably have been possible, but certainly far less fun, not to mention less well-fed, without the help of the folk at the White Mountain Research Centres both in Bishop and up in the White Mountains. Cecil, Mike, Scotty, Donna, Kathy, Daniel, the Sczusaks [I never have been able to spell that!] and everyone else on the staff, who went to such great lengths to make me so welcome. The food certainly will not be forgotten, but thanks also for the support with the various traumas of DHL, UPS, FedEx and vehicle batteries, tents, bearcans...and for introducing me to the phenomenal wilderness all around. While staying there, I met so many wonderful people who were also working [or not..] in the area. I so enjoyed learning about electro-fishing, anaesthetising mice, stamping out various non-indigenous plants and the many aspects of the regional geology about which I remain embarrassingly ignorant. I shall not forget you, nor those great nights drinking green beer on the porch, and in the hot springs.

Several people survived the hardships of the research station to help me in the field. Peet McFadzean was of course there doing his own "work", but offered many helpful suggestions, as did Nancye, Alien, Audrey and Zoë. The suggestions, advice, and insights of all the folks who came onto the Tableland have helped considerably with my interpretation of those old channels.

No-one's ideas come to them only through night-time inspiration, or from sitting silently at a desk. Over the last four years, I have benefited immensely from discussions,

informal, unintentional, and sometimes even sober, with many people, and the ideas in this thesis have been distilled from the thoughts they have triggered. Thanks in particular go to Aileen, Katie, Zoë, Peet, Nancye, Patience, Bill, Clare, Paula, Chris, Mark, Anne, Rog, Dave, Lynne, Matt, Doug, Jon, John and many others.

The last four years have been incredible. I would like to thank many people for making them brilliant, through their friendship, patience and support. it is always the things you do out of work that have the most effect on you, and so I shall always remember the days away oop north, rugby [physio] and many nights filled with alcohol, exceptionally good food and great chat. Thanks to Kath, Suse, Zoë, Clare, Amanda, Oli and his family, Rog, Ali, Dave, David, Dan, Doug, Fiona, Anna, Peet, Matt, Alien, and her folks, for introducing me to the wonders of the Scottish wilderness, scrambling, 'climbing' and midgie-avoidance tactics. You are the ones responsible for the amount of gear I have had to move across town these last four times!!!

Writing-up has not been the most fun experience of my life, but it has brought me so much kindness from so many people. Thanks and apologies go to all who have had to deal with me in the last few months, and for the millions of offers of help, food, alcohol, hugs, ears to rant into and shoulders to cry on. My family in particular have been greatly appreciated throughout the phud, for offering words of wisdom, and all their loving support. Those that have already sledged this route understand the icy wind. My thanks in particular for shelter and support, and for the great times go to my fellow travellers: Matt, Theo, Peet, Anne, Ann, Rich, Nicky, Doug, Nadia and John. Looks like I'd better turn the light out then.

This project, in particular the fieldwork, cosmogenic work and conference attendances would have been impossible without the generous support of my sponsors. This work has been funded by a NERC studentship, with additional support from industrial CASE partners Shell, Enterprise and Conoco. A University of Edinburgh Small Project Grant helped with the costs of cosmogenic isotope sample analysis.

There are so many people who have been there for me. The danger of writing a list is that you always manage to forget people who have made huge contributions. I can never thank all the people who have contributed to the work in this book, or my sanity, but those who I have forgotten/omitted to mention, you know who you are, and my heartfelt thanks go out to you.

Above all, I would like to thank the person who has done the most to get this phud handed in. Thank you Rog for your constant support and love, not to mention food [yes, I know you've been counting] and the haven you have given me from the rest of the world. I'm afraid you've been lapsing from the curm-Hutcheonliness a bit recently, though. Thank you not only for marching with me, but for pulling my sledge, and also for the many times you have carried me.

Contents

1 Introduction 1
- 1.1 Rationale . . . 1
- 1.2 What is the advantage of this particular approach? . . . 2
- 1.3 Specific aims . . . 3
- 1.4 Structure of this thesis . . . 4

2 Theory and Context 6
- 2.1 Normal faults: growth and interaction . . . 6
  - 2.1.1 Fault scaling . . . 8
  - 2.1.2 Interaction and linkage . . . 9
    - 2.1.2.1 Enhanced growth . . . 10
    - 2.1.2.2 Tip gradients . . . 15
    - 2.1.2.3 Inhibited growth . . . 16
  - 2.1.3 Evolution of a normal fault population . . . 17
  - 2.1.4 Influence of lithology . . . 19
- 2.2 Sedimentation in extensional basins - tectonic approach . . . 20
  - 2.2.1 Effect of normal fault topography . . . 20
  - 2.2.2 Effects of fault growth, interaction and linkage . . . 21
- 2.3 Fluvial processes and responses to tectonics - geomorphic approach . . . 26
  - 2.3.1 Morphology and process . . . 26
    - 2.3.1.1 Alluvial streams . . . 26
    - 2.3.1.2 Bedrock streams . . . 27
  - 2.3.2 Stream power . . . 30
    - 2.3.2.1 The stream power law . . . 32
  - 2.3.3 Responses to tectonic motion . . . 34
    - 2.3.3.1 Knickpoints . . . 34
    - 2.3.3.2 Alluvial stream responses . . . 39
    - 2.3.3.3 Bedrock stream responses . . . 43
  - 2.3.4 Modulation of fluvial response to tectonics . . . 45
    - 2.3.4.1 Climate . . . 46
    - 2.3.4.2 Lithology . . . 46
    - 2.3.4.3 Pre-existing landscape . . . 47
    - 2.3.4.4 Rates of change . . . 48
- 2.4 Numerical approach: LEM development . . . 49
  - 2.4.1 Model parameters . . . 50
    - 2.4.1.1 Surface processes . . . 50
    - 2.4.1.2 External influences . . . 54

2.4.2 Landscape modelling approaches 55
2.5 *In situ* cosmogenic isotope analysis 61
2.5.1 Calculation of exposure ages and erosion rates 62
2.5.2 Two-isotope systematics 64
2.5.2.1 Erosion Island plot 64
2.5.2.2 Al-Be comparison age plots 67
2.5.3 Previous geomorphic studies using cosmogenic isotopes 67

3 Introduction to fieldwork on the Volcanic Tableland 74
3.1 Regional Setting: Owens Valley, California 74
3.1.1 Glacial chronology 78
3.1.2 Drainage and sedimentation 81
3.1.3 Range-front structure and faults 82
3.2 The Volcanic Tableland 83
3.3 Fieldwork data used in this thesis 90

4 Stream and fault interaction in a fault overlap, Volcanic Tableland 92
4.1 Fault displacement profiles 94
4.1.1 Fault 1: bounding the northwest [back] of the central overlap . . 95
4.1.1.1 Fault cutoffs 95
4.1.1.2 Displacement-length profile 97
4.1.1.3 Small faults 98
4.1.1.3.1 Centre of Fault 1 footwall 106
4.1.2 Fault 2: bounding the east [front] of the central overlap 106
4.1.2.1 Fault cutoffs 106
4.1.2.2 Displacement-length profile 108
4.1.3 The linking fault: joining Faults 1 and 2 110
4.1.3.1 Fault cutoffs 110
4.1.3.2 Displacement-length profiles 111
4.1.4 Summary of fault profile data 113
4.2 Drainage systems in the central overlap 116
4.2.1 Main stream 117
4.2.1.1 Stream course 118
4.2.1.2 Long profile 120
4.2.1.3 Bank profiles 130
4.2.1.4 Cross-section data 131
4.2.1.5 Summary of main stream data 138
4.2.2 Minor ramp channels 140
4.2.2.1 Stream course 140
4.2.2.2 Long profile 141
4.2.2.3 Cross-section data 144
4.2.2.4 Summary of minor channel data 150
4.2.3 Rounded clasts on the central overlap 151
4.3 Summary of central overlap data 154

5 Northern and axial drainage networks, Volcanic Tableland 156
5.1 Lateral drainage system: Northern tip network 156
5.1.1 Downstream channel 158
5.1.1.1 Incised channel 160
5.1.1.2 Downstream of the main fault array 166
5.1.1.3 Summary of downstream channel data 172
5.1.2 Upstream channel 174
5.1.2.1 Stream course and long profile 174
5.1.2.2 Cross-section data 176
5.1.3 Tributaries 181
5.1.3.1 Tributary 1 182
5.1.3.2 Tributary 2 183
5.1.3.3 Tributary 3 185
5.1.3.4 Tributary 4 188
5.1.3.5 Summary of upstream northern drainages 192
5.1.4 Non-tuff clasts 194
5.1.5 Summary of northern drainage system data 197
5.2 Axial drainage system 199
5.2.1 Map and profile data 200
5.2.2 Cross-section data 208
5.2.2.1 Fault 0 footwall 208
5.2.2.2 F1 basin 209
5.2.2.3 Southern axial channel: Fault 2 to Corral Fault basin . 211
5.2.3 Hangingwall basin profiles 215
5.2.4 Tributaries of the axial system 219
5.2.4.1 Stream down F1/F0 overlap 219
5.2.4.2 Tributary from fumarole high to east 222
5.2.4.3 Hangingwall of Corral fault 222
5.2.5 'Fumarole-axial' network 223
5.2.5.1 Main fumarole-axial stream 223
5.2.5.2 'Road stream': Fault 2 basin to Casa Diablo Road . . . 226
5.2.6 Summary of axial stream data 228
5.3 Summary of Chapter 5 231

6 ^{10}Be and ^{26}Al Cosmogenic Isotope Analysis - Fieldwork and Results 233
6.1 Field approach 233
6.1.1 Sampling strategy 234
6.1.2 Analysed samples 238
6.1.2.1 Sample 2: Main channel downstream of linking fault . . 239
6.1.2.2 Sample 4: Main channel southern fork, immediately above linking fault 240
6.1.2.3 Sample 6: Main channel northern branch in linking fault scarp 241
6.1.2.4 Sample 8: Main channel upstream of linking fault . . . 242
6.1.2.5 Sample 11: Minor channel 1, immediately above linking fault scarp 243
6.1.2.6 Sample 14: Main channel in Fault 1 footwall 244
6.2 Results and calculations: AMS and ICP-AES data 246

6.2.1 Raw data . . . 246
6.2.2 Cosmogenic nuclide abundancies: N_{26} and N_{10}^* . . . 248
6.2.2.1 Pipette calibration method . . . 249
6.2.3 Erosion Island plot . . . 250
6.2.4 'Raw' production rates . . . 252
6.3 Calculations: Shielding . . . 253
6.3.1 Sample thickness . . . 253
6.3.2 Topographic shielding . . . 254
6.3.3 Sloping surfaces . . . 255
6.3.4 Surface cover . . . 255
6.4 Corrected exposure ages . . . 257
6.5 Initial interpretation . . . 257
6.5.1 Erosion histories . . . 257
6.5.2 Controls on channel formation and incision . . . 261
6.6 *In situ* cosmogenic production rate scaling factors . . . 265
6.7 Summary . . . 268

7 Discussion of Volcanic Tableland results 269
7.1 General features of the Tableland . . . 270
7.1.1 Streams . . . 270
7.1.2 Faults . . . 274
7.1.3 Stream power and cross-sectional morphology . . . 279
7.1.3.1 Stream power . . . 279
7.1.3.2 Aspect ratio . . . 281
7.1.3.3 Comparison of stream power and aspect ratio . . . 290
7.2 The central overlap: Interaction and linkage of two overlapping faults . 292
7.2.1 Constraints on fault and drainage evolution from surveying . . . 292
7.2.1.1 Linking fault evolution . . . 292
7.2.1.2 Footwall stream response to faulting . . . 293
7.2.1.3 Development of alluvial fan in Fault 1 basin . . . 295
7.2.1.4 Connection of main stream to E/SE . . . 297
7.2.1.5 Relative occupation of main and minor streams . . . 298
7.2.2 Constraints from the cosmogenic isotope data . . . 299
7.2.2.1 Correlation with regional climate cycles . . . 300
7.2.2.2 Fault and drainage evolution . . . 303
7.2.2.3 Knickpoint propagation rates . . . 305
7.2.2.4 Knickpoint propagation mechanism . . . 307
7.2.2.5 Erosion rates . . . 309
7.2.3 Model of the evolution of the central overlap . . . 310
7.3 Axial stream: Evolution and linkage of the array . . . 314
7.3.1 Early drainage from the F0 footwall . . . 314
7.3.2 Sediment supply to the F1 basin . . . 314
7.3.3 Controls on development of the axial stream . . . 315
7.3.4 Establishment of the axial stream . . . 317
7.3.5 Fumarole-axial stream . . . 318
7.3.6 Reorganisation of the array stream patterns . . . 319
7.4 Non-tuff clasts: Early drainage evolution . . . 322
7.4.1 Proposed model of large-scale Tableland drainage evolution . . . 323

7.4.2 Correlation with Owens River incision . . . 326
7.5 Comparison with the 'classic' overlap stream geometry . . . 329
7.5.1 Controls on the development of the Tableland overlap geometry . 329
7.5.2 Controls on the development of the 'classic' overlap geometry . . 332
7.6 Overview . . . 334

8 Numerical modelling approach: CASCADE **337**
8.1 Incorporation of dynamic interacting faults . . . 339
8.1.1 Fault model . . . 339
8.1.1.1 Incorporation into CASCADE . . . 340
8.1.2 Model parameters . . . 340
8.1.2.1 Model scale and resolution . . . 340
8.1.2.2 Surface processes . . . 340
8.1.3 Results . . . 342
8.1.3.1 Experiment 1: Evolution of streams around a growing fault population . . . 342
8.1.3.2 Experiment 2: Lithological resistance . . . 349
8.1.3.3 Experiment 3: Event size . . . 354
8.1.4 Other considerations: Initial topography . . . 357
8.1.5 Limitations of the dynamic model . . . 358
8.2 Discussion of the model results . . . 359

9 Synthesis **363**
9.1 Fieldwork . . . 364
9.2 Modelling . . . 366
9.3 Holistic Approach . . . 367
9.4 Future work . . . 368

A *In situ* cosmogenic isotope analysis theory **369**
A.1 Production of cosmogenic isotopes . . . 369
A.2 Advantages and disadvantages of *in situ* cosmogenic analysis . . . 371
A.3 Production rates . . . 373
A.3.1 Scaling coefficients for production rates . . . 373
A.3.2 Calculation of production rates at a sample location . . . 374
A.4 Modification of production rates: sample shielding . . . 375
A.4.1 Sample thickness . . . 376
A.4.2 Topographic shielding . . . 377
A.4.3 Sloping surfaces . . . 379
A.4.4 Surface coverage . . . 379
A.5 Calculation of exposure ages and erosion rates . . . 380

B Methodology **383**
B.1 Collection of field data using differential GPS . . . 383
B.1.1 GPS Theory . . . 383
B.1.2 Data collection on the Volcanic Tableland . . . 385
B.1.3 Data analysis and plotting . . . 387
B.2 Cosmogenic isotope target preparation . . . 388
B.2.1 Preparation of quartz concentrates . . . 388
B.2.2 Preparation of target oxides . . . 389

List of Figures

2.1 Typical features of a normal fault, modified from Schlische (1991) 7
2.2 Log-log plot of D_{max} against L for global dataset, after Schlische *et al.* (1996) 9
2.3 Changes in stress in the region around a normal fault, due to a single slip event, after King *et al.* (1994); Cowie (1998) 10
2.4 Interaction and linkage of sub-parallel faults, from Gupta and Scholz (2000) 11
2.5 Breaching of a relay ramp, after Trudgill and Cartwright (1994) 12
2.6 Early linkage of fault segments, modified from Cartwright *et al.* (1995); Cowie *et al.* (2000) 13
2.7 Late linkage of fault segments, modified from Cowie *et al.* (2000) 14
2.8 Sketch of 'slip patch', from Cowie and Shipton (1998) 15
2.9 Inhibited growth: 'anticlustering' of small faults, from Ackermann and Schlische (1997) 16
2.10 Cartoon of the healing-reloading mechanism, from Cowie (1998) 17
2.11 Fault population evolution as predicted by the healing-reloading model, from Cowie *et al.* (2000) 18
2.12 Block model of extensional half-graben sedimentation patterns, modified from Gawthorpe *et al.* (1994) 20
2.13 Streams as indicators of fault tip propagation, modified from Jackson *et al.* (1996) 23
2.14 'Classic' model of relay-zone drainage, modified after Jackson and Leeder (1994) 24
2.15 Classification of alluvial channels, from Schumm (1981) 27
2.16 Cartoon of abrasion, from Whipple *et al.* (2000a) 29
2.17 Cartoon of plucking, from Whipple *et al.* (2000a) 29
2.18 Cartoons of knickpoints in layered, jointed rock, modified from Miller (1991) 30
2.19 Evidence for knickpoint migration: terraces and profiles, from Siedl and Dietrich (1992) 35
2.20 Proposed mechanisms of headward knickpoint migration, from Gardner (1983) 36
2.21 Knickpoint morphology and bed shear stress variation, modified from Gardner (1983) 36
2.22 Numerical modelling of knickpoint evolution, modified from Howard *et al.* (1994) 38
2.23 The range of alluvial channel patterns for three channel types, from Schumm (1981) 39

2.24 Responses of experimental channels to uplift and to subsidence, from Ouchi (1985) and Schumm *et al.* (2000) 40
2.25 Adjustment of braided and mixed-load streams to uplift and to subsidence, from Ouchi (1985) and Schumm *et al.* (2000) 41
2.26 Variations in channel morphology and hydrology in response to tectonics, from Jorgensen (1990) 42
2.27 Uplift-rate curve and variations in channel gradient, from Merritts and Vincent (1989) 43
2.28 Response of different stream sections to uplift, from Merritts and Vincent (1989) 44
2.29 Schematic figure of the bedrock landsliding algorithm, from Densmore *et al.* (1998) 52
2.30 Stream patterns resulting from radial uplift using a regular and irregular grid, from Braun and Sambridge (1997) 59
2.31 Model Erosion Island plot 65
2.32 Different complex exposure histories which result in low N_{26} / N_{10}* values, from Bierman et al. (1999) 66
2.33 Cosmogenic nuclide depth profiles: correction for inheritance, modified from Phillips *et al.* (1998) 70
2.34 Cosmogenic ^{36}Cl profile down the Hebgen Lake fault, from Zreda and Noller (1998) 73

3.1 Map of Owens Valley, modified from Phillips *et al.* (1996); Berry (1997) 75
3.2 Sketch cross-section of Owens Valley, showing structure of Volcanic Tableland 77
3.3 Evolution of the Owens Valley, White Mountains and the eastern Sierra Nevada, modified from Lueddecke *et al.* (1998) 78
3.4 Overviews of the Volcanic Tableland 84
3.5 Map of the surface of the Volcanic Tableland, modified from Pinter and Keller (1995) 86
3.6 Displacement-length profile for a linked fault array on the Volcanic Tableland, eastern California, from Dawers and Anders (1995) 87
3.7 Evolution of Owens River and Rock Creek gorges, after Putnam (1960) 89
3.8 Cross-sectional profile of a channel 91

4.1 Aerial photograph of the main fault array studied 93
4.2 Aerial photograph of the main overlap 94
4.3 View of Fault 1, looking west from the top of the eastern fumarole high 95
4.4 Map and elevation profiles of the fault cutoff surveys for Fault 1 96
4.5 Displacement-length profile for Fault 1 97
4.6 Field photograph of main channel incision through Fault 1 98
4.7 Map of the small faults around Fault 1 discussed in the text 99
4.8 Map and cutoff and displacement-length profiles for the hangingwall splay fault k at the southern tip of Fault 1 100
4.9 Map and cutoff and displacement-length profiles for small fault j in the footwall of the southern tip of Fault 1 101
4.10 Map and summed displacement-length profile for the southern tip of Fault 1, including the contribution of small faults j and k 102

4.11 Overview of the overlap between the northern tip of Fault 1 and Fault 0 103
4.12 Map, cutoff and displacement-length profiles for small fault 'g' at northern tip of Fault 1 footwall . . . 104
4.13 Map, cutoff and displacement-length profiles for small fault 'h' at northern tip of Fault 1 footwall . . . 105
4.14 Map, cutoff and displacement-length profiles for small antithetic fault in centre of Fault 1 footwall . . . 106
4.15 Map of surveyed fault cutoffs for Fault 2 . . . 107
4.16 Fault 2 cutoff elevation and displacement-length profiles . . . 109
4.17 Map of surveyed fault cutoffs for the linking fault . . . 110
4.18 Cutoff and displacement-length profiles for the linking fault . . . 112
4.19 View of main channel course down the overlap, through the linking fault 113
4.20 Aerial photograph of the central overlap . . . 116
4.21 Map of the main stream course from the fork to the Fault 2 hangingwall basin . . . 117
4.22 'Dogleg' kinks in the main channel in the footwall of Fault 1: joint influence on the main channel course . . . 119
4.23 Main channel branches incising the linking fault . . . 120
4.24 Long profile of the main channel . . . 120
4.25 Long profile of main channel in the footwall of Fault 1 . . . 121
4.26 Contrasting morphologies of the three channel reaches in the footwall of Fault 1 . . . 122
4.27 Steps in the upper part of the main channel profile: footwall of Fault 1 . 123
4.28 Long profile of main channel through the ramp: Fault 1 to Fault 2 . . . 124
4.29 Channel morphologies in the lower main channel: ramp and F2 hangingwall . . . 126
4.30 Incision into the linking fault scarp by southern branch of main channel 127
4.31 Comparison of profiles of the three main streams which cut through the linking fault scarp . . . 128
4.32 Profiles of the banks of the main channel in the footwall of Fault 1 . . . 132
4.33 Map of the cross-sections surveyed in the main channel: fork to Fault 2 basin . . . 133
4.34 Cross-sectional profiles of the main channel upstream of Fault 1 . . . 134
4.35 Cross-sectional profiles of the main channel through the central overlap 136
4.36 Variation in aspect ratio of the main channel and braids in the central overlap: Faults 1 to 2 . . . 137
4.37 Variation in aspect ratio plot along the main channel from the fork to Fault 2 . . . 138
4.38 Map of the minor channels in the fault overlap . . . 140
4.39 Long profile of the minor channels in the fault overlap . . . 141
4.40 Field photographs of the minor channel at the foot of Fault 1 and cutting through Fault 2 . . . 142
4.41 Map of cross-sections measured in minor channels . . . 144
4.42 Morphology of cross-sections through minor channel 1 . . . 146
4.43 Morphology of cross-sections through minor channel 2 . . . 147
4.44 Morphology of cross-sections through minor channel 3 . . . 148
4.45 Variation in aspect ratio of minor channels through the ramp . . . 149
4.46 Variation in the surface of the Tableland: typical and central ramp surface 151

4.47 Variation in size of rounded clasts forming the ramp surface away from the channels across the central overlap 152
4.48 View of main channel incision into the ramp surface 153

5.1 Aerial photograph of the drainage network at the northern tip of the fault array 157
5.2 Map and long profile of the northern tip channel downstream of Telegraph Road 159
5.3 Map and long profile of the incised section of the channel flowing through the northern tip of the main fault array 160
5.4 Profile of the channel bed and banks through the northern tip of the array 162
5.5 Field photographs of the stream incised through the northern tip of the fault array 163
5.6 Downstream variation in cross-sectional morphology of incised northern channel 165
5.7 Map of the downstream reaches of the northern drainage network, showing cross-section locations 166
5.8 Field photographs of the downstream reaches of the northern stream . . 167
5.9 Variation in cross-sectional morphology of downstream reaches of northern stream network 170
5.10 Long profile and aspect ratio plot for downstream reaches in the northern stream network 171
5.11 Map and long profile of the upstream section of the northern tip system 175
5.12 Downstream variation in cross-sectional morphology of upstream northern channel 177
5.13 Incision depth in the footwall of the largest fault in the upstream northern channel: comparison of bank and channel bed profiles 178
5.14 Field photographs of varying morphology in main upstream northern channel 179
5.15 Map of western tributaries in northern network, showing locations of the surveyed cross-sections 181
5.16 Long profile and downstream variation in aspect ratio of northern stream tributary 1 183
5.17 Long profile and downstream variation in aspect ratio of northern stream tributary 2 184
5.18 Long profile and downstream variation in aspect ratio of northern stream tributary 3 186
5.19 Bank profiles and incision variation in incised canyon in northern stream tributary 3 187
5.20 Long profile and downstream variation in aspect ratio of northern stream tributary 4 188
5.21 View of tributary 4 incising through fault scarp 189
5.22 Bank profiles and incision variation in faulted reaches of northern tip tributary 4 190
5.23 Non-tuff clasts in the northern stream network 196
5.24 Aerial view of the axial drainage network 199
5.25 Long profile of the axial channel network and some surveyed tributaries 200
5.26 Map of the axial channel network and surveyed tributaries 201

5.27 Field photographs of axial stream in F0 basin 202
5.28 View of F0 basin, the northern axial channel and the tributary draining the F1-F0 overlap 203
5.29 Field photographs of axial stream in F1 basin 204
5.30 Map of braiding in the axial channel network in the hangingwall basin of Fault 1 205
5.31 Field photographs of southern axial stream 206
5.32 Cross-sectional profiles of axial channel in Fault 0 footwall 208
5.33 Variation in cross-section aspect ratio of axial channel in Fault 0 footwall 209
5.34 Cross-sectional profiles of the axial channel in Fault 1 basin 210
5.35 Variation in aspect ratio of the axial channel in the Fault 1 basin 211
5.36 Location of cross-sections surveyed in the southern axial channel 212
5.37 Cross-sectional profiles of axial channel in the Fault 2 to Corral fault basin 213
5.38 Variation in cross-section aspect ratio of southern axial channel: Fault 2 hangingwall to Corral Fault basin 214
5.39 Map of central axial channel showing location of measured hangingwall profiles 215
5.40 Profiles of the hangingwall basins of Faults 0, 1 and 2 216
5.41 Map of Fault 1/Fault 0 overlap showing drainage towards F0 hangingwall basin 219
5.42 Cross-sections in the F1/F0 overlap drainage: profiles and aspect ratios 220
5.43 Long profile of tributary channel from fumarole high to northeast 222
5.44 Long profile of channel in hangingwall of corral fault 223
5.45 Map of central graben, showing the relative locations of the fault proximal axial channel and the 'fumarole-axial' channel 224
5.46 Long profile of 'fumarole-axial' channel and related streams 225
5.47 View of truncation of the fumarole-axial channel 225
5.48 Downstream variation in cross-section aspect ratio of axial channel . . . 229

6.1 Location map of the cosmogenic sample sites 235
6.2 Cosmogenic sample sites 16-18 in Fault 2 scarp, at locality 9a 236
6.3 Soil lines and soil patch on Fault 2 237
6.4 Long profile of the main channel showing the location of the analysed samples 238
6.5 Field photographs of cosmogenic sample site 2 239
6.6 Field photographs of cosmogenic sample site 4 240
6.7 Field photographs of cosmogenic sample site 6 241
6.8 Field photographs of cosmogenic sample site 8 242
6.9 Field photographs of cosmogenic sample site 11 243
6.10 Long profile of minor channels, showing the location of sample VT11 . . 244
6.11 Field photographs of cosmogenic sample site 14 245
6.12 Erosion Island plot for Volcanic Tableland samples 252
6.13 Rose-diagrams showing the shielding of the analysed samples by topographic obstructions, as measured in the field 255
6.14 Comparison of ^{26}Al and ^{10}Be corrected apparent exposure ages 258
6.15 Cartoon of variation in radioactive cosmogenic isotope abundancies in a sample that has been buried for a period of time between exposures . . 260

6.16 Map of the central overlap and long profile of the main stream showing the apparent exposure ages of analysed samples 263
6.17 Comparison of ^{26}Al and ^{10}Be apparent exposure ages, using different scaling factors 267

7.1 Correlation of aspect ratio with fault displacement in the central overlap 283
7.2 Distribution of aspect ratios in surveyed streams 285
7.3 Correlation between aspect ratio and local channel bed slope 288
7.4 Simple model of linking fault evolution 294
7.5 Sketch of proposed mechanism of downwearing of the Fault 1 knickpoint 312
7.6 Palaeogeographic evolution of the central overlap 313
7.7 View of southern Fault 0 basin, and lip controlling drainage into the F1 basin 317
7.8 Palaeogeographic evolution of the axial stream 321
7.9 Proposed model of drainage evolution on the Volcanic Tableland 325
7.10 Terraces at the southern margin of the Tableland, from Pinter *et al.*, 1994327

8.1 Calculation of topography from the positive feedback model; from Cowie *et al.*, 2000 339
8.2 Evolution of faulting and topography created by positive feedback fault model, from Cowie *et al.*, 2000 341
8.3 Evolution of stream patterns and topography around a developing fault population 344
8.4 Catchments and summarised streams at four stages through model run . 347
8.5 Effect of increased lithological resistance: model topography with L_{fb}=500km 350
8.6 Comparison of drainage basins and stream patterns developed around faults in soft and hard rock 352
8.7 Effect of tectonic event magnitude: model topography and stream development with frequent small events 356

A.1 Variation of TCN production rate with depth in a target, modified from Gosse and Phillips (2001) 370
A.2 Sketch of variation in nuclide abundancy with depth 376
A.3 Sketch of topographic shielding for a sample 377
A.4 Sketch of path lengths for near normal and low angle incident radiation 379
A.5 Sketch of shielding of a sample on a sloping surface 380

B.1 The Z-Xtreme kit in the field 386

List of Tables

2.1 Targets for *in situ* TCN production 61

3.1 Late Quaternary glacial advances in the eastern Sierra Nevada 80

4.1 Calculated displacement-length values for surveyed faults 114
4.2 Comparison of gradients of channel sections for the main channel branches through linking fault 128
4.3 Variation in gradient and SL index of main channel reaches through the overlap 129
4.4 Variation in bed gradient in footwall of Fault 1, calculated perpendicular to the Fault 1 scarp 130
4.5 Variation in gradient of banks of main channel in footwall of Fault 1 . . 130
4.6 Variation in gradient and SL index of minor channels through the overlap 143

5.1 Variation in gradient of the northern channel 180
5.2 Variation in downstream bed gradient of the tributaries of the northern tip channel 193
5.3 Variation in downstream bed gradient and SL index of the main axial channel 207
5.4 Variation in downstream bed gradient of the axial stream tributaries . . 221
5.5 Variation in downstream bed gradient of the 'fumarole-axial' channel and tributaries 226

6.1 Raw field, ICP-AES and AMS data for the Volcanic Tableland samples . 247
6.2 Abundancies of ^{26}Al and ^{10}Be in the Volcanic Tableland samples, calculated from the ICP-AES data 248
6.3 Pipette calibration data 250
6.4 Abundancies of ^{26}Al and ^{10}Be in the Volcanic Tableland samples, calculated from the pipette calibrations 251
6.5 'Raw' production rates of ^{26}Al and ^{10}Be for the Tableland samples - no shielding corrections made 253
6.6 Impact of shielding on in situ cosmogenic nuclide production rates . . . 254
6.7 ^{26}Al and ^{10}Be apparent exposure ages 257
6.8 Variation in calculated exposure ages with different production rate scaling factors 266

7.1 Comparison between averaged erosion rates, stream power and aspect ratios for central overlap streams 280
7.2 ^{26}Al and ^{10}Be apparent exposure ages 300

7.3 Maximum long-term averaged erosion rates at sample sites 309

A.1 Advantages and disadvantages of the six commonly-used TCNs 372
A.2 Production rate scaling factors for ^{10}Be and ^{26}Al in quartz 373
A.3 Nuclear disintegration rates in the atmosphere, after Lal (1991) 375

Chapter 1

Introduction

This chapter explains the rationale behind the project, and introduces the approach adopted to tackle the main aims of this work. Section 1.4 outlines the structure of this thesis. A fuller picture of the previous work in each of the fields discussed here is given in Chapter 2.

1.1 Rationale

The last twenty years has seen major advances in our understanding of how normal faults accommodate strain in regions of active extension. A combination of detailed displacement/length studies, numerical modelling and palaeoseismology studies have shown fault populations to be extremely dynamic. Growth of one fault has profound effects on the growth of its neighbours, and spatial patterns of tectonic activity change constantly through time. However, the precise rates of fault growth are harder to pin down. The historical earthquake record extends back only about a hundred years, while palaeoseismology constrains events to the timescale of 10^4 to 10^7 years. Between these two lies a gulf of knowledge.

A fuller picture of the rates of fault growth, and the patterns of linkage comes not from studying the faults themselves, but from investigating their influence on the surrounding landscape. Detailed analysis of sediment distributions in extensional basins has provided information from the whole evolution of some fault populations. Study of unroofed basins, or well-characterised subsurface data can constrain the relative timing of major events within the evolution of a fault array, and also the broad rates of tectonic processes such as tip propagation and linkage, by which the faults develop. However, while providing excellent data about the large scale, basin studies are limited by the completeness of the sedimentary record, the resolution of biostratigraphy, and sedimentation rates, and typically constrain fault evolution over timescales of 10^5 to 10^7 years.

More detailed information on shorter timescales comes from young regions, where sediment transport systems have not yet been overprinted or buried. Rivers are extremely sensitive to small changes in local topography, and respond to external forcing over weeks to years, depending on the magnitude and the rate of the trigger. A record of stream evolution is preserved not only in the ultimate site of deposition,

but also within the stream course itself. Changes in local gradient are preserved as changes in sinuosity or stream pattern [e.g. braiding]; local aggradation; incision, often forming terraces or knickpoints; or through complete changes in stream course by lateral migration or avulsion. Thus the fluvial record provides a high-resolution record of changes in local topography, and through application of surface dating techniques to the stream bed, banks, terraces or deposits, can tightly constrain the rates of tectonic processes which have elicited the stream response.

However, the isolation of the tectonic trigger from the fluvial record is not always straightforward. Streams are controlled by a number of different external factors [tectonics, climate, lithology..] and their ability to respond to an external change is a delicate balance between the magnitude and rate of the trigger, and their own power. Thus a single tectonic event may cause a variety of contrasting responses, depending on the discharge and power of the affected stream. There also remains a desperate need for more quantitative information about the rates and scales of the landscape's response to tectonic forcing.

This project investigates the evolution of a series of interconnecting stream networks which drain a young extensional fault array on the Volcanic Tableland in Owens Valley, California. By investigating the morphology of streams and faults together, it is possible both to put together a detailed picture of the patterns of fault growth, and also to gain insights into the mechanisms by which streams respond to tectonic forcing. This is extremely valuable in improving our understanding of the sensitivity of streams to external controls, and also, therefore, the sensitivity of the depositional systems they produce. The study focuses on an area with a well-constrained climatic history, and a single lithology, making it simpler to extract tectonic information from the fluvial record. *In situ* cosmogenic isotope analysis is also applied to some of the surveyed streams in a fault overstep, to gain quantitative information about the rates of processes of fault growth, and stream response. In particular, the project investigates how major reorganisations of the stream patterns are related to specific stages in the evolution of the fault population.

1.2 What is the advantage of this particular approach?

The impact of fault evolution on streams has been the subject of a lot of attention. However, most of this work has been focused from two specific approaches. The 'tectonic' approach has considered the basin-scale evolution of faults, and used the avulsion and incision of streams to indicate vertical fault motions, or tip propagation [e.g. Leeder and Gawthorpe (1987); Leeder and Jackson (1993); Jackson and Leeder (1994); Stewart (1995); Jackson et al. (1996); Burbank et al. (1996b); Morewood and Roberts (1999); Goldsworthy and Jackson (2000); Morewood and Roberts (2002); Jackson et al. (2002)]. This approach has been invaluable in shedding light on the interaction of large faults, and the scale over which faults control landscape development. Nonetheless, studies have generally been qualitative, and rarely consider the streams themselves, or the specific mechanisms by which they accommodate the changes in the fault pattern.

More 'process-based' studies have come from the fluvial geomorphology community, and provided an excellent understanding of the processes by which streams respond to

external forcing [e.g. Burnett and Schumm (1983); Ouchi (1985); Merritts and Vincent (1989); Seidl and Dietrich (1992); Tinkler and Wohl (1998); Whipple et al. (2000a)]. These studies give insights into the ability of streams to respond to changes in the surrounding landscape, as well as the rates of response. However, these approaches have typically focused on broad areas of uplift or subsidence, rather than specific aspects of the developing fault pattern. Peakall (1998) and Peakall et al. (2000) carried out a detailed study of the Carson River, linking avulsions to periods of fault activity and quiescence. He was able to isolate the magnitude and rate of the tectonic forcing [through tilt], but did not link the activity to specific changes in the pattern of the controlling fault.

This study aims to combine a little of both approaches, by surveying both faults and streams in a young extensional array on the fringe of the Basin and Range, in eastern California. The combined approach makes it possible to link major reorganisations in the stream patterns, or subtle changes within a single stream, to changes in the local distribution of deformation. Surveys have been carried out using differential GPS, and hence the systems can be analysed at very high resolution. Since the fault array has already been extensively studied (Dawers and Anders, 1995), this example provides a good tectonic framework in which to investigate the sensitivity of streams to relatively well-understood fault interaction, and the gradual localisation of strain. However, it also demonstrates how much additional information can be gleaned from the stream morphologies than from analysis of the faults themselves. Dating of the streams gives absolute temporal constraints to the study, allowing the quantitative assessment of the rates of stream response to tectonic growth, as well as some clues to the relative impacts of the different external factors that have influenced these streams.

An additional aspect of the project is the use of numerical modelling to test some of the observations of the field studies. Surface process models provide valuable insights into the interaction between the different aspects of the landscape, and patterns of long-term fluvial evolution. However, they have to date used relatively simplistic faults, and hence lose much of the complexity of natural systems. This project discusses the results of some preliminary landscape evolution modelling, incorporating for the first time a fully dynamic fault evolution model, that explicitly includes stress feedback between neighbouring structures. The modelling thus makes it possible to look more closely at how changes in an external control impact on the development of the whole landscape.

1.3 Specific aims

The specific aim of the project is:

> To gain a quantitative understanding of the processes by which fluvial systems respond to extensional fault growth, and how in turn the streams can be used to gain more information about fault interaction.

And hence I have tried to answer the following questions:

1. How do fluvial systems respond to changes in the distribution of displacement? This is aimed specifically at fault interaction and linkage, and hence changes in the uplift rate, propagation rate and in the location of activity within a fault population.

2. How fast do these changes occur?
3. How does the magnitude of the tectonic trigger affect the fluvial response?
4. Can the response to a tectonic trigger be reliably isolated from the other factors which affect stream development?

1.4 Structure of this thesis

Chapter 2 provides a detailed introduction to the theory behind this project, and explains how this work fits into the context of previous studies. It falls into three areas. The first introduces fault growth, explaining how the interaction between faults governs the evolution of the population as a whole. The second considers the landscape response to extensional faulting, looking first at the basin scale [section 2.2]. Section 2.3 takes a more process-based view, considering the mechanisms by which streams adjust to external forcing, in both bedrock and alluvial systems. Section 2.4 discusses the ways that the landscape is abstracted in numerical surface process models, and acts as an introduction to CASCADE, the model used in this project to investigate fault/stream interaction. The third part of the chapter [section 2.5] describes the basic application of *in situ* cosmogenic isotope analysis to tectonic and geomorphic problems. A fuller explanation of the theory, and in particular the production rate scaling debate and shielding calculations, is in ***Appendix A***.

Chapter 3 introduces the field area on the Volcanic Tableland, eastern California. The chapter describes the setting of the Owens Valley [section 3.1], and outlines its recent climatic history [section 3.1.1]. Section 3.2 introduces the Volcanic Tableland and describes the previous work on the faults and surface streams studied in this thesis. Section 3.3 briefly outlines the data collected during two fieldseasons, and defines the cross-sectional aspect ratio, AR, used extensively through the fieldwork chapters which follow. A fuller description of the field and labwork methodology is in ***Appendix B***.

The results of GPS surveys of streams and faults in a normal fault array on the Tableland are presented in ***Chapters 4*** and ***5***. ***Chapter 4*** looks closely at a region between two overlapping faults in the centre of the array. The first part [section 4.1] presents surveys of the two main faults and the smaller fault which hard-links them, to investigate the spatial variation in displacement distribution in the overlap. Section 4.2 describes the streams which flow through the overlap, considering how features of the streams relate to the varying distribution of displacement described in section 4.1. GPS data is used to investigate features of the stream course, profiles and variation in cross-sectional morphology.

Chapter 5 contrasts the central overlap streams with two other major drainage systems from the fault array. The first stream [section 5.1] is a transverse system flowing through the northern tip of the array. Section 5.2 considers the evolution of an axial stream which connects the hangingwall basins of the southern faults. Relationships between this stream and other nearby channels provide insight into the patterns of fault interaction that occurred during linkage of faults in the array.

Chapter 6 presents the results of the *in situ* cosmogenic isotope analysis of samples from the streams on the Tableland. The sampling approach is discussed in section

6.1, along with photographs of the sampled sites. Sections 6.2 and 6.3 explain the calculation of the exposure ages in section 6.4. Initial interpretations of these data are made in section 6.5, although a fuller discussion is in ***Chapter 7***. The effect of using other scaling factors to calculate exposure ages is explored in section 6.6.

The combined evidence from the fieldwork and the cosmogenic studies is discussed in ***Chapter 7***. The first section considers the major characteristics of the Tableland streams [section 7.1.1] and faults [section 7.1.2], and discusses the sensitivity of the streams to fault movements. The relative merits of the SL index, a proxy for stream power, and the cross-sectional aspect ratio, 'AR', for evaluating the stream response to faulting, are debated in section 7.1.3. The second part of the chapter [section 7.2] focuses on the central overlap of the array, in terms of the linkage of the main faults, and the development of the streams which drain it. The implications of the cosmogenic isotope data are explored in section 7.2.2, and used to estimate rates of stream and fault processes, and maximum erosion rates. A model is proposed for the evolution of the overlap region [Fig. 7.6].

Section 7.3 assesses the factors that controlled the connectivity of the southern fault basins and hence the evolution of the axial stream. The implications of the other surveyed streams are also incorporated into a model which demonstrates the close connection between stream reorganisation and fault linkage [Fig. 7.8]. Section 7.4 considers the evolution of the Tableland streams in the wider context of the Owens Valley drainage systems, and particularly with reference to the main Owens River which has incised deeply into the Tableland surface. The final part of the chapter [section 7.5] compares the stream geometry of the central fault overlap on the Tableland with a model often assumed to describe drainage patterns in most synthetic fault overlaps. This comparison leads to a discussion of the interacting factors which control stream evolution between overlapping fault tips.

Chapter 8 outlines the results of some preliminary numerical investigations of the fieldwork conclusions. It describes the first incorporation of a dynamic fault evolution model into the surface process model CASCADE, and investigates the impact of stress feedback between faults on the development of the surrounding landscape.

The main points of each part of this thesis are summarised at the end of each chapter. Hence ***Chapter 9*** provides a short overview of the conclusions of the work, and its implications for other studies. Some potential avenues for future work are also outlined.

Two appendices present more detailed explanation of the theory behind cosmogenic isotope analysis [***Appendix A***] and the methods used, both to collect the GPS surveys in the field, and to prepare targets for cosmogenic isotope measurements [***Appendix B***].

Chapter 2

Theory and Context

This thesis presents a detailed investigation of stream evolution around a developing normal fault array in eastern California. Some of the field results are tested using a numerical model, in Chapter 8. The work combines aspects of both tectonic and geomorphic ideas, and uses a relatively young dating technique: *in situ* cosmogenic isotopes. Hence this chapter explains the basic principles drawn on in the thesis and demonstrates how the project links some studies carried out from very different angles.

The chapter falls into three main parts. The first [section 2.1] explains our understanding of the evolution of a normal fault population, demonstrating how that evolution is dominated by the interactions between neighbouring faults.

The second section looks at the development of transport and depositional systems around an evolving normal fault population. This is a complex problem, and has been tackled from a number of different directions. One approach [section 2.2] focuses mainly on the basin scale, and the impact of the growing tectonic systems. The second approach [section 2.3] is more process-based, founded on observations over relatively short time scales [hours to tens of years]. The third approach considered here [section 2.4] integrates process-based data with large-scale controls, through the development of numerical landscape evolution models [LEMs]. Landscapes are the product of a complex interplay between different controls. The ways that other external factors modulate a stream's response to faulting, and the impact of the *rate* of change, are considered in section 2.3.4.

The third part of this chapter [section 2.5] introduces *in situ* cosmogenic isotope analysis, which has been used in this project to date channels on the Volcanic Tableland. An outline of the theory is given in section 2.5, although a fuller explanation is contained in Appendix A. Some examples of applications of this technique to geomorphic and tectonic problems most relevant to this thesis are given in section 2.5.3.

2.1 Normal faults: growth and interaction

As a region undergoes active extension, planar normal faults, generally dipping between 30 and 70°, develop sub-perpendicular to the direction of extension [e.g. Jackson and McKenzie (1983); Jackson and White (1989)]. Uplift of the footwall and subsidence of

the hangingwall provide both a source of sediment, and a depocentre for deposition. Displacement is maximum near the centre of an isolated fault, and decreases to zero at the tips [e.g. Watterson (1986); Jackson and White (1989); Cowie and Scholz (1992b); Fig. 2.1a]. This is mirrored in both the footwall uplift and the hangingwall subsidence patterns. Displacement decreases with increasing distance from the fault scarp, forming a scoop-shaped hangingwall basin dipping towards the centre of the fault, and a footwall which dips away from the central high [Fig. 2.1b., c]. In large faults, this may be explained by isostatic forces [e.g. Vening-Meinesz (1950); Jackson and McKenzie (1983); Weissel and Karner (1989); Anders et al. (1993)], but is harder to understand in the case of small faults [e.g. Schlische et al. (1996)]. Faults grow vertically by the accumulation of displacement, and also laterally by the propagation of their tips [e.g. Jackson and McKenzie (1983); Watterson (1986); Cowie and Scholz (1992a)], so that idealised non-interacting faults maintain a self-similar shape as they evolve (Cowie and Scholz, 1992a).

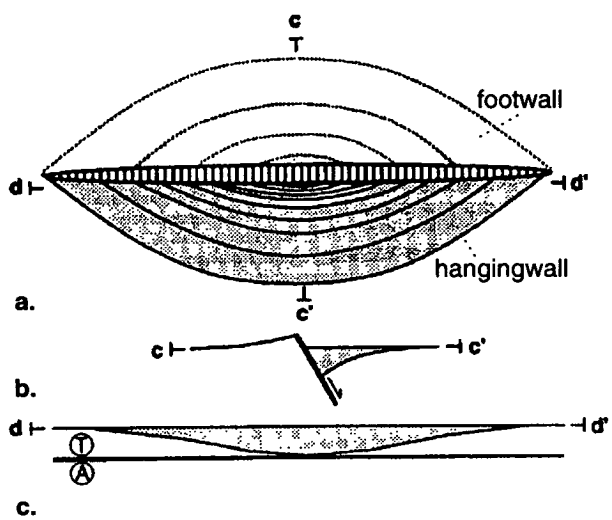

Figure 2.1: *Typical features of a normal fault, modified from Schlische (1991).*
a. Map view of fault: contours show the scoop-shaped hangingwall basin and the footwall dipping away from a central high.
b. Section through the displacement maximum of a normal fault: displacement decreases away from the scarp in both the footwall and the hangingwall.
c. View of hangingwall basin parallel to fault. Displacement maximum [D_{max}] is near the centre of an isolated fault, and decreases to zero at the fault tips. T is motion towards the reader, A is away.

Motion on faults occurs predominantly in small increments in discrete events, i.e. earthquakes, which may be clustered in time [e.g. Machette et al. (1991); Dorsey et al. (1997)]. A contribution to the displacement is also made between these events by aseismic processes such as creep. The exact ratio of uplift to subsidence is debated, partly due to the complications of footwall erosion and hangingwall deposition. Currently-used ratios range from 1:10 (Jackson and McKenzie, 1983; Jackson and White, 1989; Goldsworthy and Jackson, 2000) to around 1:1 (Anders et al., 1993; Schlische and Anders, 1996; Contreras et al., 2000). Many workers use values closer to the observation of

a 1:5 ratio in coseismic slip in the 1983 Borah Peak earthquake (Stein and Barrientos, 1985), although this underestimates the longer-term contribution of aseismic slip.

Normal faults grow on all scales, and are typically segmented along strike [e.g. Jackson and White (1989); Machette et al. (1991); DePolo et al. (1991); Crone and Haller (1991)], forming *en echelon* arrays of overstepping structures. Although arrays can reach over 100km in length [e.g. Machette et al. (1991); DePolo et al. (1991); Morley (1999); McLeod et al. (2000)], segments are rarely over 30km long, except in regions of particularly thick crust [e.g. Hayward and Ebinger (1996); Jackson and Blenkinsop (1997)], implying some degree of control by the mechanical layering of the crust [e.g. Jackson and White (1989); Scholz et al. (1993); Moore and Schultz (1999); McLeod et al. (2000); Wilkins and Gross (2002)]. Some normal faults also demonstrate a characteristic spacing [e.g. 30km lateral spacing for seismogenic faults (Jackson and White, 1989; DePolo et al., 1991; Anders et al., 1993; Cowie, 1998)].

Faults cannot really be considered in isolation, as their evolution is governed by interactions with neighbouring structures [section 2.1.2]. These interactions control the patterns and rates of displacement and tip propagation on individual segments, and are also responsible for many of the larger scale features of normal fault populations.

2.1.1 Fault scaling

Natural cumulative displacement and length data have a wide scatter on a log-log plot of maximum displacement, D_{max}, against total fault length, L [e.g. Fig. 2.2]. This is partly an inherent result of measuring difficulties [e.g. Muraoka and Kamata (1983); Cowie and Scholz (1992a)], as well as reflecting the various states of linkage within a population [e.g. Cartwright et al. (1995)], but has resulted in considerable debate about the exact relationship between D_{max} and L for growing faults, which is a fundamental function of the growth mechanism.

Many early studies of fault populations implied that the D_{max}-L relationship was non-linear, with an exponent, n, of 1.5 (Marrett and Allmendinger, 1991; Walsh and Watterson, 1991; Gillespie et al., 1992) or 2 (Watterson, 1986; Walsh and Watterson, 1988, 1989) in the equation

$$D_{max} = cL^n \tag{2.1}$$

where c is a constant incorporating rock properties [e.g. shear modulus].

While the scaling appeared to fit the data available at the time, a simple elastic growth mechanism is unrealistic, as it produces an infinite stress at the fault tip and the increment of slip rapidly becomes larger through time.

Scholz and Cowie (1990) argued that the scaling should be linear [n=1.0]. Cowie and Scholz (1992a) devised a fault growth model which incorporated *in*elastic growth in a 'frictional breakdown zone' at the tips. In this case, the peak stress at the tip is exactly equal to the shear strength of the rock, and hence dependent on the fractured lithology. Thus, Cowie and Scholz (1992c) questioned whether datasets from different lithologies and different tectonic régimes could be combined, pointing out that single lithology studies implied a more linear relationship.

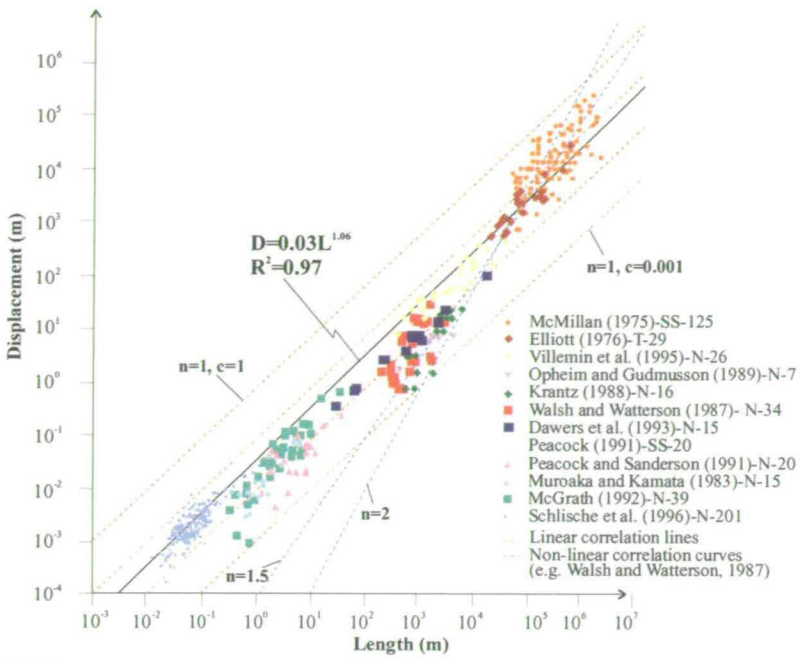

Figure 2.2: *Log-log plot of maximum displacement, D_{max}, against total fault length, L, for global dataset [after Schlische et al. (1996)].*
N - normal faults; T - thrust faults; SS - strike-slip faults
Family of linear curves [n=1, solid] best fit the data; best fit curve [$D_{max} = 0.03L^{1.06}$] darkest. Non-linear curves, n=1.5 (Marrett and Allmendinger, 1991; Walsh and Watterson, 1991; Gillespie et al., 1992) and n=2 (Watterson, 1986; Walsh and Watterson, 1988) shown for reference [dotted].

With the addition of data from large populations in single lithologies [e.g. Dawers et al. (1993); Cartwright et al. (1995); Schlische et al. (1996)], the global dataset now extends over eight orders of magnitude. Schlische et al. (1996) demonstrated that a robust scaling relationship can be determined for all measured faults, despite the combination of data from different lithologies [Eqn. 2.2 and Fig. 2.2]:

$$D_{max} = 0.03L^{1.06} \tag{2.2}$$

Modelling of syn-faulting stratigraphic geometries using a series of different fault growth patterns also produced the best correlation with natural basinfills using a linear fault growth model (Schlische, 1991; his model II).

2.1.2 Interaction and linkage

As a fault slips, it alters the stress field in the surrounding rock. For a normal fault, stress is enhanced in a small region around the tips, while stress is relaxed in the region adjacent to the main body of the fault [Fig. 2.3: King et al. (1994); Burgmann et al. (1994); Willemse et al. (1996); Cowie (1998); Cowie and Shipton (1998); Gupta and Scholz (2000)]. Thus movement on one fault influences the development of nearby faults, if they are close enough for their stress fields to overlap: there is no need

for physical linkage for interaction [e.g. Larsen (1988); Peacock and Sanderson (1991, 1994); Willemse et al. (1996); Cowie (1998)]. The region over which the stress field is felt depends on the magnitude of the slip, and hence on the length and total displacement on the fault [e.g. Burgmann et al. (1994); Willemse et al. (1996); Nicol et al. (1996); Schultz and Fossen (2002)]. Thus as faults propagate lengthways, and accumulate more displacement, they affect a larger area, and interact with more distal faults.

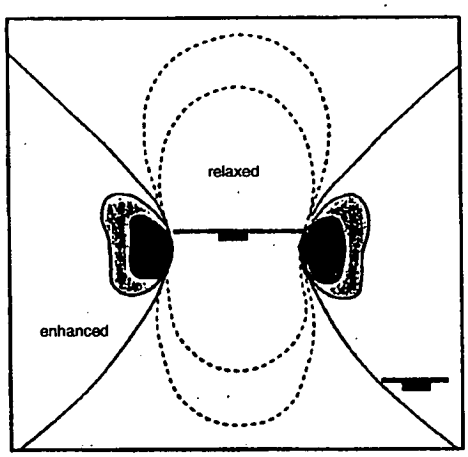

Figure 2.3: *Changes in stress in the region around a normal fault, due to a single slip event [after King et al. (1994); Cowie (1998)].*
Increased probability of failure on planes parallel or co-planar to the main fault: co-planar or closely-spaced en echelon *faults are favoured.*
Reduced probability of failure in the 'shadow zone' transverse to the fault: faults are unlikely to nucleate here, or may be abandoned if already formed, following repeated motion on the central fault.

En echelon faults that are arranged in an underlapping geometry tend to propagate towards each other, and hence are rarely seen. As they propagate past each other, or if they are widely spaced, the tips enter the region of relaxed stress ['-' in Fig. 2.3] and hence propagation is inhibited by slip on the faults [e.g. Aydin and Schultz (1990); Burgmann et al. (1994); Willemse et al. (1996); Cowie (1998); Cowie and Shipton (1998); Gupta and Scholz (2000)]. Similarly, faults are unlikely to nucleate near the centre of an active fault, where the stress is relaxed after each slip event. Faults that have already formed in this region grow very slowly, and may be entirely switched off by growth of the central fault.

2.1.2.1 Enhanced growth

Walsh and Watterson (1989) observed that overlapping *en echelon* faults often have anomalous D-L profiles: the maximum displacement on each fault being skewed towards the other fault [Fig. 2.4]. Peacock and Sanderson (1991) inferred that this was the result of interaction and displacement transfer. Essentially, as a fault tip enters the 'stress shadow' of a nearby fault [Fig. 2.3], it requires a higher stress concentration to continue to propagate. This can be achieved by increasing the displacement gradient at the tip,

as observed. 'Skewed' displacement profiles have since been used to infer interaction between overlapping 'soft-linked' faults by many authors [e.g. Scholz et al. (1993); Anders and Schlische (1994); Trudgill and Cartwright (1994); Dawers and Anders (1995); Huggins et al. (1995); Childs et al. (1995); Schlische (1995); Willemse et al. (1996); Peacock and Sanderson (1996); Schlische and Anders (1996); Nicol et al. (1996); Cartwright and Mansfield (1998); Moore and Schultz (1999); Gupta and Scholz (2000)].

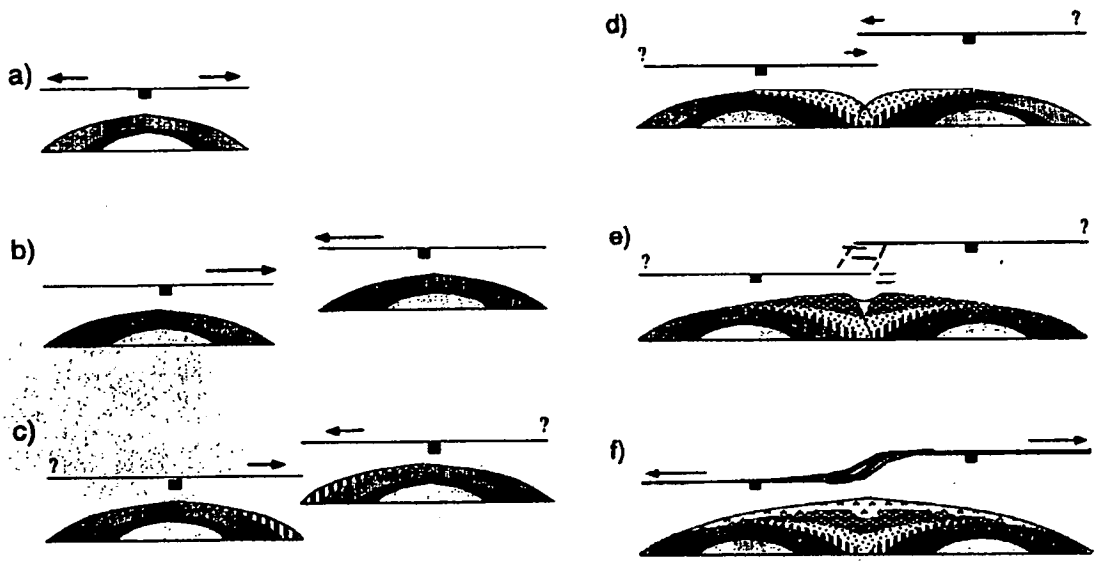

Figure 2.4: *Conceptual model showing the interaction of sub-parallel faults, from Gupta and Scholz (2000).*
a. Pre-interaction [map view]. Arrows show direction of propagation; D-L profile is symmetrical. Shading represents different periods of displacement accumulation.
b. Weak interaction: while underlapping, an increase in shear stress near tips may drive faults to accelerate towards each other, until a stress drop region is reached. Underlapping faults are rarely observed.
c. Moderate interaction: after entering the stress shadow, propagation decelerates and displacement begins to accumulate near interacting tips, and steep profiles develop on interacting ends.
d. Strong interaction: any propagation is slow, displacement profiles near interacting tips steepen. Individual profiles are now very different from the characteristic profile and the composite profile is closer to the characteristic profile.
e. Linkage: once critical stress drop is reached, propagation stops, minor linkage structures form, displacement accumulates in the linkage region, and the summed profile approaches that of a single fault.
f. Coalescence: linkage is complete, the displacement profile is now appropriate for a single long fault. Propagation of distal ends resumes, leaving segment boundary behind. Portions of the overlap zone may now become part of the fault gouge.

Transferred displacement is accommodated by warping and fracturing the rock between the two fault tips into a 'relay' zone (Larsen, 1988; Morley et al., 1990; Peacock and Sanderson, 1991; Childs et al., 1995), resulting in an apparent displacement low between the two fault tips [Fig. 2.4d]. Trudgill and Cartwright (1994) showed that displacement in the relay can be accommodated by a series of different structures, depending on the rate and magnitude of the strain, as well as on the presence of heterogeneities such as

joints. If the strain in the relay, accommodated both by ductile and brittle failure, is summed, there is no displacement deficit across the overlap [e.g. Larsen (1988); Walsh and Watterson (1989); Peacock and Sanderson (1991, 1994); Trudgill and Cartwright (1994); Dawers and Anders (1995); Childs et al. (1995); Huggins et al. (1995)].

As interaction increases, displacement increases on the overlapping fault tips, and so in turn does the stress in the intervening rock. Once this stress exceeds the critical yield strength of the rock, the relay may breach, and the two faults become 'hard-linked' by the formation of a through-going fault [e.g. Larsen (1988); Peacock and Sanderson (1991, 1994); Trudgill and Cartwright (1994); Dawers and Anders (1995); Huggins et al. (1995): Fig. 2.4f]. If the through-going fault links across the back of the overlap, forming a 'footwall-breached relay' [sensu. Larsen (1988); Trudgill and Cartwright (1994)], then the relay structures are left in the hangingwall of the final fault. The opposite occurs in the formation of a hangingwall-breached relay: Fig. 2.5.

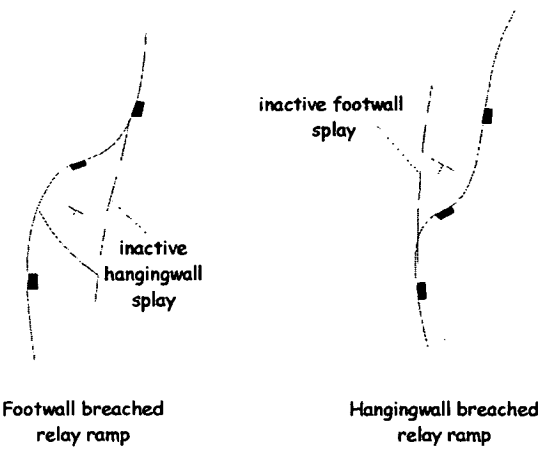

Figure 2.5: *Breaching of a relay ramp by a through-going fault, after Trudgill and Cartwright (1994).*
a. Footwall-breached ramp: the abandoned relay is left in the hangingwall of the final fault. The original tip of the right-hand fault forms an abandoned hangingwall splay.
b. Hangingwall-breached ramp: the abandoned relay is left in the footwall of the final fault. The original tip of the left-hand fault forms an abandoned footwall splay.
***NB:** Either geometry can form with either left- or right-stepping* en echelon *faults: no specific preference of structure is implied by the sketches.*

After linkage, the through-going fault behaves as a single isolated fault (Dawers and Anders, 1995), unless it also is interacting with other nearby structures, e.g. McLeod et al. (2000), and gradually develops the D-L profile of an isolated fault, with a roughly central D_{max}, scaled to the new length of the fault [e.g. Walsh and Watterson (1989); Peacock and Sanderson (1991, 1994); Huggins et al. (1995); Childs et al. (1995); Cartwright et al. (1995); Willemse et al. (1996); Gupta and Scholz (2000); Dawers and Underhill (2000); Fig. 3.6].

Segment linkage is now generally accepted as the primary mechanism of fault growth. However, a debate continues about the relative rate and timing of the linkage and accumulation of displacement as segments interact. Two endmember scenarios exist [e.g. Cowie (1998); Cowie et al. (2000)]:

Case 1: Early linkage

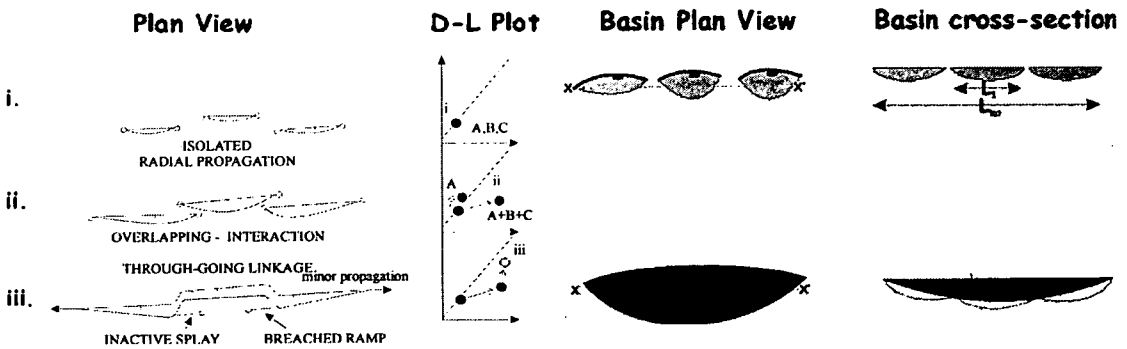

Figure 2.6: *Early linkage of fault segments: implication for D-L scaling and basin development, modified from Cartwright et al. (1995); Cowie et al. (2000).*
i. Isolated segments with ~symmetrical D-L profiles have expected D_{max} ratio.
ii. Linkage of segments occurs before significant interaction has occurred, producing an under-displaced fault: displacement is significantly less than predicted for its length. A single long basin is formed in the hangingwall.
iii. The linked fault gradually accumulates displacement without significant increase in length, approaching the expected D-L value for its summed length. The single hangingwall depocentre subsides, forming a central low.

This scenario was suggested by Cartwright et al. (1995) to explain the observed scatter in displacement-length data. Fault segments link relatively early in their development, resulting in under-displaced faults: the resultant faults have low displacement for their length, and hence plot below the expected D-L value for a fault population [Fig. 2.6b] The linked faults subsequently accumulate displacement until they again reach the expected D-L profile for their length. This late accumulation of displacement occurs without significant change in length, and returns the D-L values to the expected ratios on the log-log plot [Fig. 2.6c]. Scatter in the displacement gradients at fault tips may result from closely-spaced linkage events (Cartwright and Mansfield, 1998). Morewood and Roberts (1999, 2002) used early linkage to explain the apparent increase through time in the D_{max}-L ratio of the South Alkyonides Fault in central Greece. They argued that the fault tips were pinned at depth, and hence that growth was not self-similar. Morley (1999) invoked early linkage to explain long lenses of sediment deposited in some East African Rift basins, although he admitted that he could not resolve the early synrift, which would allow better assessment of the earlier evolution.

Case 2: Late linkage

The other end-member scenario is one in which segments interact significantly before they link: the tips propagate towards each other while the segments accrue displacement. Thus the final fault is 'overdisplaced' after linkage, although there are displacement deficits at the linkage zones due to the deformation of the relay zone. This model is consistent with a linked fault array on the Volcanic Tableland (Dawers and Anders, 1995); Fig. 3.6, and also many other observed [e.g. Anders and Schlische (1994); Schlische (1995); Huggins et al. (1995); Childs et al. (1995); Schlische and Anders (1996);

Schlische et al. (1996); Gupta and Scholz (2000)] and modelled faults [e.g. Willemse et al. (1996)].

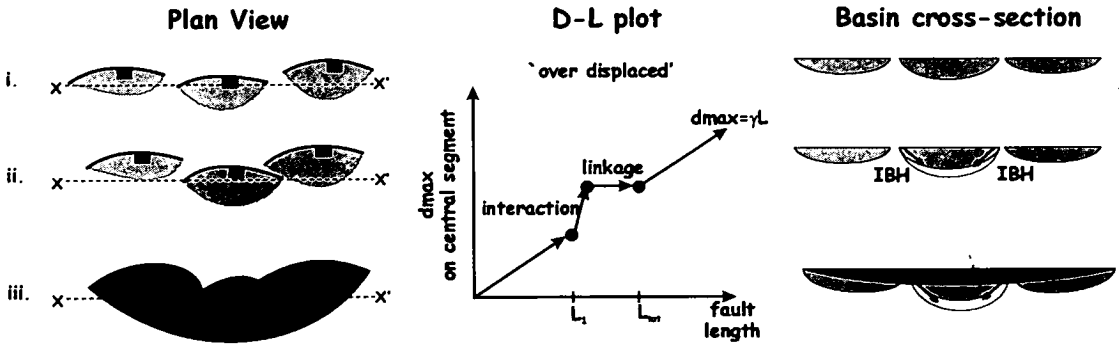

Figure 2.7: *Late linkage of fault segments: implication for D-L scaling and basin development, modified from Cowie et al. (2000).*
i. Isolated segments with ~symmetrical D-L profiles have expected D_{max} ratio.
ii. Interaction between segments causes asymmetrical D-L profiles during soft-linkage. Segments accrue quite considerable displacement before hard linkage, hence individual sub-basins develop, separated by basement highs [IBH]. Individual strata gradually onlap showing that the basin is widening as it fills.
iii. Hard-linked fault may be underdisplaced [e.g. McLeod et al. (2000)] but less so than in early linkage scenario [Case 1]. Gradual adjustment to the full isolated-fault D-L profile removes the footwall low and connects hangingwall basins as the IBHs subside.

Timing of linkage has important consequences for the hangingwall depocentre evolution. While early linkage results in a single long basin throughout most of the fault evolution [Fig. 2.6], late linkage allows the development of individual sub-basins separated along strike by basement highs [intra-basin highs, IBHs: Anders and Schlische (1994); Schlische and Anders (1996); Schlische (1995)]. Sediment is deposited in small depocentres, at the foot of each fault, which do not coalesce until the IBHs subside as the linked fault gradually accumulates more displacement [Anders and Schlische (1994); Schlische and Anders (1996); Cowie et al. (2000); Fig. 2.7]. Deposition in small isolated depocentres which later coalesce has been documented extensively [e.g. Dawers and Underhill (2000); Davies et al. (2000); McLeod et al. (2000)], implying significant interaction before linkage.

Gupta and Scholz (2000) determined a 'characteristic' D-L profile for relatively isolated faults in the Solite quarry fault population, North Carolina. Comparison with interacting fault pairs in the same population revealed anomalous tip displacements [see Fig. 2.4], which they used to assess the degree of interaction. Faults with higher displacement anomalies [i.e. tip gradient considerably higher than the isolated faults] grew further into the stress shadow of overlapping faults, although no faults grew into the regions of highest stress drop (Gupta and Scholz, 2000). As faults grew further into the stress drop regions, their combined D-L profiles approximated more closely the profile of a single long fault. The difference between the isolated faults' D_{max}/L ratio [0.021] and that of the entire fault population [0.030: Schlische et al. (1996)], implies that interaction acts to increase the D_{max}/L ratio of faults. This implies that faults do not become hard-linked until after they have accumulated most of their displacement (Gupta and Scholz, 2000).

As faults link, the structures between overlapping tips both in the footwall and hangingwall of the faults change considerably. Based largely on palaeoseismicity, segment boundaries were initially thought to be barriers to earthquake rupture [e.g. Machette et al. (1991)]. However, it is clear that many large earthquakes rupture more than one segment [e.g. DePolo et al. (1991); Crone and Haller (1991); Jackson and Leeder (1994)] and as the structures accommodating fault motion change, so the boundaries between active parts of a fault move through time. Although motion may initially be focused on individual small segments, their boundaries cannot be long term barriers to earthquake rupture [e.g. Anders and Schlische (1994); Schlische and Anders (1996); Schlische (1995); Dawers and Anders (1995); Willemse et al. (1996); Cowie (1998)].

2.1.2.2 Tip gradients

The Cowie and Scholz post-yield fracture mechanics model predicts 'bell-shaped' tip gradients. However, many workers have observed linear displacement-gradients at fault tips [e.g. Cartwright and Mansfield (1998); Cowie and Shipton (1998); Moore and Schultz (1999); McLeod et al. (2000); Morley and Wonganon (2000)] which initially appear inconsistent with this fault growth model. Cowie and Shipton (1998) explained linear tip gradients in the Chimney Rock fault array in southern Utah by considering slip occurring on only a small part of the fault in each event, rather than on the entire surface. This causes less impact on the stress field around the fault than if the entire fault moved, and also results in 'stress feedback': a *reloading* of the fault as a result of the rupture [main fault plane lies in the enhanced-stress region near the slip patch, Figs. 2.3 and 2.8]. Hence the main fault is brought closer to failure than it would be due to the regional loading alone. The model also invokes healing of the slipped rock between events, so that even this region can support the stress changes associated with a subsequent rupture on the fault. This model predicts that slip on a central part of a fault may not have a significant effect on the displacement pattern near its tip, hence reducing the maximum separation over which overlapping faults can interact significantly.

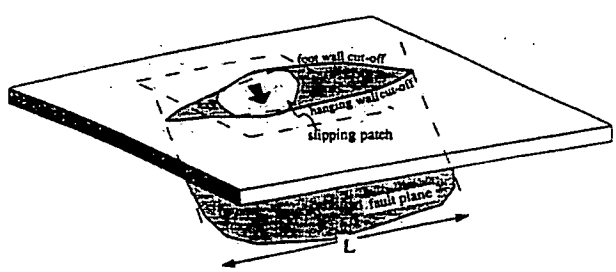

Figure 2.8: *Sketch of 'slip patch': a small rupture on a normal fault plane, from Cowie and Shipton (1998). Adjacent parts of the fault remain healed.*

Cowie and Shipton's model is consistent with the linear tip gradients observed where jointing is pervasive, on a scale far smaller than the fault dimensions, in the Canyonlands grabens (Cartwright and Mansfield, 1998; Moore and Schultz, 1999), and also on the Volcanic Tableland (Dawers et al., 1993; Dawers and Anders, 1995).

Cartwright and Mansfield (1998) described three types of fault tip structure, and along with Moore and Schultz (1999), noted a variety of displacement gradients at the fault tips. A certain amount of the scatter in this data may be explained by lithological variation, and in particular jointing, but it has also been attributed to the interaction between faults, as well as to closely-spaced linkage events (Cartwright and Mansfield, 1998).

2.1.2.3 Inhibited growth

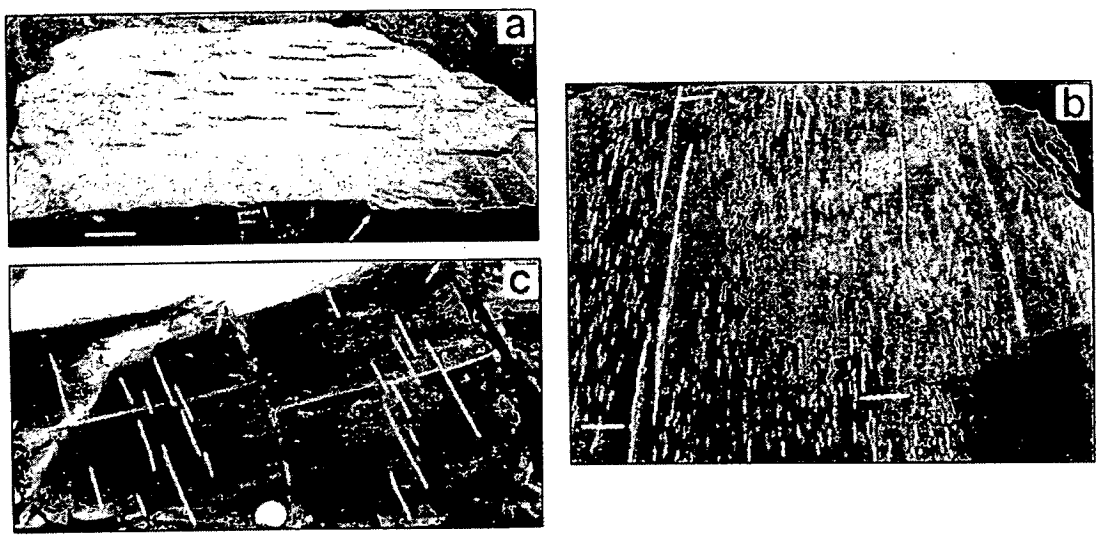

Figure 2.9: *Inhibited growth: 'anticlustering' of small faults around master faults in the Solite quarry, from Ackermann and Schlische (1997).*
a. Footwall of large 'master' fault shown in foreground. Scale bar in lower left corner is 5cm. Note breached relay at lower right.
b. Distribution of faults on bedding plane. Scale bars normal to fault traces are 10cm long.
c. Crack shields in cross-section; faults are highlighted. Arrows point to tips of master faults. Coin is 2.5cm across.

Figure 2.3 shows that other than in a small area near the tips, slip on a fault relaxes the stress in the surrounding rock, and hence reduces the probability of a subsequent rupture on nearby structures. Ackermann and Schlische (1997) described 'crack shields' around large faults in the Solite quarry, North Carolina: areas devoid of faults in an otherwise pervasively-faulted unit [Fig. 2.9]. These unfaulted regions occupy a part of the stress shadow zone of Fig. 2.3 closest to the fault, and demonstrate that the later development of the smaller structures was controlled by slip on the 'master' faults. Concentrations of small faults are seen around the tips of the large faults [Fig. 2.9], highlighting the regions of enhanced stress, and also at fault steps, consistent with growth from the linkage of separate segments.

The region of inhibited growth scales with the slip on the fault, so that the nearest faults nucleated at a distance, $S \simeq 3d$, where d is the local displacement on the fault (Ackermann and Schlische, 1997). Displacement becomes limited for large faults which break through the mechanical layer, and hence this scaling explains the observed characteristic spacing of large faults within a population [e.g. Jackson and McKenzie

(1983); Jackson and White (1989); Jackson and Blenkinsop (1997); McLeod et al. (2000)]. Gupta and Scholz (2000) observed that tip propagation was increasingly inhibited as fault overlap increased, and that no faults grew into a critical region, analagous with the crack shield in [Fig. 2.9].

Sediment distributions in the hangingwall of the large Strathspey-Brent-Statfjord [SBS] Fault in the northern North Sea show that a large number of short faults initially controlled subsidence within the hangingwall basin (McLeod et al., 2000). However, activity on these faults ceased when large segments in the major basin-bounding SBS fault linked. The death of the hangingwall faults, and localisation of strain onto the large through-going structure, was the result of stress relaxation over an increasingly wide area as the main fault accrued more displacement. Subsequent syn-rift sedimentation in the basin was controlled only by this major fault (McLeod et al., 2000).

2.1.3 Evolution of a normal fault population

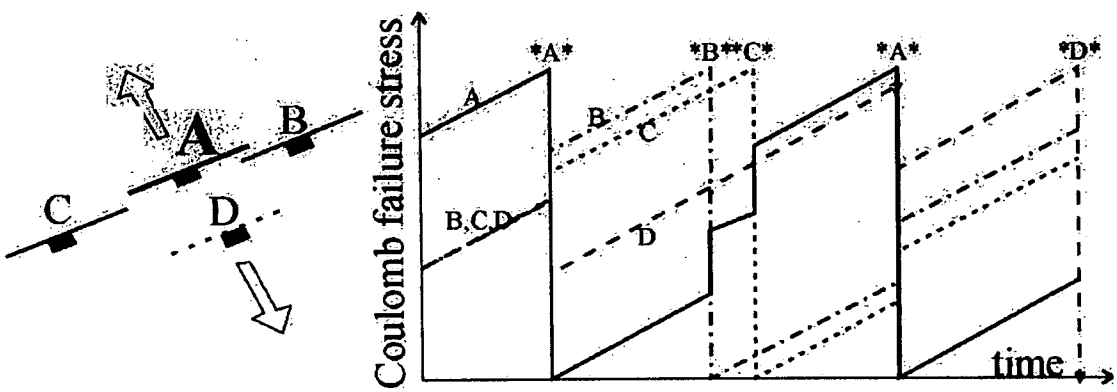

Figure 2.10: *Cartoon of the healing-reloading mechanism, demonstrating the effect of slip on rupture times of nearby elements, modified from Cowie (1998).*
Variation of Coulomb failure stress on an array of four faults, A, B and C, aligned along strike, and D, located to one side. Hollow arrows indicate the regional tectonic loading. The variation in amplitude of the static stress change due to rupture is not considered; only the sign, i.e. increase or decrease.
*A is the first segment to rupture; B and C are optimally oriented with respect to A [positive feedback] and D lies in the stress shadow of A [negative feedback]. Earthquakes on each fault are indicated by *A*, *B*, *C*, and *D*, respectively.*

Cowie (1998) extended the idea of interacting stress fields to investigate the evolution of a whole fault population, using a numerical model (Cowie et al., 1993). Small broken elements were allowed to heal instantaneously, and hence could support the stress changes due to neighbouring ruptures. Extensional loading across the model produced a pattern of fault evolution which incorporated the features discussed above, with preferential growth of overlapping *en echelon* and coplanar structures, and the inhibition of ruptures in the regions parallel to slipping faults [e.g. Fig. 2.10].

Although faults are initially nucleated throughout the lattice, the subsequent pattern of displacement accumulation at any point in the lattice is utterly dependent on its location relative to other rupturing elements. Elements which are repeatedly loaded

by slip on their neighbours become located near the centre of faults. Those nearer the tips are loaded less regularly, and hence have lower displacement rates (Cowie, 1998). The stress feedback mechanism results in the clustering of rupture events through time, as seen in natural systems [e.g. Machette et al. (1991); Dorsey et al. (1997)], and also the gradual localisation of activity onto a few structures which grow to dominate the extending region [e.g. McLeod et al. (2000)]. Despite initially fast growth, some structures are later 'switched off', due to relaxation of the stress field by the slip on larger faults to which they are parallel. Thus the pattern of fault activity changes from initially widely-distributed deformation [Fig. 2.11a], to localisation on a few large faults which grow rapidly, dominating the stress patterns in the surrounding rock [Fig. 2.11d]. Faults may die at any point, governed by the growth of nearby structures (Cowie, 1998).

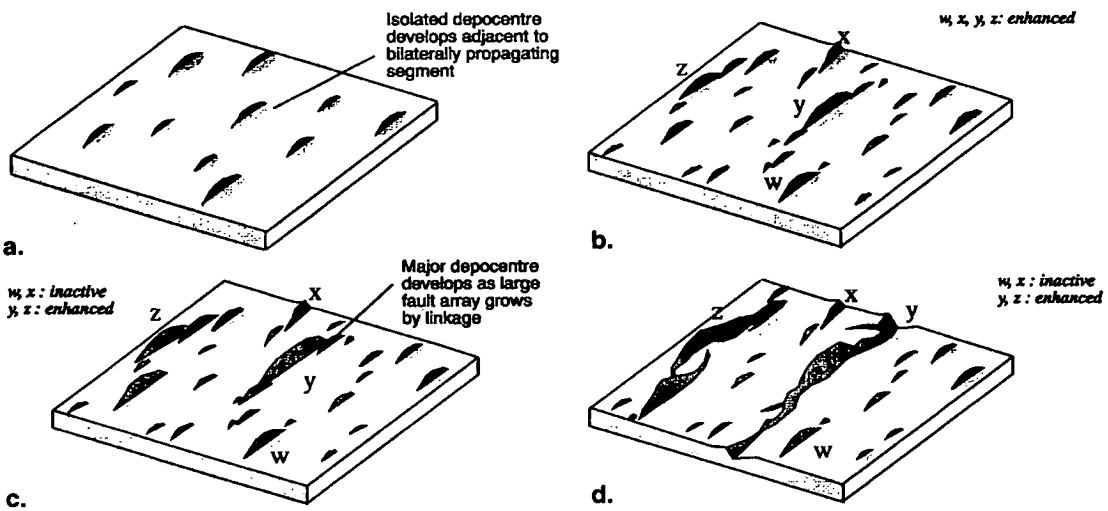

Figure 2.11: *Block diagram of fault population evolution as predicted by the healing-reloading model, modified from Cowie et al. (2000).*
a. Early rift initiation: Initial nucleation of many isolated faults. Isolated basins form in the hangingwalls [e.g. Davies et al. (2000)].
b. Mid rift initiation: Enhanced growth of those faults which are optimally located with respect to neighbouring structures [W,X,Y,Z]. Suppressed growth of faults which are not optimally located. Abrupt enlargement of early depocentres at fault linkage. major depocentres adjacent to longer segments.
c. Late rift initiation: Growth of depocentres by coalescence of smaller basins [Y,Z] as deformation localises. Depocentres adjacent to inactive fault segments [W,X] cease to subside.
d. Transition to rift climax: Localisation of deformation onto a few through-going faults [Y,Z], and activity ceasing on faults in intervening regions [W,X]. Single large depocentre develops adjacent to the major fault, with a more uniform subsidence rate along strike.

Changes in the loci of fault activity have been observed during the evolution of many extensional regions [e.g. Hayward and Ebinger (1996); Jackson (1999); Goldsworthy and Jackson (2000); Dawers and Underhill (2000); McLeod et al. (2000); Morewood and Roberts (2002)], while slower displacement and subsequent death of faults parallel to large structures has also been documented [e.g. Jackson (1999); McLeod et al. (2000)]. Nicol et al. (1997) observed that large faults have developed at consistently high displacement rates, while smaller faults are the result of lower displacement rates, and not necessarily later nucleation. They also concluded that high strain results in a

gradual localisation of deformation, as predicted by Cowie (1998). An increase in the rate of displacement during the later stages of rift evolution, commonly termed the Rift Initiation \ Rift Climax transition, has previously been attributed to an increase in the regional strain rate [e.g. Steckler et al. (1988); Prosser (1993)]. However, according to the stress feedback model, this increase in fault displacement rates is the result purely of the localisation of deformation onto a small number of structures, and hence is an inherent feature of the development of a fault population (Cowie, 1998; Gupta et al., 1998; Fig. 2.11).

This model demonstrates that fault populations are dynamic. An extending region cannot be fully understood purely by analysis of its fault pattern at any one time, as faults constantly nucleate and die, and the loci of activity can change drastically through time, as can the rates of displacement and tip propagation [e.g. Davies et al. (2000)]. Most importantly, interaction between faults is the primary control on the accumulation of displacement at any point (Cowie, 1998; McLeod et al., 2000; Gupta and Scholz, 2000), and explains many of the observed phenomena of extensional regions.

2.1.4 Influence of lithology

A factor that complicates the investigation of fault evolution is the rheology of the material that is being fractured. The faults which grow in the Tableland area studied in this thesis show evidence of growth influenced by strength variations within the tuff sheet. Cowie and Scholz (1992a) discussed the impact of lithological properties on the scaling of faults, as their growth model requires that the peak stress at the fracture tip is exactly equal to the shear stress of the deforming material. They hence questioned the combination of data from different lithologies when attempting to calculate a universal scaling law for fault populations (Cowie and Scholz, 1992c). Many other authors have also discussed the impact of lithological variations on fault growth, and particularly tip propagation [e.g. Burgmann et al. (1994); Peacock and Sanderson (1996); Nicol et al. (1996); Cowie and Shipton (1998); Cartwright and Mansfield (1998); Moore and Schultz (1999); Wilkins and Gross (2002)]. In particular, the impact of joints on fracture growth has been discussed at length. Faults in the Volcanic Tableland, California, the Canyonlands grabens in Utah and in SW Iceland show signs of joint-influenced nucleation [e.g. Gudmundsson (1992); Acocella et al. (2000)], while joints also play an important role in the structures which form at the tips of propagating faults (Gudmundsson, 1987a,b; Dawers et al., 1993; Dawers and Anders, 1995; Trudgill and Cartwright, 1994; Cartwright et al., 1995; Cartwright and Mansfield, 1998; Moore and Schultz, 1999). Refraction of faults at lithological boundaries has been observed by many workers [e.g. Peacock and Sanderson (1991, 1994, 1996); Wilkins and Gross (2002)].

2.2 Sedimentation in extensional basins - tectonic approach

Sedimentation systems are dynamic, changing with the tectonic systems, and can only be understood in the context of the *contemporary* fault pattern [e.g. Davies et al. (2000)]. This section considers how the changing patterns of fault activity and interaction described above [section 2.1] are expected to affect the development of transport systems. In contrast, section 2.3 considers the fluvial systems themselves, focusing on their ability to respond to external controls, and the mechanisms by which the changes are achieved. Section 2.3.4 emphasises that fluvial systems are the product of an interplay between a series of different external and internal controls. Hence the response to tectonic growth may vary considerably from one stream to another.

2.2.1 Effect of normal fault topography

The growth of extensional faults provides a sediment source from topographic highs, and a series of growing hangingwall depocentres. Streams drain extending regions in two main directions: 'transverse' streams drain perpendicular to faults; 'axial' streams flow parallel to the faults (Leeder and Gawthorpe, 1987; Leeder et al., 1991; Leeder and Jackson, 1993; Anders and Schlische, 1994; Schlische, 1995; Fig. 2.12).

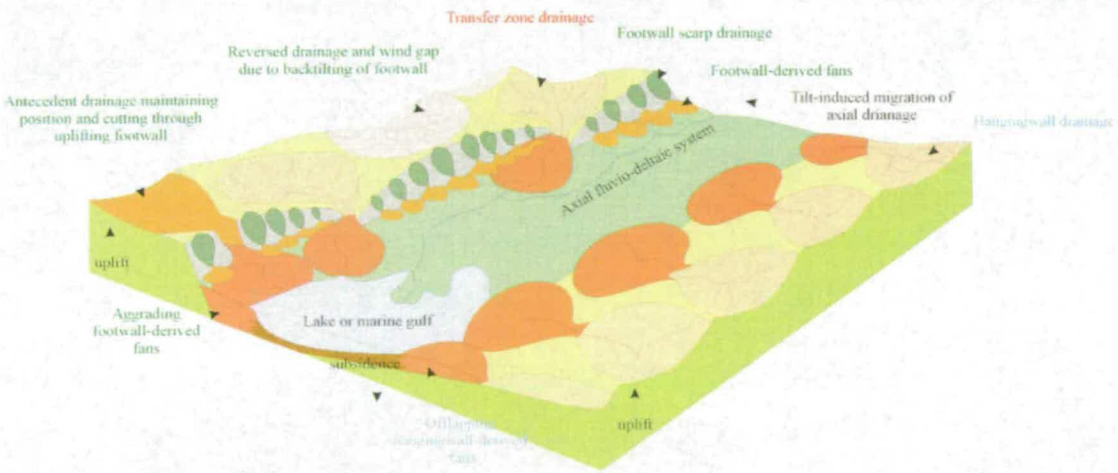

Figure 2.12: *Conceptual model of extensional half-graben sedimentation patterns, modified from Gawthorpe et al. (1994).*
Vertical scale is greatly exaggerated, three overlapping segments are each 12-50km long. A and B are fans sourced by large transfer zone drainage basins; C is a fan delta sourced from an antecedent drainage basin.

Gentle hangingwall dip slopes give rise to long narrow basins [e.g. Leeder et al. (1991); Leeder and Jackson (1993); Gawthorpe et al. (1994); Goldsworthy and Jackson (2000); 'hangingwall drainage' in Fig. 2.12] as the hangingwall rotates towards the fault with increasing subsidence. The steep scarp itself produces short catchments (Jackson et al., 1982; Leeder and Gawthorpe, 1987; Leeder and Jackson, 1993; Gawthorpe et al., 1994; Goldsworthy and Jackson, 2000; 'scarp drainage' in Fig. 2.12) as few streams have the

power to develop large basins as the footwall uplifts. Degradation of the footwall can be marked, particularly in large fault systems, aided by the high slopes and tectonic shaking, producing a relatively high supply of sediment from landsliding events (Keefer, 1984a,b; Pearce and Watson, 1986; Stewart and Hancock, 1988; Densmore et al., 1997, 1998; McLeod and Underhill, 1999; Hovius et al., 1997; Allen and Hovius, 1998; Hovius and Leeder, 1998; Hovius et al., 2000).

However, scarp drainage generally accounts for only small sediment volumes. A significant amount of drainage follows the anticlinal slopes to drain either completely away from the scarp ['backtilted drainage' in Fig. 2.12] or towards the tips of the fault, following the topographic slope produced by the along-strike reduction in displacement [e.g. Leeder and Gawthorpe (1987); Leeder and Jackson (1993); Gawthorpe et al. (1994); Goldsworthy and Jackson (2000)]. Low displacement at the fault tips provides a convenient place for streams to enter the hangingwall, and capture of other footwall streams, driven by tectonic slopes, may result in large drainage basins parallel to the scarp. These systems are particularly important in hard lithologies, where direct incision of the scarp is minimal, and also between the tips of overlapping faults, where sediment may be supplied from the footwalls of *both* faults (Jackson et al., 1982; Leeder and Gawthorpe, 1987; Morley et al., 1990; Gawthorpe and Hurst, 1993; Leeder and Jackson, 1993; Jackson and Leeder, 1994; Anders and Schlische, 1994; Schlische, 1995; Gawthorpe et al., 1994; Goldsworthy and Jackson, 2000; Gawthorpe and Leeder, 2000; 'transfer zone drainage' in Fig. 2.12) [see below].

Streams inherited from pre-fault topography are also modified by fault evolution [section 2.3.4.3], and may continue to cross the scarp ['antecedent' in Fig. 2.12] or become defeated (Jackson et al., 1982; Crossley, 1984; Leeder and Gawthorpe, 1987; Leeder and Jackson, 1993; Gawthorpe et al., 1994; Jackson et al., 1996; Keller et al., 1999; Morewood and Roberts, 1999; Goldsworthy and Jackson, 2000; 'reversed drainage' in Fig. 2.12).

Rivers flowing parallel to fault scarps generally develop during the latter stages of array development, as they require the individual fault hangingwall basins to be connected (Nanson, 1980; Leeder and Gawthorpe, 1987; Leeder and Alexander, 1987; Schlische, 1991; Leeder and Jackson, 1993; Jackson and Leeder, 1994; Anders and Schlische, 1994; Peakall, 1998; Peakall et al., 2000; Fig. 2.12). As discussed [section 2.1.2], this is achieved through sedimentation, as IBHs are covered, or by subsidence of the highs as the controlling faults link [e.g. Anders and Schlische (1994); Leeder and Jackson (1993); Jackson and Leeder (1994); Schlische (1995); Schlische and Anders (1996); Dawers and Underhill (2000); Davies et al. (2000); Cowie et al. (2000); Gawthorpe and Leeder (2000); see below].

2.2.2 Effects of fault growth, interaction and linkage

Transport and sedimentation patterns are extremely sensitive to the spatial variation in fault activity and hence are very dynamic: they constantly change in response to the evolution of the controlling fault system. These changes can be summarised as:

Increased displacement: Footwall slopes increase, favouring drainage down the topographic slope parallel to the scarp, towards displacement lows at the tips. Increased uplift may reverse cross-scarp streams (Jackson et al., 1982; Leeder and Jackson, 1993;

Jackson and Leeder, 1994; Gawthorpe et al., 1994; Jackson et al., 1996; Keller et al., 1999; Goldsworthy and Jackson, 2000). Where scarp streams can keep pace with the uplift, they develop prominent steps, or 'knickpoints', which migrate upstream with headward incision (Jackson et al., 1982; Seidl and Dietrich, 1992; Seidl et al., 1994; Goldsworthy and Jackson, 2000). Similarly, the increasing flexural 'bulge' in the hangingwall may act as a barrier to dip-slope supply, except for powerful streams.

Increased tilting of the basin floor results in lateral migration of axial streams, either gradually [e.g. Nanson (1980); Leeder and Alexander (1987); Peakall et al. (2000)] or in discrete avulsion events [e.g. Reid (1992); Peakall (1998); Peakall et al. (2000)]. If subsidence outpaces sediment supply, a major change in sedimentation may occur, leading to a transition from dominantly fluvial to lacustrine, or shallow marine facies (Leeder and Gawthorpe, 1987; Schlische, 1991; Gawthorpe et al., 1994; Schlische and Anders, 1996; Davies et al., 2000; McLeod et al., 2000). Fluvial sedimentation may recommence after rifting ends; or follow a major increase in supply if transport systems are rejuvenated, or capture new drainage basins (Schlische, 1991; Schlische and Anders, 1996; Contreras and Scholz, 1997; Ravnås and Steel, 1998).

Episodic fault activity: Peakall (1998) and Peakall et al. (2000) described avulsion of the axial Carson River towards the faults immediately after earthquakes, but migration back to a steeper, more efficient route during tectonically quiescent periods. Dorsey et al. (1997) explained alternations between rapid fan progradation and flooding in the Loreto basin, Baja California, as the result of earthquake clustering.

Fault propagation: Footwall streams avulse in an attempt to maintain a course around the tip. Earlier abandoned courses are marked by wind gaps in the scarp [e.g. Jackson et al. (1996); Fig. 2.13], which can be used to gauge rates of fault tip propagation [e.g. Jackson and Leeder (1994); Burbank et al. (1996b); Morewood and Roberts (1999); Keller et al. (1999); Morewood and Roberts (2002); Jackson et al. (2002)]. Drainage area and discharge increase as the streams migrate (Burbank et al., 1996b), leading to the development of large catchments for some transfer zone drainages [e.g. Morley et al. (1990); Leeder and Jackson (1993); Jackson and Leeder (1994); Jackson et al. (1996); Goldsworthy and Jackson (2000); Fig. 2.12]. Less successful streams may be reversed, or captured by other streams, which gradually become more likely to incise the propagating scarp [Fig. 2.13].

Tip monoclines: Schlische (1995) and Gawthorpe et al. (1997) described monoclinal warping of the ground surface above upwardly-propagating blind normal fault tips, prior to surface rupture. An evolution from blind tip to surface rupture thus occurs both at the initiation of surface faulting, and also beyond the visible surface tip of an active fault trace (Schlische, 1995; Gawthorpe et al., 1997; Gupta et al., 1999; Sharp et al., 2000; Corfield and Sharp, 2000). Sediment packages deposited in the developing hangingwall thin towards the monocline, and then are truncated against the fault; synrift sediments show thickening wedges towards a fault exposed at the surface. Stream response to motion on the scarp buried beyond the visible fault tip can be seen by anomalous incision into the hangingwall (Jackson and Leeder, 1994).

Drainage between interacting fault tips: The effect of interaction between overlapping faults is greatest for footwall streams forced between the propagating tips. Streams draining the ramp between overlapping synthetic faults are generally considered to be the major conduits of footwall sediment to the hangingwall basin,

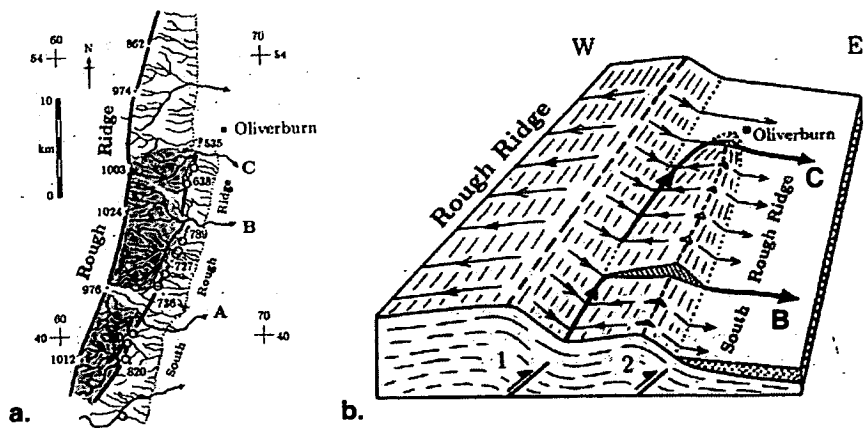

Figure 2.13: *Streams as indicators of fault tip propagation, modified from Jackson et al. (1996). a. Drainage map, and b. schematic cartoon illustrating stream development around South Rough Ridge, Otago, NZ. Ridge is asymmetrical fold developed above a blind thrust fault. Catchments of three major streams are shaded in [a]; open circles denote wind gaps: notches marking old dry stream courses.*
Stream C is diverted virtually around the tip of the fold. The gathering of streams into asymmetric catchments that cross South Rough Ridge suggests that the fault underlying it is later than the one which formed Rough Ridge, and is propagating to the north.
Stream power also affects the response: where capture has resulted in large catchments, streams [A, B] have sufficient power to incise through the fold.

sourced from large footwall catchments, and dumping volumetrically large deposits at the toe of the ramp [e.g. Jackson et al. (1982); Leeder and Gawthorpe (1987); Morley et al. (1990); Gawthorpe and Hurst (1993); Gawthorpe et al. (1994); Leeder and Jackson (1993); Jackson and Leeder (1994); Anders and Schlische (1994); Figs. 2.12 and 2.14]. As interaction between the faults increases, fracturing of the ramp increases the sediment supply, while warping may result in incision into the ramp as the stream power increases. Sediment supply in this 'classic' model is terminated by hard-linkage of the faults, as the ramp is breached by a through-going fault (Leeder and Gawthorpe, 1987; Morley et al., 1990; Gawthorpe and Hurst, 1993; Leeder and Jackson, 1993; Jackson and Leeder, 1994; Anders and Schlische, 1994; Schlische, 1995).

Although it explains some stream patterns well, the 'classic' model is too simplistic to be applied unhesitatingly to all synthetic fault overlaps. Many examples demonstrate stream incision and deflection causing different stream/fault geometries [e.g. Leeder and Jackson (1993); Armstrong (1997); Goldsworthy and Jackson (2000)] and hence different depositional patterns. This thesis considers a further example of a different overlap zone stream geometry [Fig. 4.20] and hence examines the factors that may determine which stream geometry is adopted [section 7.5 and see also section 2.3.4.4].

Early/late fault linkage: As demonstrated in section 2.1.2, the consequences of early [e.g. Cartwright et al. (1995)] or late linkage [e.g. Peacock and Sanderson (1991)] are profound for the basin evolution. Early linkage causes deposition in a long shallow basin the length of the summed fault, which gradually deepens [e.g. Morley (1999); Fig. 2.6]; late linkage implies extended isolation of small basins by IBHs (Davies et al., 2000), which only subside gradually as the faults become hard-linked [e.g. Anders and

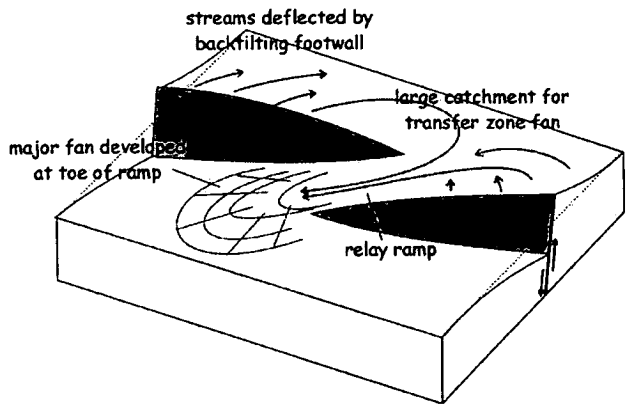

Figure 2.14: *'Classic' model of relay-zone drainage, modified after Jackson and Leeder (1994). Stream drains down natural slope of the relay ramp formed between two overlapping synthetic normal faults. Large fan deposited at the toe of the ramp, sourced from an anomalously large catchment in the footwall, which may extend far back towards D_{max}, and is the result of considerable deflection and probably stream capture as the fault tip propagated laterally. Hard-linkage of the faults breaches the relay, and is assumed to cut off supply to the hangingwall basin as the headwaters are uplifted in the footwall of the through-going fault.*

Schlische (1994); Schlische (1995); Schlische and Anders (1996); Dawers and Underhill (2000); Fig. 2.7]. Where displacement has been accommodated on a series of faults in the overlap, the IBH may persist, isolating hangingwall basins for longer (Schlische and Anders, 1996). The locations of highest subsidence migrate along-strike through time as displacement profiles adjust to interaction and linkage of fault segments. Migration of depocentres and coalescence of originally discrete depocentres has been documented in the North Sea (McLeod, 1996; Dawers and Underhill, 2000; Davies et al., 2000; McLeod et al., 2000; Cowie et al., 2000), and in the Gulf of Suez (Sharp et al., 1998; Gilpin, 1998; Gupta et al., 1999; Sharp et al., 2000), to coincide with patterns in the growth and linkage of bounding fault segments. However, few convincing examples of early linkage exist to date.

Localisation of deformation: As the fault population develops, deformation is localised onto a few faults whose displacement rates increase, often dramatically (Cowie, 1998; Gupta et al., 1999; Cowie et al., 2000). Although uplift and erosion increase, sediment supply lags subsidence (Gordon and Heller, 1993; Blair and MacPherson, 1994), and hence hangingwall basins become starved, often triggering a transition to a deeper-water facies (Schlische, 1991, 1995; Schlische and Anders, 1996; Ravnås and Steel, 1998; Gupta et al., 1999; Davies et al., 2000; Dawers and Underhill, 2000; Cowie et al., 2000; McLeod et al., 2000).

Subsidence of IBHs allows axial systems to connect originally isolated basins (Leeder and Gawthorpe, 1987; Gawthorpe et al., 1994; Jackson and Leeder, 1994; Anders and Schlische, 1994; McLeod et al., 2000). These streams are often important in providing sediment from outwith the half-graben, as well as in redistributing sediment within the rift (Leeder and Gawthorpe, 1987; Schlische, 1991; Leeder and Jackson, 1993; Jackson and Leeder, 1994; Schlische, 1995; Contreras and Scholz, 1997; Ravnås and Steel, 1998; Davies et al., 2000; McLeod et al., 2000). However, connection of basins along-strike is also dependent on the sediment flux from transverse streams. Where supply is low,

IBHs are only slowly onlapped, even after fault linkage, delaying basin connection. High sediment flux may allow basins to be connected by axial streams prior to fault linkage, as the IBH is onlapped, or aggressive streams cut headwards through the barrier (Jackson and Leeder, 1994). Leeder et al. (1996) describe varying patterns of interaction between footwall-sourced fans and axial drainage belts in the Rio Grande Rift, which they use to demonstrate variations in sediment supply from two different source areas.

Abandonment of small faults: As displacement rates increase on a few faults, many smaller nearby faults are abandoned, at varying stages through the population evolution (Cowie, 1998; Gupta et al., 1998; Cowie et al., 2000). These smaller faults may be draped by synrift sediment in the hangingwall of large faults (McLeod et al., 2000; Davies et al., 2000; Dawers and Underhill, 2000), or uplifted and eroded in the footwall of more active structures (Leeder and Jackson, 1993; McLeod, 1996; McLeod et al., 2000). Where the active faults are oriented at high angles to the initial faults, fluvial patterns are overprinted, leading to a significant change in the major geomorphic features of the original tectonic topography [e.g. Bentham et al. (1991); Leeder et al. (1991); Leeder and Jackson (1993); Goldsworthy and Jackson (2000); Morewood and Roberts (2002)].

2.3 Fluvial processes and responses to tectonics - geomorphic approach

Rivers take a wide variety of forms, governed by the material they erode, the climate, and the tectonic régime. Alluvial streams incise their own deposits, which vary with location from boulders to clay. Reach morphology varies drastically depending on the distance from the drainage divide. Bedrock streams have a much lower sediment supply relative to their discharge. Their evolution is very dependent on the strength and heterogeneity of the rock they incise. Colluvial streams are small steep headwater streams, with gradients over 20% (Seidl and Dietrich, 1992; Sklar and Dietrich, 1998), dominated by debris-flow scouring.

Many studies have focused on alluvial systems, and it has long been assumed that bedrock-incising streams develop in the same ways. However, recent work [e.g. Tinkler and Wohl (1998)] has highlighted major differences between bedrock and alluvial systems, demonstrating the need to consider the processes that govern their evolution separately. In order to investigate the mixed bedrock-alluvial streams on the Volcanic Tableland [Chapters 4 and 5], this section describes the different morphology and erosional processes in alluvial and bedrock streams. Section 2.3.2 discusses stream power, which is often used to predict aggradation and incision patterns. It emphasises the problems inherent in using the stream power law, as its scaling, and the variability of its parameters, are poorly understood.

Mackin (1948) described a stream in equilibrium as 'graded': having a discharge just high enough to transport the imposed sediment load. The gradient of a stream decreases with increasing distance from the drainage divide, so that an equilibrium stream has a logarithmic longitudinal ['long'] profile. Any change in the external controls [tectonic uplift/subsidence, base-level change, discharge or sediment flux] upsets this balance and elicits a response by which the stream acts to return to its previous equilibrium. Section 2.3.3 outlines our understanding of the mechanisms of response, emphasising the differences between alluvial and bedrock streams, and hence the ability of the different streams to adjust to external forcing. Section 2.3.4 emphasises that stream evolution is the result of the interplay between the various controlling factors. It also highlights the impact of the *rate* of external forcing.

2.3.1 Morphology and process

2.3.1.1 Alluvial streams

Schumm (1981) described five main types of alluvial stream, by differences in their pattern [simply, straight / braided / meandering] and by their dominant load [suspended / bedload / mixed: see Fig. 2.15]. Stream patterns are not fixed, but change through time, as well as along a river's course, through aggradation or incision. Water discharge determines the dimensions of the channel [width / depth and meander dimensions], but the relative proportions of large grains [bedload] and small grains [suspended load] also have an impact on the shape, width-depth ratio and pattern of the stream (Schumm, 1981; Schumm et al., 2000). Variations in these factors, and also in the total sediment flux and stream power, cause major changes in the stream pattern, and hence

Schumm's classification also indicates the relative stability of each stream type to external forcing [Fig. 2.15]. Changes between each of these main patterns occur abruptly, rather than gradually, implying that critical threshold values of gradient, stream power and sediment load control the different forms [Schumm and Kahn (1972); Fig. 2.23].

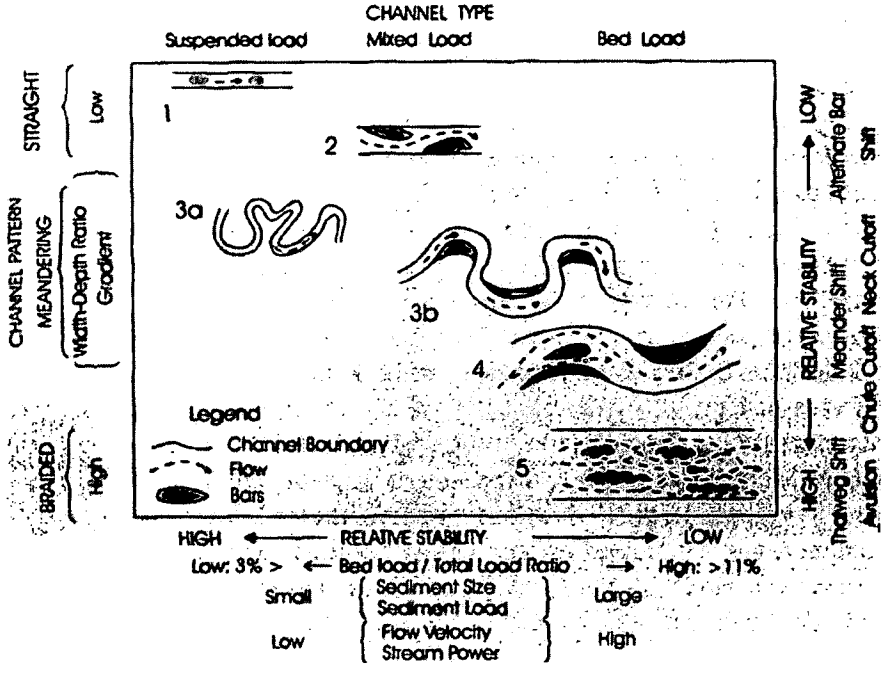

Figure 2.15: *Classification of alluvial channels, based on pattern and type of sediment load, with associated variables and relative stability indicated, from Schumm (1981); Schumm et al. (2000).*

Fine-bed streams occur primarily in lowland areas, and respond relatively quickly to external changes (Howard et al., 1994). Coarse-bed channels are more common in mountainous regions, but have relatively lower transport rates, with gradient roughly proportional to grain-size. Where sediment supply is high ['live-bed'], particles fine rapidly downstream. Lower sediment yields, dominated by periodic floods, produce 'threshold' streams. Transport and fining of grains occurs slowly, and these systems respond very slowly to external forcing (Howard et al., 1994).

Montgomery and Buffington (1997) painted a picture of a dynamic fluvial system, which changes through time in response to the length and magnitude of external forcing. Their alluvial classification was based on reach morphology, with five different types each corresponding to a specific gradient down a typical stream course, and dominated by different combination of processes. They also predicted that steep upper reaches were the most resilient to changes in sediment supply and discharge.

2.3.1.2 Bedrock streams

Bedrock is incised directly where there is insufficient sediment to mantle the channel bed (Howard et al., 1994). This may be the result of steep gradients [around 3-10%]

or low sediment supply, and thus caused by rapid uplift or base-level fall, resistant bedrock or low runoff rates. Bedrock channels may be covered by a thin veneer of alluvium during low flows, but actively incise into the underlying rock during peak flows. Alternating bedrock-alluvial reaches are also common (Miller, 1991; Seidl and Dietrich, 1992; Wohl, 1992, 1993; Howard et al., 1994; Tinkler and Wohl, 1998a; Howard, 1998). These have been attributed to oversteepening of an initially fully-alluvial stream, accommodated by episodic bedrock incision on small steep reaches; episodic variations in sediment supply; or knickpoint migration (Howard et al., 1994; section 2.3.3.1).

For a given discharge, bedrock streams are steeper than alluvial streams [e.g. Howard et al. (1994); Montgomery and Buffington (1997); Tinkler and Wohl (1998a); Wohl and Merritt (2001)]. As a result, velocities and shear stresses in bedrock channels are higher. Critical flow is common along at least short stretches during floods (Tinkler, 1993; Tinkler and Wohl, 1998a,b; Hancock et al., 1998; Wohl and Ikeda, 1998). Bedrock stream evolution is extremely dependent on lithology. Resistant walls and bed lower sediment loads, making for efficient, but supply-limited, transport. They also reduce a stream's potential to adjust its width, sinuosity and braiding (Wohl, 1992; Howard et al., 1994; Tinkler and Wohl, 1998a; Wohl and Merritt, 2001). Rock removed from the walls can only be replaced by alluvium, and hence the morphology of the stream is completely changed, whereas an alluvial channel is 'self-repairing' (Tinkler and Wohl, 1998a).

Reach morphology is controlled by a fine balance between fluvial erosive forces and bedrock resistance, and hence is more variable than in an alluvial channel, though also longer-lived, as it is determined predominantly by infrequent major discharges (Howard et al., 1994; Wohl et al., 1994; Tinkler and Wohl, 1998a; Wohl and Merritt, 2001). Exploitation of lithological heterogenities results in longitudinal grooves along joints, preferential abrasion of small cavities and protrusions, and plucking of blocks along suitably-oriented joint or bedding planes [Fig. 2.17; e.g. Miller (1991); Bishop and Goldrick (1992); Tinkler (1993); Weissel and Seidl (1997, 1998); Hancock et al. (1998); Wohl and Ikeda (1998); Whipple et al. (2000a)]. Thus morphologies vary with bed thickness and orientation, joint density and overall rock strength (Wohl and Merritt, 2001). Inputs of coarse material from tributaries or local debris-flows may also affect morphology [e.g. Bishop et al. (1985); Sklar and Dietrich (1998)].

Erosion in bedrock channels occurs by abrasion, plucking and possibly cavitation, as well as knickpoint migration [section 2.3.3.1]. Abrasion by small clasts forms flutes and potholes and is fastest on the downstream face of obstructions [e.g. Wohl (1992, 1993, 1998); Hancock et al. (1998); Sklar and Dietrich (1998); Wohl (2000); Whipple et al. (2000a); Fig. 2.16]. The removal of intact blocks of rock by plucking, or quarrying is aided by impacts from suspended or bedload clasts, and 'hydraulic wedging' of material into opened joints and bedding planes [e.g. Hancock et al. (1998); Whipple et al. (2000a); Fig. 2.17]. Cavitation has not been convincingly observed in natural rivers, but is common in artificial channels. Locally high velocities cause water vapour-filled bubbles, which implode when carried into regions of lower velocity [higher pressure], forming a high-powered jet of water which drills into nearby rock [e.g. Thompson and Wohl (1998); Hancock et al. (1998); Whipple et al. (2000a)]. Although flow conditions around steps and constrictions make cavitation viable, it is inhibited by the entrainment of air into the flow (Hancock et al., 1998).

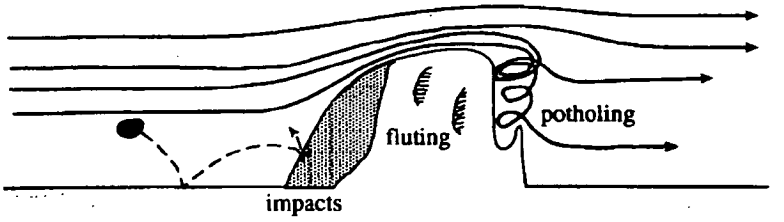

Figure 2.16: *Cartoon of abrasion, from Whipple et al. (2000a).*
Bedload and coarse suspended clasts are decoupled from the flow and impact the upstream faces of obstructions [shaded], causing smooth, polished faces, with little abrasive damage. Fine-scaled flutes occur on the flanks of large obstacles, as tight stream-wise vortices are formed by flow-separation. Large, often coalescing potholes form on the lee side of obstacles, protuberances, and knickpoints. The complete obliteration of massive, very hard rocks in these potholed zones testifies to the awesome power of the intense vortices shed in the lee of obstructions.

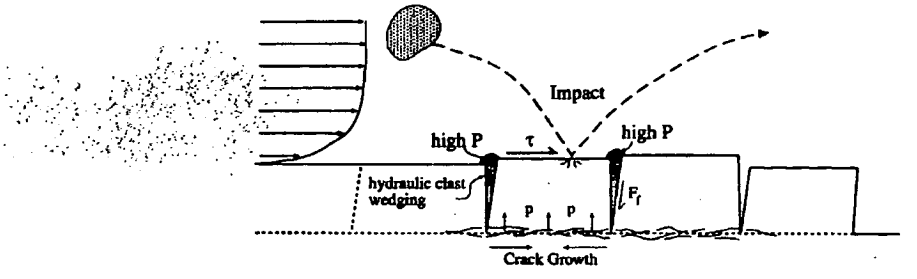

Figure 2.17: *Cartoon of plucking, from Whipple et al. (2000a).*
Impacts by large saltating grains produce some direct abrasion but contribute most importantly to the generation of stresses that drive the crack propagation necessary to loosen joint blocks. Hydraulic clast wedging works to further open cracks. Surface drag forces and differential pressures across the block act to lift loosened blocks. Where the downstream neighbour of a block has previously been removed, both rotation and sliding become possible, and extraction is greatly facilitated.

Plucking dominates where joints or bedding planes are exposed (Hancock et al., 1998; Whipple et al., 2000a; Wohl, 1998). Incision in unjointed rocks is slower as it is dominated by abrasion. The size of quarriable blocks depends on the joint or bedding spacing, and the flow velocity (Hancock et al., 1998; Wohl, 1998; Whipple et al., 2000a). Thus the transition from plucking to abrasion occurs at wider joint spacings in stronger flows. Sklar and Dietrich (1998) showed that abrasion has a maximum rate at an optimal sediment flux [enough tools to erode, but not enough to shield the bed] and an optimal discharge [sufficient impacts of sufficient energy].

Knickpoints are steepened reaches, which can form following relative base-level drops [e.g. Gardner (1983); Seidl and Dietrich (1992); Young and McDougall (1993); Wohl (1993); Wohl et al. (1994); Howard et al. (1994); Seidl et al. (1994); Wohl and Ikeda (1998); section 2.3.3.1]. Knickpoints also form at resistant beds, particularly where they are jointed, or have bedding or joint planes at high angles to the flow [e.g. Young (1985); Bishop et al. (1985); Miller (1991); Bishop and Goldrick (1992); Howard et al. (1994); Weissel and Seidl (1997, 1998); Sklar and Dietrich (1998); Fig. 2.18]. Bishop et al. (1985) and Sklar and Dietrich (1998) describe steepening of bed profiles due to

the entry of coarse clasts. Streams respond to the steepening by focusing flow in a narrowed jet. Erosive features such as potholes may be concentrated at the lip of the step, and contribute to the incision (Bishop and Goldrick, 1992; Wohl, 1993; Wohl and Ikeda, 1998; Whipple et al., 2000a). Where joints or favourably-oriented bedding planes are present, they may be exploited by the stream, either reducing the steep slope *in situ*, or by upstream migration of the knickpoint [e.g. Miller (1991); Bishop and Goldrick (1992); Weissel and Seidl (1997, 1998); Wohl and Ikeda (1998); Fig. 2.20].

The increased gradient at a knickpoint also causes a drastic increase in flow velocity [e.g. Tinkler (1993): Eqn. 2.3]:

$$v_b = \left(2gh + v_i^2\right)^{0.5} \tag{2.3}$$

where v_b is the velocity of water above the step and v_i the resultant velocity, after falling over a step of height h metres.

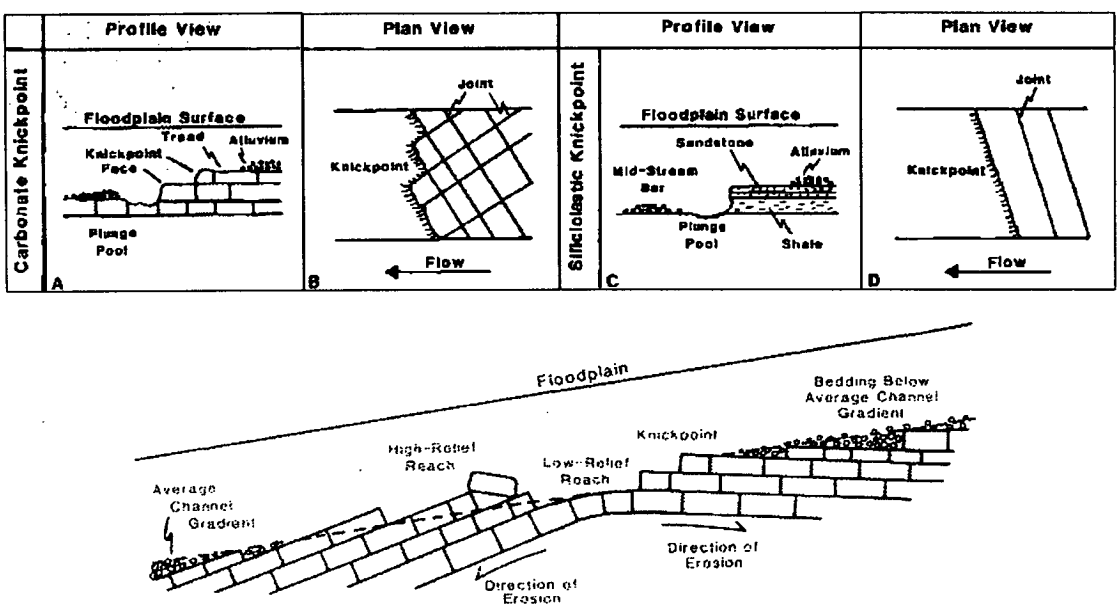

Figure 2.18: *Cartoons of knickpoints in layered, jointed rock, modified from Miller (1991).*
a. Different knickpoint forms in carbonate and siliciclastic rocks; tributaries of the Ohio River, IN.
b. Cartoon of changes in channel morphology with stratal dip. The erosion of a given bed may be reduced once it is degraded below the average gradient of the stream.

2.3.2 Stream power

Stream power is often used to predict patterns of incision and deposition within and between basins. It describes the erosive power of a stream: work carried out on the bed by the water and sediment [e.g. Stock and Montgomery (1999)], and hence is dependent on the slope, discharge and other factors such as lithology, and stream dimensions. Thus narrow steep reaches with high velocity have high stream power [e.g. Hack (1973);

Bishop et al. (1985); Merritts and Vincent (1989); Wohl et al. (1994)]. Talling and Sowter (1998) observed that incising reaches have a different pattern of downstream variation in slope, and hence in stream power, than depositing reaches.

Unit stream power, ω, is defined [e.g. Hancock et al. (1998)] as

$$\omega = \frac{\rho_w g S_e Q}{w} \tag{2.4}$$

where ρ_w is the density of water, in kgm^{-3}
g is the acceleration due to gravity, $9.81\mathrm{ms}^{-2}$ S_e is the energy slope, in kgm^{-3}
Q is the discharge of water, in $\mathrm{m}^3\mathrm{s}^{-1}$ w is the width of the channel, in m

Hack (1973) defined the *Stream-gradient* or *SL Index*, a proxy for stream power. Although the inherent assumption of equilibrium is not valid if the stream is incising, the *relative* SL index values are useful for identifying locations of anomalously high stream power in a river (Seeber and Gornitz, 1983; Bishop et al., 1985; Merritts and Vincent, 1989; Goldrick and Bishop, 1995; Wohl and Ikeda, 1998; Burbank and Anderson, 2001). SL indices have been calculated for the streams studied in the Tableland [Chapters 4 and 5] to demonstrate the downstream variation in stream power. Its value is an indication of the factors controlling stream evolution is discussed in section 7.1.3.

For a graded stream, a semi-logarithmic plot of the long profile is a straight line, with altitude, h, given by:

$$h = c - k \ln L \tag{2.5}$$

where L is the horizontal stream length from the drainage divide, in m. c and k are constants. Taking the derivative and rearranging for $k\,[= SL]$, the gradient between two points i and j on the semi-log plot is:

$$k = \frac{h_i - h_j}{\ln L_i - \ln L_j} \tag{2.6}$$

where h_i and L_i are the elevation and distance of point i, in m. For short stream sections, this can be approximated as the *SL index*:

$$\boxed{SL = \left[\frac{\Delta h}{\Delta L}\right] * L} \tag{2.7}$$

where Δh and ΔL are measured [in m] for the reach in question, and
L is the distance from the drainage divide to the midpoint of the reach, in m.

2.3.2.1 The stream power law

The *'stream power law'* in this thesis refers to Eqn. 2.10, a widely-used formulation for the average incision rate at a point in a stream, calculated at a reach-scale from either the shear stress or unit stream power [Eqn. 2.4], in combination with rules for the velocity and discharge of the flow. The use of this equation assumes that erosion rate is approximately equal to t for shear stress, or w for the stream power rule (Hancock et al., 1998). The shear-stress and stream power-based rules are, respectively:

$$\frac{dz}{dt} = K_1 \frac{Q^{1/3} S_e^{2/3}}{w^{2/3}} \tag{2.8}$$

$$\frac{dz}{dt} = K_2 \frac{Q S_e}{w} \tag{2.9}$$

where K_1 and K_2 are constants. Howard and Kerby (1983) argued that the largest shear stress on a channel is exerted by infrequent large floods, and erosion is small compared with basin relief. Hence they suggested that for these 'dominant discharges', drainage area, A, could be used as a proxy for the discharge. If width is also dependent on the discharge, then the *'stream power law'* is:

$$\boxed{\varepsilon = K A^m S^n} \tag{2.10}$$

where ε is the average erosion rate, in mmyr^{-1}
K is a constant: the coefficient of erosion, in $\mathrm{m}^{0.2}\mathrm{yr}^{-1}$
A is the contributing drainage area, in m^2
S is the [non-dimensional] gradient of the channel bed [replacing S_e], and
m and n are positive constants.

An approximation of this rule [Eqn. 2.11] has been used in a reach where no significant tributaries join the studied river [e.g. Burbank et al. (1996a); Whipple et al. (2000b)], and is compared with the long-term erosion rates obtained from cosmogenic isotope data for one of the Tableland streams, in section 7.2.2.5.

$$\varepsilon = K' \left(\frac{S'}{w} \right)^n \tag{2.11}$$

where K' is a different dimensional constant, and w is the channel width, in m.

The values of the stream power law constant, K, and the two exponents, m and n, are the subject of considerable debate. K incorporates the influences of a wide range of different factors, such as channel geometry, hydraulic roughness, the assumptions implicit in the 'dominant discharge' idea, sediment discharge and lithological resistance, which itself is a function of rock heterogeneity, uplift rates, climate and erosional process

(Sklar and Dietrich, 1998; Hancock et al., 1998; Whipple and Tucker, 1999; Whipple et al., 2000a,b). K is also implicitly linked to the slope exponent n (Sklar and Dietrich, 1998; Whipple and Tucker, 1999; Stock and Montgomery, 1999; Snyder et al., 2000).

Howard and Kerby (1983) suggested incision was dependent on shear stress, and calculated values of $m = 0.4$, $n = 0.7$. Seidl and Dietrich (1992) applied the stream power law at tributary junctions to obtain $m/n = 1.0$, implying incision is linearly related to the unit stream power. Further work on Hawaiian channels implied $m = n = 1.0$ (Seidl et al., 1994). However, Whipple and Tucker (1999) argued that constraints on the hydraulic geometry and relation of the basin area to discharge limit the ratio m/n to between 0.35 and 0.6.

Incision rate varies with the erosional process. Seidl and Dietrich (1992) and Seidl et al. (1994) noted varying values of m/n in streams dominated by knickpoint migration, suggesting that the stream power law failed to adequately predict the stream evolution. The choice of the slope exponent, n, affects the shape of migrating knickpoints (Howard et al., 1994; Weissel and Seidl, 1998). Stock and Montgomery (1999) were unable to find consistent values for K, m and n in a wide dataset of streams. They found an apparent critical dependence on the erosional process and tectonic régime: for stable Australian rivers, $m = 0.3 - 0.5$, $n = 1.0$; for Hawaiian streams dominated by abrupt base-level drops, $m = 0.1 - 0.2$. Hancock et al. (1998) and Whipple et al. (2000a) showed that incision processes are non-linear: abrasion varies with velocity^5, and hence with $n^{5/3}$; plucking varies with velocity^2; $n^{2/3-1.0}$. Whipple et al. (2000b) calculated $n = 0.4 \pm 0.2$ and $K = 2.4\text{x}10^{-4} \rightarrow 9.0\text{x}10^{-4}\text{m}^{0.2}\text{yr}^{-1}$ for incision in an Alaskan river dominated by plucking, but both K and n varied between two different rock units.

Using a value of $m = 0.4$, Stock and Montgomery (1999) calculated values for K in Japanese and Californian streams which varied with lithology by over five orders of magnitude. However, the values of K also depended on the values chosen for m and n. Wohl and Ikeda (1998) and Wohl and Merritt (2001) observed that substrate variations had more influence than drainage area on erosional patterns. Modelling by Sklar and Dietrich (1998) predicted that both K and the ratio m/n could decrease with increasing sediment supply, and therefore that the common assumption that K is constant throughout an area was flawed.

Snyder et al. (2000) showed that K was not constant even where the climate and lithology were relatively uniform, as K was linearly dependent on the uplift rate. Attempts to constrain the values of K and n emphasised their interdependence, although taking orographic rainfall into account, they obtained constant K for reasonable values of n [1.6-2.7]. However, they noted that channel width, alluvial cover, sediment flux and the frequency of debris-flows could all affect the scaling of the stream power law. Although they felt that their streams showed no downstream variation in K, they accepted that possibility by allowing K to vary downstream with incision rate [after Sklar and Dietrich (1998)] in later calculations.

In summary, although the stream power law is widely used to investigate variations in incision rate and basin evolution within and between basins, it is still poorly understood. While most studies assume that the coefficient of erosion, K, and the area and slope exponents, m and n, are constant, a considerable body of evidence suggests that they in fact vary drastically not only between basins, but also potentially within a single stream, depending on the incision process, the uplift rate, lithology and climate.

This has significant implications for the use of the stream power law to investigate fluvial systems, and limits its use as a predictive or comparative tool. The present lack of knowledge of its scaling may make it inapplicable for detailed investigations of basin and stream morphology. However, stream power itself [and e.g. the SL index, Eqn. 2.7] is a very useful tool to indicate the variation in erosivity, and hence to investigate the likely patterns of incision along a stream.

SL index is used in this thesis in the study of the Tableland streams [Chapters 4 and 5] to compare the downstream variations in stream power between the surveyed streams. Section 7.1.3 demonstrates that in this case, the SL index is a very useful tool, although attempts to correlate long-term erosion rates with the stream power law [section 7.2.2.5] were far less successful.

2.3.3 Responses to tectonic motion

The streams studied on the Tableland [Chapters 4 and 5], and those modelled using CASCADE [Chapter 8], are primarily affected by gradient changes imposed by uplift and subsidence on nearby faults. In either case, the streams act to reduce the changed gradient, by changing their course, and by local incision and aggradation. In the case of an increased lateral gradient, the stream may migrate gradually, or avulse, towards the lowest gradient, depending on the rate of the motion [e.g. Nanson (1980); Leeder and Alexander (1987); Peakall (1998); Peakall et al. (2000); and section 2.2.2]. This section considers the implications of a tectonically-induced change in the *longitudinal* gradient of a stream.

2.3.3.1 Knickpoints

The streams surveyed on the Tableland are dominated by upstream knickpoint migration. Unless a stream is defeated [see section 2.2.2], base-level drop may result in the formation of a steepened knickpoint reach at that point [see section 2.3.1.2]. Narrowing of this stream focuses its erosive power on the lip, and flow velocities increase. Seidl and Dietrich (1992) correlated knickpoints in Elder Creek, California with terraces downstream, and concluded that upstream knickpoint migration accommodated uplift of the trunk stream [Fig. 2.19].

Seidl et al. (1994, 1997) attributed knickpoints in Hawaiian bedrock channels to periodic sea level drops and cliff retreat. They also proposed headward knickpoint migration, at rates of 0.5-2mmyr^{-1}, was the dominant form of incision into the host basalt. Attempts to constrain these rates with cosmogenic studies (Seidl et al., 1997) were beset with difficulties, but broadly agreed with the original findings, favouring retreat, rather than downwearing of knickpoints [Fig. 2.19]. Knickpoint propagation under a boulder armour was particularly important to facilitate downcutting in lower reaches. Wohl et al. (1994) observed two sets of knickpoints in an Israeli gorge: a lower active set and an upstream partially buried set, which they attributed to two distinct sequences of headward propagation, triggered by discrete periods of tectonic motion.

Knickpoints formed in response to uplift are controlled by the substrate. Favourably-oriented joints in tributaries of the Macleay River, Australia, allow rates of gorge retreat to exceed the erosion rates on the knickpoint lip (Weissel and Seidl, 1998).

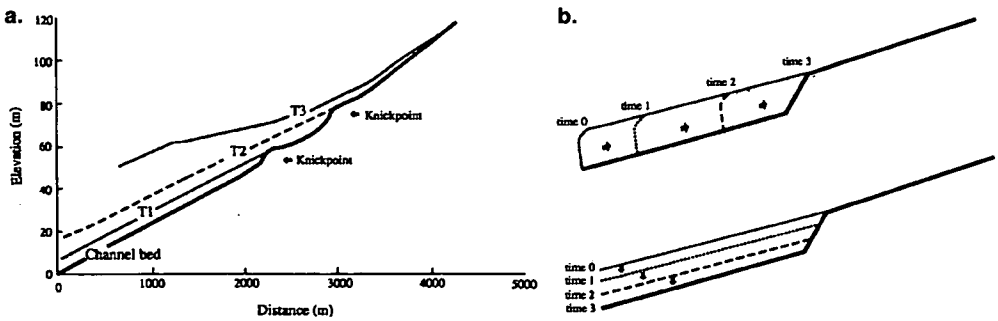

Figure 2.19: *Evidence for knickpoint migration in Elder Creek, CA, Seidl and Dietrich (1992). a. Schematic figure of Elder Creek long profile showing knickpoints and correlating downstream terraces. '0m' corresponds to the confluence of Elder Creek and the trunk south fork of the Eel River. Terraces T1 and T2 end abruptly at channel knickpoint locations. Terrace T3 terminates where the channel bed slope increases markedly. The steep headwaters above the highest knickpoint are dominated by debris flows.*
b. Schematic plot showing two suggested scenarios for knickpoint and terrace formation.
Top: knickpoint migration is the principal incision process; the progression of a knickpoint along a channel profile results in the formation of a terrace parallel to the stream.
Bottom: vertical incision caused by processes other than knickpoint propagation, including abrasion; the knickpoint forms as a result of differential rates of vertical erosion.

Wohl and Ikeda (1998) observed that knickpoints formed in response to uplift occurred preferentially in hard lithology, and where joints and bedding were oriented across the stream flow. Although a major mechanism of bedrock erosion, knickpoint evolution is not adequately predicted by the stream power law [Eqn. 2.10], in many cases occurring at a rate independent of the variation in drainage area (Seidl and Dietrich, 1992; Seidl et al., 1994; Howard et al., 1994; Weissel and Seidl, 1997; Sklar and Dietrich, 1998; Wohl and Ikeda, 1998; Whipple and Tucker, 1999; Snyder et al., 2000; Wohl and Merritt, 2001). Application of a single erosion law to a fluvial system dominated by different erosion mechanisms may be inadequate to predict the real patterns of erosion.

While knickpoints have often been described, a debate still exists about the mechanism by which they evolve, and hence how they facilitate incision. Gilbert (1895) first suggested that the Niagara Falls migrated headwards by parallel retreat of the knickpoint [Fig. 2.20b], but recent studies have suggested other possible mechanisms of knickpoint migration [Fig. 2.20].

Gardner (1983) modelled knickpoint evolution by systematic base-level drops using homogeneous cohesive bedrock in a flume. He concluded that knickpoint evolution is governed by the spatial variation in bed shear stress, τ_o, along the stream. Shear stress increases rapidly through a steepened reach upstream of the knickpoint, reaching a maximum at the knickpoint lip, and then decreases rapidly downstream [Fig. 2.21]. This is enhanced by narrowing of the stream as the knickpoint is approached, causing incision to increase towards the notch at the lip. Gardner found that sufficient energy was focused at the lip to quickly erode the knickpoint almost *in situ* by inclination, and then replacement [Fig. 2.20a.,c]. Thus, he concluded that in homogeneous bedrock, the knickpoint would not migrate far before it was fully eroded, except in cases of jointed lithologies, where retreat might be facilitated by collapse and removal of joint blocks.

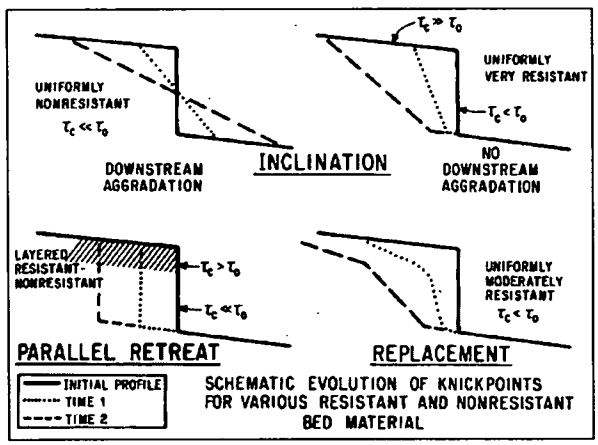

Figure 2.20: *Proposed mechanisms of headward knickpoint migration, from Gardner (1983).* τ_0 *is actual bed shear stress;* τ_c *is critical bed shear stress.*
a. Inclination: the knickpoint face rotates around its central point. The gradient of the steep reach is reduced in situ, *with very little headward migration.*
b. Parallel retreat: the gradient of the knickpoint is maintained, and the steep reach migrates headward through time. This mechanism was initially described by Gilbert, and more recently by Weissel and Seidl (1997, 1998).
c. Replacement: a steep reach is generated immediately upstream of the knickpoint lip. This 'drawdown' reach steepens and lengthens through time, while the knickpoint lip migrates headward, and the knickpoint face gradient decreases.

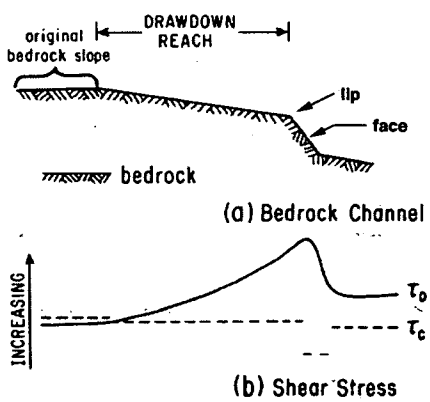

Figure 2.21: *a. Knickpoint morphology and b. variation of actual and critical bed shear stress at a knickpoint, modified from Gardner (1983).*
τ_0 *is actual bed shear stress;* τ_c *is critical bed shear stress.*
Diagram represents his run Ia at 4.5hr. Note that τ_c *will vary with the channel slope as the downslope component of gravity changes.*

However, examples of knickpoint migration over quite long distances that are *not* facilitated by joints belie this explanation [e.g. Bishop et al. (1985); Seidl and Dietrich (1992); Young and McDougall (1993); Wohl et al. (1994); Seidl et al. (1994)].

Howard et al. (1994) modelled the evolution of initially concave bedrock stream profiles perturbed by intermittent base-level drops [Fig. 2.22]. In all cases, a steep bedrock-floored knickpoint formed at the location of the base-level drop, and gradually eroded headward [Fig. 2.22], while alluvial reaches developed between the knickpoints during periods of stability. Howard et al. (1994) attributed steepening and incision immediately upstream of the knickpoint to the upstream transmission of the base-level drop, which travelled headward faster than the knickpoint itself. Thus they predicted that bedrock channels undergoing uplift could be characterised by "patchy alluvial cover, or short alternating sections of alluvial and bedrock channels".

Howard et al. (1994) demonstrated that the form of knickpoint migration is dependent on the formulation of the stream power law. A steep knickpoint migrates upstream when m and n are high [$\varepsilon \propto$ stream power; Fig. 2.22b,d]. In contrast, knickpoint faces were rapidly rounded and decreased in gradient as they propagated, when fractional values of m and n were used [$\varepsilon \propto$ shear stress; Fig. 2.22c,e]. Erosion of intervening alluvial reaches also occurred more quickly. Howard et al. (1994) concluded that the critical factor in knickpoint retreat was the relative slopes of the knickpoints and the intervening reaches [compare Fig. 2.22b and d; c and e].

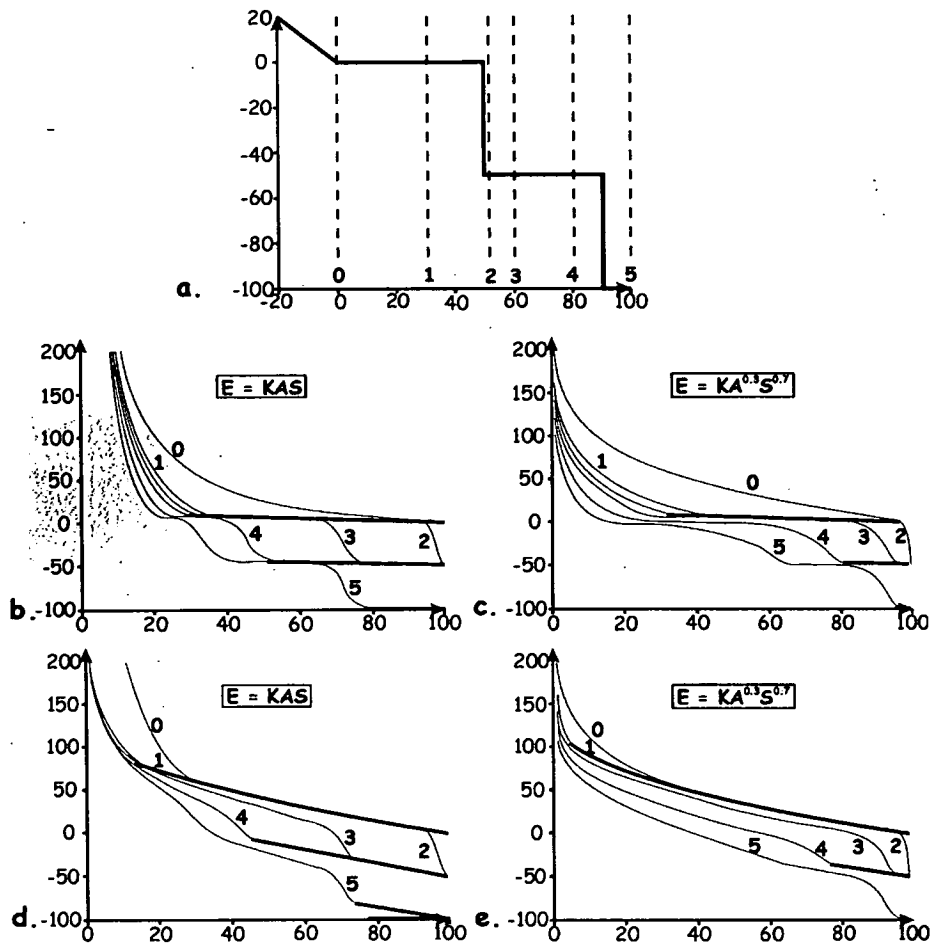

Figure 2.22: *Numerical modelling of knickpoint evolution, modified from Howard et al. (1994). Time and distance scales are in arbitrary units. Drainage area is assumed to be proportional to the square of downstream distance, with unit drainage area at unit distance. Heavy lines in plots [b] to [e] are alluvial channel segments that form during periods of base-level stability.*
a. Temporal changes in downstream base level.
b. Successive stream profiles produced for the erosional history in [a] with bedrock erosion proportional to stream power: m=1; n=1; K=0.0004 [e.g. Seidl and Dietrich (1992); Seidl et al. (1994)]. Alluvial gradient shallow [K_m=1 in $S = K_m A^{0.25}$].
c. Conditions similar to [b] but bedrock erosion proportional to shear stress: m=0.3; n=0.7; K=0.096. [e.g. Howard and Kerby (1983)]
d. Conditions as for [b] but with steeper assumed alluvial slope: [K_m=6.5 in $S = K_m A^{0.25}$.]
d. Conditions as for [c] but with steeper assumed alluvial slope: [K_m=6.5 in $S = K_m A^{0.25}$.]

2.3.3.2 Alluvial stream responses

Due to having relatively soft banks, an alluvial stream may respond to uplift or subsidence by changing its course and its morphology. The exact response depends on the type of river, and the magnitude and location of the vertical motion (Ouchi, 1985; Holbrook and Schumm, 1999; Fig. 2.24). Schumm and Kahn (1972) observed increases in sinuosity [stream length/valley length] with imposed slope in experimental flume studies of alluvial streams. Increasing sediment load, stream power or velocity also results in increased sinuosity (Schumm and Kahn, 1972). However, different streams have different stability thresholds (Schumm, 1981; Fig. 2.23). Suspended load channels respond quickly to small changes in imposed slope, while braided, bedload-dominated streams change at higher imposed slopes [Fig. 2.23].

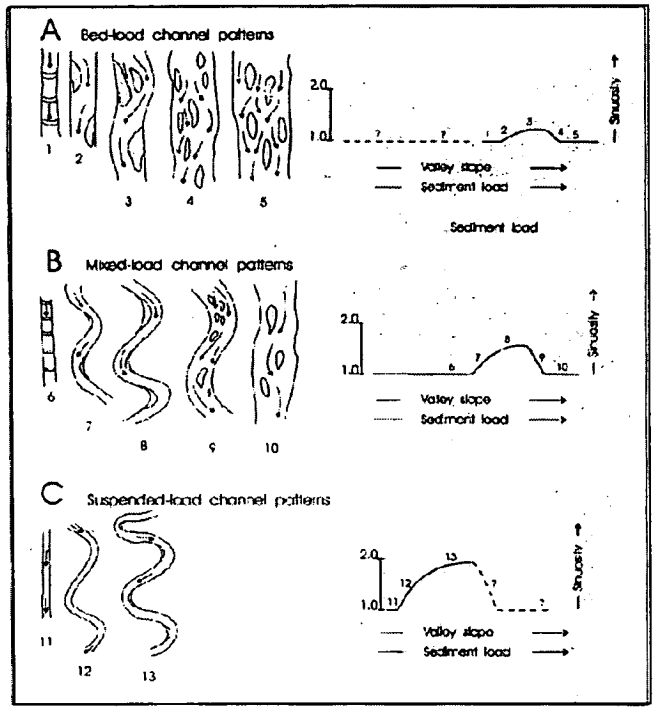

Figure 2.23: *The range of alluvial channel patterns for three channel types, from Schumm (1981); Schumm et al. (2000). Patterns can be formed with constant discharge, by increasing the valley slope [see also Schumm and Kahn (1972)].*
a. Bedload dominated. b. Mixed load. c. Suspended load dominated.

Streams can also change pattern completely, such that a meandering suspended-load stream could develop into a braided stream, as a result of a change in the type, or volume of sediment (Schumm et al., 2000). Doming produces a convexity in the stream long profile, by lowering the gradient of the reach above the uplift, but increasing the slope of the stream below the uplift. If the stream cannot divert its course around the obstacle, then aggradation may occur in the upstream low gradient reach, resulting in flooding (Burnett and Schumm, 1983; Holbrook and Schumm, 1999). The stream responds to remove the convexity, and hence will alter its morphology to achieve maximum efficiency through the uplift itself, but to reduce its efficiency in the steepened

downstream reach (Burnett and Schumm, 1983; Ouchi, 1985; Gomez and Marron, 1991; Merritts and Hesterberg, 1994; Harbor, 1997; Holbrook and Schumm, 1999; Figs. 2.24 and 2.25). The opposite is true where a stream experiences subsidence along its path [Figs. 2.24 and 2.25].

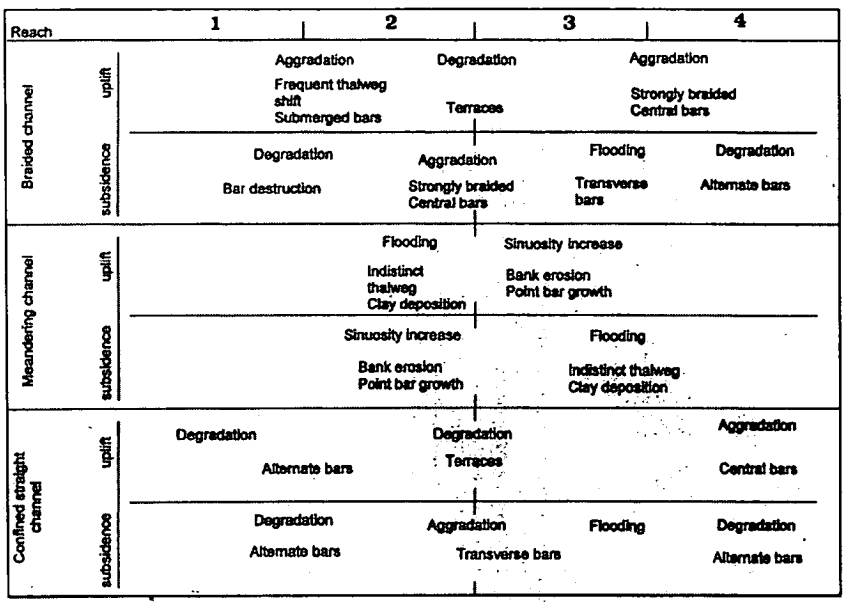

Figure 2.24: *Responses of experimental channels to uplift and to subsidence for braided, meandering and straight channels, from Ouchi (1985); Schumm et al. (2000).*
Reaches 2 and 3 are zones of deformation; reach 4 is downstream, and reach 1 is upstream of the zone of deformation.

The experimental responses produced in Ouchi's flume models are mirrored in natural examples. Burnett and Schumm (1983) describe identical patterns of response to uplift in Louisiana and Mississippi. Importantly, they noted that the response was dependent on the size of the stream: large streams had almost straight long profiles through the uplift, implying full accommodation of the uplift, while a marked convexity was preserved in the profile of smaller streams. The smallest streams were defeated. Jorgensen (1990) concluded that observed patterns of aggradation and incision reflected major changes in a large number of parameters, from channel shape and dimensions to average grainsize [Fig. 2.26]. Incision and increased transport efficiency in uplifting reaches reflected narrowing and increased unit stream power. Aggradation in subsiding reaches reflected increased width, channel instability and profile irregularity (Jorgensen, 1990; Harbor, 1998). Again, Jorgensen noted the differences between streams that were strong enough to adjust fully to the ongoing tectonic motion, and those that preserved records of displacement in their long profiles. The Sevier River did not respond by changing sinuosity as expected [Fig. 2.26b]. Harbor (1998) concluded that changes in the channel pattern were tempered by changes in the grain size and sediment load. The downstream river was swamped by the increased volume and size of material eroded from the uplift zone. He argued that an alluvial river adjusts its cross-section more rapidly than its profile.

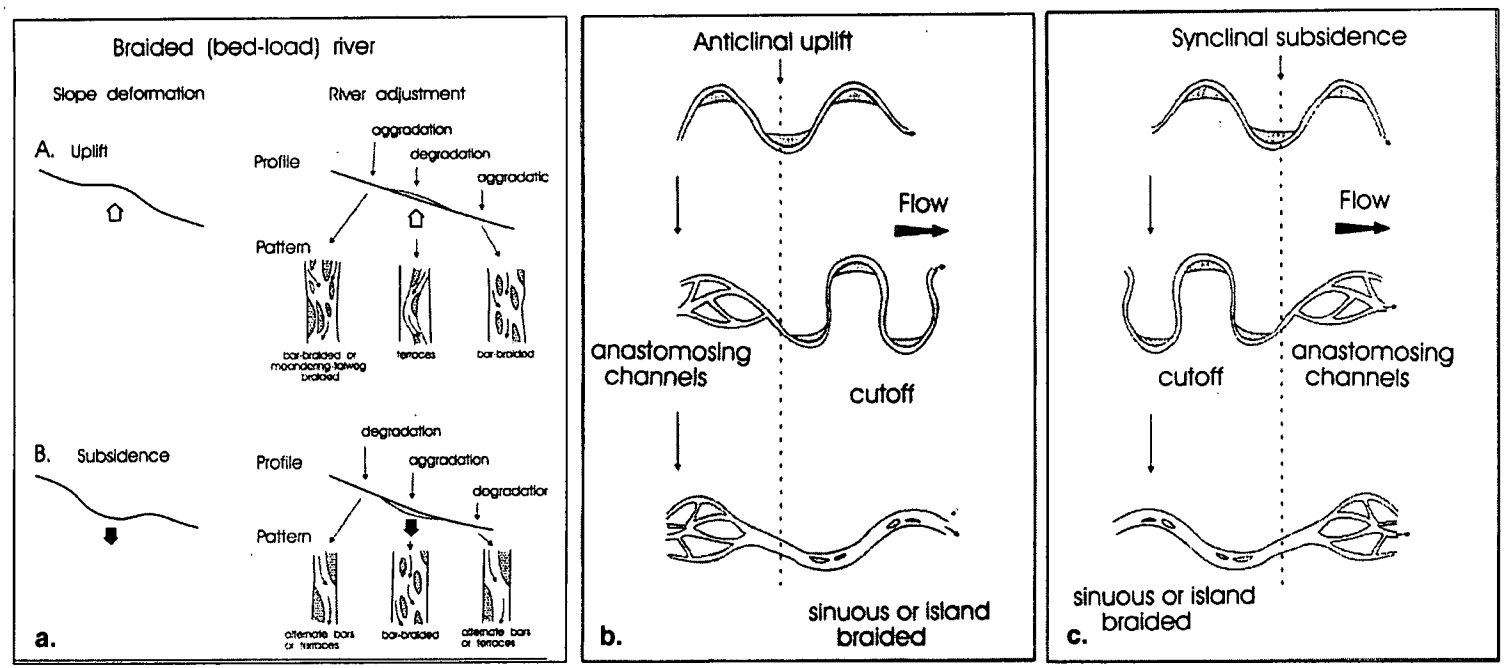

Figure 2.25: *Adjustment of a. braided and b., c. mixed-load streams to uplift and to subsidence, from Ouchi (1985); Schumm et al. (2000).*

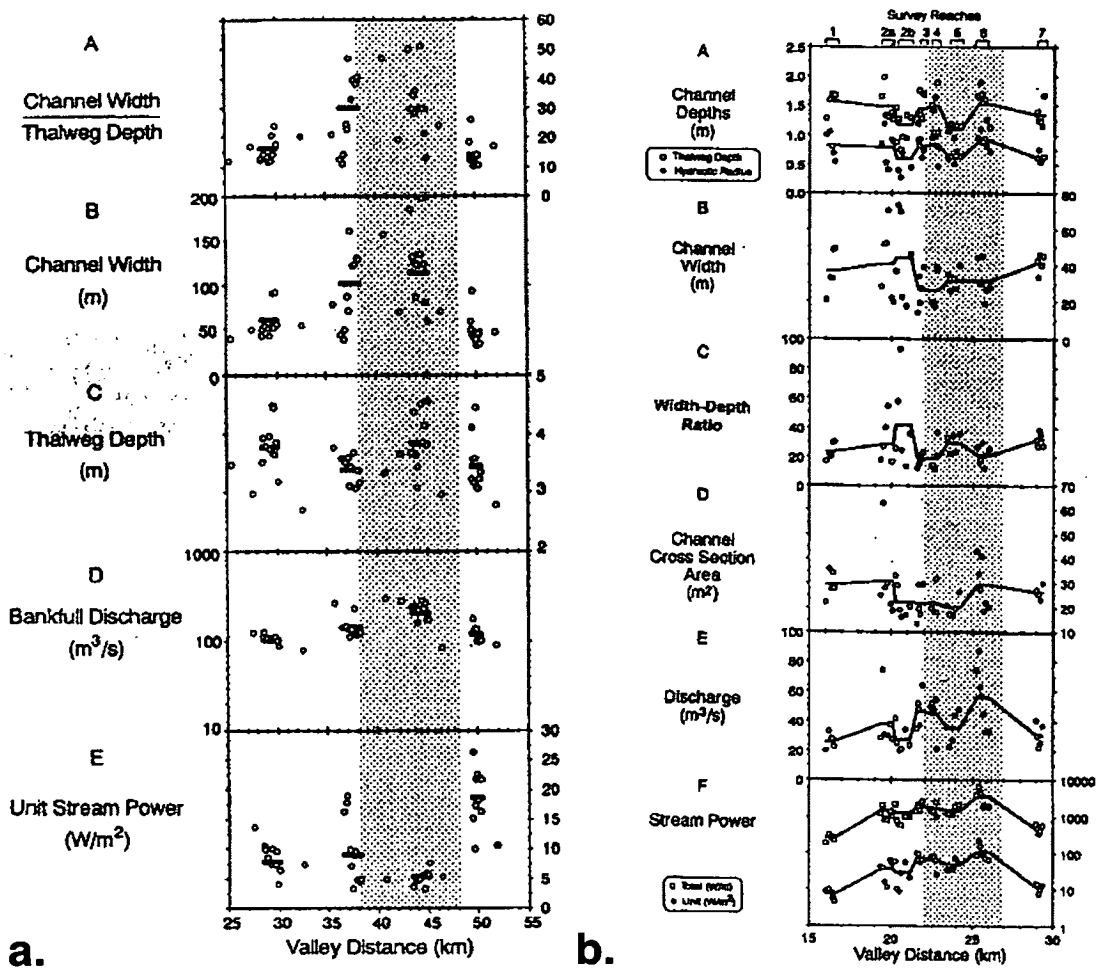

Figure 2.26: *Variations in channel morphology and hydrology in response to tectonics, from Jorgensen (1990). [Discussed in Schumm et al. (2000)].*
a. Response of the mixed-load Humboldt River, NV, to subsidence in the Rose Creek Narrows, beyond the tip of the East Range normal fault array.
b. Response of the gravel-bed Sevier River, UT, to oblique uplift on the Sevier Fault.

2.3.3.3 Bedrock stream responses

Bedrock streams are less capable of changing their width or pattern, as they are confined by resistant walls. However, incision is strongly dependent on gradient, and as in alluvial streams, uplift and steepening of the stream profile produce morphologies that localise the erosive force (Wohl and Merritt, 2001). Steep knickpoint reaches are common products of uplift, and associated with increased flow velocities and rapid incision [section 2.3.3.1]. The rates of erosive processes are strongly dependent on the velocity of the flow, and hence increase in steep reaches, and at steps (Tinkler, 1993; Hancock et al., 1998; Whipple et al., 2000a; Eqn. 2.3). Burbank et al. (1996a) and Leland et al. (1998) described incredible rates of bedrock incision from the Indus Gorge [2-12mmyr^{-1}], allowing the river to keep pace even with the very rapid uplift at the Nanga Parbat-Haramosh uplift axis. However, Sklar and Dietrich (1998) note that there is a limit to the increase in the rate of abrasion by bedload with increasing velocity, as the highest flow rates entrain all clasts, and reduce the number of effective impacts on the bed.

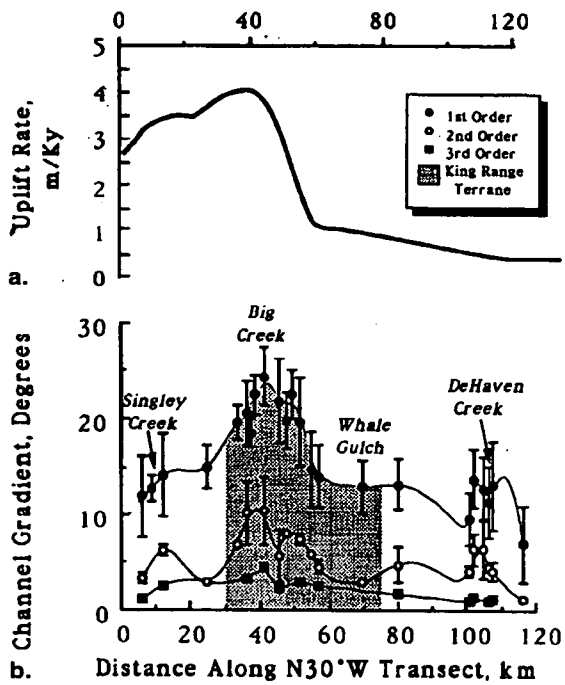

Figure 2.27: *a. Uplift-rate and b. variations in first-, second- and third-order channel gradients for coastal basins along a transect in northern California, from Merritts and Vincent (1989). Gradient variations mirror the uplift rate, with lower order streams [small tributaries] showing the greatest response to uplift rate. Generally, higher order [trunk] streams have sufficient energy to adjust to all but the highest rates of uplift, and hence show the smallest deviations in gradient.*

Narrowing of the flow on steep reaches focuses erosion, leading to the formation of inner channels by the coalescence of large potholes (Wohl, 1993; Hancock et al., 1998; Whipple et al., 2000a,b; Wohl and Merritt, 2001). Undulating walls can develop where a stream incises into softer rock, and are often found downstream of incised knickzones

(Wohl, 1998; Wohl et al., 1998; Wohl and Merritt, 2001). Where stream gradients are decreased, streams adopt morphologies that allow flow and hence erosion to spread more evenly over the channel bed (Wohl and Ikeda, 1998; Tinkler and Wohl, 1998a; Wohl, 1998; Wohl and Merritt, 2001). At very low gradients aggradation occurs, and an alluvial mantle may develop on the stream bed (Howard et al., 1994; Tinkler and Wohl, 1998a; Wohl and Merritt, 2001). Boulder armouring inhibits erosion (Seidl et al., 1994; Wohl et al., 1994; Granger et al., 2001a), and boulder bars in confined narrow gorges may help a stream to dissipate flow energy in low gradient reaches (Wohl, 1992). Wohl et al. (1994) described the burial of once active knickpoints in the upper reaches of a gorge in Israel, thus implying alternations in the governing tectonics, eliciting a change of response from incision to aggradation.

Merritts and Vincent (1989) showed the impact of different uplift rates on the evolution of bedrock streams in northern California [Fig. 2.27]. Stream gradients were very sensitive to the uplift rate, with the highest average gradients located in the regions of fastest uplift. Small [low order] tributary streams showed the greatest variation in gradients, while trunk [higher order] rivers have sufficient energy to adjust to all but the highest rates of uplift [Fig. 2.28]. Similar conclusions were reached by Burnett and Schumm (1983) and Rosenbloom and Anderson (1994).

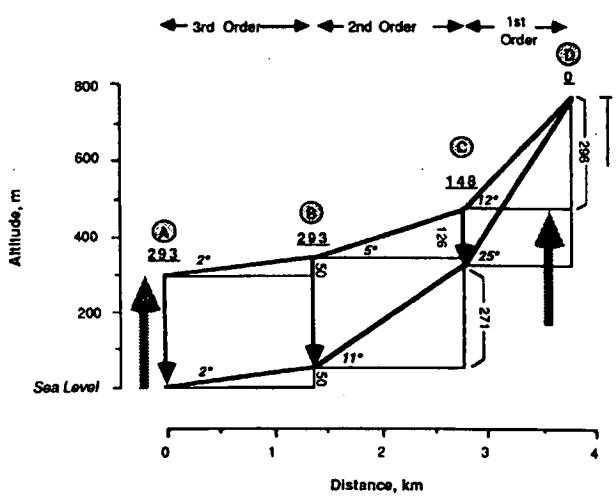

Figure 2.28: *Incision analysis: response of different parts of a stream to imposed uplift, from Merritts and Vincent (1989).*
Upper profile represents a composite of typical channel gradients, reliefs and stream lengths for first- second- and third-order sub-basins in the low uplift [southern] Fort Bragg area. Lower stream profile is the same but represents a drainage basin in the high-uplift Big Flat Creek area. Shaded arrows represent uplift; solid arrows incision. Lettered locations in circles: A - mouth of third-order stream; B - mouth of second-order stream; C - mouth of first-order stream; D - mouth of zeroth-order stream. Underlined values are amounts of downcutting, in metres. Sub-basin reliefs are in metres.

However, Merritts and Vincent were surprised that gradient alone could not distinguish northern basins undergoing intermediate uplift rates from the southern low-uplift area. They attributed this to a lag in the basin response, as the northern basins had only recently experienced increased uplift rates. However, variations in the stream-gradient

[SL] index [Eqn. 2.7], reflecting the local stream power, distinguished between these uplift régimes more convincingly.

2.3.4 Modulation of fluvial response to tectonics

Although fault evolution plays a major role in the development of transport and depositional systems, it cannot be considered in isolation: drainage systems are subject to many other controls that temper their response to tectonic movements. A footwall stream may respond to increasing rates of uplift by incising through the scarp, being deflected towards the fault tip, or by being completely reversed. The specific response is the result of a complex interaction of a number of different factors, which primarily affect the discharge and sediment supply [e.g. Leeder et al. (1991); Leeder and Jackson (1993); Gawthorpe et al. (1994); Jones et al. (1999); Humphrey and Konrad (2000); Goldsworthy and Jackson (2000)].

Discharge affects stream power [Eqn. 2.9]: the more water in a stream, the greater its capacity to erode, and to carry the resultant sediment away. Hence incision patterns and rates, and the transport capacity of a stream, are governed largely by variations in discharge. The patterns of erosion and deposition in a fluvial basin are dependent on the growing topography, but also on the availability of water to erode uplifting parts of the landscape, and to carry the products away [e.g. Jones et al. (1999)]. Aggressive streams, with high discharges, incise headwardly more rapidly, and may thus be more successful in capturing the discharge and drainage area of other streams [e.g. Burbank et al. (1996a)]. This has a major impact on the relief and the compartmentalisation of the footwall, and hence also on the locations and magnitudes of sediment inputs to the growing basins.

Patterns of stream incision are governed by the balance between upstream sediment supply and the carrying capacity of the flow [e.g. Wohl et al. (1994); Kooi and Beaumont (1994)]. Relatively subtle variations in the volume of entrained sediment can cause rapid abrasion, or protect the channel bed [e.g. Sklar and Dietrich (1998): their Fig. 11]. The availability of sediment for erosion drives variations in the sediment budget of a stream network, and hence sediment storage, abrasion and the volumes of sediment finally deposited in downstream basins. In turn, variations in deposited volumes affect the connectivity of hangingwall basins and the interaction between axial and transverse fluvial networks [e.g. Jackson and Leeder (1994); Leeder et al. (1996); McLeod et al. (2000): section 2.2.2]. Variations in sediment supply, both spatially and temporally present problems in using sediment thicknesses and distributions to piece together the patterns of fault evolution [e.g. Schlische (1991, 1995); Contreras and Scholz (1997); Ravnås and Steel (1998); Scholz and Contreras (1998); Jones et al. (1999); Contreras et al. (2000); Davies et al. (2000); McLeod et al. (2000)].

The Volcanic Tableland streams [Chapters 4 and 5] have been influenced not only by normal fault evolution, but also by the shape of the pre-existing landscape, variations in lithological resistance and a sequence of glacial-interglacial cycles. Thus the following sections consider how these other factors may have affected the ability of the streams to respond to the changing fault pattern. It is also significant that stream response is dependent on the *rate* of external forcing [section 2.3.4.4].

2.3.4.1 Climate

The influence of climate is felt primarily through variations in temperature and in the magnitude and periodicity of precipitation. These factors control the amount and distribution of water falling in a catchment, and its fate: climate also influences vegetation growth, soil cohesion and hence the surface:groundwater flow ratio [e.g. Schumm (1977); Vandenberghe (1995)]. Since all these factors are important in controlling runoff and the exposure of the landscape to denudation, erosion patterns, discharge and sediment supply are intimately linked to variations in the climate [e.g. Vandenberghe (1995); Jones et al. (1999)].

Tebbens et al. (2000) demonstrated the response of different reaches of the River Meuse to late Quaternary glacial cycles. Reduced vegetation and exposure of large tracts of land during glacials led to aggradation in upstream uplifting reaches, which were then degraded during interglacials. Subsiding lower reaches also aggraded rapidly during the glacials, but incision was focused at the glacial/interglacial transition, through decreased sediment supply and increased discharge. Subsequent highstands during the interglacials caused a wave of deposition to migrate upstream through time. Vandenberghe (1995) noted that the largest changes in stream response occurred in short periods at the transitions between glacial and interglacial periods. However, he also concluded that the timescale was of primary importance in determining the landscape response [section 2.3.4.4].

Climatic forcing has a major influence on base level changes. The interaction between eustatic and tectonic variation in base level results in varying degrees of accommodation generation through both time and space. While eustatic variations are generally low amplitude, long period effects, tectonic variations in subsidence patterns can be rapid, and extremely variable within a rift [sections 2.1.2 and 2.2.2]. Both factors are, however, important in determining depositional thicknesses and stacking patterns as well as facies relationships [e.g. Gawthorpe et al. (1990, 1994, 1997); Ravnås and Steel (1998); Gupta et al. (1999); Davies et al. (2000)]. Climatically-induced base level drops can also generate knickpoints.

2.3.4.2 Lithology

Variations in erodability have drastic implications for landscape evolution. The simplest demonstration is the distribution of alluvial and bedrock streams. While soft rocks will rapidly generate low gradient alluviated reaches with high sediment fluxes, resistant substrates will maintain steep bedrock-floored reaches, with low sediment fluxes, which are consequently less susceptible to external forcing. Within bedrock streams, the substrate is the primary control on the stream development, in terms of channel morphology, and hence flow velocity [e.g. Bishop et al. (1985); Wohl (1993); Tinkler and Wohl (1998a); Wohl and Merritt (2001)], and also erosional processes and hence incision rate [e.g. Hancock et al. (1998); Sklar and Dietrich (1998); Weissel and Seidl (1998); Whipple et al. (2000a,b); section 2.3.1.2]. These effects are demonstrated by the clear dependence of the erosional coefficient, K in Eqn. 2.10, on lithology [e.g. Stock and Montgomery (1999)]. Where heterogeneities such as joints or thin beds are exposed, they are rapidly exploited by the flow, to form characteristic bedforms [e.g. Wohl (1993); Wohl et al. (1994); Wohl (1998)], and as weaknesses which aid

erosion [e.g. Hancock et al. (1998); Whipple et al. (2000a)]. Upstream migration of knickpoints formed in response to fault motion is often modified by the geometry of joints and bedding orientations in the eroding lithology (Miller, 1991; Weissel and Seidl, 1997; Wohl and Ikeda, 1998).

The ease of erosion affects the rates and volumes of sediment that are eroded from any part of a catchment, and lithological heterogeneity consequently impacts on the spatial variation in sediment supply, as well as drainage density. The shape of drainage basins developed in different lithologies vary drastically (Leeder et al., 1991). Exploitation of oblique bedding or structural weaknesses may result in drainage orientations which are strikingly different from those predicted by the fault pattern alone (Goldsworthy and Jackson, 2000). A resistant bluff may inhibit avulsion in response to fault motion (Leeder and Alexander, 1987; Peakall et al., 2000).

Lithological variations also impact on the style of deformation, and the evolution of fault scarps. Jackson et al. (1982); Leeder and Jackson (1993) and Goldsworthy and Jackson (2000) demonstrated how lithology affects scarp morphology and fluvial patterns. Where footwalls form in resistant rock [e.g. limestone], streams are forced to follow displacement gradients, and tend to drain the steep, high footwalls through fault overlaps. However, scarps in more friable rock [e.g. Neogene sediments] are less pronounced geomorphic features, and streams may erode deep gorges directly through the scarps. Joints or preferentially-oriented bedding influence fault scarp degradation, as competent layers may slide on low angle detachment horizons, or scarps fail along exposed steep joint or bedding planes [e.g. Keefer (1984a,b); Pearce and Watson (1986); Stewart and Hancock (1988); McLeod (1996); Gilpin (1998); McLeod and Underhill (1999)].

2.3.4.3 Pre-existing landscape

During the early stages of fault evolution, while tectonic uplift is low, erosion may be focused in pre-existing highs, and inherited drainage patterns may continue to dominate the rift. As faults develop, these systems may be modified, but where they occupy deeply-incised channels, antecedent streams may remain influential long into the rift evolution (Crossley, 1984; Leeder and Jackson, 1993; Gawthorpe et al., 1994; Goldsworthy and Jackson, 2000). Thus some major sediment input points may not be determined solely by the developing fault geometry. Although footwall uplift provides new sediment sources, drainage development may be hampered by catchments already created by large antecedent systems. In other cases, uplift and backtilting of footwalls may result in the defeat of earlier streams, channelling sediment away from the developing rift, which may then become starved (Leeder and Jackson, 1993; Gawthorpe et al., 1994). Discharge from streams which originally flowed towards a new scarp from the hangingwall may be ponded in small lakes in the growing basin (Leeder and Gawthorpe, 1987; Leeder and Jackson, 1993; Gawthorpe et al., 1994; Holbrook and Schumm, 1999; Goldsworthy and Jackson, 2000; Morewood and Roberts, 2002). Where antecedent streams flow parallel to the incipient faults, much early sediment may be removed from the developing half-graben. If the antecedent stream maintains its course by incision [e.g. in response to base-level changes further downstream], hangingwall basins may remain starved through much of their development (Ravnås and Steel, 1998; Holbrook and Schumm, 1999).

2.3.4.4 Rates of change

Many studies have concluded that basin response is governed not only by the magnitude, but particularly by the *rate* of the change in an external control. Peakall et al. (2000) concluded that slow rates of lateral tilting result in gradual migration of stream courses, while rapid tilting, e.g. after a large earthquake, generally causes avulsion. The deflection of a transverse stream around a propagating fault tip depends on the propagation rate: if the fault tip migrates too quickly, the stream is more likely to be defeated, leaving a wind gap in the scarp (Jackson et al., 1996; Burbank et al., 1996b; Keller et al., 1999; Morewood and Roberts, 1999; Goldsworthy and Jackson, 2000). Similarly, uplift rates influence footwall stream courses: while incision may occur through relatively slowly uplifting scarps, an increase in uplift rate may defeat, deflect or reverse a stream (Humphrey and Konrad, 2000). The change in the rate of uplift connected with fault linkage and strain localisation is responsible for large-scale changes in the deposition patterns in rift basins, as accommodation is generated faster than erosion can produce sediment to fill it (Schlische, 1991; Schlische and Anders, 1996; Ravnås and Steel, 1998; Gupta et al., 1998; Cowie et al., 2000; McLeod et al., 2000; Davies et al., 2000; Dawers and Underhill, 2000). Tectonically-induced base level falls may have more significant impacts than eustatic changes in some regions, partly as they occur more rapidly (Gawthorpe et al., 1994; Ravnås and Steel, 1998; Davies et al., 2000).

Howard (1982) defined a time scale of response for a fluvial system, proposing that rapid fluctuations would have negligible effects on gradients, while streams could completely adjust to slower changes. Paola et al. (1992) used a simple 2D model to demonstrate the importance of the *rate* of an imposed change. Responses to changes in subsidence, water and sediment flux were all different when varied at slow, rather than fast rates, although the magnitude of the variation in each case was the same. They concluded that basins filtered the variation according to an intrinsic response time, or 'equilibrium time'. Where external perturbations occur more slowly than this response time, the response is limited by the rate of the external control; responses to rapid fluctuations are limited by the time required to modify the fluvial transport system (Marr et al., 2000).

Both Paola et al. (1992) and Marr et al. (2000) showed that while a basin may respond rapidly to fluctuations in water supply, it cannot react as rapidly to variations in subsidence rate. Merritts and Vincent (1989) showed that small basins in northern California required time to respond to increased uplift rates. Stream gradients reached a maximum 130ky after the peak in the uplift rate, while the maximum relief caused by incision was not achieved for a further 80ky. In the same region, Snyder et al. (2000) calculated a mean basin response time of 102ky after an eight-fold increase in the regional uplift rate. Vandenberghe (1995) observed that fluvial responses to glacial cycles are different over different timescales. In each case, the variation in stream response is due to the fact that climate change induces a number of other effects which influence stream evolution, and a river requires time to adapt to these perturbations.

2.4 Numerical approach: LEM development

Numerical surface process, or landscape evolution, models [LEMs] provide the ability to model the interplay of different processes over long periods of time. In Chapter 8, I outline some preliminary work with the numerical model CASCADE, to test some of the ideas arising from the field studies. This work is the first introduction of interacting faults into a surface process model, and considers their impact on stream development. This section details the main processes that are modelled in typical LEMs [section 2.4.1] and then describes a series of examples of other models, at different scales but predominantly of extensional régimes [section 2.4.2], which provide a context for the work with CASCADE.

LEMs are useful as the processes governing landscape evolution are often non-linear and also interdependent [e.g. Paola et al. (1992); Rosenbloom and Anderson (1994); Hancock et al. (1998); Sklar and Dietrich (1998); Whipple and Tucker (1999); Burbank and Anderson (2001); sections 2.1 to 2.3], making it hard to quantify the effect of any one process. LEMs make it possible to isolate a single process and specifically investigate its effect on the landscape. This has resulted in major advances in our understanding of surface processes, and the levels of coupling between parts of the landscape. LEMs play a role both in prediction and also in interpretation of landscapes. Most importantly, these models provide a *quantitative* picture of landscape evolution.

However, the complexity and interdependence of surface processes leads to a significant challenge in modelling them. Modelling is limited by the ability to abstract surface processes in a way that is simple enough to be investigated numerically, but still provides valuable information about the real world. LEMs have been used at a wide variety of scales, from a single catchment or flight of marine terraces [e.g. Rosenbloom and Anderson (1994); Anderson et al. (1999)] to an entire passive margin or orogen [e.g. Beaumont et al. (1992); Willett et al. (1993); Tucker and Slingerland (1994); van der Beek and Braun (1998)], and hence operate at different resolutions. In each case, the processes must be modelled differently, as it is not possible computationally e.g. to model grain-size variations at the orogen scale. As a result, small scale models may tell us a great deal of information about e.g. the scaling of erosional processes within a single stream or catchment. While losing this fine resolution, large scale models offer the opportunity to investigate processes that operate over bigger spatial and time scales, so that the development of specific landscape features may be investigated [e.g. Ellis et al. (1999)], provided that reasonable approximations to the driving processes can be made. Another important and complicated issue is describing the boundaries of a model space, as it is essential that the synthetic region behaves as if it is simply a small part of a continuous landscape.

LEMs have become increasingly powerful, with moves to include three-dimensional tectonic models [e.g. Gomberg and Ellis (1994); Densmore et al. (1998); Ellis et al. (1999); Cowie et al. (1993); Cowie (1998); Cowie et al. (2000)]. However, it remains essential that models are ground-truthed by comparison with natural observations. However detailed, numerical models are useless unless they can produce reasonable topography or stream profiles over feasible geological timescales, and unless the feedbacks between different processes are founded in reality. It is important to ensure that results are not artefacts of the grid resolution or time-step used within the model

[e.g. Sklar and Dietrich (1998)]. The most powerful models are those which predict relationships and features that are directly testable in the field, allowing additional constraints on rates and scales to be provided by focused fieldwork [e.g. Gupta and Cowie (2000)]. Overall, it is essential that the sensitivity of a model be rigorously tested. In particular, many authors have noted the need to test the impact of varying initial conditions [e.g. Densmore et al. (1998); van der Beek and Braun (1999); Ellis et al. (1999); Allen and Densmore (2000)]. Since one of the hardest things to reconstruct in any natural environment is its original form, testing the dependency of a modelled outcome on the initial assumptions is essential.

2.4.1 Model parameters

2.4.1.1 Surface processes

Although surface processes are simplified to different extents in different models [section 2.4.2], the basic processes may be summarised as: production of loose material, or regolith, by weathering; transport and deposition by hillslope processes; and channelised flow. In general, an interface between bedrock and the mantling alluvium is calculated at each point in the model space, and rates and scales of processes are governed by the type of material exposed at each point, taking into account the depth of cover during erosion.

Weathering: Before it can be transported across the landscape, regolith must be created from exposed bedrock. This is the rate-limiting step where bare bedrock is exposed, or in arid climates, and is partly responsible for the lag in transport systems' responses to changes in climatic and tectonic changes [e.g. Rosenbloom and Anderson (1994); Allen and Densmore (2000); Burbank and Anderson (2001)]. Regolith production is increased under a soil or alluvium mantle, as chemical attack speeds erosion, but hindered where the cover is deep, as the bedrock is effectively shielded from attack (Rosenbloom and Anderson, 1994; Small et al., 1997; Heimsath et al., 1999; Anderson et al., 1999). Although some models explicitly model weathering-limited hillslope processes [e.g. Rosenbloom and Anderson (1994); Densmore et al. (1998)], others assume that material is eroded and removed from a hillslope instantaneously, thus failing to capture some of the delayed response of the landscape to changes in external conditions [e.g. Koons (1989)].

Hillslope processes: Material is transported down hillslopes by a number of processes such as soil creep, rockfalls, rain splash, rodent burrowing and landsliding, which are dependent on the climate and lithology. Transport depends primarily on the local slope, although there is often also a dependence on the downslope distance. Combining conservation of mass and a slope dependence [e.g. Kooi and Beaumont (1994); Braun and Sambridge (1997); Burbank and Anderson (2001)] gives a general equation for these processes:

$$Q_s = -kx^a \left(\frac{\delta z}{\delta x}\right)^b \tag{2.12}$$

where Q_s is sediment flux from all hillslope processes, $\frac{\delta z}{\delta x}$ is the local slope gradient
x is the distance from the top of the slope, and k, a and b are constant.

In the simplest situation, where the processes are not influenced by the down-slope distance, and are linearly dependent on slope, this collapses to the diffusion equation:

$$\frac{\delta z}{\delta x} = \kappa_s \frac{\delta^2 z}{\delta x^2} \tag{2.13}$$

where, in 1D, $\frac{\delta z}{\delta x}$ is the erosion rate, and
κ_s is the hillslope diffusivity, given by $\kappa_s = k/\rho_s$, where ρ_s is the density of the sediment.

A linear diffusion equation is often used to model hillslope processes, particularly at large scales [e.g. Koons (1989); Kooi and Beaumont (1994); Tucker and Slingerland (1994); Braun and Sambridge (1997)] although small scale studies show that processes are more complicated than this relationship implies [e.g. Dietrich et al. (1992)]. Weathering-limited diffusion [e.g. Rosenbloom and Anderson (1994)] allows some time for the regolith to be created.

Landsliding: Although often included in the diffusion equation [e.g. Kooi and Beaumont (1994); Tucker and Slingerland (1994); Braun and Sambridge (1997)], bedrock-involved landsliding is not adequately captured by this simple relationship (Densmore et al., 1998). In many mountainous catchments, bedrock landsliding is the dominant mechanism of sediment removal [e.g. Hovius et al. (1997); Hovius and Leeder (1998); Allen and Densmore (2000); Hovius et al. (2000)], and hence use of the diffusion equation results in unrealistic model landscapes. One simple landslide rule instantaneously removes all material above a threshold slope from interfluves into the channels [e.g. Tucker and Slingerland (1994)]. Howard (1994) and Anderson (1994) used a threshold slope, but also changed κ_s, so that the rate of sediment flux increased as the critical slope was approached.

Densmore et al. (1998) developed an algorithm to capture the stochastic nature of landslides, incorporating a threshold slope, dependence on the rock strength and a probability function governed by the ratio between the actual and maximum stable height of the slope [Eqn. 2.15]. Material eroded in landslides was carried downslope in debris flow-like chutes, and deposited at the first available stable location. Thus, the maximum stable height of a slope, H_C is given by:

$$H_C = \frac{4C}{\rho g} \frac{\sin\beta \cos\phi}{[1 - \cos(\beta - \phi)]} \tag{2.14}$$

where C is the effective cohesion on the fracture plane
ϕ is the effective friction angle on the failure plane [Fig. 2.29]
β is the surface slope, ρ is the rock density.

The probability of a landslide, p_{fail}, is then given by

$$p_{fail} = \frac{H}{H_C} + A \tag{2.15}$$

EX BIBL. UNIV. EDINBURGH

where H is the hillslope height, and
A is a term which increases linearly with time, to represent the time-weakening of the rock (Densmore et al., 1997).

Landslides initiate typically at the base of a slope (Densmore et al., 1997, 1998) and hence the landslide site is defined as the lowest point on a slope whose gradient exceeds the critical internal friction angle, ϕ. Any node above this location whose elevation exceeds the projection of the failure plane contributes to the landslide volume [Fig. 2.29]. The size of the landslide is linearly related to the time since the last landslide (Densmore et al., 1997), and limited by the summed volume of all the unstable nodes. Material is carried down the steepest slope to be deposited at the first location where it will not exceed the stable slope.

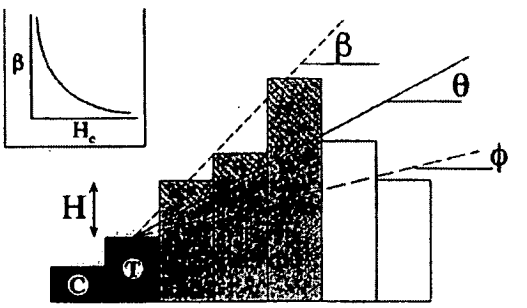

Figure 2.29: *Schematic figure of the bedrock landsliding algorithm, from Densmore et al. (1998). A landslide target, T, is assigned at the lowest point above the channel, C at which $\beta > \phi$. The potential failure plane dips at θ and is assumed to be exposed at the target. The probability of failure is given by: $p_{fail} = \frac{H}{H_C}$ [Eqn. 2.15], which in turn depends on the rock strength and the topographic gradient.*

This approach has been the most successful to date in reproducing the landsliding mechanism in LEMs, and has resulted in very realistic mountainous landscapes [e.g. Densmore et al. (1998); Ellis et al. (1999); Allen and Densmore (2000)]. Since then, similar algorithms have been incorporated into other LEMs, including CASCADE (Champel et al., 2002).

Channels: Flow in channels is most commonly modelled by stream power-governed equations [e.g. Kooi and Beaumont (1994); Tucker and Slingerland (1994); Braun and Sambridge (1997)]. Although the factors that determine channel initiation are complex [e.g. Dietrich et al. (1992)], many models define a threshold stream power (Montgomery and Dietrich, 1988, 1992), usually simply an area-slope product, and any node exceeding this threshold acts solely as a channel [e.g. Willgoose et al. (1991); Densmore et al. (1998)]. In other large scale models, each location within the grid is allowed to erode by *both* hillslope and channel processes [e.g. Kooi and Beaumont (1994); Anderson (1994)], as the model resolution is larger than either the channel or hillslope width.

Sediment transport is dependent on a stream's carrying capacity. 'Detachment-limited' [e.g. bedrock] streams are dominated by variations in the sediment flux: they are generally starved, and hence have excess discharge, which results in sediment entrainment and incision. 'Transport-limited' [e.g. alluvial] streams are limited by their

discharge: they are effectively over-supplied with sediment, and hence are constantly at capacity. Some models define streams as transport-limited throughout the model space [e.g. Willgoose et al. (1991)]. However, bedrock and alluvial stream processes differ considerably [section 2.3], and a transport-limited model is unsuitable for modelling bedrock streams [e.g. Howard et al. (1994)]. The differences between bedrock and alluvial streams are generally poorly captured in LEMs [e.g. Hancock et al. (1998); Sklar and Dietrich (1998); Burbank and Anderson (2001)], partly due to the large scale, but a better approximation is to allow the streams to adjust to the local imposed load.

Kooi and Beaumont (1994) adopted an approach that produced a certain extent of substrate control, as incision rates and length-scales varied with the type of material exposed at a node. They defined a simple carrying capacity, q_f^{eqb}, proportional to the unit stream power:

$$q_f^{eqb} = -K_f q_r \frac{dh}{dl} \tag{2.16}$$

where q_r is the river discharge per unit width, in this case proportional to *precipitation*, and hence not necessarily linked linearly to drainage area [unless the rainfall is constant over the whole model].
$\frac{dh}{dl}$ is the local slope, and K_f is the fluvial transport coefficient.
For steady-state sediment transport, the erosion rate is:

$$\frac{\delta h}{\delta l} = -\frac{dq_f}{dl} = \frac{1}{l_f}\left(q_f^{eqb} - q_f\right) \tag{2.17}$$

where q_f is the actual sediment in the stream, per unit width
l_f is the lithology-dependent length scale of fluvial erosion [$l_f = v_f t_f$, where v_f is the flow velocity; $t_f = 1/\text{rate constant}$].

The erosional length scale, l_f, is a material property of the rock: low for alluvium or soft rocks. Thus for $q_f > q_f^{eqb}$, the stream is transport-limited, and the excess sediment is deposited on the channel bed. For $q_f < q_f^{eqb}$, the stream is under capacity [detachment-limited], and able to pick up more sediment. In particular, for bedrock streams, l_f is very high, and $q_f \ll q_f^{eqb}$; Eqn. 2.17 collapses to an approximation of the stream power law [Eqn. 2.10]:

$$\frac{\delta h}{\delta l} = \frac{-q_f^{eqb}}{l_f} = -\left(\frac{K_f q_r}{l_f}\right)\frac{dh}{dl} \tag{2.18}$$

where $\frac{dh}{dl}$ is the local slope, and $m = n = 1$ in Eqn. 2.10 (Seidl and Dietrich, 1992).

Thus bedrock incision occurs, though importantly, the incision rate decreases as the stream approaches capacity. This approach has been adopted in several subsequent models, including CASCADE (Braun and Sambridge, 1997). However, unlike Kooi and

Beaumont (1994), CASCADE specifically defines streams, by connecting each node to its lowest neighbour. Water and sediment flux is calculated as above for each node in turn from the top of the stream downwards. This allows the definition of catchments, while lakes may form at local lows, where water is ponded (Braun and Sambridge, 1997).

2.4.1.2 External influences

Tectonics: Many surface process models incorporate only simple one-dimensional tectonic models, with regions of uniform or simply-varying uplift and subsidence [e.g. Koons (1989); Rosenbloom and Anderson (1994); Kooi and Beaumont (1994); Tucker and Slingerland (1994); Whipple and Trayler (1996); van der Beek and Braun (1999)]. Few LEMs have to date incorporated more realistic extensional tectonics, with the exception of *Zscape* (Densmore et al., 1998; Ellis et al., 1999), which has been developed from the *3DDEF* model (Gomberg and Ellis, 1994). In Zscape, slip is accrued in a series of discrete events, each with an associated 3D coseismic elastic stress-field. Although the evolution of a central part of a fault has been modelled (Ellis et al., 1999), and preliminary observations made from the fault tip regions (Densmore et al., 2002), no published examples have considered the evolution of an entire fault with along-strike variations in displacement. There is also no interaction between different faults in the model space. The work described in Chapter 8 couples together an LEM and a dynamic fault model, to investigate the erosion of topography created by a fully-interacting fault population. The results clearly demonstrate the role of fault interaction in controlling stream patterns, and hence the importance of modelling dynamic interacting faults if realistic tectonic landscapes are to be reproduced.

Climate: Climate variations are generally modelled by changing the amount of precipitation which falls on different parts of a model (Ellis et al., 1999; Allen and Densmore, 2000; thus also including orographic effects). The influence of climate is included in the process scaling, so that increased precipitation affects the weathering rate and the likelihood of landsliding, as well as rates and volumes of the transport by both hillslope and stream processes. Kooi and Beaumont (1994); Gilchrist et al. (1994) and van der Beek and Braun (1998) used the ratio of diffusive to fluvial erosion, R, as a proxy for climate change, as diffusion should dominate in arid climates, while increased precipitation and runoff in wet periods should favour fluvial erosion. van der Beek and Braun (1999) defined this ratio as:

$$R = \frac{\kappa_D}{\kappa_F v_R} \tag{2.19}$$

where κ_D is the diffusional constant, and κ_F the fluvial rate constant
v_R is the velocity of the flow.

Lithology: Erosion occurs at a faster rate and hence over a shorter distance in soft rocks or alluvium than in resistant material. Many models include a distinct interface between bedrock and surficial alluvial deposits. The model calculates the depth of alluvium at each point in the model space, and thus the rate and length scale of erosion. Variations in the bedrock geology may be investigated by definition of a characteristic

length scale and rate of erosion for each lithology [e.g. Kooi and Beaumont (1994); Tucker and Slingerland (1996)]. van der Beek and Braun (1999) defined a fluvial erosion efficiency, varying with lithology, as:

$$E = \frac{\kappa_F v_R}{L_{fb}} \tag{2.20}$$

where L_{fb} [L_F in Kooi and Beaumont (1994)] is the erosional length scale for that bedrock.

Isostasy: A flexural response to tectonic motion, and to the reorganisation of mass by erosion and deposition, has been incorporated into many large scale models [e.g. Kooi and Beaumont (1994); Tucker and Slingerland (1994); Braun and Sambridge (1997)]. The importance of isostatic restoring forces in controlling elevation patterns over long time scales has also been discussed by Anders et al. (1993); Montgomery (1994); Small and Anderson (1995) and Harbor (1997).

2.4.2 Landscape modelling approaches

Many surface process models have been developed over the last 10-15 years, each aimed at investigating a different aspect of landscape evolution. This section focuses specifically on the models which led to the development of CASCADE, highlighting the insights gained from each approach. The effect on the landscape of interaction between model faults is examined in Chapter 8.

Koons: Koons (1989) investigated the evolution a 40x40km region of the Southern Alps, NZ. He fixed rivers at their modern locations, and forced graded profiles to be maintained. Transport from the interfluves was modelled by simple diffusion with instantaneous creation of regolith. The pronounced asymmetry of the rainfall and erosion was reproduced by making diffusion strongly dependent on the rainfall pattern. Although simplistic, and failing to reproduce all the features of the Southern Alps, the model allowed Koons to investigate the effect of varying diffusivity, $\kappa*$, and uplift rate, on the development of topography. In his model, a steady-state was reached where elevations were determined by uplift rate, v, stream spacing, L, and the diffusivity, as

$$elevation \propto \frac{vL^2}{\kappa*} \tag{2.21}$$

Where $\kappa*$ was low, steady state was not reached, and the elevation was proportional not to the rate, but to the total amount, of uplift. Glacial cycles of 50ky duration caused 250-500ky fluctuations in the erosional rate, implying continuous adjustments to the changing climate.

Willgoose and others: Willgoose et al. (1991) developed a much more sophisticated two-dimensional model, based in continuum mechanics, and including both hillslope and channel transport rules. Streams initiated where stream power exceeded a threshold [e.g. Montgomery and Dietrich (1988, 1992)], while fluvial transport scaled non-linearly with slope and drainage area [a direct proxy for discharge]. All rivers

carried sediment at capacity: they were transport-limited throughout. Non-fluvial nodes eroded by slope-dependent diffusion.

Beaumont and others: Beaumont et al. (1992) developed an LEM along similar lines to Willgoose et al.'s model, but allowed *both* hillslope and channel transport in all nodes, as their grid was larger. A substrate-dependent length scale for erosion [section 2.4.1.1] was included by Kooi and Beaumont (1994), who investigated escarpments along passive margins for over 100My, at length scales of 150x50km and a resolution of 1km. They also incorporated an isostatic response to tectonic uplift and denudation.

Kooi and Beaumont (1994) varied rainfall patterns, lithology and flexural rigidity, and mimicked climate changes by varying the ratio, R, of fluvial to hillslope erosion [see above]. Escarpment morphology and retreat style changed with R. Gilchrist et al. (1994) investigated the controls on denudation in SW Africa, where coastal catchments are highly eroded relative to interior basins. By varying lithology, climate, uplift rate and the initial location of the drainage divide, they were able to reproduce the observed landscape quite accurately, and developed three potential scenarios for evolution of the modern SW African margin landscape.

The apparently lower erosional efficiency arising from the fact that small streams are not resolved in these models meant that unrealistically high diffusivities were needed to reproduce natural topography (Koons, 1989; Kooi and Beaumont, 1994; Anderson, 1994)]. Kooi and Beaumont (1996) looked at the effect of scale, modelling erosion of a single constant-gradient segment [fluvial or hillslope], an interfluve, and a series of connected drainage basins. Their model considered only spatially-averaged processes, with a resolution of around a kilometre, and hence all 'sub-grid' scale processes were modelled by diffusion. However, Kooi and Beaumont (1996) discussed the different timescales over which fluvial and hillslope transport systems reached equilibrium with the substrate, uplift rate and climate at each spatial scale. They reiterated that a substrate-dependency in the fluvial erosion algorithm was essential in order to successfully reproduce natural landscapes.

Tucker and Slingerland: Tucker and Slingerland (1994) introduced a threshold slope to differentiate between slow, diffusive hillslope processes and rapid mass failure. Although they considered the river sediment load, their approach differed from Beaumont et al. (1992) as there was no substrate dependence. Bedrock incision followed a linear stream power law rule, but as rainfall was uniform over the grid, discharge was effectively proportional to drainage area. In their 1994 paper, Tucker and Slingerland used a $1km^2$ resolution and a 150[x50 for 2D] km grid to compare a supply-limited bedrock landscape with a low weathering rate, with a transport-limited alluvial landscape; effectively investigating the ratio of alluvial transport efficiency to bedrock incision rate [similar to Kooi and Beaumont's erosional length scale, L_f]. Their results were broadly compatible with the escarpment morphology and location of drainage divides in SE Australia [e.g. Weissel and Seidl (1997, 1998)]. However, the model assumed that divide retreat was dominated by fluvial transport, thus, as a result of low model resolution, neglecting the potentially important contribution of subgrid processes.

In their 1996 paper, Tucker and Slingerland changed both stream and hillslope transport rules to investigate the sediment flux from part of the Zagros mountains. Incision included a substrate dependence, similar to Kooi and Beaumont's approach:

$$\frac{\delta h_b}{\delta t} = -k_v \left(\frac{Q}{Q*}^m \right) S^n \tag{2.22}$$

where $Q*$ is the total possible discharge [total grid area multiplied by the precipitation rate]
$m = 1/3$, $n = 2/3$, from observations in the Zagros [cf. $m = n = 1$ in their 1994 paper]
k_v represents the erodability of the sediment.

Due to the high relief and arid climate, they assumed that landsliding dominated hillslope erosion, and that local base-level drops would be immediately translated to failure of the critical hillslopes. Hence, as hillslope and fluvial processes occurred in each cell, elevations were determined purely by the channel bed. The model included a simple uplift function: an advancing uplift front with uniform uplift rate, and a superimposed sinusoidal folding pattern. The effect of lithological variations were modelled by using four different values of k_v, calibrated to reproduce the Zagros topography during the runs. The model again considered 1km^2 cells, but a smaller area, of only 42x82km.

The model reproduced several features of the natural landscape: deposition lagged the onset of uplift, and the peak deposition rate lagged the peak uplift rate, demonstrating a critical fluvial response time. This response time was dependent on the rock resistance, the width of the deforming region, and the uplift rate, although this last result was dependent on the use of $n \neq 1$. Lateral variations in lithology caused by folding also affected stream gradients, and hence incision rate. Tucker and Slingerland (1996) noticed the influence of the length scale of growing thrusts, which diverted antecedent rivers and controlled sediment input points.

Anderson and others: Anderson (1994) addressed the inability of large-scale models such as Beaumont et al. (1992) and Tucker and Slingerland (1994) to capture subgrid processes, and hence their need to use unrealistically high diffusivities. He proposed that since hillslopes respond significantly faster than channels, they can be represented by a steady-state relief. In a simple model of the Santa Cruz mountains, Anderson allowed one major stream in each 4x4km cell, and calculated bedrock incision using a linear stream power law. This was then scaled by the *measured* diffusivity and the hillslope length to obtain the cell's relief. He assumed that diffusion dominated in low gradient reaches, and landslides dominated in rapidly-incising reaches. Hence he defined a threshold slope and allowed the sediment flux to increase as this threshold was approached. The model was updated every 40kyr over 4 and 8-10My. With reasonable rates for these simple geomorphic rules, and a simple Gaussian uplift model, he was able to accurately reproduce the first order topography of a restraining bend of the San Andreas fault. However, Anderson (1994) dictated the stream locations in plan view, as had Koons (1989), so they remained unchanged, despite the changing tectonic field. Also, since this model did not include any mechanism for sediment deposition, it failed to reproduce alluvial regions.

Rosenbloom and Anderson (1994) considered the evolution of a small flight of marine terraces on the margin of the Santa Cruz mountains, which were cut by streams with marked convexities. Their model was constrained by detailed field observations and published terrace dates. Based on their observations, they modelled hillslope erosion

using regolith thickness-dependent weathering, and diffusion. Fluvial erosion followed a linear stream power law, though modified by a diffusion term to account for the observation of shallowing knickpoint slopes with age. Drainage area, stream diffusivity and the stream power erosion coefficient were considered to be constant throughout the model; alluvial deposition was not included, and a very simple uplift function was used. Model hillslope profiles fitted the observations well, giving a narrow range of diffusivities which agreed with local estimates. The model successfully accounted for the stream profile shapes, showing that large streams were able to incise fast enough to avoid developing convexities despite the uplift. However, the shapes and elevations of the knickpoints were not captured, implying that the stream rule was too simple to predict the complex external forcing.

Zscape: Densmore et al. (1998) were the first to include a detailed three-dimensional normal fault uplift function in a surface process model [from Gomberg and Ellis (1994)]. In an attempt to reproduce Basin and Range topography, uplift was modelled in discrete earthquakes every 500years, on 40km long normal faults dipping at 45°, with surface displacements of up to 1.4m [ratio of 1:4.67 uplift to subsidence]. Densmore et al. (1998) also explicitly modelled stochastic bedrock landsliding for the first time, with slope failure dependent on hillslope height, slope and rock strength [see above]. Following Anderson (1994), they modelled other hillslope processes by linear diffusion, but increased sediment flux as a threshold slope was approached. Weathering varied with regolith depth. Alluvial transport and bedrock incision were differentiated by the same method as Tucker and Slingerland (1994). However, a threshold stream power was defined so that stream and hillslope nodes were distinguished, which was more appropriate for their smaller grid: here 100m.

The new landslide algorithm reproduced the observed size-frequency distributions of landslides [e.g. Hovius et al. (1997)]. Densmore et al. (1998) demonstrated that explicitly modelling landslides produced far more realistic topography than simply using weathering-limited diffusion. The model predicted that in mountainous catchments like the Basin and Range, the sediment flux due to landsliding was similar to that from fluvial erosion, as implied by Hovius et al. (1997, 2000), and demonstrating the requirement for specific inclusion of this process in LEMs. Sediment flux from the diffusional processes was an order of magnitude smaller. The steep model hillslopes responded rapidly to base-level falls, implying that fluvial incision limited the rate of landscape change [see also Anderson (1994)].

Ellis et al. (1999) used *Zscape* to provide clues to the formation of key features of Basin and Range topography, such as triangular facets, benches on spur crests, and piedmonts. They considered a 10x10km grid, again with 100m nodes, at the centre of a long range-bounding fault. Steady-state topography was achieved in $\sim 10^6$ years; its form governed primarily by the spacing of rivers and the strength of the bedrock, which in turn determined the landslide distribution. Ellis et al. predicted that despite being formed by fault activity, the height of triangular facets after steady-state was *not* linked to fault slip, although this has recently been observed in field data by DePolo and Anderson (2000). Ellis et al. (1999) also investigated the rate of overprinting of stream patterns as fault activity stepped basinward. However, they did not consider any change in the earthquake magitude through time on either fault [simple 'on' or 'off'], and there was little displacement variation along the strike of the modelled part of the fault [see sections 2.1 and 2.2].

CASCADE: The model used in this thesis has one major advantage over the other LEMs described above: it can use an *ir*regular grid: nodes are not forced to be equidistant, or to lie in rows and columns (Braun and Sambridge, 1997). Distances are calculated by Delaunay triangulation, connecting each node to a set of 'natural neighbours', which are then used to calculate specific stream paths. Other geomorphic processes are defined exactly as by Kooi and Beaumont (1994). The irregular grid avoids biasing the transport pathways, which are confined to four directions in a regular rectangular grid [Fig. 2.30a]. Thus regular grids reduce the potential for stream meandering and tend to develop straight, steep rivers, draining a few large catchments. The advantage of an irregular grid is clearly demonstrated by the stream pattern around a radial uplift [Fig. 2.30b]:

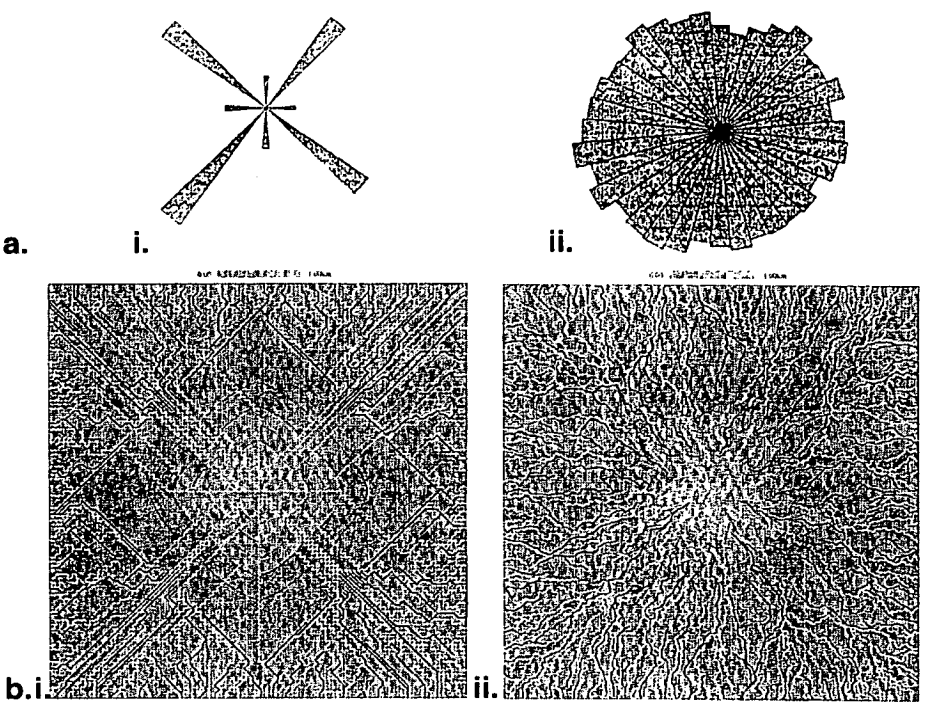

Figure 2.30: *Stream patterns resulting from radial uplift using a regular and irregular grid, from Braun and Sambridge (1997).*
a. Rose diagram of river segment orientations and lengths, showing the strong bias given to the NE-SW and NW-SE directions in a regular rectangular grid [i]. No preference is given to any direction in the unstructured grid [ii], as shown by the distribution and similar lengths of all streams.
b. Topography, stream pattern [black lines] and catchment geometry [white lines] resulting from radially symmetrical uplift function, using [i] a regular rectangular grid, and [ii] an unstructured grid.
Grid uses 10 000 nodes in a 100x100km square grid; average node is 1km^2. Results after 1My, in 100yr timesteps.

The fact that nodes do not need to be regularly spaced can be used to provide more detailed information in parts of a grid. Braun and Sambridge (1997) showed an example of self-adaptation, where nodes were automatically added to parts of the grid that became channelised, whereas no extra information was required from purely diffusional

regions. The grid can also be deformed: for example, extension can be allowed to actually pull nodes apart, and new nodes can be automatically inserted where the spacing has increased (Braun and Sambridge, 1997).

van der Beek and Braun (1998) calibrated the erosional parameters in CASCADE using the SE Australian passive margin, an average resolution of 1km, and timesteps of 100yrs. Specifically, they defined the two ratios, R and E [see above] as proxies for climatic and lithological variations, respectively. Landslides were not specifically included. However, they calibrated the model well from long-term denudation rates and rates of escarpment retreat, which proved linearly related to E (van der Beek and Braun, 1998). Fluvial erosion dominated the landscape evolution, but the diffusivity, κ_D, was less dependent on the nodal spacing than in regular grids. However, they argued that at large scales [>1km], hillslope processes should be considered as a subgrid process [e.g. Anderson (1994)].

In 1999, van der Beek and Braun specifically included a threshold slope, S_C, to allow bedrock landsliding [following Tucker and Slingerland (1994)], which dominates large river evolution in SE Australia [e.g. Weissel and Seidl (1997, 1998)]. Using an irregular ~2km grid, they constrained possible pre-rift topographies, and also used river profiles to constrain rates and processes of scarp retreat. However, they noted that the fluvial algorithm overpredicted incision in the headwaters of streams, as the incision is maximum where the stream is furthest from equilibrium [steepest], whereas in reality, incision probably reaches a maximum further downstream. Despite the simplicity of their algorithm, van der Beek and Braun (1999) demonstrated that landsliding was significant, while diffusional erosion accounted for less than 1% of the denudation, even in this stable landscape. They also demonstrated the importance of lithological variations in shaping drainage patterns. van der Beek et al. (2001) used CASCADE to demonstrate the importance of varying tectonic uplift in the production of anomalous longitudinal stream patterns in the Blue Mountains, SE Australia.

CASCADE has also been used to investigate the evolution of compressional regions. Tomkin and Braun (1999) applied a similar approach to Tucker and Slingerland (1996) to consider the evolution of fault propagation folds in Otago, NZ (Jackson et al., 1996). van der Beek et al. (2002) and Champel et al. (2002) included a more realistic tectonic displacement pattern, which they applied to thrust-cored folds in the Siwaliks of Nepal. Their results investigated the role of detachment dip and fault length in controlling stream patterns. This most recent work (van der Beek et al., 2002; Champel et al., 2002) included a more sophisticated bedrock landsliding rule, based on Densmore's stochastic algorithm, which they demonstrated was essential to achieve true steady state topography. An early form of Champel et al.'s landsliding algorithm was used in this project, and is discussed further in Chapter 8.

2.5 *In situ* cosmogenic isotope analysis

In situ cosmogenic isotopes have been used in this thesis to constrain the evolution of streams and channels in a fault overstep in an array on the Volcanic Tableland [Chapter 6 and section 7.2.2]. Terrestrial cosmogenic isotopes [TCN] are produced by the interaction of cosmic rays with nuclei in the atmosphere or on the earth's surface. Specific target atoms produce specific cosmogenic isotopes [Table 2.1], some stable, and others radiogenic. The age of a sample may be calculated from the concentration of the TCN in a sample, as the rate of production [and decay for radiogenic isotopes] is known [section A.3]. Since *in situ* cosmogenic nuclides are only produced in a thin veneer of the earth's surface, the calculated age of the sample represents the amount of time it has been exposed at the earth's surface: the *apparent 'exposure age'*. Alternatively, the TCN concentration can be used to constrain the rate at which a surface has eroded. Thus cosmogenic analysis is a powerful tool for investigating landscape development, and has been extensively used to study erosion rates, tectonic slip rates, river development, glacial advances and many other surface processes during the last decade [section 2.5.3].

The following section describes briefly the equations used to estimate the exposure ages and long-term erosion rates of samples, as used in Chapter 6, and discusses methods of investigating the data. A fuller explanation of the theory, including the mechanism of isotope production, calculation of production rates and also the derivation of the equations in section 2.5.1 is contained in Appendix A. Section 2.5.3 describes some applications of TCN analysis to tectonic and geomorphic problems.

Nuclide	Half-life (kyr)	reaction/target element	target mineral
^{3}He	stable	spallation: O, Mg, Si, Ca, Fe, Al	Ol, Px, Hbl, Gt
^{10}Be	1 500	spallation: O, Si thermal: O, Si, ^{9}Be, B, ^{13}C muon: O, Si	Qz, Ol, Mgnt, Plag
^{14}C	5.37	spallation: O, Si thermal: N, ^{16}O, ^{17}O, Si muon: O	Qz
^{21}Ne	stable	spallation: Mg, Na, Al, Fe, Si	Qz, Ol, Gt, Plag?
^{26}Al	700	spallation: Si thermal: Si muon: Si	Qz, ?Ol
^{36}Cl	300	spallation: ^{40}Ca, K thermal: ^{40}Ca, K, ^{35}Cl muon: ^{40}Ca, K	Kfsp, Plag, Calc ^{35}Cl in Calc fluid incl. in Qz Qz

Table 2.1: *Targets for in situ TCN production, modified from Gosse and Phillips (2001) and Bierman (1994). The target minerals in the final column are:*

Ol - Olivine	*Px - Pyroxene*	*Hbl - Hornblende*
Gt - Garnet	*Qz - Quartz*	*Mgnt - Magnetite*
Plag - Plagioclase	*Calc - Calcite*	*Kfsp - K-feldspar*

This project considers specifically *in situ* cosmogenic isotopes: those nuclides produced in rocks at the earth's surface. Due to the reduced flux and energy of the cosmic

radiation by this point, typically only of the order of 10^{-14}atoms are produced per gram of target rock at the surface per year. Due to these vanishingly small concentrations, targets for analysis must be produced extremely carefully, and can only be analysed in high-resolution accelerator mass spectrometers [AMS], which can measure down to concentrations of 10^{-15} atoms.

Six cosmogenic isotopes are commonly used for geomorphic studies [Tables 2.1 and A.1 and section 2.5.3]. They have a variety of half-lives [including two stable isotopes], making them useful over timescales from 10^3 - 10^6yrs. Resolution is typically high, particularly where more than one isotope is used [section 2.5.2]. TCN targets are ubiquitous: the major targets being quartz and olivine, although cosmogenic isotopes are also produced from garnet, pyroxene, hornblende and calcite [Table 2.1]. TCN analysis can be used on rock surfaces, and also for loose sediment, such as clasts in moraines, stream terraces and alluvial fans. *In situ* cosmogenic isotopes have been shown to be consistent with each other [e.g. Nishiizumi et al. (1991); Phillips et al. (1991)] and show good correlation with other dating techniques [e.g. Kubik et al. (1998); Ivy-Ochs et al. (2001)].

The main disadvantage is the extremely low concentrations of TCNs: typically 10^{-14} atoms g^{-1} target mineral. Quite large samples are required, particularly for analysing young, or low-altitude features. *In situ*-produced TCNs may be easily swamped, by the larger concentration of the same TCN produced in the atmosphere [as for ^{10}Be], or by the normal stable isotope, pushing the ratio of TCN to stable isotope below the detection limit of the AMS. Inheritance from previous exposure or from deep-seated muon-production can be a major problem. Thus although many isotopes are produced cosmogenically, only six TCNs are commonly used for geomorphic purposes: ^{3}He, ^{10}Be, ^{14}C, ^{21}Ne, ^{26}Al and ^{36}Cl.

The AMS measures the ratios, R, of the cosmogenically-produced isotopes to the naturally-occurring isotope [e.g. ratio of ^{26}Al:^{27}Al]. The production rate of each isotope at the sample site is calculated, by scaling the atmospheric nuclear disintegration rates to the sample latitude and elevation [section A.3]. Using the measured isotope ratios and the calculated production rates, apparent exposure ages or erosion rates can be calculated for the samples [section 2.5.1]. Corrections must also be made for shielding of the sample, by topographic obstructions, snow or sediment, or 'self-shielding' if the sample was taken from a sloping surface, or is very thick [section A.4].

Complex exposure, punctuated by one or more periods of burial, can be identified only by using two or more isotopes. Although estimates can be made for the period of burial and exposure, a unique solution is not possible with only two isotopes.

2.5.1 Calculation of exposure ages and erosion rates

The full calculations used in the cosmogenic isotope analysis are in Appendix A. Hence this overview occasionally refers to equations [Eqn. A.*] that are not in this chapter, but may be found at the end of this thesis.

The concentration of any cosmogenic nuclide increases through time as long as the sample remains in the productive zone near the surface. For a sample that remains at the surface, the rate of increase is the surficial production rate at the specific sample latitude and elevation [section A.3]. The concentration of radiogenic TCNs, e.g. ^{10}Be

and ^{26}Al, also *de*creases exponentially with time, as the nuclide decays. For very old samples [exposure age $\geq$ nuclide half-life], the rate of decay will equal the rate of production, and the concentration of the TCN remains constant: 'secular equilibrium'. However, for younger samples, an apparent 'exposure age' can be calculated: the amount of time that the sample has been exposed at the surface. For stable TCNs, e.g. ^{3}He, this is the measured TCN concentration divided by the production rate. For radiogenic isotopes, radioactive decay must also be considered.

If erosion is negligible, the sample can be assumed to have remained at the surface throughout. The minimum **apparent exposure age** of a sample exposed continuously at the surface may be calculated by rearranging Eqn. A.16 to give:

$$\boxed{t_{exp} = -\frac{1}{\lambda} ln \left[1 - \frac{N(t)\lambda}{P_0} \right]} \tag{2.23}$$

where
t_{exp} is the [minimum] apparent exposure age of the sample, in years
λ is the radiogenic decay constant [$= 1/t_{1/2}$], in yr^{-1}
$N(x,t)$ is the number of atoms of the cosmogenically-produced isotope at a depth x [cm], and time, t [yrs]
P_0 is the original production rate, calculated from Eqn. A.1 or A.3.

If the length of the exposure is known, then Eqn. A.15 can be used to estimate the long-term average erosion rate during the exposure. For samples that have been irradiated for a long time [$t \gg 1\,(\lambda + \mu\varepsilon)$], then Eqn. A.14 simplifies (Lal, 1991) to:

$$N(x,t) = \mathrm{e}^{-\mu x} \frac{P_0}{\lambda + \mu\varepsilon} \tag{2.24}$$

where
μ is the absorption coefficient of the rock, in cm^{-1}: $\mu = 1/z*$: $\mu = \rho/\Lambda$
ε is the [assumed constant, long-term maximum] erosion rate of the TCN, Myr^{-1}

This is the steady-state case, and hence after long term irradiation, samples will attain secular equilibrium. Rearranging Eqn. 2.24 gives the steady-state **maximum erosion rate**:

$$\boxed{\varepsilon = \frac{1}{\mu} \left[\frac{P_0}{N} - \lambda \right]} \tag{2.25}$$

Production rates of *in situ* TCNs vary considerably across the planet, due to variations in the geomagnetic field which modulates the incoming cosmic radiation [section A.3]. Most importantly, production rates vary drastically with both latitude and elevation.

Scaling equations modify the production rates, which are modelled at sea level and high latitude (SLHL), for production at the specific sampled site. However, the exact values of the scaling factors at SLHL are debated.

A plethora of scaling variations exists [Table A.2], making it hard to choose the most reliable and appropriate method to scale production for collected samples. This project uses the nuclear disintegration rates from Lal (1991), scaled using Nishiizumi et al. (1996) data, which were derived from samples collected near my study area, in the Sierra Nevada, California. However, Nishiizumi et al.'s samples were collected from considerably higher altitudes, and in the light of the scaling debate [section A.3], I have compared them with production rates calculated from alternative scaling factors, and from the Dunai (2000) disintegration rates [Table 6.8].

2.5.2 Two-isotope systematics

If multiple nuclides are used, erosion rates can be constrained more closely than by using a single TCN. Comparison of exposure ages elucidates possible periods of burial between exposures, reveals potential contamination, and may indicate where inheritance has occurred. The value of the comparison depends on the use of nuclides with widely differing half-lives, as the difference in the decay rate affects the resolution of the nuclide over different time scales. As well as being relatively simple to prepare together from quartz samples, the ^{10}Be / ^{26}Al pair used in this thesis make a very useful comparison [$t_{1/2}$: ^{10}Be 1.5Myr; ^{26}Al 0.7Myr].

2.5.2.1 Erosion Island plot

Figure 2.31 shows a log-normal Erosion Island plot for a series of samples. The plot provides a quick analysis of the samples based on the variation in the relative abundancies of the two isotopes, e.g. N_{26} / N^*_{10} for ^{26}Al and ^{10}Be [section 6.2.2]. N^*_{10}, scaled to production at sea level and high latitude, is plotted on a log scale along the horizontal axis. Since the ratio of the two production rates and the half-lives are known, the variation in the ratio of the two isotopes through time may be estimated, depending on the erosion history of the sample.

With constant erosion, a sample will move towards the ground surface at a constant rate. Assuming production by spallation, the variation in the ratio of the TCNs is given by:

$$\frac{N_{26}}{N^*_{10}} = \left[\frac{\left(\frac{P_{26}}{\lambda_{26}}\right) + \frac{\varepsilon}{\mu}}{\left(\frac{P_{10}}{\lambda_{10}}\right) + \frac{\varepsilon}{\mu}} \right] \tag{2.26}$$

where P_{26} is the production rate of ^{26}Al, in atoms g^{-1}SiO$_2$ yr^{-1} at the sample site
λ_{26} is the decay constant of ^{26}Al [$= 1/t_{1/2}$], in yr^{-1}
ε is the erosion rate [constant], in cmyr^{-1} and
μ is the absorption coefficient of the sample, in cm^{-1}, where $\mu = \rho/\Lambda$.

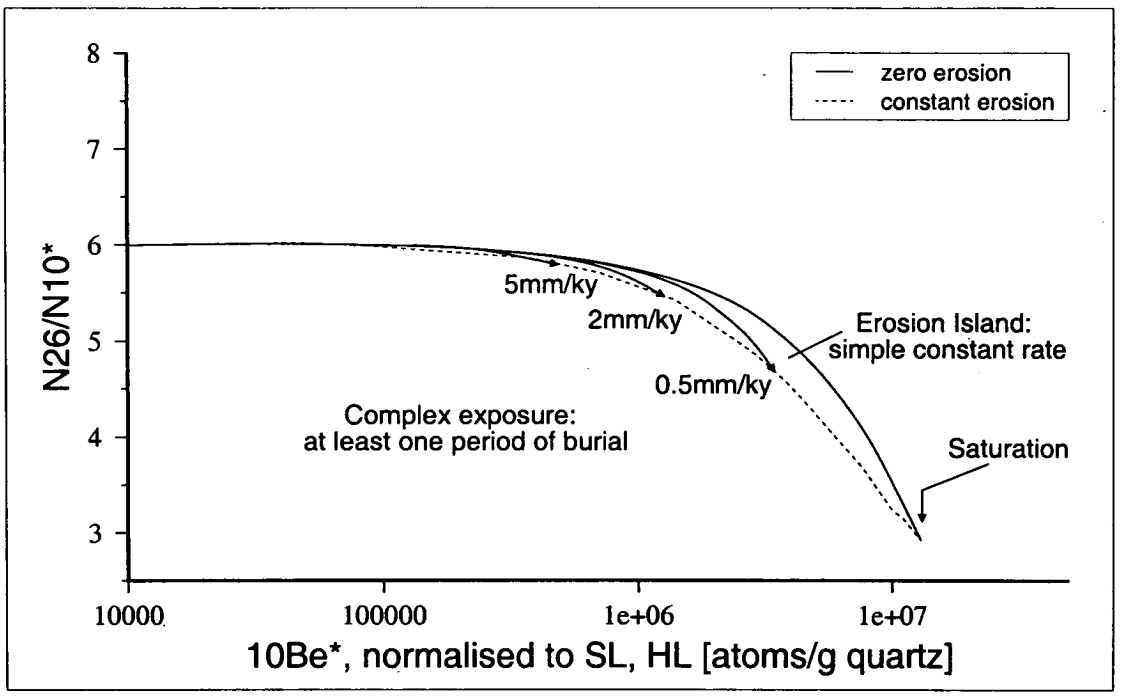

Figure 2.31: *Model Erosion Island plot.*
Log-normal plot of N_{26}/N_{10}^{*} *ratio against log* N_{10}^{*} *[blank-corrected].*
Samples plotting within the erosion island have experienced only a simple erosion history, and can be modelled by constant erosion rate trajectories, as shown.
Samples plotting below the island have undergone complex erosion - suggesting at least one period of burial between exposures. [^{26}Al *decays faster than* ^{10}Be*, and hence ratio of isotopes drops during burial: see text].*
Samples which fall above the zero erosion line imply large uncertainties in, usually, the N_{26} *value, which may be due to the limitations of AMS for young or rapidly eroding samples, or indicate contamination.*

In the case of a sample that has experienced no erosion, ε=0 in Eqn. 2.26, and the sample remains at the surface throughout its exposure. Hence the equation simplifies to:

$$\frac{N_{26}}{N_{10}^{*}} = \left[\frac{\left(\frac{P_{26}}{\lambda_{26}}\right).\left(1-e^{-\lambda_{26}t}\right)}{\left(\frac{P_{10}}{\lambda_{10}}\right).\left(1-e^{-\lambda_{10}t}\right)} \right] \tag{2.27}$$

The solid line in Fig. 2.31 represents the locus of points that experience zero erosion; the broken line is the constant erosion locus. A sample falling on the zero erosion curve has never been buried or eroded, and the exposure age may be read from the horizontal axis. The erosion history of any sample within the steady-state 'erosion island' between the lines may be modelled with a unique production rate curve and a steady erosion rate; the exposure age corresponds to the distance travelled along that curve.

Any sample plotting *above* the erosion island has a higher ratio of [here] ^{26}Al to ^{10}Be than the initial production ratio. This cannot be explained by inheritance or

by any combination of erosion and burial, as these all tend to increase the proportional concentration of the *longer*-lived isotope in the sample. However, for young or rapidly eroding samples, the low concentrations of ^{26}Al cause a large uncertainty in N_{26}. The erosion island is so narrow in this region that a high N_{26} / N^*_{10} may reflect the limitations of AMS resolution with low isotopic concentrations [e.g. Small et al. (1997)]. Samples plotting far above the island, however, may reflect a larger source of error, or possibly contamination.

A sample plotting *below* the erosion island has experienced a more complex erosion history. No unique curve of constant erosion can be drawn: exposure has been interrupted by at least one period of burial [see also Fig. 2.32]. The longer-lived isotope is proportionately enriched in the sample, as it decays less than the shorter-lived isotope during burial. This enrichment of the longer-lived isotope [here ^{10}Be] is also evident in plots of ^{26}Al vs. ^{10}Be age [e.g Fig. 6.14].

Complex exposure may be due to a single burial, a series of burial and exhumation events or relatively shallow burial, where some degree of TCN production still occurs. Although it is impossible to derive a unique erosion history with only two isotopes, Bierman et al. (1999) outline a simple method to estimate the *total* lengths of time for which a sample has been buried and exposed.

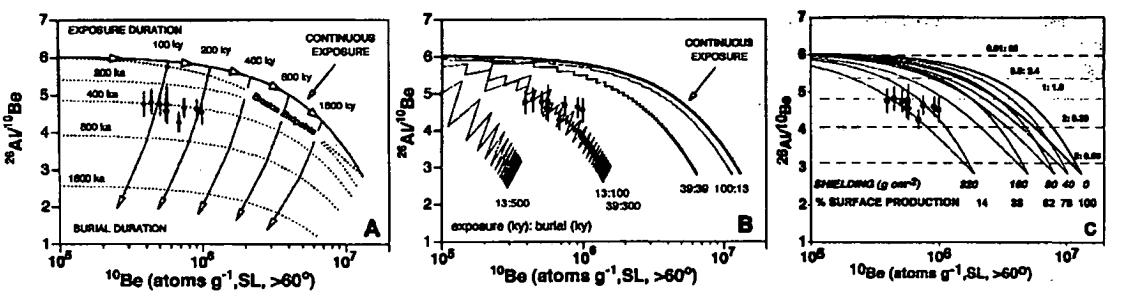

Figure 2.32: *Different complex exposure histories which result in low N_{26} / N_{10}* values, after Bierman et al. (1999).*
A. Samples are exposed at the surface, and then buried below the production zone. No further TCN production occurs.
B. Samples experience a series of periodic exposures separated by burial events. Trajectory of sample on plot reflects the relative length of the burial and exposure events.
C. Samples are not buried completely below the surface production zone, and hence some lower rate TCN production occurs during burial [section A.1]. Samples plot further to left as more deeply buried, since production is a lower proportion of the surface rate.

In principle, Bierman et al.'s method uses the different decay rates of the two isotopes to calculate a common solution to Equations 2.28 and 2.29. Radioactive decay occurs throughout, but production only occurs while a sample is exposed. Iterative solution of the equations gives an estimate of how long *in total* the sample was exposed to cosmic radiation, t_e, and the *total* burial time, t_b.

$$N_{Be} = \frac{P_{Be}}{\lambda_{Be}} [1 - exp(-\lambda_{Be} t_e)] exp(-\lambda_{Be} t_b) \tag{2.28}$$

$$N_{Al} = \frac{P_{Al}}{\lambda_{Al}} [1 - exp(-\lambda_{Al} t_e)] exp(-\lambda_{Al} t_b) \tag{2.29}$$

where N_{Be} and N_{Be} are the measured abundancies of ^{10}Be and ^{26}Al [N_{10}* and N_{26} above, respectively], in atoms g^{-1}
P_{Be} is the production rate of ^{10}Be, in atoms g^{-1} yr^{-1}
λ_{Be} is the decay constant of ^{10}Be, in yr^{-1}
t_e and t_b are the total summed exposure and burial times, respectively, in yrs.
The method is only approximate, as it assumes that the sample was exhumed and buried virtually instantaneously, and also that no production occurred during burial. As explained by the more sophisticated method of Granger and Muzikar (2001), TCN production, particularly by muons, can add considerably to the TCN content at depth, resulting in an underestimation of the burial time relative to the total exposure. This is more marked with older samples, and where a sample has not been exposed for long prior to its burial [muon production during burial is a greater proportion of the total TCN content: their Fig. 2]. However, although the errors are large, the Bierman et al. (1999) method is a powerful tool to estimate the magnitude of a possible burial [see section 6.5.1].

2.5.2.2 Al-Be comparison age plots

An alternative method of presenting ^{26}Al and ^{10}Be exposure age data is to plot the ^{26}Al age against the calculated ^{10}Be age for each sample [e.g. Fig. 6.14]. Points with near identical ^{26}Al and ^{10}Be ages have experienced only a simple erosion history, and have probably not been buried. In contrast, a sample which has a ^{10}Be age far older than its ^{26}Al age indicates that at least one period of burial has occurred [see above]. This also allows ages to be compared to certain marker events of known age [e.g. volcanic eruptions, glaciations etc.].

2.5.3 Previous geomorphic studies using cosmogenic isotopes

Cosmogenic isotopes have been widely used to estimate exposure ages and erosion rates of landforms around the world, and to constrain LEMs, as they provide a valuable method of dating surfaces over the 10^3 to 10^6 year timescale. An example is the escarpment retreat and summit denudation rate estimates from ^{36}Cl studies for the Drakensberg in SE Africa (Fleming et al., 1999). Cosmogenic isotopes have recorded

the lowest known erosion rates in the cold arid deserts of Antarctica [e.g. Nishiizumi et al. (1991); Brown et al. (1991); Brook et al. (1993); Summerfield et al. (1999)]. Exposure ages from Meteor Crater in Arizona showed close similarities between ^{26}Al / ^{10}Be (Nishiizumi et al., 1991b) and ^{36}Cl estimates (Phillips et al., 1991), providing an early confirmation that the TCN technique was viable to date landforms, and internally consistent. TCN analysis also provided estimations of varying erosion rates within the crater, and clear evidence of climatic fluctuations. Examples of some applications most relevant to the work in this thesis are described in the following section.

Bedrock weathering and basin erosion rates: Brown et al. (1995) measured ^{10}Be concentrations in quartz grains of different sizes in streams to estimate a mean erosion rate of 43mMy^{-1} for a fluvial basin in Puerto Rico. Despite high uncertainties, especially in production rates, the TCN work was better constrained than previous estimates based on river gauging [75mMy^{-1}± 50%]. Brown et al. (1995) estimated that landslides accounted for 55% of the sediment flux from the basin. Schaller et al. (2001) used ^{10}Be in fluvial sands to calculate erosion rates for river basins in continental Europe. Their data provides a good estimate of long-term averaged sediment fluxes, and also demonstrates the variation of erosion rates with lithology. Cerling et al. (1999) used ^{3}He in olivines to investigate the size and frequency of debris flows from Prospect Canyon into the Colorado in the Grand Canyon. They revealed an enormous sediment input, and also estimated a recurrence interval of 15 to 2000yrs.

Several workers have addressed the variation of weathering rates with regolith thickness [section 2.4.1]. Small et al. (1997) used ^{26}Al and ^{10}Be to investigate bare bedrock erosion on summit flats in the western US. They obtained very low rates of erosion [mean 7.6±3.9mMy^{-1}] compared to average basinwide erosion rates [e.g. 43mMy^{-1}: Brown et al. (1995)], concluding that relief increases through time. However, bedrock under a covering of ~90cm regolith eroded at almost twice the rate of the bare peaks [here 13.0-14.3±4.0mMy^{-1}] (Small et al., 1999). They argued that regolith increased weathering rates as it held water in contact with the rock for longer. The data implied that the hillslopes were in steady state: a condition attained probably within 2-3My.

Heimsath et al. (1999) used ^{26}Al and ^{10}Be to investigate the variation of soil production rate with soil thickness in northern California. Their results favoured an exponential decrease of erosion rate with soil thickness, although the data did not categorically disprove a 'humped' variation with depth [i.e. that erosion rate reaches a maximum under a finite soil thickness]. They observed a ten-fold decrease in erosion rates for bedrock covered by a metre of soil. Complex exposure of some samples [section 2.5.2] demonstrated that erosion patterns must vary through time. Heimsath et al.'s results implied that while the landscape adjusts quickly [~10ky] to achieve a *local* steady-state soil thickness, adjustment to larger scale tectonic and climatic variations may take up to ~70ky.

However, the use of *in situ* TCNs is not straightforward. Small et al. (1997) showed that summit tors erode predominantly by the episodic removal of rock chips, rather than by uniform downwearing, resulting in a large scatter in erosion rate estimations from any one area. They emphasised the difficulties in differentiating between episodic and uniform erosion of young samples, or those with low production rates, which fall at the left side of the erosion island plot [Fig. 2.31]. However, they showed that averaging results from one area provided a reasonable estimate of the true erosion rate. Bierman

and Gillespie (1991b) noted that widespread range fires in the western US caused large spallations and diffusive loss of noble gases from granite boulders. Unless taken into account, these effects could result in considerable underestimation of exposure ages. Sampling of affected rocks at least 5-10cm below the surface reduced the errors in using gaseous isotopes [e.g. ^{3}He, ^{21}Ne]. While ^{3}He is an appealing isotope to use due to its low detection limit, and also the fact that it can be measured in a normal mass spectrometer, Trull et al. (1995) observed that much of the cosmogenic ^{3}He had been lost from rock exposed in the heat of Death Valley.

Fluvial terraces: Strath terraces may be used to estimate incision rates, by assuming that the terrace exposure age records its abandonment as the river incises. Studies have demonstrated that incision is not constant through time or space, and emphasise the varying fluvial response to external controls. Repka et al. (1997) noted a three-fold variation in incision rates in the Fremont River through time, while Hancock et al. (1999) noted that incision rates in the Wind River decreased almost three-fold downstream. Burbank et al. (1996a) and Leland et al. (1998) used ^{26}Al and ^{10}Be to estimate the response of the Indus River to extremely rapid tectonic uplift near the Nanga Parbat - Haramosh axis [NPHA]. Straths revealed incredibly rapid incision rates, which increased downstream towards the uplift axis, reflecting the variation in uplift rate between the Skardu Basin and the NPHA. Correlation with fission track work and hillslope analysis implied a dynamic equilibrium between fluvial incision and rock uplift rates. A sudden marked increase in incision rates [from 1-6mky^{-1} to 9-12mky^{-1}] during the last 15ky may reflect an increase in discharge or sediment load due to the last deglaciation.

Inheritance: Wide scatter has sometimes been observed in exposure ages calculated from a single terrace, reflecting a combination of cosmogenic build-up prior to the initial erosion and processes which have modified the terrace after its deposition. Anderson et al. (1996) addressed the issue of inheritance acquired either during the erosion, or transport of sedimentary material. Assuming no systematic variation in the source of the material from the upstream catchment, rapid deposition of the terrace, and no post-depositional mixing, they showed that the concentration of ^{26}Al and ^{10}Be within a terrace should fit a logarithmic curve with depth [Fig. 2.33a], reflecting the pattern of post-depositional production [Fig. A.1a]. However, the *inherited* TCN content of samples at any depth should be constant [dotted line in Fig. 2.33a]. Anderson et al. calculated that by amalgamating 30 clasts, a meaningful representative average of the TCN concentration at the terrace surface could be obtained. Moreover, by comparing amalgamated surface samples with those from depth, the component of inherited nuclide abundance could be estimated and removed.

Anderson et al. (1996) demonstrated that amalgamation of surface clasts removed much of the scatter in calculated ages, while as much as 22-43% of the measured nuclide concentration was inherited. Thus surface ages should be considered at best as maxima. Repka et al. (1997) compared estimates of inheritance by measuring both amalgamated surface-depth pairs and a sequence of samples down a profile. While amalgamated surface samples alone overestimated the true age, comparison with subsurface samples allowed them to predict an exposure age within 5% of the true value.

Anderson et al.'s ages were dependent on rapid deposition and no post-depositional modification. The true variation of TCN concentration with depth can be assessed

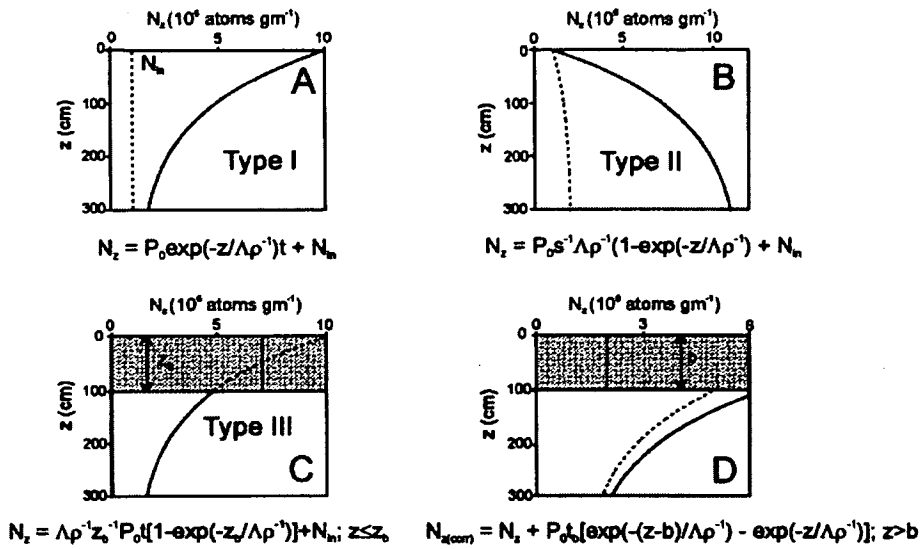

Figure 2.33: *Cosmogenic nuclide depth profiles: correction for inheritance, modified from Phillips et al. (1998). Profiles are modelled for* $N_\varepsilon = 10^6 atoms g^{-1}$; $\rho = 1.5 g cm^{-3}$.
a. Type I: downward decreasing concentrations: geomorphically stable alluvium - short deposition, minimal post-depositional burial / bioturbation. Exposure time, t = 100ky.
b. Type II: downward increasing concentrations: constant [non-instantaneous] burial rate, s. Solid line, $s = 0.001 cm yr^{-1}$; *dotted line,* $s = 0.01 cm yr^{-1}$.
c. Type III: shaded area [100cm thick] is bioturbated, and has a uniform nuclide concentration with depth. Underlying material shows downward decrease in TCN concentration. Dotted line reflects pre-bioturbation profile, for t = 100ky. Uniform profiles also occur where the landform is too young to have accumulated significant TCN concentrations.
d. Shielding of a stable geomorphic surface by a younger deposit [shaded area, 100cm thick - constant TCN conc.]. Dotted line is measured profile, solid line is corrected profile. Burial occurred at 15ka; young deposit $\rho_b = 1.5 g cm^{-3}$.

more accurately by sampling a complete depth profile through the landform. Phillips et al. (1998) demonstrated the importance of sampling continuous profiles. A series of different nuclide concentration profiles may be produced in a landform, depending on its evolution [Fig. 2.33]. Hancock et al. (1999) collected amalgamated samples in continuous profiles through Wind River terraces, using both cobble-sized clasts and sand. They obtained good exponential profiles, and demonstrated an inherited component of 7-20%.

If the inherited nuclide content is assumed to have been acquired wholly during either constant bedrock erosion, or constant fluvial transport, the rate of these processes can be constrained (Anderson et al., 1996). Mean minimum hillslope erosion rates for terraces along the Fremont and Wind Rivers have been estimated as 11 to 130mMy^{-1} (Anderson et al., 1996; Repka et al., 1997; Hancock et al., 1999). Alternatively, if inheritance was due solely to fluvial transport and storage, maximum fluvial transport times for the same terraces were estimated as 548 [Fremont] or 260ky [Wind] (Anderson et al., 1996); 166ky (Repka et al., 1997; Fremont); >10ky (Hancock et al., 1999; Wind).

Knickpoints: Seidl et al. (1997) measured a wide variety of *in situ* nuclides in basalt olivines to investigate the evolution of knickpoints in a Hawaiian channel. Their work

was fraught with difficulties, such as variable loss of gaseous nuclides, stubborn meteoric ^{10}Be, high ^{27}Al concentrations and low Cl contents, so that they were unable to attain a convincing sequence of exposure ages for any single nuclide down the channel. However, the broad pattern of exposure ages agreed with their previous qualitative study (Seidl et al., 1994), implying that knickpoint retreat, at a loosely-constrained rate of 0.4mmyr^{-1}, had dominated incision. Above the knickpoint, they estimated a bedrock incision rate of 0.01mmyr^{-1}. Old ages downstream correlated with large boulders in the channel, which they believed protected the channel bed from other incision processes; a conclusion consistent with the observations of Granger et al. (2001a).

Weissel and Seidl (1998) used ^{26}Al and ^{10}Be to investigate knickpoint retreat in the Macleay River, SE Australia. Although incision rates at the knickpoint lip were up to three times higher than those calculated from upstream straths, they were dwarfed by the downwearing of the gorge-head, where rapid erosion occurred by collapse of heavily-jointed rocks. Complex exposure of some downstream straths implied that, unlike the upstream straths, they were periodically covered by major sediment volumes from mass failure of the steep banks.

Channel bed erosion: Hancock et al. (1998) attempted to use ^{26}Al and ^{10}Be to compare medium-term [1.5-2ky] incision rates in the Indus middle gorge with present-day abrasion rates estimated from drill-holes in the channel bed. Their corrections also had to include shielding due to the seasonal variation in water depth. The production rates of ^{10}Be were so low as to preclude its use, and only three of their samples contained enough quartz to date using ^{26}Al. Their erosion rates [0.25-0.5mky^{-1} using TCNs; 0-4mky^{-1} using drillholes] were considerably lower than those calculated by Burbank et al. (1996a) and Leland et al. (1998), implying a considerable variation in incision through time, perhaps linked to glacial climatic cycles.

Fluvial incision rates using cave sediments: Granger et al. (1997) described a novel method using TCN concentrations in cave sediments, deposited in response to varying river water elevations, to constrain fluvial incision. By assuming the sediment had not experienced prior burials, and had been rapidly deposited below the production zone [>10m for muons], they estimated the burial date, and previous exposure period, of the sediment. Application to the sediment in dolomite caves near the New River, Virginia yielded an average incision rate of 27.3±4.5mMy^{-1}, and also implied a small regional tectonic tilt. Extrapolation of the prior TCN concentration allowed estimation of the bedrock exhumation rates in the catchment of the river. In a later paper, Granger et al. (2001b) investigated more extensive deposits in the enormous Mammoth Cave, Kentucky, which they used to study the Green River. The high resolution allowed correlation with climatic events, implying that evolution of the Green River was dominated by reorganisations of upstream rivers in response to major climatic events. They also demonstrated that erosion in the stream catchment had remained nearly constant [2-7mMy^{-1}] despite major variations in the incision rate.

Glacial chronology: Boulders in moraines and glacially-striated surfaces have been dated using ^{36}Cl, ^{26}Al and ^{10}Be by many workers to constrain the timing of glacial advances, and to correlate them with regional or global climatic fluctuations. North American examples include studies in the Sierra Nevada [e.g. Nishiizumi et al. (1989); Phillips et al. (1990, 1996); section 3.1.1]; Rocky Mountains [e.g. Gosse et al. (1995); Phillips et al. (1997)]; New Jersey [e.g. Clark et al. (1995)] and Baffin Island (Bierman

et al., 1999). Examples from other parts of the world include Stone et al. (1998) who dated nunataks in Scotland, and Barrows et al. (2001) in the Snowy Mountains, Australia.

Tectonics: Several workers have dated offset alluvial fan surfaces and streams to estimate rates of fault slip. Ritz et al. (1995) used ^{10}Be to date gneissic boulders embedded in alluvial fan surfaces offset by the Bogd Fault in Mongolia. Field observations and aerial photographs demonstrated a persistent sense of lateral offset of both streams and ridges. By assuming no prior burial of the sediment, rapid fan-formation and no post-depositional TCN loss, the ^{10}Be concentration provides a minimum exposure age for the landform surface. Ritz et al.'s data suggested that all the fan surfaces approached steady-state saturation, in which case the youngest surface has the most closely constrained age. As their exposure ages were minima, they used the oldest boulder on that surface to calculate a rate of lateral slip. The TCN approach yielded slip rates far lower than those previously estimated from assumptions of fluvial responses to climatic variations [1.2 vs. 22mmyr^{-1}]. However, these slip rates were consistent with stream formation occurring during major pluvial periods.

Similar approaches have used ^{10}Be and ^{26}Al to investigate other strike slip faults [e.g. Siame et al. (1997); van der Woerd et al. (1998)], compressional faults [e.g. Brown et al. (1998)] and extensional faults [e.g. Bierman et al. (1995a); Zehfuss et al. (2001)] in a variety of different locations. In each case, the *in situ* nuclides have allowed estimation of slip rates and recurrence intervals, and elucidated the relative roles of climatic and tectonic influences on the developing alluvial systems.

Jackson et al. (2002) measured *in situ* ^{10}Be concentrations in quartzite sarsen stones on the northern tip of South Rough Ridge, Otago, an asymmetric fold formed over a propagating thrust [Fig. 2.13]. Their data yielded estimates of fault uplift rate [0.10-0.15mmyr^{-1}] and an overall mean tip propagation rate [1.0-2.0mmyr^{-1}], although they favoured the interpretation of tip propagation occurring in discrete periods. However, their estimates were based on very few data points [e.g. uplift rate calculated from the elevation of one sample] spaced only over the northern 600m of the ridge, and did not use the wind gaps exposed in the scarp to the south [Fig. 2.13]. Complex exposure could not be assessed as they have as yet only used a single nuclide. Jackson et al.'s data does however, imply some of the lowest erosion rates observed outside Antarctica [$\leq$0.6mmky^{-1}], suggesting that additional data from the area should give robust constraints on geomorphic processes.

Zreda and Noller (1998) measured ^{36}Cl concentrations in a profile down the limestone scarp of the Hebgen Lake fault, and obtained a series of discrete ages which correlated with horizontal weathering bands [Fig. 2.34]. They believed these bands demonstrated the gradual exhumation of the scarp in successive earthquakes [e.g. Jackson et al. (1982)], the most recent of which occurred in 1959. Their model ages suggested that earthquakes had occurred at this location 0.4, 1.7, 2.6, 7.0, 20.3, and 23.8 ka, implying clustering of events through time [e.g. Machette et al. (1991); Dorsey et al. (1997)]. The 2.6ka event correlated with an independent estimate from diffusional modelling. However, later trench studies and other cosmogenic work in the area have cast considerable doubt on Zreda and Noller's findings [e.g. Hecker et al. (2000)].

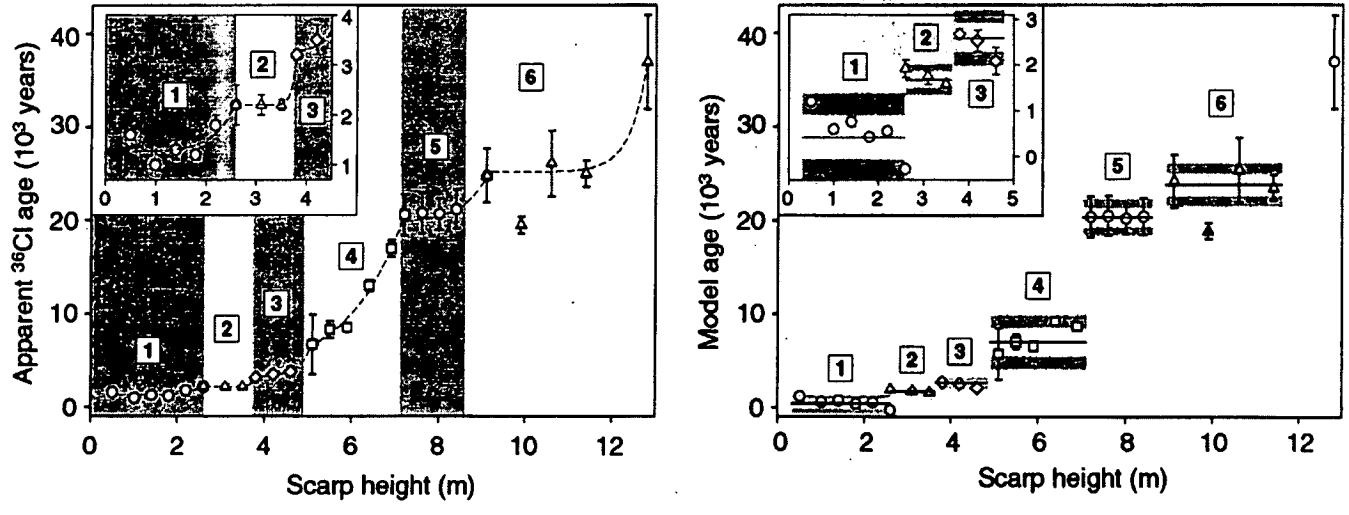

Figure 2.34: *Cosmogenic ^{36}Cl profile down the Hebgen Lake fault, from Zreda and Noller (1998).*
Group 1 is from the 1959 scarp; groups 2 to 6 are from the pre-1959 part of the scarp, 20 m east of group 1. Sections 1 to 6 were defined in the field using the degree of surface weathering and colouration. Individual apparent ages [left] form a pattern expected for scarps formed by recurring faulting. Error bars [1 SD] represent overall analytical uncertainty. Exponential best fits [dashed] delineate a trend within each group.
Model ages [right] form six groups whose means [solid lines] are statistically different at the 1 level [white bands]. At the 2 level [gray bands], groups 5 and 6, 2 and 3, and 1 and 2 are statistically indistinguishable. These parts of the scarp are considered to have been formed by different earthquakes, on the basis of differences in surface appearance.

Chapter 3

Introduction to fieldwork on the Volcanic Tableland

This project examines the drainage patterns which have developed around a fault array studied by Scholz et al. (1993) and Dawers and Anders (1995), and includes surveys of the main faults in the central overlap of the array, which put the streams into tectonic context [Chapter 4]. Differential GPS surveys of the streams are used to assess the interaction between their development and the evolution of the faults within the array [section 4.2 and Chapter 5]. *In situ* cosmogenic isotopes have been used to constrain the occupation of the channels, and hence some of the rates of stream and fault evolution [Chapter 6].

This chapter introduces the field area, on the Volcanic Tableland, Owens Valley, eastern California. The first section [3.1] places the Tableland in its regional setting. The glacial chronology of the area, which is important for considering the controls on the stream initiation and occupation [e.g. Pinter and Keller (1995)], is outlined in section 3.1.1 and Table 3.1. The subsequent sections provide a wider context in terms of both the regional drainage patterns [section 3.1.2] and constraints on the regional tectonic framework [section 3.1.3]. The Volcanic Tableland is introduced in section 3.2, which outlines the current understanding of its evolution and lithological features, as well as previous work on the faults and streams on its surface.

Section 3.3 outlines the collection of the data that is presented in Chapters 4 and 5. In particular, the aspect ratio, AR, which has been used as a quantitative assessment of the variation in stream cross-section, is defined. The methods used to collect the field data are described in more detail in Appendix B. Section B.1 briefly highlights the salient points of differential GPS surveying, and discusses the approach used to presenting this 3D data. Section B.2 outlines the laboratory preparation of ^{10}Be and ^{26}Al targets for AMS analysis, carried out at Edinburgh University.

3.1 Regional Setting: Owens Valley, California

Owens Valley lies at the extreme western margin of the Basin and Range, between the Sierra Nevada and the White-Inyo Mountains. The valley floor is 20-30km wide, and around 1230m above sea level.

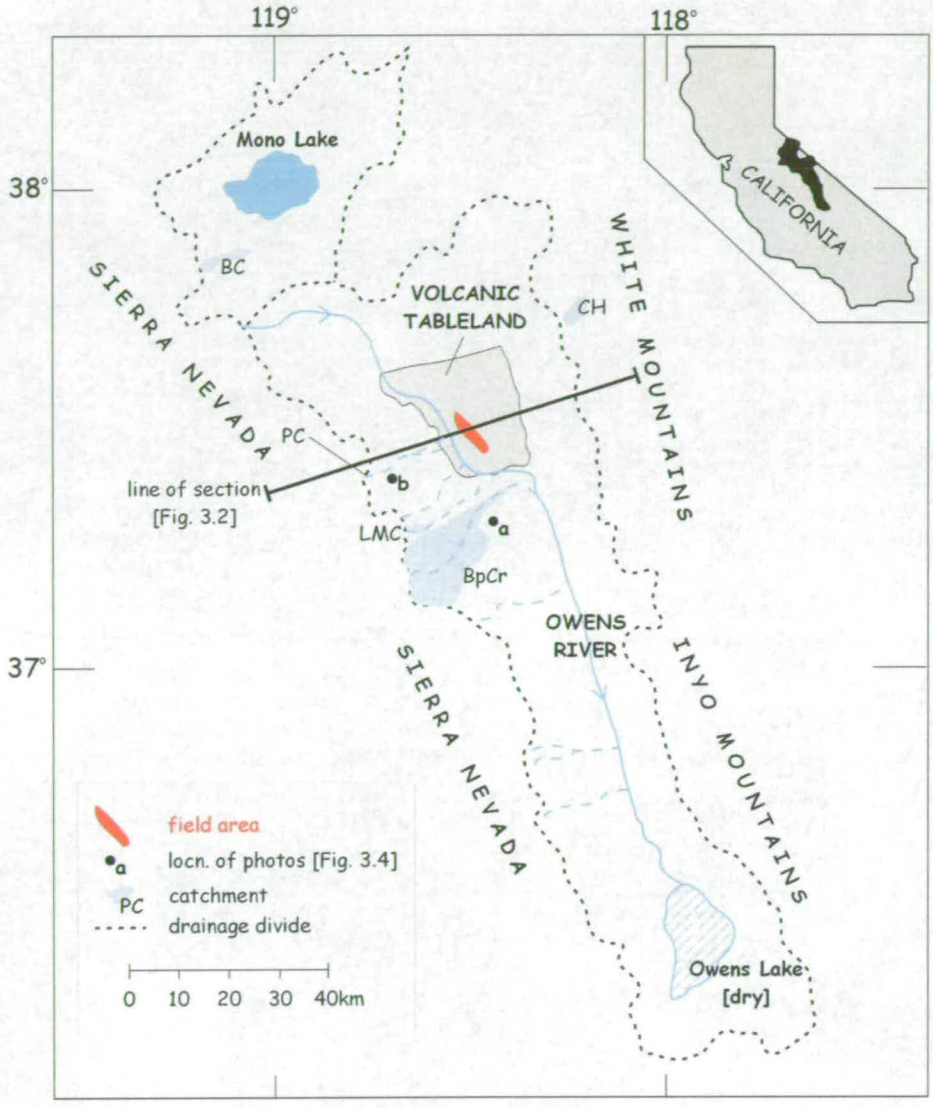

Figure 3.1: *Map of Owens Valley, showing the location of the field area and sites of glacial studies in the eastern Sierra Nevada, modified from Phillips et al. (1996); Berry (1997).*
Study area [red] is on the Volcanic Tableland, in the centre of northern Owens Valley [see also Fig. 3.5].
Glacial study sites - BC: Bloody Canyon; LMC: Little McGee Creek; PC: Pine Creek; BpCr: Bishop Creek. McGee, Pine and Bishop Creeks drain into Owens River and hence to Owens Lake. Bloody Canyon drains into Mono Lake, north of the headwaters of the Owens River (Phillips et al., 1996). Owens Lake is supplied predominantly from the eastern Sierran streams; little supply comes from the arid western flanks of the White Mountains.
Owens Lake is now desiccated, following the development of the LA aqueduct in 1913, but overflowed repeatedly during the last 800ky, supplying four lakes to the southeast. Mono Lake may have initially been connected to Owens Lake via an ancestral eastern branch of the Owens River, which flowed between the Tableland and the White Mountains (Smith and Bischoff, 1997).
Note location of the sketch section in Fig. 3.2 and the photographs in Fig. 3.4. The Volcanic Tableland [grey] is shown in more detail in Fig. 3.5.

The bounding ranges rise to over 4300m, the products mainly of extensional faulting along range-bounding faults [Fig. 3.2]. The Sierras are the erosional remnant of a batholith, made of a series of discrete acidic plutons and associated contact metamorphic rocks [e.g. Bateman (1965)]. Sedimentary and mafic igneous rocks make only a small proportion of the range. Heavy glaciation has resulted in steep slopes and knife-edged ridges, while huge moraines have built out into the valley from deeply-incised canyons. In contrast, the White Mountains consist of a thick sequence of folded and faulted Precambrian to Cambrian sedimentary rocks. Most of the precipitation which rises from the Pacific is dropped on the Sierras, and hence glaciation in the White Mountains has been considerably less pronounced. Similarly, modern streams are smaller, and drain smoother, more rounded slopes. The floor of Owens Valley covers up to 2000m of Cenozoic sediment [e.g. Bateman (1965)], deposited in the subsiding trough between the range-front faults. The climate is semi-arid, with mean annual temperatures on the valley floor of 3-11°, and only 15-20cm annual precipitation, most of which falls as snow in winter, or in brief heavy thunderstorms in summer (Bateman, 1965; Berry, 1997; Smith and Bischoff, 1997). Hence erosion rates on the valley floor are typically very low.

Intrusion of the Sierra Nevada batholith during the Cretaceous was followed by a period of erosion, exposing the batholith amidst a broad region of low relief. Westward tilting of the Sierras and the surrounding region began slowly during the late Cretaceous to Eocene, with streams draining westwards across the northern Sierras during Eocene times [~50-45Ma; Bateman and Wahrhaftig (1966)]. More rapid tilting occurred during the Miocene (Bateman, 1965). Basalt flows and some rhyolitic tuffs were extruded locally onto the erosional surface from around 10Ma [e.g. Bateman (1965); Putnam (1960); Lueddecke et al. (1998)], possibly marking the onset of Basin and Range extension to the east [Fig. 3.3a]. Regional tilting gave way to active surface faulting on the eastern Sierra range-front possibly around 5-6Ma, as inferred from the tilting of sediments in valleys to the west of the Sierras [e.g. Unruh (1991)], creating space for deposition in the Owens Valley [Fig. 3.3b]. Extensional faulting on the eastern Sierra Nevadan faults probably increased until the Pleistocene (Bateman, 1965), during which time hundreds of metres of sediment were deposited in the basin, today recording syn- and post-depositional westward tilting: e.g. 30° dip of Coso Formation, 6° dip of Waucoba lake beds [Bachman (1978)].

Extension subsequently began on the eastern side of Owens Valley, forming the White and Inyo Mountains [Fig. 3.3c]. Increased erosion accompanying uplift produced thick conglomerate sequences, deposited in huge fans into the subsiding basin (Lueddecke et al., 1998). While early sedimentation in the Waucoba lake was sourced from the Sierras, higher beds record a switch to almost solely White-Inyo sedimentary input (Bachman, 1978). Extensional faulting in the Mono Basin to the north began around 3-4Ma, implying a regional event.

After the onset of White-Inyo range faulting, sediments and stream patterns record an increasing *easterly* tilt within Owens Valley, as motion on the White-Inyo Mountain faults accelerated. The valley floor has been gradually warped into a broad arch between the faults, which is particularly evident on the Volcanic Tableland, the southwest part of which dips west towards Round Valley, while the rest dips southeast Fig. 3.2 and (Bateman, 1965; see section 3.2). Although most of the motion on the range bounding faults has been extensional, recent events have shown a high proportion

of lateral motion [e.g. 1872 Owens Valley (Lubetkin and Clark, 1988; Beanland and Clark, 1994) and 1986 Chalfant Valley earthquakes, (Lienkaemper et al., 1987; DePolo et al., 1991; Lueddecke et al., 1998)].

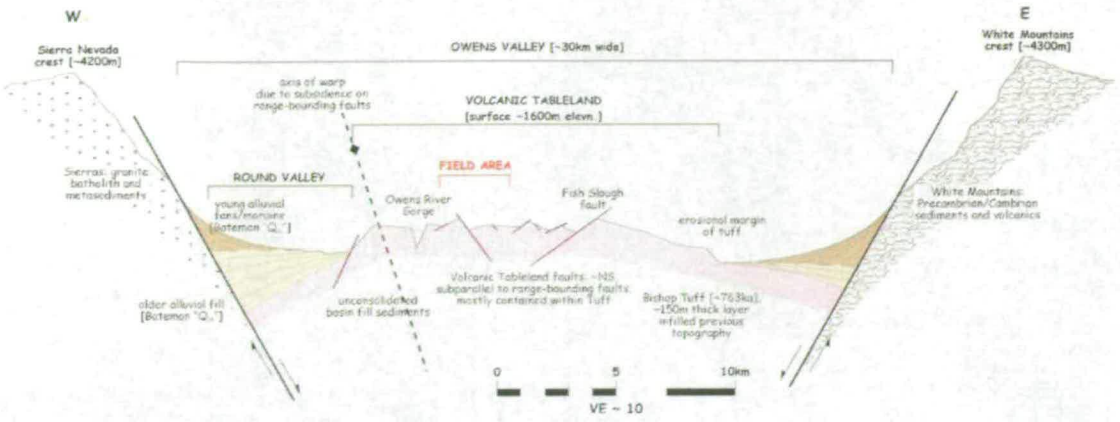

Figure 3.2: *Sketch cross-section of Owens Valley, showing structure of Volcanic Tableland. The Volcanic Tableland is the erosional remnant of a sheet of Bishop Tuff, extruded from the Long Valley caldera to the north, 759ka (Sarna-Wojcicki et al., 2000). The ignimbrite infilled the surface topography of the pre-existing basin fill: largely unconsolidated sediments, forming a sheet with an almost flat surface [hence "Tableland"].*
Extensional motion on the range-bounding faults at the base of the Sierra Nevada and White Mountains has warped the basin fill into a broad arch. At the margins of Owens Valley, Bishop Tuff has been covered by thick layers of alluvial material and moraines, sourced from both the Sierra Nevada and the White Mountains. In the centre of Owens Valley, the Tuff remains visible as a pink sheet [see Fig. 3.4a]. the Owens River has incised a deep gorge in the west of the Tableland. The structure of the Tableland and its evolution is discussed further in Fig. 7.9 on page 325, using observations from this project.
Faults on the Tableland, [discussed in Chapters 4 and 5], trend N-S, and have formed in response to the warping of the Tuff sheet due to motion on the range-bounding faults. Most of the Tableland faults are contained within the Tuff, though some [e.g. Fish Slough fault] break the entire layer, as shown by the shape of their displacement profiles (Dawers and Anders, 1995) and the occurrence of springs at the base of the scarps.

Rhyolitic volcanism accompanied the extension, with widespread deposition of several discrete ash layers over the region from craters to the north. Basaltic cinder cones and associated flows also formed along some faults (Bateman, 1965). Around 759ka, a huge eruption of the Long Valley caldera to the north extruded over 750 cubic kilometres of rhyolitic Bishop Tuff (Putnam, 1960; Bateman, 1965; Pinter, 1995; Wilson and Hildreth, 1997; Sarna-Wojcicki et al., 2000; Legros et al., 2000; see section 3.2). Ash was carried over much of western and central northern America, and pumice deposits can be found several hundred kilometres to the south. A thick sheet of ignimbrite forms the plateau of the Volcanic Tableland in the centre of Owens Valley, a few miles north of Bishop, which forms the focus of this study [Figs. 3.1, 3.2 and 3.4; section 3.2].

Climate changes have been responsible for much of the shaping of the Owens Valley landscape [e.g. Bradbury (1997)]. Glaciation may have begun in the Sierra Nevada as early as 3.2Ma, but certainly periodic glaciations dominated the late Quaternary history. Small alpine glaciers formed in high cirques, and their fluctuations are recorded by thick moraine sequences all along the Sierras, sourced from canyons

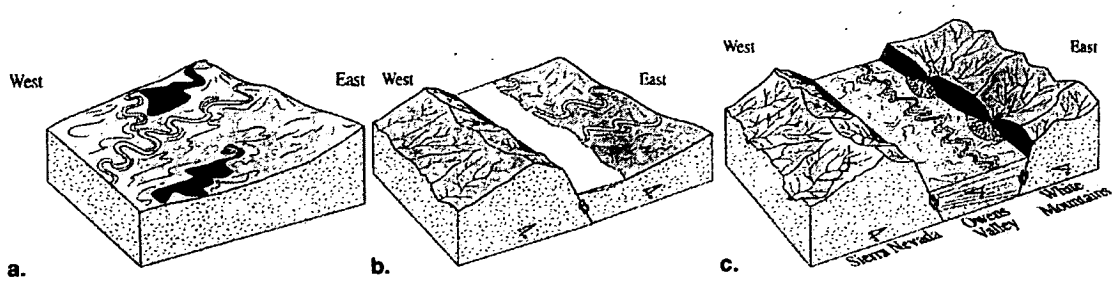

Figure 3.3: *Schematic block diagrams of the evolution of the Owens Valley area, modified from Lueddecke et al. (1998). The general locations of range-bounding faults and the tilt-polarity of each block are shown for each stage. The dates given by Lueddecke et al. (1998) for these stages have been questioned by other studies in the area.*
a. Early to Mid-Tertiary: regional planation, and extrusion of some local basalt and rhyolitic tuffs.
b. ?~6→3Ma: westward block tilting and opening of the Owens Valley. Earliest known sediments are Coso Formation: 2.5-6Ma. Sediment was derived predominantly from the Sierras [e.g. Waucoba lake beds] implying significant relief. Syn- and post-depositional westward tilts are preserved in Owens Valley sediments.
c ?~3Ma→present White-Inyo Mountain faults began to move, causing huge erosion from the uplifting range, and deposition of fanglomerates in the rapidly subsiding basin. Basin floor deposits record an overall easterly dip from this time onwards. WMtn fault stepped basinward, uplifting and dissecting previous alluvial deposits. Recent shift to more lateral motion on the faults.

incised several hundred metres into the range front. In contrast, considerably lower precipitation meant that glaciation in the White Mountains was insignificant until the later Pleistocene, and then never as widespread as in the Sierras (Bateman, 1965; Lueddecke et al., 1998)].

3.1.1 Glacial chronology

Despite the application of many techniques of both absolute [e.g. Bailey et al. (1976); Dalrymple et al. (1982); Dorn et al. (1987, 1990); Phillips et al. (1990); Zreda and Phillips (1995); Phillips et al. (1996); Smith and Bischoff (1997)] and relative dating [e.g. Blackwelder (1931); Sharp and Birman (1963); Burke and Birkeland (1979); Bursik and Gillespie (1993); Berry (1994); Pinter et al. (1994)], the timing of Sierra Nevadan glacial events remains the subject of debate [Table 3.1]. Much of this uncertainty stems from the fact that cold periods produced a series of small alpine glaciers, rather than a single large ice sheet, in the Sierras, and that moraines are inherently temporary, being overprinted or destroyed by later advances. The best evidence is preserved in locations where ice streams took slightly different routes in subsequent cold periods [e.g. Bloody Canyon: Sharp and Birman (1963)]. However, there are few locations where all workers agree on the assignment of even relative ages by weathering and geomorphic techniques [e.g. summaries of relative dating approaches in Berry (1994)]. Attempts at absolute dating of the moraines have been contentious [e.g. Dorn et al. (1987, 1990); Phillips et al. (1990)], particularly as the techniques used were often in their infancy at the

time. The difficulty of correlating evidence between locations remains a major obstacle [e.g. Bursik and Gillespie (1993); Berry (1994)].

Blackwelder (1931) recognised four distinct Pleistocene glacial periods: from oldest to youngest, McGee, Sherwin, Tahoe and Tioga. He also suggested there might be another stage between the Sherwin and the Tahoe. Since then, additional stages have been proposed: the Tenaya [before the Tioga: Sharp and Birman (1963)]; the Mono Basin (Sharp and Birman, 1963), Casa Diablo (Curry, 1971) and the Rovana in Bishop and Pine Creeks (Dorn et al., 1990) each predating the Tahoe stage. However, the assignment of 'full glaciation' status to these advances is questioned [e.g. Burke and Birkeland (1979); Bursik and Gillespie (1993); Berry (1994)]. Several later advances [e.g. Recess Peak, Hilgard, Neoglacial] have also been discussed [e.g. Clark and Gillespie (1995); Zreda and Phillips (1995); Dorn (1996)]. The Sherwin Till immediately underlies the Bishop Tuff, as seen at the Big Pumice Cut [e.g. Sharp and Glazner (1997)], and hence is >759ka (Sarna-Wojcicki et al., 2000). The Tioga glaciation has generally been accepted to fall between 25 and 10ka (Berry, 1994). However, the dating of intermediate events is more complicated [Table 3.1].

Dorn et al. (1987, 1990) used rock varnish to date moraines at Pine Creek [Fig. 3.1], but the accuracy of this technique has been severely questioned [e.g. Gillespie (1988); Bierman and Gillespie (1991a, 1992)]. Phillips et al. (1990) measured cosmogenic ^{36}Cl in moraine crestal boulders at Bloody Canyon [Fig. 3.1]. They proposed that the Tenaya was an early advance of the Tioga glaciation, explaining why it may not have been widely described, as their ages were identical within error. Bursik and Gillespie (1993) proposed that the Tenaya moraines were $\geq$5ky older than the Tioga moraines. More contentiously, Phillips et al. (1990) proposed two distinct phases in the Tahoe stage: the 'older Tahoe' with two advances around 200ka and 140ka; the 'younger Tahoe' centred at 65ka. They also placed the Mono Basin glaciation *between* the two phases of the Tahoe stage, at 110-120ka, which Bursik and Gillespie (1993) and Hallet and Putkonen (1994) argued contradicted the stratigraphic relationships.

Phillips et al.'s younger ages are generally accepted, but major scepticism surrounds their older ages, particularly due to concerns about the erosion of moraine crests and boulders [e.g. Bursik and Gillespie (1993); Hallet and Putkonen (1994)]. Birkeland et al. (1991) and Berry (1994) emphasised the importance of sampling both the crest and the footslopes to assess a moraine's age. The Tahoe stage has been generally the source of much of the argument, with some authors assigning it to the marine δ^{18}O stage 6 [~188-130ka; e.g. Burke and Birkeland (1979); Atwater et al. (1986)], although most others place it in stage 4 [~73-59ka (Martinson et al., 1987); e.g. Gillespie (1984); Dorn et al. (1990)]. However, Gillespie (1984) felt that the glacial was defined broadly enough to include deposition throughout the stage 6-4 period. A revised chronology for the last 50ky, based on ^{36}Cl measurements from Sierran and White Mountain moraines and correlated with a sediment record from Owens Lake [Fig. 3.1], has been presented by Phillips et al. (1996) and Benson et al. (1996) [Table 3.1].

Constraints on the glacial sequence have also come from comparisons with other deposits. Bailey et al. (1976); Burke and Birkeland (1979); Dalrymple et al. (1982) and Bursik and Gillespie (1993) constrained glacial outwash ages by dating intercalated volcanic material. Atwater et al. (1986) used Tulare Lake sediments from the *western* side of the Sierras to infer that the Tioga stage started around 26ka, as glacial outwash

Stage	Bishop Ck (a)	Bishop Ck (b)	L. McGee Ck (a)	Pine Ck (c)	Sawmill Ck	Bloody Cyn (f)‡	Bloody Cyn (a)	Av. SN/WM (g)	Lakes
post-Tioga/ Holocene		MJII 0.140†; 0.160# MJI 0.600†; 0.560# HP 1.395† TLk 2.595† SLk 8.574†; 10.7§	Neog <1 Hilg 7 E Hilg 8						
Tioga-Tenaya Ti-Te	LE/Sv 18 SC 19	Sv 14.81†; 14.36§ LE 20.267† LEmax 23.59†; 24.633§ SC 34.64†; 37.70§	L Ti2 12 L Ti 14 Ti 20 E Ti 26	Ti rec ≥16.3 Ti ≥22.2	Ti <53±44[d]	Ti 21.4 Te 24.3	Ti 11-14 Te 15	Ti4: 16±1 Ti3: 19±1 Ti2: 25±1 Ti1: 31±1	Ti >18->13[i] Ti 15-20[l] Ti <25.2[j] Ti <26[k] Te ≥30.7[j] Te 33-28[j$]
Younger Tahoe Ta II	Bk 65		Ta 65		Ta >53±44[d] Ta? >62±13[e] <126±25[e]	Y Ta 65.8	Y Ta 45	Y Ta: 49±2	
Mono Basin MB	Y Bp 75 O Bp 85					MB 92-119	MB 75		
Older Tahoe Ta I	Cyt 110 Y TH 120 TH 160 Birch >150		Shwn 110	Ta 143-156 pre-Ta 182-187		O Ta 2 149 O Ta 1 189-218	O Ta 100		Ta? >100[k] Ta? 125-150[l]
Sherwin								>759[h]	

Table 3.1: *Late Quaternary glacial advances in the eastern Sierra Nevada. Eastern Sierra streams arranged south to north. Ages all in ka [thousand years BP].*
(a): Zreda and Phillips (1995) from ^{36}Cl; (b): Dorn (1996) uncalibrated ^{14}C in: †aeolian biome, §weathering rind, #wood; (c): Dorn et al. (1987) ^{14}C / cation-ratio in rock varnish, Tioga 'U-Th calibrated' by Bursik and Gillespie (1993); (d): Dalrymple et al. (1982) K-Ar age on basalt between Tioga and Tahoe tills; (e): Burke and Birkeland (1979) correlations based on Bailey et al. (1976) K-Ar age on basalts above and below Tahoe till; (f): Phillips et al. (1990) from ^{36}Cl; ‡ mean ages quoted for Tioga/Tenaya; range for older stages; (g): Phillips et al. (1996) - averaged ^{36}Cl ages from Sierra Nevada (SN) [Bishop Creek, Little McGee Creek, Bloody Canyon] and eastern White Mountains, Nevada (WM) [Chiatovich Creek]; (h): Bishop Tuff age from Sarna-Wojcicki et al. (2000); (i): Clark et al. (1995) ^{14}C in lake seds; (j): Bursik and Gillespie (1993) intercalated basalts at June Lake, $Lake Russell highstand; (k): Atwater et al. (1986) ^{14}C in Tulare Lake; (l): Smith et al. (1997) multiple-technique analysis on Owens Lake core OL-92.
Labels are abbreviations for the local moraine names. See map for locations of Sierran canyons: Fig. 3.1.

from the King's River dammed the lake. They placed an earlier glaciation, possibly the Tahoe, before 100ka. Smith and Bischoff (1997) and Smith et al. (1997) described evidence of Sierran glacial advances from the 800ky core OL-92 in southern Owens Lake, which is supplied chiefly from east Sierran streams. A combination of biological, chemical, geophysical, stratigraphic and sedimentological data point to four distinct climatic régimes within the last 800ka. These are overprinted by two major glaciations: 15-20ka [correlated with the Tenaya-Tioga] and 125-150ka [correlated with the Tahoe and Mono Basin; Smith et al. (1997)]. Less well-defined, and hence probably less widespread, glacial signals are seen at 50, 70 and 90ka. Although not correlated with events in the moraine record of the Sierras themselves, Smith et al. (1997) described additional evidence of three [four?] earlier glacials at 300, 360 [455?] and 670ka. The deepest part of the core, which dates back to pre-Bishop Tuff times, indicates the waning of an earlier glacial stage, which may be the Sherwin.

3.1.2 Drainage and sedimentation

High runoff during late Quaternary glacial periods is evident from the enormous moraines which have formed from canyons cut into the eastern margin of the Sierras [e.g. Putnam (1960)]. Due to the regionally low rainfall, glacier fluctuations may have been more sensitive to changes in precipitation than to changes in temperature, and hence valley streams might be expected to record maximum runoff during the glacial stage itself rather than at the glacial-interglacial boundary (Bateman, 1965). Pluvial periods are recorded in terraces of the Owens River, which incised repeatedly in response to easterly tilting of the valley floor [Fig. 3.1]. Pinter et al. (1994) described three terraces along the southern margin of the Tableland [Fig. 7.10], which they attributed to incision during the Tioga, Tahoe and pre-Tahoe stages, by relative dating of the surfaces, and comparison with Sierran moraines [e.g. Berry (1994)]. Two terraces cut into the eastern margin of the Tableland have been correlated temporally with the last two of these incisions along the Owens River, and are thought to record downcutting of an ancestral tributary of the Owens River which flowed down Adobe and Chalfant Valleys, draining some of the White Mountains (Bateman, 1965). Overflow of Mono Lake during pluvial periods may have contributed additional runoff which accelerated the cutting of the terraces (Bateman, 1965; Pinter et al., 1994; Smith and Bischoff, 1997). Zehfuss et al. (2001) correlated alluvial deposits near Fish Springs [Fig. 3.1] with the Tahoe and late Tioga stages. However, Bursik and Gillespie (1993) note that glacial maxima did not always correlate with pluvial periods as recorded by highstands in the Pleistocene Long Valley lake.

The route of Owens River along the southern margin of the Tableland, and then down the eastern side of Owens Valley [Fig. 3.1], is probably the result of continued easterly tilt of the valley in response to rapid subsidence on the White-Inyo Mountain range front (Bateman, 1965). Gravity and seismic surveys by Pakiser and Kane [in Bateman (1965)] demonstrated that despite the overall symmetry of the current ground surface, the deepest part of the basin is at the eastern margin, explaining the present course of the Owens River. Most of the supply to this river comes from the eastern flank of the Sierras, as the arid western flank of the White-Inyo Mountains receives comparatively little precipitation. Hence changes in the Sierran runoff dominate the evolution of the Owens River, and also of its destination: Owens Lake. Although now desiccated

following the diversion of much of the Owens River discharge into the Los Angeles aqueduct in 1913, cores from the Owens Lake record detailed changes over 800ky within the upstream catchment [e.g. Litwin et al. (1997); Bradbury (1997); Smith et al. (1997)]. Increased runoff during the wettest parts of the Pleistocene resulted in overflow of Owens Lake, supplying a series of lakes to the southeast: in turn China Lake, Searles Lake, Panamint Lake and Death Valley Lake [Fig. 3.1]. Due to lower runoff and high evaporation rates, perennial lakes in these southern valleys could only be supported by the addition of water from Owens Lake, and hence evidence of persistent lakes for long periods in the past is testament to considerably higher runoff from the Sierras than at present (Smith and Bischoff, 1997; Smith et al., 1997).

Late Quaternary fluvial systems draining the Sierra Nevada and White-Inyo Mountains have deposited wide alluvial aprons onto the valley floor [e.g. Bierman et al. (1995a)]. Alluvial fans cover the Bishop Tuff to a depth of several hundred metres in Round Valley (Bateman, 1965), and abut against the western margin of the Volcanic Tableland [Figs. 3.1 and 3.2; section 7.4]. Uplift of the White Mountains triggered the deposition of enormous quantities of conglomerates (Lueddecke et al., 1998). Progradation of the enormous fans along the eastern margin of Owens Valley are probably responsible for maintaining the location of Owens River away from the immediate base of the White Mountains, despite the ongoing subsidence.

3.1.3 Range-front structure and faults

The NNW-trending Owens Valley is bounded by major faults along both its eastern and western margins. The northern part of the valley is undergoing predominantly E-W extension, while extension is oriented NW-SE in the southern and central parts of the valley [e.g. Savage et al. (1981)], resulting in a larger proportion of oblique slip. Small normal faults accommodating the regional extension are evident in many places in the floor of the valley, and are particularly well-developed on the surface of the Tableland [Fig. 3.2 and section 3.2].

The eastern flank of the Sierra Nevada is bounded by a series of left-stepping *en echelon* normal faults. Individual segments are 20-40km in length, and have cumulative throws of 1-2km (Berry, 1997). The segments are offset along strike by a series of warps and ramps, the most prominent of which is the Coyote Warp, immediately west of Bishop [Fig. 3.1], a broad bulge with surface slopes of only around 10°. Although cross-cut by a large number of faults, both syn- and anti-thetic to the range, there is no evidence of activity on the Coyote Warp faults in the last 15-25ky (Berry, 1997). Recent motion all along the Sierra Nevada to the north and south of Bishop is evident from scarps formed in Quaternary moraines and alluvial fans [e.g. Bateman (1965); Bierman et al. (1995a); Berry (1997); Zehfuss et al. (2001)]. Berry (1997) observed cumulative offsets of tens of metres on Tioga, Tahoe and pre-Tahoe moraines north of Coyote Warp, demonstrating repeated events throughout the late Quaternary, causing slips of 1.5-4m on the Round Valley and Hilton Creek faults, in events separated by 2-4ky. Slip rates are not constant along the range: the Hilton Creek fault having moved almost twice as fast as the Round Valley fault during the last 140-180ky. Estimated vertical slip rates vary from 0.4 to 2.0mmyr^{-1}.

Despite beginning later than on the Sierran range front, slip on the White-Inyo

Mountains has resulted in similar relief [over 3km] on the eastern side of the valley [Fig. 3.2]. However, as with the Sierra Nevada, recent earthquakes have had a large proportion of lateral motion. Slip in the Chalfant Valley earthquakes in 1986 was recorded on faults along the White-Inyo Mountains (DePolo and Ramelli, 1987) and also in the valley block, within the Volcanic Tableland (Lienkaemper et al., 1987).

3.2 The Volcanic Tableland

An enormous eruption from Long Valley 758.9±1.8ka (Sarna-Wojcicki et al., 2000) extruded around 750km^3 of rhyolitic tuff, resulting in the subsequent collapse of the caldera [e.g. Bateman (1965); Sheridan (1970); Wilson and Hildreth (1997); Legros et al. (2000)]. Fine ash was carried over much of western and central north America [e.g. see Fig. 1B in Sarna-Wojcicki et al. (2000)]. Thick ignimbrites were intercalated with ashfall deposits to the north, east and south of the crater, and sporadically through the Sierra Nevada (Bailey et al., 1976; Wilson and Hildreth, 1997). The Volcanic Tableland is a plateau formed by the majority of this material, which initially filled the northern end of Owens Valley [Figs. 3.1, 3.2 and 3.4]. Young alluvial fans cover the tuff in Round Valley (Bateman, 1965), and the Owens River has cut into the southern margin, creating a steep bluff [Fig. 3.4a]. Wilson and Hildreth (1997) estimate that the last ignimbrite lobe extended at least 15km further to the south than this present bluff.

Interbedded fall and flow deposits imply coeval deposition, and thus that the entire sequence was deposited in around 90hours, from a sequence of vents around the caldera margin (Wilson and Hildreth, 1997, 1998). The ignimbrite was deposited in a series of overlapping lobes, the largest volumes forming the present Tableland plateau (Wilson and Hildreth, 1997). The tuff is underlain by granite [e.g. in Rock Creek gorge], basalt [e.g. in Owens Gorge] and alluvial deposits. Varying thickness of the tuff reflects the pre-existing topography, as lobes flowed around and between highs [e.g. the Benton Range and Casa Diablo Mountain], and completely infilled previous fluvial channels [e.g. Chidago Canyon and the present Owens Gorge (Sheridan, 1970; Wilson and Hildreth, 1997; Holt and Taylor, 1998)]. Relatively high velocities of emplacement allowed some lobes to overflow basement highs, seen in cross-section along Owens Gorge (Wilson and Hildreth, 1997).

Although around 400m of tuff was initially deposited, this compacted to an average of around 150-200m as the internal heat welded the central part into a dense mass (Sheridan, 1970; Wilson and Hildreth, 1997; Holt and Taylor, 1998). The upper and lower margins of the sheet cooled more rapidly, remaining unconsolidated and hence easily eroded. A partially-welded layer above the truly-welded section reflects the gradual growth of crystallites on cooling. The thickness of the various layers is controlled by the total thickness of the sheet, and hence the underlying topography: the dense central layer is 100m thick near Chidago Canyon and Owens Gorge, but only ~40m thick where the tuff is thinnest.

Joints and fumaroles: Numerous mounds and ridges over the surface of the Tableland were formed by degassing of the tuff shortly after emplacement (Putnam, 1960; Bateman, 1965; Sheridan, 1970). These fumarolic mounds reach 30m in height and up to 60m diameter, while the ridges, which are generally 1.5-5m high, can reach

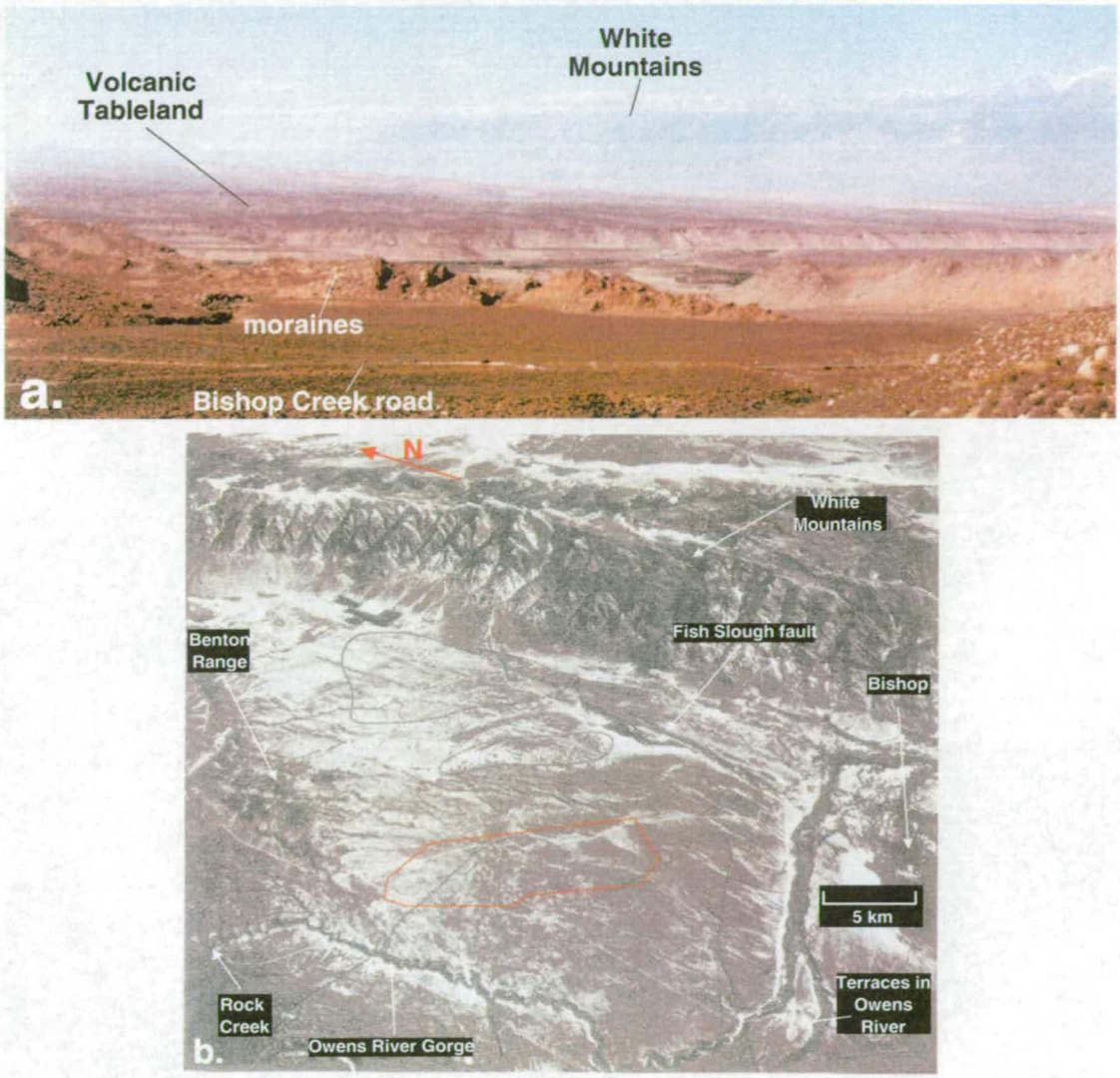

Figure 3.4: *Overviews of the Volcanic Tableland*
a. Photograph from the foothills of the Sierra Nevada looking NE towards the White Mountains [White Mountain Peak 4382m] across the Bishop Creek moraines in the foreground. [See Fig. 3.1 for location.] Pink Bishop Tuff forms most of the view in the valley floor [top of tuff ~1600m elevation]. The erosional escarpment formed by lateral incision of the Owens River forms the steep bluff [up to 150m high] at the southern margin of the Tableland. North-striking normal fault scarps can be seen on the surface of the Tableland. This angle emphasises those dipping west, though roughly even numbers dip both east and west.
b. Oblique aerial photo looking east across the Volcanic Tableland, from Sheridan (1970). [See Fig. 3.1 for location.] The White Mountain range forms the background; Bishop town is in the right foreground. The Tableland is approx. 24km across. Benton Range and Casa Diablo Mountain form the high ground at the north of the Tableland. Owens River and Rock Creek incise into the tuff in the foreground, before Owens River cuts across the southern margin of the Tableland, forming the steep Chalk Bluffs. The area studied in this thesis is outlined in red. Black lines outline the three regions of intense fumarolic activity.

600m in length. Heavy chemical alteration has resulted in significant induration of the fumaroles, and they have generally been considered as erosional remnants, recording the removal of many metres of unconsolidated ash from the original surface [e.g. Putnam (1960); Bateman (1965); Sheridan (1970)].

Preferential alignment of these mounds and ridges implies the underlying control of major joint patterns on the extrusion of gases from the ignimbrite (Sheridan, 1970). Bateman (1965) noted that the fumaroles are aligned along lines which broadly match the orientations of major joints in the Sierras [approx. NW and NE strike, though locally variable]. Sheridan (1970) noted two sets of joints, one with bimodal distribution [4 modes at his site1] showing heavy alteration in hot mineral reactions; the other with no preferred orientation, and no alteration. He concluded that the altered joints, which penetrate up to 120m into the tuff, are conjugate shear joints, formed soon after the tuff's emplacement. Devitrification of the tuff formed anhydrous minerals, prompting the release of volatiles, which escaped along conjugate joints and altered the rock which they encountered. The more 'random' unaltered joints are cooling joints, outlining polygonal columns, and penetrate only the upper 9-15m affected by the escaping gases. Striking radial patterns of columnar joints visible in the walls of Rock Creek and Owens Gorge probably formed due to the bending of isotherms by anomalous heatflow around the fumarole pipes (Sheridan, 1970). The long conjugate joint sets can be seen clearly on some parts of aerial photographs [e.g. Fig. 4.1], though they are often hard to pick out on the ground.

The highest concentrations of fumarolic mounds and ridges occur in three discrete regions in the Tableland, which appear to coincide with the thickest tuff, above the previous drainage routes (Sheridan, 1970; Fig. 3.4b). The thicker layer of tuff probably provided sufficient heat to fuel hydrothermal alteration. However, $\delta^{18}O$ variations in phenocrysts and groundmass imply that alteration involved recharge by enormous volumes of meteoric water (Holt and Taylor, 1998). Holt and Taylor calculated that the fumaroles may have formed during an intense period of degassing lasting only around ten years from the time of emplacement; consistent with observations from the 1912 Novarupta ash flow in the Valley of Ten Thousand Smokes, Alaska. Holt and Taylor invoked recharge by groundwater flow, possibly fed by seepage from the lake which formed in the Long Valley caldera, dammed by the ignimbrite [e.g. Bailey et al. (1976)], and whose highest margins were at a similar elevation to the highly altered zone of the tuff. The coincidence of the heavily-altered regions with the pre-existing drainage pattern may reflect water flow preferentially down the previous topographic lows, as the lack of alteration of the lower parts of the sheet refutes the entry of meteoric water from under the tuff. However, their model requires that the lake formed and filled to a depth of several hundred metres within ten years of the eruption, which is fast even if mountain glaciers were catastrophically melted by falling ash (Bailey et al., 1976).

Faults: The Tableland is warped into an arch about a horizontal axis oriented roughly north-south, due to the tectonic tilting of the Owens Valley in response to motion on the range-bounding faults [Fig. 3.2]. While most of the Tableland surface dips towards the southeast at around 4°, the southwest corner dips southwest towards the Sierra Nevada (Bateman, 1965; Pinter and Keller, 1995). The surface of the tuff is fractured by a large population of normal faults, all striking 340-350°, roughly paralleling the axis of the arch, and dipping to the west and east in equal numbers (Dawers et al.,

1993; Dawers and Anders, 1995; Pinter, 1995; Fig. 3.5). The largest throw, of ~120m, is on the 8km long Fish Slough fault, at the eastern margin of the Tableland. Other faults are isolated or arranged in *en echelon* arrays up to 8-9km in length.

Fault dips observed in cross-section are high: usually 70-90° (Dawers et al., 1993; Pinter, 1995), although Bateman describes some faults dipping at 55°. Despite the high dips, motion on the faults is pure dip-slip: there is no evidence of significant oblique or lateral motion (Dawers et al., 1993; Dawers and Anders, 1995; Pinter, 1995). In places, there are signs that the fault orientations are controlled on a small scale by the orientations of the conjugate joints (Pinter, 1995), while others also coincide with fumarole locations [e.g. P. McFadzean pers. comm. 1998, and Fig. 4.20]. Although there is some degradation of the scarps forming blocky debris-flow and sandy slope-wash deposits (Pinter, 1995), footwall topography is well preserved, and volumes of hangingwall deposition are generally low (Dawers et al., 1993; Dawers and Anders, 1995). This has made it possible to construct scarp profiles of the Tableland faults, and to use the profiles as reliable indicators of fault displacement.

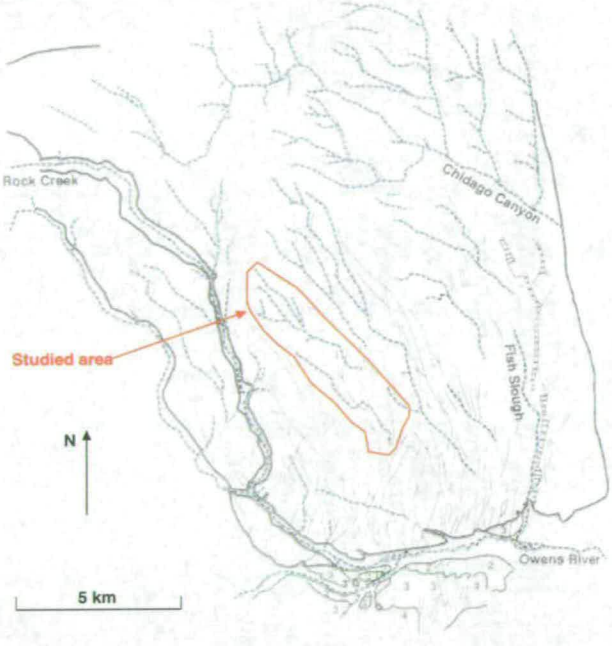

Figure 3.5: *Map of the surface of the Volcanic Tableland, modified from Pinter and Keller (1995) - map corresponds to grey area in Fig. 3.1.*
Black lines mark small normal fault scarps. The location of the fault array studied in this thesis, and by Dawers and Anders (1995) is outlined in red. Blue lines mark the location of ancestral, now dry, streams which drain the surface of the Tableland. Active drainage is limited to the canyons incised over 150m into the tuff surface by the Owens River and Rock Creek.

Dawers et al. (1993) constructed displacement-length profiles for a number of isolated faults on the Volcanic Tableland from their footwall and hangingwall cutoffs. This population provided key evidence of linear scaling [e.g. Cowie and Scholz (1992a), Fig. 2.2], evident over three orders of magnitude, with $D_{avg} \sim 0.61 D_{max}$. However, they noted *linear* tip gradients, not predicted by the simple Dugdale fracture model [section 2.1.1]. Lienkaemper et al. (1987) observed fractures in the Tableland caused

by the 1986 Chalfant Valley earthquake sequence, and inferred that the Tableland faults were effectively decoupled from the observed oblique faulting in the basement by unconsolidated material below the welded tuff. Dawers et al. inferred from this, and the consistent tip gradients, that the Tableland faults nucleated at or near the surface of the tuff. They also observed that faults less than ~200m long had generally 'peaked' displacement profiles, with D_{max}/L ~0.016-0.020, while long faults had flat-topped profiles, with D_{max}/L ~0.009-0.014 [their Fig. 2]. Dawers et al. argued that this reflected the influence of the tuff layer thickness on the fault growth: the short faults were entirely contained within the tuff, but the flat-topped profiles resulted from rupture of the entire sheet.

Pinter (1995) investigated perpendicular profiles across 226 scarps, and used them to estimate a total of 290m extension across the Tableland since its emplacement, implying an extension rate of around 400mMy^{-1}. He attributed the Tableland fault geometries to flexural warping of the tuff sheet due to the differential tilting of the Sierra Nevada and White Mountain fault blocks [his Fig. 10], as had Bateman (1965). Pinter also predicted a recurrence interval of $\leq$3000yrs, consistent with his observation of repeated motion on faults cutting young fluvial terraces at the southern margin of the Tableland. However, there seems little basis for the assumptions inherent in this prediction.

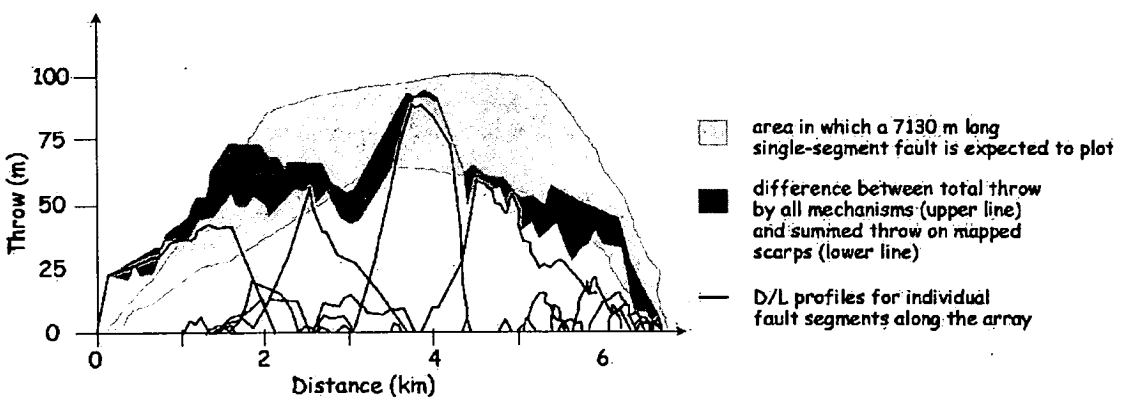

Figure 3.6: *Displacement-length profile for a linked fault array on the Volcanic Tableland, eastern California, from Dawers and Anders (1995).*
Black lines show the displacement profiles of the individual surveyed faults: the four largest segments have throws >40m. These values were calculated from the footwall and hangingwall cutoffs, measured with a theodolite. Errors are of the order of 1-5m, due to hangingwall fill and erosion of the footwall.
Dark grey region is the difference between a summed throw profile for all the surveyed faults [lower margin] and that including the contribution of 'continuous' deformation by tilting within the overlaps, as well as unmapped scarps [upper margin].
Pale grey zone is the area in which a single-segment fault of L=7130m [total summed length] would be expected to plot, given the observations of Dawers et al. (1993).

Dawers et al. surveyed the fault array which is a major focus of this thesis (Scholz et al., 1993; Dawers and Anders, 1995; Fig. 3.5). By summing the displacement on each of the faults in the >7km long array, and including displacement accommodated by warping and fracturing of the tuff in overlaps, Dawers and Anders demonstrated that the entire array acted as a single isolated fault of >7km length [Fig. 3.6]. Individual faults had

distinctly asymmetrical profiles, and steep tip gradients, demonstrating interaction with overlapping *en echelon* segments [Case 2 linkage of Cowie et al. (2000); Fig. 2.7]. Despite the appearance of displacement lows between segments, inclusion of the ductile extension and the displacement on small faults demonstrated that the overlaps were not true displacement minima. This data showed definitively the growth of large faults from the coalescence of smaller segments [e.g. Peacock and Sanderson (1991); Gupta and Scholz (2000)], and that self-similar scaling was achieved. The linear displacement-length scaling of this array was consistent with their earlier (1993) results.

Streams: The surface of the Tableland is incised to a depth of up to 20m by a series of streams which drain towards the southeast (Putnam, 1960; Bateman, 1965; Pinter and Keller, 1995; Fig. 3.5). Interaction between these streams and the surface faults is widespread. Bateman (1965) observed that streams in the southwestern corner of the tuff sheet appeared to have adjusted their paths, to drain more to the southwest. He therefore inferred that at least some of the southwesterly warping of this part of the Tableland occurred after the initial formation of the streams [see section 7.4]. Pinter and Keller (1995) observed that the stream segments have an overall bimodal distribution, draining predominantly towards 121-125° and 161-165°. They interpreted this as evidence that when the streams formed, the main part of the Tableland surface dipped towards 121-125°, but that some stream segments were diverted along the face of west-dipping normal faults, which were aligned 161-169°. Since the Tableland surface presently dips 2.8° towards 113°, Pinter and Keller inferred that eastward tilting of 0.6-0.8° about a horizontal axis had occurred since the formation of the streams, consistent with the observed tilting of terraces and alluvial fans in Owens Valley. The combination of Bateman's and Pinter and Keller's evidence fits the pattern of warping implied by the fault pattern on the Tableland.

The active Owens River and Rock Creek have incised gorges over 150m into the tuff [Fig. 3.2 and also Fig. 3.7], but the streams on the Tableland surface are no longer occupied, and most of the present drainage flows through the porous tuff below the surface (Putnam, 1960; Bateman, 1965; Pinter and Keller, 1995). Since increased precipitation was experienced in the late Quaternary glacial periods, Pinter and Keller argued that the streams on the surface of the Volcanic Tableland formed during the first major glacial period after the emplacement of the tuff: a pre-Tahoe stage, variously constrained to be 206-135ka [their Table 1; see also Table 3.1]. Where the surficial streams drained the southern margin of the Tableland, they graded to the 'Q3' terrace, which Pinter et al. (1994) correlated with Tahoe moraines, variously constrained to 79-56ka [their Table 1]. Thus Pinter and Keller (1995) interpreted the Tableland streams as formed during a pre-Tahoe glaciation, and subsequently reoccupied only during the Tahoe glacial, since when they have remained inactive. This hypothesis is tested by the cosmogenic dating in Chapter 6.

Evolution of Owens Gorge: Putnam (1960) agreed with Mayo (1934) that the deeply-incised Owens Gorge formed through catastrophic draining of the Long Valley lake, which had filled the caldera against the dam of the Tableland tuff sheet [Fig. 3.7]. Mayo's theory was based on the pronounced elevation difference of ~740m between the floors of the Long and Owens Valleys, and observations made shortly before Owens River was dammed to form the present Lake Crowley. Profiles of the rim of the Owens Gorge show a steep topographic slope which Putnam argued was sufficient to have driven relatively rapid headward incision of the Owens River into the tuff during periods

of heavy precipitation. In his model, northward incision eventually allowed the Owens River to capture and reverse a small stream which had drained into the Long Valley Lake from the west, emptying the lake to the south. The catastrophic volumes were sufficient to incise a deep gorge through the Volcanic Tableland [Fig. 3.7b].

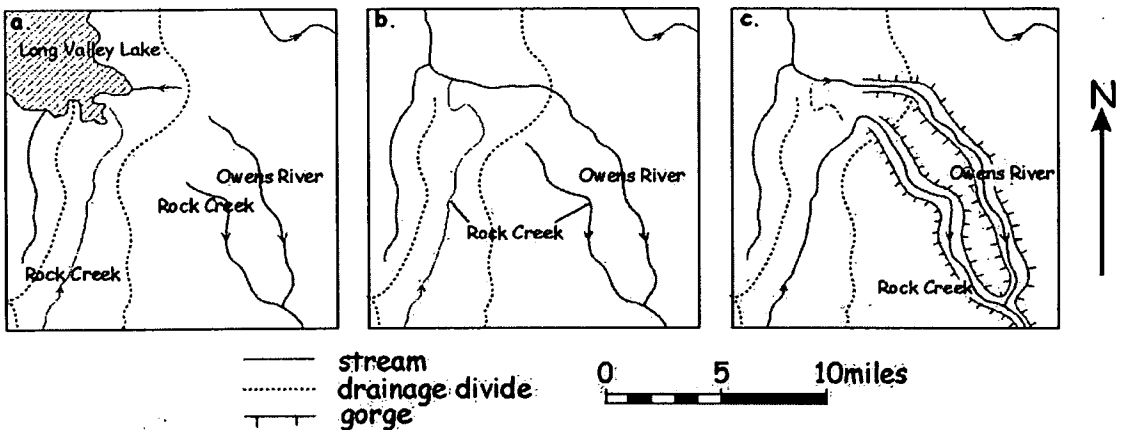

Figure 3.7: *Evolution of Owens River and Rock Creek gorges, after Putnam (1960).*
a. Dotted line marks drainage divide between the catchment for Long Valley lake to the north, and Owens Lake via Owens River and tributaries, to the south. Headward incision of Owens River and southern Rock Creek towards the north. Main discharge from Rock Creek Canyon in the Sierran flank directed towards Long Valley lake to the north by moraine from Whisky Canyon.
b. Headward incision by Owens River finally captures the stream entering Long Valley lake from the west, catastrophically draining Long Valley lake through the new channel. Owens River Gorge is incised through the Tableland to a depth of up to ~280m. Headward incision of the southern Rock Creek is slowed by resistant bedrock at Sherwin Hill.
c. Southern Rock Creek incises through the drainage divide and captures the drainage from the Sierran flank, which is subsequently directed towards the south, through a canyon incised ~220m into the Tableland.

The huge Sherwin moraine which had flowed from the eastern Sierras out of Whisky Canyon initially blocked drainage of Rock Creek to the south, forcing it to drain into Long Valley Lake to the north. However, headward incision of a tributary of Owens River eventually incised through a bedrock barrier to intercept the Rock Creek drainage, and reroute it to the south [Fig. 3.7c]. Although unable to make precise age constraints, Putnam (1960) suggested that Long Valley lake was captured shortly after its highstand, which he tentatively placed during the Tahoe glacial: the increased precipitation during the glaciation could have supplied sufficient discharge to drive headward incision. Putnam placed the formation of Rock Creek Gorge after the capture of Long Valley lake for several reasons, but particularly as the tiny remnant of the northern Rock Creek grades to the *present* lake level, and not the much higher Pleistocene lake, implying that the lake level had dropped before the northern stream was superseded.

However, Bailey et al. (1976) argued that caldera collapse was rapid, and the Long Valley lake filled extremely quickly, simply overflowing over the Tableland once it was higher than the damming tuff wall. Rhyolites on the resurgent dome imply that the lake reached its highest level [2380m above SL] and then rapidly dropped 60m before

634ka (Bailey et al., 1976; their Fig. 6). In their model, the flooding water incised into the tuff until it reached the densely-welded layer, at which point the lake level stabilised. Bailey et al. attributed an early stream cut into the southwestern corner of the Tableland to an early outflow stream. Correlation of lake terraces with dated volcanic material around Long Valley implied that the lake levels dropped in stages over the next 600ky, as the valley floor subsided due to motion on the Sierran faults, and that the lake drained completely sometime within the last 100ky (Bailey et al., 1976; their Fig. 6).

3.3 Fieldwork data used in this thesis

Normal faults and channels on part of the Volcanic Tableland were surveyed using differential GPS in two separate field seasons, and the 3D data analysed using graphical techniques. Differential GPS [Appendix B] provides an incredibly fine resolution [subcentimetre in 3D] and is relatively quick and simple to collect, as well as requiring only one operator, making it much more valuable than a theodolite for the data collected here. Displacement-length profiles are presented in section 4.1 for the key faults in the central overlap of the array studied by Scholz et al. (1993) and Dawers and Anders (1995). The profiles are calculated from the vertical separation of the footwall and hangingwall cutoffs and include a correction for significant talus aprons [sections 4.1 and B.1.3]. Profiles of the main fault overlaps, and the hangingwalls were measured, perpendicular to the main faults, to assess the cross-sectional shape of the [partially-filled] basins [section 5.2.3].

Section 4.2 and Chapter 5 present data from detailed surveys of around 30 channels draining the fault array. Variations in gradient can be calculated and related to the fault pattern using the long profiles [section B.1.3]. Cross-sectional profiles perpendicular to the local flow were measured every 50-100m along each stream, to assess variations in stream morphology. Since I was interested in the varying patterns of stream incision, I chose a method of plotting the data which emphasised these vertical variations in cross-section. I defined the *'aspect ratio' [AR]* as the incised depth [bank crest→channel floor] divided by the total channel width between the bank crests [Fig. 3.8]. Thus the AR [or depth/width ratio] is the *inverse* of the width-depth [W/D] ratio used by many authors to investigate the changing morphology of [especially alluvial] streams [e.g. Schumm (1977); Jorgensen (1990)-Fig. 2.26; Wohl (1993); Tinkler and Wohl (1998a); Wohl (1998); Holbrook and Schumm (1999); Schumm et al. (2000)]. However, I believe it provides a more useful tool for investigating channel incision, in this particular case.

Due to lateral migration during incision, or lithological variation, the two banks of a stream are often not both at the same elevation above the channel floor. In such cases, I measured the depth to the *lower* of the two bank tops, to ensure that the depth was not overestimated due to the presence of pre-existing topography [e.g. fumaroles or faults], or deposition on one bank. Since a stream generally narrows as it incises, the active part may be a small inner channel near the base of the overall cross-section [Fig. 3.8b]. In this case, the aspect ratio as calculated in this thesis will drastically *underestimate* the true AR of the active part of the channel. The use of the lower bank of an unequal pair similarly may result in an underestimation of the true aspect ratio. Hence the ARs quoted in this thesis are very conservative and should be considered

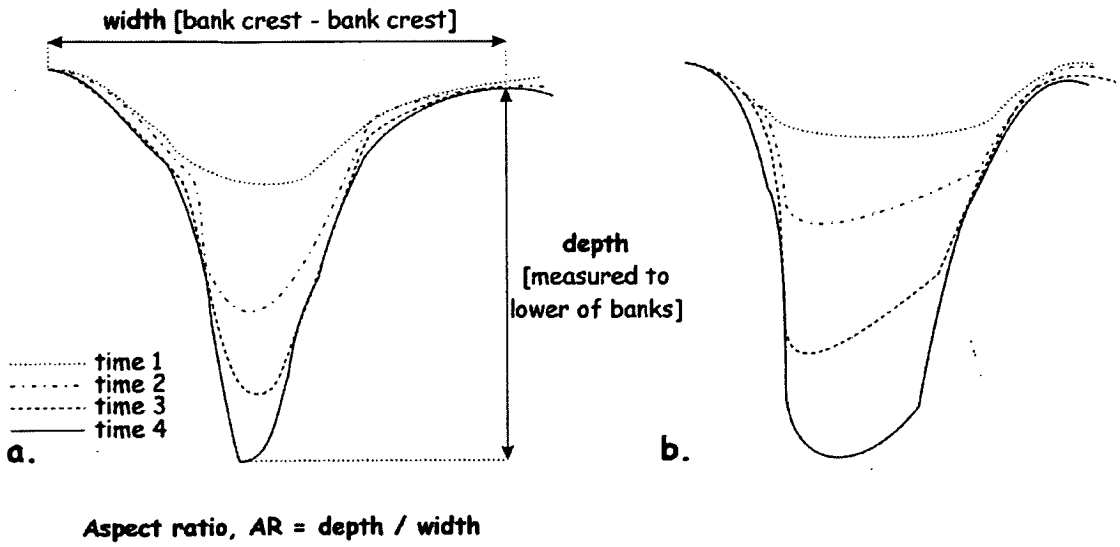

Figure 3.8: *Cross-sectional profile of a channel.*
Depth and width of the channel cross-section defined as shown. Depth is always measured to the lower of two unequal bank crests. The ***aspect ratio [AR]*** *is calculated as the bank-midpoint depth divided by the bank-bank width. This is the inverse of the more commonly plotted width/depth [W/D] ratio of a stream: deeply-incised narrow streams have high aspect ratios.*
Comparison of AR ratios for two different hypothetical streams: a. developing an inner channel, and b. with constant width maintained during incision. The AR calculation used in this thesis underestimates the true AR of the inner channel, so both streams would appear to have the same aspect ratio, despite the different cross-sectional forms. Full cross-sectional profiles have therefore been included for most of the streams discussed in the thesis, to allow the reader to assess the morphology in each case. AR values should always be considered as minima.

minima. However, since the surveyed streams are dry, and in many cases preserve no reliable indication of the contemporary water depth, this approach was chosen to be consistent throughout the surveyed area. The original full cross-sectional profiles are presented for each stream as 'common base' plots [except for the northern stream tributaries, section 5.1.3], and hence the reader may assess how conservative the AR estimates are in each case. The methodology is outlined in more detail in Appendix B.

Chapter 6 presents *in situ* cosmogenic isotope exposure ages for a series of samples taken from the streams in the central overlap of the array. The sampling pattern is discussed in section 6.1, and the calculation of the results in the following section [6.2]. The preparation of the targets for analysis is outlined in section B.2. The results are discussed along with the survey results in Chapter 7.

Chapter 4

Stream and fault interaction in a fault overlap, Volcanic Tableland

The fieldwork, carried out during two seasons in the summers of 1999 and 2001, focuses primarily on the drainage patterns in and around a single fault array [Fig. 4.1], previously described by Dawers and Anders (1995). The data is presented in two chapters. This first chapter focuses on features of a fault overstep in the centre of the array, and discusses its evolution, based on surveys of the streams and faults. Chapter 5 compares the features of these central streams with those of two other large drainage systems around the array.

The first part of this chapter [section 4.1] considers the accommodation of displacement on the main faults in the overstep. A study of the faulting in this array has already been carried out Dawers and Anders (1995), but the largest faults bounding the central overlap have been resurveyed in this project to investigate how the accommodation of displacement relates to the drainage pattern, which is described in the second part of the chapter [section 4.2]. This also makes a good comparison with the numerical modelling [e.g. Fig. 8.3]. *In situ* cosmogenic isotope exposure ages from the main channel in this central overlap, presented in Chapter 6, provide important time constraints on the processes that occurred in the developing overlap zone [see section 7.2.2].

The distribution of deformation on the main faults in the central overlap discusses displacement profiles calculated from footwall and hangingwall cutoffs surveyed along the exposed scarps in the field using differential GPS [section B.1.2]. Section 4.2.1 discusses stream courses, channel long profiles and cross-section data from GPS surveying, together with other important observations made in the field. Initial interpretations of this field data are discussed at the end of each section and brought together at the end of the chapter.

The drainage evolution of the central overlap is put into the context of the array by comparison with two other important networks in Chapter 5: a lateral system which flows through distributed faults at the northern tip of the array [section 5.1] and the system which flows axially to the southern part of the array [section 5.2]. The implications of the observations presented in Chapters 4 and 5, and the additional constraints of the cosmogenic data, are discussed in Chapter 7.

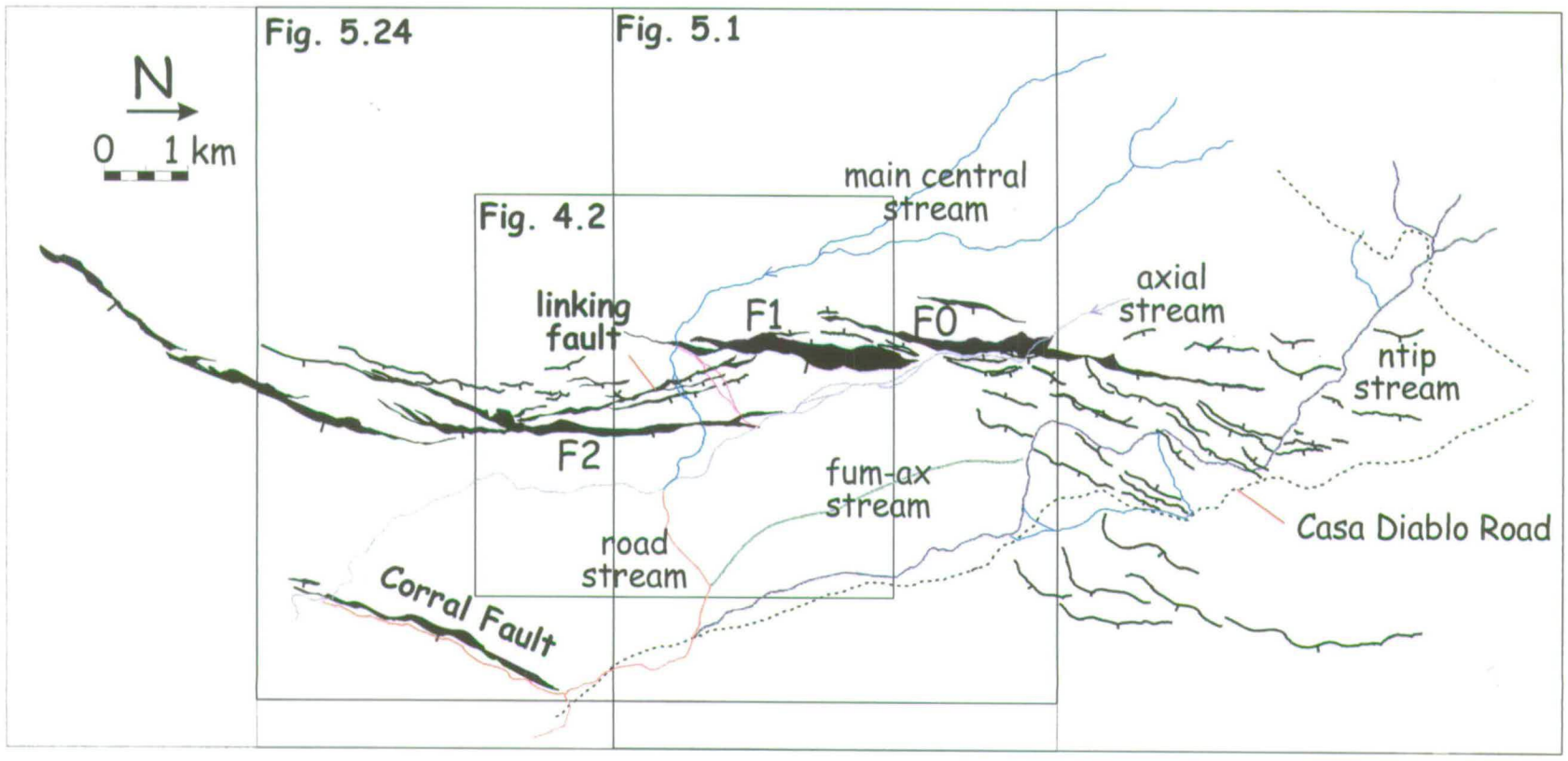

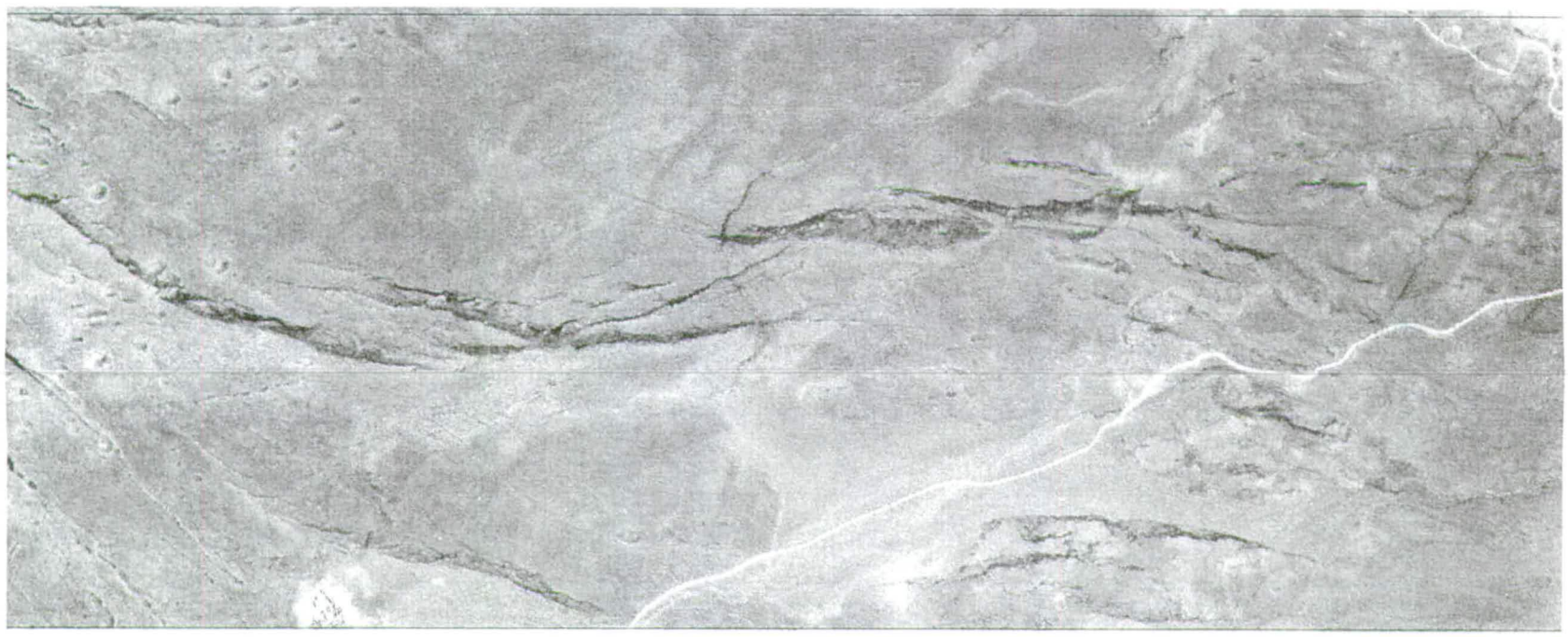

Figure 4.1: *Aerial photograph of the main fault array studied.*
Dark shadows are extensional fault scarps, dipping east [towards bottom]. D_{max} on Fault 1 is approx. 90m. The array is approx. 7.1km in length, and the two main faults bounding the central overlap [see Fig. 4.20], are approx. 800m apart across the overlap. A large channel [section 4.2.1] incises through this overlap, snaking nearly around the tips of the two main faults. It is incised approx. 8m into Fault 1 at the back (top) of the overlap. Smaller streams [section 4.2.2] diverge from the main stream at the base of this fault and drain towards the northern tip of Fault 2. A large drainage system cuts through the northern tip of the array [section 5.1]; the main axial system [section 5.2] runs sub-parallel to the southern part of the area. Pale areas on the photograph are sand deposited by the various channel systems. The small 'blebs' on the photograph are vent mounds, or fumaroles, through which the tuff degassed after emplacement. Major conjugate joint sets can also be seen.

4.1 Fault displacement profiles

This section discusses the distribution of displacement on the faults in the central overlap of the array [Fig. 4.2]. The array has already been described in detail [Dawers and Anders (1995)], and hence the intention of this study is to consider the distribution of displacement and the timing of motion, relative to the development of the drainage systems in the overlap. Fault cutoff profiles were surveyed in the first fieldseason [1999], and used to construct displacement-length profiles for the main faults in the overlap [section B.1.2]. This section discusses each of the major faults in turn, looking at the style of faulting, through observations of the fault shape, displacement-length profile, and some of the interactions with joints and fumaroles.

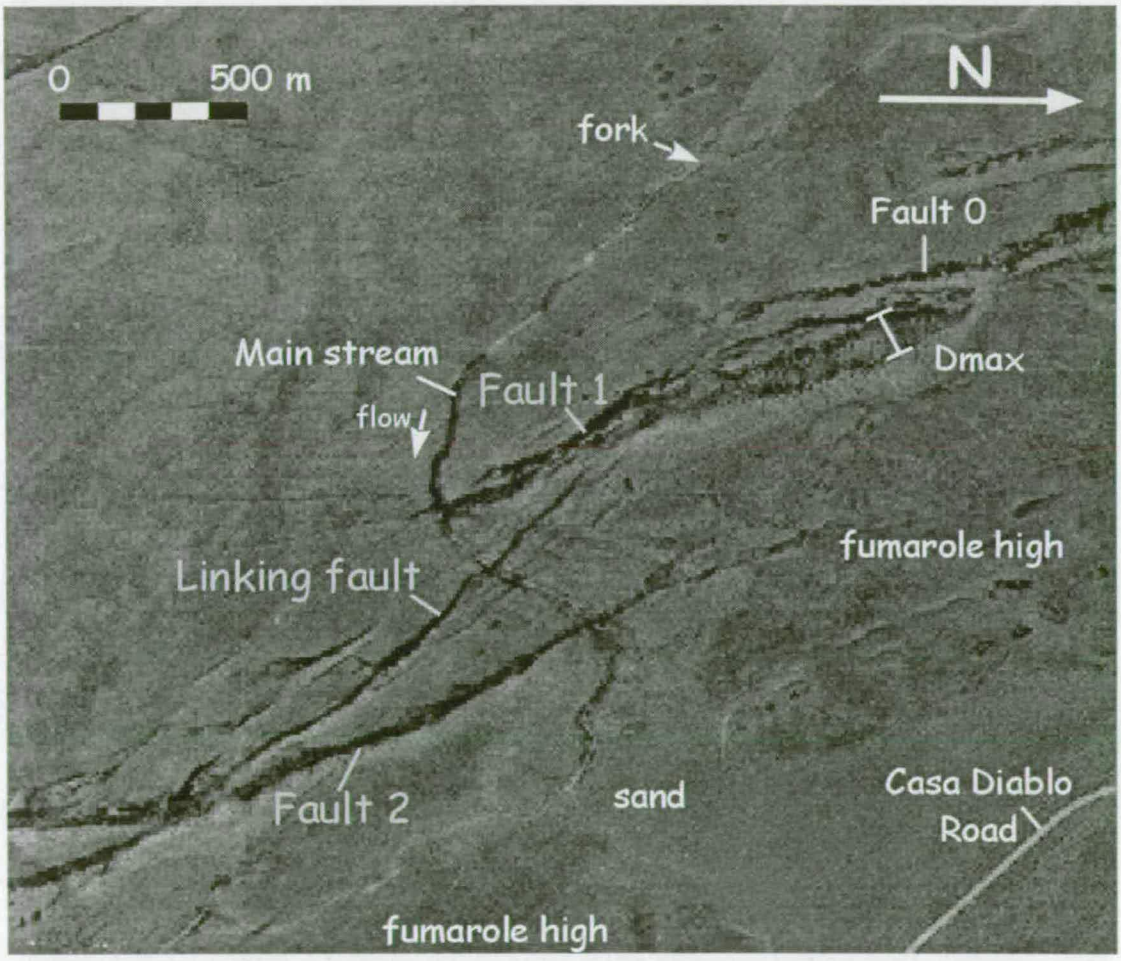

Figure 4.2: *Aerial photograph of the main overlap: see Fig. 4.1 for location.*
Dark shadows are extensional fault scarps dipping towards the east (bottom) with throws up to 90m ['D_{max}'] on Fault 1. The overlap is approx. 1km north-south, and the two main faults [Fault 1 and Fault 2] are approx. 800m apart at the widest part. The 'Linking fault' hard-links these two largest faults. The channels discussed in section 4.2 snake through the overlap. The main channel [section 4.2.1] incises through both Fault 1 and Fault 2, and also the linking fault, as marked. Several less distinct minor channels [section 4.2.2] diverge from the main channel at the foot of Fault 1, and flow towards the northern tip of Fault 2.

Locations of the main channel incisions are indicated, but the streams are discussed in detail in section 4.2. The main features of the faulting styles are summarised in section 4.1.4. Additionally, some profiles surveyed across the hangingwall basins perpendicular to the faults are shown in Fig. 5.40. Weathering bands in the Fault 2 scarp are discussed with the cosmogenic isotope analysis, in Chapter 6.

4.1.1 Fault 1: bounding the northwest [back] of the central overlap

Fault 1 bounds the west-northwest of the central overlap region [Figs. 4.1 and 4.3], and a maximum displacement of 92.7 metres was calculated by Dawers and Anders (1995) near its centre [Fig. 3.6]. Interaction between the southern part of this fault and Fault 2 is responsible for the formation of a warped relay ramp which has been hard-linked by a through-going fault ['linkf' in Fig. 4.20]. However, the overlap between the northern tip of Fault 1 and 'Fault 0' has not been breached by a through-going fault, although there are several small faults and fractures within it [section 4.1.1.3].

Figure 4.3: *View of Fault 1, looking west from the top of the eastern fumarole high. The fault is approx 1.5km long, and the scarp reaches ~80m high.*

4.1.1.1 Fault cutoffs

Fault cutoff profiles were collected around the upper and lower margins of the exposed scarp of Fault 1. Elevation profiles of the cutoffs [Fig. 4.4c] were calculated along a 'spine' between the two fault tips. The small splay ['fault k': Fig. 4.7] has not been included in this calculation, but is considered in section 4.1.1.3. A series of small consecutive surveys were made to collect the fault cutoffs, but due to GPS problems, three small gaps occur in the footwall data [Fig. 4.4]. These parts of the profile have been interpolated using the Generic Mapping Tools [GMT: see section B.1.3].

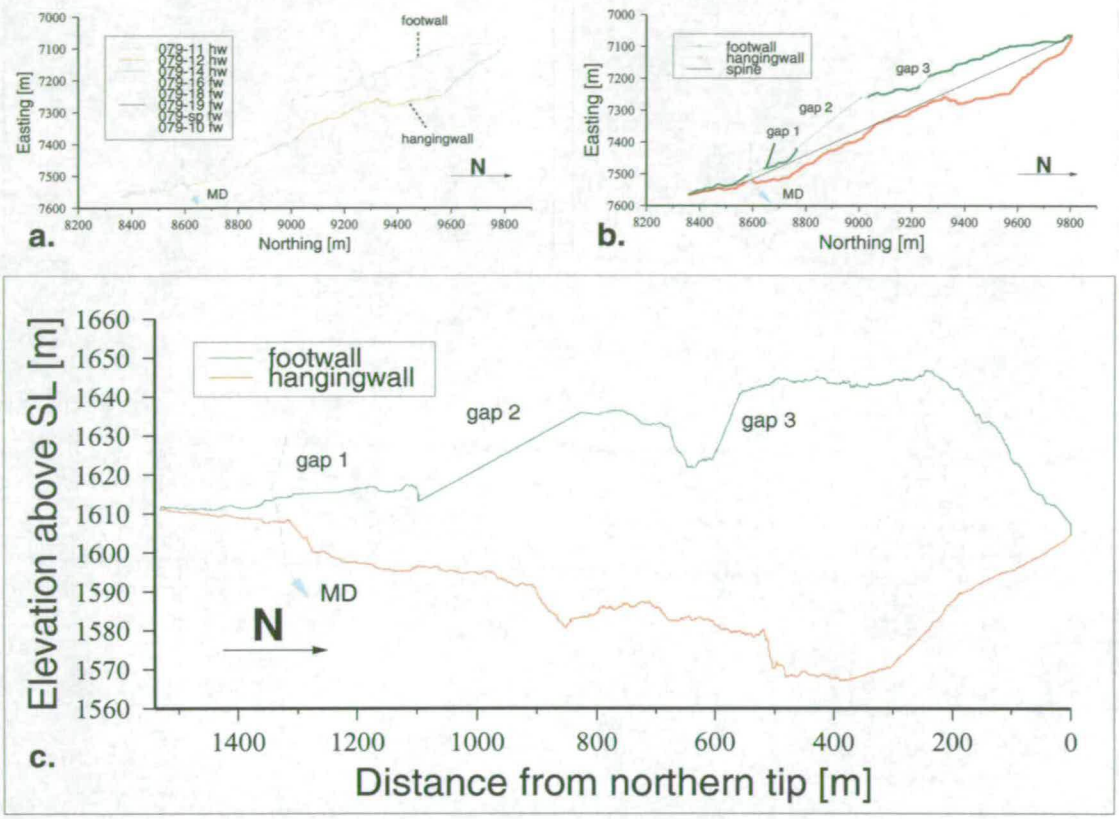

Figure 4.4: *Maps and elevation profiles of fault cutoff surveys for Fault 1.*
a. Map of the surveys collected in the field. Gaps between the surveys are the result of mobile receiver problems.
b. Map of the summed cutoff datasets used to calculate the profiles. Straight line sections indicate the interpolated gaps between surveys. The black line joining the tips of the fault is the 'spine' used to calculate distance along the fault.
c. Elevation profiles of the cutoffs, calculated as distance from the northern tip of the fault [along the 'spine']. Straight line interpolation was used in gaps between surveys.
Footwall cutoff surveyed at top edge of visible scarp; hangingwall cutoff surveyed at base of visible fault scarp. [Dawers and Anders (1995) surveyed the lowest point in the hangingwall] 'MD' marks the location of the main channel incision. Note the distinct change in the fault trace and profile shape at this point. A small splay ['fault k' in Fig. 4.7] has not been included here [see section 4.1.1.3].

4.1.1.2 Displacement-length profile

Figure 4.5 is the displacement profile calculated for the entire fault, using the upper and lower margins of the fault scarp.

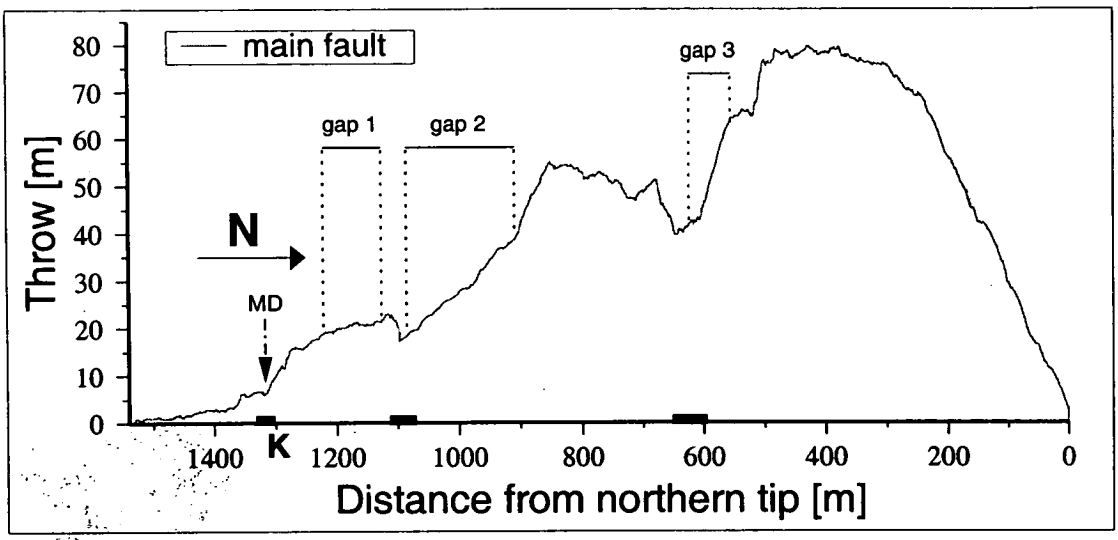

Figure 4.5: *Displacement-length profile for Fault 1, using the elevations of the footwall and hangingwall cutoffs, and a dip of 75°. 'Gaps' refer to interpolated parts where footwall data was missing.*
Locations of probable major old segment boundaries are marked by grey boxes on the x-axis. 'K' marks the location of the abandoned hangingwall splay fault 'k' [section 4.1.1.3].
'MD' marks the location of the main channel incision. Note the distinct change in displacement on the fault at this point, consistent with the location of an old segment boundary.

The calculated maximum displacement for the fault is 79.65m. Using a total surveyed length of 1530.2m, this gives an overall displacement-length [D/L] ratio of 0.052. [Dawers and Anders (1995) measured D_{max} = 92.7m: a D/L ratio of 0.061. The discrepancy is probably due to the different locations used for the hangingwall cutoffs - Dawers and Anders (1995) surveyed typically the lowest point in the hangingwall.] The D/L ratio is high as D_{max} in fact scales for the entire 7.1km fault array (Dawers and Anders, 1995). However, the value of 0.052 calculated here is based solely on the main fault scarp itself, and does not take into account the contribution of small faults [section 4.1.1.3] or the warping and fracturing of the tuff, by which a large proportion of the strain is accommodated [e.g. Fig. 3.6]. Table 4.1 on page 114 compares the values calculated for Fault 1 with those for the other faults on the Tableland surveyed in this project.

Fault 1 is very asymmetrical, with D_{max} skewed towards the northern tip, implying recent interaction with the overlapping Fault 0 to the north. The northern tip also has a very steep gradient [0.271], which can be clearly seen in the bed gradient of the axial channel [Fig. 5.25] and profiles surveyed across the Fault 1 hangingwall basin [Fig. 5.40]. In contrast, despite interaction with Fault 2, which formed the warped overlap, the southern tip of Fault 1 shows a much gentler tip gradient [0.021]. The distinctly different morphologies of the tips and their profiles probably reflects a difference in the

relative timing of the activity on the three faults. These differences may also play a role in the contrasting drainage patterns in the two overlaps [sections 4.2.1 and 5.2].

The displacement profile consists of at least four 'lobes', implying the linkage of a series of segments [e.g. McLeod et al. (2000); their Fig. 9]. Segmentation is clear in the field, on a variety of scales [e.g. Fig. 4.6], as predicted by the model of fault growth suggested by Anders and Schlische (1994); Cartwright et al. (1995); Schlische (1995); Cowie (1998) and others. The main channel through the overlap [section 4.2.1] incises through Fault 1 near its southern tip [Fig 4.5]. This incision coincides with a marked change in the shape of the cutoff traces [Fig 4.4] and of the displacement profile [Fig 4.5]; a small splay fault in the hangingwall of Fault 1 ['k' in Fig. 4.7] and the tip of a further subsidiary fault [fault 'j' in Fig. 4.7] in the footwall of Fault 1. These factors all imply that this is a palaeo-segment boundary and that the channel probably exploited a contemporary topographic low in the Fault 1 scarp.

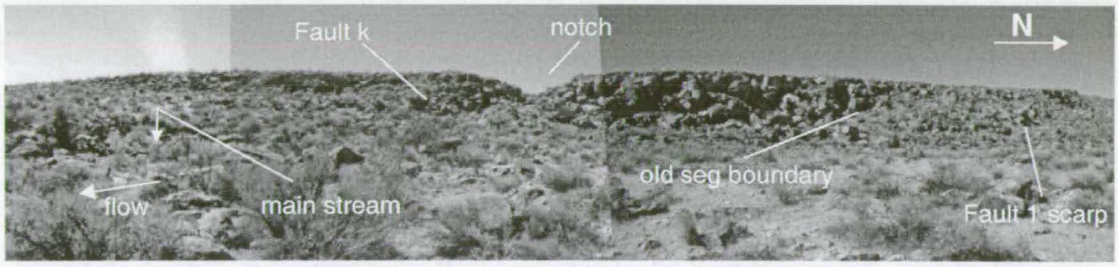

Figure 4.6: *Field photographs of main channel incision through Fault 1.*
A large notch has been cut into the fault scarp. Small linked segments can be seen within the fault scarp to the north-east [right], as implied by the apparent segmentation of the displacement profile.
'Fault k' [Fig. 4.7] is a small hangingwall splay fault, whose displacement increases dramatically towards Fault 1 [Fig. 4.8c]. This is probably the relic tip remaining after linkage of early small segments. A low in the 'raw' displacement profile of the main fault [Fig. 4.5], and a marked change in the fault trace [Fig. 4.4] are both apparent at this location.
Incision of the stream into the ramp surface [section 4.2.3] can be seen in the foreground.

Field relations show clear evidence of the influence of large conjugate joints on the location and development of the faults. Many of the faults on the Tableland show evidence of growth influenced by jointing [sections 4.1.1.3, 4.1.2, 4.1.3 and McFadzean (2002)]. Fault 1 has a marked bend in its trace [see Fig. 4.4], and becomes parallel to one of the main joint sets at its southern tip. However, the change in orientation may also facilitate a change in the method of strain accommodation, with more displacement distributed onto joints running subparallel to the southern tip of Fault 1. This can be seen in the long profile of the main stream, Fig. 4.24; see Chapter 7.

4.1.1.3 Small faults

The profile in Fig 4.5 considers only the displacement on the main fault scarp. It does not include any contribution from warping or small-scale fracturing of the tuff, which between them accommodate a considerable amount of the strain [e.g. Cartwright et al. (1995); Dawers and Anders (1995): Fig. 3.6; McLeod et al. (2000)]. A series of extensional structures occur around Fault 1, both at the tips, and also in the footwall

of the fault [see Fig. 4.1]. Most of the small faults are sub-parallel to Fault 1, probably due to the influence of jointing; few faults strike perpendicular to the main fault. This is consistent with the positive feedback model [Cowie (1998), section 2.1.3]: small faults parallel to Fault 1 may be preferentially loaded by slip on the large fault. Some examples of small faults are shown in the following section, focusing particularly on the differences between the northern and southern tips of Fault 1 [Fig. 4.7].

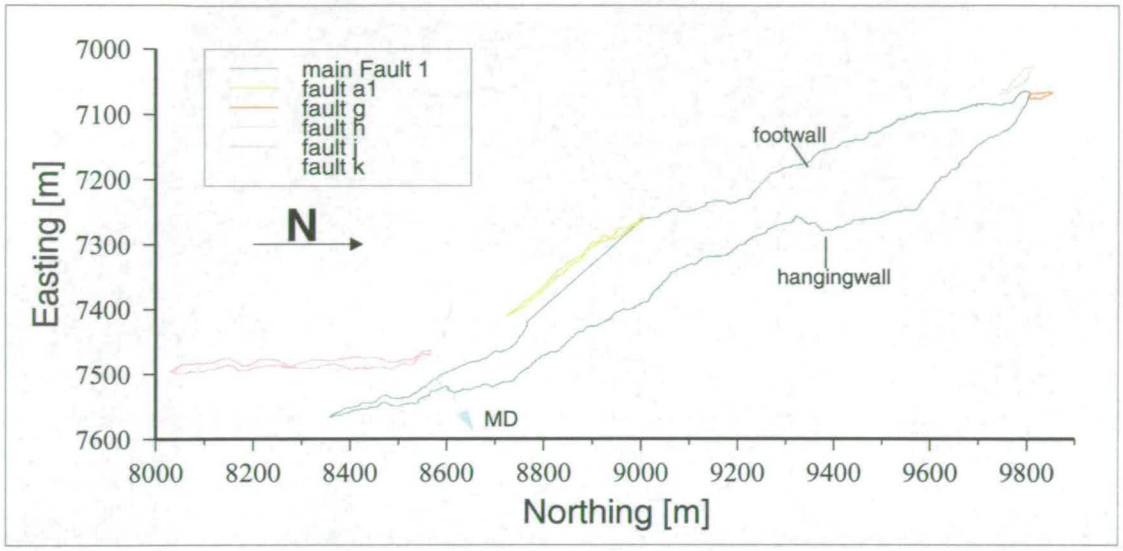

Figure 4.7: *Map of the small faults around Fault 1 discussed in the text.*
The cutoff data collected for the footwall and hangingwall of Fault 1 is shown in dark green. Small faults in the footwall of the main fault discussed here [g-k and a1] are colour-coded as shown.
'MD' marks the approximate location of the gorge incised by the main channel: see Fig. 4.1.

Southern tip of Fault 1: Two small faults occur at the southern tip of Fault 1 near the incision by the main channel: a hangingwall splay [fault k], and a small footwall fault [j, Fig. 4.7].

Cutoff profiles and a displacement profile of the hangingwall splay, fault k, are shown in Fig. 4.8. Displacement on the splay increases rapidly towards its termination against Fault 1. Since the northern tip of fault k is not visible, its original shape cannot be inferred but, the main Fault 1 displacement profile has a corresponding marked low at their junction [Fig. 4.5]. The orientation and the relative displacement profiles of the splay and the main fault [Figs. 4.6 and 4.7] are very similar to descriptions of hangingwall splays abandoned after linkage of two fault segments [e.g. Morley et al. (1990); Anders and Schlische (1994); Cartwright et al. (1995); McLeod et al. (2000), Fig. 2.5].

A small fault [j in Fig. 4.7] in the footwall of Fault 1 extends southwards for several hundred metres from the southern bank of the incised main channel [Figs. 4.1 and 4.7]. The fault strikes 002°, subparallel to a major joint set, and has a series of southward-stepping 'jogs', each along 155°, subparallel to a second joint set. At both tips, fault j dies into a joint, a characteristic which is seen in many places on the Volcanic Tableland

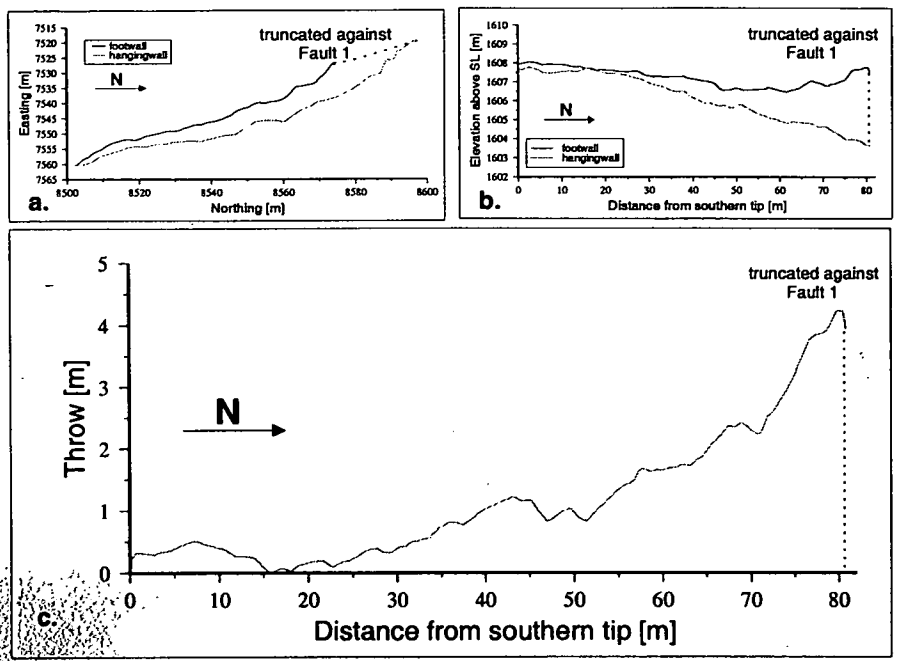

Figure 4.8: a. Map, b. cutoff and c. displacement-length profile for the hangingwall splay, fault k, at the southern tip of Fault 1. See Fig. 4.7 for location relative to Fault 1. Displacement increases dramatically towards the truncation against Fault 1. This splay is probably a remnant abandoned splay left from linkage of Fault 1 and a smaller fault.

[e.g. at the northern tip of the array; fault a1; and see McFadzean (2002)], indicating the influence of joints on later structural development on the Tableland surface.

Figure 4.9 shows that displacement associated with Fault 1 is accommodated far beyond its mapped southern tip on smaller structures: fault j extends over 250m beyond the main fault tip. Thus, although largely focused on a single structure in the centre, displacement is more distributed at the southern tip of Fault 1. In particular, the orientation and stepped trace of fault j imply that where extension is roughly perpendicular to a major joint set, the pre-existing fractures are used to accommodate some strain. If the displacements on these two faults at the southern tip of Fault 1 are added to the displacements measured on the main scarp [Fig. 4.5], its southern tip profile changes dramatically, as the effective length and the tip gradient of the summed fault is increased [Fig. 4.10 and Table 4.1].

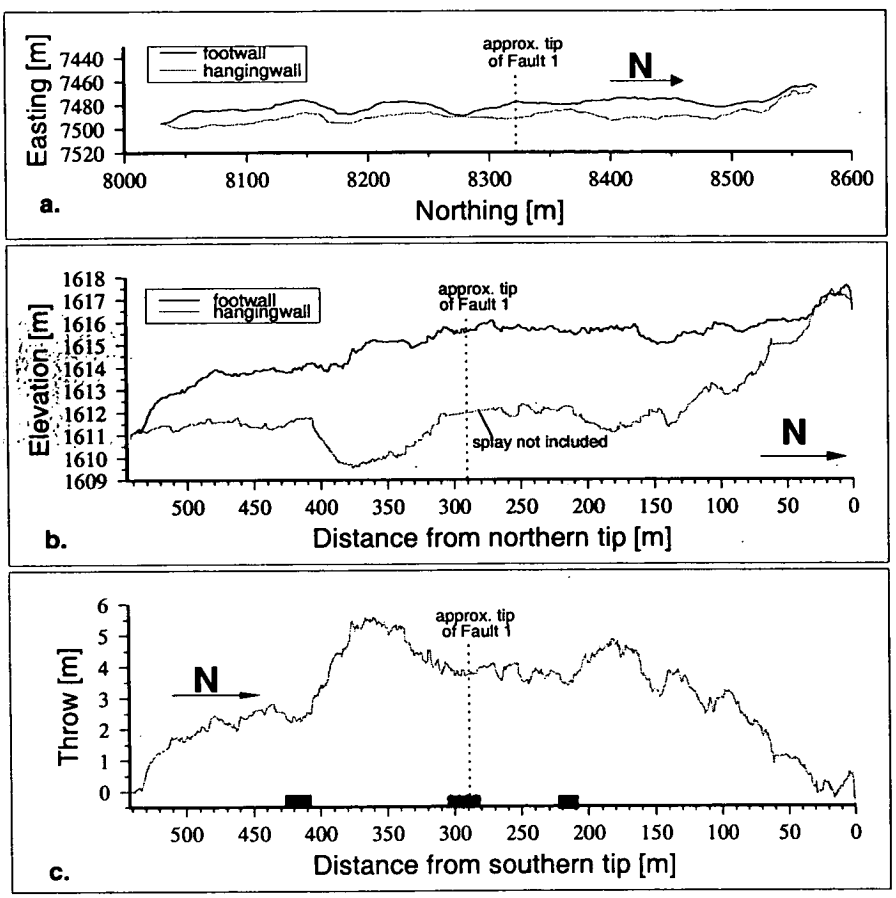

Figure 4.9: *a. Map, b. cutoff and c. displacement-length profile for small fault j in the footwall of the southern tip of Fault 1.*
NB *the scale of the map in [a] slightly distorts the true undulations of the fault trace. The fault extends for 255m beyond the southern tip of Fault 1 and dies into a joint at both tips. A small splay [marked in b] has not been included in the cutoff profiles.*
Major segment boundaries are marked with red boxes on the x-axis. Some probable lower-order segment boundaries occur towards the northern tip.

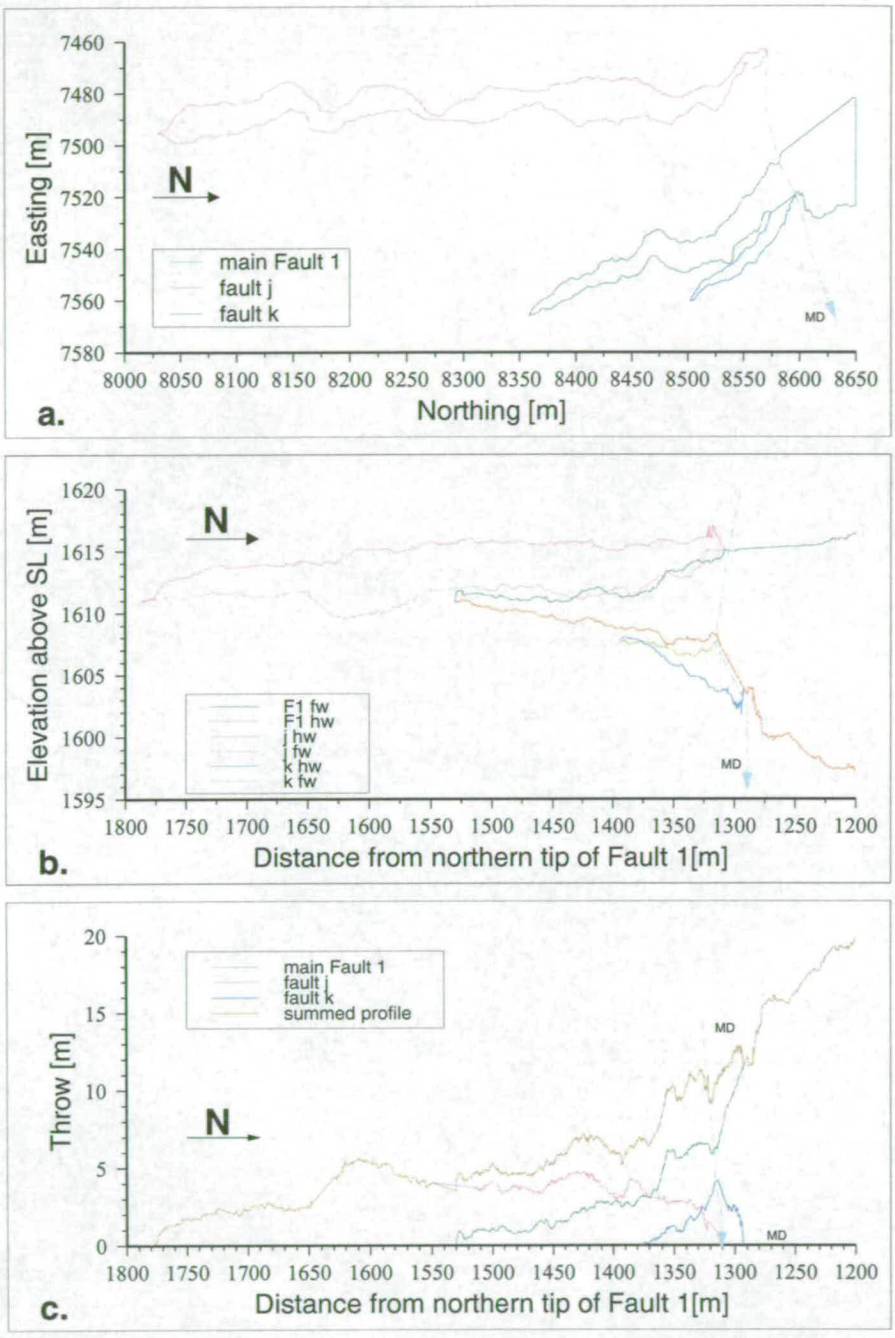

Figure 4.10: *a. Close-up map of southern tip of Fault 1.*
b. Cutoff profiles for faults j and k, calculated along the spine of Fault 1.
c. Summed displacement-length profile for the southern tip of Fault 1, including the contributions of the small footwall fault j, and the abandoned hangingwall splay, fault k. The original D-L profile of Fault 1 [green] is as shown in Fig. 4.5.
The approximate location of the incised main channel is marked 'MD'. The channel clearly incises through the main scarp at the point where fault k has joined the main structure, and immediately north of the fault j tip. This point is a displacement low in the summed profile. [See also section 4.2.1.]

Northern tip of Fault 1: Unlike the ramp at the southern tip of Fault 1, the ramp between Fault 1 and Fault 0 is not breached. However, the overlap zone is steeply warped and broken by a number of small fractures [e.g. Fig. 4.11]. Two of the largest of these fractures, near the tip of Fault 1, are discussed below [see Fig. 4.7].

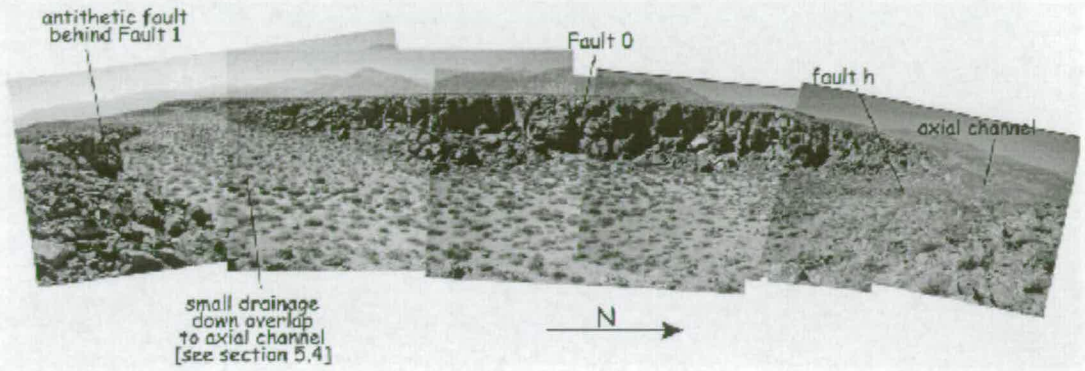

Figure 4.11: *Overview of the overlap between the northern tip of Fault 1 and Fault 0. Field photograph montage taken from the top of the Fault 1 scarp, looking towards Fault 0 [west]. The Sierra Nevada form the background. Note the number of small fractures in the ramp, although there is no hard-linkage between the two main faults. Fault h, described below, is marked. Fault g can be seen in Fig. 7.7. A small channel [Figs. 5.41 and 5.42] drains [left-right] down the ramp towards the axial channel which flows around the northern tip of Fault 1 [section 5.2].*

'Fault g' is a small fault [~50m long] right at the northern tip of Fault 1 [Fig. 4.7]. The profile is clearly skewed towards F1 [Fig. 4.12], giving a steep tip near Fault 1 but a shallow tapering northern tip profile. Both features indicate interaction with Fault 1, as expected. A double peak near the D_{max} implies linkage of two smaller structures, whose displacement profiles reflect mutual growth and interaction. 'Fault h' lies further west, sub-parallel to the trace of Fault 1 [Fig. 4.7]. Fault h is ~85m long and again not symmetrical, with two distinct 'lobes' suggestive of earlier segmentation. The more northerly lobe has more than twice the displacement of the southern lobe, indicating the effect of Fault 0 to the north.

Brittle deformation accommodates some of the strain in this overlap, but the small faults are predominantly found near Fault 1. Since the tip of Fault 1 is near the centre of Fault 0, this fault pattern is consistent with the stress-shadow pattern shown in Fig. 2.3. Faults g and h are much smaller than the faults at the southern tip of Fault 1, and accommodate less displacement, hence making very little contribution to the overall displacement profile of Fault 1. The number of small faults [Fig. 4.11] and the evidence for interaction between them suggests that displacement is being transferred between Faults 0 and 1, although there is no through-going fault visible at the surface. This may well reflect that most of the strain in the overlap has so far been accommodated by warping of the tuff, resulting in a steeply angled ramp surface [stream draining the ramp has an overall gradient of ~9° towards the north: Fig. 5.42]. Jointing is much less conspicuous in this region [Fig. 4.2], in comparison with the southern tip of Fault 1, and may be partly responsible for the larger ratio of ductile to brittle deformation in this overlap.

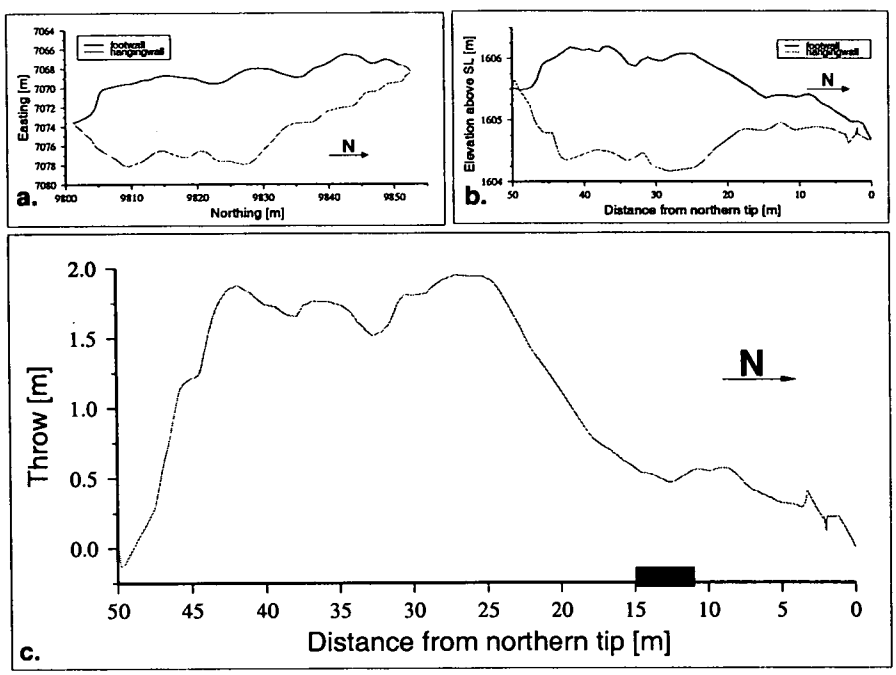

Figure 4.12: *a. Map, b. cutoff and c. displacement-length profile for small fault 'g' at northern tip of Fault 1 footwall. Fault 1 is immediately to the south of this fault, explaining the massive difference in displacement and tip gradients between the northern and southern tips. An old segment boundary is marked by the red box on the x-axis.*

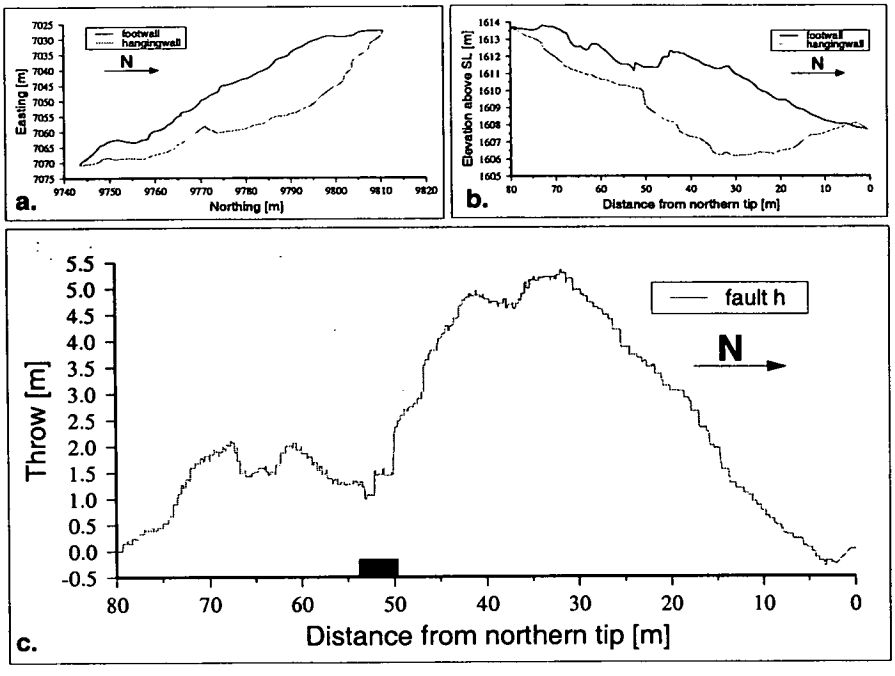

Figure 4.13: *a. Map, b. cutoff and c. displacement-length profile for small fault 'h' at northern tip of Fault 1 footwall. The marked difference in the displacement and also the tip gradient on this fault suggests that it is interacting predominantly with Fault 0 to the north-west. Linkage of at least two original segments is indicated by the presence of two distinct lobes in the profile. Red box marks the probable location of an earlier segment boundary.*

4.1.1.3.1 Centre of Fault 1 footwall A whole series of small faults, both syn- and anti-thetic, and oriented subparallel to Fault 1, occur in the central footwall of Fault 1 [Fig. 4.1]. Only one is considered here: a typical antithetic structure, fault a1 [Fig. 4.7]. This fault, dipping west, has a long [~ 320m] thin trace, similar to that of fault j [Fig. 4.14a]. A series of 'lobes' in the displacement profile suggest the linkage of up to five original segments. The profile is, however, far more symmetrical than the other small fault profiles described, suggesting a considerably smaller degree of interaction with nearby faults [Fig. 4.14c].

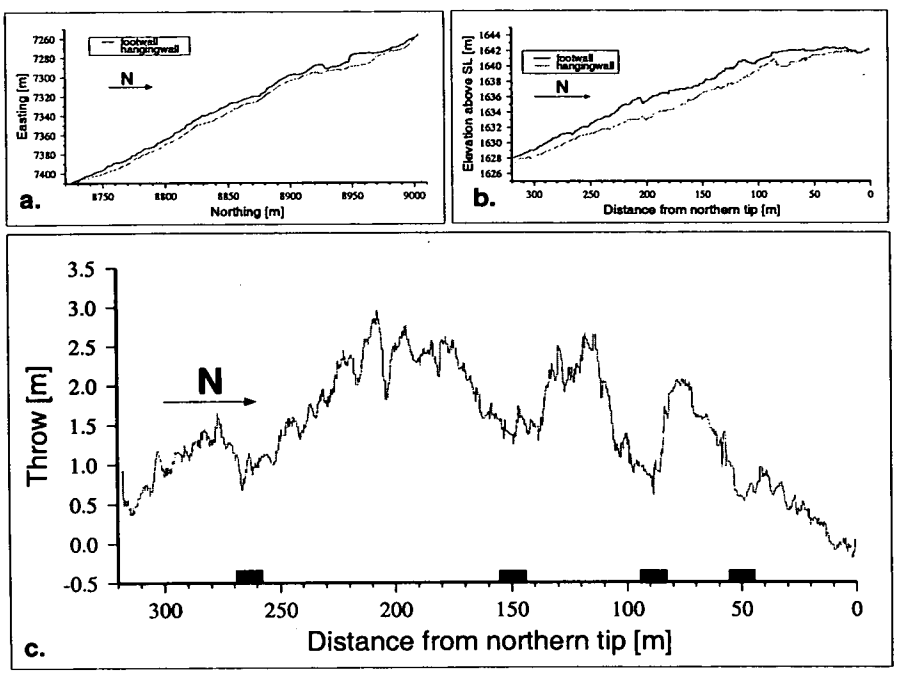

Figure 4.14: *a. Map, b. cutoff and c. displacement-length profile for small antithetic fault 'a1' in centre of Fault 1 footwall. Red boxes mark palaeo-segment boundaries.*

Fault a1 is typical of the numerous footwall faults in this region. Their number demonstrates the point that a reasonable proportion of the extension is accommodated on small structures, many of which appear to have originated as joints, particularly towards the south, as demonstrated by their traces, and in some cases their spacing. Some structures also die into joints at their tips [e.g. fault j].

4.1.2 Fault 2: bounding the east [front] of the central overlap

4.1.2.1 Fault cutoffs

Fault 2 is virtually straight, striking 333°. The northern tip of the fault splits into two, the western splay longer than the eastern. This splitting occurs at a series of small fumaroles, which correlate with slightly wider parts of the traces ['Fum' in Fig. 4.15; see also Fig. 4.40a,b]. Fumaroles appear on the aerial photographs [Figs. 4.1 and 4.20] as small rounded 'blebs': the remnants of vents through which the hot tuff degassed [Sheridan (1970)]. They are pervasively jointed, and indurated, so they may

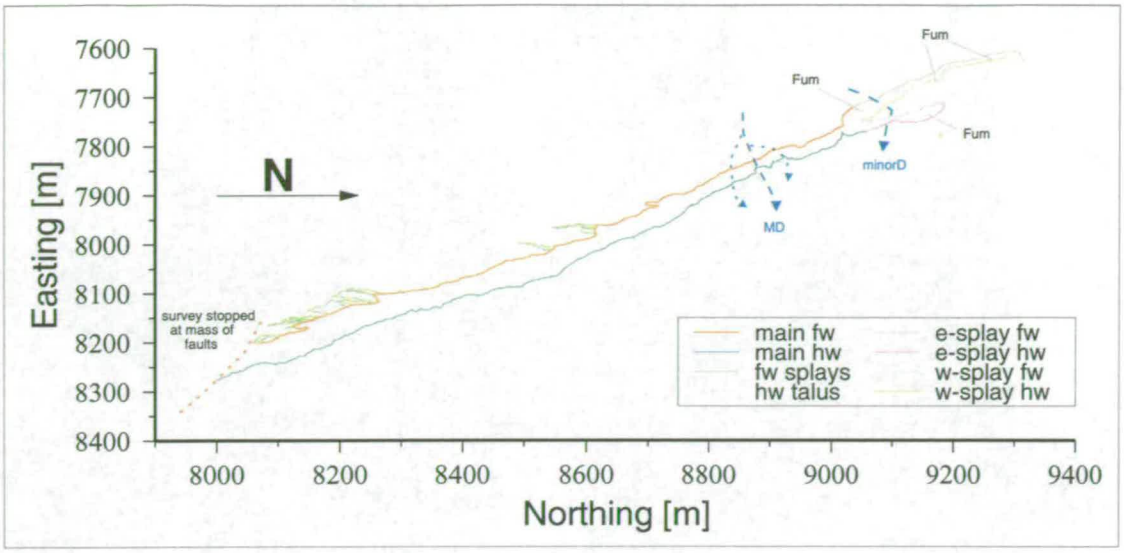

Figure 4.15: *Map of surveyed fault cutoffs for Fault 2. The survey was stopped where this fault is joined to large faults to the south.*
'Fum' marks the location of fumaroles, where the fault trace widens.
'MD' and 'minorD' indicate the location of the main and minor stream channels through the scarp.

be expected to have influenced the growth of later fractures. Surveying was stopped in the south where the fault changes orientation sharply, and becomes hard to distinguish from other large scarps [Fig. 4.1]. Thus this survey corresponds to the northern part of the fault surveyed by Dawers and Anders (1995) [Fig. 3.6]. Linkage to southern faults is probably responsible for the increase in fault width, and scarp height, towards the southern tip of the survey.

A series of fault-tip splays occur in the southern footwall of the fault [dark green in Fig. 4.15]. The splays all have very similar orientations, striking 009-017°, which may simply reflect the stress orientation during their growth, or possibly indicate the influence of an underlying structural heterogeneity, such as the jointing [joints oriented 136-150° and 350-012° here]. Comparison with fault k and Fault 1 suggests these faults are abandoned footwall splays, left after linkage of a series of initially small fault segments.

A number of small talus fans occur along the hangingwall, increasing in size towards the south. The large southern fans lie at the toe of a large overlap zone. Other fans along the hangingwall of the fault correspond with small channels draining the footwall. Towards the south, supplying streams cascaded off the scarp, as indicated by black staining on the scarp [e.g. Fig. 6.2]. In contrast, the main channel and minor channels towards the north ['MD' and 'minorD' in Fig. 4.15] have incised through all or part of the scarp [e.g. Fig. 4.29c], and left 'nicks' in the fault trace.

Splays from the southern part of the fault footwall are not included in the profiles here, and hence some parts of the southern footwall profile appear more linear than expected [Fig. 4.16a]. Cutoff profiles have been calculated separately for the two fault splays at the northern tip of the fault. Fumaroles in the fault scarps ['Fum'] correspond with local footwall highs but not hangingwall lows, suggesting that these sites had

a surface topography before faulting, and that the footwall highs do not reflect true tectonic displacement highs. Sharp lows in the footwall elevation mark stream incision, particularly at 'MD' and 'minord' [section 4.2].

4.1.2.2 Displacement-length profile

Displacement on the surveyed part of Fault 2 increases towards the south: D_{max} is located over 1200m from the northern tip [Fig. 4.16b; compare with the survey in Fig. 3.6]. This implies a high degree of interaction with the large faults to the south, and is similar to the asymmetry of Fault 1, which implies interaction with Fault 0 to the north. These profiles, and the steep warping and pervasive fracturing of the overlap zone [e.g. Fig. 4.2], imply that much of the strain has been accommodated in the intervening rock, and not on the two main faults themselves.

Although segmentation of Fault 2 is not as pronounced on the medium scale seen in Fault 1 [3-500m length], linkage can be inferred over the 50-100m scale [Fig. 4.16b]. This may imply linkage and formation of a through-going Fault 2 relatively earlier than for Fault 1, where much larger-scale segmentation remains [Fig. 4.5].

Local displacement lows occur at several of the hangingwall talus fans [Fig. 4.16b], which are *not* supplied by incised channels. This implies that streams originally exploited displacement lows between small segments, but that supply to the subsiding hangingwall was cut off as the footwall uplifted further, and possibly faster, following segment linkage. In contrast, where channels have incised through the scarp, [e.g 'MD': Fig. 4.16b], local displacement lows remain, although less evident when a correction is made for the talus fan elevation [gold]. In these cases, once established, the drainage routes were maintained, despite the later growth and development of the through-going fault.

Displacement accumulation at the northern tip of Fault 2 is clouded by the presence of a series of fumarole mounds [Figs. 4.16c and4.40b], which are closely associated with the splitting of the fault into two splays. The real tip gradient is hard to determine through the mounds, which form 'highs' every ~100m. When the two splay profiles are summed [ochre line in Fig. 4.16c], it becomes obvious that the minor channel [section 4.2.2] crosses the scarp at the lowest local elevation, and between two fumarole mounds.

Figure 6.2 shows a series of distinct weathering bands in the Fault 2 scarp. The most highly-weathered bands occur towards the top, while the lowest part of the scarp appears very fresh [Fig. 6.2]. Soil lines are visible on the lowest part of the scarp, and a couple of small soil patches cling to the surface of the tuff [Fig. 6.3]; implying that the lowest part of the scarp was buried until relatively recently. Together, these observations imply exhumation in periodic movements. Each band is 1-3m high, and hence may be too large for a single event on particularly the young fault [slip scales with length; $\leq$1m slip expected per event on a $\leq$1.5km fault]. However, the distinct differences in weathering imply that a relatively long period elapsed between the exposure of the bands, particularly given the low erosion in this area. Thus the bands may represent clusters of fault events. Similar weathering bands have been described on normal fault scarps in central Greece [e.g. Jackson et al. (1982)]; and on the Hebgen Lake scarp, (Zreda and Noller, 1998).

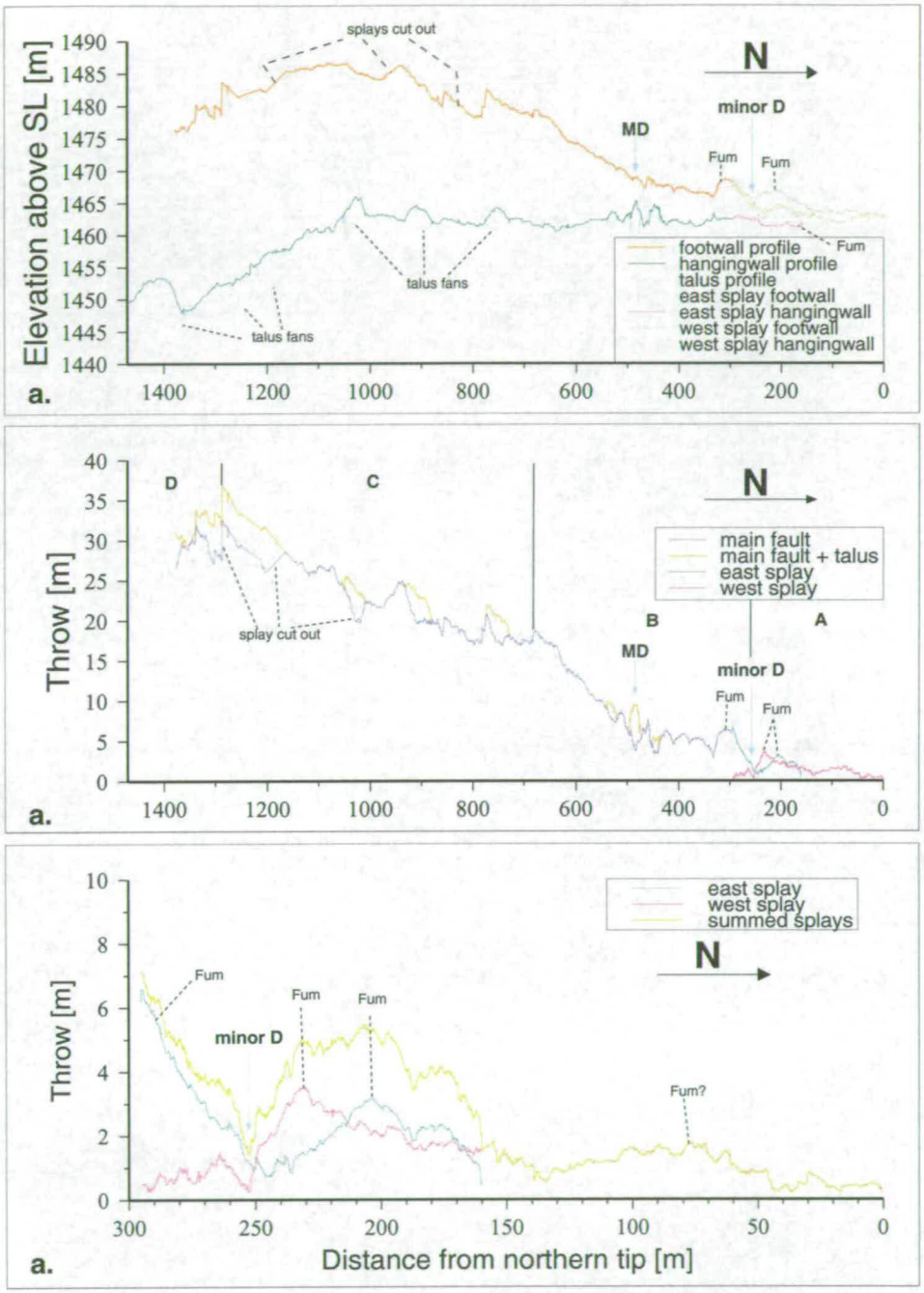

Figure 4.16: *a. Fault 2 cutoff elevation profiles. Distances are calculated from the northern tip of the western splay.*
b. Fault 2 displacement-length profile. Four sections occur along the fault, distinct by the variation in the displacement along strike, as marked: A to D.
c. Close-up of the d-l profile of the northern splays of the fault.
'Fum' marks the location of fumaroles along the fault: footwall elevation highs do not coincide with hangingwall lows.
'MD', and 'minorD' mark the location of the streams discussed in section 4.2. The minor channel crosses Fault 2 between two fumaroles, implying a strong influence of lithological heterogeneity, and the pre-existing topography, on stream development.

4.1.3 The linking fault: joining Faults 1 and 2

4.1.3.1 Fault cutoffs

Figure 4.17 shows the surveyed cutoffs of the main linking fault scarp, which joins Faults 1 and 2, and a large splay fault near Fault 1. The linking fault trace is almost straight, striking broadly 320°, although slight undulations may reflect old segment boundaries. Close cutoffs mark where drainage channels cut through the fault, e.g. 'MD'. There is no clear association of the linking fault or northern splay with fumaroles in the ramp.

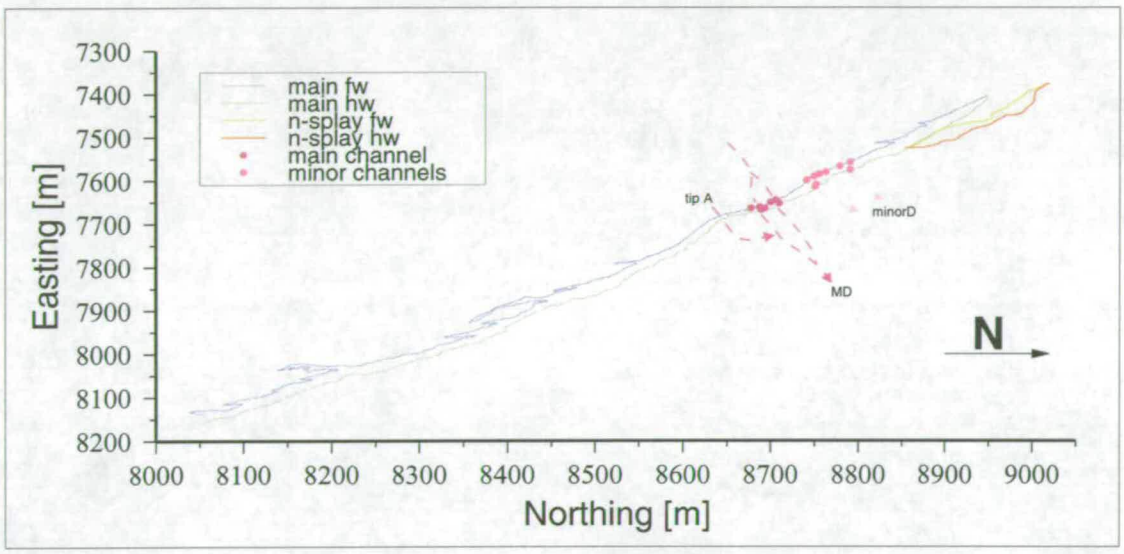

Figure 4.17: *Map of surveyed fault cutoffs for the linking fault.*
The location of the main ['MD'] and minor ['minorD'] channels are marked. Dots demonstrate the braiding of each stream branch at the scarp. Many small footwall splays occur towards the southern part of the fault, and a large splay fault has grown near Fault 1. A slight change in orientation coincides with the thinnest part of the fault map trace, immediately south of the main channel incision. A small channel incises the scarp at this point ['tip A': see Fig. 4.23].

A series of footwall splays occur towards the south. Almost all have a portion of their scarps striking 004-010°, similar to the orientations of the Fault 2 footwall splays, and roughly paralleling one of the main joint sets. The largest splays occur at changes in strike of the southern part of the fault, and again, the footwall splays are interpreted as abandoned remnants from previous linkage events. The hangingwall of the fault is generally devoid of splays. A series of discrete larger faults occur in the hangingwall of the linking fault [Fig. 4.2], but since they do not directly join the linking fault scarp, they have not been included in this discussion.

The highest point in the main footwall elevation is approximately in the centre of the fault, around 650m from the northern tip [Fig. 4.18a]. The elevation drops dramatically northwards to a pronounced low around 400m from the northern tip, where a channel incises right through the scarp; and then increases again towards the northern tip. In contrast, a much more gradual decrease in elevation is seen towards the south, where the linking fault merges into a group of larger faults [Fig. 4.1]. The large northern

splay has two discrete segments, on either side of the tip of the main fault [~25m on scale].

4.1.3.2 Displacement-length profiles

The d-l profile [green in Fig. 4.18b] shows a maximum displacement of 16.31m approximately at the centre of the fault. However, several local displacement highs approximately 150m apart correspond with footwall splays, and are probably remnant displacement highs, retained from earlier pre-linkage times. The retention of these highs may indicate that linkage was relatively recent, and that the displacement has not been equilibrated. A dramatic displacement low [throw $\simeq$ 0m] around 400m from the northern tip corresponds with the change in orientation of the map trace. A 1.5m wide channel [tip A] incises through the scarp at this point, although it cannot be traced far into the footwall [Fig. 4.23b]. This evidence suggests a major structural boundary, and thus fault segmentation on the order of 400m, similar to that of Fault 1 [Fig. 4.5].

The northern section of the linking fault has a generally lower displacement than the southern part. A steep northern tip gradient [0.084] indicates strong interaction with Fault 1, although the fault was also enhanced by growth on the splay fault [red]. In contrast, although the linking fault does not die to a discrete tip at its southern end, the tip gradient is much more gradual [0.019]. The largest footwall splay has a D_{max} of 5.67m, immediately south of the main fault D_{max}. All the splay profiles are skewed to the north, as seen with fault k, and suggesting that a similar pattern of segment linkage generated the linking fault.

The northern splay fault [red] consists of two clear segments, each approximately 100m long. [*Displacements at the southern tip are not reliable, as the cutoff elevations disagree by almost 4m, although measured the same elevation. However, the northern part of the data appears reliable.*] The maximum displacement is huge: although only 223m long, the fault has a similar D_{max} to the linking fault: 15.89m. The D_{max} is near Fault 1, which probably dominated its development. Consequently the northern tip gradient is also incredibly steep [0.317].

The raw profile [green] has a central D_{max}, and shows segmentation on the order of 150m: the separation of the footwall splays. Inclusion of the splay fault data [lime] shows two discrete displacement maxima, separated by a low displacement region, through which all the major streams have incised [Fig. 4.19]. The two forks of the main channel incise deep notches [Fig. 4.23a] while a third channel 'A' has cut down directly through the point with lowest displacement [Fig. 4.23b]. The summed southern data implies linkage of small segments to form two segments of around 400m length near Fault 2, separated from a further fault pair growing near Fault 1 [see Chapter 7 and Fig. 7.4].

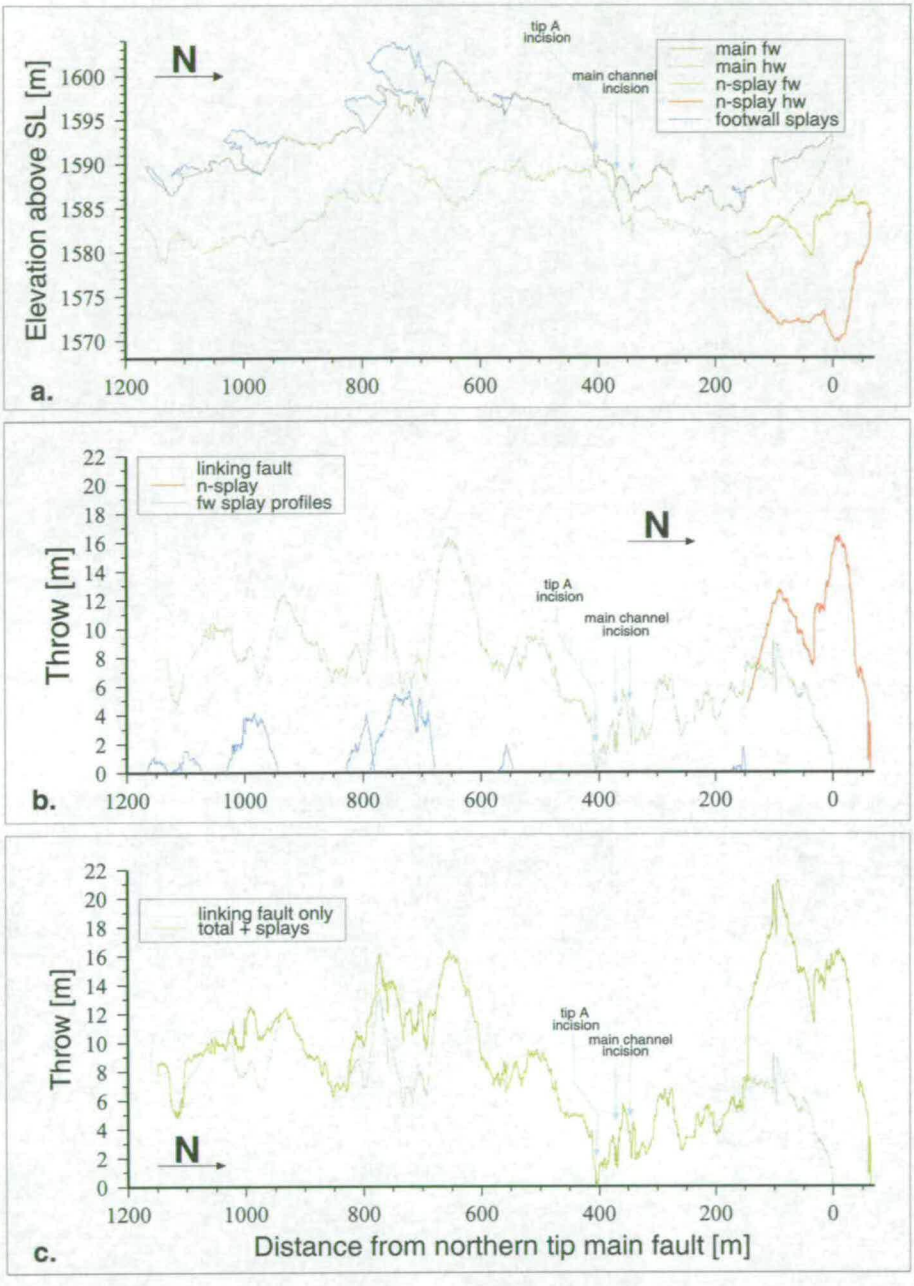

Figure 4.18: *a. Cutoff profiles for the linking fault. Main footwall and hangingwall [lilac and green]; splays in the southern footwall [blue]; northern splay fault [red and yellow].*
b. Displacement-length profiles for the linking fault and splays, calculated using a fault dip of 75°. Note the huge displacement on the northern splay fault, despite its short length. However, the southern tip of the northern splay has apparently erroneous elevations: see text.
c. Summed displacement-length profile for the entire fault, including the contribution of the footwall splays and northern splay fault [lime]. The profile of the main fault alone [green] is shown for comparison.
'MD', and 'minorD' mark the location of the incised channel branches. The sudden drop in displacement around 400m from the northern tip implies a major segment boundary. This displacement low coincides with the thinnest part of the map trace [Fig. 4.17], the slight change in fault orientation, and is cut through by a channel [tip A].

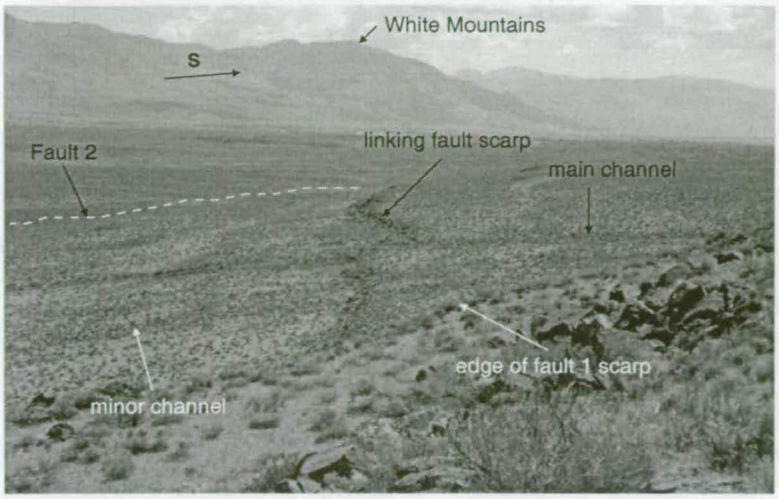

Figure 4.19: *View of main channel path down the overlap, through the linking fault. Photograph taken from the top of the Fault 1 scarp, looking SE. Main channel course exploits the displacement low between the two ends of the linking fault. Minor channel course visible in the foreground. Fault 2 footwall forms the lower edge of the ramp. The main stream is ~350m from F1 where it incises the linking fault.*

4.1.4 Summary of fault profile data

Surveying of the three main faults in the central overlap highlights several important features of faulting on the Tableland. Each of the surveyed faults shows various orders of segmentation, over scales of 50 to 400m in length.

The largest fault, Fault 1, has the highest displacement, and also an extremely high D_{max}/L ratio [Table 4.1]. This reflects its location at the centre of the whole fault array and may hint at a relatively early linkage of its subsidiary segments. The skewing of the displacement profile and the asymmetry of the tip gradients imply that much of the recent development of Fault 1 has been dominated by interaction with Fault 0 to the north. Many small faults occur around the main structure, reflecting the large-scale fracturing of the tuff associated with the high extension. Small faults at both tips play an important role in accommodating extension, and also emphasise the differences between the two fault tips. Many of the small faults appear to have nucleated or propagated along joint planes, reflecting the influence of lithological heterogeneity within the Bishop Tuff on the style of later deformation.

Fault 2 has a similar length to Fault 1, but considerably lower displacement [Table 4.1]. A discrete fault tip was not surveyed at the southern end, as the fault is hard-linked to faults to the south, and hence a tip is hard to distinguish. This interaction is also responsible for the location of the maximum displacement towards the southern end of the survey. Displacement decreases rapidly towards the north, and several different displacement gradients occur along the fault. Fault 2 splits into two strands at its northern tip, following the lines of prominent fumaroles, and demonstrating the influence of these more-welded heterogeneities in the tuff on the fault development.

Numerous splay faults are evident in the southern part of the footwall, striking 009-017°, parallel to one of the main joint orientations; again indicating the influence of joints on fault nucleation.

Fault	D_{max} (m)	L (m)	D_{max} / L ratio
Fault 1	79.58	1530.20	0.052
Fault 1 + southern tip faults	79.58	1785.961	0.045
F1 fault g [N]	1.95	49.95	0.0390
F1 fault h [N]	5.34	79.90	0.0669
F1 fault j [S]	5.57	542.10	0.0103
F1 fault k [S]†	4.24†	80.77†	0.052†
F1 fault a1 [C]	5.62	318.21	0.0177
Fault 2§	32.75§	1466.67§	0.022§
Fault 2 (incl. talus)§	37.59§	1466.67§	0.026§
Linking fault	16.31	1149.51	0.0142
Linkf + all splays	21.26	1213.55	0.0175
Linkf north splay‡	15.89	223.40	0.071

Table 4.1: *Calculated displacement-length values for surveyed faults.*
Dawers et al. (1993) observed that small isolated faults on the Tableland have D_{max}/L in the range 0.016-0.020; large isolated faults have D_{max}/L in the range 0.009-0.014.
Values are all based on differential GPS surveying during the summer of 1999.
† *Fault 'k' has been truncated: this is the remnant hangingwall splay after segment linkage during the earlier development of Fault 1, hence the length and possibly the D_{max} are underestimated; D_{max}/L is probably heavily* over*estimated.*
§ *A southern tip was not surveyed for Fault 2, hence the length is underestimated, and D_{max} / L consequently overestimated. This survey corresponds to only the northern ~1500m of this fault surveyed by Dawers and Anders (1995): Fig. 3.6.*
‡ *This is the 'northern splay fault' to the east of the northern tip of the linking fault.*

The linking fault which joins these two faults across the warped relay has a much lower displacement, but a complicated profile. Inclusion of the displacement contributions of numerous small splay faults indicates a complex history of segment linkage. The linking fault appears to have grown in two main parts, each nucleated at one end of the relay, near the bounding faults. A wide region with a marked displacement low, exploited by both the main and minor streams, still exists between the two displacement maxima, implying that the present through-going structure may have formed only comparatively recently.

Study of the faults also sheds a great deal of light on the development of the drainage systems through this central overlap. In general, streams and talus deposits are associated with palaeo-displacement lows, some of which have been lost due to subsequent displacement accumulation after segment linkage. In the cases of Fault 1 and the linking fault, the main channel ['MD' in the figures] crosses the scarps at pronounced displacement lows, probably marking old segment boundaries. The main channel crosses Fault 2 at a point with generally low displacement, but a steep displacement gradient. The minor channels cut through the northern tip of this fault between fumarolic highs. Talus fans without associated incised channels at old segment boundaries in the southern part of Fault 2 imply that these sediment supplies were cut off, possibly following segment linkage. Other incised streams [e.g. main and minor

channels discussed in section 4.2] have been able to keep pace with the fault uplift, maintaining supply to the subsiding hangingwall.

Further discussion of the implications of this data, particularly for the development of the stream networks in and around the overlap zone, can be found in Chapter 7.

4.2 Drainage systems in the central overlap

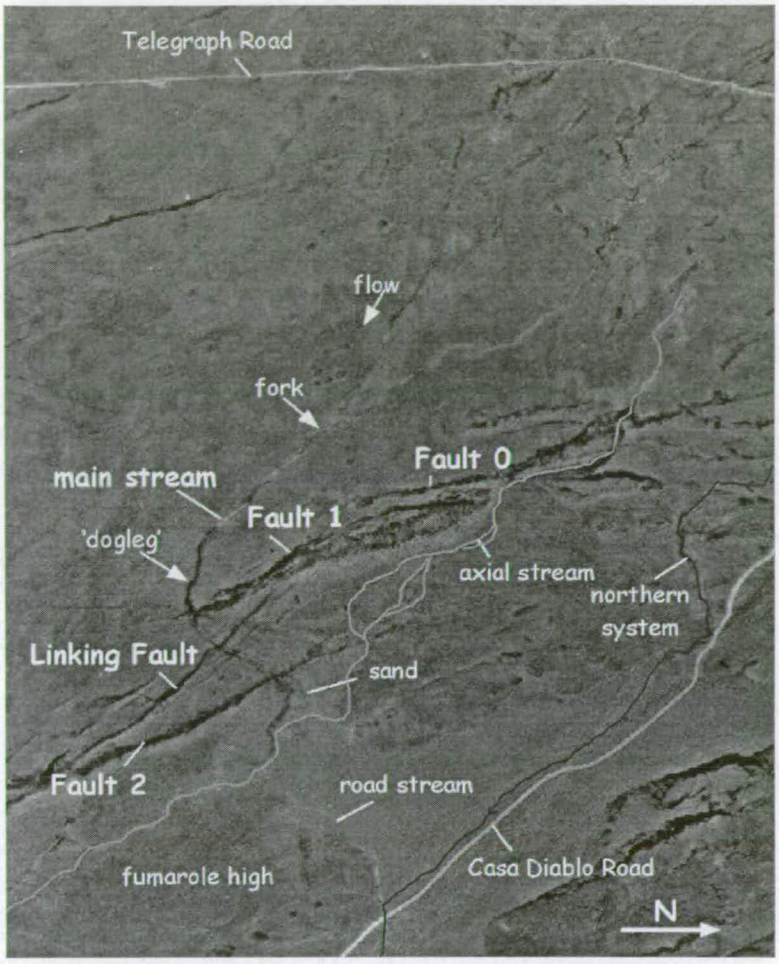

Figure 4.20: *Aerial photograph of the central overlap.*
Dark shadows are extensional fault scarps dipping towards the east [bottom] with throws up to 90m [D_{max}]. The overlap is approx. 1km north-south, and the two main faults [Fault 1 and Fault 2] are approx. 800m apart at the widest part, joined by the linking fault.
The main stream incises through all three of these main faults, as marked. It deposits a fan of sand in the hangingwall basin of Fault 2 [pale area].
Smaller channels diverge from the largest stream at the foot of the Fault 1 scarp and drain towards the northern tip of Fault 2, into its hangingwall basin.
The channel flowing axially to the whole fault array [see Fig. 4.1] has reworked some of the sand from the main channel towards the south.
The downstream part of the northern tip drainage system [section 5.1] can also be seen.

This section focuses on the streams flowing through the central overlap, across and between the faults described in section 4.1 above. The streams were surveyed using differential GPS over two fieldseasons. Discussion of their development is based predominantly on the features of the stream courses, longitudinal profiles and variations in cross-sectional morphology.

Section 4.2.1 concentrates on the largest channel ['MD' in section 4.1], which can clearly be seen snaking through the centre of the overlap. Section 4.2.2 looks at the contrasting

development of the smaller channels which diverge from the main channel at the foot of Fault 1, and flow across the north of the overlap towards the northern tip of Fault 2 [Fig. 4.20; 'minord' in section 4.1]. The features of these streams are compared with those of the other major systems around the array in Chapter 5. Exposure ages for samples from these channels are calculated in Chapter 6, and discussed in Chapter 7.

4.2.1 Main stream

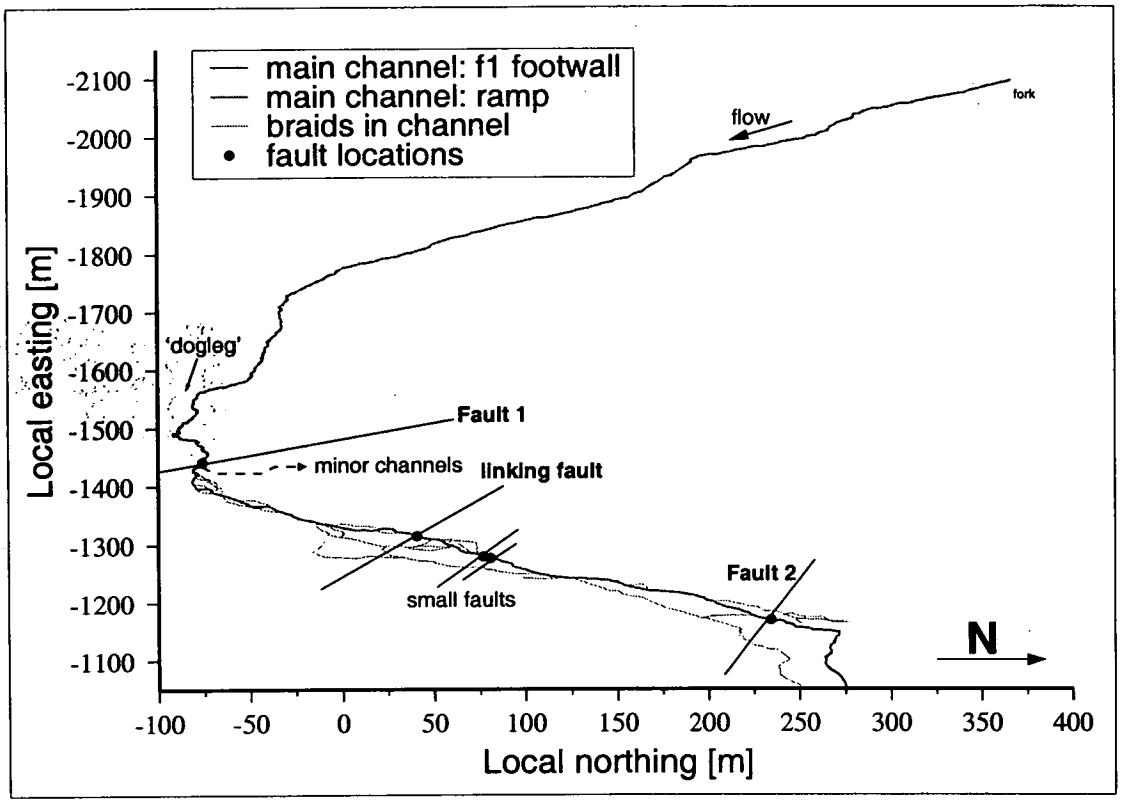

Figure 4.21: *Map of the main stream course from the fork to the Fault 2 hangingwall basin. The channel is sinuous, but not diverted around the tips of either Faults 1 or 2: all of the major scarps are incised. Sinuosity increases in the immediate footwall of Fault 1, preserved by incision along a series of joints ['dogleg'].*
Braiding occurs upstream of both the linking fault and Fault 2, the braids rejoining a short distance downstream from each scarp. Two large branches cut through the linking fault. A third branch cuts through the linking fault scarp at the displacement low marking the point of segment linkage ['A' in Fig. 4.18c]. [See also Figs. 4.23 and 4.31].
Smaller channels [section 4.2.2] diverge from the main stream at the base of Fault 1.

The main stream is the most striking feature of the central overlap. It shows prominent bends near the two main faults, but, in contrast to the many published examples of streams flowing through normal fault oversteps [e.g. Leeder and Gawthorpe (1987); Gawthorpe et al. (1994); Fig. 2.12], is not diverted around the tips of both fault segments to deposit sediment at the toe of the ramp. Instead, the channel incises through the scarps of all the major faults [Faults 1, 2 and the linking fault: see Fig. 4.24], to deposit its load in the hangingwall basin, over 400m from the northern tip

of Fault 2 [section 7.5]. However, prominent bends imply that the fault development had a major impact on the stream development and provide a stark contrast to the virtually straight channel through the northern tip of the array [Fig. 5.3a]. This section gradually builds a picture of the response of this main stream to the growth of the faults, focusing on the stretch from the fork upstream of Fault 1 through the ramp and into the Fault 2 basin. The channel's course is studied first, and followed by observations made from the longitudinal and cross-sectional profiles of the channel. Other observations from the ramp are presented after the description of the minor channels, in section 4.2.3.

4.2.1.1 Stream course

The main stream follows a fairly straight course for most of the distance from the fork towards the Fault 1 scarp [Fig. 4.21]. However, as it approaches the scarp, the channel deviates sharply from this line, and becomes increasingly sinuous. There are two wide bends in the channel course, ~300 and ~100m from the scarp, where the channel bends through almost 90°. The stream then winds through several tighter bends before incising through the scarp. This increased sinuosity continues for ~30m into the hangingwall of Fault 1, before the stream resumes a straight course towards the linking fault.

The channel course in the footwall of Fault 1 is largely controlled by joints. The long straight part of the channel immediately downstream of the fork follows a joint [Fig. 4.20]. Sharp kinks in the channel course at the 'dogleg' in Fig. 4.21 also coincide with joints, the channel flowing in turn along each of two main joint orientations [see Fig. 4.22]. The clear change in morphology at this point, and greatly increased incision [section 4.2.1.2], demonstrates the exploitation of joint planes by the downcutting stream.

Sixty metres upstream of the linking fault, the main stream forks, and several smaller branches form in the immediate footwall of the fault. Both main branches incise deep notches through the linking fault scarp and a pair of smaller faults further downstream, subparallel to the linking fault [Fig. 4.20], before recombining [Fig. 4.23a]. Another small channel joining the southern fork flows through the segment boundary at the displacement low in the linking fault scarp [Fig. 4.23b.; at 'A' in Fig. 4.18c]. Although the aerial photo implies that this channel branches off the main stream ~100m downstream of Fault 1 [Fig. 4.20], on the ground, it can only be reliably traced for ~5m upstream of the fault. More minor braiding of the main channel occurs around a series of small N-S trending faults downstream of the linking fault, although most braids are short [Fig. 4.21].

Similar braiding occurs ~45m upstream of Fault 2, resulting in a series of small waterfalls along the scarp. The main channel is incised deeply into the Fault 2 scarp [Fig. 4.29c]. Branches rejoin the main channel over a range of distances up to 200m into the hangingwall. Most transported material is deposited in the immediate hangingwall of Fault 2, in small fans are along the scarp. Cobbles [5-20cm diameter] are deposited near the scarp, while the main trunk stream carries fine sand to more distal regions; although much has been reworked towards the south by the axial channel [see the shape of the sand deposit [pale area] on the aerial photograph, Fig. 4.20; and section 5.2].

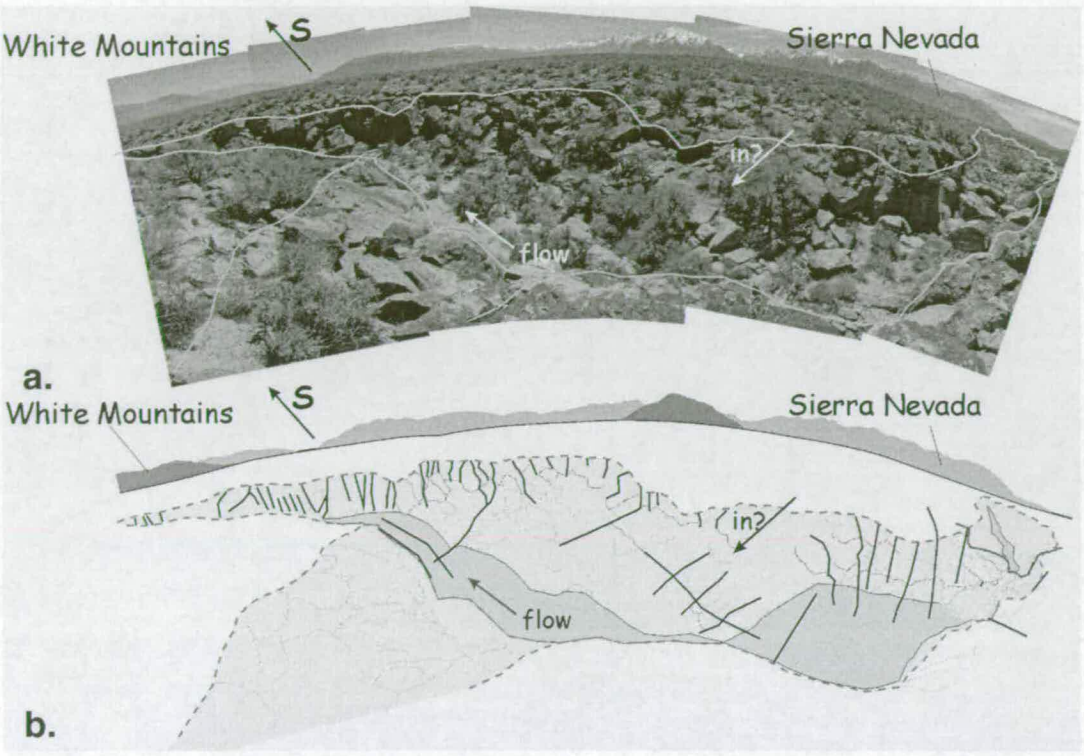

Figure 4.22: *'Dogleg' kinks in the main channel in the footwall of Fault 1: joint influence on the main channel.*
a. Field photographs and b. sketch interpretation of the sharp changes in channel direction. The channel flows along a joint, and cuts down another [right] before switching to flow parallel to a second dominant joint direction. The channel returns to its original direction further downstream [left]. Water also appears to have entered this channel from the ground surface ['in'], along a small inlet in the western bank, carved along a joint plane.
c. Stereographic representations of joint orientations measured at two locations in the channel banks [see photographs for locations]. Stream flow directions are superimposed in red.

Both the braiding and increased sinuosity seen at the faults are typical stream responses to a reduction in gradient. The relative location of the stream changes with respect to the faults is very similar to the pattern in Holbrook and Schumm (1999) [their Fig. 8b], which shows the response of alluvial channels to tectonic uplift. The different responses [sinuosity in F1 footwall versus braiding at the linking fault and F2] probably reflect the different environments: prior incision and the well-developed joint pattern restrict the development of braiding in the immediate footwall of Fault 1. When superimposed on the displacement-length graph for the linking fault [Fig. 4.18c], incisions of the three branches of the main stream all occur in the central displacement low [Fig. 4.19], suggesting that they exploited a structural 'gap' in the developing linking fault scarp. The occurrence of three discrete channels may possibly reflect a more detailed response to fault growth, as 'A' incises at the lowest displacement, while the other forks incise on either side of a local displacement high [Fig. 4.18c].

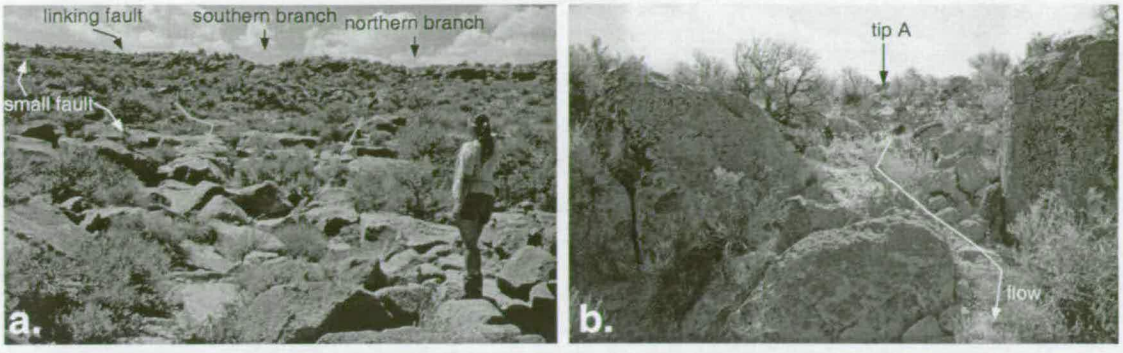

Figure 4.23: *Main channel branches incising the linking fault.*
a. View upstream [to west] of the branching of the main channel at the linking fault. Photograph taken from downstream of the subsidiary faults: note the two branches through each fault, and the two notches in the linking fault which forms the skyline.
b. View upstream [to west] of incision into the linking fault scarp by the small channel 'A', at the displacement low [see Fig. 4.18]. Blocks forming scarp here are 80cm high. Despite the clear incision, the channel can only be traced into the footwall for ~5m.

4.2.1.2 Long profile

Sharp knickpoints are evident at each fault crossed by the main stream [Fig. 4.24]. Pronounced differences in morphology and gradient are evident between the reach incised into the footwall of Fault 1, and the downstream reaches. Gradients and SL indices of each reach are presented in Table 4.3 on page 129.

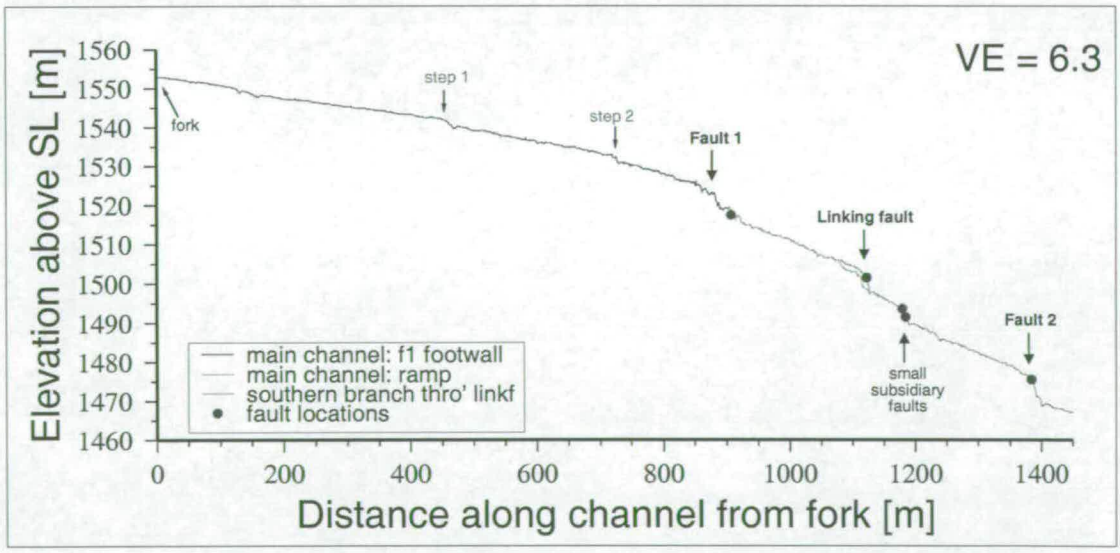

Figure 4.24: *Long profile of the main channel from the fork in the footwall of Fault 1 to the hangingwall basin of Fault 2, showing the locations of the main steps in the channel bed.*

Footwall of Fault 1: Three distinct reaches in the Fault 1 footwall are separated by sharp steps in the profile. The channel gradient increases towards the main fault in each of these sections [Fig. 4.25 and Table 4.3], and correlates with an increase in

incision evident from the bank profiles [Fig. 4.32], and channel cross-sections [section 4.2.1.4]. Each reach has a characteristic morphology, as shown in Fig. 4.26.

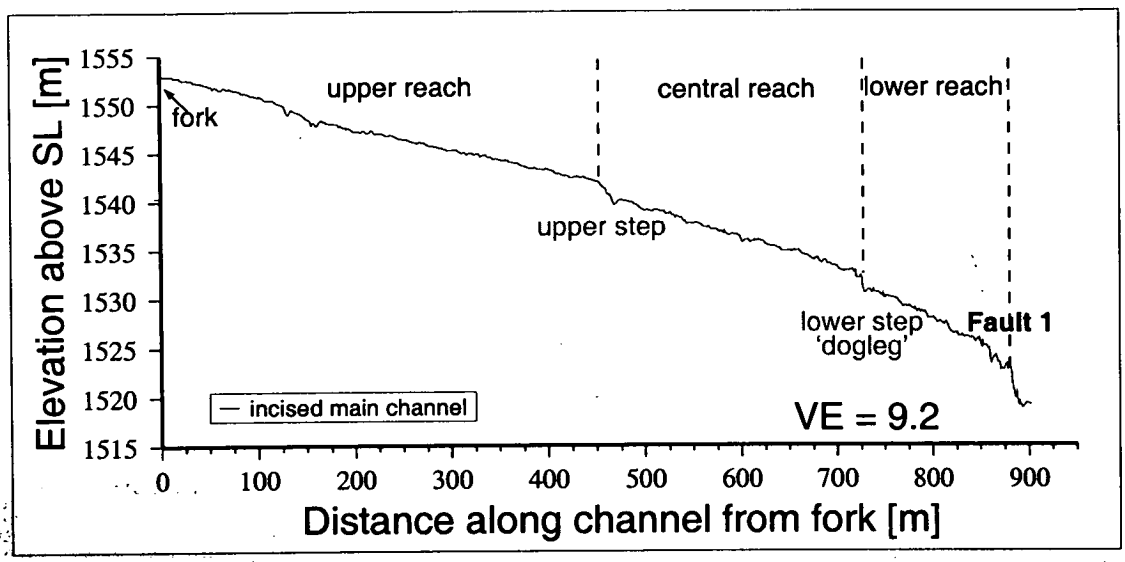

Figure 4.25: *Long profile of main channel in the footwall of Fault 1. Three distinct reaches are separated by two pronounced steps in the profile [see text for discussion]. The knickpoint at Fault 1 consists of a series of small steps of 1.5-2m in height, where the channel has eroded out joint planes in the tuff.*

The upper reach is predominantly straight [Fig. 4.20]. It is characterised by a broad shallow channel, reaching a width of 20-22m between bank tops, but only 0.5-3m depth. Polygonal cooling blocks in the tuff are exposed as bedrock sheets [Fig. 4.26a] along some parts of the channel floor, with sand and occasional pebble lags against the jointed sheet margins. Bedrock is exposed along parts of the shallow, and often sharply asymmetrical, banks. Local steep-sided canyons or 'slots' mark deeper excavation of joints. Incision increases downstream, with lateral cobble bars gradually becoming visible on bends. Water-smoothed surfaces are well-preserved on many bedrock slabs, particularly at the lip of 'slots'.

In the central reach, the channel begins to bend towards the main fault. This section has much steeper walls, reaches up to 20m width between the bank tops, and 4-5m depth [Fig. 4.26c]. The floor generally exposes jointed bedrock, although more cobbles line the bed than further upstream, sometimes forming small bars 1-3m in length. Small steps of 20-80cm are common where joint planes oriented across the channel have been eroded. Sand and pebble lags partially fill small pools and cavities immediately downstream of these steps. The banks are steep, exposing jointed bedrock blocks, and often quite degraded, with many subangular 30-100cm blocks lying on the channel floor. Some of these blocks have been reworked a short distance downstream, indicating some failure of the banks during channel occupation. Rarely, lateral cobble bars have formed on the inside of bends, to a depth of 2-3m.

The channel course is more tortuous in the lowest footwall reach, bend orientations implying exploitation of joint planes. The stream is deeply incised, with bank-bank widths of only 10-12m, but depths of 5-8m towards the main Fault 1 scarp [Fig. 4.26e].

Figure 4.26: *Contrasting morphologies of the three channel reaches in the footwall of Fault 1.*
a. Upper channel reach: small fork. Channel barely 60cm wide, shallow, sand and pebble-lined. Red notebook is 30cm high.
b. Wider section of upper reach, exposing 'plates' of bedrock in channel. Channel is 2-4m wide, and incised 20-40cm into tuff. Camera case for scale in foreground.
c. Central reach: 'kp1' to dogleg. Immediately downstream of 'kp1': beginning of incision. Depth 80-120cm, width 10-12m. Camera case for scale in foreground.
d. Lower reach: immediately downstream of 'kp2'. Channel 3-4m deep with steeper bedrock walls. Channel base only 2-5m across. Red notebook is 30cm high.
e. Steep bedrock-walled gorge immediately above Fault 1. Sagebrush in channel are ~3m high. Incision reaches 8m at F1 scarp.
f. Eroded joint exposed in northern bank of channel, ~150m upstream of Fault 1. Bank is ~4.5m high, joint opened to 70cm width.
Gradients and SL indices of the different sections are presented in Table 4.3.

The banks are subvertical, incised along planes in the tuff [Fig. 4.26f]. In many places, the walls have failed along joint planes, leaving fallen blocks 1-3m in diameter in the channel floor. A few blocks have been reworked downstream, but most have become jammed and locally constrict the channel. Small piles of sand, pebbles and cobbles are trapped behind these obstructions, and smoothing is excellently preserved on many blocks, demonstrating active abrasion. Otherwise, the channel floor is incised into bedrock, although now often obscured by thick sagebrush growth [Fig. 4.26e]. Steps of 0.5-1.5m occur in several places in this reach, where water cascades over jammed blocks in the channel bed, and also at some steps where joint planes have been eroded *in situ*.

The first major step in the profile [Fig. 4.25] is a drop of 2.5m across a transverse joint, 450m upstream of Fault 1, separating the shallow upper and incised central reaches. This is the largest vertical drop upstream of Fault 1, and corresponds with the largest change in the channel morphology, as incision is minimal upstream of this point, except in the short 'slots' where joints have been excavated.

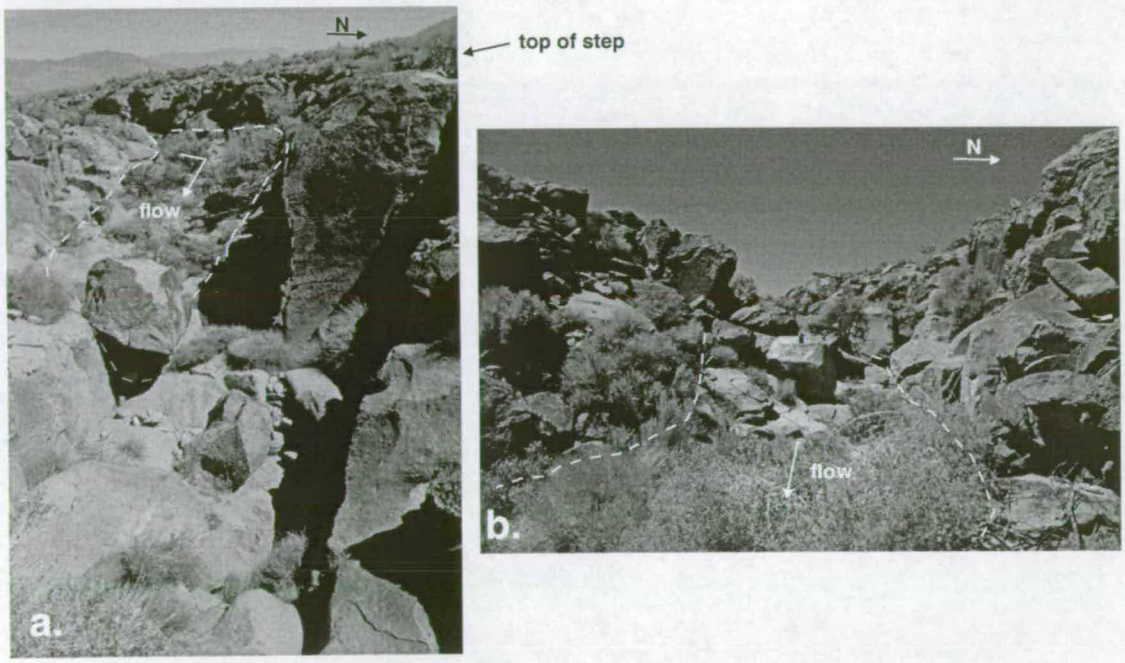

Figure 4.27: *Steps in the upper part of the main channel profile: footwall of Fault 1.*
a. First joint step in dogleg looking upstream into the central reach. The drop here is about 2m. [See also wider view of dogleg bends: Fig. 4.22]. Camera case in foreground for scale.
b. Looking upstream from the base of the Fault 1 scarp at joint steps in the scarp. Each step is 1-2.5m high, making a total drop of 10.5m through the fault scarp. Red notebook on joint in centre of photo is 30cm high [see also section 7.2.2.3].

The second step in the profile [Fig. 4.27a] occurs at the upstream bend of the dogleg [Fig. 4.27a]. The channel drops 2m at this upstream bend, marking a sharp change from the central reach into the steep-sided gorge of the lower reach [Fig. 4.26c,d]. From this point, the channel gradient increases sharply as it gradually incises more deeply towards the main fault scarp. Bends are more common, and their orientations suggest that the downcutting channel made use of weak joint planes.

The most prominent feature of the channel profile at the Fault 1 scarp is the series of steps in which the channel drops from the footwall to the base of Fault 1 [Figs. 4.24 and 4.25]. The overall elevation drop is 10.5m, accommodated in a series of drops of 1-2.5m [Fig. 4.27b]. This is roughly equivalent to the horizontal spacing of joints in this part of the tuff and implies that the stream exploited weaknesses to adjust its profile [section 7.2.2.4]. Water-smoothed surfaces are evident on many exposed joint planes. The flight is not vertical, but steps back in an upstream direction over a distance of 80m, reflecting upstream erosion of the fault scarp as well as the downcutting action of the river. This stepped knickpoint is very different from those at the other faults downstream [see Figs. 4.24, 4.29c, 4.23 and Table 4.3].

Ramp: Fault 1 to Fault 2 hangingwall basin: The main stream does not flow down the steepest gradient of the ramp, but follows a much shorter course to Fault 2. The steepest slopes on the present-day surface drain away to the north, closer to the route taken by the minor channels [section 4.2.2]. Steep knickpoints occur at the scarps, even at the small faults downstream of the linking fault. However, in contrast with its profile in the footwall of Fault 1, the main channel shows little change in gradient in the three reaches between the faults in the ramp [Table 4.3]. The gradient of the channel bed is considerably steeper than even the last incised reach immediately upstream of the Fault 1 scarp [Fig. 4.24 and Table 4.3]. This part of the profile accounts for an overall elevation drop of 44m, but over roughly half the distance taken for the 40m drop between the fork and the base of Fault 1.

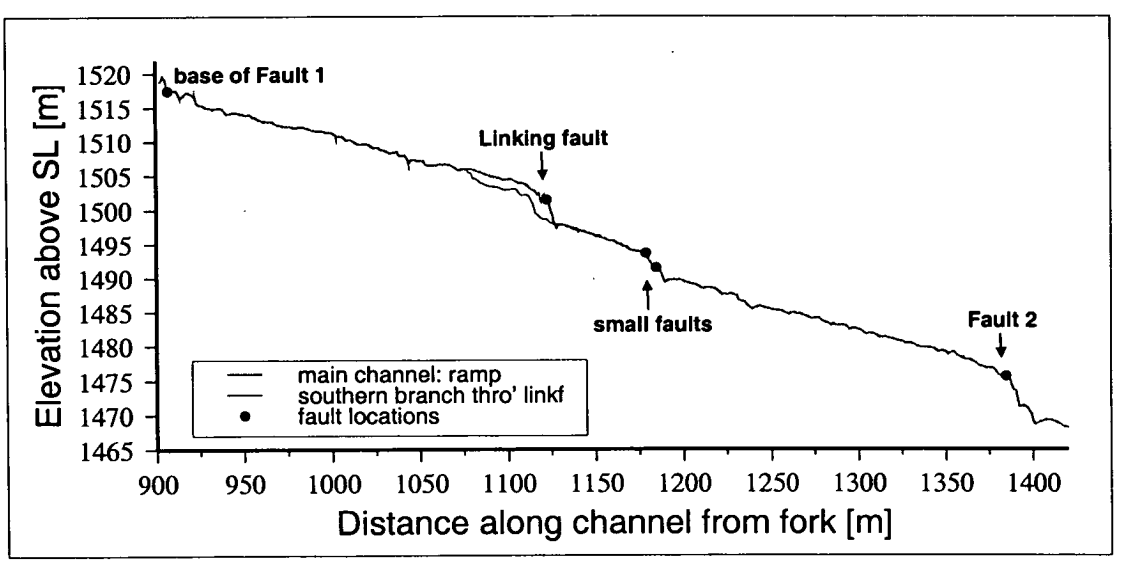

Figure 4.28: *Long profile of main channel through the ramp: Fault 1 to Fault 2. The southern branch of the channel through the linking fault is shown in pink.*

The lack of gradient change between non-faulted reaches in the ramp is coupled with an almost uniform channel morphology [Fig. 4.29a,b], although varying degrees of braiding are observed [section 4.2.1.1]. In non-faulted reaches, the main channel has a width of 5-10m between bank tops, and a depth of generally 0.5-1.5m. The channel incises bedrock, exposing jointed slabs, as seen in the upper footwall reaches [Fig. 4.29a]. The bed surface is very irregular, partly due to uneven erosion of the jointed slabs, with

evidence of plucking, particularly in the immediate footwalls of the faults. Erosion of joints has formed some steps of 20-80cm in the channel floor, partially filled by fine sand and pebbles up to a few centimetres across. Channel banks are composed of jointed bedrock slabs, much like the channel base, though deposition of cobbles up to 20cm across is common, forming lateral and point bars in braided parts of the stream. Cobbles cover much of the ramp surface for some distance away from the channel [e.g. Fig. 4.46], but their size [up to 30 cm] and distribution are not consistent with overbank deposition [section 4.2.3].

The channel gradient decreases sharply in the hangingwall of Fault 2 [Fig. 4.28 and Table 4.3]. The channel narrows to less than a metre in width, and is less than 50-80cm deep. Bedrock is incised for the first few metres from Fault 2, where the channel is choked with subangular boulders reworked from the scarp [Fig. 4.29]. Further downstream, cobbles line the channel banks and floor for around 200m, beyond the main cobble fan. Beyond this, the bed material fines, and the channel lies between soft banks of fine sand up to 70cm high. Occasional pebble lags are visible. The axial stream [section 5.2] joins this overlap channel 240m downstream of Fault 2. From this point on, it is hard to distinguish how many of the channel features were original, and how many have been overprinted by the southward axial discharge.

The knickpoints at the ramp faults [linking fault, small faults and Fault 2] are much steeper than that at Fault 1. The elevation drops are also more commonly single steps, rather than flights of smaller steps as seen at Fault 1. Where the main channel incises scarps, it narrows considerably: the main channel is only ~4m wide [bank-bank top] where it incises Fault 2. Plungepools [e.g. Fig. 4.29c,d] are developed at each fault scarp, and downstream of some of the larger joint steps. Smoothing of the bedrock is well-preserved both in the pools and also on some parts of the fault scarps, with sand, and sometimes rounded cobbles, in the base.

Figure 4.29: *Channel morphologies in the lower main channel: ramp and F2 hangingwall.*
a. Typical view upstream in the main channel looking towards the linking fault. Hammer is 40cm long. Pitted bedrock slabs exposed in channel base. Erosion evident between blocks, partially filled with clasts.
b. Smoothing of bedrock steps in channel upstream of the linking fault. Large potholes eroded between joint 'plates'. A small pool can be seen below the smoothed step.
c. View upstream at the main channel incision through Fault 2. Nancye Dawers stands in the upper of two plungepools. The foreground shows the scoured pool at the scarp base, partially filled with large rounded cobbles, up to 30cm diameter. Angular blocks line the waterfall. Total elevation drop is 10.5 m.
d. View of Fault 2 hangingwall, from the top of Fault 2 scarp. Lower plungepool is seen in the foreground. Branches of the main channel snake off to the left and right, initially filled with coarse material: angular blocks from the fault scarp, and rounded cobbles up to 35cm across. The course of the channel in the distance can be picked out by the line of the green sagebrush snaking towards the south [right].

The two main stream branches show slightly differing responses to the linking fault growth, with the southern branch incising more deeply [3m in comparison with 2m] into the scarp itself. However, this incision extends only 40m into the footwall, at which point incision rapidly decreases, forming a 'spade'-shaped incision [Fig. 4.30]. Water also appears to have entered this branch through an overspill channel from the main stream to the north ['in': Fig. 4.30a], which itself is only incised a few centimetres into the tuff. Incision is considerably lower in the northern branch, and decreases rapidly upstream. Both branches thus show some degree of upstream migration of the incision, as reflected by the shape of the knickpoint crest [Fig. 4.28]. However, most of the elevation drop still occurs at the fault scarp in a single sharp step, in contrast to that at the F1 knickpoint [Figs. 4.25 and 4.27]. A third channel crosses the linking fault scarp at the point with lowest displacement ['A' in Fig. 4.18c]. This channel is incised right through the scarp, but can only be traced ~5m into the footwall of the fault.

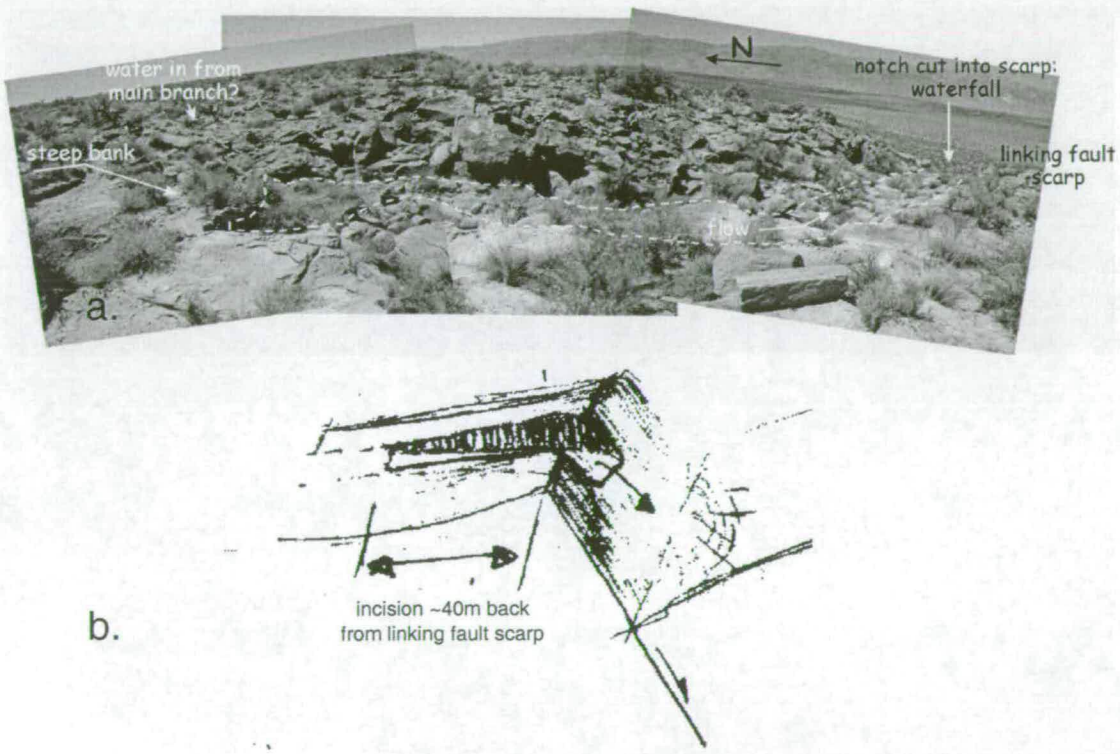

Figure 4.30: *a. View from southwest of spade-shaped incision into the linking fault scarp by southern branch of main channel.*
b. Field sketch of spade-shaped incision: the channel is 3m deep at the scarp, shallowing gradually upstream to the current low knickpoint 40m west of the fault. The incision decreases to 0 west of the knickpoint.
Water appears to have also entered this channel from overspill of the main northern branch ['in'].

Figure 4.31 shows the three channel branch profiles where they incise the linking fault. The *overall* gradient of the three branches is very similar, but in detail, the individual channels have very different shapes [Table 4.2]. The most obvious difference is in the

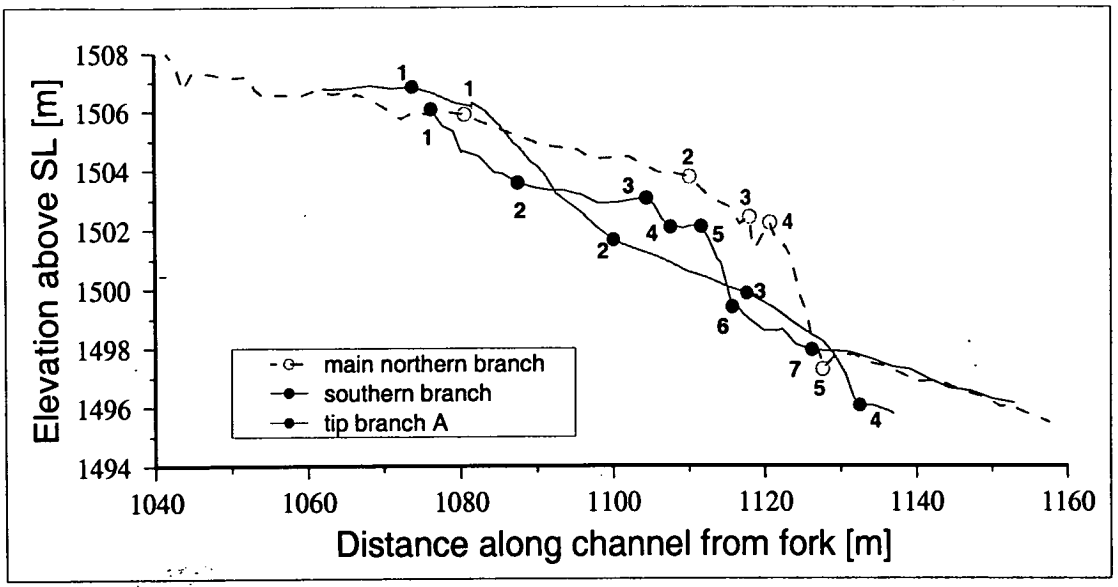

Figure 4.31: *Comparison of profiles of the three main streams which cut through the linking fault scarp.*
'Main' northern branch [blue], southern branch [pink] and tip branch 'A' [green].
The numbers on each plot refer to the separate sections of each channel whose gradients have been calculated in Table 4.2.
The profile of the channel through the displacement low ['A'] has a much smoother, shallower profile than those of the northern branches [see also Fig. 4.18].

maximum gradient: the channel which incises at the displacement low [A] has a much lower maximum gradient [14.419°] than the main [northern] and southern channel branches [35.429 and 33.730° respectively]. The consequently smoother profile may reflect the lower local displacement on the linking fault [see D-L profile: Fig. 4.18c], but also suggests a greater adjustment to fault displacement. Knickpoints at the smaller faults are also steep, although the southern branch appears to have incised into them more deeply than the northern stream. This may indicate either a higher discharge, or a longer period of occupancy of this branch.

Section	Main [N] branch		South branch		Tip branch (A)	
	Lgth(m)	Grad(°)	Lgth(m)	Grad(°)	Lgth(m)	Grad(°)
Overall	**46.99**	**10.403**	**49.95**	**9.264**	**58.71**	**10.394**
1 - 2	29.54	4.118	11.37	12.329	26.29	11.111
2 - 3	7.88	9.699	16.89	1.789	17.63	5.838
3 - 4	2.60	4.339	3.12	17.430	14.80	14.419
4 - 5	6.97	35.429	4.09	-0.284		
5 - 6			4.07	33.730		
6 - 7			10.42	7.979		
Max. grad		**35.429**		**33.730**		**14.80**

Table 4.2: *Comparison of gradients of channel sections for the main channel branches through linking fault. Channel sections are numbered as in Fig. 4.31.*

The Fault 2 knickpoint, in contrast, consists of two large steps, forming two waterfalls in the field [Fig. 4.29c]. Some upstream erosion of the scarp has occurred, facilitated by

joints, as shown by the large blocks eroded from the scarp [Fig. 4.29c,d]. Incision into the top of the scarp is less marked than at the linking fault, as shown by the sharper crest of the knickpoint in Fig. 4.28. The reduced crestal incision may reflect a reduced discharge, due to braiding of the stream [Fig. 4.21].

Overall profile: Table 4.3 shows the downstream variation in bed gradient and SL indices of the main channel. Gradients are averaged for each reach, and compared with the reaches across the fault scarps. Equivalent values have been calculated for the minor channels [page 143], the transverse northern tip channel [page 180], and the axial channel [page 207].

Reach	Description	Length (m)	Gradient (°)	SL index
(F1 footwall)	Fork to kp1	452.48	-1.399	-28.74
	kp1 to dogleg	243.70	-1.721	-17.95
	Dogleg to top F1	117.71	-2.792	-41.41
Unfaulted	Base F1 to linkf	182.74	-3.586	-69.29
	Linkf to small fs	46.99	-4.800	-98.57
(ramp)	Small fs to F2	161.78	-3.733	-88.19
	F2 immed basin	96.31	-2.451	-132.76
	F2 basin: join axial	133.83	-0.752	-42.24
Fault scarps	Fault 1	**43.02**	**-8.404**	-132.02
	Linking Fault	19.80	-18.523	-374.47†
	Small fault 1	7.93	-16.113	-340.95†
	Small fault 2	3.37	-32.509	-756.91†
	Fault 2	**47.03**	**-12.605**	-292.00
Footwall steps	Upper (kp1)	15.61	-8.546	-69.17
	Lower (kp2: dogleg)	10.58	-12.136	-155.81

Table 4.3: *Variation in gradient and SL index of main channel reaches through the overlap, calculated from differential GPS surveys of the main channel.*
Gradients are averaged for each reach from the fork to the hangingwall basin of F2. Gradient increases towards the Fault 1 scarp, remains roughly constant and high through the ramp to Fault 2, then decreases sharply in the F2 hangingwall basin. Incised reach gradients are also averaged through the fault scarps and the two steps in the footwall of Fault 1. The knickpoint gradient through Fault 1 is considerably lower than through the other faults in the ramp. Together with the greater length of this reach, this implies that more of the uplift at Fault 1 has been accommodated. Fault 2 is the only downstream fault to approach the Fault 1 values.
SL index is a proxy for stream power: $SL = \frac{\Delta elevn}{\Delta length} * dist, L$ *[sections 2.3.2 and 7.1.3]. L calculated from the fork. Fault reaches have locally high stream power, but the highest values occur at the smallest faults in the ramp [†].*

Variations in the channel gradient correlate closely with changes in morphology. The increased gradient towards Fault 1 reflects steepening of the footwall stream by F1 motion, but this has been partially accommodated by increased incision. In contrast, the gradient is higher in the ramp than even in the immediate footwall of Fault 1, which, along with the lower incision, implies that the channel has not adjusted as much to tectonic motion in the ramp as to that on Fault 1.

The main stream profile shape is very different at each scarp. The channel incises virtually right through Fault 1, forming a stepped profile; the elevation drop accommodated over tens of metres along the stream. In contrast, the elevation drop at the smaller faults within the ramp is sharp, and occurs virtually right at the present scarp.

Of these downstream scarps, only the Fault 2 knickpoint shows any significant evidence of a stepped profile, although the main elevation drop remains at the present fault scarp, implying that there has been little upstream migration of the knickpoint to date. The profiles imply that the channel has adjusted more fully to the displacement on Fault 1 than to the other faults, which is consistent with the contrasting bed gradient. Thus the river may have begun to adjust to uplift on Fault 1 considerably earlier than it began to interact with the other faults downstream [see also Chapter 7]. However, braiding, and the different incision patterns at the linking fault also indicate a response to motion on the downstream faults, facilitated by the increased stream power [high SL] in the steepened reaches.

4.2.1.3 Bank profiles

Figure 4.32 shows the profiles of the two banks of the main channel in the footwall of Fault 1. Distances are calculated *perpendicular to the fault scarp*, to allow comparison with published footwall surface profiles. Letters [A-H] refer to the gradients shown in Table 4.5, to be compared with the channel floor gradients in Table 4.4.

Channel section	Equiv. bank	Length (m)	Gradient (°)
Fork to start 'slot'	**AB**	139.18	1.041
'slot' step, kp0		54.77	2.792
'slot' step to kp1	**CD**	329.14	1.093
kp1		20.75	6.828
kp1 to dogleg	**EF**	245.92	1.687
Dogleg [kp2]		13.72	9.726
Dogleg to top F1	**GH**	120.76	3.744

Table 4.4: *Variation in bed gradient in footwall of Fault 1, calculated perpendicular to the Fault 1 scarp [see Fig. 4.32].*

Channel section	North bank		South bank	
	Length (m)	Grad. (°)	Length (m)	Grad. (°)
AB:Fork to slot	136.60	1.131	139.94	1.109
BC	121.45	0.689	118.49	0.508
CD:to kp1	280.55	1.342	282.86	1.446
DE	82.20	0.572	136.95	0.800
EF :to kp2	167.52	2.271	124.706	2.836
GH:to top F1	138.18	3.257	118.26	3.456

Table 4.5: *Variation in gradient of banks of main channel in footwall of Fault 1, calculated perpendicular to the Fault 1 scarp [see Fig. 4.32].*

The profiles of both banks are very similar, indicating that incision of the channel was fairly symmetrical along most of the footwall channel. The banks show an overall decline in elevation towards the Fault 1 scarp, rather than increasing to a regional high at the scarp, as might be expected from a typical footwall profile [e.g. Fig. 2.1]. This implies a reasonable amount of erosion of the fault crest, possibly by removal of jointed blocks from the footwall [section 7.2.2.4].

The bank profile shapes and the absolute gradients of the main sections mirror the

gradient pattern of the channel floor, becoming increasingly steep towards the Fault 1 scarp [Tables 4.4 and 4.5]. Incision increases downstream towards Fault 1, particularly steeply in the lowermost reach. Steps in the channel floor coincide closely with sharp elevation and gradient changes in the profiles of both banks. This supports the idea that steps in the bed profile [Fig. 4.27] represent important morphological features of the channel, and probably relate to important stages in the channel development [section 7.2.2.3].

Steps in both bank profiles reflect pervasive jointing and a series of small footwall faults which accommodate displacement near the southern tip of Fault 1. Joints can be correlated across the stream, and with steps in the channel floor [e.g. Fig. 4.26f and 4.27b]. The change in elevation of the bank profiles across the joints suggests that they accommodate a degree of the extension, as shown by the small faults j and also a1 [section 4.1.1.3]. Hence the elevation drops in the channel floor profile which coincide with joints may result in part from extensional opening of the joints [Chapter 7].

4.2.1.4 Cross-section data

Cross-sections were surveyed every 50-100m in the channel upstream of Fault 1, and every 25-50m along the channel between Faults 1 and 2 [Fig. 4.33]. Ramp cross-sections were extended to include all stream braids. Hence the cross-sectional profiles [Fig. 4.35] show a series of elevation lows, reflecting the braiding of the stream.

Footwall of Fault 1: Cross-sectional profiles are shown in three panels in Fig. 4.34b, corresponding to the three reaches discussed in section 4.2.1.2. Lower-numbered sections are further downstream. All panels are plotted on the same scale [VE = 9.0] to allow direct comparison. Channel depth [incision] increases downstream, but not constantly: a gradual increase occurs within each reach [except section 8], but a sharp increase occurs between each of the three reaches. Channel width also decreases downstream, although the difference is most pronounced between the upper and central reaches. The combination of these two effects results in the deeply incised, steep walled gorge near Fault 1, in marked contrast with the shallow wide profiles of the uppermost reach [see Fig. 4.26].

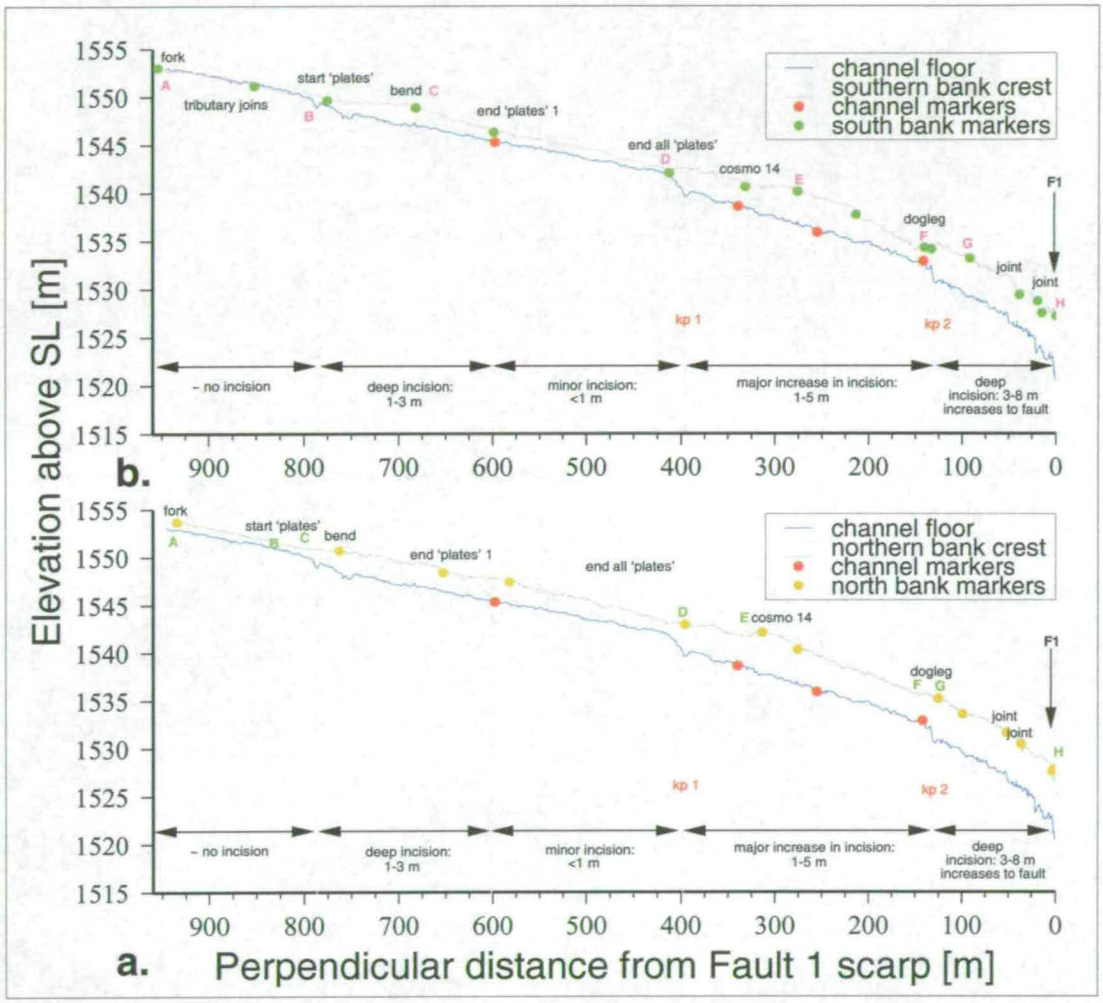

Figure 4.32: *Profiles of a. southern and b. northern banks of the main channel in the footwall of Fault 1, calculated perpendicular to Fault 1. Slight differences therefore occur from the profile in Fig. 4.25.*
'kp1' and 'kp2' are the two bedrock steps [section 4.2.1.2].
Letters refer to the sections of the bank profiles whose gradients have been calculated in Table 4.5. 'Plates' refers to the tops of polygonal cooling blocks exposed in the channel floor. Gradients of the channel reaches discussed in section 4.2.1.2 are recalculated for comparison, in Table 4.4, perpendicular to F1.

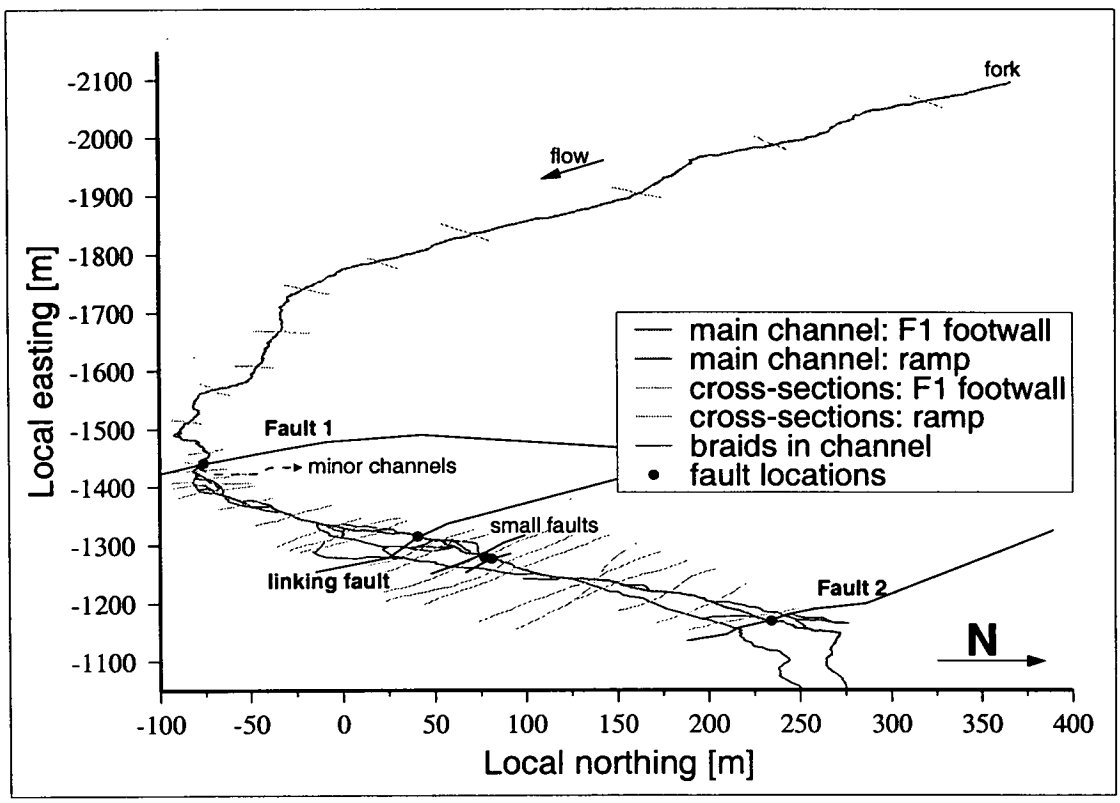

Figure 4.33: *Map of the cross-sections surveyed in the main channel: fork to Fault 2 basin. Section profiles were surveyed perpendicular to the channel flow every 50-100m in the footwall of Fault 1, and every 25-50m along the channel through the ramp.*

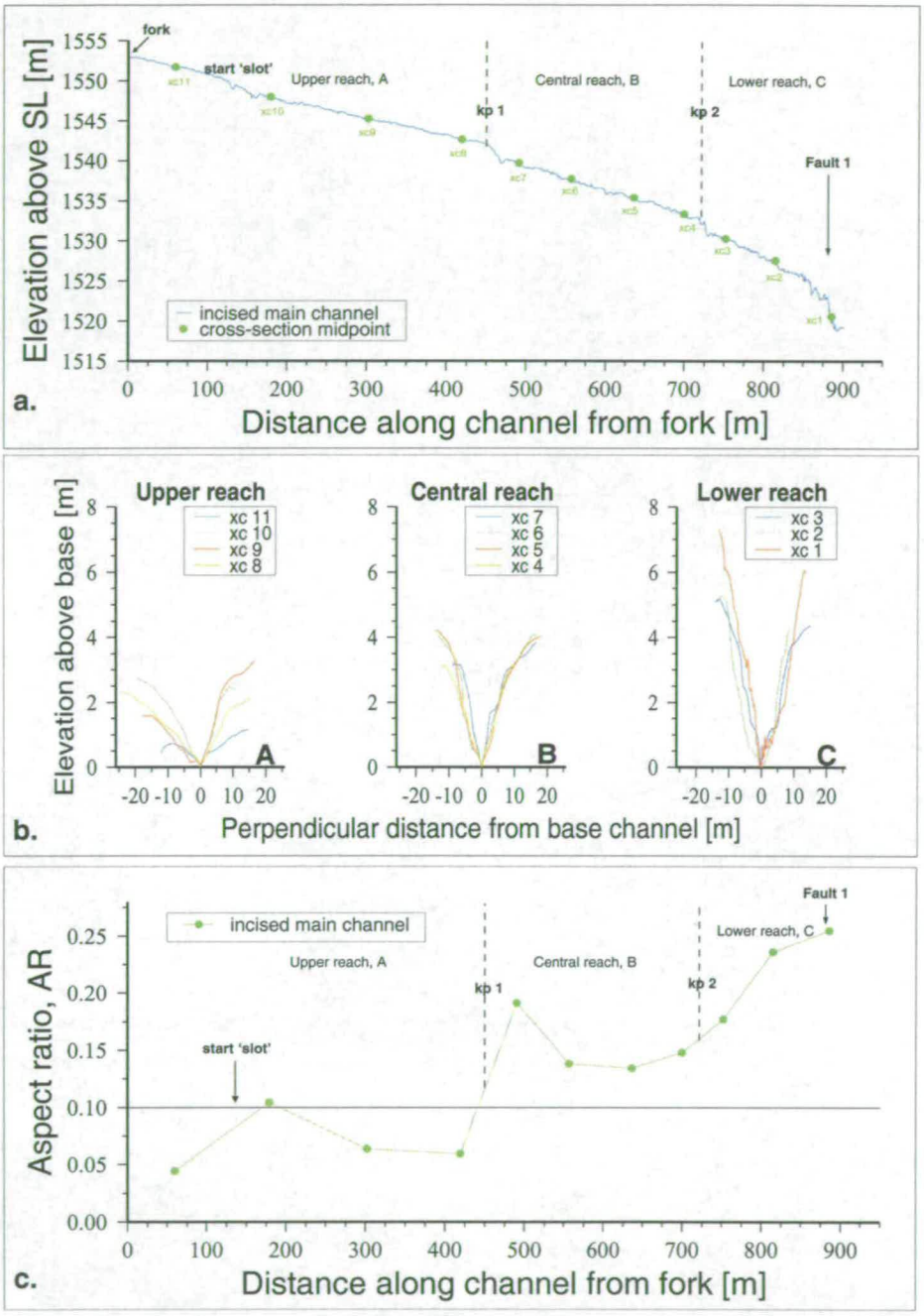

Figure 4.34: *a. Long profile of the main channel in Fault 1 footwall, showing the cross-sections midpoints [green circles and numbers].*
b. Cross-sectional profiles upstream of Fault 1. The panels refer to the three reaches described in section 4.2.1.2, separated by the steps 'kp1' and 'kp2'. Each reach has a characteristic profile shape. All panels are plotted on the same scale; VE = 9.0. South(west) is to the left in each case. Lower numbers [blue →green →red →yellow] are further downstream.
c. Variation in aspect ratio, AR [bank-base depth / bank-bank width]. Sharp increases in AR occur immediately downstream of each step. The upstream section with high [≃ 0.1] AR marks the 'slot' canyon which can be seen in the bank profiles [Fig. 4.32]. AR=0.1 appears to separate shallow profiles from the gradual incision in response to uplift on Fault 1.

The downstream variation in cross-sectional morphology is seen more clearly by plotting the channel's aspect ratio, AR, along the stream [section 3.3]. Figure 4.34c shows the variation in the AR downstream: the total depth normalised by the width: thus my 'aspect ratio' [AR] is the *inverse* of the width-depth ratio used by e.g. Schumm (1972, 1977); Jorgensen (1990). However, the AR emphasises the variation in incision of the channel [see section 3.3].

The three distinct profile shapes of Fig. 4.34b correlate with three distinct parts of the aspect ratio plot, showing respectively low [$\leq$ 0.1], medium [0.125-0.2], and rapidly increasing high [$\geq$ 0.2] aspect ratios. The three reaches show internally similar AR values, but there is no overlap between the AR values of the three sections. Most pronounced is the sharp increase in aspect ratio over the last 300m towards the Fault 1 scarp. Sudden increases in aspect ratio occur across each of the steps [kp1, kp2] in the floor profile [at 454m and 716m from the fork]. The upstream cross-section showing a high [$\simeq$ 0.1] AR marks the beginning of the 'slot' canyon, $\simeq$150m from the fork, which is clear in Fig. 4.32.

The aspect ratio therefore provides a quantitative assessment of the observed morphological differences between the three reaches, and is consistent with the observed gradient changes in Fig. 4.25. The correlation of the sharp changes in morphology with the steps in the channel implies that the steps represent fundamental structural features in the channel. It is most likely that these steps are related to the upstream migration of the knickpoint formed by periodic slip on Fault 1 [section 7.2.2.3]. The change in AR between sections 7 and 8, which correlates with step 'kp1', is more pronounced than the changes at 'kp0' and 'kp2'. This reflects the stark change in channel width at kp1, [compare A and B in Fig. 4.34b] but also suggests that kp1 may be a more important feature of the channel. The relevance of these steps, and the mechanism of their formation, is discussed in the light of the cosmogenic work, in Chapter 7.

Ramp: Fault 1 to Fault 2 hangingwall basin: Figure 4.35 shows cross-section profiles of the main channel through the ramp [see Figs. 4.33 and 4.36b for locations]. The panels each show a different morphology, corresponding to a separate part of the ramp. All profiles are plotted from north [left] to south [right] and were extended to included all the braids of the trunk stream [see Fig. 4.21], which in some cases have a greater degree of incision than the main braid, particularly near the linking fault. All panels are plotted on the same scale as the footwall sections [VE = 9.0].

Section 21, in the immediate hangingwall of Fault 1, shows a narrow channel with a northern bank reaching 1.5m in elevation. The steep high bank on the south side, however, includes the talus apron in the hangingwall of splay fault k. The channel widens and becomes shallower away from Fault 1 [A: xcs 20-16]. As the linking fault is approached, the stream incises more deeply into the tuff, reaching around 1m depth, and again narrows [B: xcs 15-12]. Braiding [section 4.2.1.1] is evident from section 19. Interestingly, the incision of the channel reaches a maximum in the immediate footwall of the *smaller* faults, generating a very large difference in the incision and width of the channel across the faults [compare xcs 9 and 8 in C]. The southern branch rejoins the trunk stream downstream of the small faults, and a consistent morphology is maintained to F2 [D: xcs 7-1]. A gentle increase in incision and decrease in width occurs as Fault 2 is approached, in marked contrast to the sharp morphological changes in the immediate footwall of Fault 1 [Fig. 4.34].

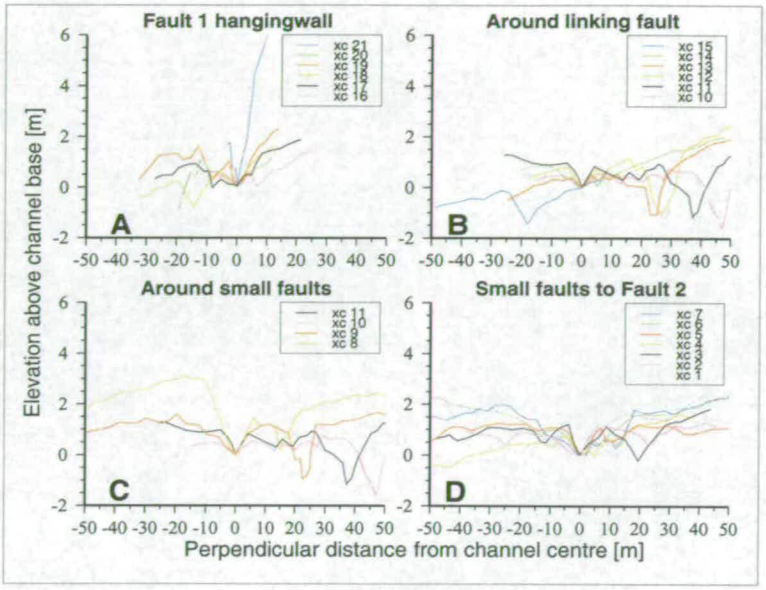

Figure 4.35: *Cross-sectional profiles of the main channel through the central overlap.*
Four panels represent different morphologies down the stream. The sections are overlain with '0' in each at the base of the trunk stream. ***NB*** *sections 11 and 10 are shown in both panels 2 and 3.*
All panels are plotted on the same scale; VE = 9.0, and were extended to include all the braids of the main drainage system to the south and north of the main stream. North is to the left [negative distances from centre] throughout.

Figure 4.36a shows the variation in aspect ratio down the lower part of the trunk stream and the other branches. In some cases, notably near the linking fault, the northern fork is not the deepest channel. Again, the faults are the most prominent features of Fig. 4.36a, with the highest aspect ratios around the transverse faults. Sharp increases in aspect ratio are seen immediately upstream of the faults, with corresponding drops in aspect ratio in the hangingwalls. The highest AR values occur at the largest fault, Fault 1, but the small faults produce higher ARs than Fault 2 or the linking fault. Away from the faults, the channel has a consistently low aspect ratio, AR<0.1. This agrees with observations of a broadly uniform morphology, and the small variation in bed gradient between faults [Table 4.3]. Interestingly, as in the incised footwall [Fig. 4.34c], there appears to be a cutoff at around AR= 0.1 between the unfaulted reaches and those showing incision in response to uplift [see Chapter 7].

A similar pattern is evident in the southern branch [brown], with localised AR highs around the central faults. However, the aspect ratios are higher than those of the main [northern] branch, and through the small faults, the southern branch has ARs equivalent to those of the footwall channel. The southern branch is more deeply incised through the linking fault and the smaller faults; and as reflected by its comparatively smoother long profile [Fig. 4.31], appears to have accommodated more of the uplift. This may reflect a higher discharge, or possibly an earlier or longer occupation of this southern branch. Most of the smaller braids show lower aspect ratios than the main branches, reflecting shallower incision and their lower discharge. Again, the aspect ratios in the braids remain below 0.1, with the exception of braid 'b', and in the

downstream reaches AR<0.065 [see section 7.1.3.2]. Most discharge across the linking fault is focused through the main northern and southern braids.

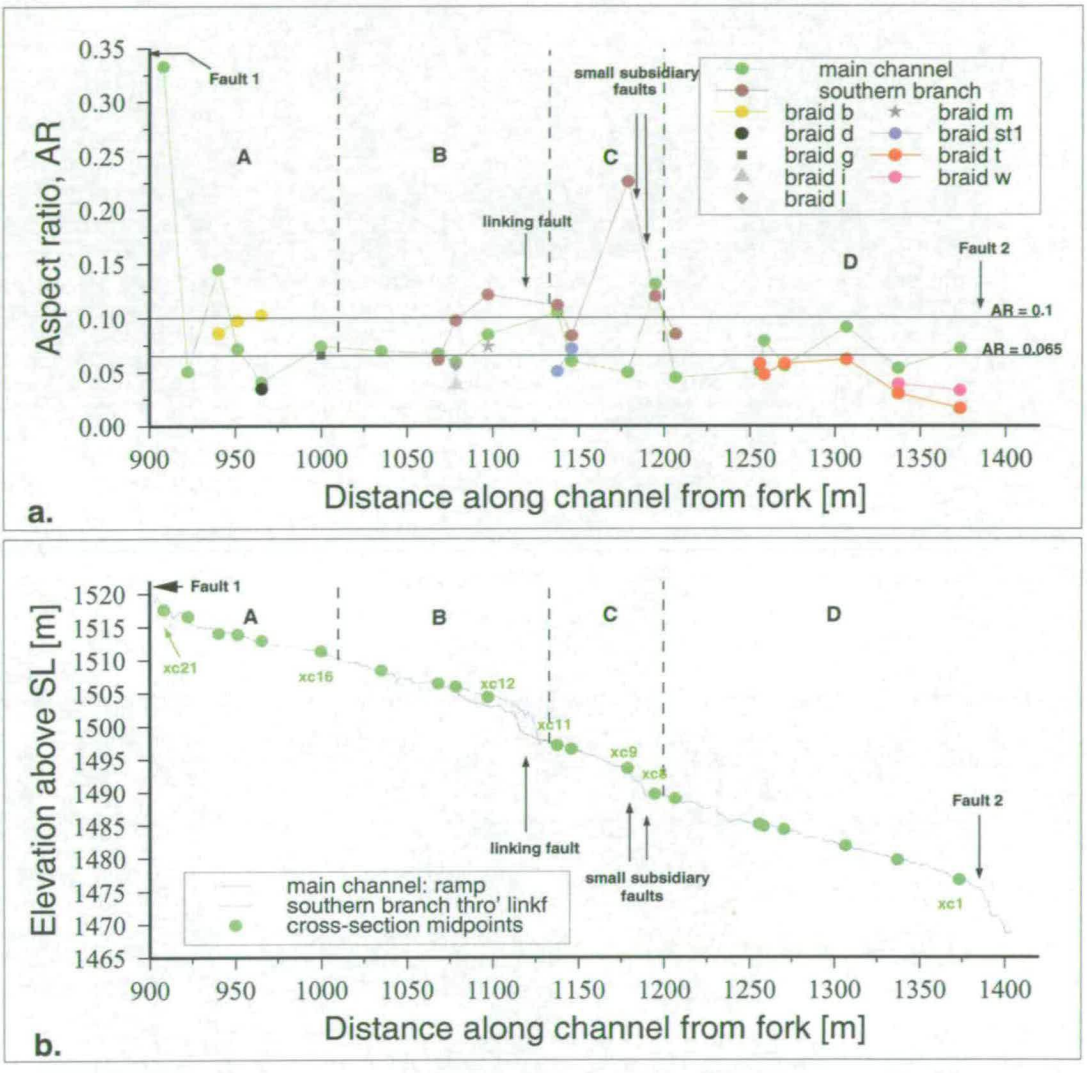

Figure 4.36: *Variation in aspect ratio of the main channel and braids in the central overlap: Faults 1 to 2.*
a. Aspect ratio, AR [bank-base depth / bank-bank width] of the main channel [green] against distance along the channel. Aspect ratio variation in the southern branch is compared [brown].
b. Long profile of the main channel, showing cross-section locations.
The straight lines in [a] are at aspect ratios of 0.1 and 0.065 [see section 7.1.3].

4.2.1.5 Summary of main stream data

The main stream flows across a series of faults, in each case from the footwalls into the downthrown hangingwalls. The course, profile, and morphology of the river show a clear connection between the development of these faults and of the stream itself. The channel may be considered in two markedly different parts: the upstream section, in the footwall of Fault 1; and the downstream reach, where the channel crosses the overlap zone between Faults 1 and 2.

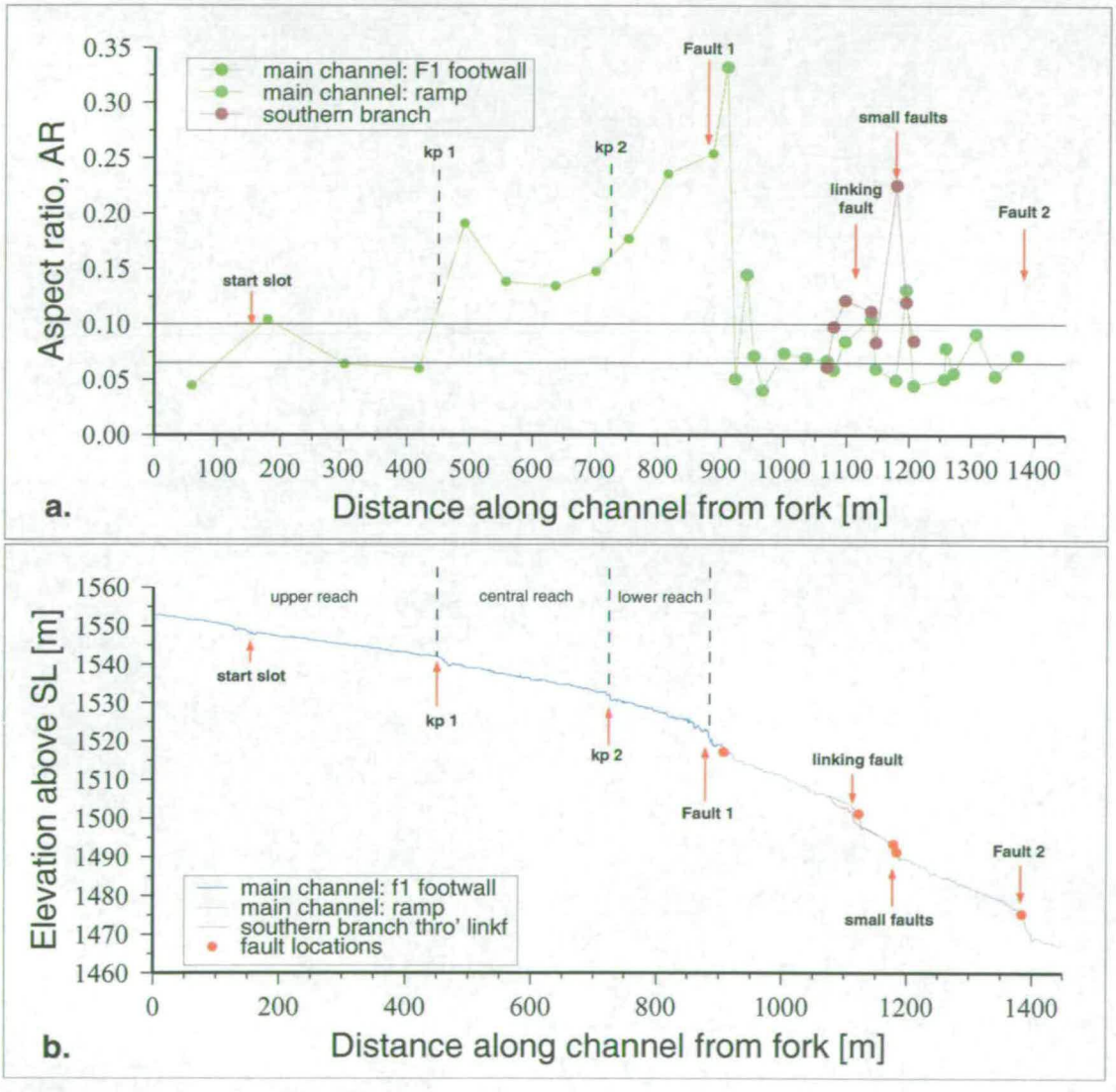

Figure 4.37: *Variation in aspect ratio plot along the main channel from the fork to Fault 2.*
a. Aspect ratio, AR [bank-base depth / bank-bank width] of the main channel [green] and southern fork [brown], plotted against distance from the fork.
b. Long profile of the main channel from the fork to Fault 2. Profile of the southern branch is superimposed in brown. See Fig. 4.21 for map of stream course.

The main channel steepens, narrows and becomes increasingly more incised throughout the upper part of its course, as it approaches the main Fault 1. This upstream part of

the stream has three distinct reaches, separated by clear steps in the channel bed profile [kp1 and kp2]. These reaches are distinct by morphology in the field [Fig. 4.26], channel bed gradient [Table 4.3], and can also be distinguished by a quantitative assessment of their morphology: the aspect ratio, AR [Fig. 4.37a]. Despite the high displacement on Fault 1, only a comparatively small step in the profile remains at the scarp itself, as the stream has accommodated at least 8m of fault slip by incision in the immediate footwall of the fault [Fig. 4.37b]. The smaller upstream steps [kp1 and kp2] mark morphological boundaries in the channel, and thus are probably important structural features of this part of the channel [Chapter 7].

Once the stream crosses Fault 1, its morphology changes drastically [Fig. 4.29]. The channel gradient is considerably higher than in the footwall of Fault 1 [Table 4.3], and yet the aspect ratios are more like those in the upper reach of the footwall, furthest from Fault 1 [Fig. 4.37a]. Sharp changes in the channel occur around each transverse fault, the channel becoming narrower and more incised into the uplifted footwall. Plungepools scoured at the base of each fault [e.g. Fig. 4.29c,d] are testament to slip during stream occupation. However, the morphological modifications at each downstream fault are considerably smaller than those in the upstream part of the channel in response to Fault 1 motion [Fig. 4.37a]. This is partly due to the lower displacement on these faults [Table 4.1], but the steeper channel profiles through the faults [Table 4.3] and the lesser degree of fault crest erosion [Fig. 4.37b] also imply a lower erosive power, or a shorter period of time in which to accommodate the fault motion [see Chapter 7].

The aspect ratio plot [Fig. 4.37a] shows sharper, shorter-wavelength morphological changes in the ramp than the smooth changes seen in the footwall. While the sampling frequency in the ramp is higher, this 'spikiness' reflects the higher fault density, and also the higher bed gradient, implying a system that has not yet fully responded to the development of the faults across which it flows. Although the bed gradient is high, the main stream does not flow down the *present* steepest gradient, which slopes away to the north, towards the northern tip of Fault 2. This may be the result of a relatively early development of the channel [see Chapter 7].

Another key feature of the channel's response to faulting is the localised braiding seen particularly around the faults in the downstream overlap [Fig. 4.21]. The stream braids a few tens of metres upstream of the faults, with the branches recombining downstream of the scarp, in response to the local change in gradient caused by faulting [e.g. Holbrook and Schumm (1999)]. Examination of the profiles of three channels incised through the linking fault scarp [Fig. 4.31], their aspect ratios [Fig. 4.36a] and the displacement profile of the linking fault [Fig. 4.18c] implies a series of fine adjustments of the stream in response to both the temporal and the spatial variation in the accumulation of displacement on the linking fault.

These points are considered in Chapter 7 in the light of the cosmogenic data [Chapter 6], and of the observations from other key drainage networks in this part of the Tableland which follow [sections 4.2.2 to 5.1].

4.2.2 Minor ramp channels

A channel diverges from the main stream at the base of Fault 1, from which a series of smaller tributaries stem, draining much of the northern part of the ramp [Fig. 4.20]. Most of these channels are very shallow, incised only a few centimetres into the tuff, and in many cases, cannot be traced for more than a few tens of metres on the ground. However, the largest of these minor channels can be followed from the base of Fault 1 to the hangingwall basin at the tip of Fault 2, down almost the steepest slope on the ramp. This section considers this small stream, and two of its tributaries. The map, long profile and cross-section data for these channels provide a good comparison with the main channel data [section 4.2.1] and so shed more light on the evolution of the overlap zone.

4.2.2.1 Stream course

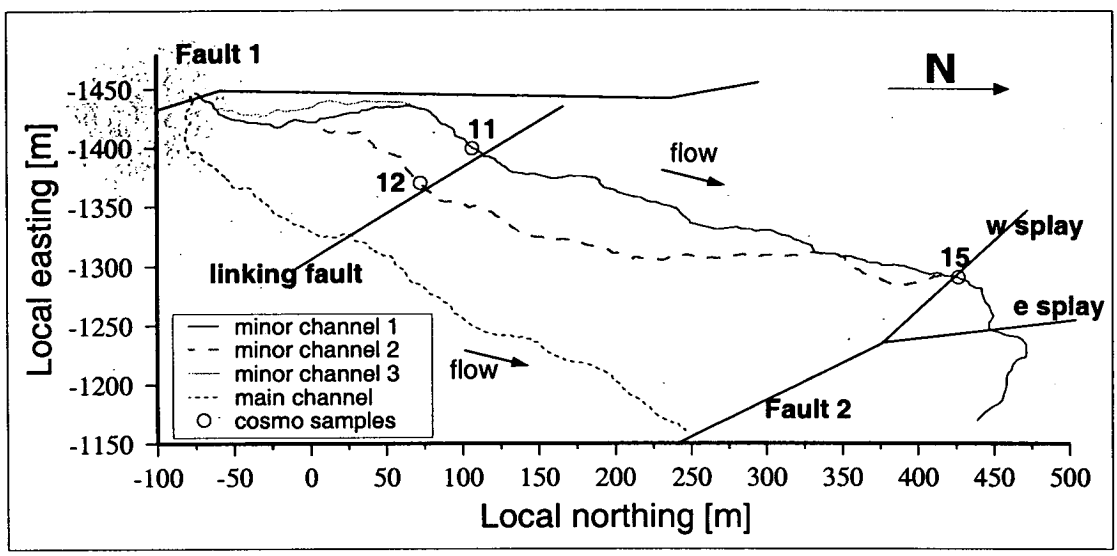

Figure 4.38: *Map view of the minor channels in the fault overlap.*
The main channel is included [pink], to show the stream divergence at the base of Fault 1.
Two large channels flow across the transverse linking and small faults, before channels recombining immediately upstream of the fumarole in the west splay of Fault 2.
Orange circles show the location of the cosmogenic samples collected from the minor channels, at the linking fault and Fault 2 scarps. Work on sample 11 is detailed in Chapter 6.

The largest of the channels considered here, 'minord1', flows across the linking fault scarp and past splays of the northern tip of Fault 2, to deposit its load in the hangingwall basin [Fig. 4.38]. As with the main channel, this stream braids in the vicinity of the faults it crosses within the ramp, with as many as seven small streams crossing the linking fault. The largest of these branches, 'minord2', diverges from the trunk stream in the footwall of the linking fault, and itself spawns a series of braids around the transverse faults. Most of these braids are short, and minord2 rejoins the trunk stream immediately above F2. This is very similar to the relationship between the north and south forks of the main channel, [Figs. 4.21 and 4.31].

Minord1 deflects quite sharply around a large fumarole at which the Fault 2 trace splits

in two [Fig. 4.15]. Relatively sharp bends allow the stream to pass between fumaroles in both the western and eastern tip splays of Fault 2, rather than passing across the higher scarp to the south [see Fig. 4.40a]. This implies an early formation relative to the growth of Fault 2, allowing the streams to drain into the hangingwall basin despite the growing fault. It also highlights the influence of pre-existing topographic highs on drainage development on the Tableland [fumaroles formed during the initial degassing of the tuff, possibly for around 10-100 years after emplacement, (Holt and Taylor, 1998)].

'Minord3' is an example of one of the considerably smaller branches, which can be traced for only a couple of hundred metres along the base of the talus slope of Fault 1, where it is deeply incised into the tuff.

4.2.2.2 Long profile

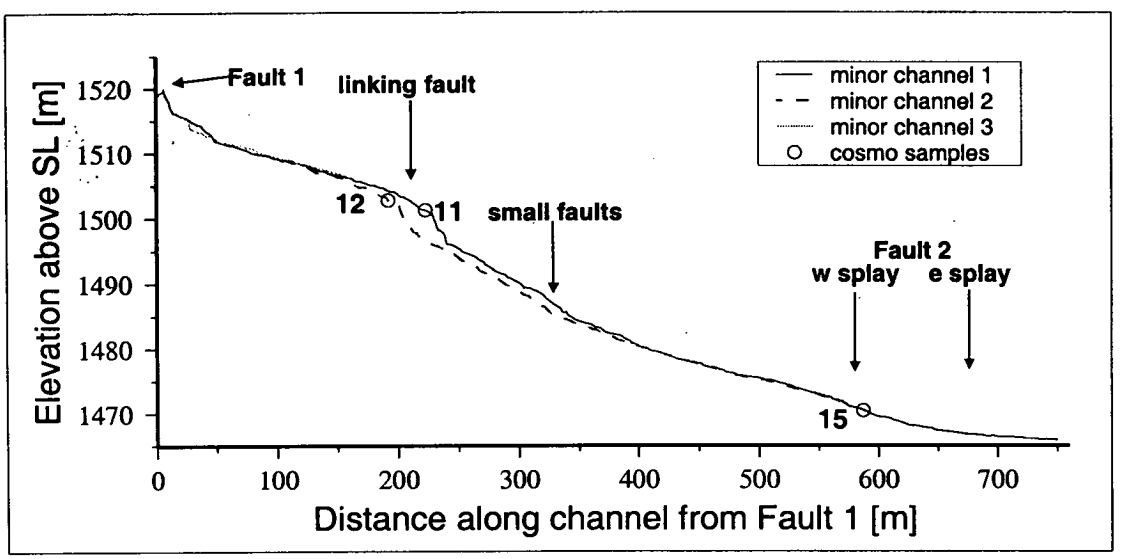

Figure 4.39: *Long profile of the minor channels in the fault overlap.*
Channel 3 rejoins the trunk stream [channel 1] in the footwall of the linking fault; the two larger streams recombine immediately upstream of Fault 2.
Orange circles show the location of the cosmogenic samples collected from the minor channels, at the linking fault and Fault 2 scarps. Work using sample 11 is detailed in Chapter 6.

The profile of both the larger branches down the ramp are very similar, except through, and immediately downstream of, the linking fault [Fig. 4.39].

The initial section of the trunk channel is extremely steep, where it navigates a large pile of angular blocky debris, with some clasts up to 3m across, carried from the gorge through Fault 1 [Fig. 4.48]. This debris would now present a barrier to the passage of water from the channel cut through Fault 1 into these small channels, unless the water level was sufficiently high to overcome it. This debris pile may therefore post-date the formation of the northern channels, as water flowing from the F1 footwall would currently be funnelled into the main channel, despite the ramp gradient downstream [see section 4.2.3 and Chapter 7].

Below the debris pile, the streams reduce in gradient rapidly, then maintain a steep

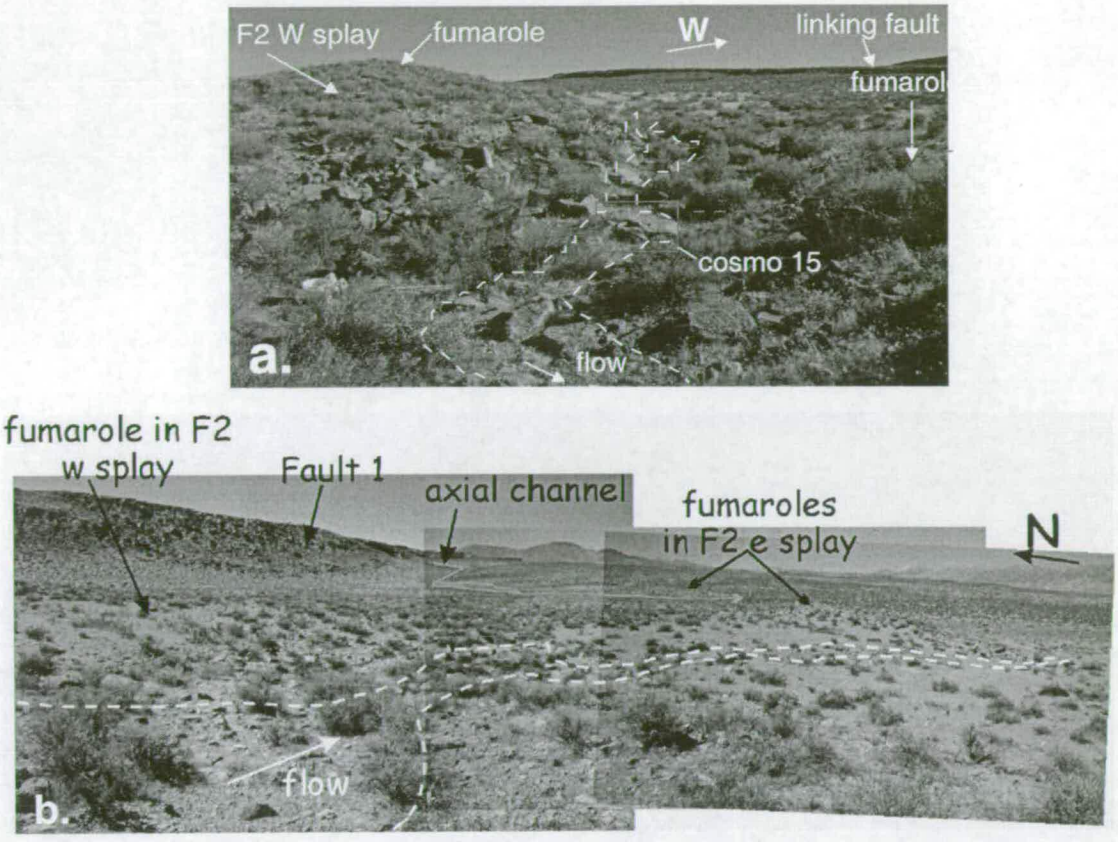

Figure 4.40: *Field photographs of the minor channel:*
a. View of minor channel flowing through western splay of Fault 2 tip. Photograph looking upstream [to southwest] from the east splay of Fault 2. Large mound behind the channel is a fumarole. The minor channels 1 and 2 recombine immediately upstream of this fault. Cosmogenic sample 15 collection site is marked: see Chapter 6.
b. View to north from base of fumarole. Minor channel 1 flows between fumarole mounds in the splays of fault 2 into the hangingwall basin. Fault splays are 60m apart at this point.

but fairly uniform gradient to a sharp knickpoint at the linking fault crest [Fig. 4.39]. Bedrock slabs are exposed in many places along the upper channel course, though there are also small pebble and cobble [5-25cm diameter] deposits along the stream. The channel floor is smoothed or grooved, with little evidence of the plucking and potholes seen in the main channel [e.g. Fig. 6.9]. As with the northern branch of the main stream, the knickpoint in the northern trunk stream occurs at the scarp itself, and is steep [Table 4.6]. Steepening of the profile occurs over 55m in the immediate footwall, but so far little of this motion appears to have been accommodated by incision. In contrast, and again like the *southern* branch of the main channel [Fig. 4.31], minord2 has a slightly shallower profile over the linking fault [Table 4.6], as well as a longer steepened reach, implying a slightly fuller response to the linking fault motion.

Downstream of the linking fault, the channels flow over a series of small faults, each with a displacement of 0.3-2.4m. The small faults are marked not by individual steps in the profiles, but instead a very steep reach in both channels 1 and 2, which shallows downstream where the faults become smaller and further apart. Steepening of the

profile occurs immediately upstream of Fault 2, where channels 1 and 2 recombine. However, since the stream flows between fumaroles in the western and eastern splays of Fault 2, [Fig. 4.40a], there is only a small elevation drop across the western splay, and virtually none at the eastern splay of Fault 2. This is very different from the main channel [Fig. 4.28], where a steep stepped knickpoint has formed at Fault 2, along with considerable braiding.

Minord1 becomes increasingly alluviated in the lower reaches, and bedrock exposures are generally limited to the immediate fault crests and scarps. Clast size decreases to only 1-15cm in diameter, fining to gravel and coarse sand near Fault 2. Plungepools, like those in the main channel [Fig. 4.29c], occur at the base of larger faults; scoured up to 30cm into bedrock at the linking fault, but filled with sand and pebbles downstream of the small faults. Bedrock is exposed where the channel incises into the tuff through the western splay [sample 15: see Chapter 6], and towards the eastern splay, of Fault 2. Minord3 incises bedrock where it leaves the trunk stream, but downstream is largely filled with cobbles [15-30cm diameter], and some coarse sand from the Fault 1 talus slope.

Channel gradients: Averaged gradients of reaches between major faults are shown in Table 4.6, and can be compared with those of the main channel [Table 4.3].

Minord1			
Reach	**Length (m)**	**Grad (°)**	**SL (m)**
F1-linkf	219.24	-4.89	-89.08
Linkf total	16.74	-16.58	-345.11
Linkf max.	1.04	**-40.34**	-982.55
Linkf-small fs	62.26	-5.91	-124.68
Small fs total	37.98	-7.35	-161.68
Small fs-w-splay F2	273.84	-3.33	-82.05
F2 w to e-splay	**98.13**	-1.25	-34.78
F2 basin	30.26	-0.70	-20.20
Minord2			
F1-linkf	100.39	-3.87	-72.72
Linkf total	21.92	-15.07	-305.70
Linkf max.	6.12	**-23.65**	-493.58
Linkf-above F2	366.15	-4.08	-94.91
Minord3			
whole channel [Linkf fw]	161.07	-3.95	-70.33

Table 4.6: *Variation in gradient and SL index of minor channels through the overlap. Length (m) and averaged gradient (degrees) of channel and faulted reaches from the base of Fault 1 to the F2 basin. Minord2 has generally a lower gradient than the equivalent reach of minord1. See also cross-sections [Figs. 4.42 to 4.44], and main stream values [Table 4.3]. Main stream gradients are lower in the upper reaches, but higher in the lower reaches, due to the different routes across the ramp, and the reduced displacement on the northern F2. Stream-length-gradient index, SL is a proxy for stream power: $SL = \frac{\Delta elevn}{\Delta length} * dist, L$ [sections 2.3.2 and 7.1.3]. L is calculated from the fork in the footwall of Fault 1, so the main and minor stream values can be compared directly.*

Minord2 has a generally shallower gradient than minord1. Gradients of the minor

channels are generally higher than those of the main channel in the upper part of the ramp. This partly reflects the tectonically-produced slope of the ramp: minord1 follows almost the steepest gradient of the overlap zone. Nearer to Fault 2, the minor channels have a gradient shallower than, or similar to, the main channel, reflecting the considerably lower displacement at the tip of Fault 2, and hence smaller rejuvenation of the northern streams. The maximum gradient of minord1 through the linking fault is similar to that of the two main channel branches, though minord2 has a far shallower profile, nearer to that of tip branch 'A' [Table 4.2].

Table 4.6 also includes values of the stream-length-gradient index [SL], which gives a proxy for the stream power [sections 2.3.2 and 7.1.3]. Locally increased SL indices highlight differences in stream power through the faulted reaches, but also highlight the beginnings of profile adjustment to uplift in the steepened reaches upstream of each fault.

4.2.2.3 Cross-section data

Figure 4.41 shows the location of the cross-sections surveyed across the minor channels. Cross-sections are numbered 1-10 downstream in the footwall of the linking fault, and 28-11 downstream in its hangingwall. The variation in cross-sectional morphology of each channel is discussed in turn, and hence only the relevant part of the profile is plotted in each case. All cross-sections are plotted on the same scale [VE = 28.74] and from south [left] to north [right]. The variation in these morphologies is then summarised by comparing the downstream variation in aspect ratio, AR, between these branches, and with the main stream, in Fig. 4.45.

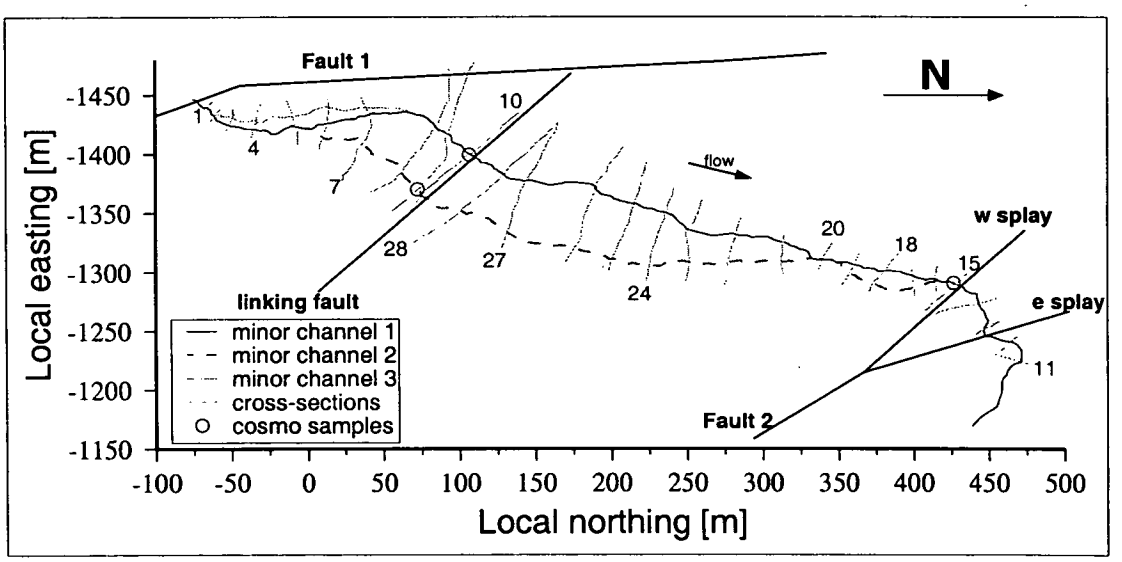

Figure 4.41: *Map of cross-sections measured in minor channels.*
Channels 1 and 2 recombine above section 16, immediately upstream of Fault 2. Channel 3 is only crossed by sections 2-7.

Minor channel 1: Seven distinct morphologies correspond to discrete parts of minord1 [Fig. 4.42b]. Incised narrow channels mark the steep faulted reaches, while

the channel is wider and alluviated in the gentler reaches downstream. The stream is confined between high, steep banks over the pile of debris at the base of Fault 1 [Fig. 4.48]. The banks reduce away from the fault, although the width does not increase markedly. This is consistent with the relatively steep gradient in this upper reach. Alluvial deposition occurs below the small faults [E]. Locally-increased incision, and the topographic highs of fumaroles in the western splay of Fault 2 form steep banks in xcs 16-14 [see Fig. 4.40a]. Incision decreases rapidly downstream of this splay, resulting in the very shallow channel profile of xcs 13-11 [G]. The higher northern bank marks a fumarole in the eastern splay of Fault 2.

Minor channel 2: Minord2 is only crossed by sections 6-10 and 28-17. Five distinct cross-section morphologies are visible downstream [see Fig. 4.43], broadly correlating with the divisions of the profile for the main trunk stream shapes described above. The cross-sectional profiles of minord2 are very similar to those of the main trunk stream, although the channel is generally slightly wider and incision through the linking fault is deeper than in minord1. This is consistent with the lower gradient through the linking fault [Fig. 4.43b and Table 4.6], which implies a greater adjustment to fault motion. Braiding of the channel is particularly evident in sections 8 and 10 upstream of the linking fault, and in section 24 at one of the small faults. Although a distinct morphological change is evident in minord1 at the linking fault crest [B/C, Fig. 4.42a], the clearest division in the smaller channel [B/C, Fig. 4.43a] in fact occurs *downstream* of this fault, in the steep reach above the small faults.

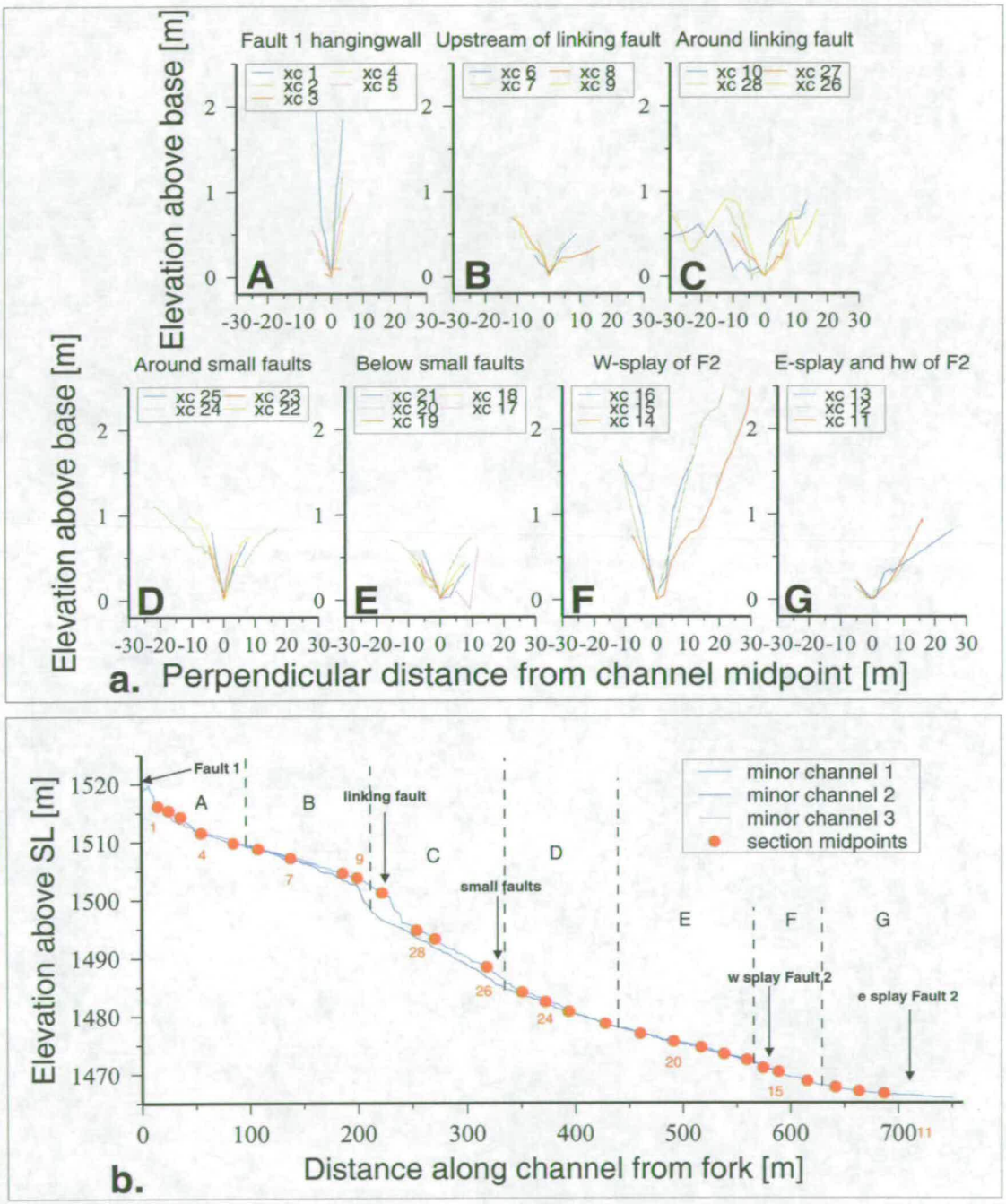

Figure 4.42: *Morphology of cross-sections through minor channel 1.*
a. Cross-section morphologies, in seven panels [A - G], with south on the left, representing the different sections downstream.
Sections 1-10 in the linking fault footwall increase in number downstream; sections 28-11 decrease in number downstream from the linking fault. VE = 28.74.
b. Long profile of the minor channels showing the location of the cross-sections.
Profile divided according to the section morphologies [A - G] in [a]. Major faults are marked.

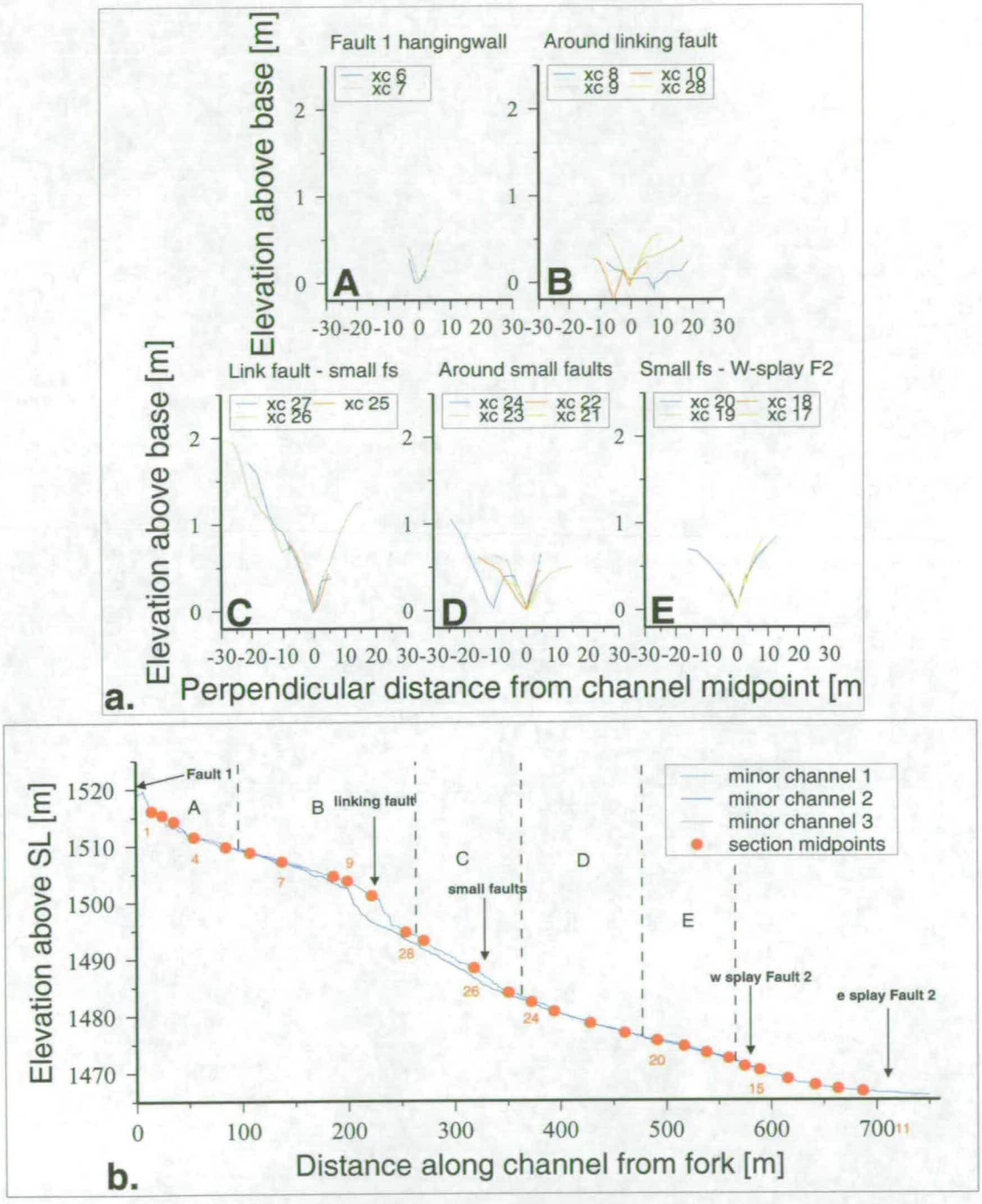

Figure 4.43: *Morphology of cross-sections through minor channel 2.*
a. Cross-section morphologies, in five panels representing different reaches downstream. Sections 6-10 in the linking fault footwall increase in number downstream; sections 28-17 decrease in number downstream from the linking fault. The channel rejoins channel 1 after section 17. VE = 28.74.
b. Long profile of the minor channels showing the location of the cross-sections. Profile divided according to the section morphologies [A - E] in [a]. Major faults are marked.

Minor channel 3: The small stream, minord3, is only crossed by sections 2-7. However, a very marked change occurs in the channel's morphology even over this short [~170m] stretch.

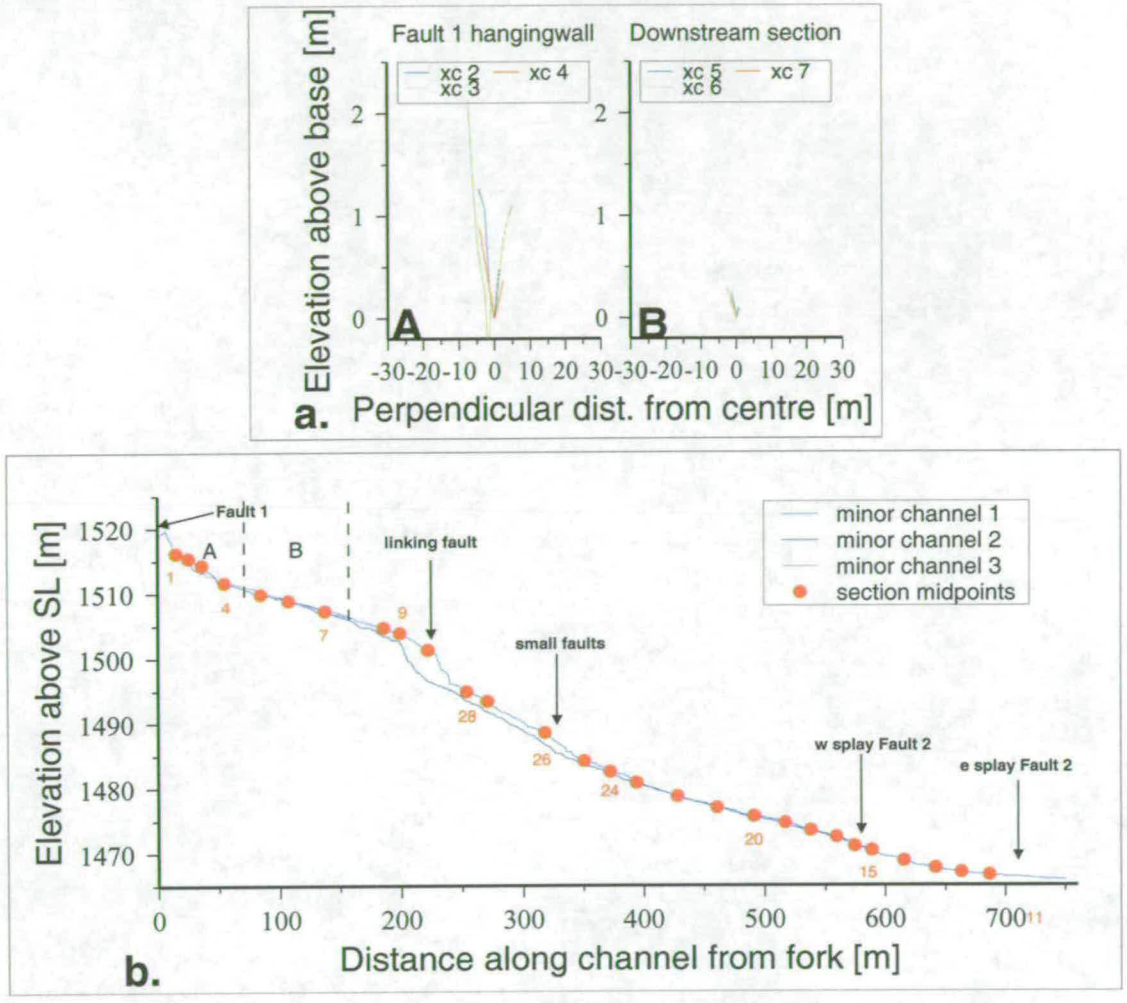

Figure 4.44: *Morphology of cross-sections through minor channel 3.*
a. Cross-section morphologies, in two panels representing the different sections downstream. This channel is short, and hence only crossed by sections 2 - 7 [numbers increase downstream]. VE = 28.74.
b. Long profile of the minor channels showing the cross-section locations. Profile divided according to the section morphologies in [a].

In the immediate hangingwall of Fault 1, the channel has extremely steep banks, formed by debris piled at the exit of the footwall stream, and incision of up to 50cm. The channel flows along the base of Fault 1 for around a hundred metres, incised into bedrock. Around xc5, the channel bends towards the trunk stream, and becomes increasingly alluviated until it peters out where it joins the trunk stream downstream of section 7.

Aspect ratios: The variation in aspect ratio [bank-base depth / bank-bank width; Fig. 4.45] summarises the cross-section data.

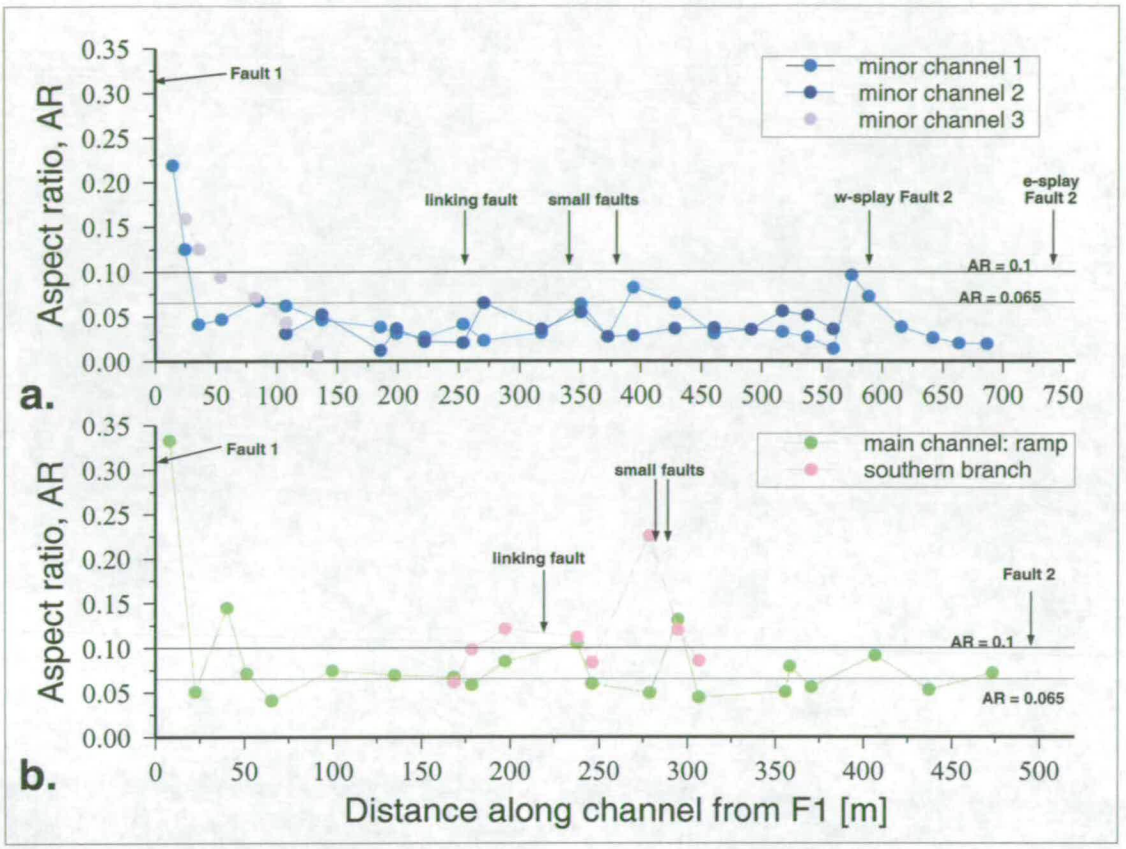

Figure 4.45: *Variation in aspect ratio of minor channels through the ramp.*
a. Aspect ratio of minor channels 1-3.
b. Aspect ratio of main stream northern and southern forks.

The largest northern channel [minord1] has the highest AR values, except at the linking fault and immediately upstream of fault 2, where minord2 is more deeply incised. High AR values correspond with the deep, narrow channel shapes in the immediate hangingwall of Fault 1, where the channels cross the debris pile and incise in response to rapid subsidence. Elsewhere, the aspect ratio of the minor channels remains below 0.065, except near faults. Higher aspect ratios occur in minord1 around the small faults [xc 24] than at the linking fault, implying a higher degree of adjustment to these small uplifts than to the linking fault itself. The opposite is true of minord2. Incision through the western splay of Fault 2 results in the highest aspect ratio away from Fault 1.

Minor channel ARs broadly mirror the downstream variation in morphology of the main channel [Fig. 4.45b]. However, the aspect ratios are consistently lower, reflecting the lower discharge. This difference is most marked around the linking fault, where the incision, particularly by the southern fork of the main channel, results in aspect ratios 1.5-2.5 times those of the minor channels. Very low AR values in the northern channels downstream of the small faults reflect the lower displacement at the tip of Fault 2, and hence reduced rejuvenation of the small streams.

4.2.2.4 Summary of minor channel data

The northern part of the central overlap of this array is drained by a series of small channels, many of which are indistinct, and can only be traced on the ground for a few tens of metres. The small channels diverge from the main stream at the base of Fault 1, and flow down the steepest ramp gradient to the northern tip of Fault 2. The largest of these streams crosses Fault 2 at virtually its lowest displacement, cutting a path between the topographic highs formed by fumaroles in the fault tip splays.

As with the main stream [section 4.2.1], the development of these minor streams has been dominated by the evolution of the faults they cross. Braiding is pronounced in the immediate footwall and hangingwall of transverse faults, as seen in the main channel [Fig. 4.21], caused by the tectonically-driven changes in local gradient. While the main stream has an almost uniform gradient throughout the non-faulted reaches of the ramp, the minor stream profiles are smoother, with shallow lower reaches reflecting the insignificant rejuvenation by Fault 2. The steep knickpoint at the linking fault scarp is therefore extremely prominent. Alluviation is more marked in the lower reaches of the smaller streams. The profile of the small minord3 emphasises the local control of fault motion on the channel incision, with incision focused at the rapidly subsiding areas near Fault 1, and decreasing away from the scarp.

The linking fault knickpoint in minord1 has a similar steep gradient to that of the two large main channel branches [Table 4.2], indicating that motion on this fault was late relative to the channel development. Although there is some steepening of the reach immediately upstream of the fault, the gradient and position of the steep knickpoint at the scarp itself indicate that profile adjustment has barely begun. Minord2 shows a greater degree of profile adjustment, with a lower gradient, especially through the fault, approaching that of the stream draining through the segment boundary in the linking fault [tip branch 'A', Fig. 4.31].

The variation in morphology of these minor channels follows a similar pattern to that of the main channel, as shown by the overall shape of the aspect ratio plot [Fig. 4.45]. As with the main channel, the main controlling features of the channel morphology are the faults, with narrowing of the stream and incision focused around the fault scarps. However, the smaller channels have a considerably lower aspect ratio throughout their length, reflecting a lower discharge than in the main channel. The aspect ratio normalises depth by the width of the channel, and hence the lower AR values reflect genuinely lower incision per unit width. [The streams are not simply mathematically similar.] This is consistent with the difference in the channel courses across the ramp: greater incision would be expected in a channel which experiences higher base level drops downstream.

A pile of angular debris at the exit of the gorge cut by the channel through Fault 1 [Fig. 4.48] presently forms a barrier to the passage of water from the footwall into the minor channels, except in flood stages, and funnels most of the water into the main channel. This may give some indication of the relative timing and style of development of the main and minor channels [see also section 4.2.3 and Chapter 7].

4.2.3 Rounded clasts on the central overlap

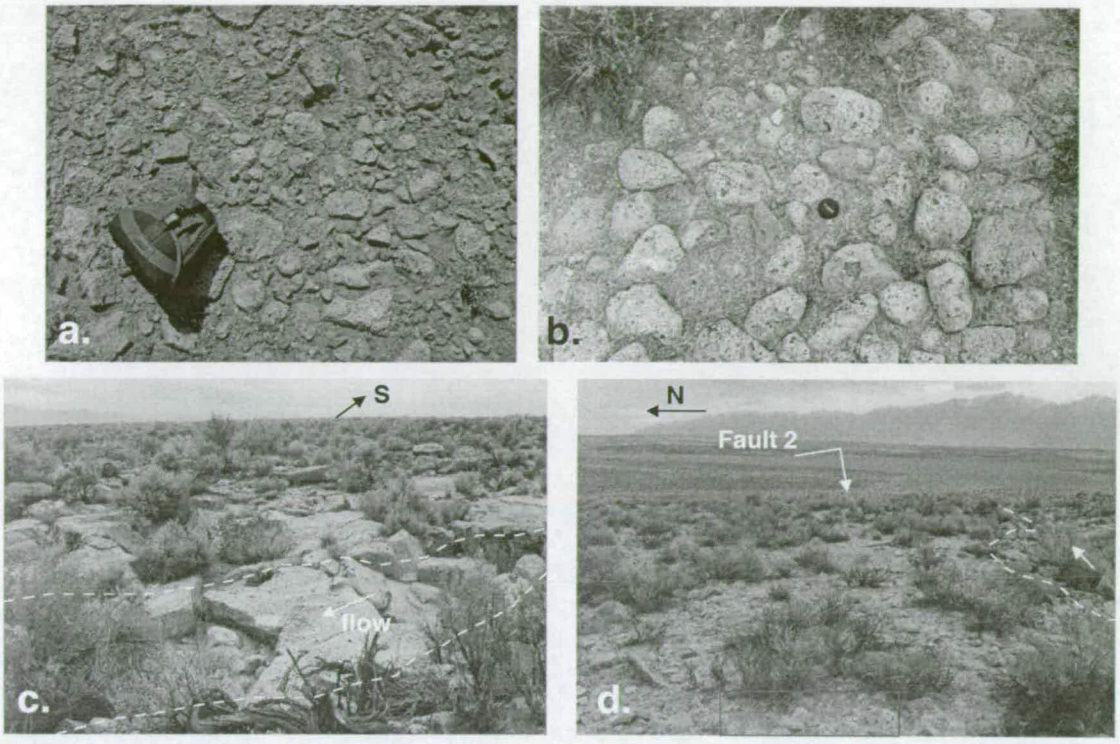

Figure 4.46: *Variation in the surface of the Tableland.*
a. Typical surface of the Volcanic Tableland [this in footwall of Fault 0]. Surface covered in randomly-oriented angular fragments of tuff, and thin soil.
b. View of surface of central overlap, 5m north of the main channel. Surface covered in well-rounded cobbles up to 30cm in diameter, well-tessellated in a sandy matrix.
c. View south across main channel, approx. 150m upstream of the linking fault. Channel bed incises into bedrock in the foreground, ramp surface to south is covered in angular blocks and fragments of tuff but few rounded cobbles. [Well-hidden] notebook is 20cm high.
d. View NE across main channel, approx. 150m upstream of the linking fault [same location as [c], other bank]. Main channel flows towards the top at the extreme right of the photograph. In contrast with [c], the foreground shows extensive rounded cobble deposits stretching over the ramp surface. Red box outlines part of ramp surface shown in [b]: cobbles are 5-35cm in diameter. See also the banks of the channels where cosmogenic samples were collected: Figs. 6.5, 6.8 and 6.9.

Most of the surface of the Volcanic Tableland is covered in a thin veneer of soil and angular fragments of tuff varying from 3-20cm diameter, in between meagre grass and desert plants [Fig. 4.46a]. However, much of the central overlap is different, as the channels cut through a surface covered in well-rounded pebbles and cobbles of tuff, reaching up to 30cm in diameter, and quite well-tessellated [Fig. 4.46b]. These rounded clasts are not limited to the immediate margins of the channels crossing the ramp, but are found over the entire of the overlap north of the main channel, although they are rare more than a hundred metres to the south of the main channel. In many places along the main channel, these deposits have been incised into, and neatly-arranged rounded cobbles form raised banks on the sides of the channel [e.g. Figs. 4.46c,d, 6.5,

and 6.8]. Although most marked along the main channel, incision into rounded cobble deposits is also evident along parts of the minor channels, e.g. Fig. 6.9.

However, there is no systematic variation in size of the cobbles away from the channels, as would be anticipated if they were overbank deposits from flooding of the streams. Similarly the deposits do not correlate with the size of clasts which occur in parts of the channel beds themselves, as would be anticipated if they were lateral bars formed during the evolution of the main channel itself. Instead, they show an overall decrease in size *with distance from the stream incision through Fault 1* [Fig. 4.47], over the entire of the northern part of the ramp, at least 270 000 m^2.

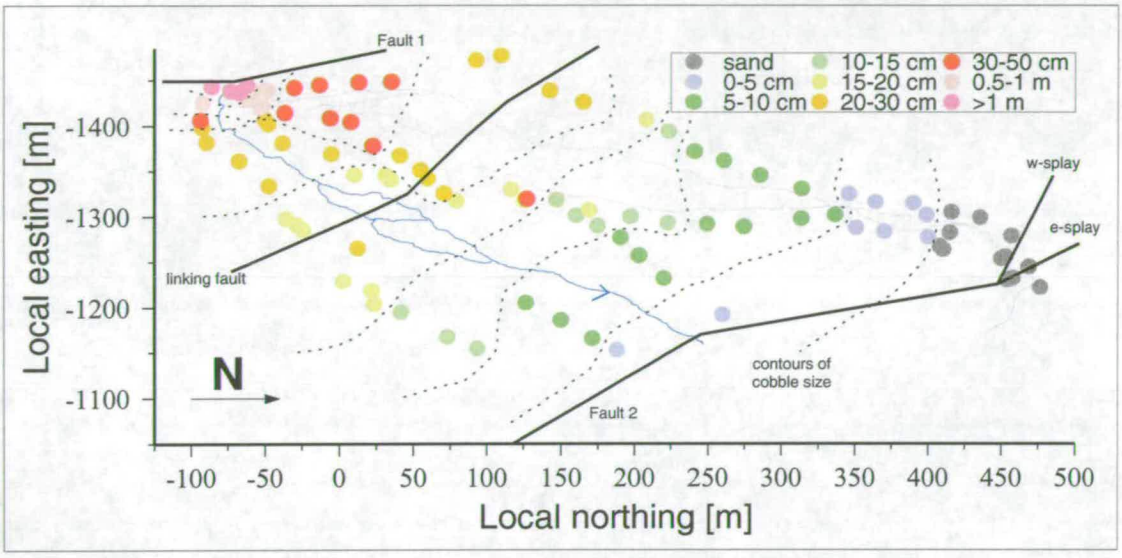

Figure 4.47: *Variation in size of rounded clasts forming the ramp surface away from the channels across the central overlap.*
Contours [dotted] show variation in average size of rounded clasts measured on the ramp surface away from the channels: samples measured at each end of the surveyed cross-sections.
Channels shown in navy [main] and lilac [minor] for reference. Approximate location of main faults marked by grey lines.
Grain size is not related to the channels, but decreases away from the point source at the base of Fault 1, towards the rapidly subsiding area at the centre of Fault 1, to the north.

The variation in size, the tessellation, roundness, and distribution of the clasts, and the fact that the present channels are incised into the rounded deposits, all suggest that they were deposited in a relatively mature large alluvial system *prior* to the development of the channels which currently flow across the ramp. The simplest explanation for this is a large alluvial fan system, sourced from the exit of the main channel at the base of Fault 1, supplied by the early channel which had begun to incise through the Fault 1 scarp [see Fig. 7.2.3]. Accumulation of displacement on Fault 1 would tend to drive the deposition towards the rapidly subsiding area in the centre of Fault 1, to the north of the present overlap, resulting in clast deposition predominantly on the northern part of the present ramp, as seen. Distal fan deposits may form part of the thick sand deposits which are seen in the hangingwall of Fault 1, around and beyond the northern tip of Fault 2 [see large pale area on the aerial photograph, Fig. 4.1]. The main channel which now connects the Fault 1 footwall channel to the Fault 2 basin

must be a relatively late development, as suggested by its incision into the rounded fan deposits. This may also partly explain why it does not flow, as might be anticipated, down the steepest slope of the overlap zone, towards the centre of Fault 1 [see Chapter 7].

Late incision of the main channel into a previous depositional system is also consistent with the large pile of angular material at the base of Fault 1 [Fig. 4.48]. If a fan was sourced from this point at the Fault 1 scarp, then deposition of large material would be anticipated close to the channel exit from the scarp. The present pile of debris here effectively blocks all but flood-stage flow from draining down the channels at the north of the ramp. Base-level drop caused by incision of the main channel into the ramp would drive further incision into the Fault 1 scarp, producing large quantities of angular debris. That the incision was driven by incision in the main channel is evident from the fact that the course of the main channel itself is not blocked by this debris, which has been dumped immediately outside the narrow gorge in Fault 1.

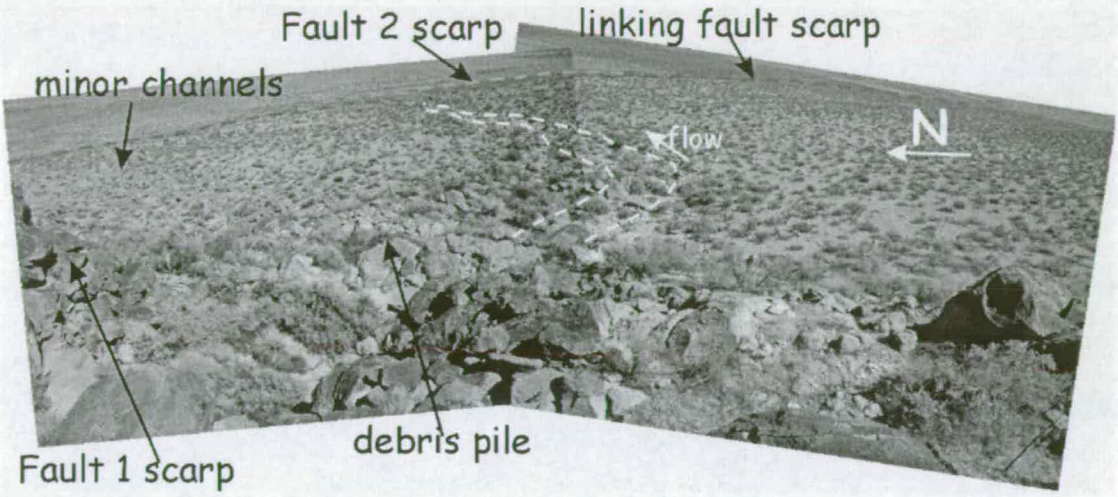

Figure 4.48: *View of main channel incision into the ramp surface.*
Photograph from the inside of the canyon cut through Fault 1. The main channel incises deep into the tuff away to the linking fault in the distance. Minor channels diverge off to the north [left]. Note the large debris pile between these channels, probably deposited during an earlier stage of the stream development. Following incision of the main channel, water flow into the minor [northern] channels is restricted due to this debris pile.

This model brings up various important timing questions: the relative timing of motion on, and the incision through, the Fault 1 scarp and then of the subsequent incision of the main channel into the ramp surface, presumably in response to uplift on the propagating Fault 2; as well as the rate of knickpoint migration in the Fault 1 scarp. Some of these questions may be addressed by the dating of various parts of the channel system, and hence these points, and the viability of this hypothesised two-stage depositional model, are discussed more fully in Chapter 7, in the light of the cosmogenic isotope study outlined in Chapter 6.

4.3 Summary of central overlap data

The central overlap zone lies between two large faults ['1' and '2'], each over 1.5km in length, which are hard-linked by a third long fault [the 'linking fault']. Although these faults accommodate much of the displacement, a large amount of strain is also accommodated by smaller fractures and warping within the overlap itself, which dips steeply towards the northeast. Segmentation is pronounced in all the surveyed faults, on a variety of scales from 50 to 400m in length.

Fault 1, the northwestern, largest fault, has a D_{max} of almost 80m [92m in Dawers and Anders (1995)], which is located towards its northern tip, reflecting the influence of Fault 0, to the north, on its development. Small faults are well developed in its footwall and at both tips, and often developed along joint planes. Fault 2, at the front of the overlap, has a similar length to Fault 1, but much lower displacement [D_{max} ~38m]. The influence of lithological heterogeneity is pronounced, with the fault splitting at its northern tip along two lines of fumaroles, while splays in the southern footwall are oriented parallel to prominent joint sets. The fault which links these two main structures appears to have had a complex development [Fig. 7.4], and again shows the influence of joints on fault nucleation, particularly towards the south of the overlap. This linking fault appears to have been nucleated in two distinct places, at the ends of the relay, close to the bounding faults, and to have grown by linkage of *en echelon* segments. A pronounced displacement low remains between these two regions, implying a relatively recent linkage.

Drainage of the central overlap is dominated by local fault motion, resulting in braiding, incision of channels into the tuff surface, and the development of prominent knickpoints. Streams generally exploit displacement lows in the scarps, and particularly the regional low between the two parts of the linking fault. However, the observation of several talus fans at the base of Fault 2 which are not associated with incised streams implies that segment linkage may have cut off the sediment supply from at least some of the streams that originally drained the developing relay. There is also considerable evidence of the influence of lithological heterogeneity, and particularly joints and fumaroles, on the channel development.

The ramp itself is now drained by two separate drainage systems: a major stream which flows across the ramp to deposit a large fan of material in the hangingwall, 400m from the northern tip of Fault 2; and a series of smaller streams, many of which cannot be traced far, which drain predominantly the northern part of the ramp towards the northern tip of Fault 2. The main stream does not flow down the steepest slope of the ramp towards the toe of the relay, but incises relatively deeply into the tuff, with prominent knickpoints developed at each of the transverse faults, showing only minor profile adjustment to their uplift. Braiding occurs immediately upstream and downstream of each fault scarp. The channel dimensions, amount of incision, clast size and sediment volume imply a high discharge.

The minor channels which drain the northern part of the ramp are much less distinct than this main stream, being only shallowly incised into the tuff surface. Those that can be traced flow down the steepest slope of the ramp, to deposit their load in the low area at the northern tip of Fault 2, towards the centre of the Fault 1 hangingwall basin. The stream profiles are smoother, reflecting the lower uplift at the Fault 2 tip,

although a prominent knickpoint is still evident at the linking fault, again showing little stream adjustment to this motion. Discharge in these channels was probably considerably lower than in the main channel.

Both these ramp systems stem from a single source channel incised into the footwall of Fault 1. This supply channel is dominated by the development of Fault 1, with two sharp knickpoints upstream of the present scarp, implying a long history of profile adjustment to periodic base-level drops. Channel morphology is closely linked to the knickpoints, as shown by the aspect ratio of the channel which increases dramatically towards the Fault 1 scarp. In contrast to the sharp steep downstream knickpoints, the Fault 1 scarp is incised to a depth of almost 8m by the channel, and has a much shallower, step-like profile, implying a considerably greater adjustment to fault motion.

Most of the northern part of the ramp surface is covered in rounded clasts, in marked contrast with the rest of the Tableland surface. The rounded deposits are well tessellated, and are clearly incised by the present channels. The clasts show a distribution and size variation consistent with deposition in an earlier alluvial system, rather than as overbank, or lateral bar, deposits from the channels currently visible on the ramp. The present main channel across the ramp thus probably incised through the fan deposits, in response to motion on Fault 2 at a relatively late stage. Large angular blocks, some up to 3m across, form a large pile at the exit of the gorge cut through Fault 1, which would today prevent all but flood-stage discharge from draining down the minor channels to the north; instead focusing any flow down the main channel across the ramp. This is consistent with a two-stage depositional model, with late incision of the main ramp channel into the previous alluvial deposits.

Constraints on the suggested evolution of these drainage systems are provided by the cosmogenic isotope study, which is described in Chapter 6. The implications of the cosmogenic work are discussed with reference to the above observations in Chapter 7.

Chapter 5

Northern and axial drainage networks, Volcanic Tableland

The previous chapter described the features of the central fault overlap of an array on the Volcanic Tableland, leading to some initial suggestions about the evolution of the drainage network which runs through it. This second fieldwork chapter compares those findings with two other stream networks from the same array: the lateral system which drains the northern tip of the array [section 5.1], and the stream network which flows axially to the southern part of the array [section 5.2]. The two networks are described using stream data in the same way: differential GPS surveys show the stream courses, long profiles and cross-sectional morphologies.

The northern tip system provides a direct comparison with the central overlap channel, as it also flows broadly from west to east across the array, but it encounters a very different structural environment. The axial stream developed as individual fault sub-basins connected along strike, and hence provides more information about the downstream part of the central stream network, which flows into the hangingwall basin of Fault 2 [see Fig. 4.1], and the interconnectivity of southern streams. Perpendicular profiles of the hangingwall basins of Faults 0, 1 and 2 are also presented in this second section [see Fig. 5.40].

A summary of each system follows the field observations, and the whole chapter is discussed in the light of the central overlap data and the cosmogenic isotope data, in Chapter 7.

5.1 Lateral drainage system: Northern tip network

This section considers the drainage network that flows through the northern tip of the fault array [Fig. 5.1], as a direct comparison with the drainage through the central overlap [section 4.2]. Although both streams may have originally flowed in a similar direction, in response to the tilt of the Tableland surface [towards 121-125°: Pinter and Keller (1995), see Chapter 3], the current course of this northern channel is very different from that of the central overlap stream, implying that the two streams experienced very different tectonic environments.

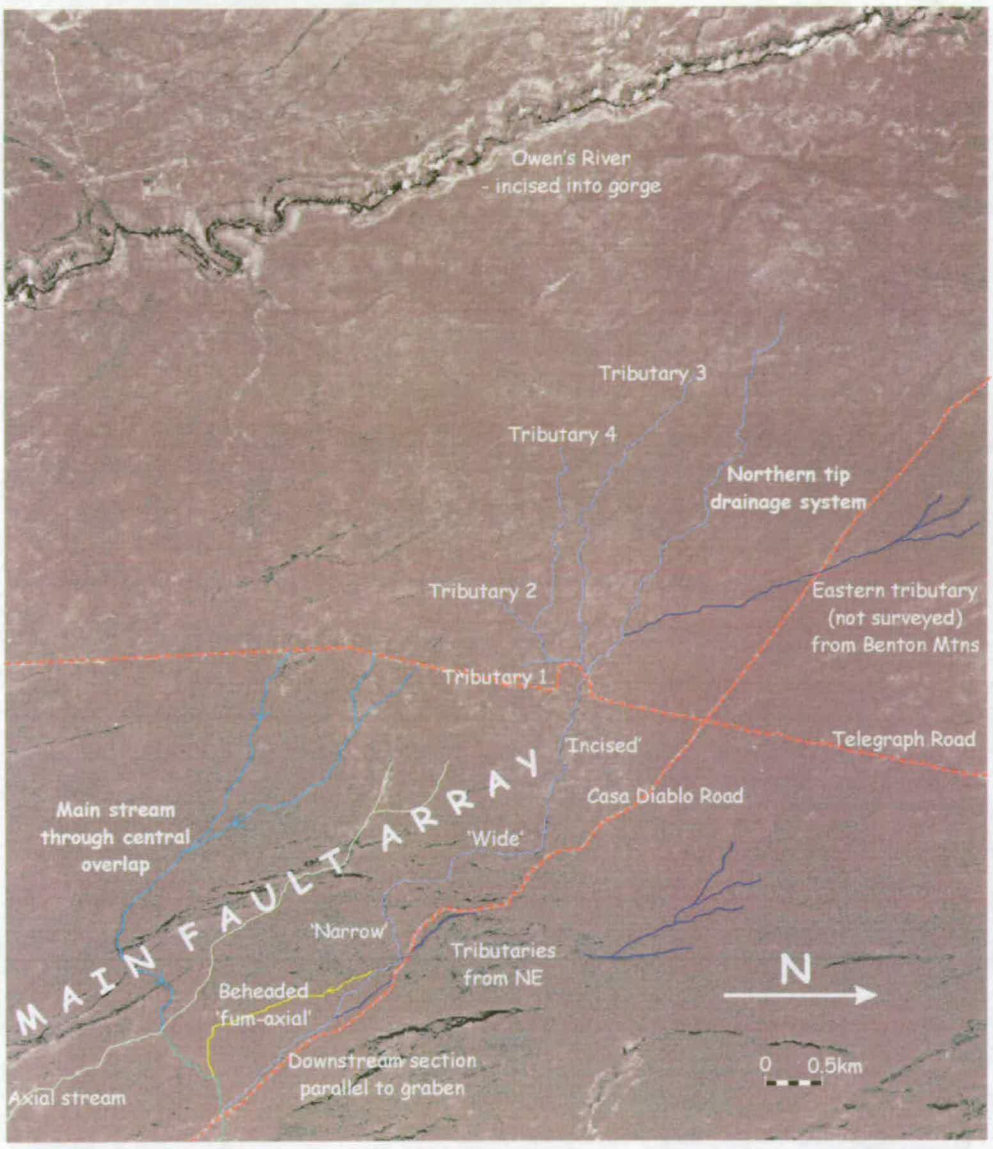

Figure 5.1: *Aerial photograph of the drainage network at the northern tip of the fault array. Dark shadows are extensional fault scarps dipping east; faults which dip to the west cast thinner shadows. A gorge is incised through the northern tip of the main array, where faults have throws* $\leq$*30m. Compare with the main stream through the central overlap, where* D_{max} *is* $\sim$*90m. West of the main array, a series of tributaries snake between and through fault scarps, and then join together near the dense fumarole blebs at the Telegraph Road, which cuts left to right across the photograph. Casa Diablo Road runs NW-SE along the bottom of the photograph. Paler areas indicate sand-rich deposits, while darker colours are generally higher, fumarole-rich ground, or uplifted footwalls.*
Downstream of the main array, the northern stream negotiates a series of major bends, then flows subparallel to the array, towards the SE, near Casa Diablo Road, roughly down the centre of the graben. 'The fumarole-axial channel' is a beheaded stream discussed in section 5.2.5.
The gorge [up to $\sim$*150m deep] cut by the incision of the Owens River is prominent at the top of the photograph, draining towards the SSE [left]. The Benton Mountains (predominantly acidic igneous rocks) form higher ground beyond the photo to the north and north-west: see Fig. 3.4b].*

The northern drainage system is discussed in two main parts. The first section [5.1.1] focuses on the downstream channel, which incises through the tip of the fault array, then flows eastwards towards the centre of the graben by Casa Diablo Road; and investigates the factors controlling the morphology along its course. The second part turns to the upstream part of the network [section 5.1.2], and a series of tributaries [section 5.1.3], to provide more insight into the development of the marked differences from the central overlap channels [section 4.2]. The surprising observation of non-tuff clasts in the channel bed is discussed in section 5.1.4, and brought together with the rest of the northern stream data in section 5.1.5.

5.1.1 Downstream channel

Downstream of Telegraph Road, on the east side of the main fault array, the northern stream experiences a series of large morphological changes, governed largely by the local fault pattern [Fig. 5.2]. A deeply-incised gorge is carved almost straight through the main fault array. Downstream of this, the river turns sharply to flow southwards, parallel to the array, and opens out into a broad plain bordered by small fault scarps and fumaroles; a low-gradient migrating channel depositing fine sand. Another sharp turn in its course directs the channel between transverse faults, where it is constricted into a narrow gorge, though less deeply-incised than through the main fault array. After passing through a fumarole-rich area, the stream bends to flow once more parallel to the main graben, in a shallow, low-gradient channel. This section investigates the different morphologies of these reaches, and the features which govern them, beginning with the deeply-incised gorge through the main fault array.

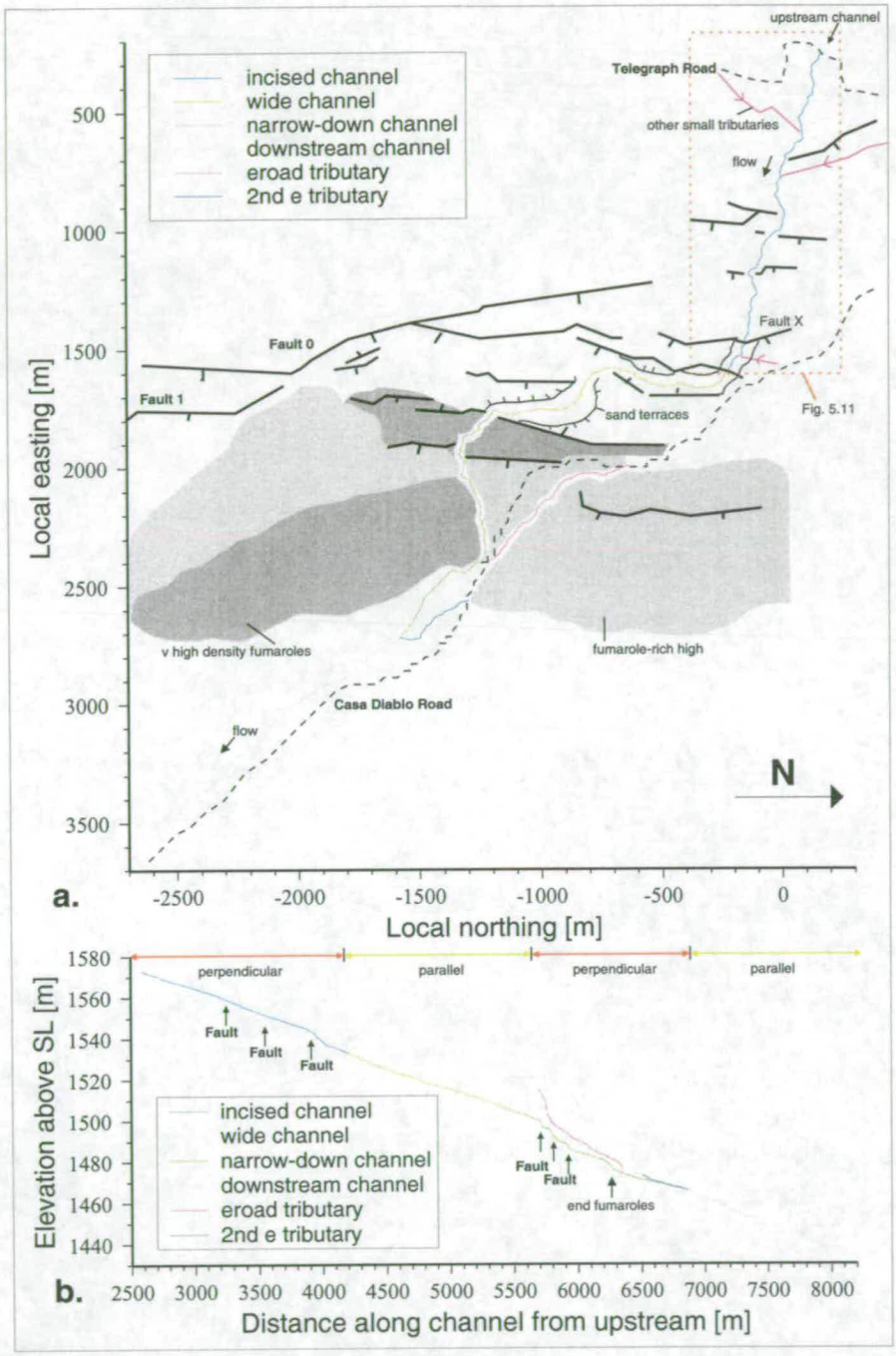

Figure 5.2: *a. Map and b. long profile of the northern tip channel downstream of Telegraph Road. See Fig. 5.11 for upstream map.*
The channel shows widely-varying morphologies in four distinct sections downstream:
blue: incised gorge through main array [Fig. 5.5]
orange: wide depositional channel parallel to main array [Fig. 5.8a]
green: narrow gorge steps down small faults [Fig. 5.8b]; channel widens out downstream [Fig. 5.8c]
lilac: shallow low-gradient channel parallel to main graben
Purple and navy streams are the downstream sections of tributaries from the northeast.

5.1.1.1 Incised channel

Stream course and long profile: The channel incised through the northern tip of the array has a much straighter course than the central overlap stream [see Fig. 4.1]; flowing towards 104°. Bends in the channel course are caused by the tips of small faults striking 336-021° [Fig. 5.3a], although the deflections are far less severe than in the central overlap.

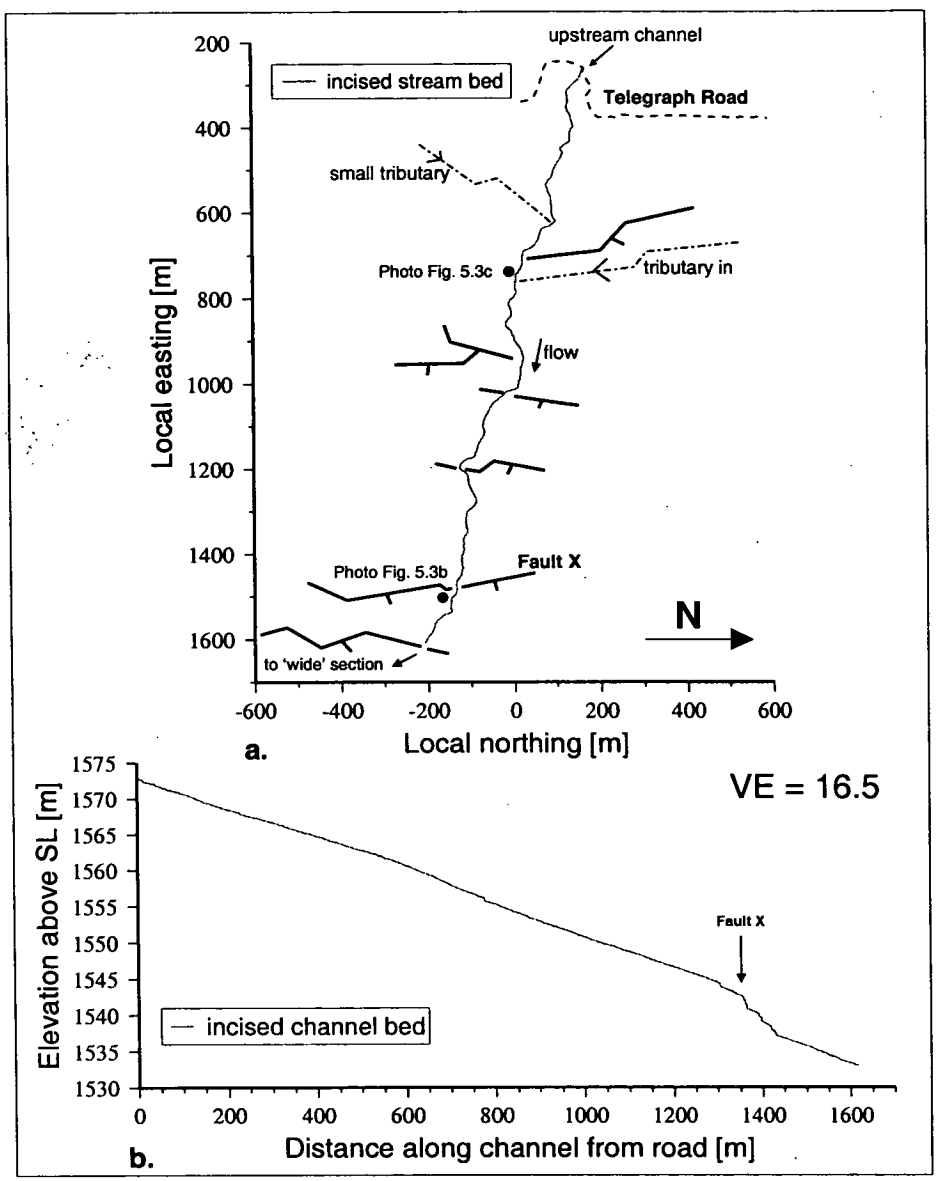

Figure 5.3: *a. Map and b. long profile of the incised section of the channel flowing through the northern tip of the main fault array.*

Deformation at this tip of the array is distributed onto a series of small faults, averaging 100-500m in length, with maximum displacements of 2-30m. In contrast, most of the extension in the central overlap is focused on the two large structures, Faults 1 and 2,

with D_{max} of 40-90m [section 4.1]. Hence the contrasting amounts of channel deflection are probably at least partly a result of the distribution of deformation.

The profile of the incised northern channel is very smooth [Fig. 5.3b], with an almost uniform gradient of 1.21° [Table 5.1]; considerably lower than that of the main channel through either the gorge incised into the footwall of Fault 1, or across the ramp itself. It is much more akin to the central stream gradient near the fork, far upstream of Fault 1, or in the F2 basin. One pronounced step in the profile towards the end of the gorge correlates with Fault X [Fig. 5.3a]. However, there are no steep knickpoints at any of the upstream faults in the array; in marked contrast with the profile of the main channel through the central ramp [Fig. 4.24], which has a far steeper profile, interrupted by a series of very steep knickpoints where the stream crosses normal faults.

The low gradient and lack of steep knickpoints imply that this northern channel has adjusted its profile to accommodate virtually all the fault motion, and is more in equilibrium with the local tectonic environment. The steep knickpoint at Fault X prompts the question of the timing and magnitude of this unaccommodated uplift, which may have occurred more recently, than motion on more westerly faults.

Bank profiles: When the bank profiles are compared with the channel profile [Fig. 5.4], the deep incision can be appreciated. High bank elevations locate the fault scarps along the gorge, showing that the low gradient of the channel bed is the result of major adjustment to differential uplift. The channel bed is at least 2m below the bank crests throughout the gorge, and in places, is incised more than 10m, deeper than the incision of the central footwall stream at the Fault 1 scarp [Fig. 4.32], despite the more distributed deformation at this tip of the array [see Fig. 5.5a].

Where a high occurs in one bank only [Fig. 4.32], the stream has deviated towards, or around, a fault tip [e.g. Fig. 5.3a]. Paired elevation highs indicate incision through a scarp, e.g. Fig. 5.5b, and demonstrate that the channel has not been deflected around all the faults. This stark comparison with the central overlap stream implies a different balance between stream power and the fault uplift at this northern tip. Uplift is distributed onto a number of small faults, but the stream must also be relatively more powerful and mature. However, some parts of the tuff in this northern part of the array are slightly different, being in general coarser-grained, and often less consolidated. In this case, the channel may have been able to incise more easily than into the tuff than in the central overlap.

Figure 5.5 shows the steep gorge incised into the northern tip of the array. The depth of incision, particularly at the fault scarps [Fig. 5.5b] is immense for the Tableland, and the scale of the channel [see also cross-sections, Fig. 5.6] is much larger than the streams through the central overlap. Even where the banks are lower [Fig. 5.5c], the channel has a broad flat bed, and 1.5m clasts line the margins. Many large clasts of dense igneous material occur [section 5.1.4], which indicate a particularly powerful stream.

In constricted parts of the channel, where faults have been incised, notches are cut into the walls up to 2.5m above the stream bed, and clasts have been plucked from the tuff all along them. Below this notch, the tuff is smoothed and stained. The stream bed is now almost uniformly covered in sand, probably the result of later deposition, and aeolian reworking of sand from elsewhere on the Tableland. While some fumaroles cause

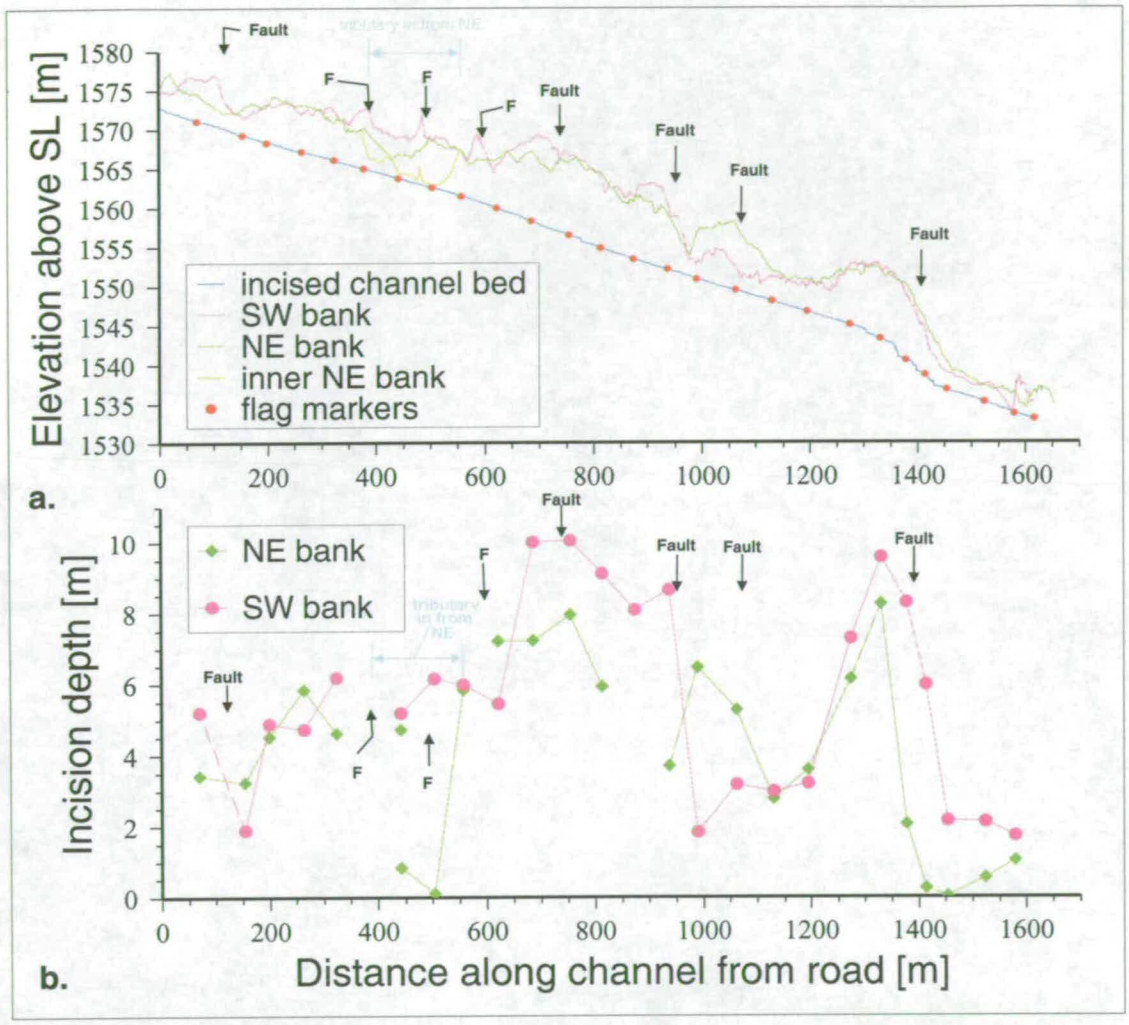

Figure 5.4: *a. Profile of the channel bed and banks through the northern tip of the array. The 'inner NE bank' [ochre] shows the location of a large tributary joining the channel from the NE, resulting in a low inner bank to the channel along this one margin. 'Flags' are the points where incision depths have been calculated in [b].*
b. Incision depth: elevation difference between channel bed and crest of banks. Fault scarps are high elevations in one ['F'] or both ['Fault'] banks. Where high elevations occur in both banks, the channel has incised through a scarp; unpaired elevation highs reflect deviation of the channel towards, or around, a fault tip. Note in particular the large scarp at the knickpoint in the channel, at the downstream end of the gorge: Fault X in Fig. 5.3.

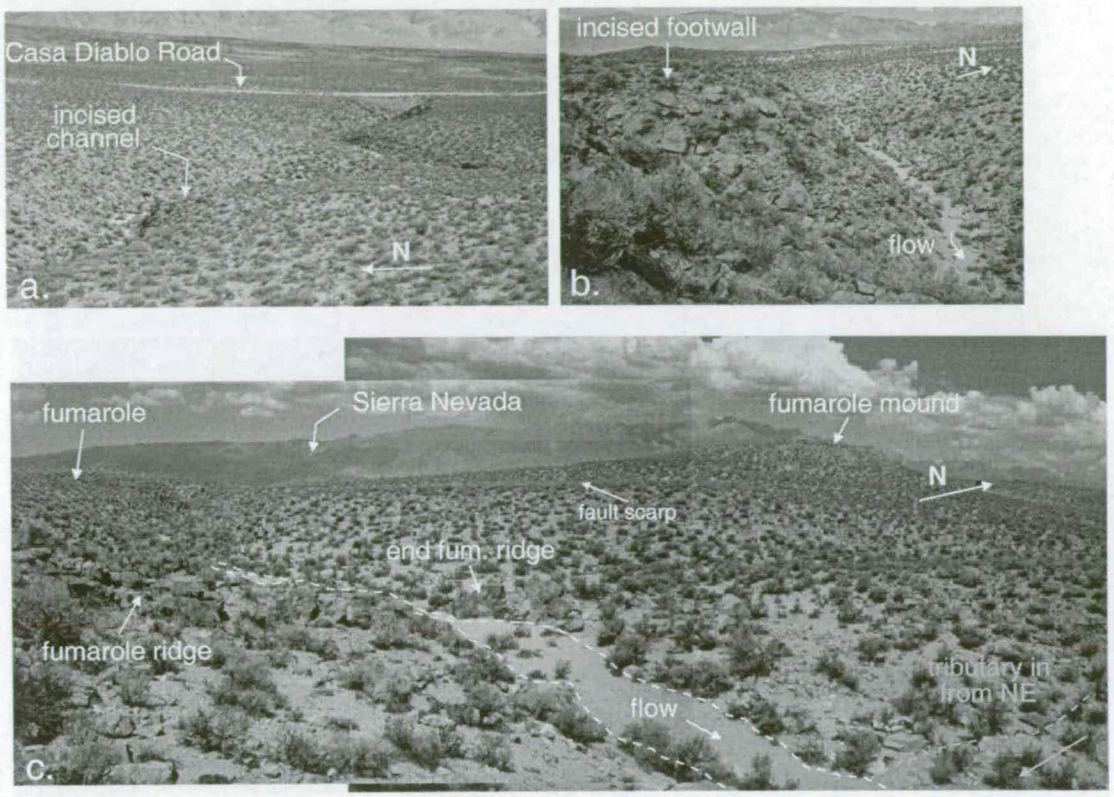

Figure 5.5: *Field photographs of the stream incised through the northern tip of the fault array.*
a. View to the east [downstream] of incision into the Tableland surface. Stream has cut down over 10m at the deepest part. Stream bed in the foreground is approx. 3m wide.
b. View to west [upstream] of deepest part of channel, near eastern end of incised reach, xc 34. Stream has incised over 10m in the footwall of this E-dipping fault. Channel floor is approx. 2m wide.
c. View to west [upstream] towards western end of incised reach, section tx2. Stream winds around a fault tip and between fumarole mounds, though a prominent fumarole ridge has been incised. Northern bank in centre of photograph is lower than where fumaroles form southern bank. Southern [high] bank is approx. 6m high, northern bank only 1-2m. Channel floor is 3m wide, flat and sandy, though large clasts line the banks. Large tributary supply enters just on far right of photograph [Fig. 5.3a].

deviation, other fumarole ridges have been entirely obliterated by the flow [Fig. 5.5c]. Thus the response of this channel to the local structure and topography contrasts sharply with the channel through the central overlap, where steep knickpoints and sharp deviations are preserved [Figs. 4.24 and 4.21].

Cross-section data: Cross-sectional profiles [Fig. 5.6a] emphasise the deep incision evident in the bank profiles. As in section 4.2, profiles are presented in separate panels, showing the contrasting morphologies along the channel. All profiles are plotted from the NE to SW, perpendicular to the flow, and all at the same scale [VE=9.0]. The deepest incision occurs in the central part of the canyon [panel B], at the axis of deformation of the fault array. Incision decreases slightly through the first part of section C, but then increases again as a further fault is incised. No cross-sections were measured in the steep channel between panels C and D, through the Fault X scarp.

The lowest banks [D] occur not only downstream of Fault X, but also on the apex of two sharp upstream bends [purple in Fig. 5.6b], where the channel is deflected around fault tips. The second of these lows [tx2] is also near a large tributary channel from the north-east, which itself exploits a low along the base of a fault to join the main canyon [Fig. 5.5c]. Reduced incision in xcs 33 and 32 marks a wider channel downstream of Fault X, and beyond the main canyon.

Cross-section morphologies are summarised by the aspect ratio [bank-base depth/bank-bank width: Fig. 5.6c]. Two sets of AR values have been calculated: one using the cross-section profiles; the second using the bank data at the flagged points [Fig. 5.4], as no continuous cross-sections were surveyed through the steep reach in Fault X. The two datasets have a broadly similar shape, but where available, the continuous profiles should be used, as the bank data are based on only three points.

The high incision through fault scarps [high AR, $\geq$0.175], contrasts sharply with parts of the gorge between faults, or where the stream has bent around fault tips [AR$\leq$0.125]. Although the depth of incision is higher than that in the central overlap [Fig. 4.32], the variation in aspect ratio follows a similar pattern, reflecting a similar response to the fault development [e.g. compare incision in Fault X: Fig. 5.6c with the main stream incision through Fault 1: Figs. 4.34c and 4.37]. Aspect ratios are similar to those of the deeply-incised main channel in the footwall of Fault 1 [Fig. 4.34c]: the deepest part of the northern canyon has a similar aspect ratio to the stream in the immediate footwall of Fault 1 [AR$\simeq$0.25].

In summary, the smooth profile of the present bed of the northern gorge is the result of massive incision, accommodating virtually all of the differential movement across faults in the main array. Large variations in incision depth over a scale of only 100-200m highlight the stream's sensitivity to relatively small fault motions, and also imply quite rapid profile adjustment [Chapter 7]. The coincidence of the highest incision, and highest AR values, with the steepened profile at Fault X implies that the step is the result of fault motion that occurred more recently than on the faults further west: although the channel has clearly begun to incise deeply to accommodate the Fault X movement, a knickpoint remains in the profile.

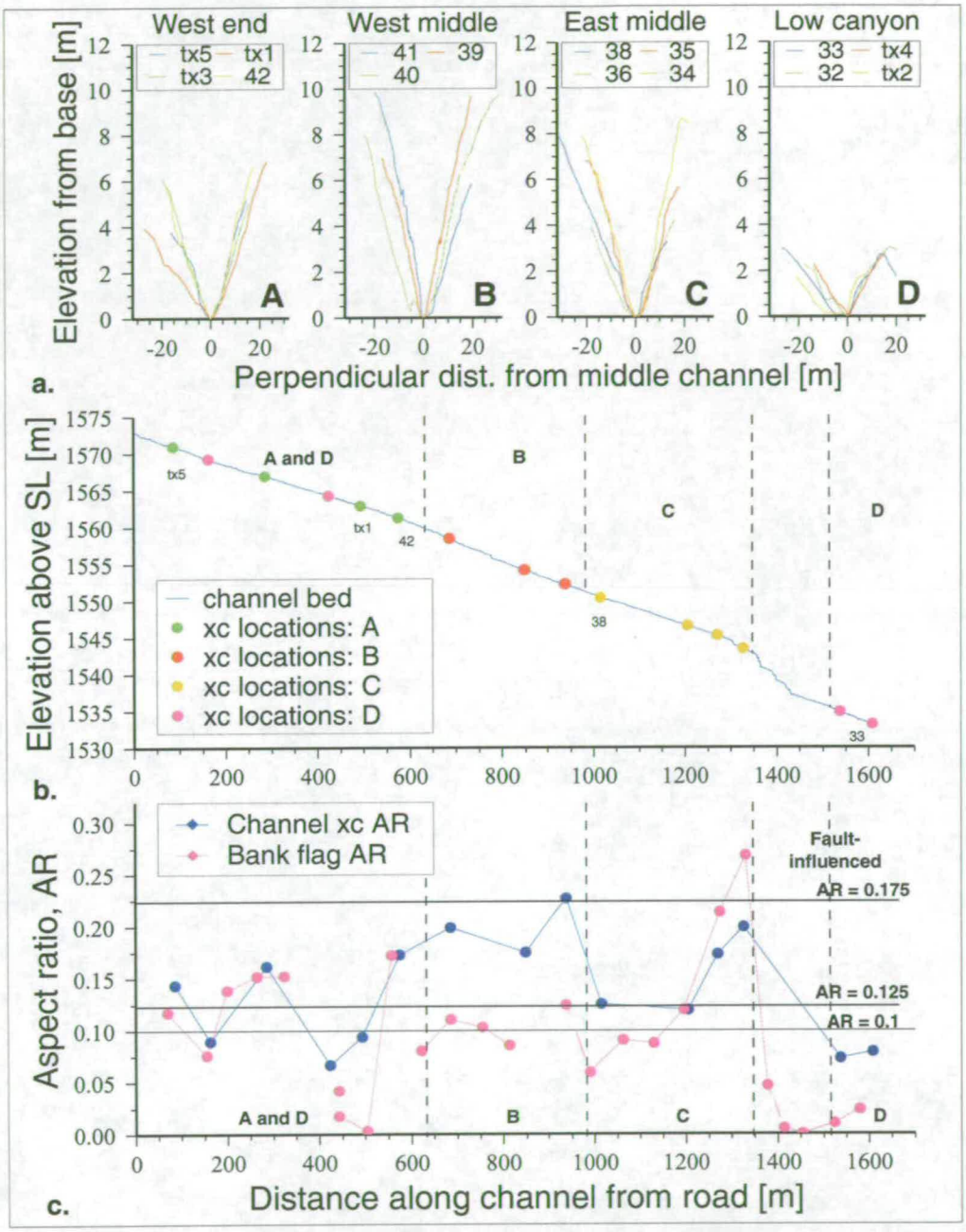

Figure 5.6: *Downstream variation in cross-sectional morphology of incised northern channel.*
a. Cross-sections in the incised channel, separated into the 4 main morphologies. All profiles are plotted from the NE to SW, perpendicular to the flow, and all at the same scale: VE=9.0.
b. Long profile showing locations of the 4 varying morphologies downstream. The lowest banks [D] occur at the downstream [east] end of the canyon, and on the bends upstream, sections tx4, tx2 [Fig. 5.5c], where the stream is deflected around/towards faults, or tributaries join the gorge.
c. Variation in aspect ratio [bank-base depth / bank-bank width]. No cross-sections were surveyed through the Fault X footwall, hence two sets of data: navy line from cross-sections; purple line using bank crest profiles at the flagged locations [Fig. 5.4a]. The AR profiles are similar, but differ near the crucial downstream knickpoint.

5.1.1.2 Downstream of the main fault array

Once the northern stream has navigated the main fault array, it flows south-southwest sub-parallel to the faults, and its morphology changes drastically. This section looks at the series of changes in the channel downstream of the gorge, as it flows towards the centre of the graben [roughly followed by the Casa Diablo Road: see Fig. 4.1]. The channel undergoes three large morphological changes in this section, each corresponding with a large change in its flow direction, as the stream flows alternately parallel and perpendicular to the dominant structural grain [see Fig. 5.1].

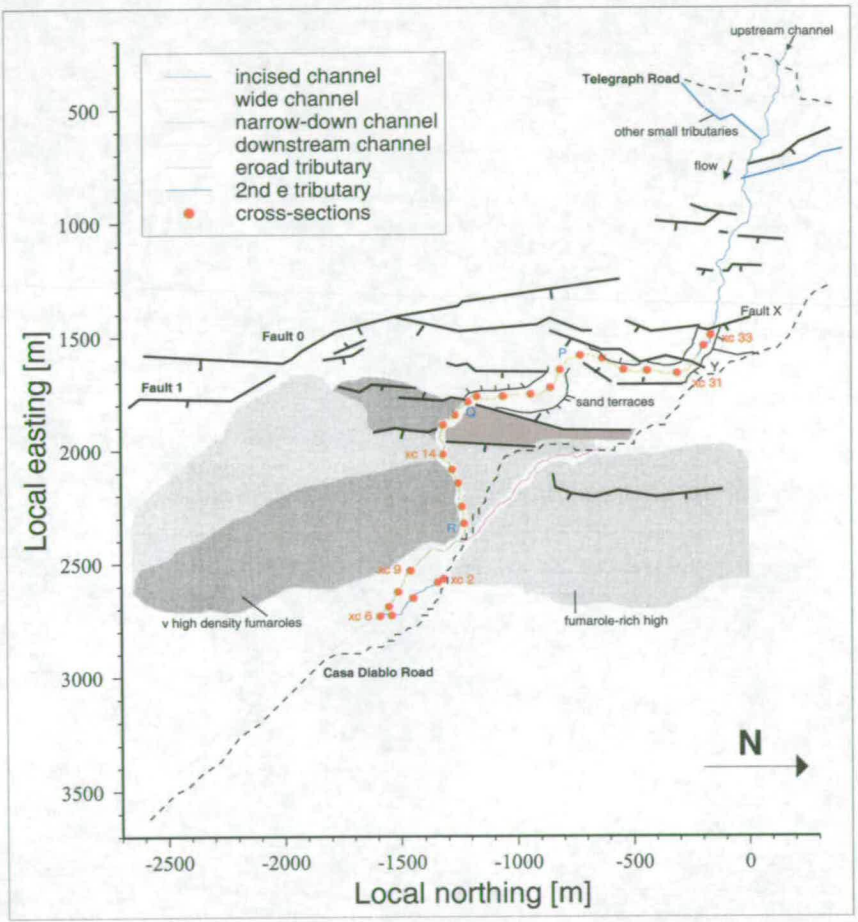

Figure 5.7: *Map of the downstream reaches of the northern drainage network. Channel reaches are coloured by morphology, as in Fig. 5.2. Locations of cross-sections discussed in Fig. 5.9 are marked with red circles. Cross-sections 33 and 32 at the downstream end of the incised channel are included for reference. 'P', 'Q' and 'R' refer to prominent changes in morphology described in the text.*

As it reaches the eastern end of the main fault array, the northern stream becomes less confined. Instead of the narrow, deeply-incised gorge cut through the array [Fig. 5.5], the river opens out into a sandy channel over 7m wide [xcs 33, 32]. The initial reach [up to 250m] downstream of the last fault [Fig. 5.2b] is littered with large rounded to subangular clasts, including crystalline granites, diorites and basalts [see section 5.1.4], reaching 1m in diameter. However, these clasts die out rapidly downstream,

and the channel deposits predominantly fine sand, and occasionally small pebbles on inner bends. Sand terraces are built up to 2m on both margins, and appear very fresh [Fig. 5.8a].

One final scarp [Fault Y: Fig. 5.7] is incised, with smoothed notches cut into the tuff up to 1.5m above the sandy channel floor, as upstream. After this, the stream rounds a bend to flow towards 191°, subparallel to the fault array, and changes morphology dramatically [A in Figs. 5.9 and 5.10]. The margins of the channel are fault-controlled, but as the stream flows along-strike, it is able to migrate laterally over a broad virtually flat area, up to 200m wide [orange reach in Fig. 5.7]. The plain is covered in fine sand, and has a very low downstream gradient [Table 5.1]. High sand terraces are developed on both sides of this plain, up to 7m above the channel bed, against the fault scarps [Fig. 5.8a], indicating deep incision along this entire stream in response to tectonic motion.

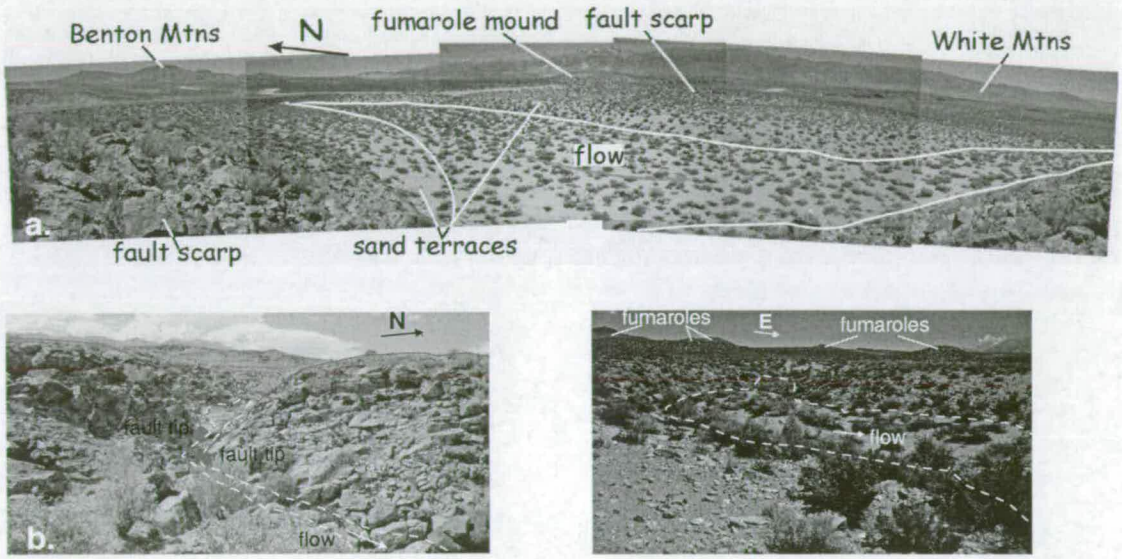

Figure 5.8: *Field photographs of the downstream reaches of the northern stream.*
a. 'Wide' reach [orange in Fig. 5.2]. Shallow channel migrates over broad sandy floodplain, depositing fines. Fresh-looking sand terraces are well-preserved along one or both margins against the faults. Course defined between lateral faults and small fumaroles [see also Fig. 5.1]
b. 'Narrow' reach [green in Fig. 5.2]. Stream incises a narrow gorge between overlapping fault tips, subparallel to the main fault array. Channel morphology broadly similar to the incised gorge upstream through the main fault array upstream [Fig. 5.5], though smaller: here ~4m deep.
c. Downstream part of 'narrow' reach: channel has widened out downstream of the small faults, but remains incised to a depth of 2m.

At **P** [Fig. 5.7], the stream bends towards 120° for around 200m before continuing on its southerly course [towards 174°] along the base of a small W-dipping fault. This change in direction occurs at the tip of the small fault that formed the eastern boundary to the channel up to this point. The channel narrows sharply as it is funnelled around this fault tip, before opening out again into a broad plain, flanked by high sand terraces [Fig. 5.1]. Some larger clasts occur at the constriction, but few non-tuff clasts are seen [section 5.1.4].

Fumarolic ridges and mounds are quite abundant, often aligned along a similar trend to the faults [320-020° strike: see Fig. 5.1], and associated with the fault tips [e.g. Figs. 5.8a, 4.40b], as at **P**. A large fumarole-rich area can be seen on the aerial photographs [darker grey colour: slightly higher ground, no sand deposition], to the east of the channel [Figs. 4.1 and 5.1]. The orientation of these strongly-welded highs directs the channel subparallel to the fault array along this reach [Fig. 5.8a], as seen elsewhere on the Tableland, e.g. axial channel [Figs. 5.26 and 5.29].

At **Q** [start green reach, Fig. 5.7], the stream turns sharply towards 134°, funnelled between two fumaroles in the scarp of a small W-dipping fault, which forms one side of a small horst. On the other side of this horst, the stream is squeezed between the tips of two overlapping E-dipping faults [Fig. 5.8b]. The faults cause a very steep profile, which drops 18m over only 420m [see Fig. 5.2b]. In response, the stream occupies a deep, narrow channel, littered with angular blocks, testament to rapid downcutting, as well as the constriction by fault tips and fumarole mounds.

Downstream of this horst, the stream flows through a region of hummocky topography, resulting from a high concentration of fumarolic mounds and ridges [see Fig. 5.7], aligned subparallel to the faults [325-010° strike]. This reach has a lower gradient and the channel gradually becomes less incised, though remaining relatively narrow, confined between rocky walls near hard fumaroles [Fig. 5.1]. The channel floor is generally sandy, but very different from the wide reach [orange in Fig. 5.7], with rounded to subangular cobbles [$\leq$20cm] in several places as the channel flows towards 079°, oblique to the fault array.

At **R** [Fig. 5.7], a further sharp bend again marks a fault scarp, causing a steepened reach [Fig. 5.2b and Table 5.1] and a junction with a large tributary from the northwest [purple channel in Fig. 5.7]. The steep profile of this tributary immediately upstream of its junction is the result of a course incised parallel to a small fault to the east of Casa Diablo Road [see Fig. 5.1]. **R** marks virtually the last local tectonic influence on the channel course. The stream finally leaves the fumarole-rich area, opening into a shallow, low gradient, sandy channel [lilac in Fig. 5.7], which can be traced for several kilometres along 132-138°, immediately west of Casa Diablo Road. The stream follows the graben between the array discussed here and a westerly-dipping array further east. The sharp change in topography and welding is marked by sudden broadening of the channel bed, which has until this point been strictly confined.

Cross-section data: Cross-sections were surveyed up to the beginning of the shallow broad reach [lilac in Fig. 5.7]. The reaches highlighted in Fig. 5.7 ['wide' orange; 'narrow' green; 'shallow' lilac] can each be distinguished clearly. Little variation in cross-section occurs in the final downstream reach [lilac in Fig. 5.9]. The six panels, A-F, in Fig. 5.9 correspond to 6 distinct cross-sectional shapes. Figure 5.10 shows the location of the cross-sections on the stream profile [see also map: Fig. 5.7], and the variation in aspect ratio [bank-base depth/bank-bank width] of the surveyed sections. All cross-sections are plotted from the centre of the channel on the same scale [VE = 10.25], with west/southwest on the left.

The stream shows an alternation in cross-sectional morphology and aspect ratio which correlates with the changes between fault-parallel and fault-normal stream flow. Sharp changes occur at each boundary.

Panel A in Fig. 5.9 corresponds to the orange reach in Fig. 5.7 where a shallow sandy channel migrates across a broad flat plain, parallel to the north-south structural grain. Terraces were included, but surveys were terminated against the fault scarps, and hence the margins in Fig. 5.9 are the sand terraces built against bounding faults. The margins do not coincide as the meandering channel is not maintained at a constant distance from the banks. Narrowing at xc 27 [purple] corresponds with the bend at the tip of the eastern bounding fault [**P** in Fig. 5.7], but the morphology is identical both upstream and downstream of this point. Aspect ratios [Fig. 5.10b] in this reach are universally low [AR$\leq$0.035]; a slight increase marks the bend. Similarly low AR values occur in sandy reaches of the smallest channels in the central overlap [Fig. 4.45].

Funnelling of the channel between the fumaroles in the fault at **Q**, [Fig. 5.7] causes a sharp increase in the depth, and decrease in the width, of the channel [xcs 22 and 19: A$\rightarrow$B; Fig. 5.9]. AR values are similar to those of the incised canyon further upstream [Fig. 5.6c] but the steep gradient implies that through this reach, the stream has not yet fully adjusted to the fault motion. Depth decreases rapidly downstream, in the low gradient reach C [xcs 17 and 15; Fig. 5.9], correlating with very low aspect ratios [Fig. 5.10b]. However, the confinement by hard tuff walls results in a narrower cross-section and correspondingly higher aspect ratios than in the 'wide' reach [panel A; Figs. 5.9 and Fig. 5.10b].

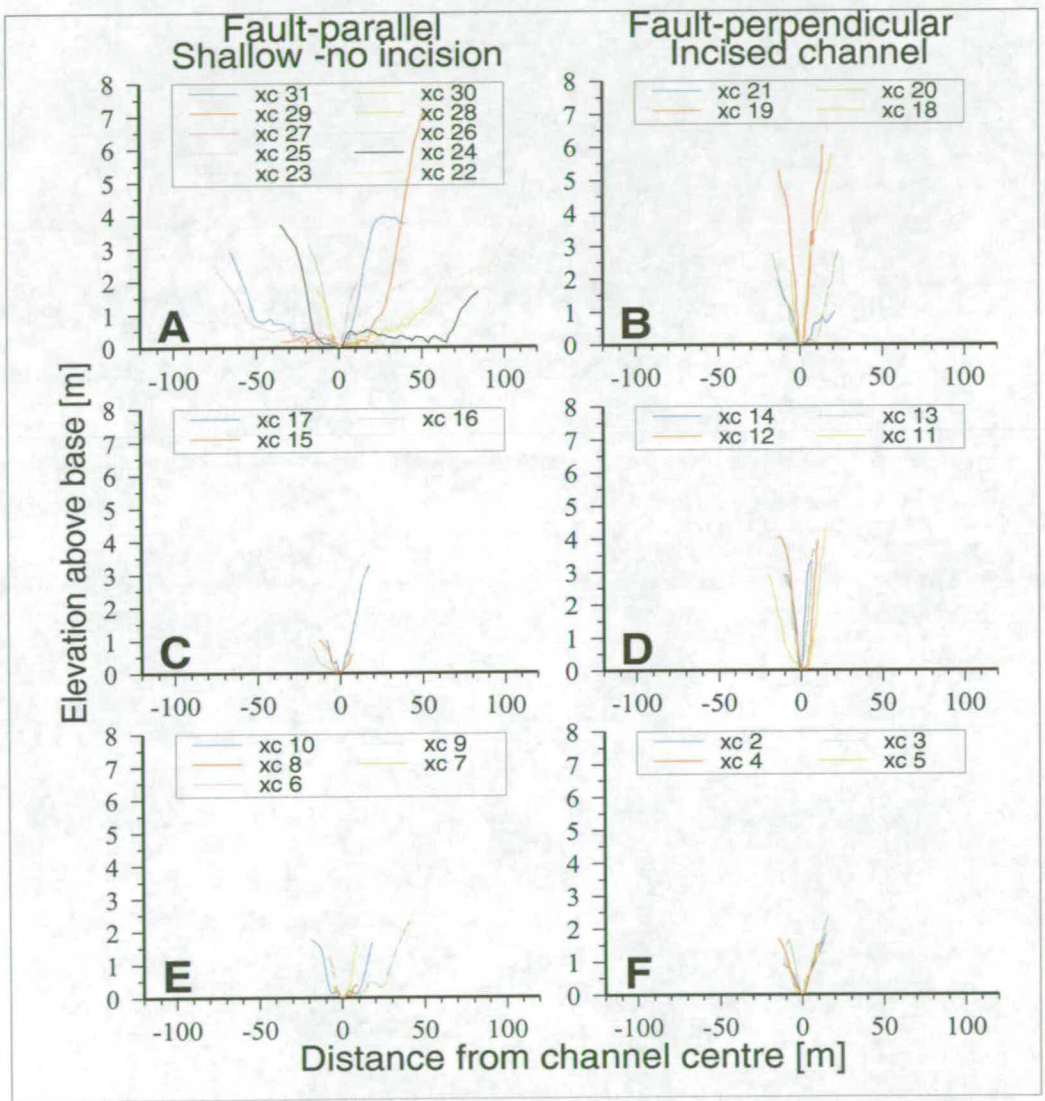

Figure 5.9: *Variation in cross-sectional morphology of downstream reaches of northern stream network.*
The 6 panels, A-F downstream, show distinct morphologies and are labelled on the profile in Fig. 5.10a. All profiles are plotted with W/SW on the left and to the same scale; VE = 10.25. Due to the fault pattern, the morphologies alternate downstream, and hence the panels on the left show shallow channels, whereas the profiles on the right are of incised stream reaches.

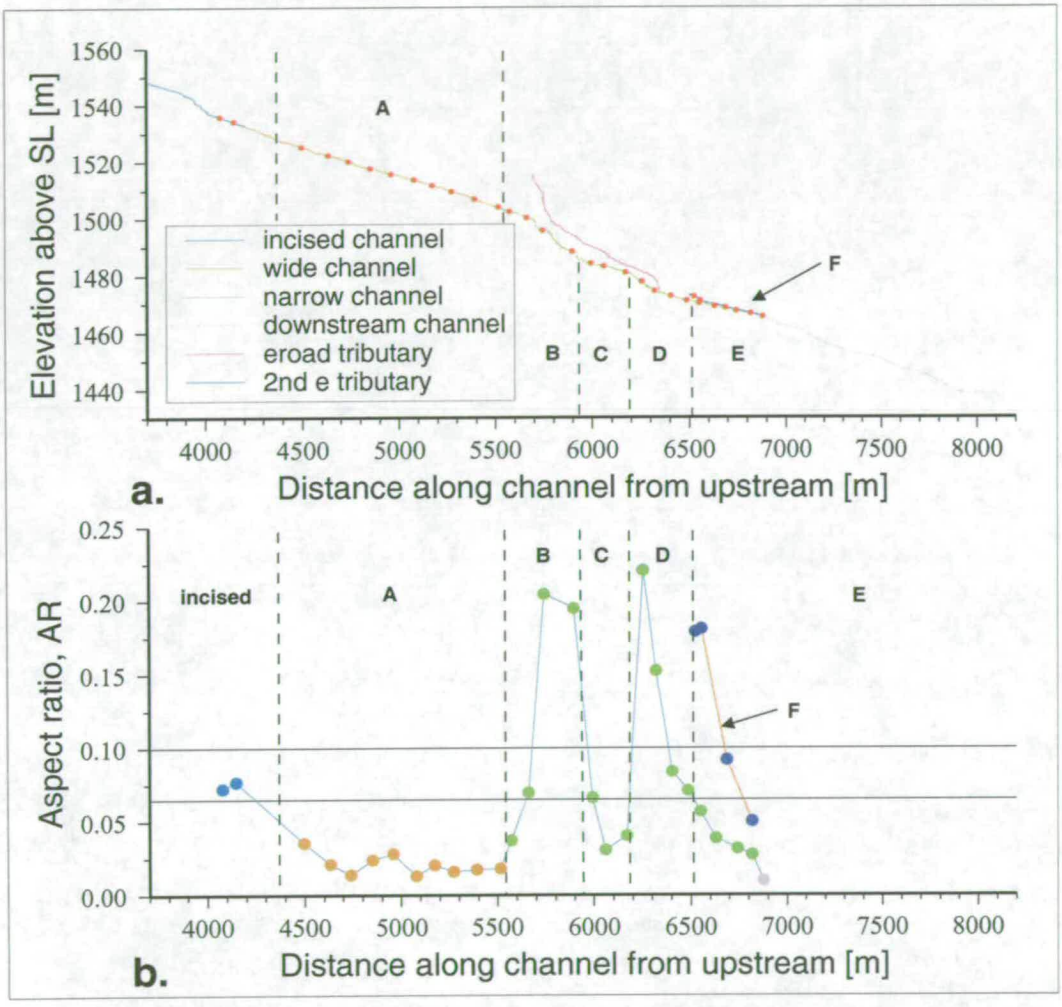

Figure 5.10: *a. Long profile and b. aspect ratio plot for downstream reaches in the northern stream network.*
Labelled reaches correspond with the 6 panels [A-F] marked on Fig. 5.9, which each show differing cross-sectional morphologies. Incised streams, with steep walls and high aspect ratios, correspond with steep gradient reaches. Particularly low aspect ratios are seen in the 'wide' reach [orange] where the channel flows subparallel to the fault array, and migrates over a broad floodplain, constrained by more widely-separated faults and fumaroles.

Response to the fault at **R** [Fig. 5.7; C→D, Fig. 5.9] is similar to the change between panels A and B upstream, although the width decrease is less dramatic, as the stream is confined by hard tuff throughout the green reach [Fig. 5.7]. Aspect ratios are similar to those in the upstream incised reaches [Fig. 5.10b]. Downstream of the fumaroles, the gradient is lower and the channel is wider [E, Fig. 5.9], resulting in low aspect ratios, as in the upstream broad reach [A, Fig. 5.10b].

Panel F shows cross-sectional profiles in the downstream end of a small tributary joining from the northeast [navy, Fig. 5.7]. Cross-section profiles are steeply-Ved, showing up to 2m of incision in response to the fault at **R** [Fig. 5.7], in the fumarole-rich area. Aspect ratios in the channel are similar to those in the corresponding part of the main channel downstream of this fault [xc 12-11, panel D, Fig. 5.9].

5.1.1.3 Summary of downstream channel data

The downstream northern tip channel shows a series of changes in morphology which correlate directly with sharp bends, where the stream becomes oriented parallel to, or perpendicular to, the prevailing structural trend. Where the stream flows roughly south, parallel to the fault array, as in the 'wide' and 'shallow' reaches [orange and lilac in Fig. 5.2], it occupies a shallow broad channel, with a low gradient, dominated by deposition of fine material. Where the channel is forced to flow across the faults ['incised' and 'narrow' reaches, blue and green in Fig. 5.2], a narrow incised channel forms, confined between steep, often rocky, walls. Incision increases in the footwalls to a maximum at the fault scarp, then decreases rapidly downstream. Varying degrees of adjustment to faulting are evident from the differences in gradient. The majority of the canyon through the main part of the fault array shows virtually complete adjustment by incision [gradient <1.5°], whereas steepened slopes at the end of the canyon [gradient 3-4°] and through small faults further downstream [gradient >11°] imply progressively lower degrees of accommodation of the uplift by the channel [Table 5.1].

These changes in flow direction are predominantly caused by variations in the local fault pattern. Where possible, the stream exploits lows between widely-spaced faults to flow along strike, in the immediate hangingwall of the faults. However, sharp bends also occur where the stream is focused through narrow gaps between overlapping fault tips, where it is confined by tectonically-produced topography [e.g. immediately downstream of **Q** in Fig. 5.7; Fig. 5.8b].

Fumaroles, aligned in ridges subparallel to the faults [320-010°], often play an important role in stream development. The harder fumarole-rich area to the east of the main fault array combines with the faults to channel the northern stream towards the south, subparallel to the array, when it leaves the gorge cut through the array [Figs. 5.1 and 5.2]. A gap between fumarole mounds provides a topographic low for the stream at **Q** [Fig. 5.7], but downstream of this bend, it is forced to cut through the denser tuff and hence remains narrow, even away from direct fault influence [Fig. 5.9]. The gradient in this reach is significantly steeper than in the reaches which are oriented parallel to the faults. Once the channel leaves this harder, raised area, it immediately settles into a shallower, low gradient sandier course, once again dominated by deposition.

The variations in morphology are evident in the stream course and long profile, and

in the shape of the channel cross-section [Figs. 5.2 and 5.9] and the aspect ratios [Fig. 5.10b].

5.1.2 Upstream channel

Analysis of the downstream channel, particularly the deeply-incised channel through the main array, implies that this northern system had a considerably larger discharge than the streams through the centre of the fault array. This section focuses on the the trunk stream west of the main fault array, while section 5.1.3 investigates four tributaries which supplied water from the southwest [Fig. 5.11]. A series of small faults, subparallel to the main array, are crossed by both the main upstream channel and several of the tributaries [Figs. 5.1 and 5.11a]. The interaction between these channels and the faults is considered, in comparison with the responses of channels crossing other faults in the main array.

5.1.2.1 Stream course and long profile

The main northern stream extends upstream of the incised gorge for several kilometres towards the north-west. Over much of this distance, the channel has a fairly straight course, flowing towards 117°, though it bends locally in response to faults, excavated joint planes and some groups of fumaroles, as seen where a series of channels flow around a plethora of fumaroles near Telegraph Road [Fig. 5.1]. The stream was only surveyed for 2.6km upstream of Telegraph Road [Fig. 5.11a], but over this stretch alone, it is evident that the channel is considerably larger and more powerful than the upstream reaches of the main central channel [section 4.2.1].

The upstream part of the surveyed northern stream is incised into bedrock, as are several jointed reaches nearer the road. Large rounded clasts up to 80cm in diameter occur in the lower reaches, and at some wider sections over 1.5km from the road. Clasts of this size are only seen in the largest central channel around the incised Fault 1 scarp, where they are generally angular blocks reworked from collapse of jointed canyon walls, rather than mature rounded clasts. In many places, relatively dense igneous clasts are present in this northern channel [see section 5.1.4], again indicating a powerful current. Since the Tableland consists solely of Bishop Tuff, these clasts must have been reworked from distant deposits, demonstrating a large upstream catchment.

The main northern channel [navy in Fig. 5.11b] has a smooth profile over the surveyed distance, implying relative maturity. The gradient is steeper than that of the incised reach [Table 5.1], and roughly equivalent to that of the central channel in the footwall of Fault 1 [Table 4.3]. As with the central channel, faults dominate the stream. Two flights of steps [500-700m and 1300m from the survey start, Fig. 5.11b] and a small step further downstream [around 1950m] occur where the channel crosses transverse faults, and, as shown in Figs. 5.12 and 5.14, correspond with marked morphological changes.

The fault furthest upstream causes an overall drop of 11m in the channel bed [Fig. 5.13]. The detailed profile reflects a great deal of adjustment by the channel, so that its gradient through the footwall is low [Table 5.1]. The elevation drop occurs in small steps over two hundred metres along the stream, and the reach immediately above the top of this knickpoint is also steepened. In contrast, the knickpoints at the downstream steps [around 1300 and 1950m] are sharper, and show less evidence of profile adjustment, even though the displacement at the faults [3 and 1.2m, respectively] is considerably smaller than on the upstream fault.

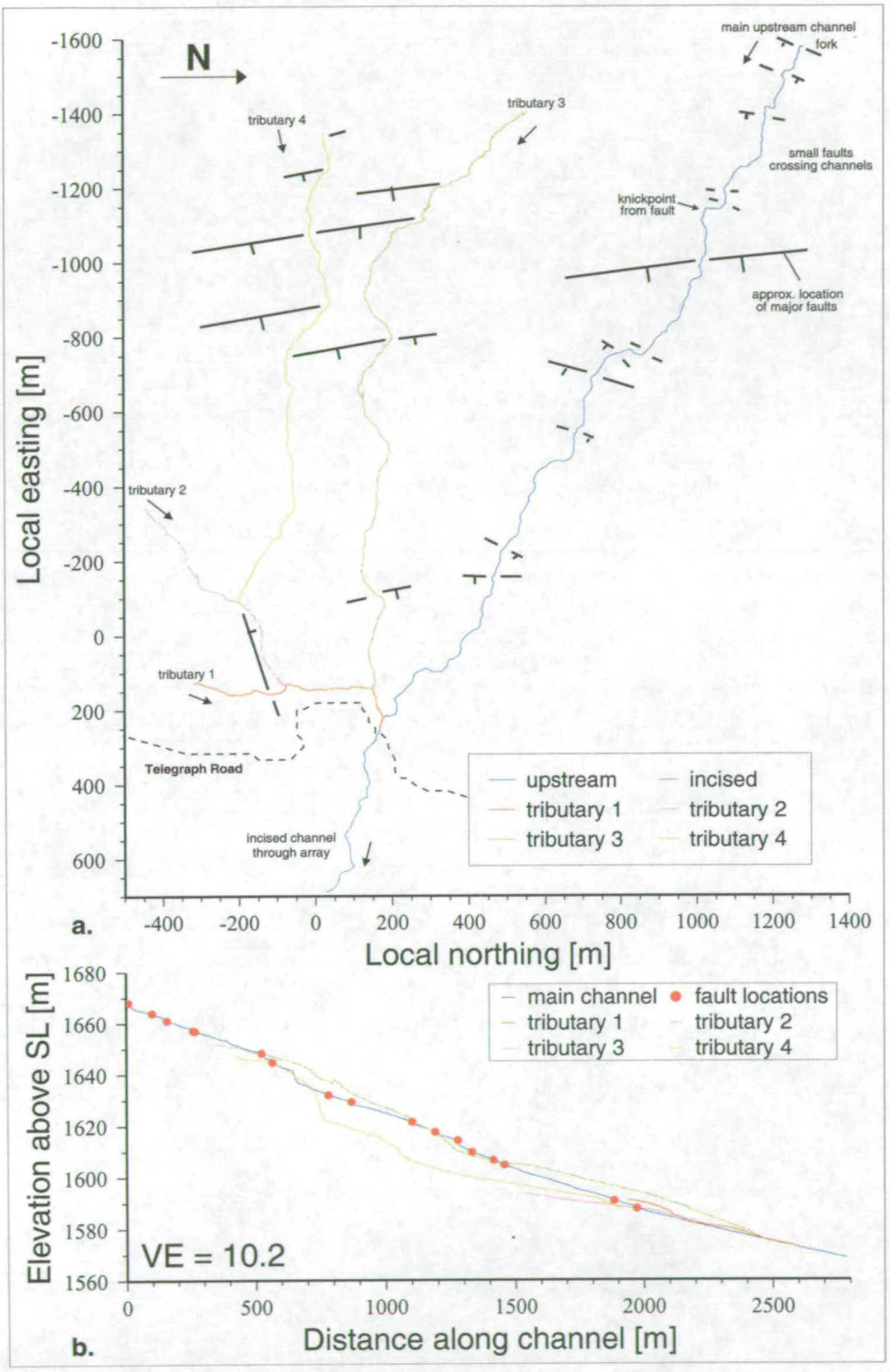

Figure 5.11: *a. Map and b. long profile of the upstream section of the northern tip system. The main stream was not traced to its source, hence the map and profile represent only the surveyed part of this channel. Tributaries 1 to 4 were surveyed as far as they could be traced. Red circles in the profile show the locations of faults which are crossed by the trunk stream.*

5.1.2.2 Cross-section data

Variations in the channel morphology, particularly in reference to these faults, are shown in Figs. 5.12 and 5.14. Cross-sections were only surveyed for the downstream 2km of the channel. Despite the relatively smooth profile, the channel shows considerable morphological variation, with eight reaches distinct by cross-sectional morphology, as shown by panels A-H in Fig. 5.12a. All the cross-sections were surveyed perpendicular to flow, and have been drawn to the same scale as the sections in the incised gorge downstream [Fig. 5.6]: VE = 9, with N/NE on the left.

For most of the surveyed distance, the channel is 2-4m deep, but varies from 20-50m in width. The tuff in this part of the Tableland is considerably more heterogeneous than in the central part of the array, varying from well-cemented and pervasively jointed to friable, poorly cemented tuff, from which clasts up to 5-10cm across have been removed. These variations in lithology have a major influence on the channel style. Steep-sided 'slots' are developed in heavily jointed reaches [e.g. E: xc 17-21; Fig. 5.14e]. Grooving and scouring of the jointed walls is evident to a height of 1-3m, and rounded tuff clasts up to 50cm in diameter lie at the downstream end of these slots. Similar steep-sided reaches are seen in the upstream part of the main central channel, but are less incised, and less abraded, implying a lower discharge. Reaches without significant jointing are shallower and broader, with thick deposits of coarse sand in the channel base [e.g. G: xc 7-4; Fig. 5.14f,g]; large clasts are rare. More friable tuff, largely in the upstream part of the survey [<750m from the survey start] is more deeply incised, and forms more rounded banks. The change between morphologies G and H reflects the proximity of a group of fumaroles near the confluence of tributaries 1-4, north of Telegraph Road [Fig. 5.1]. Steep banks in the lower reach reflect the hard fumarolic mounds, against which bars of cobbles up to 20-30cm diameter have developed. Non-tuff clasts are particularly common in this reach [section 5.1.4].

The more dramatic changes in morphology between panels A/B/C and D/E reflect the responses to faults at 700 and 1300m along the channel, respectively [Fig. 5.12b]. The size of the change in incision, and the length scale of this change, is related to the fault displacement; the large fault causing channel adjustment over several hundred metres [see also Fig. 5.13]. The small fault at 1950m [Fig. 5.14g; xcs 10/10a], causes only a short wavelength change in morphology, which is evident from a sharp local dip in aspect ratio [Fig. 5.12c].

Immediately downstream of the largest fault [xc 29], the channel is broad and shallow, with thick deposits of sand in its base. However, xcs 30 and 30a [B] show incision of over ten metres into the immediate footwall, in response to faulting. The knickpoint is currently 112m upstream of the fault, and the channel narrows sharply from the upstream sections [xc 32-31: A in Fig. 5.12], as seen in the central streams [Fig. 4.30]. Relatively friable tuff is exposed in the footwall, aiding the removal of huge volumes of rock downstream to form a canyon over fifty metres wide [Fig. 5.13].

Fault-induced incision between sections 22 and 21 has exposed a heavily jointed part of the tuff, and hence the morphological change is reversed: a broad, open stream drops over 2m into a narrow inner channel, confined by steep joints [Fig. 5.14a.→e], which has been cut into a previous broad open bend [Fig. 5.14b]. The knickpoint is considerably sharper than at the upstream fault, reflecting joint control on the upstream migration

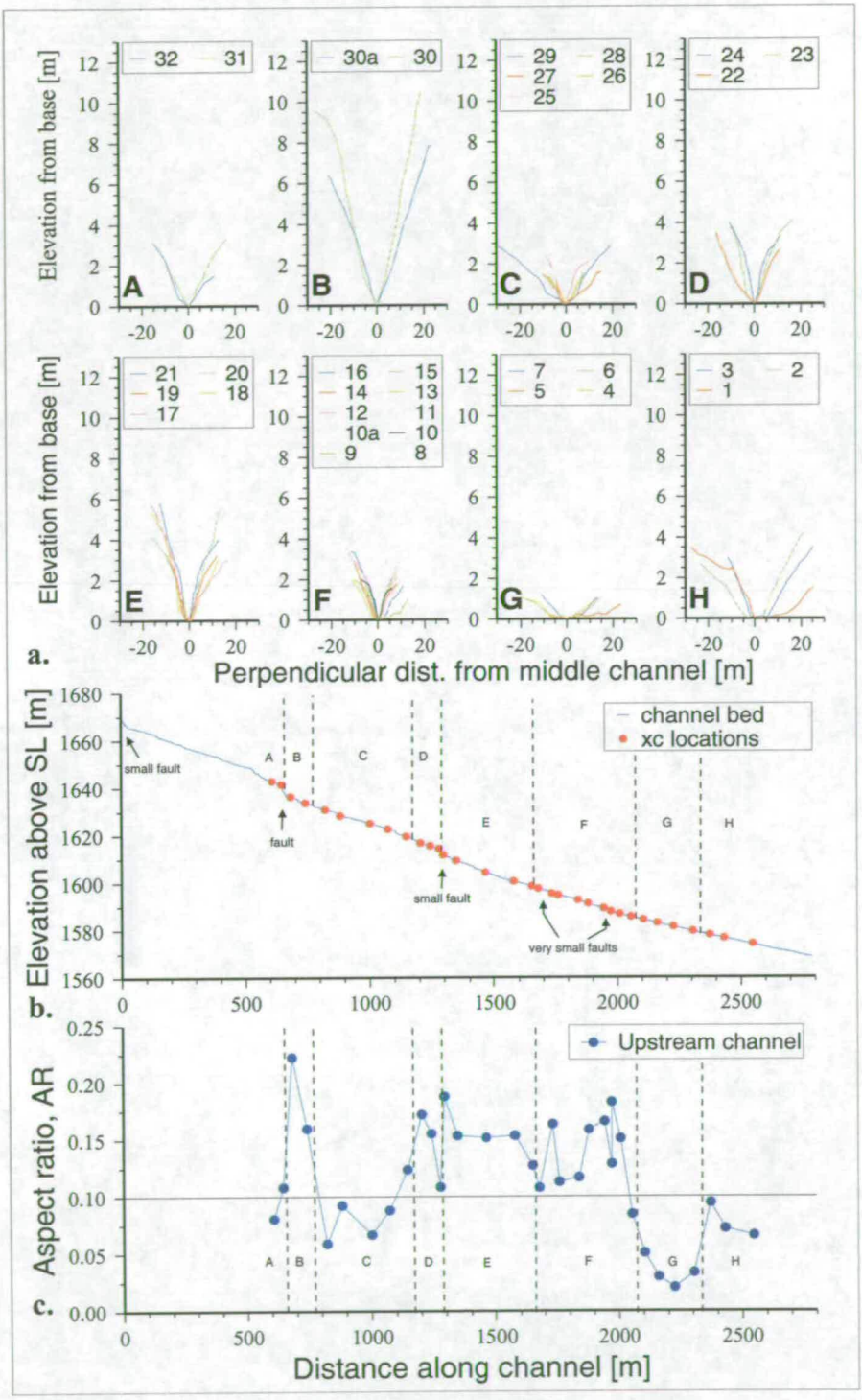

Figure 5.12: *Downstream variation in cross-sectional morphology of upstream northern channel.*
a. Cross-section profiles in the upstream channel, separated into eight morphologies, A-H. All profiles are plotted from NE to SW perpendicular to flow and at the same scale; VE = 9. Compare with the downstream incised gorge [Fig. 5.6].
b. Locations of the cross-sections, relative to the long profile of the channel.
c. Variation in aspect ratio of the channel [bank-base depth/bank-bank width] downstream.

of the step [e.g. Miller (1991)]. Abrasion is very marked on the lip of the knickpoint [Fig. 5.14d].

The aspect ratio plot, Fig. 5.12c, emphasises the hierarchy of the faults. Steepening of the channel upstream of the largest fault corresponds with the largest increase in aspect ratio. The highest AR values occur in the deeply-incised canyon in its footwall; hangingwall subsidence and deposition causes a drop in AR. Lithologically-influenced changes in the channel morphology are evident from the difference between the central part of the channel, eroding relatively hard tuff, [AR $\simeq$0.15], and the broader reach G, with very low aspect ratio [AR $\leq$ 0.1]. The local influence of fumaroles at the beginning of reach H is marked by a slight increase in the aspect ratio, although they have a much smaller impact than the faults.

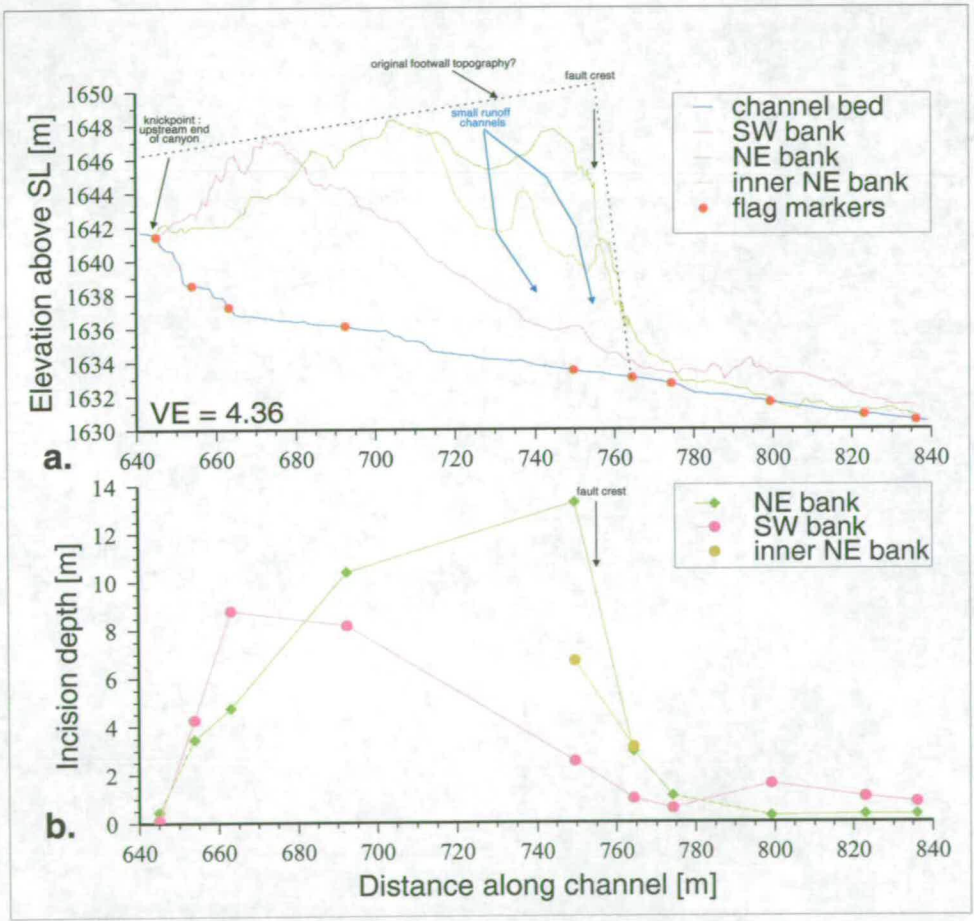

Figure 5.13: *Incision depth in the footwall of the largest fault in the upstream northern channel:a. Comparison of bank and channel floor profiles.*
b. Downstream variation in incision depth in the footwall.
Distances are measured downstream from the limit of the survey: compare with the main profile in Fig. 5.12b. The current knickpoint is 112m upstream of the fault scarp, and no step remains at the scarp, although there is a sudden drop in incision across the fault. Channel is braided and deposits fine sediment in the immediate hangingwall. Elevation differences between the 'NE' and 'inner NE' banks reflect two broad channels which have eroded the bank crest. The tuff in this region is relatively soft and friable, and probably aided the deep incision.

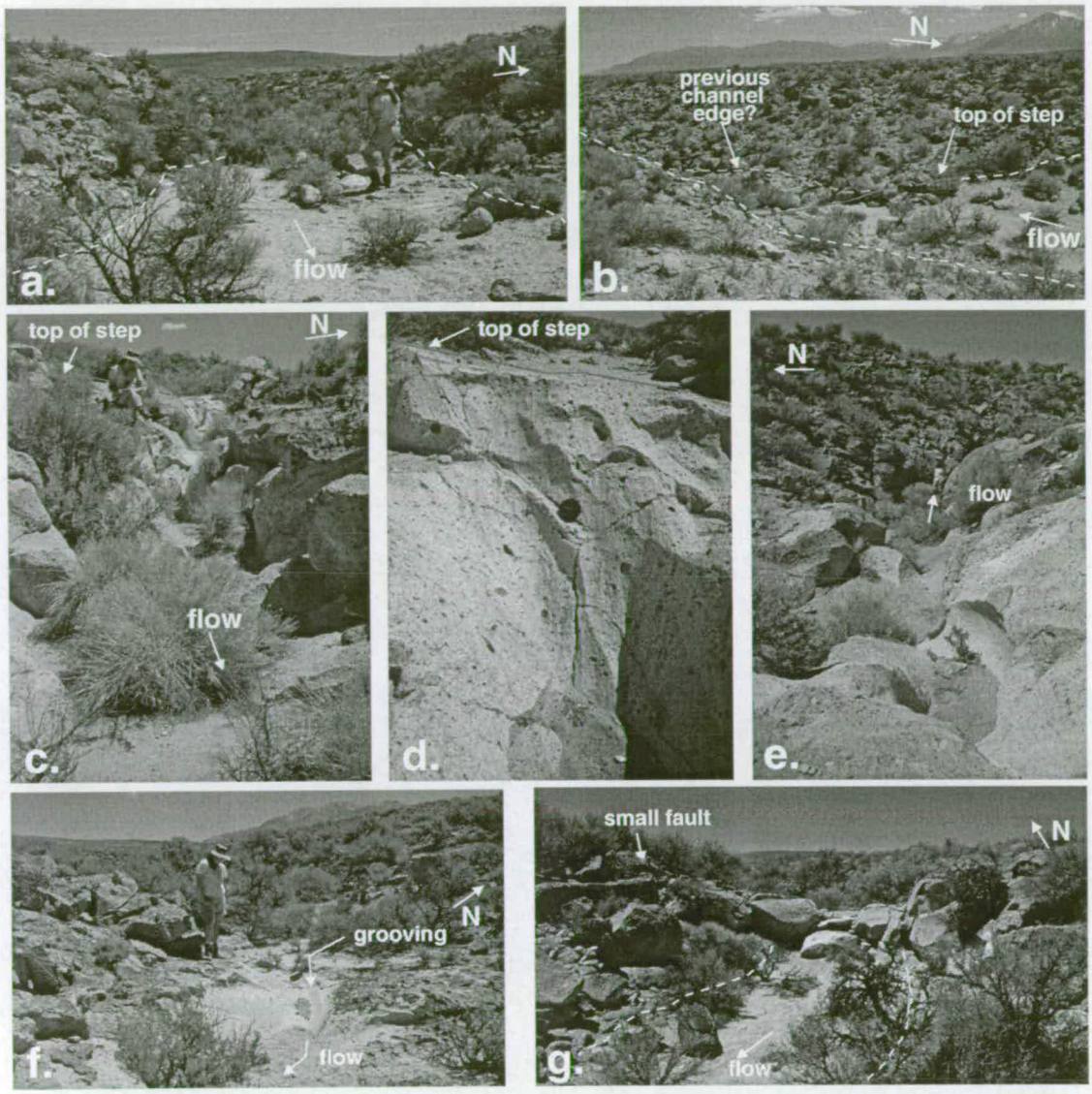

Figure 5.14: *Field photographs of varying morphology in main upstream northern channel.*
a. Photograph looking upstream from xc 22. Upstream of knickpoint: shallow open channel. Banks 2.5-3m high, sandy floor, though many large clasts [up to 70cm diameter] occur.
b. View downstream of top of knickpoint at xc 22. Wide terraces mark original broad channel. Downstream inner channel is incised over 2m into this original path, as joint planes have been exploited.
c. Knickpoint between xcs 21 and 22. Channel drops over 2m at this step.
d. Close-up of water-scoured tuff on the lip of the knickpoint. Lens cap is 5cm across.
e. Downstream channel [xc 21] eroded into hard tuff: potholed tuff in channel base, steep inner bedrock walls within original wider banks. Channel confined between steep walls: incision has exploited joint planes. 10m downstream, inner 'slot' is cut, with ~vertical walls.
f. Bend in channel, xc 15, morphology G. Longitudinal grooves cut into bedrock surface, visible over 1-2m.
g. Step at small fault crossing channel, xc 10/10a. Notebook is 20cm long: step approx. 120cm high. Top of step again very abraded.

Location	Reach	Length (m)	Gradient (°)	SL index (grad. m)
'Upstream'	1	641.06	-2.51	-14.06
	2	24.94	*-11.13*	*-123.70*
	3	610.53	-2.11	-13.27
	4	8.99	*-13.70*	*-310.01*
	5	1501.87	-1.66	-15.53
	Total	**2787.39**	**-2.08**	**-68.68**
'Incised'	1	749.92	-1.23	-63.70
	2	0.89	*-26.85*	*-1703.79*
	3	525.74	-1.24	-89.59
	4	131.94	*-3.18*	*-227.13*
	5	181.21	-1.28	-96.10
	Total	**1609.70**	**-1.41**	**-83.78**
'Wide'	***Total***	**793.02**	**-1.253**	**-44.17**
'Narrow'	1	11.87	*-11.58*	*-638.24*
	2	209.29	-2.60	-146.48
	3	9.90	*-11.375*	*-671.04*
	4	932.51	-1.23	-81.84
	Total	**1163.57**	**-1.67**	**-107.78**
'Shallow'	1	1076.32	-1.469	-123.46
	2	181.08	-0.309	-29.39
	Total	**1257.40**	**-1.30**	
'Eroad trib'	1	99.32	-9.47	-526.64
	2	54.67	-2.24	-136.23
	3	7.12	*-25.271*	*-1771.47*
	Total	**650.12**	**-3.63**	**-217.64**
'Etrib 2'	1	62.96	-1.878	-129.35
	2	296.028	-0.954	-68.71
	Total	**359.03**		

Table 5.1: *Variation in gradient and SL index of the northern channel.*
Averaged gradient of channel reaches from upstream reaches measured through the array. SL index is a proxy for stream-power [sections 2.3.2 and 7.1.3]. Distances measured from the furthest upstream extent of the surveyed main northern channel. SL increases gradually downstream in a graded river. Absolute SL values are not comparable between streams, but local anomalous SL highs indicate high stream power, caused by high gradients. In these streams, high stream power correlates with faulted reaches [italic].

5.1.3 Tributaries

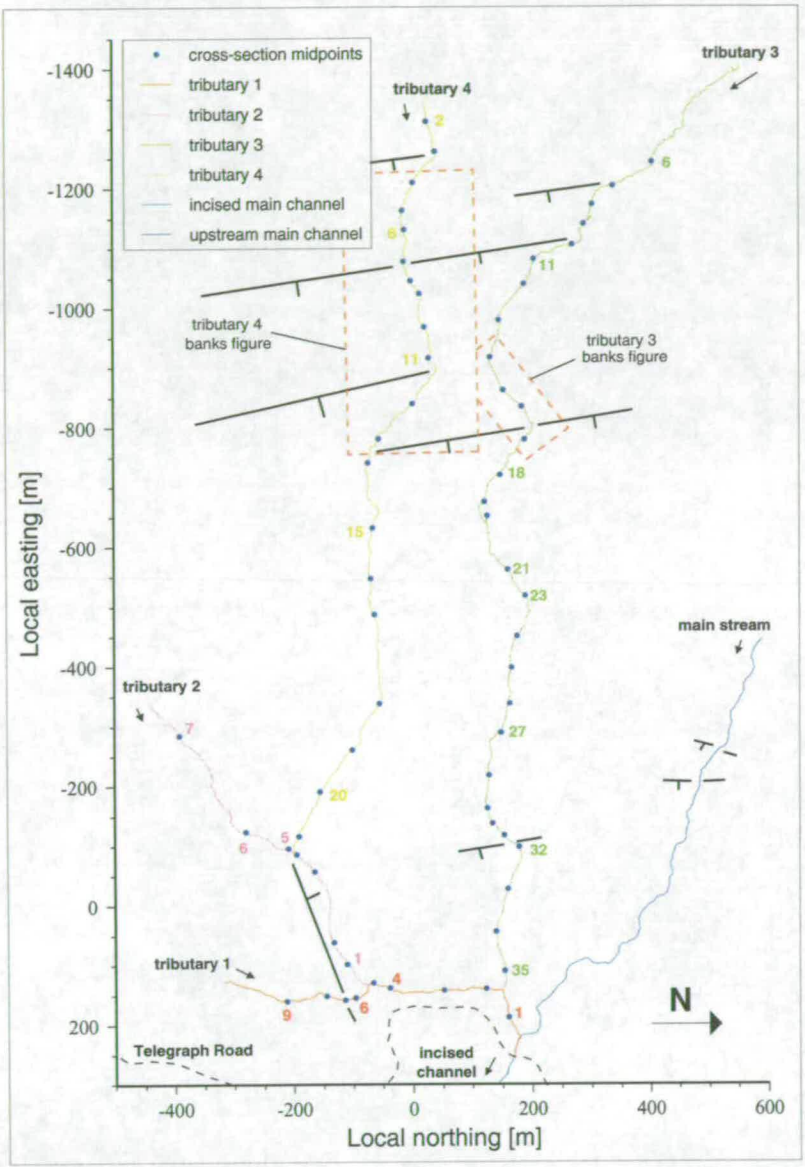

Figure 5.15: *Map of western tributaries in northern network, showing locations of the surveyed cross-sections. Cross-section numbers in each channel are marked in the aspect ratio and long profile plots: Figs. 5.16, 5.17, 5.18 and 5.20.*

The northern network receives a reasonable amount of discharge from four tributaries that join the main channel immediately west of Telegraph Road, upstream of the deep gorge [see Figs. 5.1 and 5.15]. No tributaries joining the main upstream channel from the north/north-east have been surveyed, although the aerial photograph suggests that water may have been delivered from the Benton Mountains, and diffuse sub-rounded clasts on the Tableland surface to the N/NE of the stream [see section 5.1.4] imply that there may have been some earlier sediment transport from this area. This section discusses the features of the western tributaries, surveyed upstream to their sources, over a few kilometres from the road. Tributaries 1 and 2 are small, and disappear

upstream into flat sandy areas only a few hundred metres from the main channel. Tributaries 3 and 4 are much larger, and have been traced for 1-3 kilometres upstream to wide flat areas covered in small rounded pebbles and cobbles [1-8cm diameter] where no channel could be discerned.

Where the tributaries join the main channel, they are diverted and often funnelled into narrow channels around fumarolic mounds ['blebs' on Fig. 5.1; sharp bends in Fig. 5.15]. The particularly high density of fumarolic mounds here may indicate a broad area of more welded tuff around from the mounds themselves, from early fluid flow along fissures connecting the cooling vents. Deflection of stream courses by fumaroles is seen elsewhere [e.g. N tip of Fault 2, section 4.2.2; and in the axial channel, section 5.2], and hence it may not be coincidence that the tributary discharge is distributed through a series of small shallow streams, rather than carried by one large channel.

Upstream of their confluence with the trunk stream, in this fumarole-littered area, the tributaries are incised only a few centimetres into the tuff, meandering gently over a very low gradient surface. The channels change dramatically in the vicinity of transverse faults upstream. Sharp bends in the channel courses [e.g. centre of tributary 4, Fig. 5.15], reflect deflection around fault tips. Deep incision is seen into other scarps [e.g. centre of tributary 3, upstream tributary 4, Figs. 5.19, 5.22]. In each case, the magnitude and the wavelength of the response appears roughly proportional to the displacement on the fault [section 7.1.2].

The tributary profiles [Figs. 5.16a, 5.17a, 5.18a and 5.20a], have a low gradient away from the fault scarps, although steepened near fumaroles downstream [Table 5.2]. Sharp knickpoints, and corresponding high bed gradients, occur at each transverse fault [Table 5.2]. The morphology of each step in the bed is different, depending on the discharge, and the displacement on the fault scarp at the point of incision [see also Chapter 7].

The variations in morphology are summarised by aspect ratio plots calculated from surveyed cross-sectional profiles, plotted alongside the long profile of each channel [Figs. 5.16, 5.17, 5.18 and 5.20]. The local influence of tectonic uplift on the channel development can be clearly seen in each tributary. Bank profiles of the fault-dominated reaches in tributaries 3 and 4 are shown in Figs. 5.19 and 5.22, respectively.

5.1.3.1 Tributary 1

Figure 5.16 shows the long profile of tributary 1, which flows subparallel to Telegraph Road for a few hundred metres before joining the main channel [Fig. 5.15]. Tributaries 2 and 3 flow into this channel, and cause a slight incision. A sharp change from a broad shallow channel [<0.5m deep] to a constricted canyon incised up to 2.5m occurs in response to a small fault, dipping north. In the hangingwall [xcs 7-4] the channel is wide and shallow, and small pebbles [1-5cm] line the channel bed. A series of small bedrock steps [each <1m] result in local steepening and narrowing [xcs 3-1], as the stream incises along the base of a fumarole. The channel floor is sandy, with blocky walls up to 2m high along the incised section. Tributary 3 brings a large influx of cobbly material [5-25cm] into the channel which then broadens again to its confluence with the main stream.

The aspect ratio reflects these morphology changes, with higher AR marking increased incision in the footwall of the small fault and along the base of the fumarole. Slight increases in aspect ratio occur where larger tributaries join, but the generally low aspect ratio [AR < 0.1] indicates a small, low gradient channel, and little active incision.

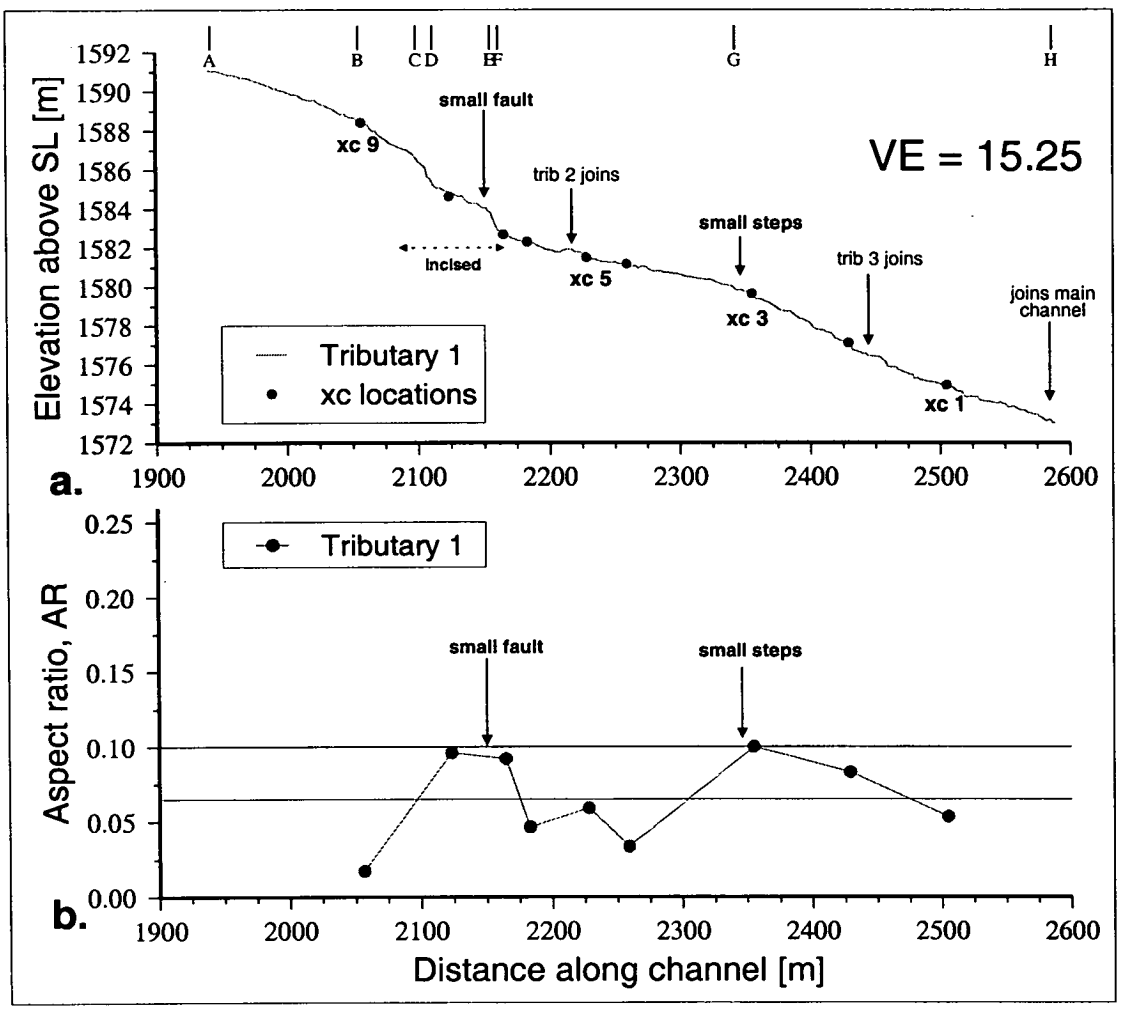

Figure 5.16: *a. Long profile of northern stream tributary 1.*
b. Downstream variation in aspect ratio of tributary 1.
Distances are calculated upstream relative to the main channel; the road crosses the main channel at 2588m. Letters along the top of the plot label reaches for which the gradient has been calculated - see Table 5.2.

5.1.3.2 Tributary 2

Much of the upstream channel is broad and sandy, often split into 40-80cm wide braids, around sand-, or later, small pebble-bars, and with minimal incision. The channel broadens considerably downstream of the influx of tributary 4 [~xc 4]. Steepening in the downstream reaches [B→D: Fig. 5.17a and Table 5.2] corresponds with narrowing of the channel, an increase in clast size [cobbles 5-40 cm] and incision of up to 2.5m at xc 3. This correlates with a sharp bend at the probable location of the tip of the small

fault through which tributary 1 is incised [Fig. 5.15a]. A large fumarole also lies on the western side of this bend. Thus the morphological change may be in response to uplift beyond the visible tip of this fault [e.g. Jackson and Leeder (1994); Gawthorpe et al. (1997); Corfield and Sharp (2000)], while the fumarole to the west prevents lateral migration and hence deflection around the fault tip.

Downstream of the bend, tributary 2 flows towards 064°, subparallel to the small fault, until it joins tributary 1. The channel broadens as it drops over a series of bedrock steps, each 15-50cm in height. Rounded cobbles up to 50cm in diameter lie on the steps, and are reworked into tributary 1.

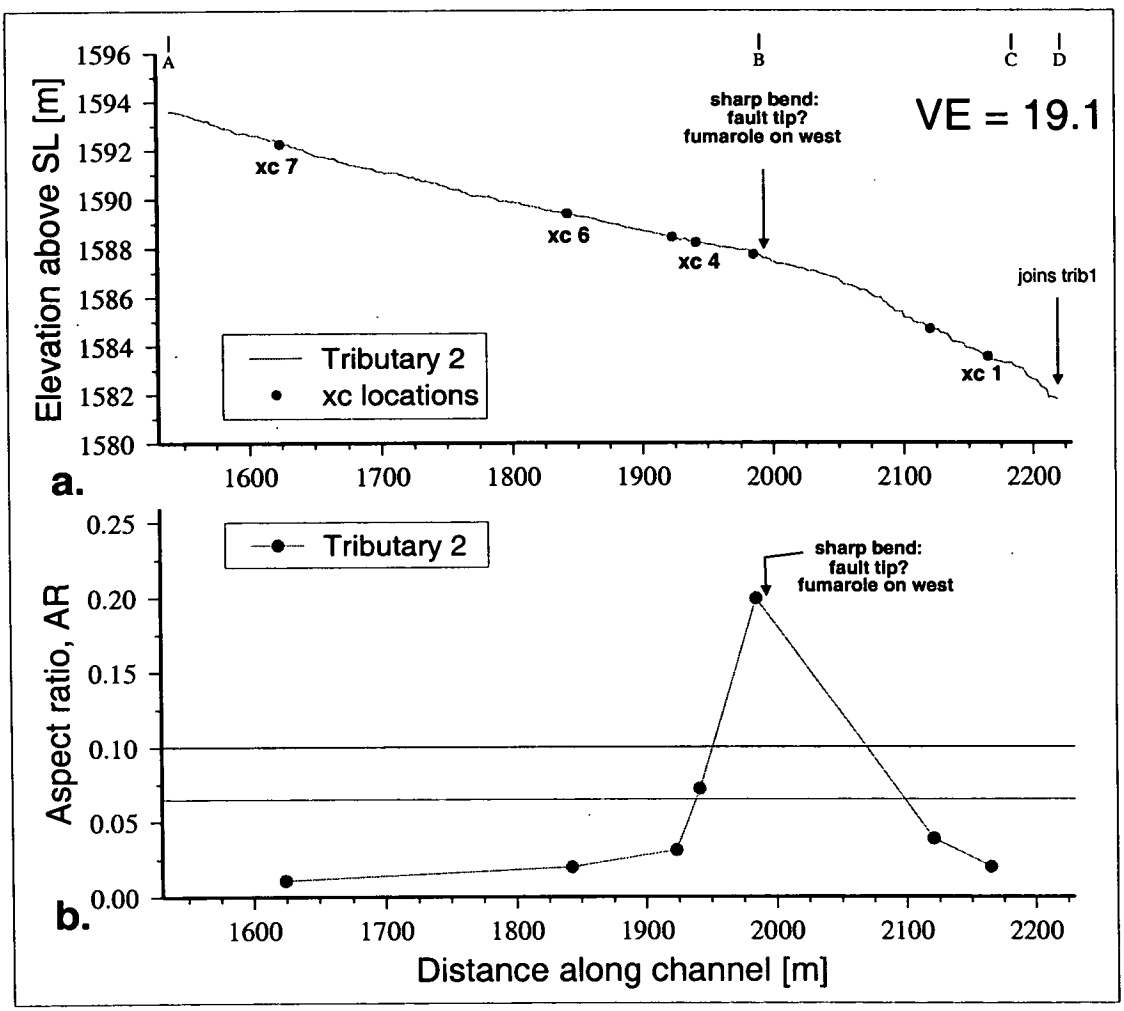

Figure 5.17: *a. Long profile of northern stream tributary 2.*
b. Downstream variation in aspect ratio of tributary 2.
The change in gradient and aspect ratio around xc 3 coincides with a sharp bend, in response to uplift beyond the visible tip of the small fault which tributary 1 incises through. A fumarole on the western bank of the same bend probably prevents deflection of the channel around the tip.
Distances are calculated upstream relative to the main channel; the road crosses the main channel at 2588m. Letters along the top of the plot label reaches for which the gradient has been calculated - see Table 5.2.

The aspect ratio plot [Fig. 5.17b] is dominated by the increase in incision towards the bend at the fault tip [xc 3]. Aspect ratios in the downstream reach decrease towards the values in the upstream shallow reach. As with tributary 1, the response to the tectonic uplift is visible over only 200-250m around the fault, reflecting the relatively small fault displacement.

5.1.3.3 Tributary 3

Tributary 3 follows a very low gradient course for several hundred metres [Fig. 5.18a] to large fault which extends for at least several hundred metres to the west at xc 7. Here, the alluviated braided channel incises into bedrock, with occasional piles of cobbles [≤20cm].

Over the next two hundred metres, the channel drops over a series of small faults, each with displacement of less than 2m. Each drop is associated with upstream bedrock incision footwall and deposition of cobbles or occasionally pebbles and sand downstream. The small faults lie between the tips of two larger faults; one small structure with very low displacement disappears away to the northwest, while the other, larger fault extends towards the south-southeast for several hundred metres.

Away from the channel, parts of the Tableland surface are covered with rounded clasts [≤20cm], well-tessellated in a sandy matrix, and reminiscent of the surface of the central ramp [Fig. 4.46]. This comparison suggests the possible existence of an earlier alluvial system, which has been subsequently incised by tributary 3, in response to the increasing strain between the two fault tips. The stream flows round the northern tip of the large fault, then along its hangingwall [xcs 10-11], gradually becoming shallower. At xc 11 the stream bends through 120° to flow away from the fault towards the east, with a corresponding sharp reduction in the bed gradient.

A drop of around a metre occurs at a further large fault [xc 17, Fig. 5.18] and a 200m long steep canyon is incised up to 4.6m into the footwall. Large angular boulders, up to 1.5m across, have been carried from the canyon to the lip of the knickpoint at the scarp, against which sand and pebbles have built up. A number of small steps occur in the canyon floor, but there is no steep knickpoint upstream [Fig. 5.19], in contrast with the upstream migration of over 100m of the knickpoint in the trunk stream, and where no drop remains at the fault [Fig. 5.13]. However, the overall elevation drop in the canyon is 17m, showing that a considerable proportion of the uplift has been accommodated by steepening and incision.

The channel is braided for 150m in the immediate hangingwall of the fault, where the sudden drop in gradient causes deposition of sand and small pebbles. This is similar to the braiding seen in the hangingwall of faults in the central overlap [Fig. 4.21]. An increase in gradient at xc 29 reflects bedrock incision of ≤6m, and the development of a canyon in response to a small transverse fault at xc 32. Downstream, the channel is broad [5m wide base] and sandy, though dotted with tuff clasts up to 70cm across.

The aspect ratio plot [Fig. 5.18b] again highlights the faults, with footwall AR increasing towards the scarp, and a sharp drop in the hangingwall. No pronounced incision [AR<0.065] is seen upstream of the canyon formed in response to the fault near xc 17. The increase in aspect ratio at this fault, and the absolute values, are higher than elsewhere along the channel, reflecting the displacement on this fault relative to

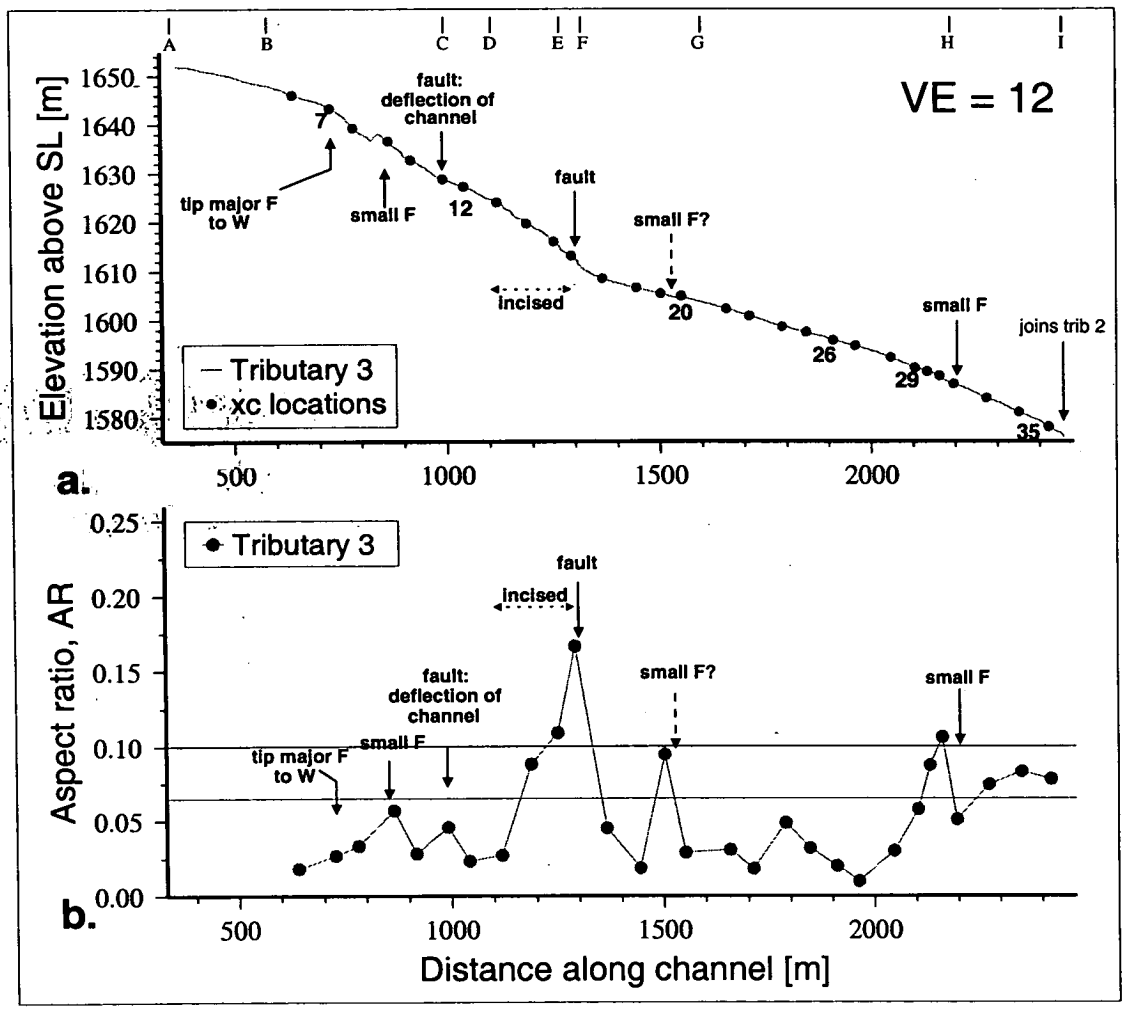

Figure 5.18: *a. Long profile of northern stream tributary 3.*
b. Downstream variation in aspect ratio of tributary 3.
The channel also responds to two small faults whose scarps it does not cross: at xc 7, a large scarp extends for several hundred metres to the west; downstream, the channel flows parallel to another major fault, then bends through 120° to flow away to the NE [see Fig. 5.15].
Distances are calculated upstream relative to the main channel; the road crosses the main channel at 2588m. Letters along the top of the plot label reaches for which the gradient has been calculated - see Table 5.2.

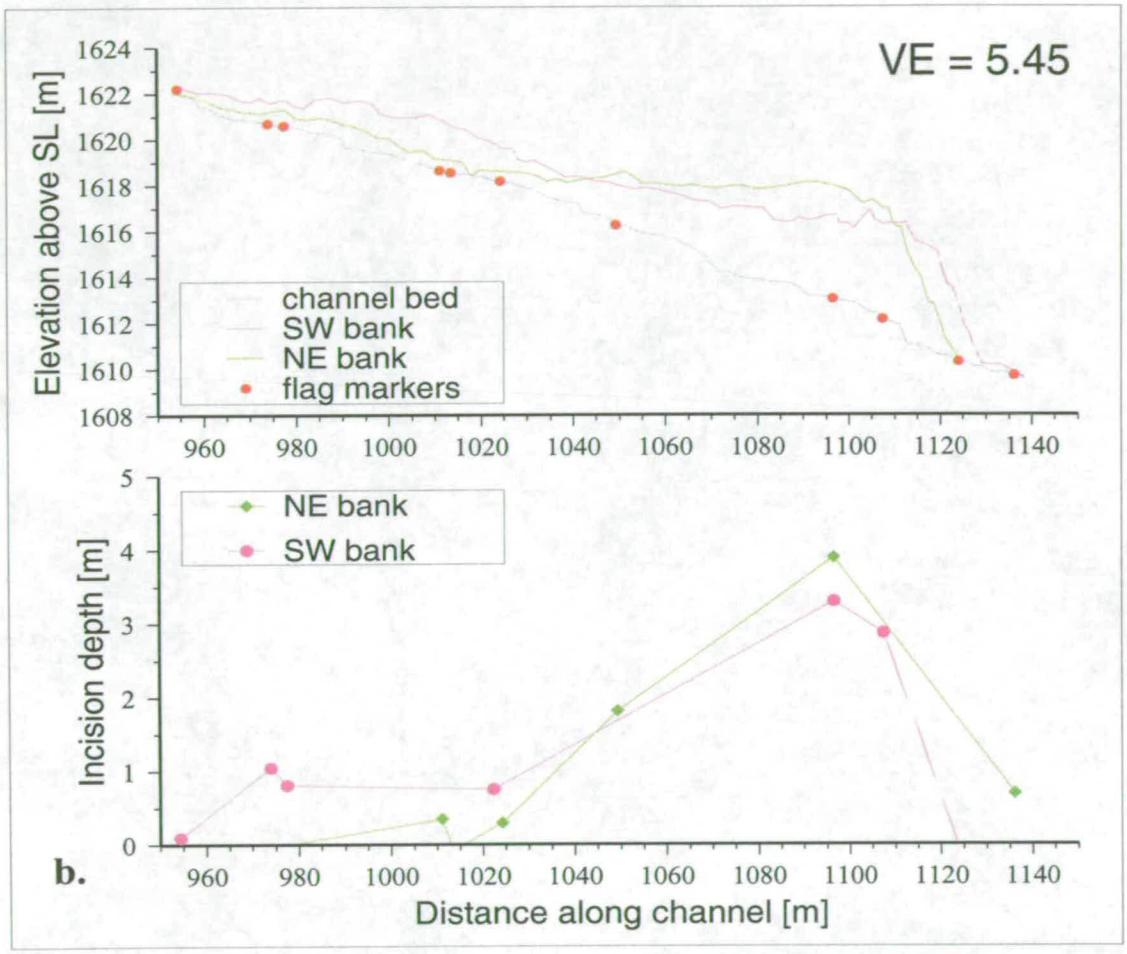

Figure 5.19: *a. Comparison of bank and channel bed profiles in incised canyon in northern stream tributary 3.*
b. Downstream variation in incision in faulted reach of tributary 3: calculated from the bank and floor profiles at a series of control points [marked].
The channel has developed a fairly constant steep gradient through the incised canyon, although there are still a series of steps at, and upstream of, the fault scarp. Most of the uplift is accommodated by steepening of the profile and incision.

smaller faults downstream [xcs 20 and 31-2]. Low gradient reaches with small bedload grainsize have correspondingly low aspect ratios.

5.1.3.4 Tributary 4

Tributary 4 is initially shallow and indistinct, but becomes more pronounced as it flows down a shallow incline, where cobbles [≤20cm] line its bed. After a hundred metres, the channel bends sharply towards the northeast near the northern tip of a fault [Fig. 5.15]. Downstream of this bend, the channel is less distinct, until it steepens in response to a large fault at xc 7 [Figs. 5.21 and 5.22].

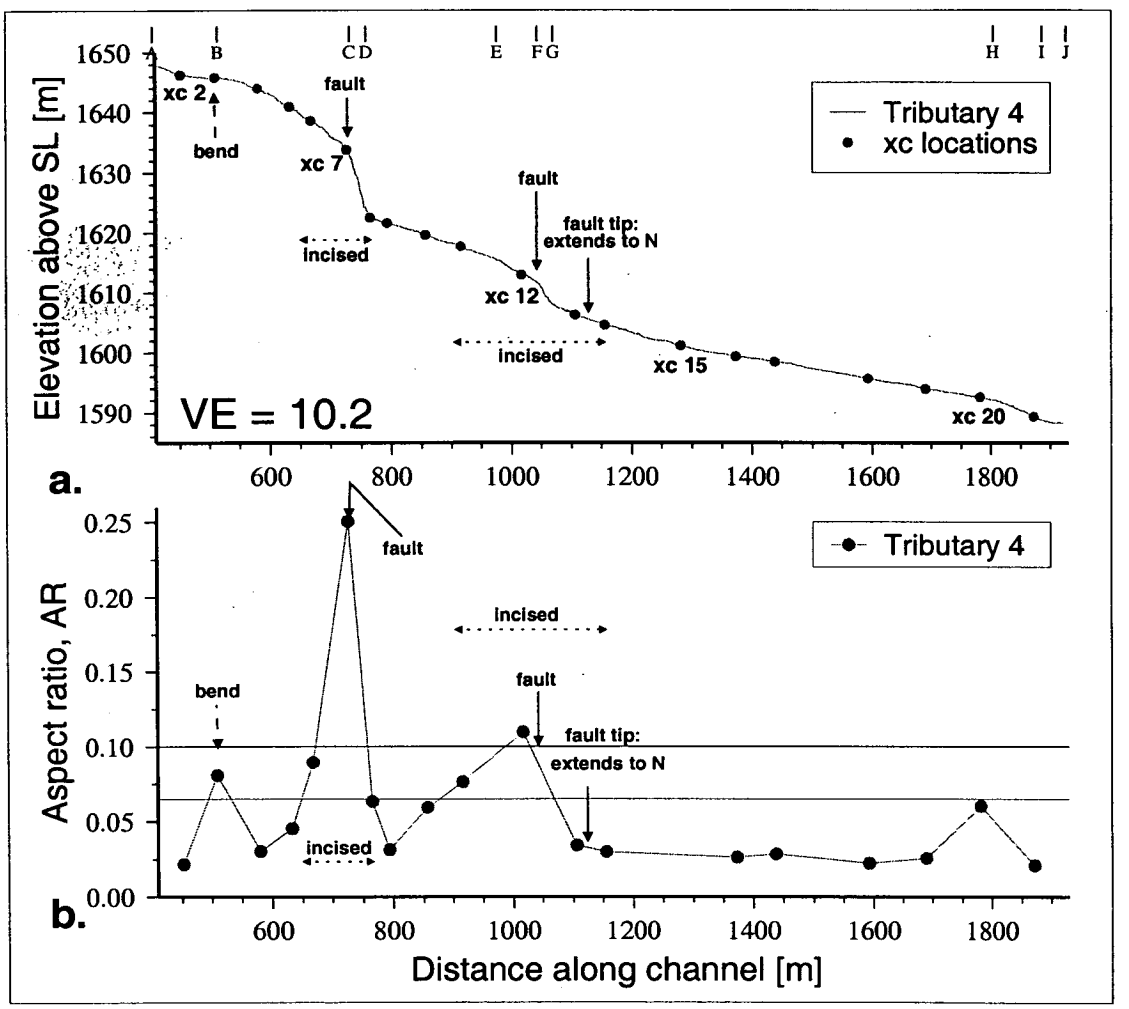

Figure 5.20: *a. Long profile of northern stream tributary 4.*
b. Downstream variation in aspect ratio of tributary 4.
The channel incises through one large scarp at xc7, and winds around the tip of several others, most notably incising through an overstep between 2 very close faults [xcs 12-10]. Another bend upstream marks the probable location of a fault tip propagating from the SE [see Fig. 5.15]. Distances are calculated upstream relative to the main channel; the road crosses the main channel at 2588m. Letters along the top of the plot label reaches for which the gradient has been calculated - see Table 5.2.

Upstream of the fault, the channel narrows, carving out a 3m wide canyon that reaches over 6m depth [Fig. 5.22c]. A few small faults cut the canyon, and the walls are very degraded, with angular blocks up to 3m in diameter in the canyon, or reworked a short way downstream. A deep notch is carved into the fault crest [Fig. 5.21], and large boulders line the waterfall down the scarp. A wide plungepool is scoured out at the base of the 11m elevation drop [xc 8].

The stream braids downstream of the incised scarp, depositing sand and small cobbles [≤20cm] in the low gradient reach to xc 10. However, it remains incised up to 60cm, and has sand terraces on either side, up to 2m high [Fig. 5.21]. The channel winds between the tips of two faults which overlap around xcs 12-13 [Fig. 5.22a]. The stream incises a v-shaped bed up to 2.8m into the footwall of the first fault, which extends towards the southwest, and then remains incised to a depth of over 1.5m as it winds around the tip of the second fault, which extends to the northeast [Fig. 5.22a], where it is incised by tributary 3 [see Fig. 5.15]. Overall, the channel drops 7m in this region, in a series of 1-1.5m bedrock steps. Throughout this reach, bedrock is exposed in the channel bed, with angular blocks reworked downstream.

The channel subsequently becomes shallower as it flows southeast [Fig. 5.22b,c], but drops a further 9m over 120m down the ramp towards the area of maximum subsidence in the centre of the southern fault. A small amount of this incision may be caused by a series of fumaroles aligned along the southeast of the faulted area. Rounded cobbles [≤80cm] lie at the base of the flight of steps, but these fine downstream to sand.

The stream bends east away from the fault and maintains a fairly uniform low gradient, locally braided, depositing sand or rounded clasts up to 40cm across. A slight increase in gradient at xc 20 may reflect the local influence of the fumarole at its confluence with tributary 2. However, it may also be rejuvenation of the stream following incision in tributary 2 [Fig. 5.17] controlled by the uplift on the fault which tips out at this pronounced bend.

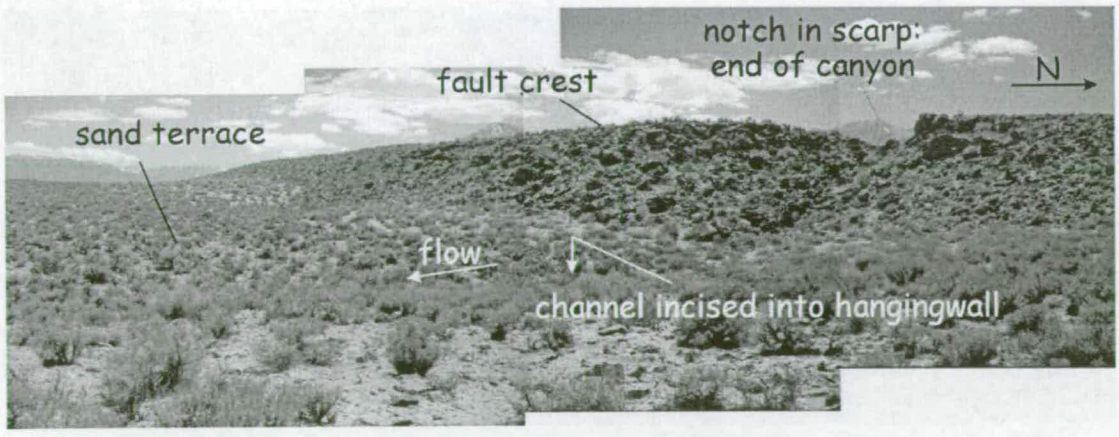

Figure 5.21: *View of tributary 4 incising through fault scarp.*

The aspect ratio plot [Fig. 5.20] is dominated by sharp peaks at the two largest faults, with the downstream increase in values above these peaks marking the incised footwall canyons. The largest change in aspect ratio occurs at the deepest incision; a similar pattern, but considerably lower AR marks the fault overlap at xcs 10-13. The low

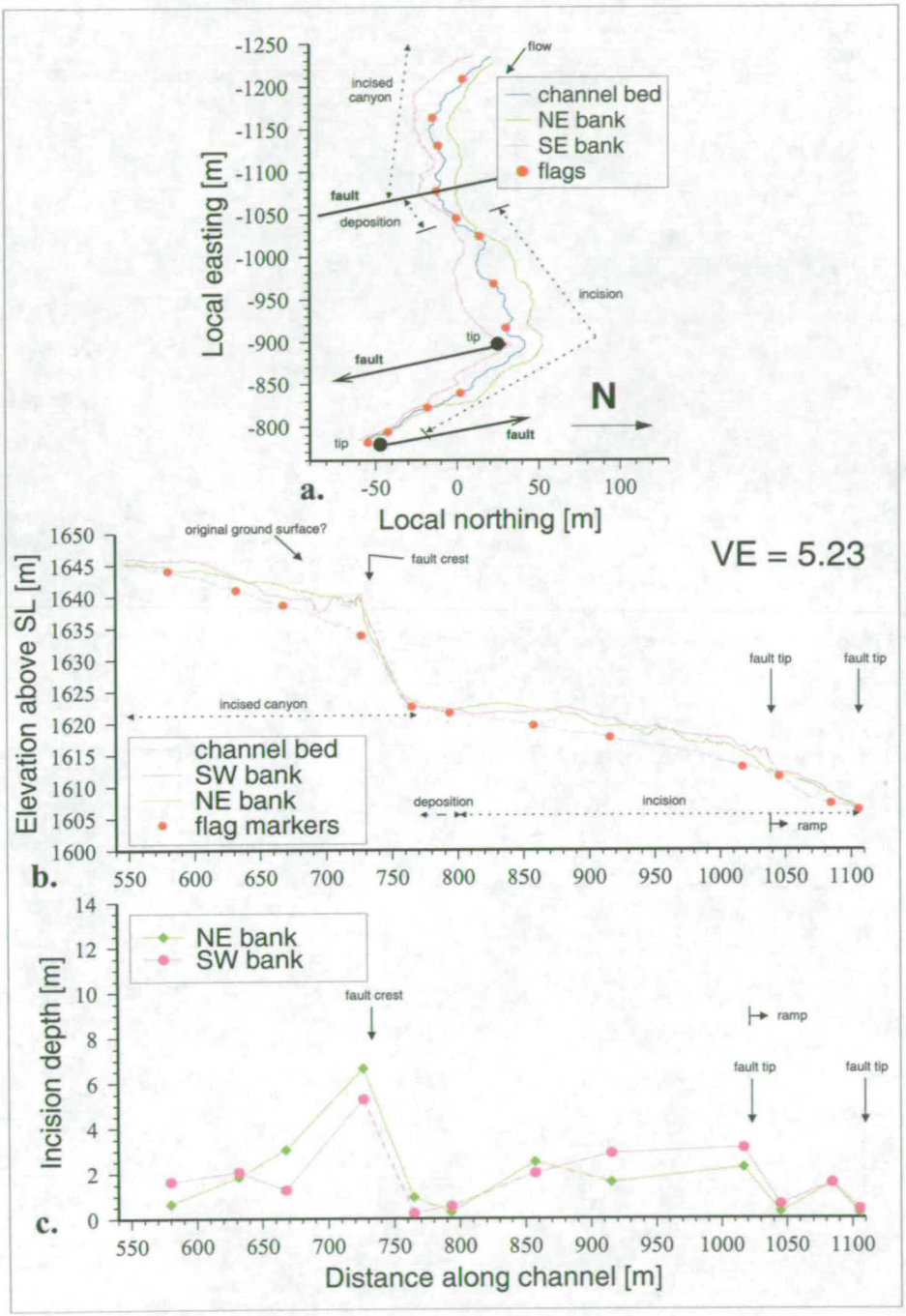

Figure 5.22: *a. Map of channel, bank crests and fault scarps in the faulted reaches of northern tip tributary 4.*
b. Comparison of bank and channel bed profiles in faulted reaches.
c. Downstream variation in incision in faulted reaches of northern tip tributary 4: calculated from the bank and floor profiles at various control points [flagged].
The channel incises a canyon through the footwall of the upstream fault, which has over 20m local displacement. Deposition occurs in the hangingwall, but the channel incises again downstream as it winds between the tips of two overlapping faults. Incision then decreases as the channel flows down the relay ramp towards the centre of the southern fault.

gradient, sandy braided reaches have very low aspect ratios [AR<0.065]. Smaller peaks in the aspect ratio occur at the upstream bend [xc 3], possibly marking a fault tip, and the steepened reach upstream of the confluence with tributary 2, which may be the effect of the fault on this lower stream [Figs. 5.15 and 5.17].

5.1.3.5 Summary of upstream northern drainages

The upstream reaches of the northern drainage system lie in a large channel, flowing towards the southeast [117°]. Although only the lower 2.6km of this stream have been surveyed, it shows evidence of powerful flow, with many large clasts, in some cases dense igneous material, littering the stream. Channel morphologies and bedforms are consistently larger than the upstream reaches of the main channel through the central overlap [Fig. 4.26]. Four smaller tributaries, 700-2500m long, feed this system from the west-southwest. The tributaries join the main stream in small channels between large fumarole mounds, immediately west of Telegraph Road. The bedforms and cross-sectional shapes of these streams are considerably smaller than those of the main stream.

While the downstream incised part of the northern system flows through a series of closely-spaced faults at the northern tip of the main fault array [section 5.1.1.1], the development of the channels upstream of the main array has been influenced predominantly by large but generally well-separated faults [Fig. 5.11a].

In each channel, changes in channel course and morphology can be linked to the local tectonic framework. As with the central overlap streams [section 4.2], uplift on transverse faults crossed by the channels results in steepening of upstream reaches and bedrock incision into the uplifting footwall. Subsidence in the immediate hangingwall of the fault causes braiding and deposition, although plungepools are usually scoured at the base of the scarps. Aspect ratios in the upstream channel increase towards the fault scarp, then drop rapidly in the immediate hangingwall, with unfaulted reaches away from the zone of faulting having similar very low values. Where channels have been deflected around fault tips, they tend to flow parallel to the fault towards the area of greatest subsidence at the centre of the fault [e.g. Figs. 5.17 and 5.20]. In some cases, major incision in one channel is caused by a fault which simply deflects, or causes shallow incision of, another channel along-strike. Hence channel evolution is influenced dramatically by the displacement variation along the faults [e.g. tributaries 1 and 2, see Fig. 5.11a].

In each case, the magnitude and wavelength of the channel response is roughly proportional to the uplift on the fault, with deep incision over several hundred metres for the largest displacements, but smaller, shorter-wavelength responses to lower displacements, as around fault tips [e.g. Figs. 5.17 and 5.20]. Large uplifts result in high-amplitude aspect ratio variations, and high absolute ARs. However, the channels are incredibly sensitive to variations in topography, and even channels with relatively low discharge [e.g. upstream tributary 1, Fig. 5.16] have incised several metres in response to motion on relatively small faults. Lithological features, such as fumaroles and joints, rarely influence channel development over similar wavelengths, nor produce such large local morphological variations. However, deep incision by the trunk stream into the footwall of the westernmost fault was probably aided by friable tuff. Incision has exploited joint planes where exposed, resulting in a narrow steep-walled inner channel incised into a previously broad stream [Fig. 5.14a→e]

The main upstream channel has adjusted more fully to tectonic activity than the tributaries, attaining a low bed gradient in the canyon even through the largest surveyed scarp, by deep incision, and over 100m upstream migration of the knickpoint

[Fig. 5.13a]. In contrast, canyons incised by the tributaries into footwalls have universally steep bed gradients [Figs. 5.16a, 5.19 and 5.22].

Tributary	Reach	Length (m)	Gradient (°)
Ntip1	AB	117.02	-1.28
	BC	45.37	-2.69
	CD	*9.35*	*-6.68*
	DE	41.71	-1.77
	EF	*7.50*	*-7.58*
	FG	185.80	-0.95
	GH	242.39	-1.61
	Total	**649.15**	**-1.59**
Ntip2	AB	511.40	-0.78
	BC	132.47	-1.47
	CD	35.27	-2.46
	Total	**679.14**	**-1.00**
Ntip3	AB	254.39	-1.18
	BC	345.94	-2.77
	CD	159.47	-2.24
	DE	124.87	-3.57
	EF	*77.22*	*-4.51*
	FG	219.42	-1.43
	GH	609.27	-1.48
	HI	300.74	-2.43
	Total	**2091.31**	**-2.08**
Ntip4	AB	127.97	-1.03
	BC	176.76	-3.57
	CD	*42.67*	*-15.15*
	DE	247.83	-2.16
	EF	39.64	-3.73
	FG	*16.96*	*-9.02*
	GH	743.97	-1.25
	HI	76.17	-2.36
	IJ	35.24	-0.88
	Total	**1507.20**	**-2.26**

Table 5.2: *Variation in downstream bed gradient of the tributaries of the northern tip channel. Averaged gradient of channel reaches from upstream towards the main stream. Reaches are labelled as in the long profile plots, Figs. 5.16, 5.17, 5.18 and 5.20. Italics indicate faulted reaches.*

5.1.4 Non-tuff clasts

The northern channel system is unique amongst the surveyed channels in that non-tuff clasts, reaching up to a metre in diameter, are found in parts of the channel bed [Fig. 5.23]. All the other channels draining through the array contain only Bishop Tuff clasts, indicating a catchment solely on the Tableland surface itself. The observation of non-tuff clasts in this stream implies a source outside the Tableland, thus requiring a significantly larger catchment. The only other observation of non-tuff material on the Volcanic Tableland is in a large channel to the south of the array, close to the western edge of the Tableland [N. Dawers, pers. comm. and section 7.4].

Over 10 different lithologies are seen in the northern stream. The clasts are predominantly igneous in nature, and span the entire range from acidic to basic and from fine- to relatively coarse-grained [Fig. 5.23], though some low-grade metamorphic clasts also occur. Clast sizes vary from a few millimetres to almost a metre in diameter, although they average around 15-25cm. All the observed clasts are sub- to well-rounded, and generally tend towards sub-spherical, rather than oblate shapes. Many of the clasts also show a high degree of weathering, with green chlorite weathering on granite clasts, and red to purple colouration developed on the more basic and metamorphic rocks. Some of the clasts have red-orange rinds on their outer rims [Fig. 5.23c,d], again suggesting a long period of sub-aerial exposure. Similar weathering rinds have been described on clasts on the Owens River terraces south of the Tableland, and used to help correlate the terraces with Sierran moraines from the late Pleistocene glacials (Pinter et al., 1994; section 3.1.2).

No specific sorting of any of the deposits is seen in terms of lithology, several lithologies, as well as the Tuff, occurring in each location, implying sampling of a heterolithic source, rather than a single rock unit. The high degree of weathering is inconsistent with the appearance of the tuffaceous deposits in this and other channels on the Tableland, which are generally very well-preserved, and show very little degradation [e.g. Figs. 4.46, 4.29a,b and 5.8]. The nature of the vast majority of the deposits on the Tableland, and the low volumes of hangingwall sedimentation, are testament to a low rate of erosion on the Tableland surface [see also section 7.2.2.5], which may suggest that these clasts weathered elsewhere before being carried onto the Volcanic Tableland.

The Tableland consists of a 150m thick layer of Bishop Tuff, and hence these non-tuff clasts must have been transported some distance before deposition here. Granite and other acidic rocks are exposed in the Benton Mountains approx. 7km to the northeast. The closest basaltic deposits are exposed in the wall of the Owens River gorge, approx. 5km west, following incision of the river into the earlier deposits, but underlie the Bishop Tuff, and hence are unlikely to have been sampled by a channel on the surface. The other obvious potential source of diverse igneous clasts is the Sierra Nevada range to the west [Fig. 5.1]. The large stream to the south which contains non-tuff clasts is very close to the western edge of the Tableland, and hence to the outer edges of the alluvial fan systems which drain off the Round Valley faults to the west [see Chapter 3]. Thus these large transport systems may have provided an initial source of material which has been reworked across the Tableland. However, this has important implications for the relative timing of the incision of the Owens River (Putnam, 1960; Bailey et al., 1976), whose deep gorge now separates the main part of the Tableland from the Sierra Nevada faults to the west [Chapter 7]. Considerably longer transport

would be required for the Sierras to have provided a source of material for streams through this northern part of the array.

Non-tuff clasts in the northern drainage system are found principally in the canyon incised through the northern tip of the main fault array [section 5.1.1.1], and in the main channel upstream of the road. Particularly high concentrations of the clasts are seen at the upstream [western] end of the incised canyon [Fig. 5.23c], where they account for over 40% of the total clasts. The concentration of these clasts decreases down the gorge, accounting for only around 10% of the clasts deposited at the eastern mouth of the canyon. Although some acidic and rare mafic clasts have collected on bends downstream of this incised reach, they are generally very small [<6cm in diameter; locally-derived tuff clasts reach 1m across], and rapidly dwindle to zero concentration downstream of the 'wide' reach [section 5.1.1.2].

The clasts are not seen in any of the western tributaries of the upstream northern channel, which is consistent with the fact that these channels have relatively small catchments [channels fully surveyed: section 5.1.3], draining only Bishop Tuff on the surface of the Tableland. Upstream of the Telegraph Road, non-tuff clasts are seen in the main channel, particularly in its lower reaches, up to 1.5km northwest of the road. The concentration of these clasts oscillates up the channel bed, with some locations showing high numbers of non-tuff clasts, while deposits in other parts of the channel bed consist virtually solely of Bishop Tuff. The concentration of non-tuff clasts appears to correlate broadly with small tributary channels from the north-northeast, which in many cases can only be traced for a few metres from their junction with the main stream. However, this relationship has not been fully investigated. Non-tuff clasts are also found distributed on the surface of the Tableland east of Telegraph Road for several hundred metres NNE of the main channel. Initial observations suggest that these diffuse deposits have no consistent orientation, and do not correlate with the main northern channel.

The size of the clasts, particularly given their high density, indicates transport by a high velocity, high discharge system. Their roundness, again given their hardness, is testament to long carriage in a mature transport system. That these clasts have been carried any distance in the northern channel is testament to at least some periods of strong, high discharge, consistent with the deep incision and the high levels of adjustment to local fault activity [e.g. Figs. 5.4 and 5.13]. However, the surveyed northern stream may not be wholly responsible for the long transport and abrasion required to round off these non-tuff clasts, and the high degree of weathering also is in stark contrast with the more typical fresh state of the tuff clasts in the Tableland streams. The appearance of large numbers of clasts to the north of the upstream channel may indicate a prior depositional system [see Chapter 7], while at least some of the clasts in the drainage may have been washed in from the nearby surface of the Tableland.

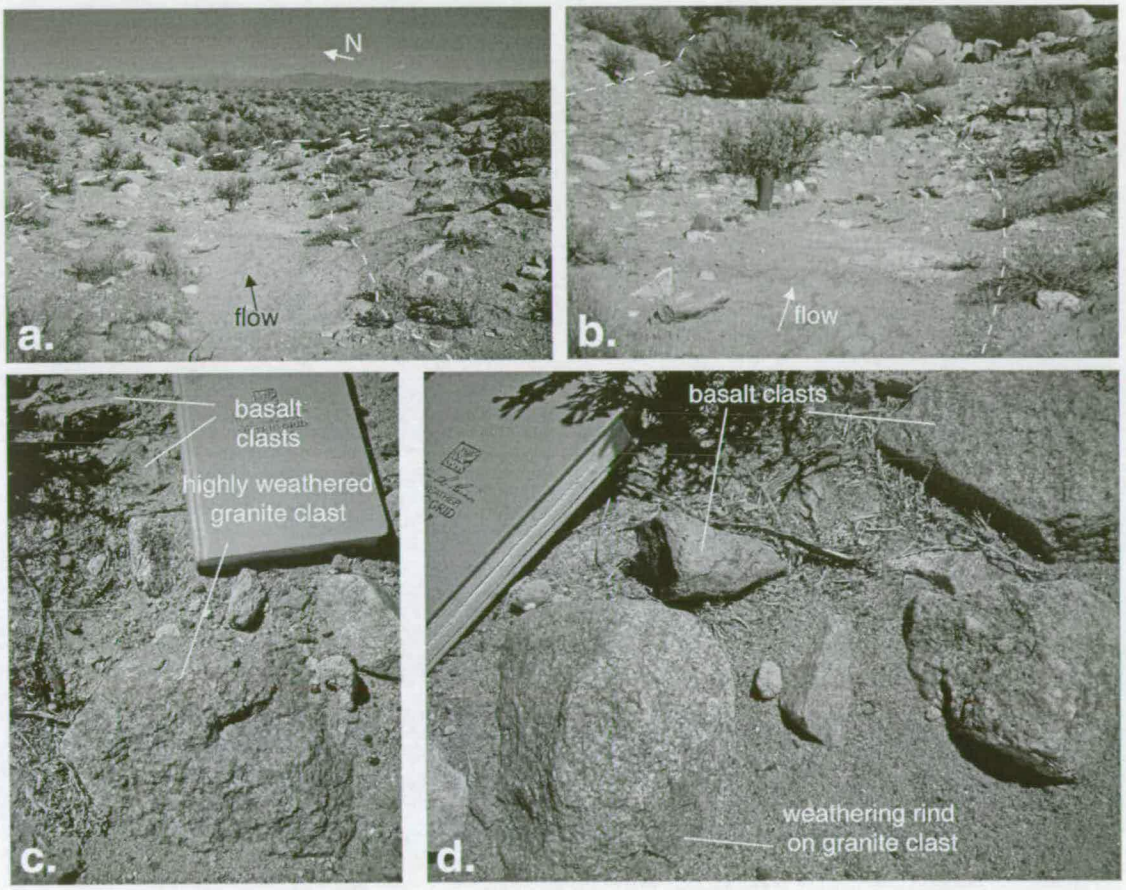

Figure 5.23: *Non-tuff clasts in the northern stream network.*
a. View looking downstream at non-tuff clasts in the centre of the canyon incised into the northern tip of the fault array. Non-tuff clasts in the foreground are marked with red spots: note the contrast with the pink tuff. Many clasts are seen near the water bottle downstream [b].
b. Close up of non-tuff clasts: basalt and granite clasts around the central part of the incised canyon. This photograph is from the centre of [a].
Water bottle in red holder is around 50cm high.
c. and d. Close ups of weathered clasts. Note the highly weathered granites, including a well-developed rind. Basalt clasts are generally smoother, with some almost planar surfaces. [Photos [c], [d] courtesy of Tim Sheehan, Tulane Univ.]
See also basalt clasts on the top of the small fault step in Fig. 5.14g.
All clasts are sub- to well-rounded and have a significantly higher density than the Bishop Tuff. Non-tuff clasts are specific to this drainage system and imply an original source in a catchment away from the main Tableland surface.

5.1.5 Summary of northern drainage system data

The northern stream system is considerably larger, and drains a larger catchment, than the streams draining the central overlap [section 4.2.1: see Fig. 4.1]. The trunk stream was not surveyed to its source upstream, but the surveyed channel is consistently larger than the main central overlap channel throughout. Four small tributaries which drain a faulted area to the southwest of the upstream channel were surveyed to their sources [section 5.1.3], and several small tributaries were also noted which join the main channel from the north-northeast. The channel flows perpendicular to faults through the northern tip of the main fault array, in a deep canyon, and then changes morphology dramatically as it bends to flow first parallel to the array, and then perpendicular to faults again further downstream. Finally, the northern stream opens into a shallow broad channel which flows subparallel to the main graben [towards 135°], now the route of Casa Diablo Road [Fig. 4.1].

Development of the northern channel network is closely linked to the evolution of the local fault pattern. Where streams cross transverse faults, they respond either by incision [e.g. Figs. 5.13, 5.19 and 5.21] or by deflection [e.g. Figs. 5.2, 5.15 and 5.22]. Fault-controlled changes in stream course can be small deflections [e.g. Tributary 3], or can be dramatic, as in the downstream part of the system, where the main channel bends first parallel, and then perpendicular, to the main array, depending on the pattern of confinement by local faults [Fig. 5.2]. The amplitude and the wavelength of the response appears roughly proportional to the fault displacement, with dramatically different responses by channels which cross near the centre, or the tips, of a given fault [see Chapter 7].

Some of the changes in stream course and incision are also due to variations in lithology. Hard fumarolic mounds and ridges help small faults force sharp changes in flow direction in the downstream channel [section 5.1.1.2], as it flows around raised fumarole-rich areas to the east of the main fault array [Figs. 5.1 and 5.2]. The presence of scattered fumaroles west of the main array may be responsible for the tributary discharge being distributed in a series of channels, rather than a single stream. Softer parts of the tuff, which have a more 'lumpy' texture, are easier to erode, and give rise to deep, wide canyons [e.g. Fig. 5.13]. Channel morphology is dramatically different between reaches that are pervasively jointed, and unjointed reaches [see Fig. 5.12]. Exposure of joint planes can result in narrow inner channels, incised into broader shallower original courses developed in less jointed rock layers [Fig. 5.14a→e].

Where the stream flows through the main array [incised reach, section 5.1.1.1] it provides a stark contrast with the main stream through the central fault overlap [section 4.2.1]. Although it flows in broadly the same overall direction, possibly reflecting the original tilt of the Tableland palaeo-surface [e.g. towards 121-125°; Pinter and Keller (1995)], this northern stream has a much straighter course through the array than the sinuous central overlap stream [compare Figs. 5.1 and 4.20]. Over 10m of incision has occurred through some of the fault scarps, and comparatively little sharp lateral deviation [Fig. 5.3a]. The smaller deflection may partly reflect the distribution of deformation between a series of small faults, in contrast with more localised strain in the central overlap [Faults 1 and 2]. However, the northern stream also shows evidence of a much larger discharge. High stream power is indicated by deep incision, resulting in a large canyon with a shallow, smooth gradient despite differential motion on a series

of faults. A knickpoint only remains at the extreme downstream end of the canyon, possibly related to later faulting. However, the stream gradient at this point is still lower than at knickpoints in the central overlap [compare Tables 5.1 and 4.3].

Non-tuff clasts are found in the bed and banks of parts of this stream network, although all the other studied channels on the Tableland erode and deposit only Bishop Tuff. The only other observation of non-tuff material is in a large channel in the southwestern corner of the Tableland [N. Dawers, pers. comm.]. These alien clasts are predominantly igneous, although they span a wide range of textures and compositions; and well-weathered, implying a long exposure [Fig. 5.23]. The distribution of the clasts, variation in lithology, maturity and their size all belie an origin as pristine outcrops eroded by the northern Tableland stream. Diffuse deposits of these clasts distributed over the Tableland surface away from the channel, to the north-northeast of Telegraph Road, possibly indicate a prior transport system which may have brought the clasts from distant outcrops, and could reflect some reworking into the northern stream. Thus this northern drainage network may provide an important link between the development of the Tableland channels and the wider evolution of the Owens Valley river systems [see Chapter 7].

5.2 Axial drainage system

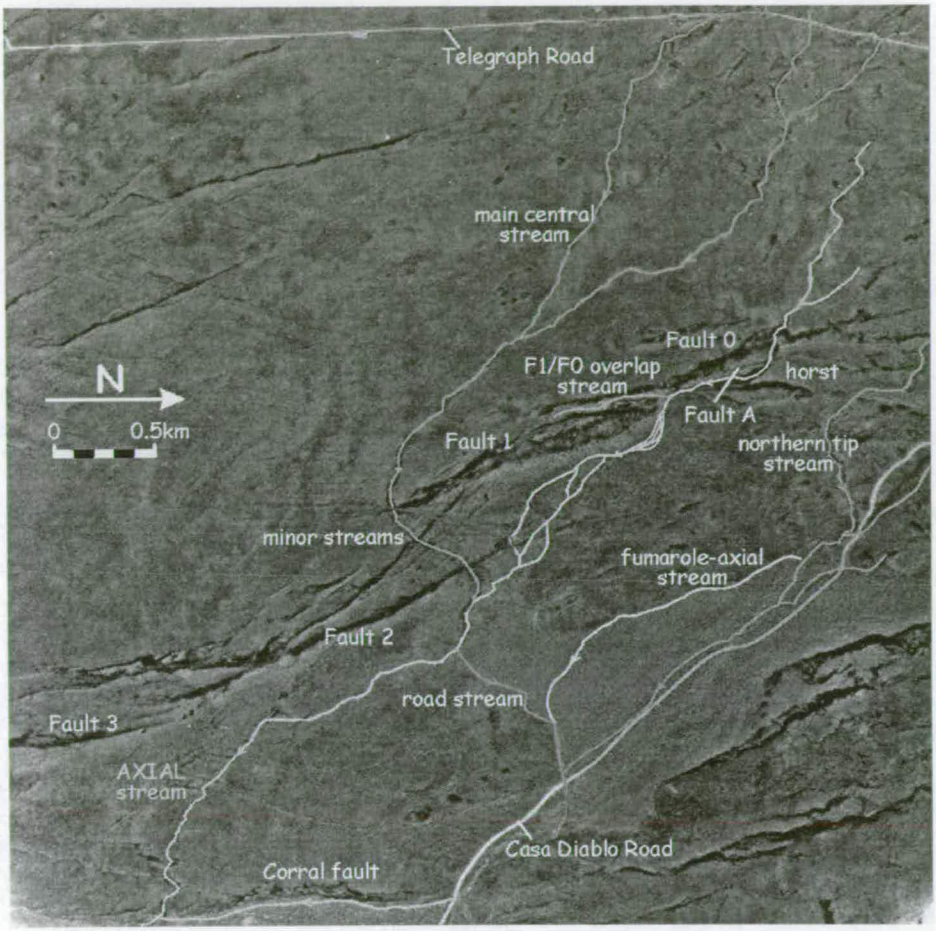

Figure 5.24: *Aerial view of the axial drainage network.*
Dark shadows are extensional fault scarps dipping towards the east (bottom) with throws reaching approx. 90m on Fault 1. Faults which dip west can be made out as thinner dark shadows.
The axial stream drains from the footwall of Fault 0 into the narrow F0 basin, confined by fumaroles and a horst to the east; then southwards connecting the Fault 0 and 1 basins with basins to the south. Tributaries supply water draining off the footwalls to the west and the raised fumarole areas to the east. Braiding occurs in the steep northern F1 basin, and around isolated fumaroles near the northern tip of Fault 2. Note the point where the axial channel intersects the main stream from the central overlap [section 4.2]. Further south, the axial stream flows more SE, to incise the Corral fault. Recent irrigation has destroyed evidence of the original stream patterns in the hangingwall of this fault.

While the previous section, and Chapter 4, considered transverse drainage systems, this section focuses on the large stream network which flows axially to the southern part of the array [Fig. 5.24]. The axial stream rises in the footwall of Fault 0, crosses its scarp and then flows southwards, connecting the hangingwall basins of Faults 0 and 1 with the basins of the southern faults. The course becomes hard to trace in deep sand, but gradually moves away from the main array to incise through the scarp o the smaller 'corral fault' to the southeast. The hangingwall of this fault has been artificially

modified to irrigate a corral and hence the axial channel is not considered beyond this point. The evolution of the axial stream is investigated through its course, long profile and cross-section data, as well as from perpendicular profiles of the hangingwall basins through which it flows [Fig. 5.40].

A series of tributaries flow into the axial channel [Figs. 5.26 and 5.25], from high ground in the footwall of the main fault array [from the central overlap: section 4.2; from the F1/F0 overlap: section 5.2.4.1], and from the indurated region around fumaroles which forms a high to the east [section 5.2.4.2]. A small stream runs along the hangingwall of the Corral Fault, to join the axial channel at the foot of the scarp [section 5.2.4.3]. These tributaries and other related stream provide useful insights into the axial stream development [section 5.2.4]. section 5.2.6 summarises the axial data.

5.2.1 Map and profile data

The axial survey is restricted to the area shown in Fig. 5.26, but a shallow channel can be traced on the aerial photograph [Fig. 5.24] for several kilometres WNW from Fault 0 beyond the limit of the survey. Although sourced from quite a large catchment, the channel is small and fairly indistinct upstream of the fault scarps, with very thin sand deposits draping the rubbly Tableland surface. Low topography is evident from the profile [Fig. 5.25 and Table 5.3] and the pronounced braiding. Two small surveyed tributaries [Fig. 5.26] are each scarcely a metre wide, and only a few centimetres deep.

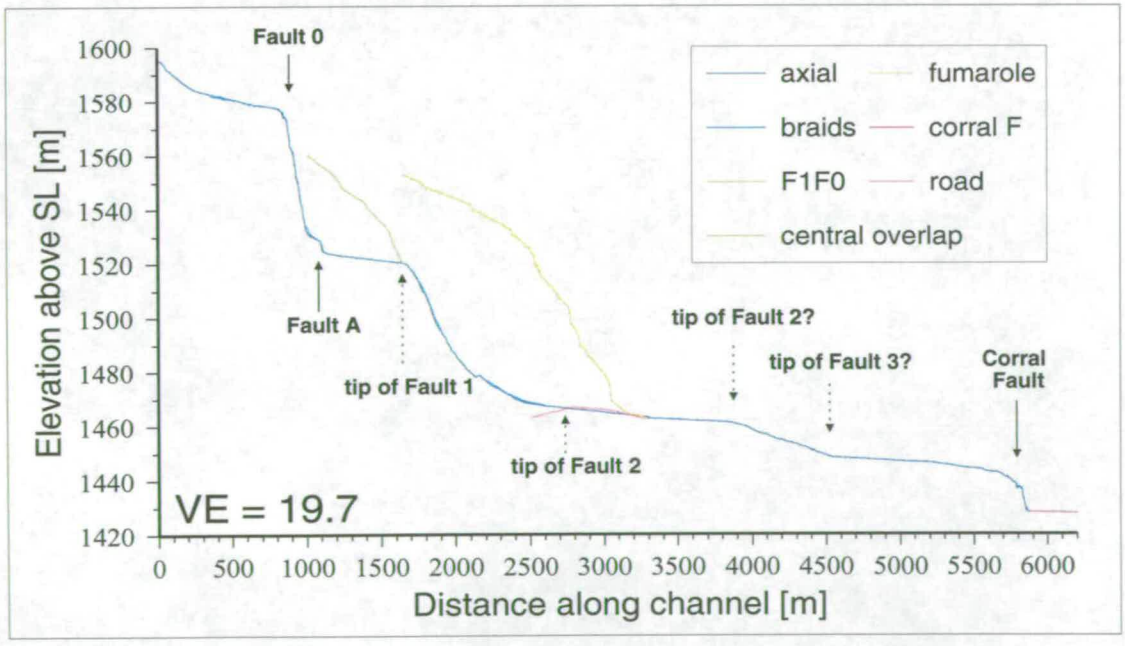

Figure 5.25: *Long profile of the axial channel network and some surveyed tributaries. Note the 'road' tributary gradient changes polarity near Fault 2: see section 5.2.5.2.*

As the fault array is approached, the stream drops down a series of bedrock steps. The bedload increases in size, with clasts up to 20cm diameter lining plucked cavities in the channel floor. Incision increases rapidly towards the scarp, with the gradient [Fig. 5.25

and Table 5.3]. Plucking and hydraulic wedging [section 2.3.1] are pronounced at the top of the Fault 0 scarp, where a broad flat 'pavement' is exposed; joints incised over a metre, and in some places also opened to almost a metre in width by the infiltration of water and clasts. The channel itself lies in one of these slits: a narrow steep-walled channel over a metre deep, littered with small angular blocks.

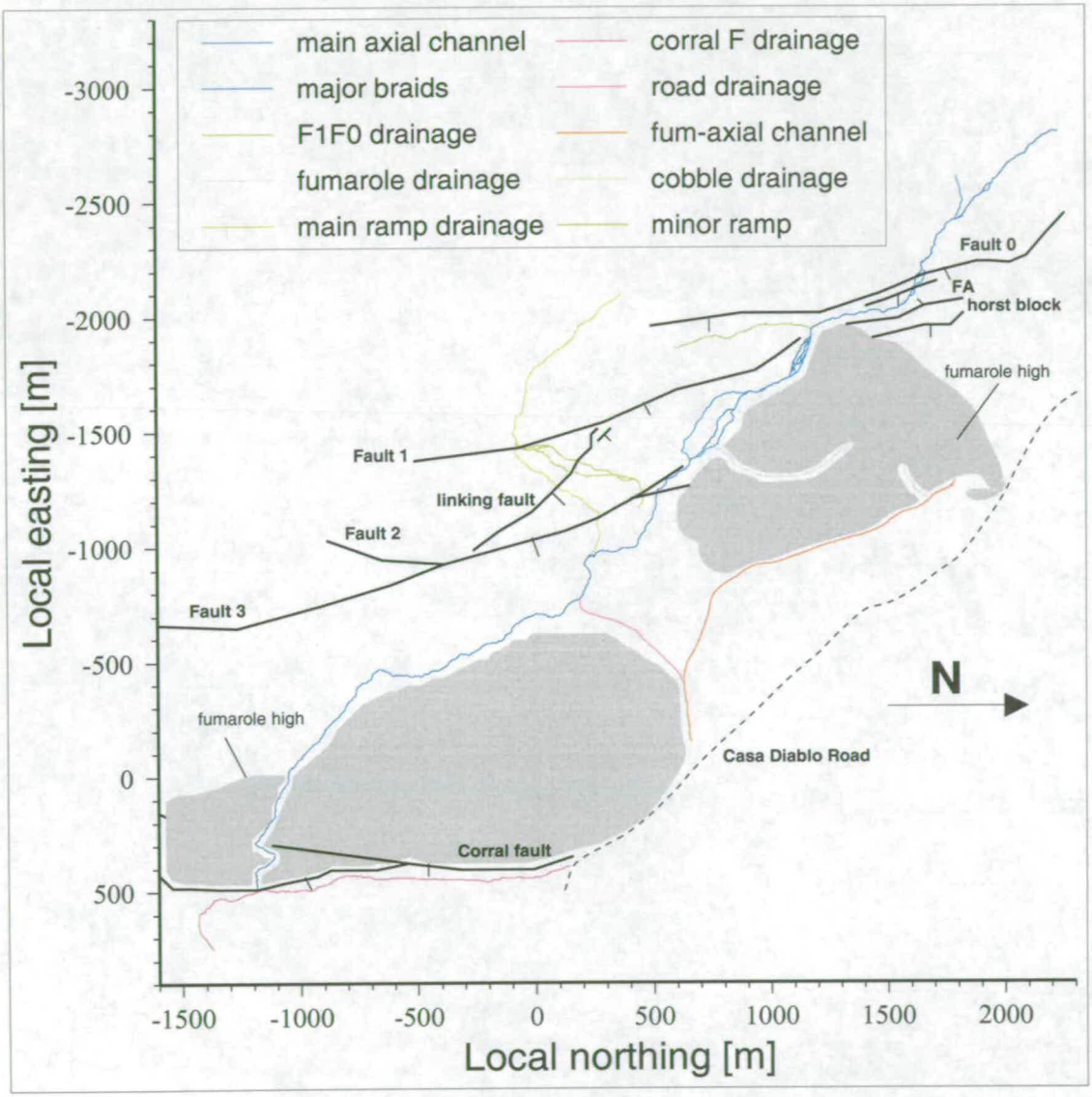

Figure 5.26: *Map of the axial channel network and surveyed tributaries. Grey areas mark the approx. locations of fumarole-rich high ground.*

The axial channel cascades 50m down the Fault 0 scarp [Figs. 5.25 and 5.27a], and has eroded a deep plungepool in the hangingwall. The knickpoint is very steep, but as at Fault 1, consists of several large steps, and the channel is choked with large angular boulders over 2m across, which balance precariously on each other and on ledges and cavities eroded by the stream [section 7.2.2.4]. Two stream branches are incised over a metre into the Fault 0 hangingwall, armoured with rounded cobbles [$\leq$30cm] and

littered with angular boulders from the waterfall. The two forks recombine downstream of Fault A Once across the Fault A scarp, the bedload decreases in size dramatically, with only sand in the channel ~100m downstream of the scarp.

A steep-sided horst to the east, subparallel to the main fault array, constrains the axial channel in a narrow elongate basin [Figs. 5.26 and 5.28]. The basin has a very low gradient today [Fig. 5.25 and Table 5.3], due to thick sand deposits across the whole of the basin; coarser material is limited to talus piles at the base of Fault A and near small fumaroles at the southeast margin of the basin [Fig. 5.28]. Sand and coarser material is also derived from a channel which flows northward down the F1/F0 overlap [Fig. 5.28 and section 5.2.4.1]. An enormous mound of sand at the toe of this steep overlap [Fig. 5.27b] demonstrates a significant supply to this basin over time.

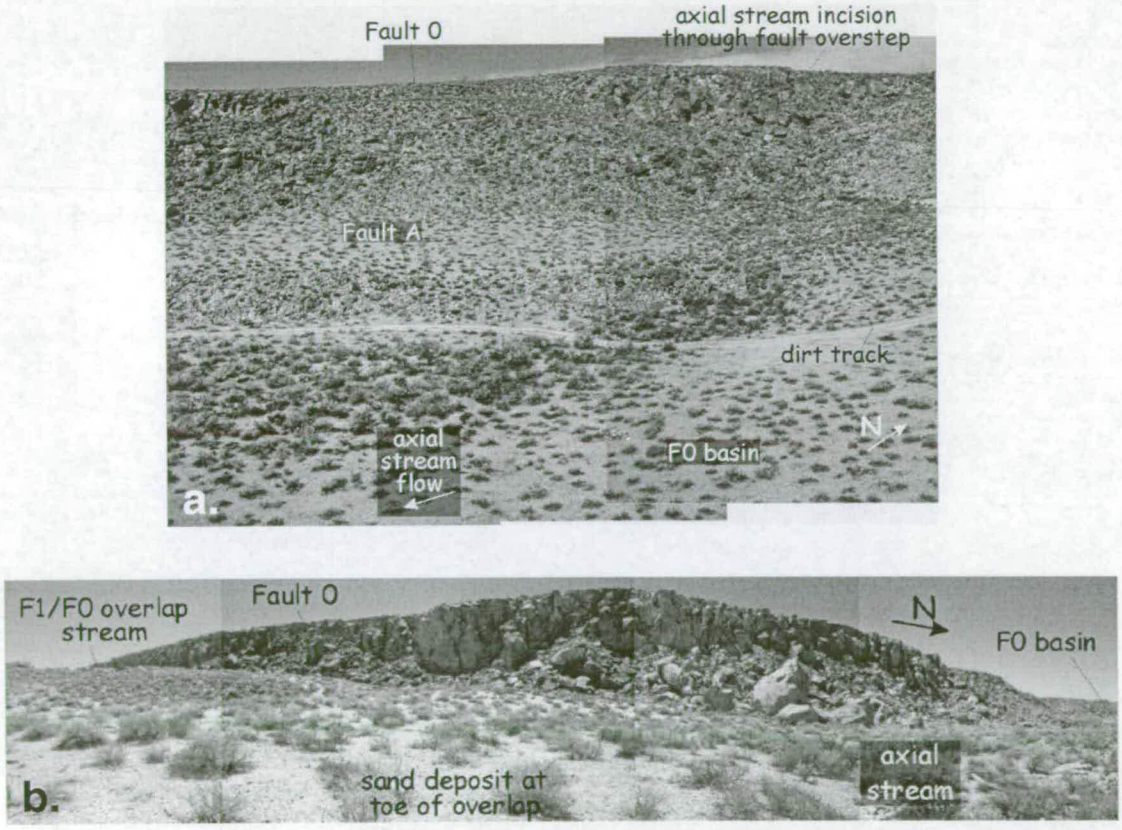

Figure 5.27: *Field photographs of axial stream in F0 basin.*
a. Waterfalls down Fault 0 and Fault A scarps, seen from the top of the horst block to the east. Main scarp is 50m high. Green line of sagebrushes marks course of channel into hangingwall basin.
b. Sand pile at the base of the F1/F0 overlap. F0 scarp reaches ~50m high; largest block at its base is ~15m diameter.

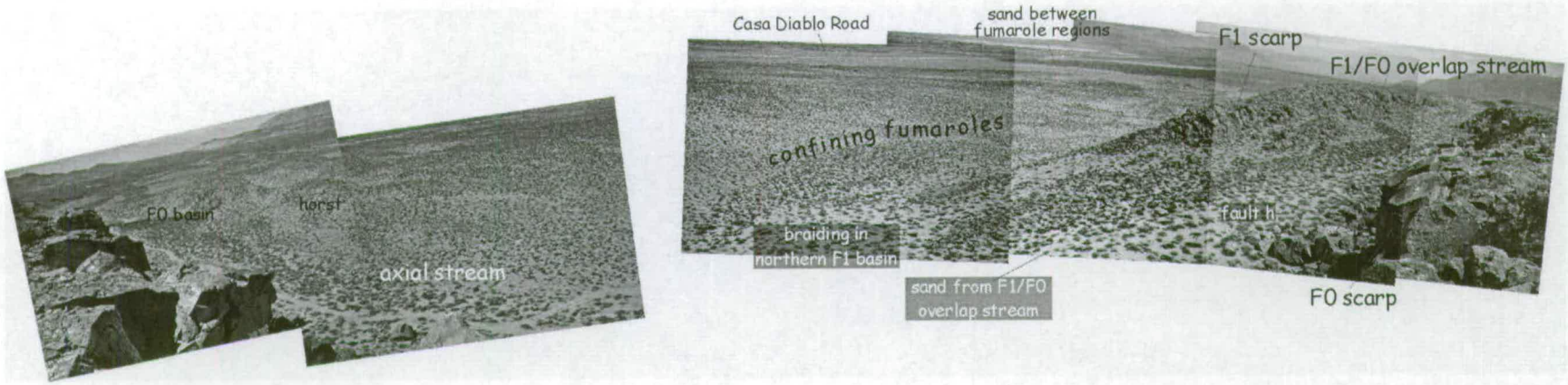

Figure 5.28: *View of F0 basin, the northern axial channel and the tributary draining the F1-F0 overlap. Photographs were taken from the top of the F0 scarp. Antithetic fault behind F1 bounds the eastern side of the F1/F0 overlap. Horst block limits the eastern margin of the hangingwall basin. Axial channel flows left to right [N-S], marked by the deep green line of large sagebrush. Sand currently fills the F0 basin to the IBH lip, so that material from the F1/F0 overlap is carried into the F1 basin by the axial channel around the F1 tip, rather than being deposited in the F0 basin.*

The axial stream spills over the F0 basin lip [IBH] into the hangingwall of Fault 1 to the south. The northern tip of Fault 1 has a very steep displacement gradient, D_{max} located only around 400m from the tip [Fig. 4.5]. The axial stream therefore experiences a steep drop as it rounds the tip of Fault 1: increasing from 0.5° to almost 8° gradient in less than 200m [Fig. 5.25 and Table 5.3]. This gradient change causes a dramatic change in morphology; the gentle sandy channel instantly splitting into a series of interconnecting braids [Fig. 5.29a and Fig. 5.30]. The stream branches are incised up to 3m into the tuff at the steepest slope [panel D in Fig. 5.34], and lined with rounded clasts from 5cm to 1m across. An elevation drop of over 50m is accommodated in a series of small bedrock steps of 50-150cm. The stream bends slightly away from the fault, but confined between the steep talus slope of Fault 1 and an indurated fumarole bank to the east, the stream cuts deeply into the slope [see also Fig. 5.40].

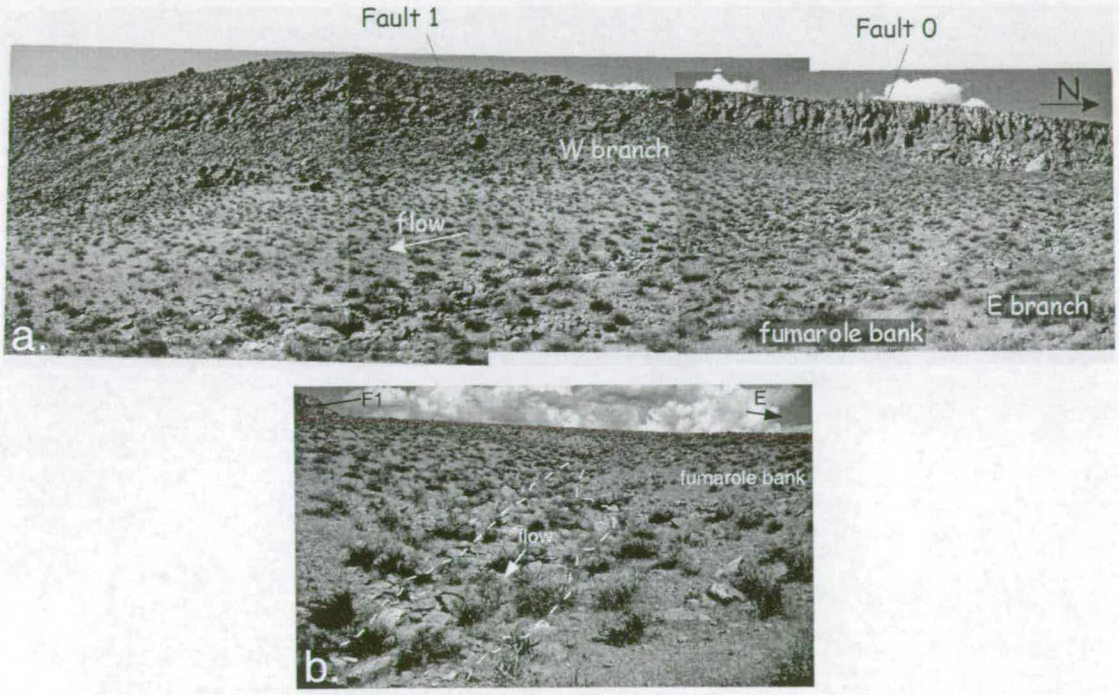

Figure 5.29: *Field photographs of axial stream in F1 basin.*
a. View from top of fumarole bank of braiding at the northern tip of the Fault 1 basin.
b. Single channel in sandy F1 basin, downstream of steep slope, looking upstream from xc10. Channel lies in notch cut between fumaroles and talus: about 15-20m wide.

As the slope of the channel reduces, the branches recombine [Fig. 5.30]. This reach is initially still deeply incised into the F1 basin, confined by the fumarole bank to the east, and smoothed bedrock steps are exposed in the channel floor [Fig. 5.29b]. Blocks up to 2m in diameter, from the F1 talus slope, obstruct parts of the channel. The axial stream splits again into smaller channels around isolated fumaroles in the southern F1 basin [see also section 4.1.2 and Fig. 5.30] but the branches spread widely over the shallow sandy floor. Incision decreases downstream with the bed gradient, from over a metre to less than 20cm where the branches rejoin, immediately upstream of the Fault 2 tip [xc 2 in Fig. 5.30]. Similar widely-spread braids fan over the shallow topography of the sandy northern Fault 2 basin. Where the axial stream receives input from

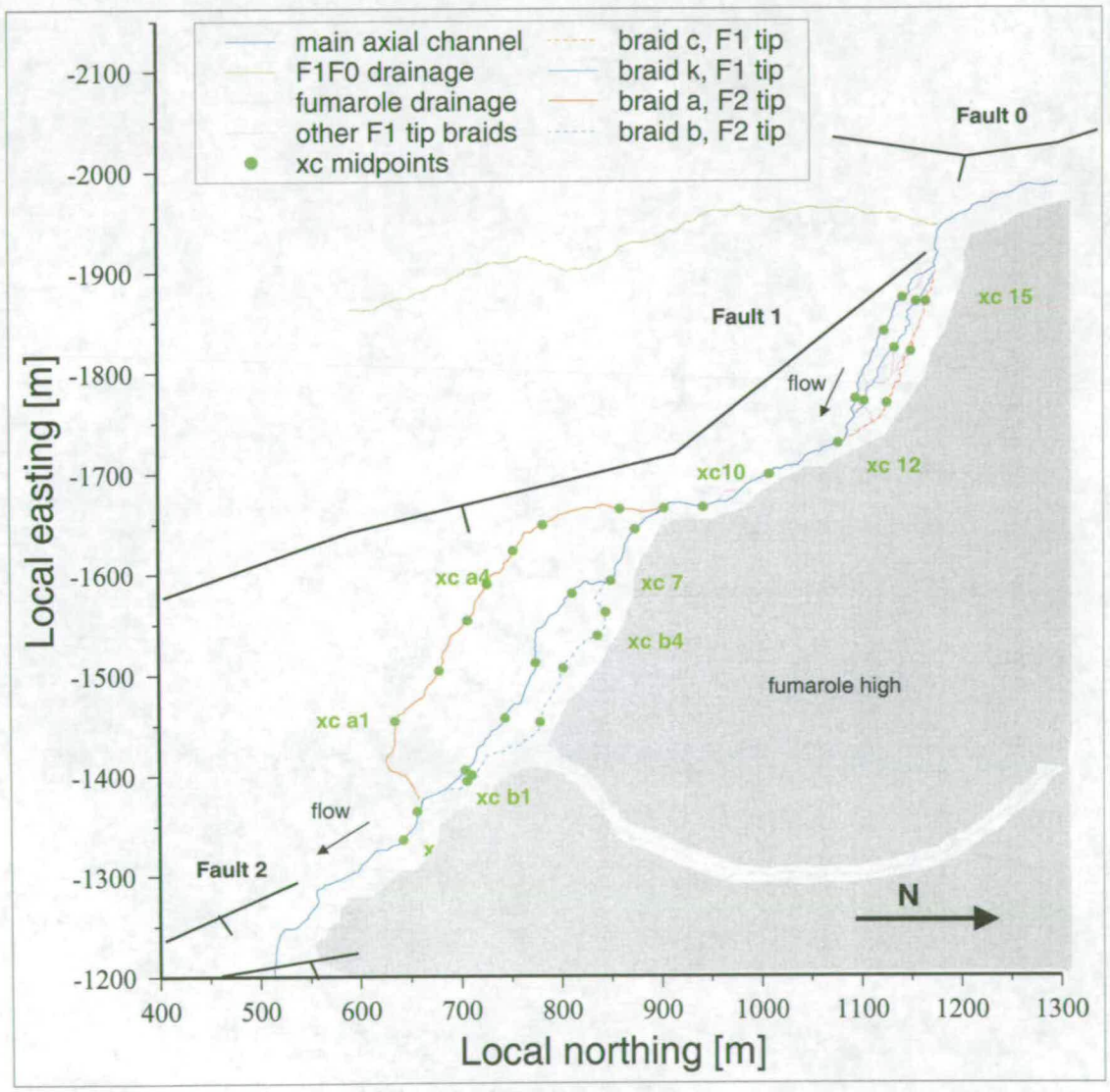

Figure 5.30: *Map of braiding in the axial channel network in the hangingwall basin of Fault 1.*

the central overlap stream, the difference is dramatic. Up to 60% of the downstream channel bed is covered in rounded cobbles [≤25cm], confined by sandy banks over 50cm high. The gradient of the channel is not significantly altered [Table 5.3], but the change in morphology is pronounced, reflecting the high discharge and sediment supply.

For most of the surveyed southern course, the axial stream flows across a sandy basin, in a channel 5-15m wide, and 20-60cm deep. Short branches split off the channel every 50-250m, and wind across the shallow basin topography. Fumaroles forming the eastern margin are smaller and further apart, and considerably further from the fault array [Fig. 5.26]. Consequently, the axial stream gradually migrates further from the scarps; further north, confined by fumaroles, it lies within 250m of the scarp base.

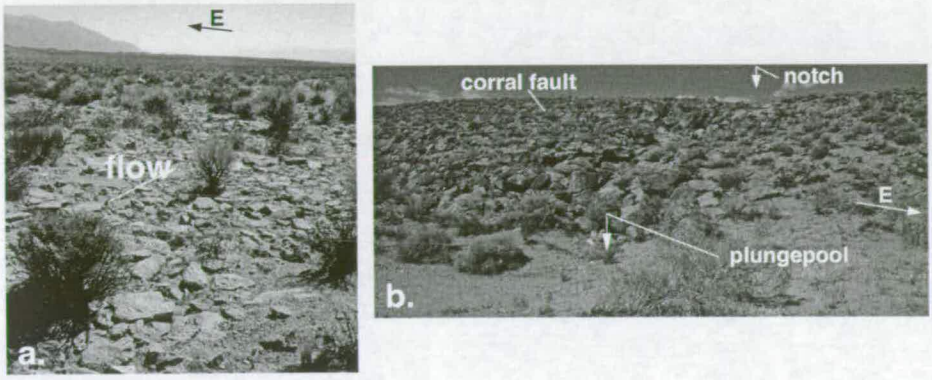

Figure 5.31: *Field photographs of southern axial stream.*
a. Bedrock incision in the southern axial stream: influence of fumaroles on the eastern margin of the hangingwall basin. Stream is <1.5m wide.
b. Incision through the Corral fault scarp. Scarp is ~11m high. Plungepool is scoured out at the base to a depth of ~0.8m.

However, where the axial channel flows close to the eastern margin of the basin, it has a steeper gradient [Fig. 5.25 and Table 5.3] and incises up to a metre into bedrock [Fig. 5.31a]. Cobbles and rounded pebbles are common, in contrast with the typical sand deposits both upstream and downstream of this incised reach. This is also evident in the aerial photograph, with pale areas, implying thick sediment deposits, where the central overlap supply enters the F2 basin, and also near the F2/F3 overlap at the southern tip of F2 [Fig. 5.24]. The centre of the basin is more starved, and appears much darker in Fig. 5.24, with thin pale strands showing sediment deposition only at the immediate base of the F2 scarp, and along the axial channel itself.

A wide bend to the SE occurs around 750m downstream of the central overlap stream, taking the axial channel towards the small Corral fault [Figs. 5.26 and 5.25]. The stream deflects sharply upstream of this fault in response to a small overlapping fault pair [see Fig. 5.26]. Uplift on these small faults [D_{max} ~4-5 m] and the Corral fault [D_{max} ~40 m] causes dramatic steepening [Fig. 5.25], driving narrowing of the channel from 15 to 5m, and incision of almost 4m depth at the Corral fault scarp. A large plungepool, almost 2m deep, is scoured out at the base of this scarp [Fig. 5.31b], downstream of which the stream widens out over a very low gradient [Fig. 5.25]. The axial stream probably originally continued southwards [see Fig. 5.26], but has recently been disrupted by irrigation attempts.

Reach	Section	Length (m)	Gradient (°)	SL index (grad m)
Fault 0 footwall	upper	223.16	-2.76	-5.39
	lower	593.84	-0.745	-6.77
	immed FW	42.82	**-3.884**	-56.93
Fault 0 basin	Fault 0 hw	14.89	**-4.887**	-86.16
	FA fw	82.82	-1.649	-30.41
	FA to tip F1	564.51	-0.514	-12.49
(braided) F1 basin	1	54.16	-3.570	-106.08
	2	58.57	-5.912	-181.90
	3	77.29	**-7.921**	-253.83
	4	115.48	-5.843	-196.58
	5	159.76	-3.533	-127.10
	6	191.51	-2.031	-80.11
tip F2 - MD	fw F2 tip	21.42	-0.613	-25.31
	immed hw	70.13	**-1.113**	-47.38
	F2 basin	727.96	-0.357	-4.54
	to MD	91.21	-0.625	-35.40
F2 - corral F	F2 to MD	530.60	-0.159	-140.82
	MD to fumaroles	122.02	-0.670	-22.58
	near fumaroles	595.08	-1.113	-67.78
	bend to SW	661.70	-0.175	-16.66
	5	257.66	-0.455	-29.30
	6	90.32	-0.247	-9.88
	near small fs	55.06	-0.986	-50.61
	8	53.14	-0.324	-26.27
	Corral F fw	172.43	**-1.964**	-5.33
Faults	Fault 0	140.33	-16.795	-280.69
	Fault A	10.69	**-18.339**	-365.68
	Fault 2 tip	27.53	-3.466	-144.70
	Corral Fault	50.80	-9.859	-732.94

Table 5.3: *Variation in downstream average bed gradient of the main axial channel reaches from the footwall of F0 to the Corral fault basin. The highest gradient non-faulted reach in each part of the channel is marked in bold; faulted reaches are separate.*
SL index, a proxy for stream power [Eqn. 2.7] is calculated from the start of the survey in the footwall of F0. As with the other streams [Tables 4.3; 4.6 and 5.1], locally high SL [stream power] is observed predominantly in reaches steepened by fault activity. All other reaches have very low stream power, reflecting the low gradient.

5.2.2 Cross-section data

Cross-sections were measured in three parts of the axial channel: the footwall of Fault 0, the Fault 1 hangingwall basin, and the reach from the central overlap / axial junction in the Fault 2 basin to the Corral Fault basin [see Fig. 5.48]. Profiles of the channel sections are all plotted at the same scale, to allow comparison of the channel morphology. As in previous sections, the cross-section aspect ratio is used to compare the different reaches. Figure 5.48 is a plot of the variation in aspect ratio along the entire axial channel.

5.2.2.1 Fault 0 footwall

Cross-sections in the footwall of Fault 0 show a shallow channel upstream of the fault, with significant stream incision only in the last 150m of the footwall [xcs 8-10: panel D, Fig. 5.32]. A few fumaroles provide high banks to some parts of the stream [e.g. xc 1, panel C].The shallow incision is reflected in the aspect ratios, which are uniformly low throughout the surveyed footwall reach of the stream [Fig. 5.33] and similar to those in the shallow downstream reaches of the northern tip channel [Fig. 5.10], and in the small channels in the central overlap [Fig. 4.45]. Aspect ratios increase in the steepened reach immediately upstream the Fault 0 scarp, as seen in other streams [e.g. in central overlap, northern tip upstream channel: Figs. 4.36 and 5.12].

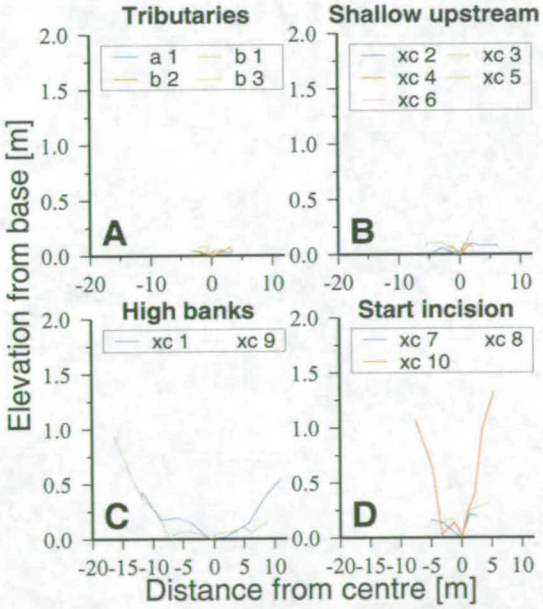

Figure 5.32: *Cross-sectional profiles of axial channel in Fault 0 footwall. The 4 panels show the varying morphology along the stream. All profiles are plotted with N(E) on the left and at the same scale as the downstream sections [Figs. 5.34 and 5.37]: VE = 18.7.*

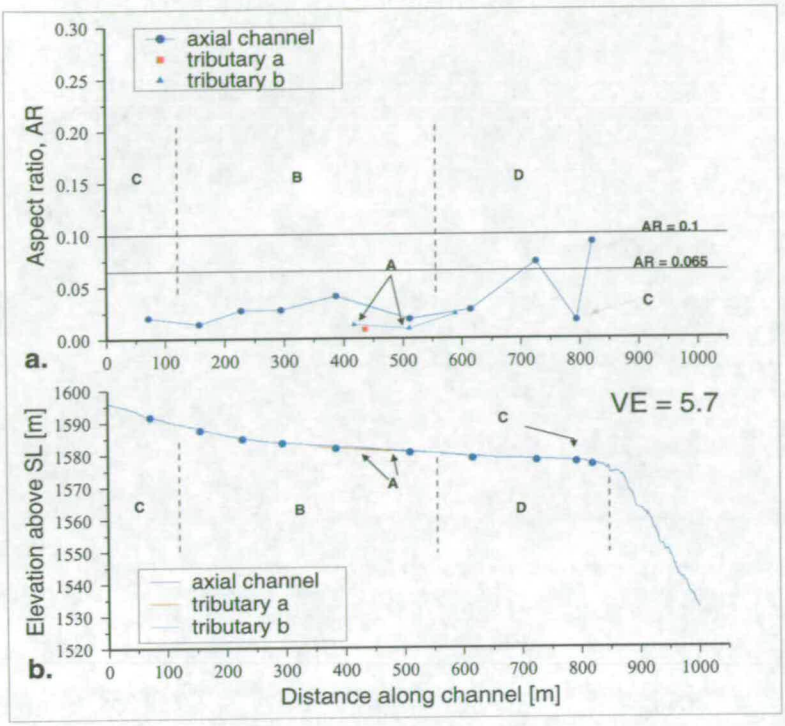

Figure 5.33: *Variation in cross-section aspect ratio of axial channel in Fault 0 footwall.*
a. Aspect ratio [bank-base depth/bank-bank width] plot of main channel and tributaries.
b. Long profile of this part of main axial system. Morphologies are marked as in Fig. 5.32.
[Sections in tributaries a and b have morphology A. Cross-section 9 is similar to xc 1: morphology C]

5.2.2.2 F1 basin

Cross-sections in the hangingwall basin of Fault 1 [Fig. 5.34] are plotted in panels representing the braiding of the stream: panels A-C are from the three main branches in the steep northern basin: panels E-G are from the three southern braids [see inset in Fig. 5.34 and Fig. 5.30 for locations]. The comparison with the Fault 0 footwall profiles is striking.

In the steepest part of the channel [panels A-C: Fig. 5.35], each braid occupies a very narrow channel, the two largest [A, C] incised over a metre into the tuff. Incision in the smaller braid k [panel B] increases with slope downstream, as the main [western] branch narrows. The fumarole bank on the eastern side of the basin confining the stream forms the high steep eastern [right] bank of sections in panels C and D. The single channel remains very deeply incised throughout reach D [see also Fig. 5.29], and barely wider than the steep braided reach. Braiding in the low gradient central basin occurs around isolated fumaroles [Figs. 5.30 and 5.35b]. Incision decreases sharply with gradient, although the width is only slightly greater than in the steep braids. By the Fault 2 basin [panel H], the stream is a mere scratch in the sandy floor, barely 10cm deep.

The width of the branches varies only slightly, but the major differences in incision result in an aspect ratio pattern closely mirroring the gradient variation in the basin

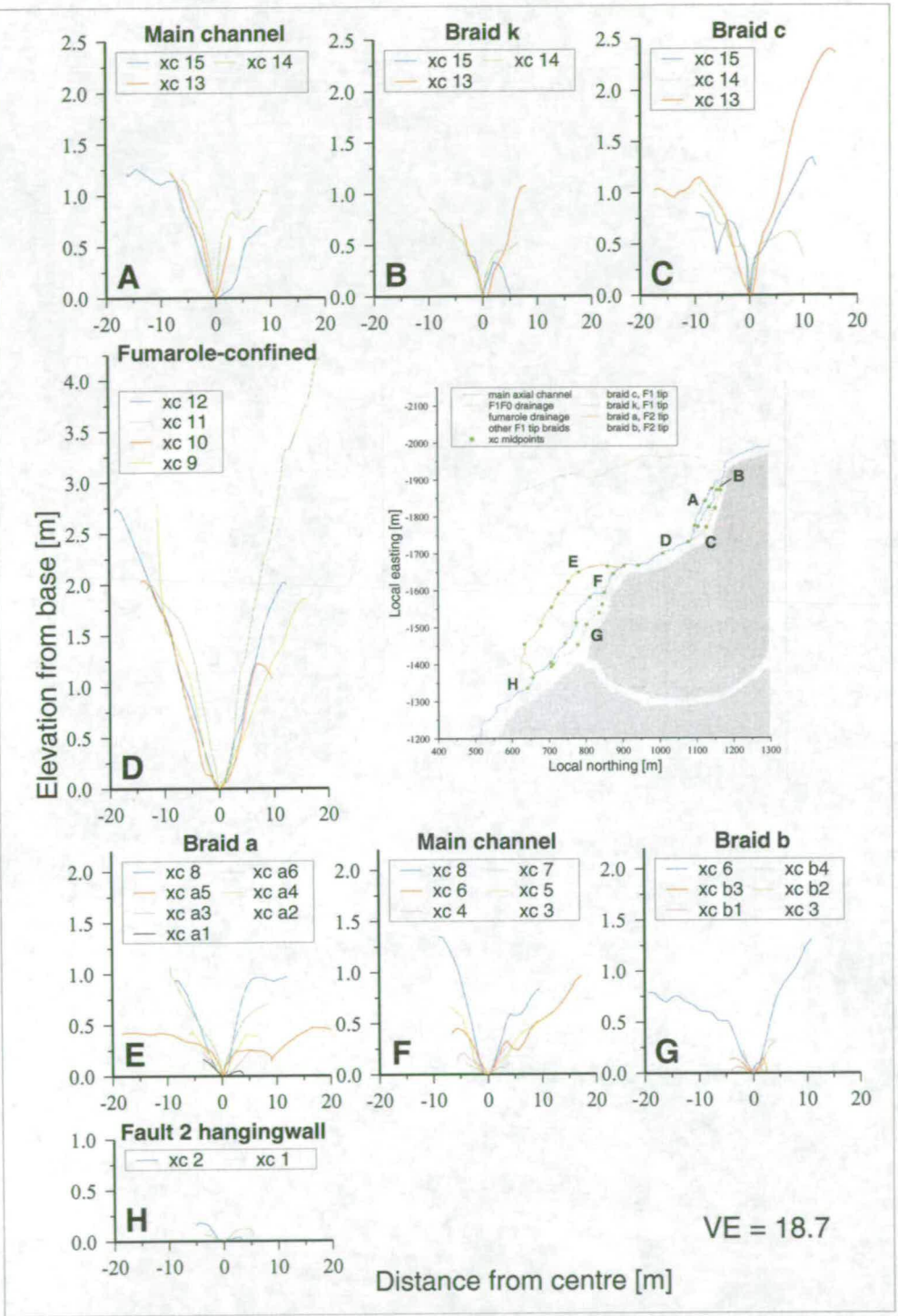

Figure 5.34: *Cross-sectional profiles of the axial channel in Fault 1 basin.*
The 4 rows correspond to the downstream variation in braiding [see inset and Fig. 5.30]. Each panel corresponds to a different branch of the stream, with (S)W always on the left. The morphology is very consistent within each branch.
All profiles are plotted at the same scale as in the other figures [5.32 and 5.37], despite the varying lengths of the axes: VE = 18.7.

[Fig. 5.35]. Thus the channel has adjusted to the varying slope of the F1 hangingwall basin not only by variations in stream pattern [braiding in Fig. 5.30], but also by quite dramatic variations in channel cross-section. Steep parts of the channel are braided, and have a high aspect ratio, due to their narrow, deep cross-section. Aspect ratio decreases with slope, such that the widely separated strands in the shallower central parts of the basin are easily distinguishable by morphology from the steep braided reach upstream.

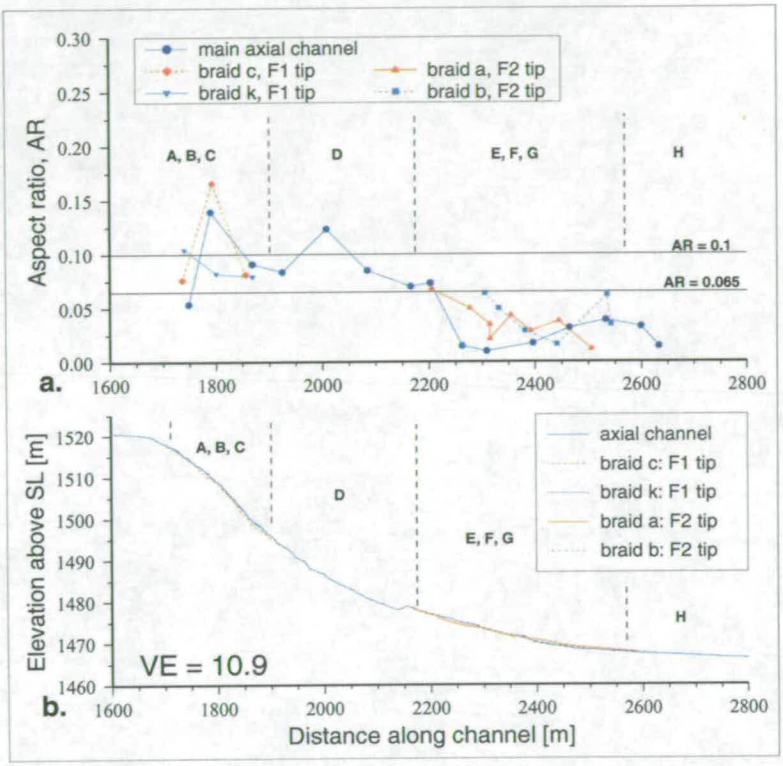

Figure 5.35: *Variation in cross-section aspect ratio of the axial channel in the Fault 1 basin.*
a. Aspect ratio [bank-base depth/bank-bank width] plot of main channel and braids.
b. Long profile of this part of main axial system. Reaches are marked according to the morphologies in Fig. 5.34. See inset in Fig. 5.34 and Fig. 5.30.

5.2.2.3 Southern axial channel: Fault 2 to Corral Fault basin

Cross-sections downstream of the central overlap stream fall into 5 groups [Fig. 5.37]. Bedrock incision, accompanied by an increase in bedload size, occurs in the stream at xcs 4-9, where the stream lies to the east, near the fumarole mounds [Fig. 5.36]. The profiles are in marked contrast to those measured immediately up- and down-stream [sections 2-3, 10-11: panel B], where there is little topography across the channel. Braiding is common, but each strand is shallow. Section 1, at the junction with the road stream [Fig. 5.36], is an exception, as it is incised only a few centimetres, but has high banks, particularly on the east [right].

Sections 10 and 11 were measured on the reach which bends west [Fig. 5.36], after which the stream turns southeast, and becomes narrower and slightly deeper. Little change

occurs where the channels flows across a uniformly shallow sandy basin floor [C]. A dramatic increase in incision and decrease in depth occurs in the steepened reach, 250m upstream of the Corral Fault [D]. Incision reduces immediately in the hangingwall [xcs 26-29, E].

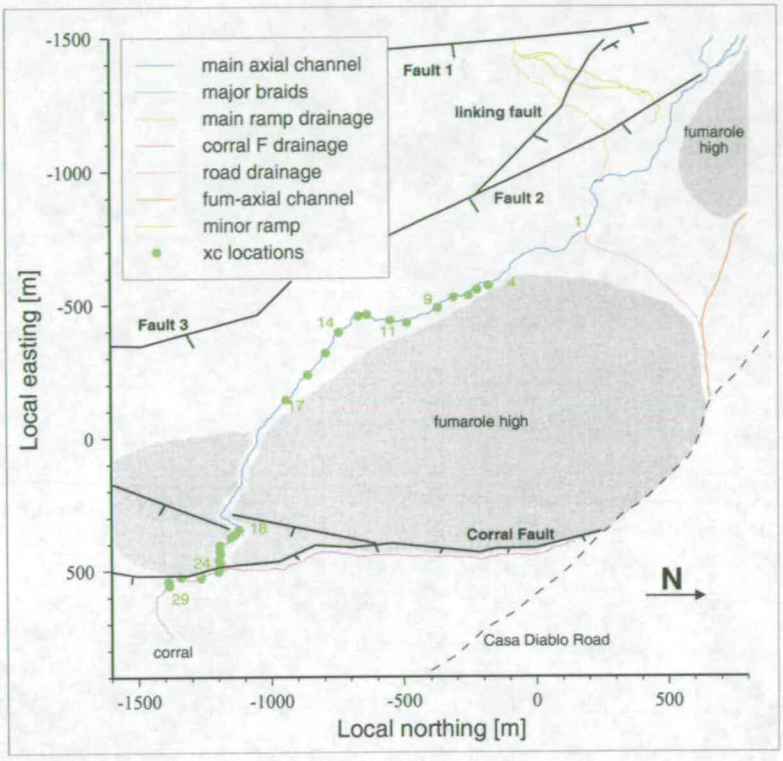

Figure 5.36: *Location of cross-sections surveyed in the southern axial channel. Green numbers refer to the numbers of the cross-sections: higher numbers are further downstream.*

The aspect ratio variation around the corral fault [Fig. 5.38] is very similar to that in other streams which cross fault scarps [e.g. central overlap, Fig. 4.36; northern upstream channel, Fig. 5.12c]. Aspect ratios further north are less easily correlated with the long profile, as the aspect ratio remains uniformly low until the fault-dominated reaches downstream [DE]. The distinct shapes of profiles in panels A and B [Fig. 5.37] are not clearly differentiated by aspect ratio, since it shows relative, not absolute, dimensions, and is based only on the water-carrying part of the surveyed profile. This is a limitation of the aspect ratio, demonstrating the need to also study the cross-sectional profiles themselves, as AR cannot distinguish a variation in morphology where the *shape* of the *channel* cross-section remains similar.

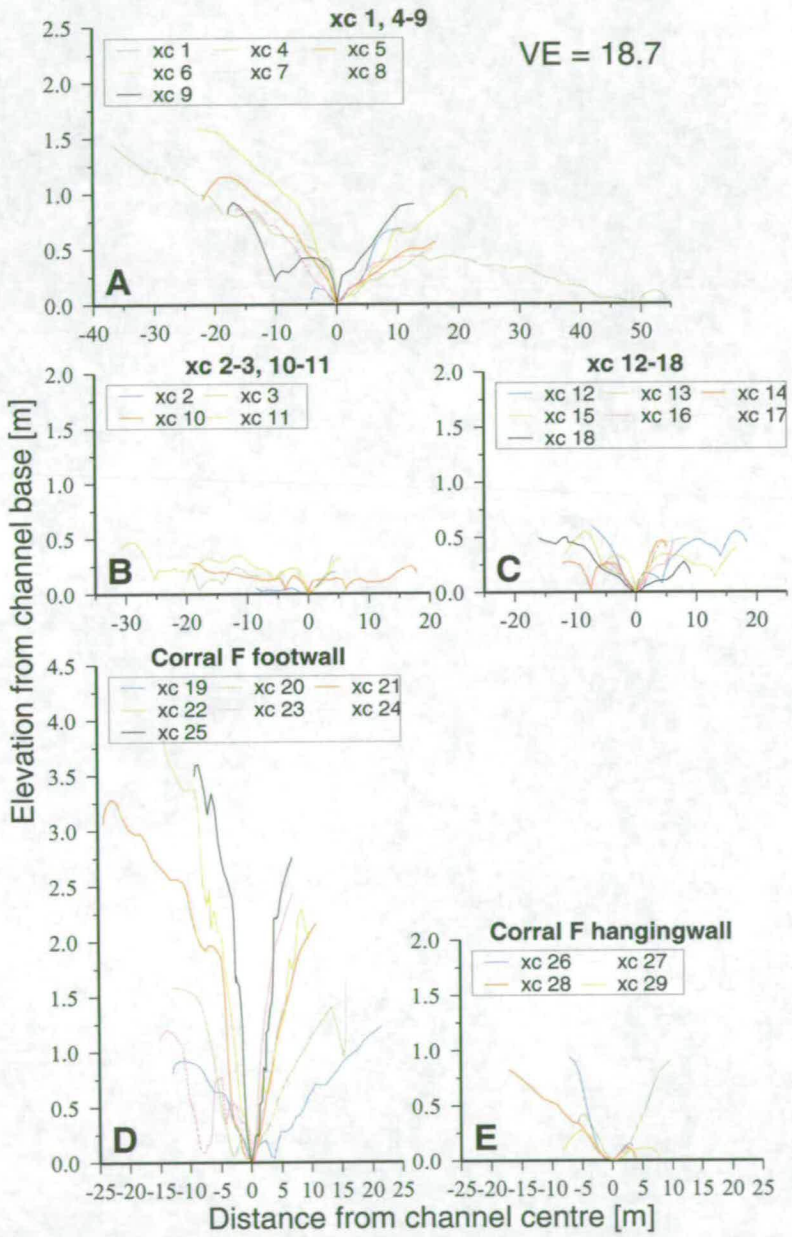

Figure 5.37: *Cross-sectional profiles of axial channel in the Fault 2 to Corral fault basin. All profiles are plotted with N(E) on the left and at the same scale as the upstream sections [Figs. 5.32 and 5.34], despite the varying lengths of the axes: VE = 18.7. See Fig. 5.36 for cross-section locations.*

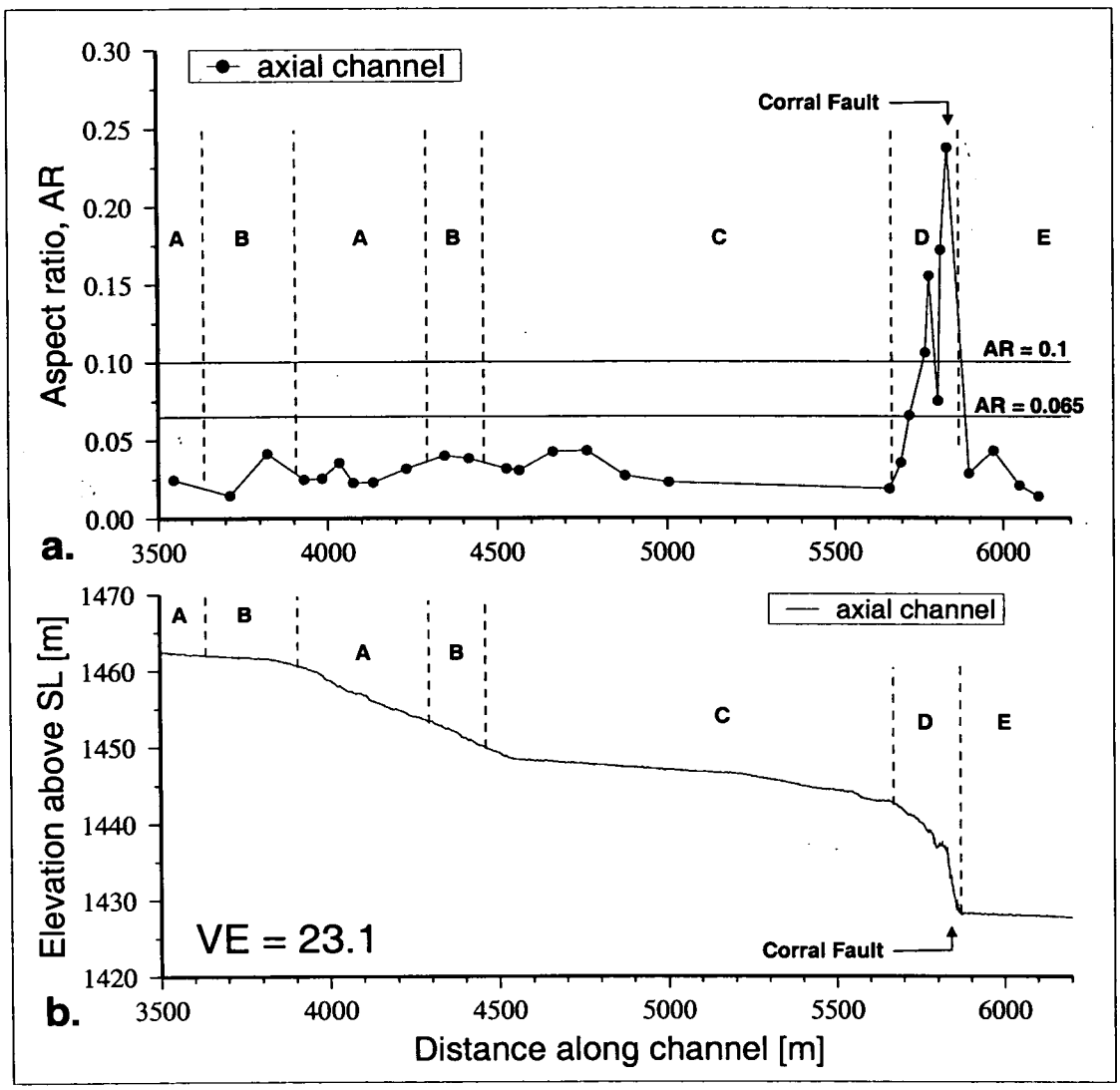

Figure 5.38: *Variation in aspect ratio of southern axial channel: Fault 2 hangingwall to Corral Fault basin.*

a. Aspect ratio [bank-base depth/bank-bank width] plot of main channel.

b. Long profile of this part of main axial system. Reaches are marked according to the morphologies in Fig. 5.37.

5.2.3 Hangingwall basin profiles

The variation in gradient perpendicular to the bounding faults is a vital factor controlling the location of the axial system, and its location relative to the base of the fault scarps. Subsidence of the hangingwall is maximum at the base of the fault scarp, and reduces with distance into the basin [Fig. 2.1]. Thus a channel flowing parallel to a fault often migrates laterally or avulses towards the scarp, as it responds to the subsidence pattern produced by the fault [e.g. Leeder et al. (1991); Peakall (1998); Peakall et al. (2000)]. Study of the surveyed profiles can thus be used to determine some of the development history, and the reasons behind the present location, of the axial channel.

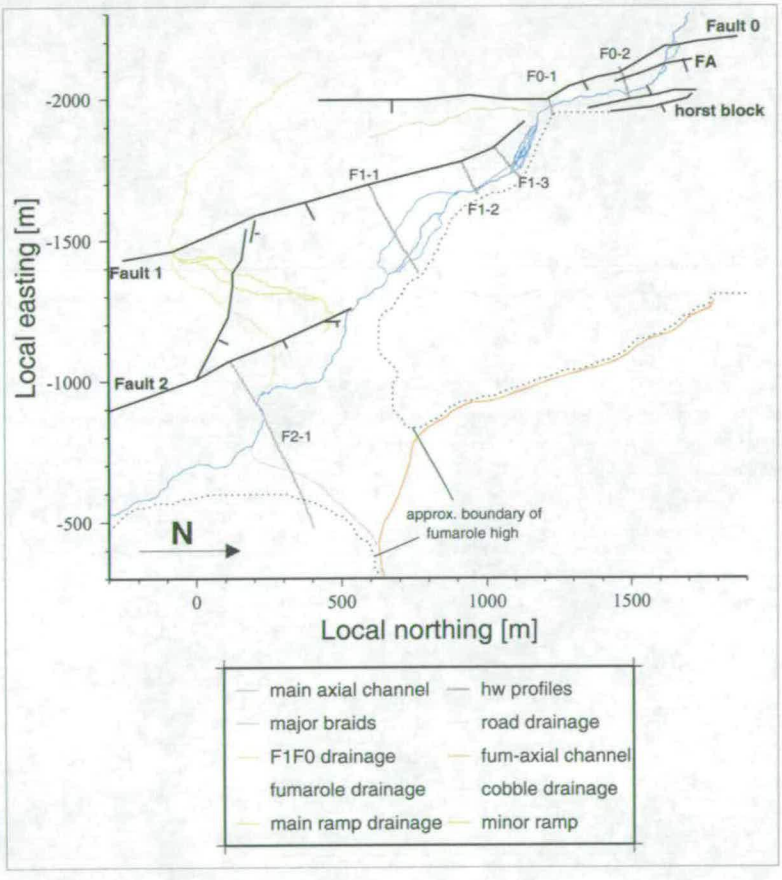

Figure 5.39: *Map of central axial channel showing location of measured hangingwall profiles.*

Figure 5.40 shows perpendicular profiles of the Fault 0, Fault 1 and northern Fault 2 hangingwall basins. Profiles are all plotted on the same scale, and surveyed from the base of the bounding fault scarp on the west [left]. The northernmost profile is at the top, and hence the gradient between basins, and within each basin, can also be seen.

The two profiles measured from the foot of Fault 0 are quite different [Fig. 5.40]. The northern profile [2] shows a virtually flat basin floor stretching almost 100m from the base of Fault A to the horst block on the east. The axial channel is braided, and closer to the antithetic fault than to Fault A. Further south, the basin is considerably

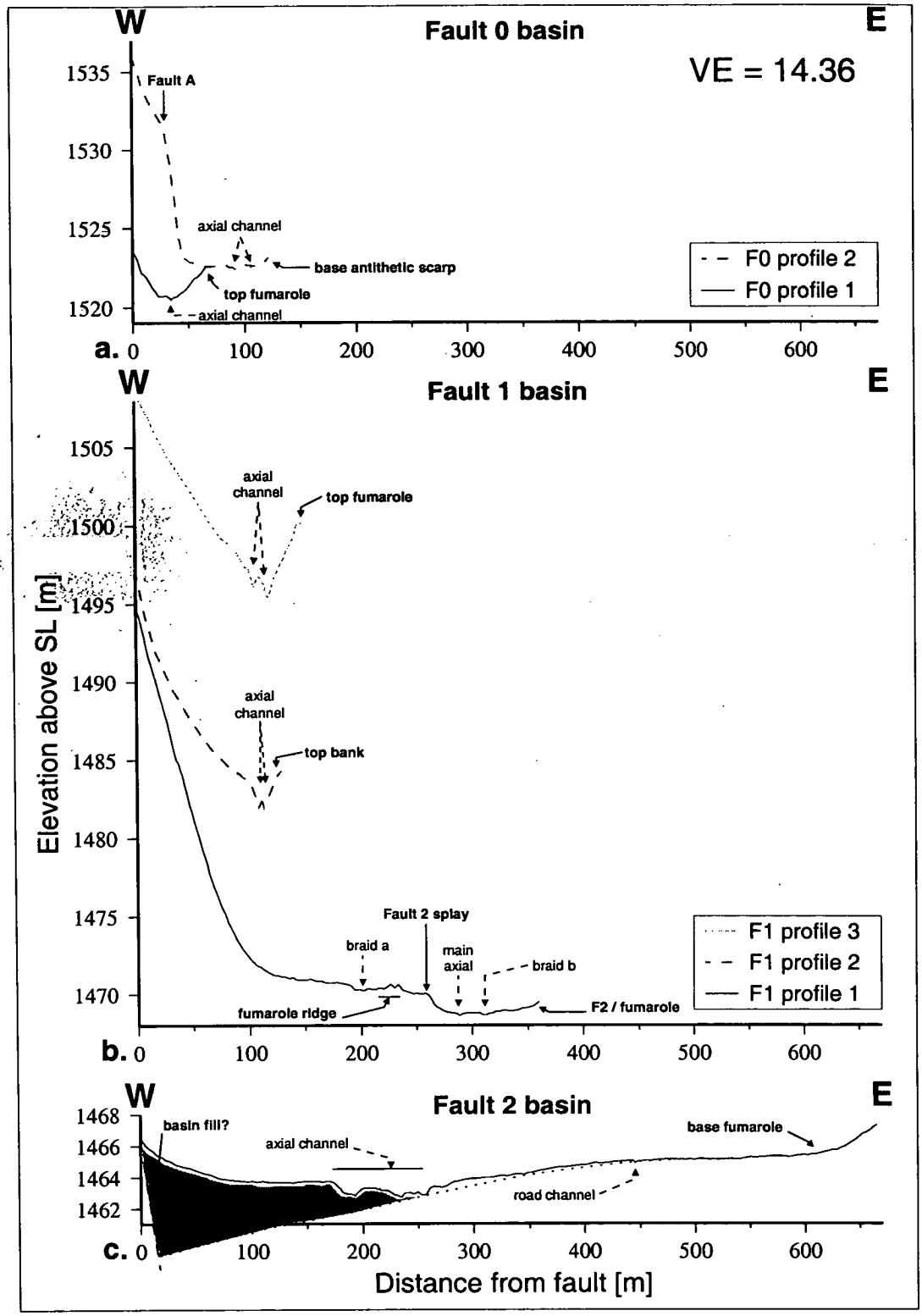

Figure 5.40: *Profiles of the hangingwall basins of a. Fault 0, b. Fault 1 and c. Fault 2. All profiles are plotted from west [fault scarp] to east, and at the same scale: VE = 14.36. Northern profiles are towards the top of the page [higher elevations] in each basin.*

narrower, the stream restricted to a 15m wide basin floor between the base of Fault 0 and a fumarole on the eastern margin. The basin floor is only 2m lower than at profile 2, 150m further upstream, despite the different fault patterns, which, combined with the flat basin floor in profile 2, implies that a lot of the original basin topography has been infilled by sediment.

The axial channel is ~25m lower by profile 3 in the F1 basin, demonstrating the high displacement and low supply to the F1 basin, relative to the F0 basin. The channel bed drops almost 27m further in 500m between the three F1 profiles. The northern profiles explain the deep incision of the stream, between a steep talus slope to the west and a hard fumarole bank on the east [however note the vertical exaggeration of the plot]. Incision is deepest in the north [profile 3], where the talus slope is steepest and the fumarole bank highest. This is also closer to the northern tip of the fault, where hangingwall subsidence is lower than at profile 2. Although the gradient of the talus apron is slightly lower in profile 2, nearer D_{max}, the axial stream is still confined by fumaroles to the east, and now unlikely to migrate laterally, as it has incised a ~2-3m deep channel.

By profile 1, however, the fumarole high is considerably further from Fault 1, creating a sandy basin ~250m wide. The axial stream occupies three distinct channels, winding between isolated fumaroles and the northern tip splays of Fault 2. Braid **a** is closer to Fault 1, and around 2m higher than the other two branches, which lie in the hangingwall of the western splay of Fault 2. Avulsion of these streams is thus not simply controlled by displacement on Fault 1, but also by motion on the Fault 2 splays, which determine the local topography within the F1 basin, the western splay having effectively divided the basin floor in two.

Only one profile was surveyed in the Fault 2 basin, but it shows a pronounced difference from the shape of the northern basins. Both the F0 and F1 basins are narrow, the axial channel confined by antithetic faults or hard fumarole-rich highs to the east. The Fault 2 basin is much wider, with a much lower fumarole region located over 600m east of the scarp. Consequently, the axial channel is much freer to migrate laterally across the low-gradient basin floor. A much gentler talus apron lies against the base of the fault, although incision of the axial channel is evident. [The apparent huge width of the channel is due to a bend, such that the stream runs subparallel to the profile: see Fig. 5.39.] Extrapolating the basin margin from the east towards the base of the fault implies that 4-8m of sediment has been deposited against the fault, although some of the original material may have been reworked towards the south by the axial channel, as seen in the shape of the sand body on the aerial photos [Fig 4.1]. Similar estimations of sediment thickness are not possible in the northern basins, as other structures obscure the dip-slopes of the western faults.

The hangingwall profiles demonstrate the influence of displacement variations both along-strike and perpendicular to the channel floor. Antithetic faulting in the north Fault 0 basin restricts the lateral stream migration, but also causes faster subsidence of this narrow basin. However, the low gradient stream within the F0 basin [~2m elevation drop over 150m] implies that sediment supply has also been relatively high, reducing the expected basin floor gradient. This is in marked contrast with the preservation of very steep slopes [see the 51m elevation drop between F0 profile 1 and F1 profile 1, and the axial stream profile, Fig. 5.25], mirroring the displacement profile of the

fault [Fig. 4.5], and implying that the basin has been relatively starved. Shallow basin floors produce are characterised by a shallow fine-grained alluviated channel, while the steep slope of the northern F1 basin drives bedrock incision, and a sharp change in channel pattern. The additional confining role of the fumarole high to the east is demonstrated by the progressive decrease in incision, and increase in the potential for lateral migration towards the south, as fumarole density decreases, and the high becomes more distant from the fault array. The gradual shift of the axial stream course to a less fault-proximal location towards the south [see Fig. 5.26] may reflect the recent pattern of fault activity since the development of the axial stream, as well as the reduced confinement by the fumarole highs [see Chapter 7].

5.2.4 Tributaries of the axial system

The largest contributor to the axial stream is the main channel from the central overlap [section 4.2.1], as demonstrated by the sharp change in morphology of the axial channel at their confluence [section 5.2.2.3]. The sediment from the central overlap channel does not radiate symmetrically from the source at the base of Fault 2, but is elongated towards the south. A thin pale line outlines the course of the axial channel in Fig. 4.1. This implies that the axial stream developed later than the central overlap stream, and has reworked a proportion of the ramp-derived sediment towards the south. A further tongue of sediment snakes towards the east from the central overlap stream [section 7.2], marking the course of the road stream [purple in Fig. 5.26] around the edge of the fumarole high [section 5.2.5.2]. The smaller streams from the central overlap [section 4.2.2] drain into the Fault 2 basin near its northern tip. The streams do not now flow directly into the axial system [Fig. 5.26], but their fine-grained deposits may well also be partially reworked towards the south.

The central overlap streams were the focus of section 4.2]. The following section discusses the contribution of the other tributaries to the axial stream, putting it into the wider context of the developing graben [Fig. 5.45].

5.2.4.1 Stream down F1/F0 overlap

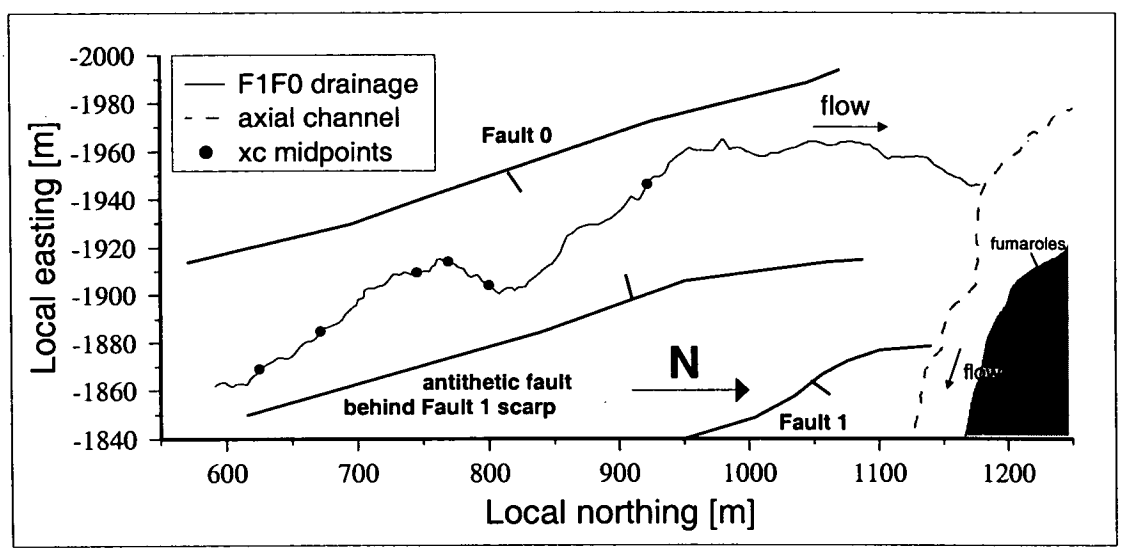

Figure 5.41: *Map of Fault 1/Fault 0 overlap showing drainage towards F0 hangingwall basin. Cross-section locations are marked for reference [see Fig. 5.42].*

The stream which flows down the overlap between Faults 0 and 1 [Figs. 4.11, 5.28 and 7.7] is the main tributary to the northern axial system. A channel can be traced from the top of the F1/F0 ramp, some 600m from the tip of Fault 1, and is probably supplied by runoff from a large relatively flat area in the footwall of Fault 1, north of the central overlap catchment. The ramp is steep [Table 5.4], reflecting the high displacement gradient on the northern tip of Fault 1 and also on Fault 0 [see Fig. 4.5].

Cobbles [$\leq$40cm diameter] in the upper reaches of the F1/F0 stream indicate a

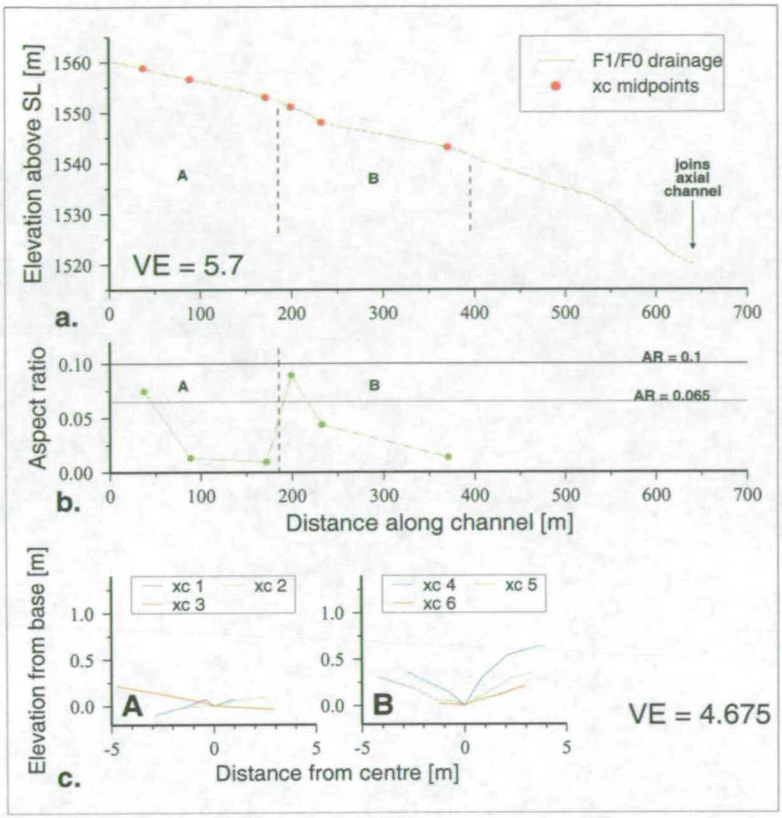

Figure 5.42: *a. Long profile of F1/F0 overlap drainage, showing the location of the surveyed cross-sections [VE = 5.7].*
b. Aspect ratio variation in the upper part of the F1/F0 overlap drainage.
c. Cross-sectional profiles in the upper F1/F0 overlap drainage.
Cross-sections were only surveyed in the upper part of this stream, due to GPS difficulties. Note that the cross-sections here are so small that they have been plotted at 4x the horizontal scale of the axial channel plots, although the vertical scale is identical. Hence VE = 4.675.
See also map in Fig. 5.41, and Table 5.4 for averaged reach gradients.

relatively large discharge. Bedrock incision occurs along some small steep stretches [Fig. 5.42a]. The lower reaches of the channel are sandy, and drain over a huge fan of sand built up at the base of the ramp [Fig. 5.27b], whose volume is testament to a prolonged high discharge down the overlap. The axial stream has probably already stripped a lot of sediment from the F0 basin, into the F1 basin, and thus the sand pile at the base of the F1/F0 overlap may be the erosional remnant of an originally much larger contribution. Certainly, with the present topography, little sediment from the ramp would be preserved in the F0 basin, as most would be rapidly carried down into the lower Fault 1 basin [Fig. 7.7]. Thus development of the through-going axial system has shifted the locus of deposition away from this narrow high basin and down into the relatively starved Fault 1 basin.

Channel	Length (m)	Gradient (°)
F1/F0 overlap stream	168.41	-2.378
	55.61	-4.116
	8.60	-7.346
	147.17	-2.118
	150.18	-3.560
	23.01	-5.079
	34.60	-8.919
	8.72	-4.748
	38.26	-6.947
	168.41	-2.378
whole stream	**802.97**	**-2.85**
Fumarole drainage	587.75	-3.172
	2.61	-12.676†
	117.39	-2.331
whole stream	**707.75**	**-3.07**
Corral F stream (axial to fault)	446.71	-0.978
	148.32	-0.803
	273.10	-0.686
	499.53	-0.385
	15.97	-5.291‡
	314.55	-0.087
	159.21	-0.358
whole stream	**1857.39**	**-0.59**
Main central overlap stream		
Average whole	476.54	-5.60
Average non-faulted		-3.53

Table 5.4: *Variation in downstream bed gradient of the axial stream tributaries.*
Averaged gradient of reaches from upstream to the junction with the main axial channel. See Figs. 5.42a, 5.43 and 5.44 for long profiles.
†*:small fault ridge.* ‡*:plungepool from axial incision through Corral fault.*
The low gradient of the stream axial to the corral fault is very similar to the sandy reaches of the main axial channel, Table 5.3.
The main central overlap channel crosses three major faults, while these other tributaries do not cross scarps. Hence the average gradient of the whole channel and of the non-faulted reaches are included for comparison. See also Table 4.3.

5.2.4.2 Tributary from fumarole high to east

Sediment is not only supplied to the axial system from the uplifting footwall highs, but also from the fumarole-rich high to the east of the faulted basins. The mounds themselves are extensively fractured, and the high ground generally covered in angular tuff fragments up to 30cm across. Drainage systems can be traced across this high ground by the increased concentration of well-rounded clasts, although distinct channels are rare, implying a more diffuse flow. One stream surveyed from the fumarole high ground to the east of the Fault 1 basin is included here as a comparison with the larger F1/F0 overlap channel [Fig. 5.26]. The channel itself is small and shallow, though occasionally incising bedrock at breaks in slope, on fumarolic ridges. Rounded cobbles [≤30cm] occur throughout the upper reaches, but fine downstream to sand at the confluence with the axial stream. The stream has a fairly constant gradient, which may suggest that it is quite long-lived [Fig. 5.43 and Table 5.4]. A similar channel drains NE off the fumarolic high ground into the 'fumarole-axial' channel discussed in section 5.2.5.1 [Fig. 5.47].

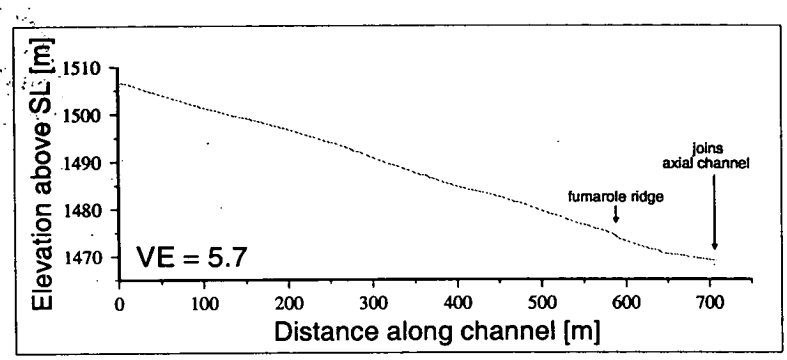

Figure 5.43: *Long profile of tributary channel from fumarole high to northeast. Gradients are given in Table 5.4.*

5.2.4.3 Hangingwall of Corral fault

A small stream flows very proximal to the base of the Corral fault [Fig. 5.26]. The stream was surveyed from the tip of the fault at Casa Diablo Road to a small corral southwest of the fault, which has been artificially irrigated recently. The hangingwall channel is 1-2m wide, but rarely over a few centimetres deep. Rounded pebbles 5-20cm in diameter dot the upstream reaches and occasionally the base of small overlaps in the fault, but the channel is predominantly lined with fine sand. The gradient is very low, except where the channel flows into the plungepool scoured out by the axial discharge through the Corral fault scarp [see Fig. 5.44 and Table 5.4]. Gradients are equivalent to those in sandy low gradient reaches of the main axial channel [compare Tables 5.4 and 5.3].

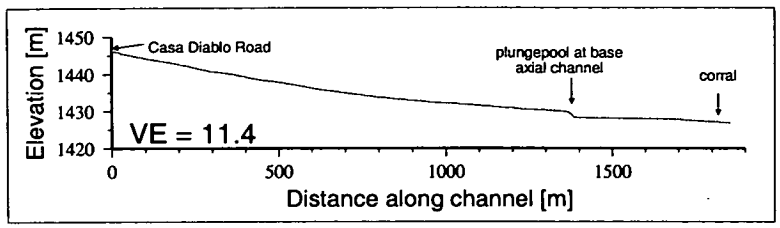

Figure 5.44: *Long profile of channel in hangingwall of corral fault.*
NB Vertical scale 2x other profiles. The channel was only traced to the corral [see Fig. 5.26]. The pronounced step marks where the channel flows into the plungepool scoured out by the axial channel incising the Corral Fault scarp. Gradients are given in Table 5.4.

5.2.5 'Fumarole-axial' network

5.2.5.1 Main fumarole-axial stream

The 'fumarole-axial' channel [red in Figs. 5.26 and 5.45] flows along the eastern margin of the fumarole-dense area east of Fault 1. It flows southward, into the stream which runs down the centre of the graben, roughly parallel with Casa Diablo Road [see section 5.1.1.2].

The fumarole-axial channel is 2-5m wide, and alluviated along all of its surveyed length. Rounded cobbles, up to 30cm across, litter its upstream reaches. Many of these clasts are supplied from the fumarole high immediately to the west, by tributaries very similar to the one which drains westwards towards the fault array [section 5.2.4.2, and see Figs. 5.46 and 5.47]. Near the largest fumaroles, the fumarole-axial stream increases in depth to almost a metre. Further downstream, the channel is shallow and sandier, though still broad, with occasional rounded pebbles.

The long profile is surprisingly smooth, with a uniform low gradient for over a kilometre, equivalent to the lower reach of the main fault array axial channel where it flows close to fumaroles in the southern [F2/F4] basin [Fig. 5.46 and compare Tables 5.3 and 5.5]. Steepening only occurs at Casa Diablo Road [Fig. 5.46 and Table 5.5]. There are no knickpoints and no significant morphological change occurs at the southern end of the fumarole-rich area [Figs. 5.24 and 5.45]. The channel is therefore relatively mature, having already compensated for lithological differences.

However, the surveyed profile does not include a steepened headwater reach, as the channel is apparently beheaded by the incision of the downstream northern channel [section 5.1.1.2] through this fumarole high in response to motion on faults downstream [Figs. 5.45 and 5.47]. The beheaded fumarole-axial channel may have been an early course of this northern channel which was cut off by incision of another [now main] branch; or possibly been connected to a stream which originally flowed from further northeast.

The fumaroles along this channel prevent lateral migration to the west. The fumarole-axial channel may have developed early relative to the development of the fault array, carrying water and sediment from the northern faults towards the south. Subsidence of the fault-proximal sub-basins provided a depocentre for sediment from the uplifting footwalls, and also for some runoff from the fumarole high. However, being confined

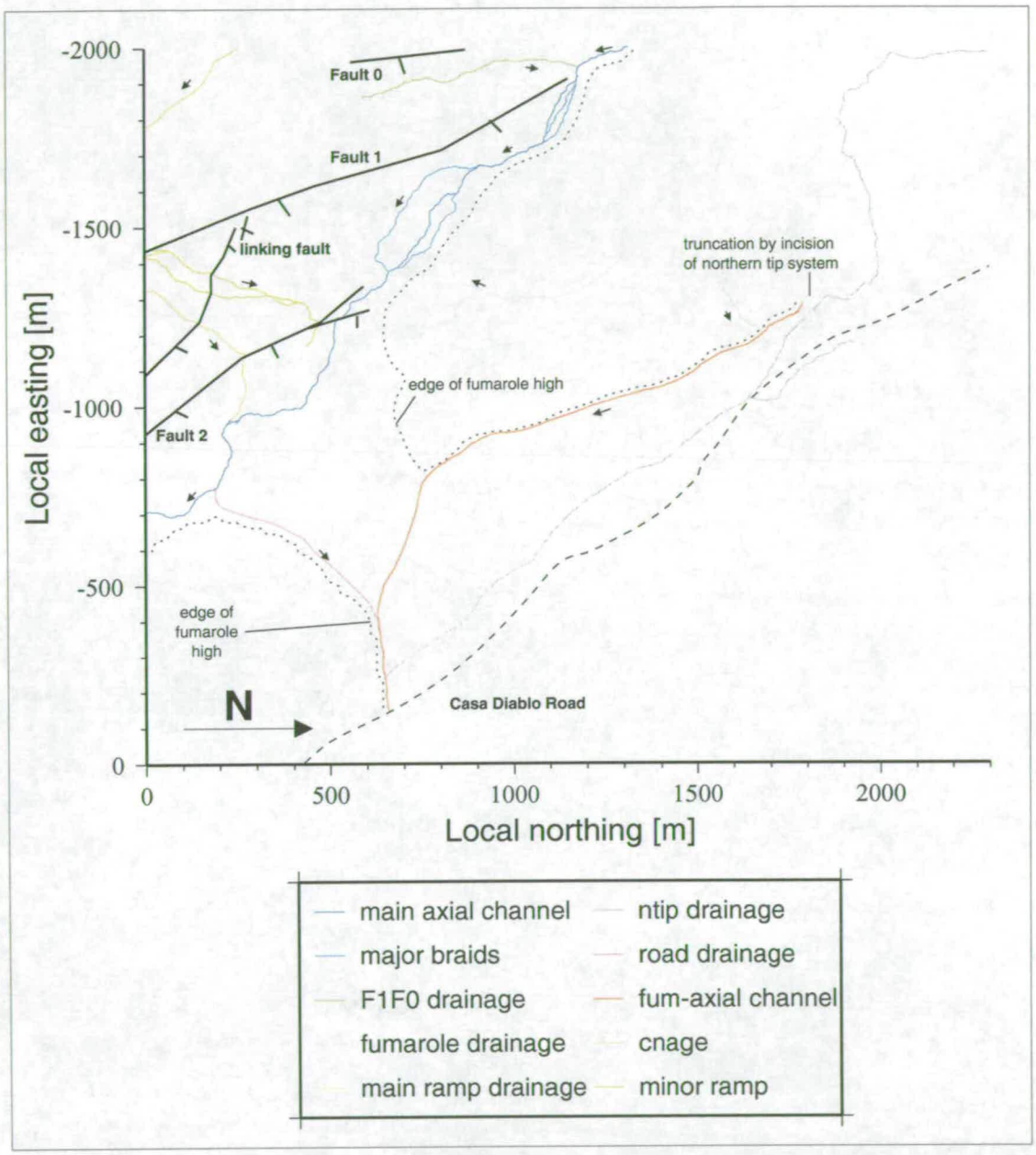

Figure 5.45: *Map of central graben, showing the relative locations of the fault-proximal 'main' axial channel and the 'fumarole-axial' channel.*
Small arrows show the direction of flow in each stream. Note the course of the northern tip stream. Incision of the downstream northern channel has beheaded the fumarole-axial stream [see text and Fig. 5.47].

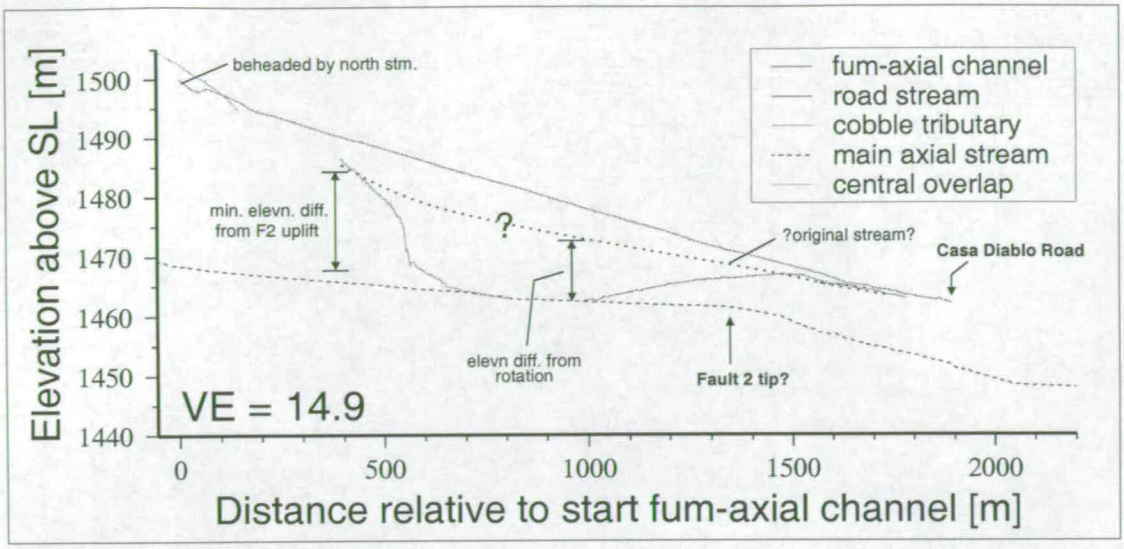

Figure 5.46: *Long profile of 'fumarole-axial' channel and related streams. Note the relative gradient of the fault-proximal axial stream, dotted.*
The change in polarity of the 'road stream' profile demonstrates the impact of the Fault 2 growth. The dotted line is a potential earlier stream profile, connecting the central overlap to the east; cut off y the growth of Fault2, and the subsidence/rotation of the hangingwall [see text].

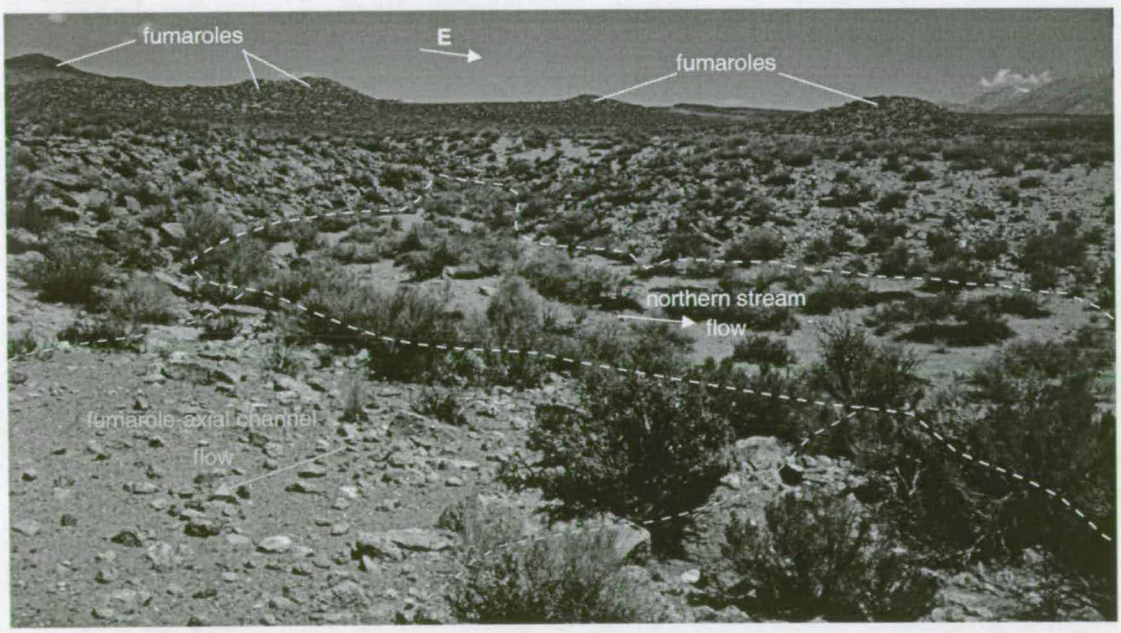

Figure 5.47: *View of truncation of the fumarole-axial channel.*
Fumarole-axial channel flows to the south [lower left of photo]. Cobbles are supplied by runoff from the high fumarole-dense ground to the west. Broad incised channel flowing southeast [left to right] is part of the incised reach of the downstream northern stream [section 5.1.1.2]. The stream bed is ~2m lower than the fumarole-axial channel. The fumarole-axial channel appears to have been beheaded by incision of this reach of the northern stream, probably due to motion on faults further east. See section 5.1.1.2 and Chapter 7].

bey the fumaroles, the fumarole-axial stream could not have responded to fault-induced subsidence by westerly avulsion towards the scarps. Hence, the new axial system developed proximal to the array ['main' axial channel, navy in Fig. 5.45], controlled by the gradual connection of the hangingwall sub-basins. It appears that at some point, the northern supply to this channel was re-routed down the present downstream northern tip channel. Hence, due to confinement by the fumaroles, the fumarole-axial stream has been left an irrelevant dinosaur between a proximal axial system, developed in response to the interaction and linkage of the western fault array; and a stream which carries sediment from the northern part of the array down the centre of the developing graben [~ present Casa Diablo Road].

Reach	Length (m)	Gradient (°)
Fumarole-axial stream	45.41	-1.09
	100.37	-0.29
	1017.38	**-0.77**
	355.18	-1.34
	70.31	-1.09
	192.44	-1.19
	36.38	-1.89
	35.53	-2.57
whole stream	**1853.00**	**-1.17**
Fumarole tributary	38.56	-4.20
	163.81	-2.51
whole stream	**202.37**	**-2.83**
Road stream	233.64	**+0.77**
	111.00	**+0.43**
	132.34	**+0.26**
	64.53	-0.20
	49.92	-1.25

Table 5.5: *Variation in downstream bed gradient of the 'fumarole-axial' channel and tributaries. Averaged gradient of channel reaches from upstream to Casa Diablo Road. The whole channel has a uniformly low gradient, steepening only immediately upstream of Casa Diablo Road. Gradients are also calculated for the tributary from the fumarole high to the northwest, and the east-west 'road' channel which runs from the Fault 2 basin [pale green and purple in Fig. 5.45, respectively]. Gradients of the latter channel are calculated from its junction with the* main *axial channel, west to east. Positive gradients in bold reflect a western slope, probably due to a change in the topography after the initial development of this channel [see text].*

5.2.5.2 'Road stream': Fault 2 basin to Casa Diablo Road

A small channel can be seen , running virtually east-west along the margin of the southern fumarole high and connecting the main central overlap channel to Casa Diablo Road [red in Figs. 5.26 and 5.45]; highlighted by pale sand deposits on the aerial photograph [Fig. 5.24]. This stream looks similar in the field to the sandy part of the fumarole-axial channel, which it joins near the fumarole high, 250m from Casa Diablo Road, being on average 2m wide and around 40cm deep, and carrying predominantly

sand. The long profile of this channel [Fig. 5.46] changes slope direction shortly before joining the fumarole-axial channels, while the western part of this profile appears to follow a very smooth curve. However, there is no change in morphology or sediment load in the channel at the change in polarity.

This evidence suggests that the present profile is the result of a subsequent change in topography and that it does not reflect two originally distinct channels draining a topographic high. The coincidence of this channel with the course of the main central overlap channel and the clear sand trail along its course suggest a likely connection of the two channels [Fig. 5.24]. The angle of the junction of the road stream and the fumarole-axial channel implies that both originally drained in the same direction: to the E/SE. The fumarole-axial profile [Fig. 5.46] confirms that the current slope of the eastern portion of the road stream [to east] is likely to be original.

Pinter and Keller (1995) suggested that the Tableland streams initiated flowing down a regional tilt towards 121-125°. This would imply that the central overlap streams drained towards Casa Diablo Road. The location of the fumarole highs to the north and south probably had a major influence on the downstream development of these streams, and hence the road stream seems a feasible early downstream route for any supply that left the F1/F2 overlap. Rotation of the F2 hangingwall, demonstrated by the hangingwall profile [Fig. 5.40] was probably responsible for the present slope of the western part of the road stream. Motion on Fault 2 similarly resulted in the formation of the knickpoint in the central overlap stream. Thus as Fault 2 grew, the connection to the east was cut off through subsidence and rotation of the hangingwall, ponding sediment derived from the central overlap in the growing Fault 2 basin. Some of this material has subsequently been reworked southwards by the fault-proximal axial system [see Fig. 5.24].

5.2.6 Summary of axial stream data

The axial channel drains from the footwall of Fault 0, parallel and quite proximal to the southern part of the fault array. No significant discharge is derived from the hangingwalls to the north. In the northern basins, the channel is closely confined near the base of the western faults by an antithetic fault and then a hard fumarolic high. As the fumaroles become more distant from the faults further south, the channel is freer to migrate laterally, and gradually moves further from the scarp bases. Although it probably originally continued southwards into the central graben, the stream is lost as it enters a recently irrigated area in the hangingwall of a small fault oblique to the main array [Fig. 5.26].

The axial stream evolution is closely controlled by the tectonic development. Where faults are crossed, the channel morphology follows a similar pattern to that seen in other surveyed streams. The aspect ratio increases dramatically in the steepened reach upstream of the scarp, and then instantly decreases in the hangingwall basin [Fig. 5.48]. Dramatic changes in bed gradient in the northern Fault 1 basin reflect the along-strike variation in displacement on the fault. Cross-sectional morphology is strongly correlated with bed gradient, particularly in the Fault 1 hangingwall basin, where aspect ratio decreases rapidly down the steep northern slope. Uniformly low aspect ratios are seen in the shallow sandy basins [southern part of F1 basin, and southern [F2-F4] basin], and in the footwall of Fault 0, upstream of the fault's influence.

Connection of individual fault sub-basins is dependent on the along-strike variation in subsidence of the individual basins, and on the sediment supply to each basin. Much of the sediment is supplied from the footwalls to the west, predominantly from the fault oversteps [e.g. sections 4.2.1 and 5.2.4.1]. A smaller volume reaches the axial system from the fumarole high to the east [e.g. section 5.2.4.2] and along the hangingwall of the Corral Fault to the south [section 5.2.4.3]. Due to the geometry of the faults and the incision of the main stream through the F1/F2 overlap, little sediment derived from the F1 footwall high enters the F1 basin directly. Instead, the main F1/F2 overlap stream and the F1/F0 overlap channel funnel sediment into the F2 and F0 basins, respectively. Consequently, the narrow F0 basin has obtained a relatively large sediment fill, and developed a flat basin floor, while the F1 basin has remained relatively starved [Fig. 5.40]. However, a high supply to the Fault 0 basin, and lower subsidence than in the Fault 1 basin, has allowed the through-going axial stream to spill over into the lower basin to the south. Hence sediment supplied particularly from the F1/F0 overlap now bypasses the Fault 0 basin, and is instead carried into the large 'hole' in the F1 hangingwall. The axial stream is also responsible for reworking of sediment away from the Fault 2 basin towards the Corral fault basin to the south.

Fumaroles play a critical role in the evolution of this stream, by restricting its lateral migration and causing deep incision, particularly in the northern F1 basin. Fumaroles also constrict the southern Fault 0 basin, allowing the basin to fill quite rapidly. Further downstream, isolated fumaroles deviate and split the axial stream.

Other nearby systems provide insight into the relative timing of their development [section 5.2.4]. Reworking of sediment derived from the central overlap [Fig. 5.24] places the axial development in this region later than the ponding of sediment in a discrete Fault 2 basin. This must also postdate the rotation of the F2 basin, which

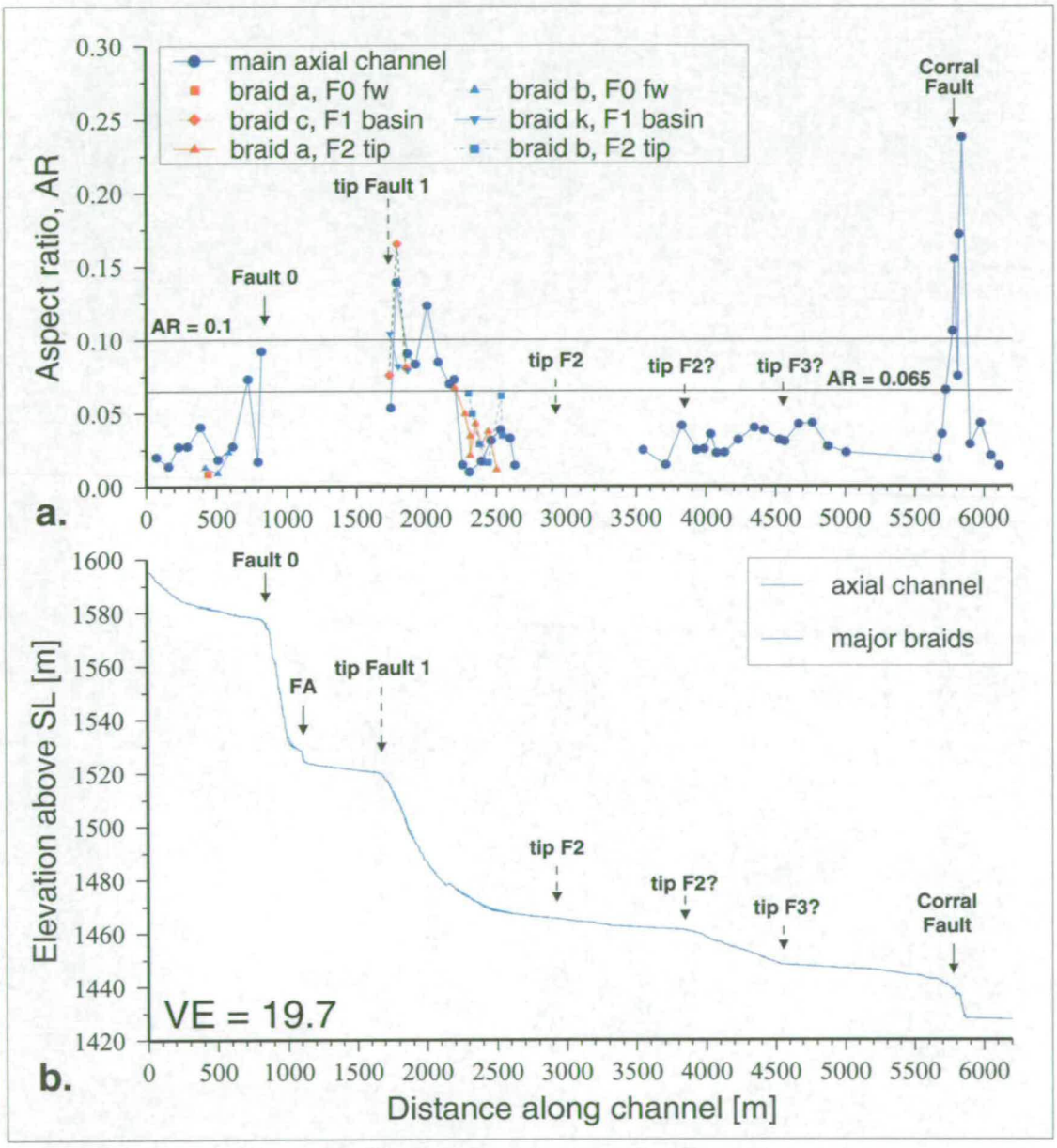

Figure 5.48: *Downstream variation in aspect ratio of axial channel.*
a. Aspect ratio [bank-base depth/bank-bank width] plot of main channel and braids.
b. Long profile of main axial system.
Variations in AR match the broad shape of the long profile, with higher aspect ratios in the steepest reaches. The stream flows perpendicular to the faults for the first 1100m [through F0 and FA], and the last 300m [through Corral fault]. The drop in the northern F1 basin is almost as steep as through the fault scarps [Table 5.3].

appears to have cut off supply from the F1/F2 [central] overlap towards the main graben to the east [section 5.2.5.2]. The south-flowing stream along the eastern margin of the eastern fumarole high ['fumarole-axial' stream: section 5.2.5.1] demonstrates a potential early route for sediment from the north of the array. However, confinement by the fumarole high probably prevented lateral migration of this fumarole-axial channel, resulting in the subsequent development of the main axial system proximal to the fault array, as basins developed in the subsiding hangingwalls and then linked along strike. The fumarole-axial channel has also been cut off from supply from the north by incision of the northern tip system into the fumarole high, resulting in transport of the northern sediment in a channel down the centre of the graben, near Casa Diablo Road [sections 5.1.1.2 and 5.2.5.1].

5.3 Summary of Chapter 5

The central overlap streams [section 4.2], have been compared with two other drainage networks from the fault array: a northern transverse system, and the stream which flows axially to the southern part of the array. Both these systems show evolution dominated by normal fault development, and also influenced by lithological heterogeneities. Similarities between these systems and the central overlap drainages lend weight to the observations made in Chapter 4, while differences between them constrain the respective influences of the faults and lithological variations, and their interaction with other factors such as sediment supply and stream power. These systems thus put the central overlap streams into the wider context of the evolution of drainage systems around the array as a whole.

The northern tip system [section 5.1] flows in a similar direction to the streams which drain the central overlap, but drains a far larger catchment [Fig. 5.1] and demonstrates a higher discharge. The deep gorge incised through the northern tip of the array has a far lower gradient than that through the footwall of Fault 1, and only a single knickpoint remains, at the downstream end of this gorge, despite the number of faults crossed. This partly reflects the distribution of deformation onto a series of small faults, but also points to the influence of stream power: the high discharge stream has adjusted more fully, and probably more rapidly, to the tectonic uplift [section 7.1.3]. Large, heavy non-tuff clasts in the northern stream are also testament to a high discharge, as well as implying a larger catchment, or the influence of a prior distributary system over this area [section 7.4].

The northern stream crosses a series of faults, showing a similar pattern of incision, and hence aspect ratio, as seen in the central overlap streams. Overall, the wavelength and amplitude of the response is roughly proportional to the fault uplift [section 7.1.3.2]. Tributaries to the northern stream [section 5.1.3] demonstrate the effects of along-strike variation in displacement on the faults they cross, resulting in stream responses varying from incision to lateral deflection. Downstream of the main array, the channelling effects of the faults force the northern stream to bend alternately parallel and perpendicular to the structural grain. The influences of lithological heterogeneities observed in the central overlap are also seen here, with fumaroles helping to funnel the streams, and stream morphology varying with the jointing of the tuff. Although the tuff in the central overlap was relatively uniform, variations in its strength and consolidation in this northern region drive some variations in incision.

The axial stream, in contrast, appears to be sourced from a much smaller catchment in the footwalls of the western faults, squeezed between the central overlap and northern tip drainages [Fig. 5.1]. Some water comes from the fumarole high-ground to the east [Fig. 5.26]. Despite its initially small catchment, the axial system is important in reworking sediment between the hangingwall basins of faults in the array. Where the axial stream crosses fault scarps, it responds in a similar way to the transverse systems above, incision increasing towards the scarp, and deposition occurring in the low-gradient hangingwall. However, the axial stream predominantly provides information on the along-strike variation in displacement accommodation, particularly on Fault 1, where the displacement profile [Fig. 4.5] has a major impact on the morphology of the stream in the hangingwall basin.

The main value of the study of the axial stream is in constraining the relative timing of development of different parts of the local drainage pattern, and hence of the fault array. The development of a through-going axial system is dependent on the along-strike connection of individual fault sub-basins, and hence the stream system constrains the linkage of faults, and provides information about the sediment supply. Water could not enter the F1 basin until the high IBH lip was overcome [see Chapter 2], here dependent on filling the higher F0 basin over the lip [section 7.3]. The importance of the F1/F0 overlap as a sediment supply route is shown. The preservation of steep slopes in the F1 basin shows that sediment supply to the F1 basin was incredibly low prior to the development of the axial stream. Extrapolation to the central overlap implies that most sediment carried by the footwall stream was focused down the main [southern] channel into the F2 basin, and comparatively little was carried down the smaller streams draining the north of the ramp [section 7.2].

Other small streams constrain the downstream deposition of sediment derived from the central overlap. The road channel implies a temporary supply to the east. Connection of the hangingwall basins along-strike was followed by southward reworking of the ponded sediment by the axial system. The south-flowing stream which flows along the fumarole high [section 5.2.5.1] constrains the development of the northern stream which beheads it. It also highlights once more the influence of fumaroles on the lateral migration of streams, here isolating different parts of the graben, and leading to the development of discrete axial streams.

More quantitative constraints on the development of the central overlap streams are provided by the cosmogenic isotope study which follows, in Chapter 6. A detailed discussion of the fieldwork results, and models for the stream evolution are in Chapter 7.

Chapter 6

^{10}Be and ^{26}Al Cosmogenic Isotope Analysis - Fieldwork and Results

This chapter describes the cosmogenic isotope analysis carried out on samples from the Volcanic Tableland. The intention of this study was to obtain apparent exposure ages for samples from the channels in the main overlap [section 4.2]. These ages may then be used to assess the rates at which the channels changed in response to the fault growth in this overlap, and to cast light on fault-influenced channel evolution in similar overlap zones elsewhere.

The basic application of *in situ* cosmogenic isotope analysis to geomorphic problems is explained in section 2.5, with examples of previous geomorphic and tectonic studies in section 2.5.3. A fuller explanation of the theory is in Appendix A and a brief outline of the laboratory procedures referred to extensively in the second part of this chapter is given in section B.2. The glacial periods referred to in this chapter are discussed in section 3.1.1 and the data constraining their timing is presented in Table 3.1.

6.1 Field approach

The cosmogenic isotope data collected from the Volcanic Tableland sites may also be used to answer several questions about landscape evolution in this area. Pinter and Keller (1995) suggest that increased runoff during the first of the two major Sierran glaciations that occurred after the emplacement of the tuff [pre-Tahoe, 206 - 131ka: see section 3.1.1], acted as a trigger for the formation of channels on the Tableland. They also suggest that the channels may have been reoccupied during the following Tahoe glacial stage [79 - 56 ka: Pinter and Keller (1995), but see Table 3.1]. If true, this should be reflected in the exposure ages of the channel samples.

The particular pattern of sampling described below was chosen in the hope of gaining information about the style of channel evolution in the central fault overstep of the array, and particularly in the main channel [section 4.2.1]. The channel cuts through several fault scarps, each marked by a pronounced step in the long profile [see Fig. 4.24].

Analysis of the variation in apparent exposure ages along the channel should cast light not only on the rate, but also on the method of channel incision, and potentially also on the migration of the knickpoints formed by repeated uplift at these fault steps. This is discussed in more detail in section 7.2.2.

Another important question is the rate of erosion on the Volcanic Tableland. Although the current semi-arid climate indicates a low erosion rate, this may not have been the case for the entire history of the Tableland. However, the Tableland is famous for the petroglyphs exposed on tuff blocks in various places, including a fantastic collection at Chidago Canyon. Such amazing preservation of symbols scratched into the relatively soft tuff possibly more than 4000 years ago is indicative of very low erosion rates at least during this period. Long-term low erosion rates are further indicated by the excellent preservation of the fault scarps [e.g. Figs. 4.3 and 4.23], and also of fine-scale erosional textures in the channels [see Figs. 5.14d and 4.29a,b.]. Sediment deposition on the Tableland is again volumetrically small in comparison with many extensional basins, despite the number of channels crossing the tuff surface. Cosmogenic analysis can be used to estimate *minimum* erosion rates, and hence is also a useful tool in assessing the evolution of structures on the surface of the Tableland [section 7.2.2.5].

Nishiizumi et al. (1989) collected a sample [their W86-20] from the base of the Bishop Tuff nearby, to calibrate their exposure ages for the underlying Sherwin Till. However, no other samples are known to have been collected from the Bishop Tuff, and *in situ* cosmogenic analysis has not been used to investigate the evolution of surface features on the Volcanic Tableland before. Hence one of the other main aims of this part of the project was to establish whether cosmogenic analysis could be used successfully with this rock type, and in this environment. As such, the work described below has also proved the feasibility of cosmogenic ^{10}Be and ^{26}Al work to constrain rates of geomorphic processes in the area [section 7.2.2].

6.1.1 Sampling strategy

Eighteen samples of the tuff were collected for cosmogenic ^{10}Be / ^{26}Al analysis [Fig. 6.1]. Samples 1-15 were collected from the drainage channels in and around the main overlap [section 4.2]. Of these, samples 1-9 were in the main channel in the ramp; 13 and 14 were taken from the bank and floor, respectively, of the main channel within the footwall of the large fault, Fault 1; and samples 11, 12 and 15 were taken in the minor channels further north in the overlap [section 4.2.2].

It was important that I sampled bedrock that had been exposed by deep incision of the channels into the surface of the tuff. Most of the main channel through the ramp and especially in the immediate footwall of the main fault, Fault 1, incises bedrock [section 4.2.1] and there is relatively little sediment storage in the channel bed. In sampling, I avoided areas with a veneer of sand or small pebbles, instead choosing bedrock where there was no nearby sediment which might have shielded the rock from cosmic radiation. I also looked for tuff that showed the lowest signs of physical weathering after its exposure. Dark coloured desert varnish has developed on many of the tuff surfaces on the Tableland, but in some places, there is pronounced flaking and spalling of this varnished surface that could be a problem for measuring cosmogenic abundances. In many parts of the channels, fine-scale abrasional features are preserved from the fluvial

scouring [e.g. Figs. 4.29b and 5.14d], indicating low rates of post-fluvial erosion. Hence sites with evidence of well-defined scouring or smoothing, and dark desert varnish were selected. Photographs of the sites of the analysed samples are shown in sections 6.1.2.1 to 6.1.2.6.

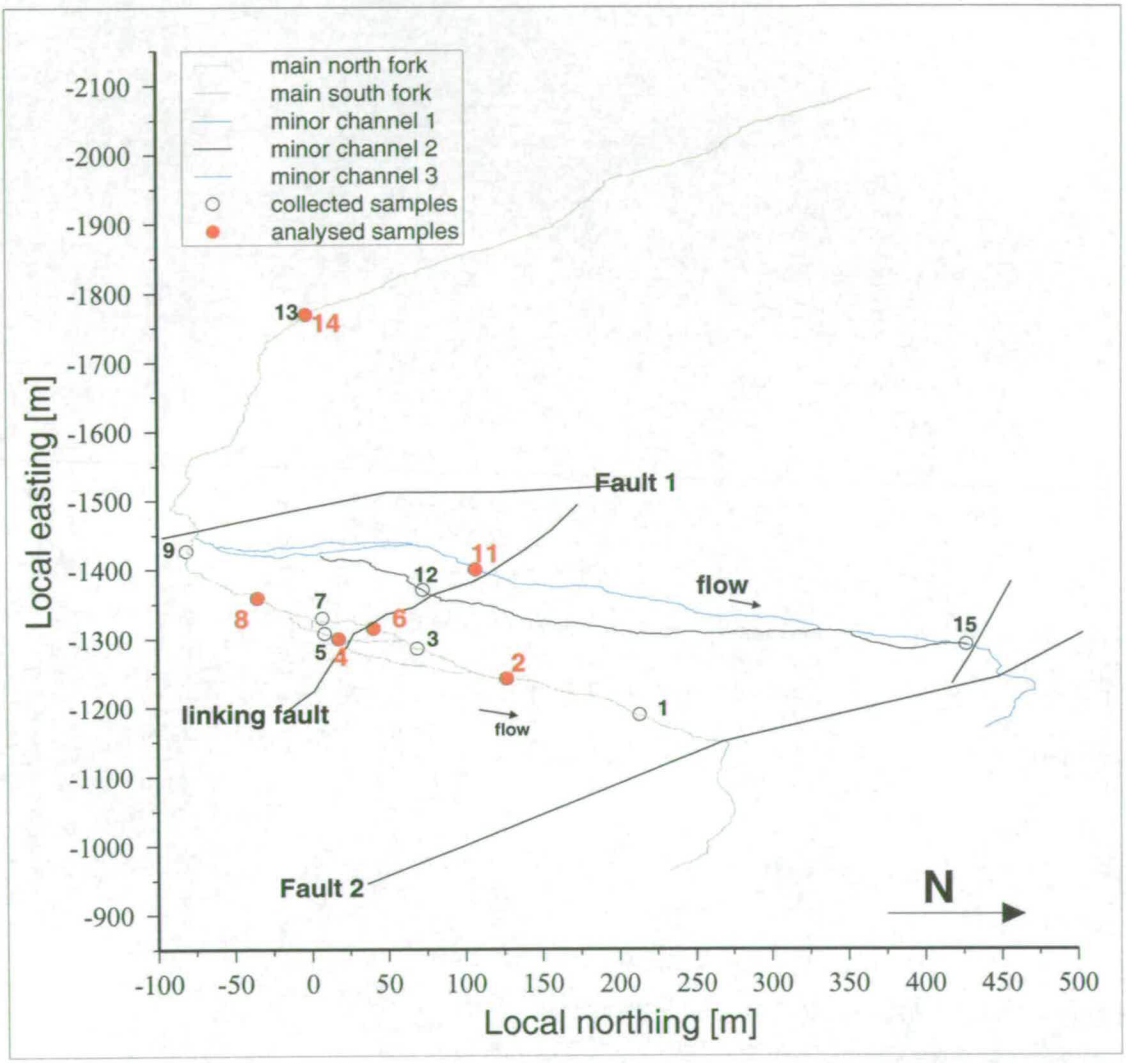

Figure 6.1: *Map showing the locations of the eighteen cosmogenic samples collected from the overlap area. Samples 1-12 and 14-15 were taken from the base of channels; sample 13 was collected in the bank above sample 14. Samples 16-18 were taken from the fault scarp at locality 9a. Samples highlighted in red were analysed in this project [see below].*

Samples 16-18 were collected from a steeply dipping [~80°] planar surface on the scarp of Fault 2. Distinct bands in the scarp are highlighted by different weathering patterns, with degradation increasing towards the top (oldest part) [Fig. 6.2]. Soil lines and a couple of small soil patches on the lowest band [Fig. 6.3] imply that this part of the scarp was below the ground surface until relatively recently. Similar variations in the degree of weathering of scarps have been described on normal fault scarps in Greece [e.g. Jackson et al. (1982)] and the Hebgen Lake fault scarp, Montana (Zreda and Noller, 1998): Fig. 2.34], and interpreted as parts of the scarp exhumed in successive

earthquake events. The pronounced differences in weathering between the bands imply a significant hiatus between the exhumation of the different parts of the scarp, and hence these bands may represent at least clusters of events, if not single slip episodes. Samples 16-18 were taken from the lowest three of these weathering bands [Fig. 6.2].

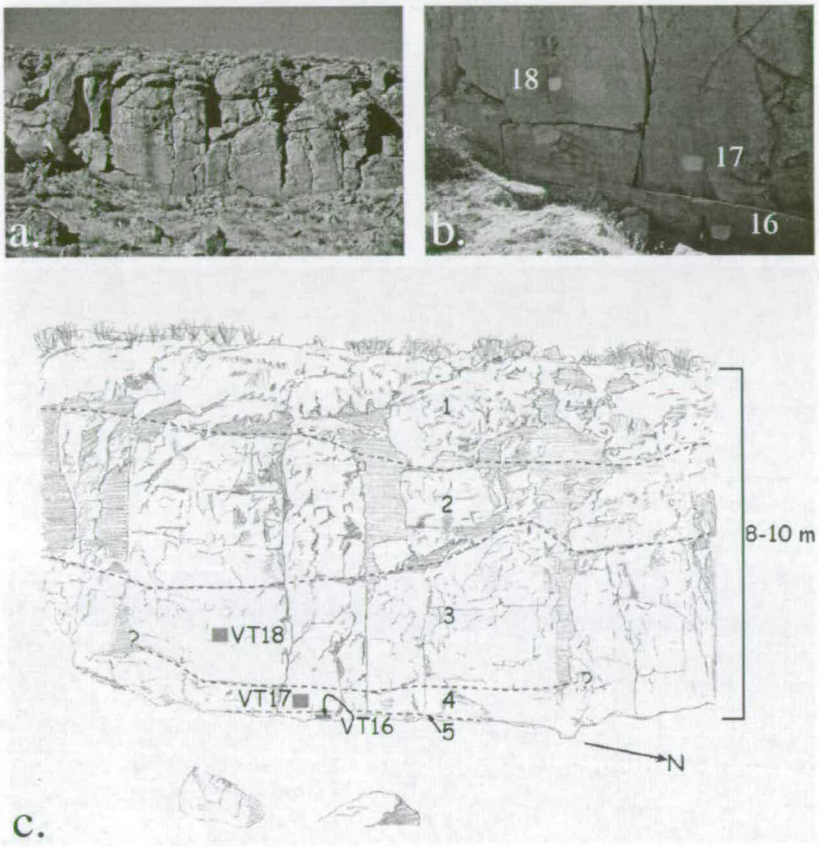

Figure 6.2: *Near-planar surface in Fault 2 scarp, at locality* ***9a****.*
a. and b. Field photograph of scarp showing the locations of samples 16-18 in the lowest three weathering bands. The red box in [a] marks the part of the scarp visible in [b]
Hammer for scale by sample 16 location is 40cm long.
c. Field sketch interpretation of the weathering bands. Field description:
1 - dark patina, rounded edges to blocks, well-flaked, some smooth surfaces, brown-yellow; good lichen covering; loose blocks mostly in place
2 - most of surface lost, leaving flaked irregular surface; brown to pink; little lichen; much recessively weathered; blocks fallen out
3 - patchy surface, parts 60% smooth, rest as '2'; horizontal fabric of aligned grains evident; plucked-out phenocrysts; patches weather dark, esp. where water stained; rest pink
4 - virtually intact smooth outer surface; fabric evident; smooth to touch; pink; some soil lines
5 - [lowest part visible in centre of block only]: below soil patches and lines; fully smooth, pink

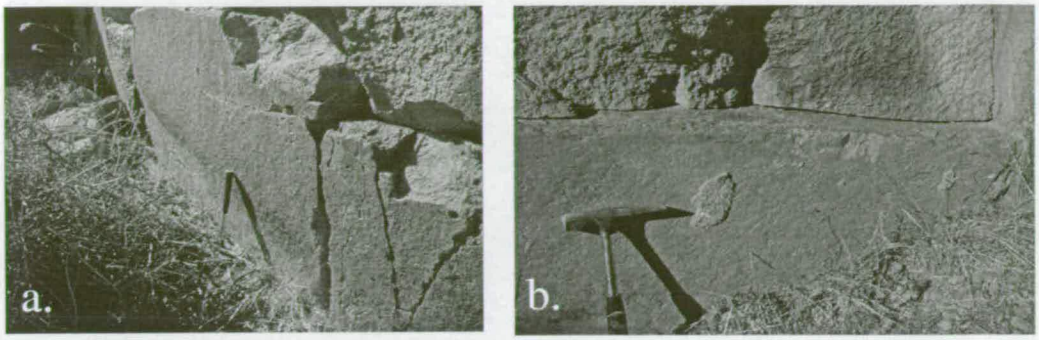

Figure 6.3: *a. Soil lines and b. soil patch attached to the planar surface of Fault 2 scarp at locality 9a. Hammer (40cm long) for scale.*

^{10}Be and ^{26}Al in these samples are produced from cosmic ray bombardment predominantly of Si and O atoms within quartz crystals. Cosmogenic isotope production decreases exponentially with depth, so if calculations of exposure age and erosion are based on the sample being at the surface of the outcrop, then errors are introduced if thick samples are collected [section A.1: Fig. A.2]. As the exact cosmic ray flux hitting the target must be known, any obstructions shielding the target site must also be quantified. This therefore requires that the topographic shielding be measured, and that the the sample be collected from as small an area as possible, to ensure that the shielding measurements are valid for the entire of the sample [see also section A.4.2 and Fig. A.3]. The targets for AMS needed to be made from at least 15-30g pure quartz after the mineral separation and etching [see section B.2]. Thus determining the exact sample size to collect is a case of obtaining a balance between having enough material for analysis and ensuring that the sample is collected from as small an area, and as thin a slice of the top of the exposure, as possible.

I collected samples of 500-900g in weight [whole rock], depending on the ease of collection, and while ensuring that the samples were no more than 3cm thick, this meant that I sampled an area usually much less than 20cm in diameter, [see photographs in Sections 6.1.2.1 to 6.1.2.6 below]. Shielding [section A.4] of the sample was determined by measuring the inclination of the horizon from the sample site in sixteen sectors around each sample [e.g. Fig. 6.13]. Corrections for sample thickness and topographic shielding are made in section 6.3.

The cosmic ray flux varies with latitude and elevation, as explained in section A.1. Hence for calculation of the production rate, the exact latitude and elevation must be known at the sample site. I measured the location of the sample sites using differential GPS [as described in section B.1] by collecting stationary carrier-phase data over half an hour. Thus the latitude, longitude and elevation above sea-level of each sample are known to less than a centimetre.

6.1.2 Analysed samples

Although eighteen samples were collected in the field, the time-intensive nature of the target preparation, as well as the high costs of AMS analysis, dictated that only a few of these samples could be analysed in this project. Targets are prepared in fours, where one sample in each batch is a blank or control, to assess any possible effects on the samples of the addition of the various reagents [see section B.2]. Thus I chose 6 samples [marked in red in Fig. 6.1] - making 2 full batches including the blanks. Although the three fault scarp samples were interesting, these samples are the smallest samples collected and have the greatest topographic shielding. If young, their cosmogenic content might be below detection. Their analysis would also only allow investigation of three channel samples. Since widely varying ages are expected along channels where incision is dominated by knickpoint retreat [e.g. Seidl et al. (1997)], analysis of only three samples would provide less information about the evolution of the overlap.

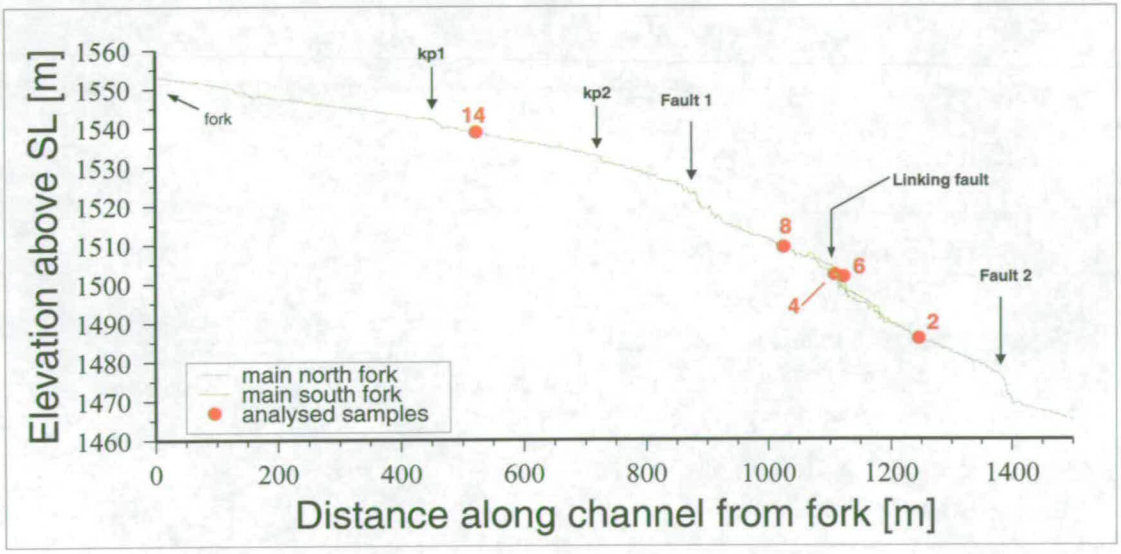

Figure 6.4: *Long profile of the main channel showing the location of the analysed samples. Note that the sample 4 is in the southern fork of the channel where it crosses the linking fault [Fig. 4.30].*
Sample 11 was taken in a minor channel further north in the ramp. Its location relative to the linking fault is similar to that of sample 4.

I also hoped to analyse the pair of samples from the bank and base of the main channel in the footwall of F1 [13 and 14, respectively], in the hope of gaining information about the incision rate in the footwall of Fault 1. However, after crushing and etching sample 13 [see section B.2], there was insufficient quartz to continue with the target preparation.

Thus samples 2, 4, 6, 8, 11 and 14 were decided upon as the key samples to analyse [marked in red in Fig. 6.1]. Samples 2, 6 and 8 provide a series up the main channel through the ramp; respectively below, in and above the linking fault scarp [Fig. 6.4]. Sample 14 is further upstream in this channel, about 375m upstream of Fault 1. Sample 4 is from the southern fork of the main channel ['spade'] where it crosses the linking

fault, and hence provides a good comparison with the age of sample 6. Sample 11 was taken from one of the minor channels further north in the overlap, but again located at the top of the linking fault scarp [see Figs. 6.1 and 6.9].

The following pages describe the sampled locations in more detail, including pictures of each site both before and after sampling. The location of the samples along the main channel is illustrated in the long profile in Fig. 6.4 [see also map: Fig. 6.1].

6.1.2.1 Sample 2: Main channel downstream of linking fault

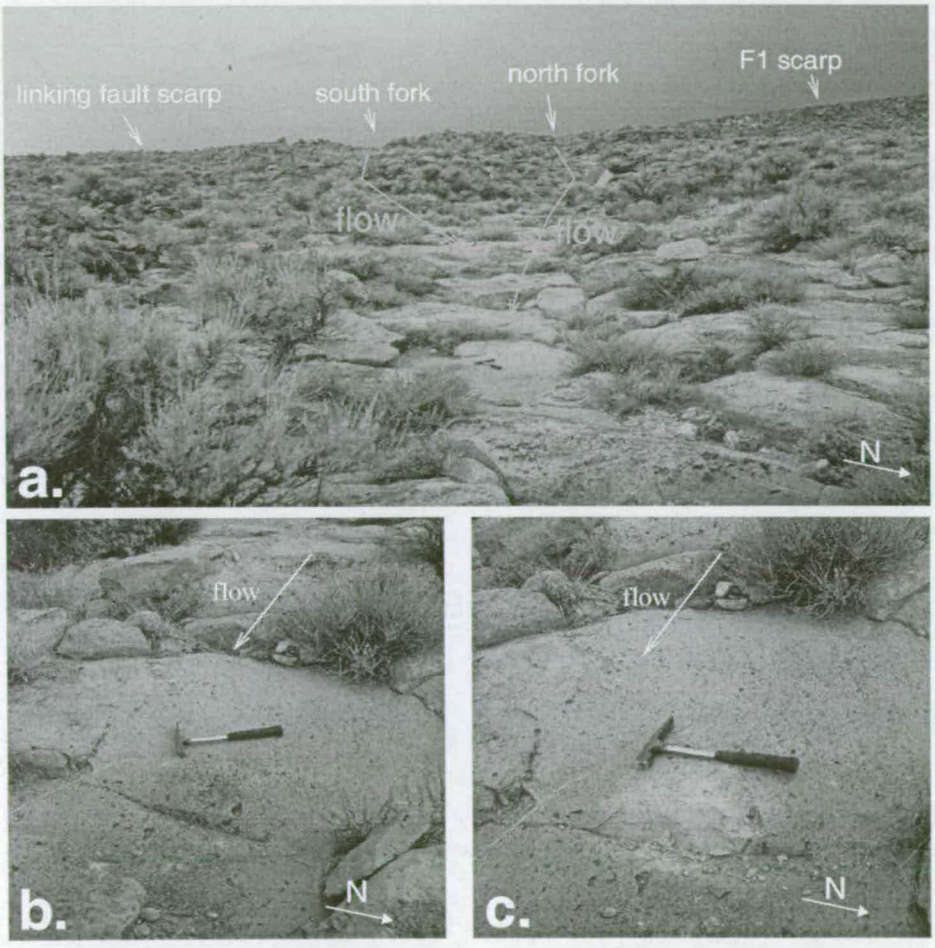

Figure 6.5: *Photographs of Sample site 2.*
a. From the east looking upstream. Note the notches where the channel cuts through the linking fault scarp that forms the skyline in the centre of the photograph. The larger Fault 1 can be seen in the distance, forming the skyline along the right-hand edge of the photograph. Hammer [40cm long] marks the sample site.
b. Close-up of the sample site before and c. after sampling.

This sample was taken from the main channel about half-way between the front fault of the ramp, Fault 2, and the linking fault. The channel is 7-8m wide and has incised the bedrock surface to around a metre. The long profile [Fig. 6.4] suggests that the erosion of the immediate footwall of Fault 2 has not propagated this far upstream, and

hence the apparent exposure age of the sample should be unaffected by the fault crest erosion [see Chapter 4].

6.1.2.2 Sample 4: Main channel southern fork, immediately above linking fault

This sample was taken from the base of the southern branch channel of the main stream [Fig. 4.30] about 3m upstream of the top of the scarp. The channel is about 12m wide between the bank tops and is incised over 2.5m into the footwall. This sample is within the part of the linking fault footwall that has undergone significant erosion [see Fig. 6.4], which should be reflected in its apparent exposure age.

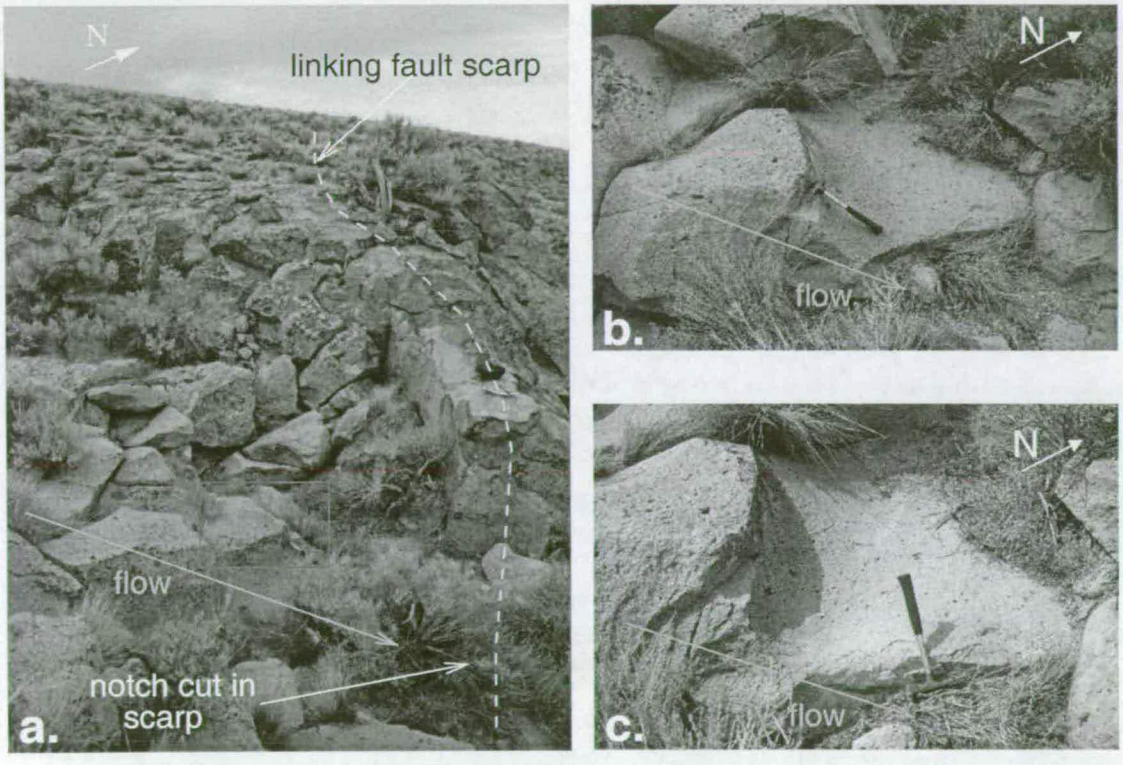

Figure 6.6: *Photographs of Sample site 4.*
a. From the fault scarp on the southern bank looking into and across the channel. The fault scarp on the northern side of the channel can be seen as the ridge on the right-hand side of the photo. Incision of 2.5-3m into the uplifting scarp, formed the notch visible e.g. in Fig. 6.5. Hammer [40cm long] and red box mark the sample site.
b. Close-up of the sample site before and c. after sampling.

6.1.2.3 Sample 6: Main channel northern branch in linking fault scarp

This sample was taken from the top of the 6m high waterfall formed where the northern fork of the main channel crosses the linking fault scarp [see Fig. 6.4]. Although shielding is higher for this sample, due to its position in the notch in the linking fault scarp, this is a very valuable sample in terms of the information it provides about the incision of the channel at the linking fault scarp. Comparison with Sample 4 may also be useful in explaining something of the relative timing of occupation of the two main stream braids at the linking fault.

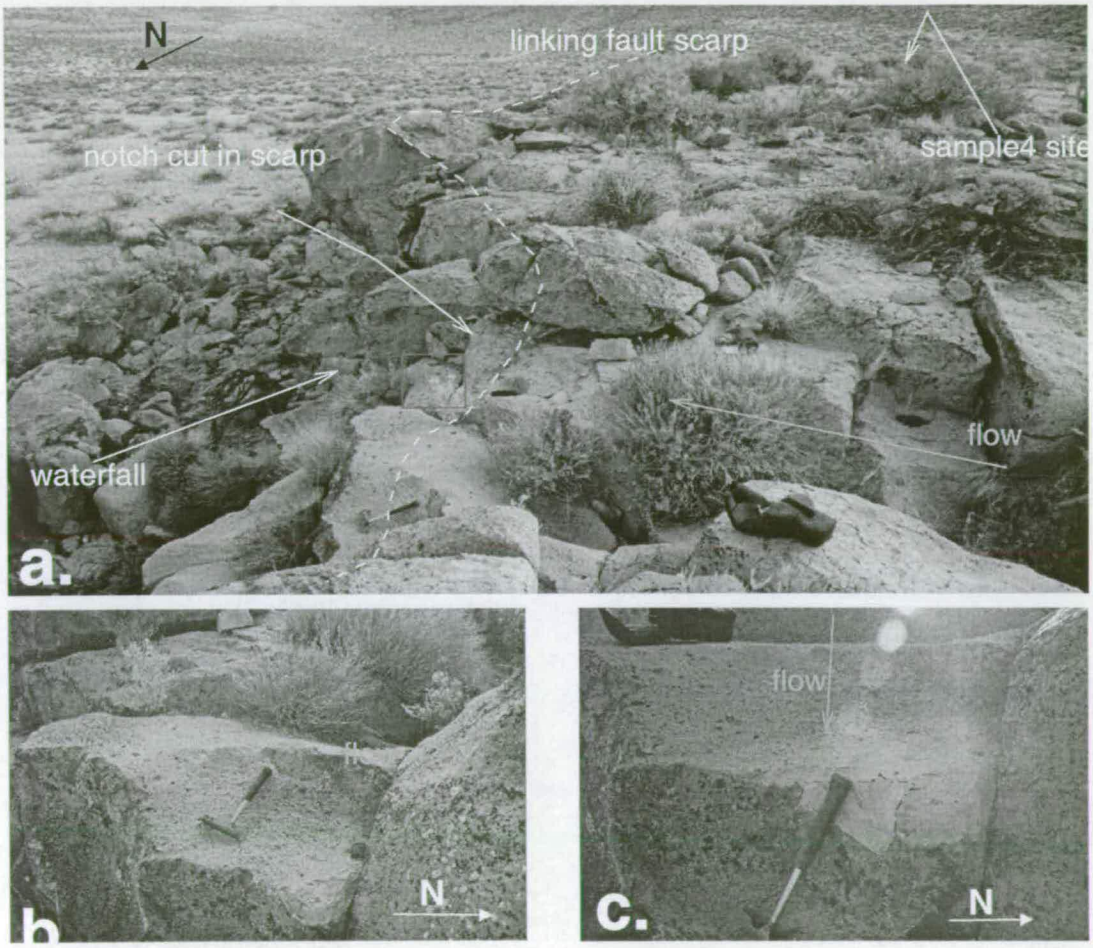

Figure 6.7: *Photographs of Sample site 6.*
a. View from the top of the fault scarp on the northern side of the channel. Channel flows from right to left - note the smoothed path incised into the footwall and through the scarp of the linking fault. The red box shows the sample location at the top of the waterfall. Hammer is 40cm long.
Sample 4 is from immediately behind the ridge of the southern bank at the top of this photo.
b. Close-up of the sample site before and c. after sampling. The dotted red box outlines where a thin piece of the tuff flaked off during sampling. This part was not collected for analysis - the material analysed came solely from the top of this step.

6.1.2.4 Sample 8: Main channel upstream of linking fault

This sample was taken from the base of the main channel about half-way between the linking fault and the largest fault at the back of the ramp, Fault 1. The channel here is about 6-7m wide between bank tops and incised around 1-1.5m into the tuff. The long profile of the main channel [Fig. 6.4] suggests that sample 8 is upstream of the part of the channel affected by propagation of the linking fault knickpoint. Hence the apparent exposure age may well be older than that of the samples 4 and 6 nearer to the scarp. Thus the four samples [2, 4, 6 and 8] provide a series up the channel that may shed light on the evolution of the channel in response to the growth of the linking fault. However, the proximity of sample 8 to the large Fault 1 may mean that this sample has also been affected by comparatively large sediment volumes eroded from incision in the footwall of this fault [see section 4.2.3 and Fig. 4.48].

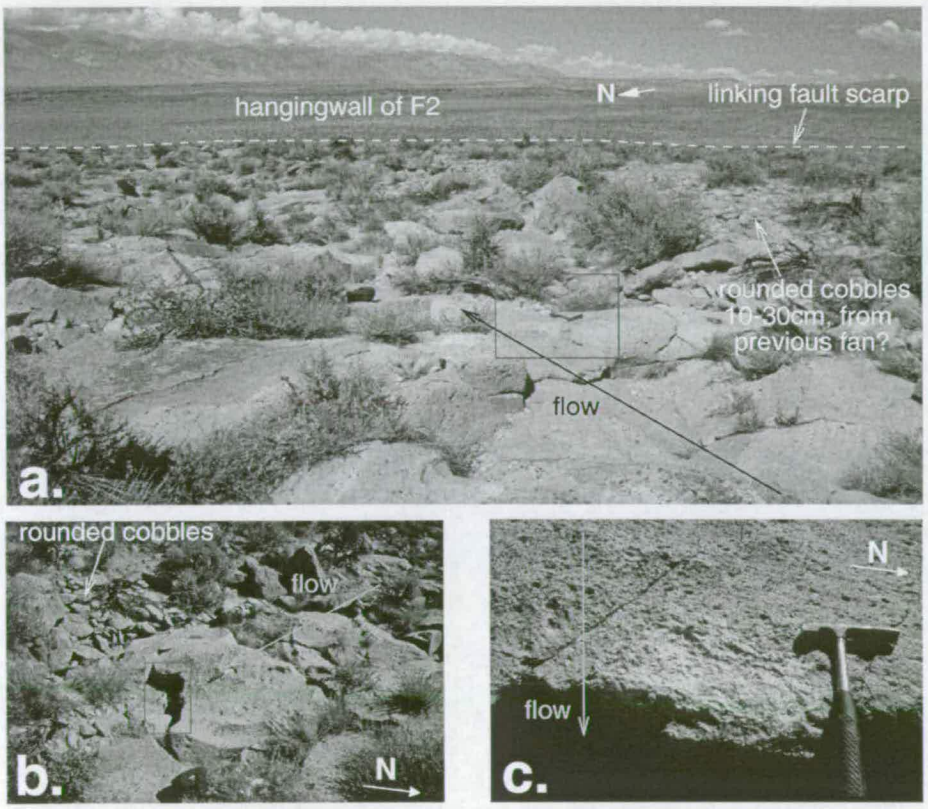

Figure 6.8: *Photographs of Sample site 8.*
a. Looking south-east across the channel towards the White Mountains in the distance. Channel flows from bottom right to top left. Cobbles on the right of the photo may be previous fan deposits incised by the present channel system [see section 4.2.3]. Red box and hammer [40cm long] show location of the sampled site.
b. Close-up of the sample site before sampling. Note the rounded cobbles again on the left. The red box in b. marks the area shown in c. after sampling.

6.1.2.5 Sample 11: Minor channel 1, immediately above linking fault scarp

This sample was taken from one of the minor channels north of the main channel in the overlap [Figs. 4.39 and 6.1]. The location is about 3m upstream of the linking fault scarp [see Fig. 6.10], and hence is analagous to the position of sample 4 relative to the linking fault. The minor channel here is approximately 2m wide, and very shallow - it is incised only 50cm into the surface of the tuff. The comparison between the long profiles of this minor channel [Fig. 6.10] and the main channel [Fig. 6.4] shows clearly that the immediate footwall of the linking fault has been eroded far more in the main channel than here. This is consistent with the deeper incision in the main channel than here [compare Figs. 6.6 and 6.7 with Fig. 6.9].

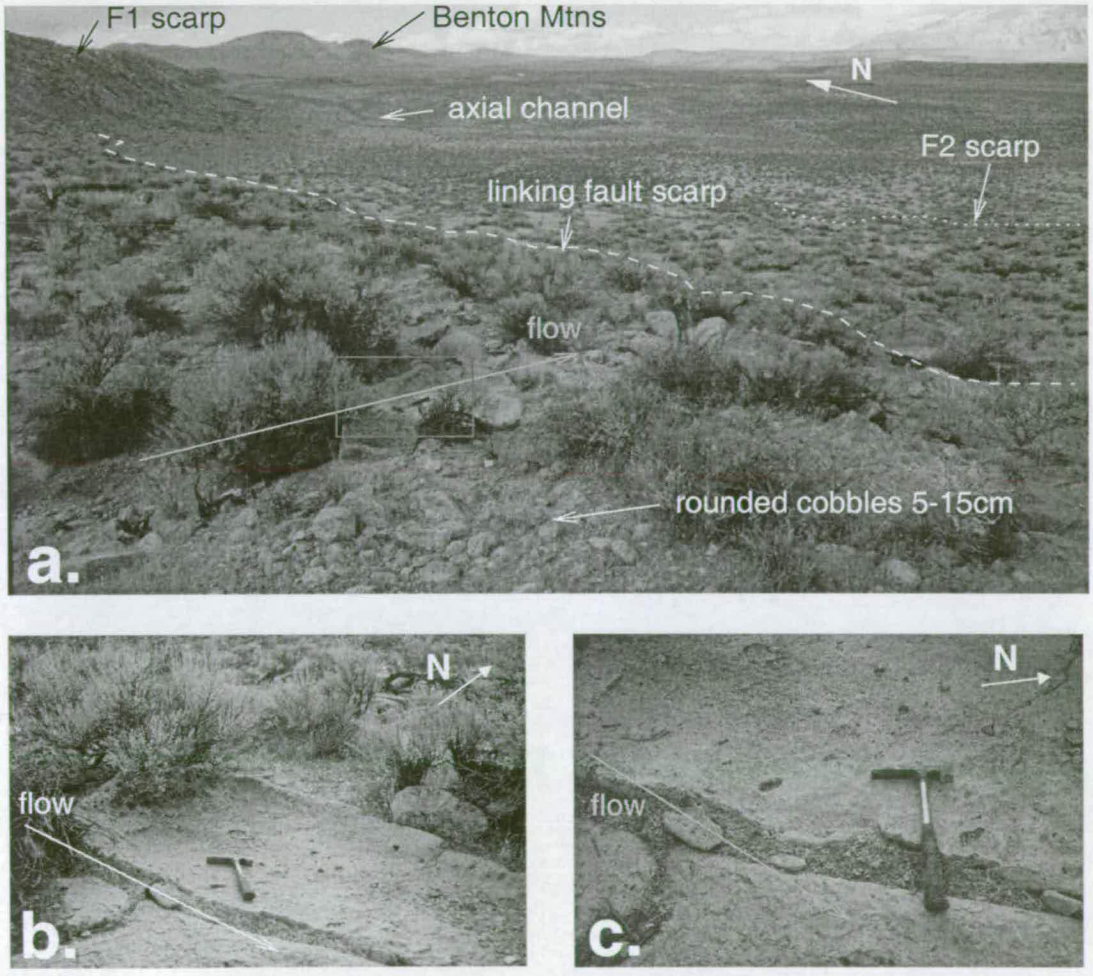

Figure 6.9: *Photographs of Sample site 11.*
a. Looking across the minor channel from the south-west towards Fault 1 in the immediate background, and the Benton Mountains in the distance. Channel flows from left to right. The top of the linking fault scarp is clear as the ridge running from top left to bottom right of the foreground. Again, cobble deposits, possibly from an earlier fan system, can be seen in the immediate foreground, incised by this minor channel. Red box and hammer [40cm long] mark the location of the sampled site.
b. Close-up of the sample site before and c. after sampling.

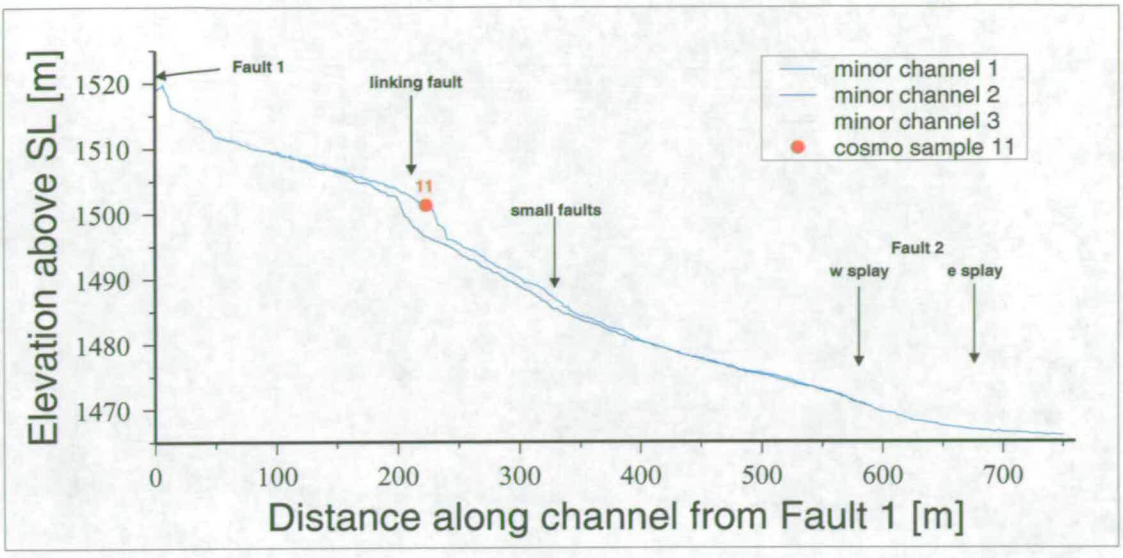

Figure 6.10: *Long profile of minor channel 1, showing the location of sample VT11. Compare with the location of sample 4 in the main channel [southern fork] in Fig. 6.4 above.*

6.1.2.6 Sample 14: Main channel in Fault 1 footwall

This sample was taken from the base of the main channel about 375m upstream of the large Fault 1 scarp [Fig. 6.1]. The channel here is incised over 3m into the footwall of Fault 1 and is approximately 18m wide from bank to bank. The long profile of the main channel [Fig. 6.4] shows that the current position of the knickpoint formed due to the displacement of Fault 1 [kp1] is ~70m further upstream than this sample. Thus the apparent exposure age of sample 14 may well be quite young, reflecting relatively recent deep incision of this channel into the tuff surface.

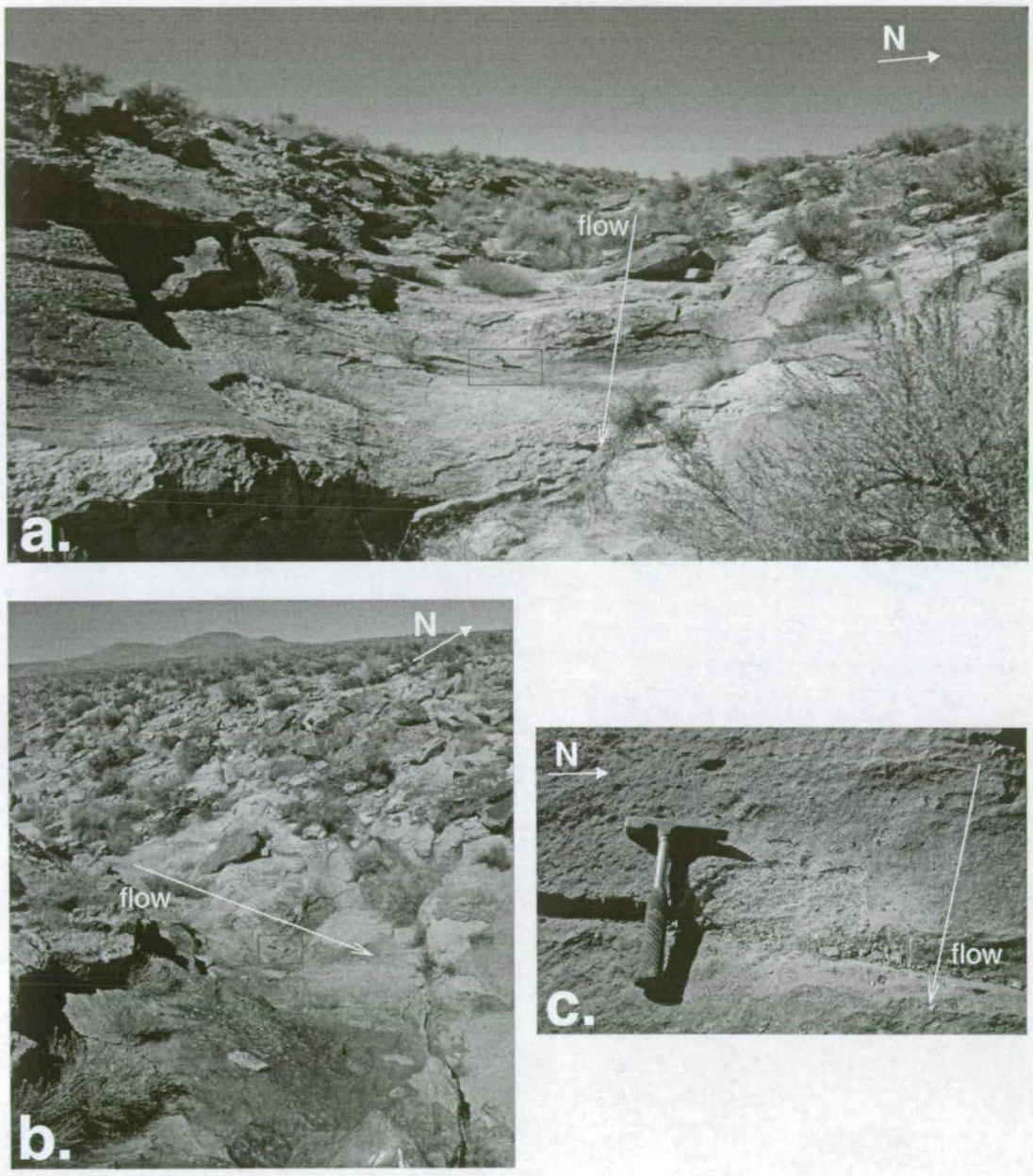

Figure 6.11: *Photographs of Sample site 14.*
a. Looking upstream [to northwest] in the main channel. Site of sample 14 is marked by the red box and the hammer [40cm long] in the channel base.
b. View down at sample 14 site from the top of the western bank (above site of sample 13 collection). Sample position is marked by the red box and the hammer in the channel base.
c. Close-up of the site after sampling.

6.2 Results and calculations: AMS and ICP-AES data

This section contains the raw data collected on the analysed samples. Table 6.1 contains field measurements of latitude and elevation, results from the Accelerator Mass Spectrometer [AMS] analysis at ANU in Canberra, and also data from the ICP analysis of aliquots carried out in the Chemistry department here at Edinburgh. A brief description of the target preparation may be found in section B.2. The equations detailed in section A.5 are used to calculate cosmogenic nuclide concentrations, N_{26} and N_{10} *, and hence production rates [P_{26} and P_{10}] at the sample latitude and elevation. The effect of sample thickness and topographic shielding is then calculated in section 6.3 [see section A.4], and an apparent exposure age calculated for each sample based on this data [section 2.5.1] and the scaling factors of Nishiizumi et al. (1996), which are derived from samples collected nearby in the Sierra Nevada (Nishiizumi et al., 1989) [section 6.3 and Table 6.7].

An initial interpretation of the corrected data is given in section 6.5. Section 6.6 discusses the use of different published scaling values [see section A.3] for the production rate of *in situ* cosmogenic isotopes, and their effects on the apparent exposure ages calculated. A full discussion of the implications of these data for the development of the Volcanic Tableland may be found in the following chapter, in section 7.2.2.

6.2.1 Raw data

The cosmic ray flux varies with latitude and elevation [section A.3]. Hence for calculation of the production rate, the exact latitude and elevation of the sample site must be known. The latitude and elevation, measured in the field using differential GPS are given below. The AMS measures the ratio of $^{26}Al/^{27}Al$ and $^{10}Be/^{9}Be$ in the samples. However, calculation of the actual concentration [N-value] of the cosmogenic isotopes [^{26}Al and ^{10}Be] requires knowledge of the *total* concentration of aluminium and beryllium in the samples. The beryllium concentration is known, as a known volume of carrier was added to each sample at the beginning of the dissolution, but independent measurement of the aluminium concentration is required. Hence a very small aliquot of each target is analysed by ICP-AES [section B.2]. This independent analysis also allows a correction to be made for any aluminium that may have been added in reagents during the target preparation, by comparing the measured Al content in the blanks with the Al initially added [to the blanks only] at the beginning of dissolution [see also B.2].

Table 6.1 on the following page shows the raw data for each sample: the field GPS data [latitude and elevation]; the mass of pure quartz after separation and etching; concentrations of Al and Be as measured in the aliquot sent for ICP [see above and section B.2] and the $^{26}Al/^{27}Al$ and $^{10}Be/^{9}Be$ ratios measured in the AMS. The samples are grouped in the two batches in which the targets were prepared, with the blank at the end of each.

Sample	Field data		Mass (g)	ICP-AES data (mg/l)		AMS data (atoms/g SiO_2 x 10^{-12})	
	Latitude (deg)	Elevation (km)		[Al]	[Be]	$^{26}Al/^{27}Al$	$^{10}Be/^{9}Be$
VT2	37.47638	1.48563	17.05735 ± 5.e-6	0.476 ± 0.022	0.1062 ± 0.0005	6.19 ± 0.390	1.59 ± 0.060
VT6	37.47580	1.50144	12.10941 ± 5.e-6	0.463 ± 0.018	0.1056 ± 0.0004	1.92 ± 0.160	0.490 ± 0.020
VT11	37.47580	1.50123	17.72079 ± 5.e-6	0.490 ± 0.016	0.0984 ± 0.0005	7.50 ± 0.280	2.08 ± 0.070
Blank 10ANU	n/a	n/a	n/a	0.106 ± 0.013	0.0940 ± 0.0005	0.0120 ± 0.0020	0.0120 ± 0.0020
VT4	37.47577	1.50210	10.88311 ± 5.e-6	0.316 ± 0.022	0.0607 ± 0.0005	1.57 ± 0.120	0.409 ± 0.021
VT8	37.47511	1.50909	17.89770 ± 5.e-6	0.510 ± 0.022	0.0610 ± 0.0005	4.22 ± 0.250	2.58 ± 0.096
VT14	37.47530	1.53867	12.14320 ± 5.e-6	0.123 ± 0.022	0.0444 ± 0.0005	2.20 ± 0.140	0.429 ± 0.011
Blank 12ANU	n/a	n/a	n/a	0.027 ± 0.022	0.0293 ± 0.0005	0.0100 ± 0.0050	0.0100 ± 0.00500

Table 6.1: *Raw field, ICP-AES and AMS data for the Volcanic Tableland samples.*
Samples are listed in the two batches in which they were prepared, with the blank at the bottom of each.
Latitude and elevation values were measured in the field using differential GPS, accurate to less than a centimetre. Latitudes are given in degrees, quoted here to 5dp, elevations are in kilometres above sea level, given here to 5dp [nearest cm].
Quartz masses were measured at the beginning of dissolution [after mineral separation, etching for 5 days in HF, and handpicking [section B.2]].
Errors in ICP-AES [Chemistry dept, Edinburgh University] and AMS [Australian National University at Canberra] data are as quoted.
***NB**: ICP-AES data for the first batch of samples was within the expected boundaries for the known volume of Be carrier added: [Be] 0.09-0.11 mgl^{-1}. [Be] values in the second batch are far lower than expected suggesting an error occurred in the aliquot production [see text].*

6.2.2 Cosmogenic nuclide abundancies: N_{26} and N^*_{10}

The raw data in Table 6.1 were used to calculate the absolute abundancies of ^{26}Al and ^{10}Be in the samples, in atoms per gram of quartz: N_{26} and N_{10} respectively [section A.5]. Traces of aluminium may be added during the target production from tiny concentrations in lab reagents [section B.2]. However, the aliquot prepared for ICP analysis is simply a tiny fraction of the sample diluted to a known concentration [section B.2]. Since all the original Be and Al in the blanks were added in known volumes of carrier [using the first pipette calibration: columns 2&3, Table 6.3], comparison of the ICP measurement of the [Al] in the blank with the known volume of Al added, allows corrections to be made to each sample for any trace Al additions during preparation [see section B.2].

As a known volume of beryllium is added to all the samples [including blanks] at the beginning of the dissolution, the ICP analysis should show virtually the same Be concentration in all the samples: between 0.09 and 0.11mgl^{-1}. This is the case with the first batch of samples [VT2, VT6, VT11 and Blank 10ANU: see Table 6.1].

N-values calculated from ICP-AES measurements				
Sample	N_{10} (atoms g^{-1} SiO_2) (x 10^4)	N_{10} * (atoms g^{-1} SiO_2) (x 10^4)	N_{26} † (atoms g^{-1} SiO_2) (x 10^4)	N_{26}/N_{10} *
VT2	329.65 ± 12.54	327.45 ± 12.54	1903.20 ± 158.05	5.81 ± 0.53
VT6	142.30 ± 5.83	139.19 ± 5.86	808.48 ± 77.89	5.81 ± 0.61
VT11	384.62 ± 13.09	382.50 ± 13.10	2282.59 ± 129.02	5.97 ± 0.39
VT4	75.75 ± 3.94	74.85 ± 3.97	624.89 ± 68.96	8.35 ± 1.02
VT8	292.46 ± 11.14	291.92 ± 11.14	1528.27 ± 121.69	5.24 ± 0.46
VT14	52.19 ± 1.46	51.39 ± 1.52	415.34 ± 67.83	8.08 ± 1.34

Table 6.2: *Abundancies of* ^{26}Al *and* ^{10}Be *in the Volcanic Tableland samples, calculated from the ICP-AES data.*
As in Table 6.1, the samples are grouped in the batches in which they were prepared.
The N^*_{10} *value is the abundancy of* ^{10}Be *corrected using the relevant Blank* N_{10} *value to allow for the component of Be added to the samples in the carrier [see section B.2].*
† *No similar correction needs to be made for Al, as an Al carrier is only added to the blanks. The* N_{26} *values however do include a correction for trace Al added [e.g. in reagents] during the target production [see text].*
***NB**: Due to the unexpectedly low ICP values for the second batch of samples, the values quoted above for samples VT4, VT8 and VT14 include a significant error [see text, and compare with Table 6.4].*

However, the analyses for the second batch of samples [VT4, VT8, VT14 and Blank 12ANU] do not fall within these boundaries [Table 6.1]. This suggests that errors were introduced in the making of the aliquots for this second batch of samples. If too small a volume of sample was put into each aliquot sent for analysis, then this could result in the lower than expected [and apparently random] measured concentrations. However, no obvious mechanism for this could be found, including obvious signs of human error.

However caused, this problem introduces an uncertainty into the data for these samples, as there is no independent measure of the amount of total Al [predominantly ^{27}Al] in these three samples. Calculation of the abundancies of ^{26}Al and ^{10}Be in these samples [N-values] using the ICP values for [Al], produces erroneous $^{26}Al/^{10}Be$ ratios, since the Be content in the second batch, measured by ICP, was far lower than expected. The Be carrier had been added to all the samples in this batch, and hence the true Be content was known to be higher than measured. Hence an alternative method of calculation of the abundancies of ^{26}Al and ^{10}Be in the second batch of samples had to be designed [section 6.2.2.1].

Values of the abundancies of ^{26}Al and ^{10}Be in the samples, calculated by the normal method [from the reported ICP data], are given in Table 6.2. N_{10}^{*} is the abundancy of ^{10}Be in the sample *after correction* for the known volume of Be carrier added to the samples at the beginning of dissolution. An Al carrier is added *only to the blank* and not to the other samples, so no similar correction needs to be made to the value of N_{26}. However, the N_{26} value has been corrected for trace Al addition during target preparation. Compare these data with the values calculated using the alternative method [pipette calibration], in Table 6.4 on page 251.

6.2.2.1 Pipette calibration method

The discrepancy between the measured ICP-AES concentrations and the expected values for the second batch of samples [Table 6.1] implies that the exact dilution of the aliquot was not as expected, and hence the ICP concentrations could not be scaled to obtain the Al content of the samples. Calculation of N-values by the 'normal' method hence introduces a significant error, and an alternative method must be used for the calculations. The amount of beryllium initially added to the samples in the carrier is known accurately, as it was added using a calibrated micropipette. Calibrations were carried out each time these pipettes were used, both when adding the carrier at the beginning of the dissolution, and also when making up the aliquots for ICP analysis [Table 6.3 and section B.2].

The first calibration is used to calculate the exact volume of Be [and Al for the blanks] added at the start of the dissolution, and also helps to calculate the amount of trace Al added during target preparation. In the 'normal' method, the second calibration is used to calculate the exact dilution of the aliquot [section B.2], and hence to calculate the total aluminium content of the samples; an approach which is unusable with the second batch of samples. However, the first pipette calibration data can be used to calculate the aluminium content of the samples if it is assumed that the *ratio* [Al]:[Be] measured by ICP is the same as that in the sample, within analytical error. This is reasonable, as the aliquot production involves purely a straight dilution, and there is no potential for separation or concentration of either element. Thus,

$$\frac{[Al]_{sample}}{[Be]_{sample}} \pm \sigma_{pip} = \frac{[Al]_{ICP}}{[Be]_{ICP}} \pm \sigma_{ICP} \qquad (6.1)$$

where $[Al]$ is the concentration of Al, so that
$[Al]_{sample}$ and $[Al]_{ICP}$ are the concentrations in the original sample and the ICP aliquot

Pipette calibration data				
	Calibration 1: carrier		Calibration 2: ICP	
	Batch 1 vol (ml)	Batch 2 vol (ml)	Batch 1 vol (ml)	Batch 2 vol (ml)
1	0.50591	0.50273	0.50185	0.49879
2	0.50095	0.49862	0.50197	0.50334
3	0.50266	0.49958	0.50281	0.50323
4	0.50208	0.49977	0.50245	0.50347
5	0.50308	0.49800	0.50243	0.50367
6	0.50412	0.50240	0.49921	0.50383
7	0.50362	0.49960	0.50483	0.50434
8	0.50238	0.49980	0.50267	0.50338
9	0.50098	0.49893	0.50259	0.50438
10	0.50342	0.49702	0.50241	0.50294
Mean (ml)	0.50292	0.499645	0.502322	0.503138
St. Dev., σ (ml)	0.001485	0.00177	0.00177	0.001596
% error:	0.29	0.35	0.35	0.32

Table 6.3: *Pipette calibration data.*
Pipette calibrations were carried out for the micro-pipette used for adding the carrier[s] at the beginning of dissolution [Calibration 1], and for making up the aliquots for ICP [Calibration 2]. Each separate column gives data for the two different batches [1: VT2,VT6,VT11; 2: VT4,VT8,VT14]. The mean and standard deviation, σ, are calculated for each calibration.

σ_{pip} and σ_{ICP} are the errors in the pipette calibration and ICP data respectively, calculated from the values in Table 6.1.

The basic assumption implicit in this approach, and not made during the 'normal' calculations, is that all the beryllium in the samples was added in the carrier. Since the ICP measures concentrations only to parts per million, and all the beryllium originally in the sample was cosmogenically-produced ^{10}Be [of the order of 10^{-12} atoms g^{-1}], the error introduced by this method is vanishingly small.

This pipette calibration method has been used to recalculate the Al concentration, and thus the abundancies of ^{26}Al and ^{10}Be, in all the Tableland samples. The results of these calculations are shown in Table 6.4, and should be compared with the values shown in Table 6.2, which were calculated from the 'raw' ICP data. For the first batch of samples [VT2, VT6 and VT11], this approximation results in only a small alteration from the values of both N_{10}^* and the ratio of isotopes, N_{26} / N_{10}^*, calculated using the ICP data. Thus there is some justification in using this method to calculate the abundancies for the second batch of samples [VT4, VT8 and VT14]. These final recalculated values have been used for all later calculations, and also to calculate the apparent exposure ages for the samples, discussed in section 6.4.

6.2.3 Erosion Island plot

Figure 6.12 shows the erosion island plot for the Volcanic Tableland samples. This plot allows a quick analysis of the samples based on the variation in the relative abundancies of the two isotopes, N_{26} / N_{10} * [see detailed explanation in section 2.5.2].

The solid line in Fig. 6.12 represents the locus of points that experience zero erosion; the broken line is the constant erosion locus. The erosion history of any points falling within the steady-state 'erosion island' between the lines may be modelled by a unique

N-values calculated from pipette calibrations				
Sample	N_{10} (atoms g^{-1} SiO_2) (x 10^4)	N_{10}* (atoms g^{-1} SiO_2) (x 10^4)	N_{26} (atoms g^{-1} SiO_2) (x 10^4)	N_{26}/N_{10}*
VT2	317.75 ± 12.03	315.36 ± 12.03	1849.74 ± 144.54	5.87 ± 0.51
VT6	137.94 ± 5.64	134.56 ± 5.67	790.43 ± 72.69	5.87 ± 0.59
VT11	400.12 ± 13.52	397.81 ± 13.52	2393.80 ± 118.82	6.02 ± 0.36
VT4	127.12 ± 6.55	124.01 ± 6.73	847.80 ± 87.70	6.84 ± 0.80
VT8	488.38 ± 18.25	486.49 ± 18.27	2225.38 ± 163.20	4.57 ± 0.38
VT14	119.74 ± 3.10	116.95 ± 3.40	608.03 ± 108.52	5.20 ± 0.94

Table 6.4: *Abundancies of* ^{26}Al *and* ^{10}Be*, calculated using the pipette calibrations: Table 6.3. Samples are grouped as in Table 6.2. The total Be and total Al in the samples was calculated using the pipette calibrations [see text].* N_{10}*,* N_{10}^* *and* N_{26} *values have been calculated as for the 'normal' ICP method [see text and Table 6.2].*

production curve, for a specific production ratio of ^{26}Al : ^{10}Be, and a steady erosion rate. The exposure age corresponds to the distance travelled along that curve. However, if a sample plots *below* the constant-erosion line, the exposure of the sample has probably been interrupted by a period of burial [see section 2.5.2.1 and Fig. 6.15].

Any sample plotting *above* the erosion island has a higher ratio of [in this case] ^{26}Al to ^{10}Be than the initial production ratio. This cannot be explained by any combination of erosion, burial or inheritance. However, for samples plotting in the left-hand part of the graph, i.e. with low production rates, or young samples, the errors even in exceptional AMS results cause a large uncertainty in N_{26} / N_{10}*, relative to the width of the erosion island, and reflect partly the present limits of the resolution of the technique (Small et al., 1997). Samples plotting far above the erosion island, however, usually indicate some other source of uncertainty, due to contamination or measurement problems.

Triangles in Fig. 6.12 represent the data from the first batch of samples, while the circles are the values from the second batch. Errors have been propagated from the raw data [Tables 6.1 and 6.3]. The first batch of samples [VT2, VT6, VT11] all plot in or near the erosion island, indicating simple, constant erosion. VT4 and VT14 are younger samples, and have much larger uncertainties in their N_{26} / N_{10}* values, due predominantly to the N_{26} errors [Table 6.3, and see also Small et al. (1997)]. However, the uncertainty in the VT14 data overlaps the entire of the erosion island, while VT4 errors almost impinge on it.

In contrast, VT8 is located far below the erosion island, even when the error margins are considered. This implies complex exposure, with at least one significant period of burial punctuating its exposure history. The implications of this are discussed in more detail in sections 6.4 and 6.5, and also in section 7.2.2.

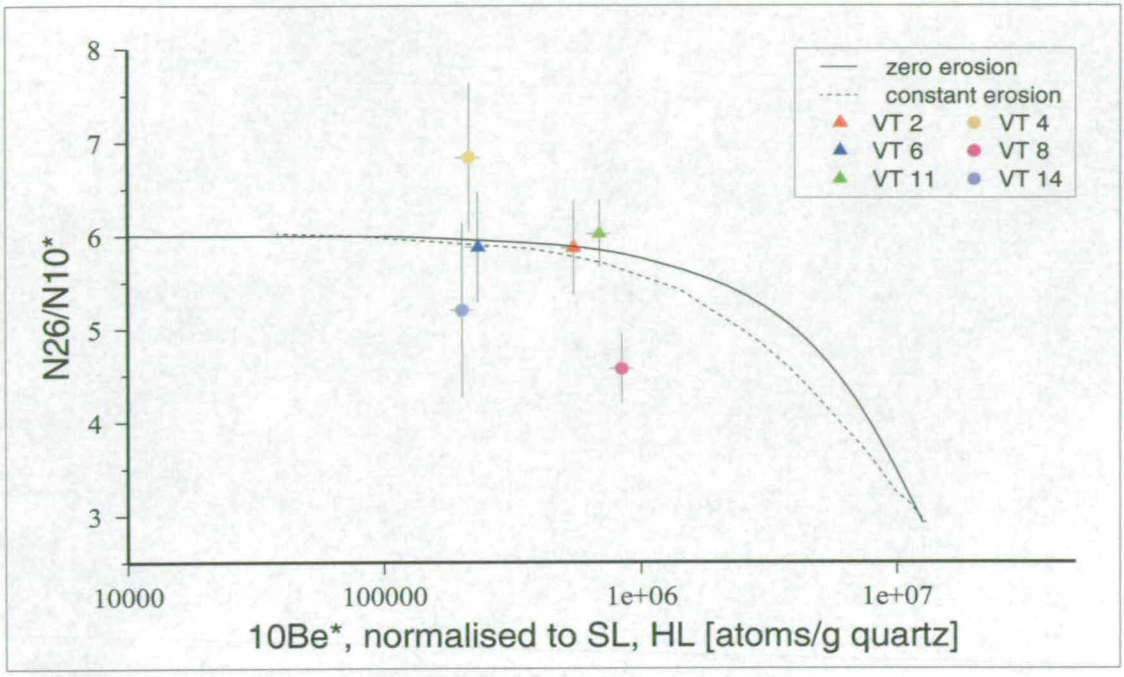

Figure 6.12: *Erosion Island plot for Volcanic Tableland samples.*
Log-normal plot of N_{26}/N^*_{10} *ratio against log* N^*_{10} *[i.e. blank-corrected] for the six Tableland samples. Triangles represent the data calculated from the first batch of samples, while the circles are the values calculated from the second batch. Errors are marked as shown in Table 6.3. Samples VT2, VT6 and VT11 have probably experienced simple constant erosion. the errors in VT4 and VT14 are much larger, predominantly reflecting the uncertainty in the* N_{26} *value [Table 6.3]. Sample 8 in contrast has probably undergone complex erosion - suggesting at least one period of burial between exposures. [*^{26}Al *decays faster than* ^{10}Be*, and hence ratio of isotopes drops during burial: see text for full explanation].*

6.2.4 'Raw' production rates

As discussed in section A.3, *in situ* production rates of cosmogenic isotopes vary considerably across the planet, due to variations in the geomagnetic field, and hence the way this modulates the incoming cosmic radiation. Most importantly, production rates vary drastically with both latitude and elevation [section A.3]. For the initial calculations shown in this section, the scaling factors of Nishiizumi et al. (1996) were used to calculate the production rates of ^{26}Al and ^{10}Be at the Tableland sample sites. These scaling factors were chosen as they are rescaled from samples collected in the Owens Valley, and include one sample from the ashfall deposits at the base of the Bishop Tuff (Nishiizumi et al., 1989). However, the particular choice of scaling factor used has a marked effect on the calculated apparent exposure age of the samples. In the light of the continuing debate about scaling production rates [section A.3], exposure ages have also been calculated for the Tableland samples using the scaling factors published by Schaller et al. (2001), Nishiizumi et al. (1996), Barrows et al. (2001) and others [Table 6.8 on page 266].

Table 6.5 contains the 'raw' production rates calculated for the Tableland sample locations using the scaling factors of Nishiizumi et al. (1996) and the GPS location

'Raw' production rates - no shielding		
Sample	'Raw' production rate (atoms g^{-1} SiO_2 yr^{-1})	
	^{26}Al	^{10}Be
VT2	17.427 ± 1.743	105.254 ± 1.053
VT6	17.269 ± 1.763	106.473 ± 1.065
VT11	17.626 ± 1.763	106.457 ± 1.065
VT4	17.637 ± 1.764	106.524 ± 1.065
VT8	17.727 ± 1.773	107.067 ± 1.071
VT14	18.113 ± 1.811	109.396 ± 1.094

Table 6.5: *'Raw' production rates of* ^{26}Al *and* ^{10}Be *- no shielding corrections. Production rates were calculated using the scaling factors of Nishiizumi et al. (1996), from the nuclear disintegration rates of Lal (1991) and the sample latitude and elevations in Table 6.1. The effect of using other scaling factors is discussed in section 6.6 [see also section A.3]. Compare with the corrected production rates in Table 6.6 on the following page.*

data from Table 6.2.1. I call these data 'raw' as they do not include any corrections for topographic shielding of the samples or sample thickness [section 6.3]. Corrected values for the production rates including these effects are given in Table 6.6.

6.3 Calculations: Shielding

The ages calculated in section 6.2.4 are based on four main assumptions:

1. The sample has been taken from an infinitely thin layer at the surface of the outcrop [i.e. it has zero thickness].
2. The sample has been exposed to cosmic radiation from the entire of the sky - from the full 90° from horizontal to vertical inclination, and through the full 360° azimuth range.
3. The sample has been taken from a horizontal surface.
4. The sample has not been covered [e.g. by sediment or snow etc.] during its exposure.

However, these assumptions are not all valid [section A.4], introducing errors in the calculated nuclide concentrations, and also the production rates. To obtain true exposure ages, corrections must be made for each of these factors. The theory behind the corrections is explained in section A.4. This section discusses the values of the shielding corrections for the six analysed Tableland samples.

6.3.1 Sample thickness

The equations for calculating the exposure ages used in section 6.2.4 above assume that the sample is taken at the surface of the outcrop. As the production rate decreases exponentially with depth from the surface, an error is introduced into the calculated ages by the fact that all samples have a finite thickness.

The equations given in section A.4.1 [Dunne et al. (1999)] may be used to calculate N_0, the *actual* isotope concentration at the surface, for both nuclides, thus removing the error due to sample thickness. As stated in section 6.1.1, care was taken to ensure that all the samples collected in the Volcanic Tableland were less than 3cm thick. Using this as the maximum value, it is possible to calculate the effect on the nuclide abundancies. For a sample thickness of 3cm, this correction yields a change of **2.32%** in the nuclide abundancies calculated in Table 6.4.

6.3.2 Topographic shielding

The production rates quoted in Table 6.5 assume that the samples are exposed to cosmic radiation from the entire sky. However, in reality, samples are shielded from at least part of the sky by topographic obstructions, in this case mountains, fault scarps and channel banks [Fig. A.3].

Figure 6.13 shows the topographic shielding of each of the six Tableland samples as measured in the field [see also section 6.1.1]. Obstructions were measured in sixteen sectors [each 22.5°] around each sample. The inclination of the horizon from the sample was measured in each sector; this shielded [lower] part of the sky is shaded in the rose diagrams. Only incident radiation from higher angles [unshaded] reaches the samples [see section A.4.2].

Thus, using the shielding data for each of the samples, and Eqns. A.7 and A.9 [Dunne et al. (1999)], the impact of the topographic shielding of each sample may be calculated. Column 2 in Table 6.6 shows the impact of the sample thickness: the effective production rate is reduced, due to the fact that not all the sample was exposed at the surface. The topographic shielding [column 3] also reduces the effective production rate, as the radiation is only incident on the sample from part of the sky. The final effective production rates given here should be compared with the 'raw' values in Table 6.5 on the page before.

Impact of shielding on production rate				
Sample	Thickness	Topography S_P	Effective Production Rate P_I (atoms $g^{-1}SiO^2$ yr^{-1}) ^{10}Be	^{26}Al
VT2	0.977	0.986	16.798 ± 1.680	101.452 ± 1.015
VT6	0.977	0.823	14.183 ± 1.418	85.657 ± 0.857
VT11	0.977	0.971	16.721 ± 1.672	100.992 ± 1.010
VT4	0.977	0.878	15.141 ± 1.514	91.448 ± 0.914
VT8	0.977	0.967	16.760 ± 1.676	101.226 ± 1.012
VT14	0.977	0.915	16.194 ± 1.619	97.809 ± 0.978

Table 6.6: *Impact of shielding on in situ cosmogenic nuclide production rates.*
Thickness - correction for reduction in production rate with depth, based on a maximum thickness of 3cm for each sample [section 6.3.1].
S_P - topographic scaling factor for production rates based on rectangular obstacles, calculated from Eqn. A.7 (Dunne et al., 1999).
The final column shows the corrected production rates, allowing for the combination of sample thickness and topographic shielding at each site. Compare with the 'raw' values calculated directly from the SLHL scaling factors, in Table 6.5.

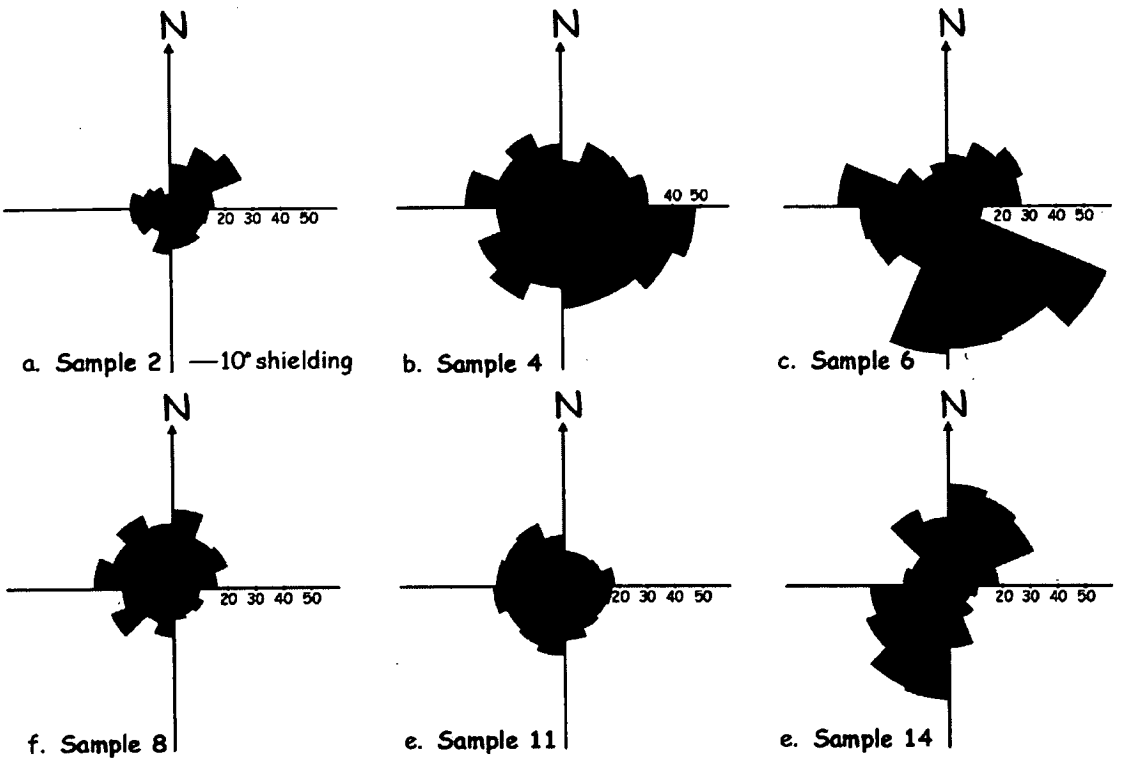

Figure 6.13: *Rose-diagrams showing the shielding of the analysed samples by topographic obstructions, as measured in the field.*
The shaded area represents the part of the sky from which incident radiation is blocked. The bar in [a] represents 10° shielding on the plots. Only radiation from higher angles [unshaded] can reach the sample sites over the obstructions. As seen in the photographs [Figs. 6.5 to 6.11], the shielding is greatest where the incision is deepest: for samples 4 and 6 in the footwall of the linking fault, and for sample 14, in the deeply incised channel in the Fault 1 footwall.

6.3.3 Sloping surfaces

The third assumption listed above is that the sampled surface was horizontal. If a sample lies on a steeply sloping surface, then up to half of the incident radiation is blocked from reaching the target [Fig. A.5 on page 380].

However, none of the analysed samples from the Volcanic Tableland were collected from steeply dipping surfaces. Although dipping surfaces were sampled in the field [fault profile samples 16-18; bank sample 13], those samples were not analysed [see section 6.1.1]. In all six analysed samples, the rock surfaces were dipping at less than 5° [see photographs in section 6.1.2.1 to 6.1.2.6]. This was even true in the case of sample VT6, which was specifically taken from a sub-horizontal surface at the apex of the scarp [see photographs: Fig. 6.5]. Thus no corrections have been made for surface slope.

6.3.4 Surface cover

The final assumption on page 253 was that the sample had not been covered for a significant amount of time during its exposure, e.g. by snow or sediment. Potential

cover is very hard to determine for the history of the Tableland samples. However, their location in the centre of the Owens Valley makes them less likely to have been covered for significant lengths of time by thick snow than samples from mountainous areas, in the Sierra Nevada or White Mountains, on either side of the valley. Also, due to the low erosion rates suggested by the small volumes of sediment on the Tableland, it is likely that the samples have not been covered by thick sediment for significant periods of time, with the possible exception of sample VT8 [see section 6.5]. Thus no correction has been calculated for surface coverage of the samples.

6.4 Corrected exposure ages

Apparent exposure ages		
Sample	Corrected exposure age (x 10^3 years)	
	^{10}Be	^{26}Al
VT2	**196.32**±10.10	**200.21**±16.16
VT6	**97.00** ± 5.83	**96.57** ± 9.14
VT11	**251.92**±11.99	**268.53**±14.03
VT4	**83.48** ± 5.87	**97.05** ±10.29
VT8 †	**311.51**±15.96	**246.58**±18.72
VT14	**73.44** ± 3.24	**64.08** ±11.60

Table 6.7: *^{26}Al and ^{10}Be exposure ages, corrected for sample thickness and topographic shielding.*
Exposure ages are calculated using Eqn. 2.23 [Dunne et al. (1999)] from the data in Table 6.6. The exposure ages are based on the production rate scaling factors of Nishiizumi et al. (1996); see Table 6.8 for calculations using other published scaling factors.
† *The widely different exposure ages for sample VT8 imply complex exposure.*

Table 6.7 contains corrected ^{26}Al and ^{10}Be exposure ages for the Tableland samples, calculated from these new production rates. The ^{26}Al and ^{10}Be apparent exposure ages are generally identical within the error margins. In all cases, the ^{26}Al uncertainty is larger than that in the ^{10}Be age, and hence the ^{10}Be age can be considered the more robust date for each sample. The advantage of using the two isotopes, however, is the provision of an internal check on the calculated ages, so that any inconsistencies are obvious. The value of the two-isotope system is also demonstrated in the case of VT8, where the ^{10}Be age is vastly greater than the ^{26}Al age [by ~65 kyr: 21%]. This implies that VT8 has experienced complex exposure [as implied by the erosion island plot, Fig. 6.12], which would not have been evident had ^{10}Be been used alone. In this case, even the ^{10}Be age underestimates the true exposure of the sample, as discussed below.

6.5 Initial interpretation

Figure 6.14 compares the ^{26}Al and ^{10}Be corrected apparent exposure ages for the Tableland samples. The reported periods of the Tahoe and pre-Tahoe glaciations, thought to have influenced the formation and development of the channels [Pinter and Keller (1995) and references therein], are marked in grey. All the calculated sample ages are older than 50 ka, despite the fine fluvial textures seen in the field; testament to the low erosion rates on the Tableland.

6.5.1 Erosion histories

Most of the samples lie on, or close to, the dotted line in Fig. 6.14, showing equal ^{26}Al and ^{10}Be apparent exposure ages, indicative of simple exposure, with no significant

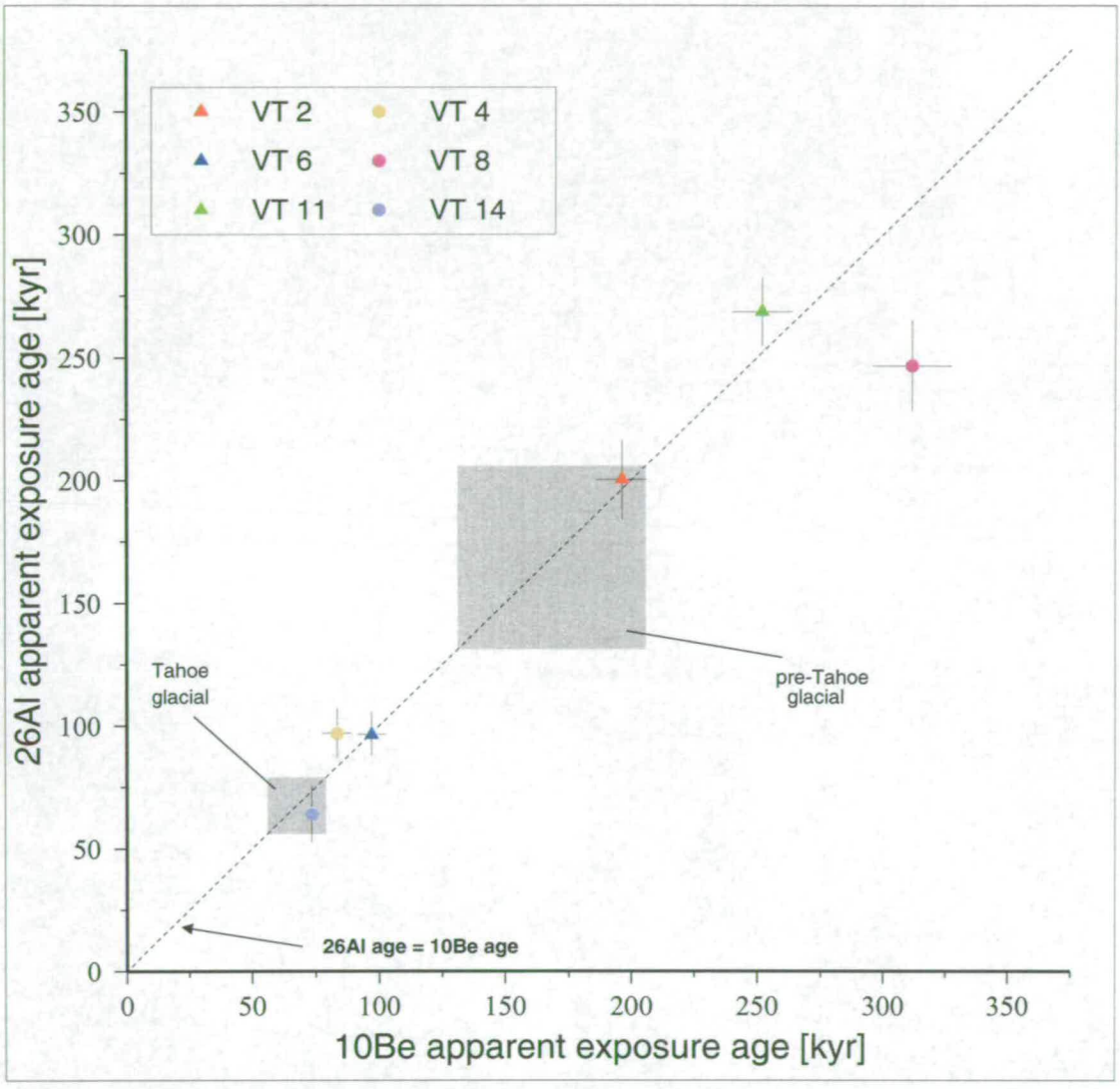

Figure 6.14: *Comparison of ^{26}Al and ^{10}Be corrected apparent exposure ages, using scaling factors from Nishiizumi et al. (1996).*
Data has been corrected for topographic shielding and sample thickness, see above. The dotted line shows the locus of points with equal ^{26}Al and ^{10}Be ages. Most samples plot on or near this line, implying simple erosion histories. VT8 lies far to the right, implying significant burial during its exposure history.
The periods of the Tahoe and pre-Tahoe glaciations, thought to have influenced the formation and development of the channels (Pinter and Keller, 1995), are marked in grey. Only VT2 and VT14 lie within the glacial periods. Other ages imply channel formation and incision occurred outside the expected times [see text].

periods of burial. However, sample VT8 is an exception to this, clearly showing a ^{10}Be apparent exposure age that is ~65kyr older than its calculated ^{26}Al age.

As stated in the discussion of the erosion island plot [page 252, and section 2.5.2], the longer half life of ^{10}Be means that it decays much more slowly than ^{26}Al, and hence becomes relatively enriched in a sample during a period of burial below the surface cosmogenic isotope production zone [~2m for the Bishop Tuff]. Erosion of the overburden brings the sample back into the production zone, and production of *both* isotopes recommences, in the characteristic ratio. Hence the imbalance in the isotope concentrations, formed during the period of burial, remains locked in the sample. Apparent exposure ages calculated in Table 6.7 assume that all the samples have remained at the surface throughout their exposure history, and so do not account for periods when the sample has been protected from cosmogenic bombardment. Burial is evident only from the discrepancy in the two isotope ages, but this difference alone is not sufficient to allow calculation of a unique solution to the burial history. Figure 6.15 demonstrates the discrepancy between the calculated and 'true' exposure ages for a sample that has been buried once between exposures. Thus *both* the ^{10}Be and ^{26}Al ages calculated in Table 6.7 underestimate the true exposure time of this sample.

In the case of sample VT8, the large relative enhancement of ^{10}Be relative to ^{26}Al suggests that either this sample has been buried for a significant period of time, or that it has experienced several burial-erosion cycles [see Fig. 2.32]. This indication of burial is consistent with the erosion island plot for the Tableland samples, Fig. 6.12: sample VT8 lies below the steady-state erosion island, implying that at least one period of burial punctuated its exposure history.

The total loss of ^{10}Be in a sample during all its burial periods is smaller than that of ^{26}Al, and hence the ^{10}Be age more accurately represents the *total* length of the surface exposure of the sample [i.e. in Fig. 6.15, $\mathbf{D}_{Be}$ is a better approximation of $\mathbf{A+C}$ than is $\mathbf{D}_{Al}$]. However, the period(s) of burial of the sample may have happened at any point relative to the calculated age of the sample, and so, as shown in Fig. 6.15, neither age can be used with confidence to determine the total exposure, or the timing of incisions or major erosion events.

Although a unique burial history cannot be determined with just two isotopes, Bierman et al. (1999) provide a simple method for calculating an approximation to the total lengths of time the sample has been exposed and buried since its initial exhumation [section 2.5.2.1]. The method is only approximate [see also Granger and Muzikar (2001)], as it relies on the assumption that the sample is exhumed and buried virtually instantaneously, and also that burial is deep, so that no production occurs during the period of burial. This method is likely to underestimate the true length of the burial, relative to the exposure, but the errors are more marked with older samples, and where a sample has not been exposed for long prior to its burial [section 2.5.2 and Granger and Muzikar (2001)].

If the Bierman et al. (1999) method is applied to VT8, the best solution to Eqns. 2.28 and 2.29 supplies:

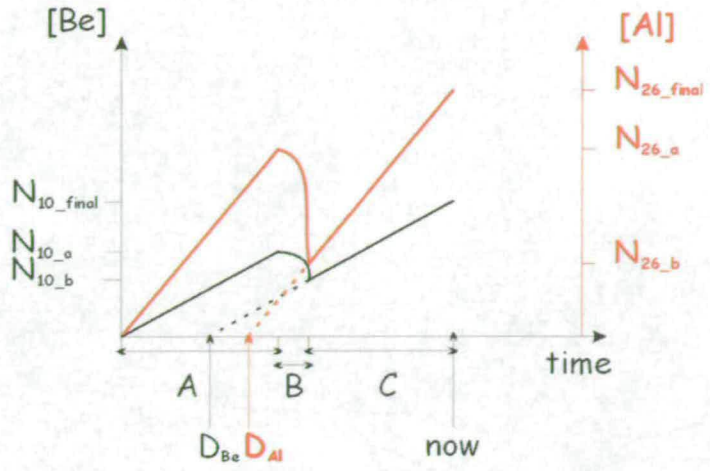

Figure 6.15: *Cartoon of radioactive cosmogenic isotope build-up in a sample that has been buried for a period of time between exposures.*
The plot shows the variation in the concentration of the two different cosmogenic isotopes through time. During the two periods of exposure [A,C], the concentration of in situ*-produced isotopes increases linearly. The gradient of each line is equal to the production rate of that isotope at the sample location. Each isotope reaches a concentration of N_a by the beginning of the burial period [B].*
During the period of burial [B], the radioactive isotopes decay according to their half-lives, to concentration N_b. The decrease in concentration is most marked for the shorter-lived isotope [here ^{26}Al].
Calculation of the apparent exposure age does not account for the period of burial, as it is based purely on constant isotope production through time - dotted line. Thus the apparent exposure age is $\boldsymbol{D_{Be}}$, or $\boldsymbol{D_{Al}}$, years for the two isotopes, whereas the sample has actually been exposed for $\boldsymbol{A+C}$ years, and buried for $\boldsymbol{B}$ years.
The burial period is evident only due to the discrepancy in the ages [$\boldsymbol{D_{Be}}$-$\boldsymbol{D_{Al}}$] predicted by the two isotope systems. A large discrepancy develops during a long period of burial or multiple burial / erosion cycles.

$$\begin{aligned} \text{total surface exposure, } t_e &= 377.5\text{kyr} \\ \text{total burial, } t_b &= 386.1\text{kyr} \\ \text{total exposure history, } t_{hist} &= 763.6\text{kyr} \end{aligned}$$

The error margins on this calculation are huge. Granger et al. (2001a) show the error scales with burial time and the uncertainty in the ^{26}Al :^{10}Be ratio [their equation 8], but for VT8, it is likely that the errors in the total exposure history, t_{hist}, are at least 200 kyr. We have an external check in that the main Bishop Tuff ash flow was emplaced 762.2±4.7ka (Sarna-Wojcicki et al., 2000), and hence the scale of the calculation above is probably reasonable for the Volcanic Tableland. While the absolute numbers are by no means precise, what this method does give us is an idea of the *magnitude* of burial time that is required to produce the observed discrepancy in the ^{26}Al and ^{10}Be exposure ages [Table 6.7]. Clearly the size of the discrepancy requires burial at least of

the order of 10^5 yrs. Hence, given that even the ^{10}Be age underestimates the exposure of the sample, the Bierman et al. (1999) calculation implies that VT8 was initially exposed at least 400-500ka. This has important consequences for the development of the fault overlap in particular, but also for our understanding of fluvial evolution on the Tableland [see section 7.2.2].

6.5.2 Controls on channel formation and incision

There is great debate about the exact timing of the onset and length of glaciations in the Sierra Nevada [see section 3.1.1 and Table 3.1], and particularly regarding stages which may have occurred between the Tahoe and Sherwin glacials. Pinter and Keller (1995) suggested that the Tableland stream development was influenced by the first two glacials that are recorded by Owens River terraces at the southern margin of the Tableland, correlated by Pinter et al. (1994) with the Tahoe and an unspecified 'pre-Tahoe' stage [see section 3.1.2]. Pinter and Keller (1995) used the published data [Table 3.1] to put boundaries on the possible extents of these stages as 79 - 56ka [Tahoe] and 206 - 131ka ['pre-Tahoe'], shown by the grey boxes in Fig. 6.14. They suggested that increased runoff during a pre-Tahoe event was responsible for the formation of the Tableland channels, and that they have since been unoccupied, with most water flowing through the subsurface, except possibly for a brief period during the wetter climate of the Tahoe glacial [see Chapter 3.2].

Where complex burial-erosion histories have *not* occurred, exposure ages in channels record the last significant incision at the location of the sample. The sample has then remained at the ground surface since the dated time of this incision. If the Pinter and Keller (1995) channel histories are right, the Tableland sample exposure ages should reflect the influence of the glacial cycles. Thus exposure ages should group around the Tahoe stage if significant incision occurred at the sample location during this second period of occupation, or otherwise around the pre-Tahoe stage, recording the channel formation. Also, if the channels were unoccupied in the interglacials both before the pre-Tahoe glacial and between the glacial events, then no exposure ages should fall far outside the events marked in grey, except possibly in cases where complex burial has occurred.

The exposure ages do appear to fall into two groups, one significantly older than the other. However, these groups do not shown any clear relationship to the glacial events marked by the grey boxes in Fig. 6.14. Significantly, only VT2 and VT14 lie within the marked periods, while all the rest of the calculated exposure ages fall both between the glacials and also before the pre-Tahoe stage, which Pinter and Keller (1995) believe was responsible for the formation of the channels. Since only VT8 shows evidence of complex burial, these ages must be considered indicators of 'true' exposure. While six ages, including one showing evidence of very significant burial, cannot be considered statistically significant, the lack of any obvious grouping around either glacial suggests there may be a more important control on the channel incision.

Figure 6.16a shows the calculated exposure ages in relation to the geographical location of the samples. The youngest samples are located in the main channel, in the immediate footwall of the linking fault and in the footwall of Fault 1. Figure 6.16b shows the calculated exposure ages relative to the long profile of the main channel [see Fig. 4.24].

Sample VT4 was taken from the southern fork of the main channel through the linking fault, and sample VT11 is not marked in the profile itself as it was taken from the minor channel further north in the ramp [see Fig. 6.16a].

The exposure ages show a marked pattern in relation to changes in gradient of the channel profile. The youngest samples occur at or immediately upstream of, the linking fault [VT4, VT6] and upstream of the large Fault 1 [VT14]. Significantly, these samples were taken from parts of the channel through which fault-driven knickpoints have propagated [see section 4.2.1.2]. Although sample VT14 was taken ~365m upstream of the fault scarp, the long profile shows a clear step, and corresponding gradient change, ~65m *up*stream of the sample location ['kp1' in Figs. 4.25 and 6.16b]. As discussed in Chapter 4, this step is an important structural feature of the channel, and probably the present location of a knickpoint which has migrated upstream from where it was initially formed in response to tectonically-induced base level fall at Fault 1. In contrast, the samples showing the older exposure ages were taken from points beyond the parts of the channel affected by knickpoint propagation. VT2 was taken upstream of the Fault 2 knickpoint, and VT8 is upstream of the linking fault knickpoint [see Fig. 6.16b and also section 4.2.1.2].

The correlation of the exposure ages with the fault pattern points to the influence of knickpoint propagation on channel incision on the Tableland. The variation in exposure ages along the main channel is similar to the pattern seen in bedrock samples from a Hawaiian channel sampled by Seidl et al. (1997) [their Fig. 6] thought to be dominated by knickpoint migration. The lack of correlation of the exposure ages with glacial events, and the link between the calculated ages and observed incision patterns, suggests that these channels have been more influenced by the local fault growth than by regional climate variations.

Sample VT11, from the minor channel to the north, has a very old exposure age, closer to that of VT2 than to the ages of other samples taken in the immediate footwall of the linking fault [VT4 and VT6]. This is consistent with the lack of incision in the minor channel here [see Fig. 6.9], and suggests that this smaller channel was less active during the later deformation of the ramp that influenced the main channel so strongly in the vicinity of the linking fault. This is consistent with the lack of any significant upstream migration of the linking fault knickpoint in the minor channel [Figs. 4.39 and 6.10]. The lack of significant movement at the tip of Fault 2, where it is crossed by the minor channel, would also reduce the amount of rejuvenation of the lower part of this stream [section 7.2.2].

The clear difference in the age of VT11 from those of the other samples in the linking fault footwall [VT4 and VT6] implies that no significant incision occurred after ~250ka in the *minor* channel in the linking fault footwall, which is consistent with the shallow channel at the sampled site. In contrast, the pronounced incision seen in the *main* channel in response to fault motion shows that it was still active much later, and the samples show that marked incision occurred around 97[-83]ka in the two branches of the main channel, upstream of the linking fault. Thus constraints may be put on the timing not only of the minor channel's activity, but also, by comparison with the main channel, on the timing of motion on the linking fault [section 7.2.2]. Significant amounts of motion occurred at least in the central part of the fault [VT4 and VT6 locations] by 97[-83]ka, resulting in this later and deeper incision.

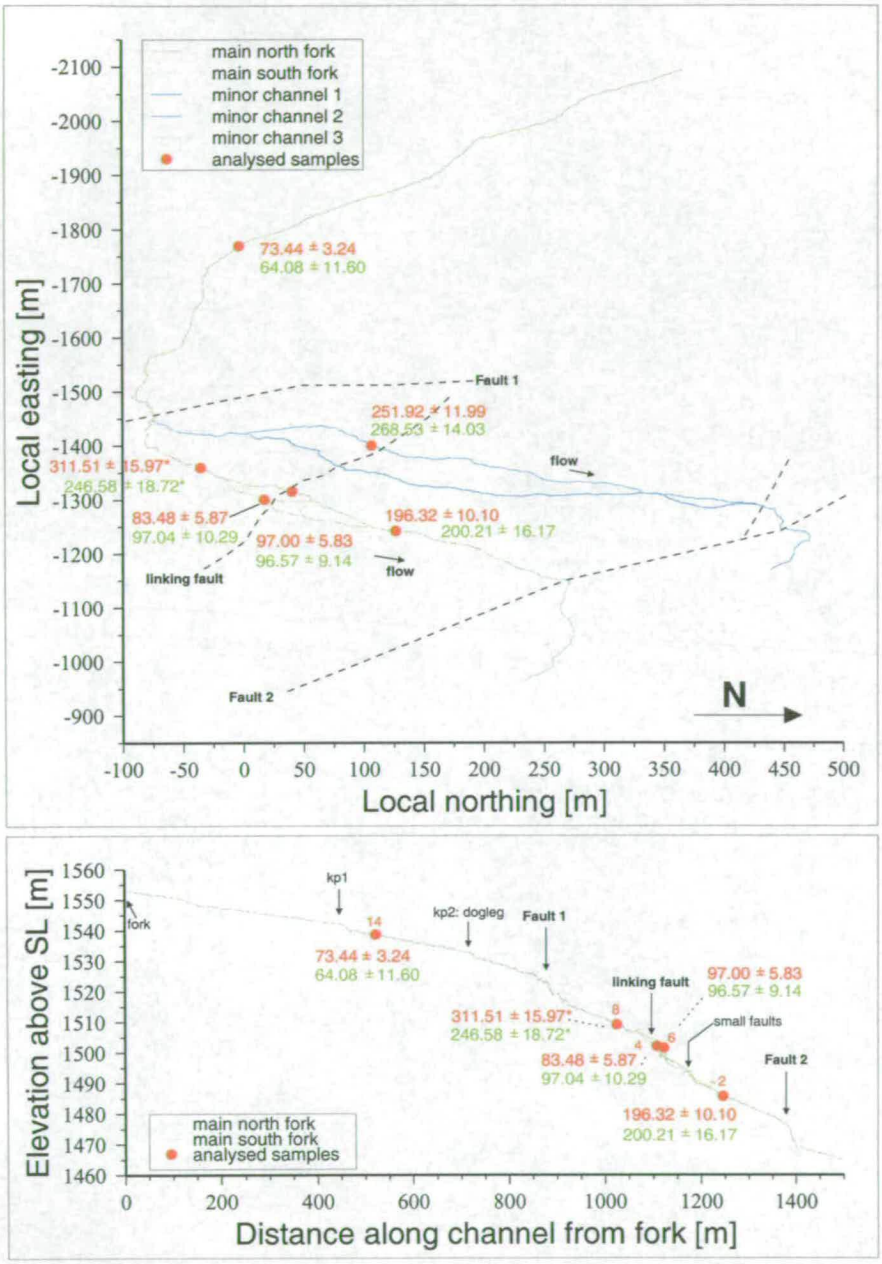

Figure 6.16: *a. Map of the central overlap and b. long profile of the main stream showing the apparent exposure ages of analysed samples.*
Ages have been calculated using the scaling factors of Nishiizumi et al. (1996). ^{26}Al *ages are marked in green and* ^{10}Be *ages in red for each sample.*
Sample 8 shows evidence of significant burial [see also Figs. 6.12 and 6.14].
Sample 11 was collected from the minor channel further to the north in the main overlap, but immediately upstream of the linking fault: at a location similar to that of sample 4 relative to the fault.
The figures imply that faulting may be the dominant control on the stream development: Samples 2 and 8 are upstream of the knickpoints formed in response to Fault 2 and the linking fault, respectively. However, the knickpoint from Fault 1 has propagated upstream even further than the sampled site for VT14 [to kp1].

Sample 8, which shows evidence of complex burial, is located immediately downstream of Fault 1, at the western side of the ramp. In section 4.2.3, evidence was presented which suggested that a broad alluvial fan was previously deposited over what has become the overlap zone, sourced from the point where the main channel cut through Fault 1. In this scenario, a sample collected from the location of Sample 8, near the source of the fan's sediment supply, may well have become covered by material deposited by the low gradient distributary channel [e.g. cobbles, Fig. 4.46 and larger material as seen in the debris pile at the foot of Fault 1, Fig. 4.48]. Sample 8 may have undergone periodic exposure and re-burial as channel systems migrated across the developing fan. The effects of this sediment deposition would have been greater at the location of sample 8 than at any of the other sampled sites, as it is proximal to the proposed sediment source from the Fault 1 scarp. Later 'fixing' of the main stream course by incision of the present channel through the deposited fan material would have again exposed the sampled slab to cosmogenic radiation at the surface. This series of events could have led to the complex exposure history of sample 8 seen in the comparison of ^{26}Al and ^{10}Be exposure ages [Fig. 6.14] and in the erosion island plot [Fig. 6.12]. The Bierman et al. (1999) calculation implies that burial of VT8 lasted for the order of 10^5 years, although not necessarily in one single stretch. This puts important constraints on the development of the transport systems in the region of this fault overlap, and also on the fault evolution, if, as suggested in Chapter 4, later incision of the main stream was driven by displacement and northward propagation of Fault 2. This is discussed in more detail in section 7.2.2.

6.6 *In situ* cosmogenic production rate scaling factors

In the light of the continuing debate about the best way to calculate production rates [section A.3], I have included a comparison of the data described above with apparent exposure ages calculated from other published scaling factors. I decided to use the scaling factors of Nishiizumi et al. (1996) as they are derived from samples collected from the Owens Valley, and include a sample taken from the Sherwin Till, under the Bishop Tuff (Nishiizumi et al., 1989), although most of the samples are taken from elevations much greater than those of the Volcanic Tableland. However, a plethora of other scaling factors exist, each derived from different field measurements or theoretical calculations. In particular, those of Schaller et al. (2001), rescaling the values of Kubik et al. (1998), are based on samples collected at very similar altitudes to those of the Volcanic Tableland. Table 6.8 compares apparent exposure ages calculated for the Tableland samples using a variety of different scaling factors. These data are then plotted in Fig. 6.17, as a comparison with the data calculated from the Nishiizumi et al. (1996) scaling factors, and also the Tahoe and pre-Tahoe glacial stages.

The last values in Table 6.8b are calculated using the Nishiizumi et al. (1996) scaling factors, but based on disintegration rates calculated following Dunai (2000), rather than those quoted in Lal (1991) [see section A.3]. These disintegration rates are based on two recent datasets, rather than the 1950s observations which form the basis of the Lal (1991) scaling approach. The debate continues as to the best approach to production rate scaling, and Table 6.8b and Fig. 6.17 show that the Dunai (2000) method [open triangles] gives consistently lower production rates, and consequently older exposure ages, for the Volcanic Tableland samples than those calculated by scaling the Lal (1991) data [filled red circles].

The difference in scaling factors and particularly in the calculated production ratio of ^{26}Al :^{10}Be, results in a relatively large scatter in the ages for each sample [Table 6.8 and Fig. 6.17]. However, the overall pattern of the data is consistent with that discussed above. Only VT8 shows any significant evidence of complex burial, and this is maintained with all the scaling factors, as well as with the Dunai (2000) disintegration rates. None of these scaling factors result in the ages showing a better correlation with the glacial events [206 - 131ka and 79 - 56ka; (Pinter and Keller, 1995) and references therein] marked in grey on Fig. 6.14. Thus the lack of evidence for a significant glacial trigger in the channel data is not simply an artefact of the particular choice of the Nishiizumi et al. (1996) scaling factors, or the Lal (1991) disintegration rates.

a. Alternative scaling factors: SLHL			
Reference	**Scaling Factor (atoms g^{-1} yr^{-1})**		**Production ratio**
	^{26}Al	**^{10}Be**	**^{26}Al : ^{10}Be**
Nishiizumi et al. (1996, 1989)†	35.03 ± 0.35	5.80 ± 0.58	6.04
Schaller et al. (2001); Kubik et al. (1998)§	35.01 ± 2.7	5.37 ± 0.22	6.52
Barrows et al. (2001)	30.62 ± 1.6	5.02 ± 0.27	6.10
Stone (2000)	31.1 ± 1.9	5.1 ± 0.3	6.10

b. Apparent exposure ages, from different scaling factors						
Reference	**Calculated Exposure Age (^{10}Be : ^{26}Al, years x 10^3)**					
	VT2	**VT6**	**VT11**	**VT4**	**VT8**	**VT14**
Nishiizumi et al. (1996)†	196.32 : 200.21	97.00 : 96.57	251.92 : 268.53	83.48 : 97.05	311.51 : 246.58	73.44 : 64.08
Schaller et al. (2001)	212.84 : 200.33	104.96 : 96.63	273.42 : 268.70	90.30 : 97.10	338.49 : 246.74	79.43 : 64.11
Barrows et al. (2001)	228.48 : 232.45	112.47 : 111.24	293.82 : 313.53	96.74 : 111.79	364.18 : 287.38	85.08 : 73.63
Stone (2000)	224.71 : 228.44	110.66 : 109.43	288.89 : 307.91	95.19 : 109.97	357.97 : 282.29	83.72 : 72.46
Nishiizumi et al. (1996)‡ Dunai (2000)	208.25 : 213.04	102.67 : 102.36	267.21 : 286.13	88.34 : 102.86	330.56 : 262.43	77.55 : 67.72

Table 6.8: *Variation in apparent exposure ages with different production rate scaling factors [see discussion in section A.3].*
a. Scaling factors from various authors, quoted for SLHL [Sea Level, High Latitude]. These are then scaled to calculate the production rates at the sample latitude and elevation [see Chapter 2].
b. Exposure ages, corrected for sample thickness and topographic shielding, calculated using the scaling factors in Table 6.8a. The values discussed previously [using Nishiizumi et al. (1996) scaling factors] are shown for comparison. Errors are not quoted here for simplicity. The data is based on samples from:
citetnish89 - Sierra Nevada and Owens Valley, California; Kubik et al. (1998) - Ötz Valley, Austria
Barrows et al. (2001) - Snowy Mountains, Australia Stone (2000) - Antarctica
Dunai (2000) - two datasets: airborne data from high latitudes in Europe and Asia and shipboard data from all latitudes in the Atlantic
† These values have been used throughout the thesis. Nishiizumi et al. (1996) values were rescaled from the initial calculations in Nishiizumi et al. (1989) following recalculation of the ages of the sampled surfaces.
§ Schaller et al. (2001) values are based on those calculated by Kubik et al. (1998), but rescaled for lower muon contributions.
‡ These values are calculated using the scaling factors of Nishiizumi et al. (1996), but from the disintegration rates of Dunai (2000). All the other data are calculated from the disintegration calculations of Lal (1991): see section A.3.

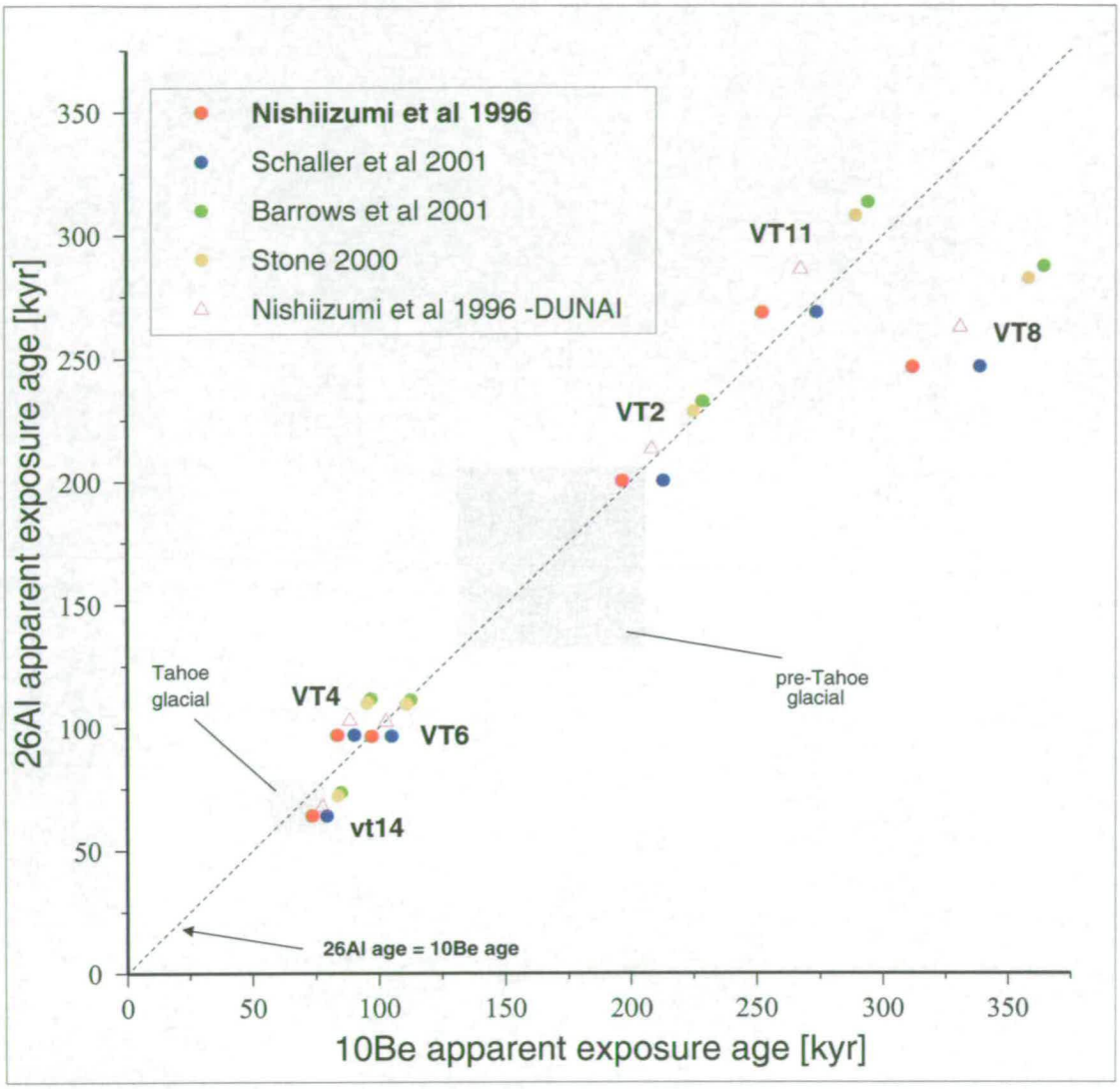

Figure 6.17: *Comparison of* ^{26}Al *and* ^{10}Be *apparent exposure ages, using different scaling factors.*
Data has been corrected for topographic shielding and sample thickness, see above. Filled circles are based on the disintegration rates of Lal (1991); open triangles are based on the methodology of Dunai (2000).
The dotted line shows the locus of points with equal ^{26}Al *and* ^{10}Be *ages. Points plotting to the right of this line may have undergone some burial, as the* ^{26}Al *age is lower than the* ^{10}Be *age [*^{26}Al *decays faster than* ^{10}Be*, and hence the ratio of isotopes drops during burial]. Again, the reported periods of the Tahoe and pre-Tahoe glaciations, thought to have influenced the formation and development of the channels [206-131ka; 79-56ka: references in Pinter and Keller (1995)], are marked in grey.*
Although the absolute ages, and the exact ^{26}Al */* ^{10}Be *ratio depend on the choice of scaling factor, the overall pattern is maintained, and no significant correlation with the glaciations is seen using any of the scaling factors in Table 6.8.*

6.7 Summary

This chapter has described the collection of samples for ^{26}Al and ^{10}Be cosmogenic radionuclide analysis from the Volcanic Tableland. Section 6.1.1 described the choice of sample sites in the field, and then explained the reasons for the choice of only 6 of these samples for final analysis. Field photographs of the locations of analysed samples, both before and after sampling, are shown in sections 6.1.2.1 to 6.1.2.6.

The second part of this chapter [sections 6.2 and 6.3] detailed the calculations of ^{26}Al and ^{10}Be exposure ages from the raw data in Table 6.1. Data for the second batch of samples showed that an error had been made in the dilution of the aliquots sent for ICP, and hence Al and Be concentrations in the targets have been assessed using pipette calibrations, as well as the using the 'normal' method, from the ICP measurements [Tables 6.4 and 6.2, respectively]. The erosion island plots for the Tableland samples [Fig. 6.12] shows that within error, most of the samples lie in the erosion island. However, VT8 shows evidence of complex burial, with a very low N_{26} / N_{10}* value.

Corrections were made to the 'raw' production rates for the sample thickness and topographic shielding of the samples in the field [section 6.3]. Since all samples were taken from subhorizontal surfaces and the sample locations were assumed not to have been significantly covered by snow or sediment during their exposure, no corrections were made for slope or for surface coverage. Apparent exposure ages were then calculated for the samples, taking into account shielding corrections [section 6.4].

Section 6.5 describes some initial interpretations of the exposure age data. Figure 6.14 compares the final ^{26}Al and ^{10}Be exposure ages, showing evidence for complex exposure for sample VT8, as implied by the erosion island plot, while the other analysed samples have been exposed continuously. Calculations following Bierman et al. (1999) suggest that VT8 may have been buried for the order of 10^5 years, and hence imply an initial exposure around 400-500ka. Comparison with published data for glacial events in the region [summarised in Pinter and Keller (1995)] suggests that regional climate may have had a smaller effect on the channel evolution than previously assumed (Pinter and Keller, 1995; and see Table 3.1). Exposure ages greater than 206ky, and particularly the complex exposure history of VT8, suggest that climate fluctuations may not have been the primary control on the formation of channels on the Volcanic Tableland. In contrast, ages plotted onto the map of the fault overlap [Fig. 6.16a] and the main channel long profile [Fig. 6.16b] indicate the role of extensional faulting, particularly through knickpoint propagation, in the evolution of the channels in the main overlap. The fact that the apparent exposure ages correlate better with the fault pattern than with the timing of glacial stages implies that local faulting, rather than the regional climatic variation, may have been the dominant influence on the drainage development in this area.

Table 6.8 shows the variation in the exposure ages of the Tableland samples when different scaling factors are used. These ages show that the lack of correlation with the glacial events cited by Pinter and Keller (1995) is not an artefact of the choice of production rate scaling factor.

Further discussion of the cosmogenic results, particularly in light of the field observations from Chapters 4 and 5, may be found in the following chapter: see section 7.2.2.

Chapter 7

Discussion of Volcanic Tableland results

This chapter considers the implications of the observations made around the fault array on the Volcanic Tableland in the preceding Chapters 4, 5 and 6. The first part [section 7.1.1] discusses the stream patterns on the Tableland, concluding that stream evolution is dominated by responses to the tectonic displacement pattern, and the interaction between the growing faults; but that streams with different discharges respond in contrasting ways. Section 7.1.2 describes the main features of the faults, and how many of the fault characteristics are demonstrated by the stream responses, and not just by the D/L profiles. Section 7.1.3 compares the tools used in Chapters 4 and 5 to investigate the downstream variation in the channel morphology: the SL index [see section 2.3.2] and the aspect ratio, AR [defined in section 3.3]. Both these parameters are numerical assessments of channel morphology, but provide different information about the evolution of the channels which incise the Tableland surface.

Section 7.2 considers the evolution of the central overlap [Chapter 4] in some detail, and uses the cosmogenic isotope data from Chapter 6 to constrain the rates of the processes which have dominated its evolution. This section discusses aspects of the tectonic and drainage development of the overlap, culminating in a model for its overall evolution [Fig. 7.6]. Section 7.3 looks in more detail at the information gained from the axial stream and its tributaries [see section 5.2], to piece together information about the linkage of the whole array, and the implications of this tectonic evolution for the streams which drain the surrounding area. A palaeogeographic model is presented in Fig. 7.8. Section 7.4 considers the implications of the observation of non-tuff clasts in the northern tip drainage network, and another channel on the Tableland [section 5.1.4]. These observations are compared with published hypotheses about the regional drainage evolution to produce a simple model for the larger-scale pattern of drainage evolution on the Tableland [Fig. 7.9]. The central overlap stream geometry is compared with the 'classic' model of relay ramp drainage development in section 7.5. The interacting factors that govern the final stream geometries are explored.

These discussions are summarised in section 7.6 and in the synthesis in Chapter 9.

7.1 General features of the Tableland

7.1.1 Streams

The influence of fault growth is felt principally through changes in local gradient, which drive changes in stream course and channel bed gradient. Local variations in channel slope affect stream power and incision rates, which in turn control the distribution of bedrock and alluvial reaches. Changes in the distribution of slip on the faults in the array are responsible for the current styles and patterns of incision and deposition on the Tableland, and the way that these patterns have evolved through time.

Stream course: The growth and propagation of extensional faults has perturbed the regional slope, and hence had major impacts on the stream patterns through time. Pinter and Keller (1995) used stream segment orientations to infer that the Tableland streams initially flowed down a regional slope towards 121-125°, but had later been affected by the growth of faults. The surveyed streams encounter predominantly E-dipping faults, and hence flow from the uplifted footwalls across the scarps into the subsiding hangingwall basins. Where powerful enough, the streams have incised through fault scarps [e.g. northern incised canyon], but fault-induced changes in stream course are widespread. Changes in course vary from small increases in sinuosity and braiding [e.g. around faults in central overlap streams, Figs. 4.21; 4.38] to large scale deviations towards local topographic lows. Streams are deflected both in the footwalls - towards lower displacement at segment tips [e.g. north stream tributary 4, Fig. 5.22], and in the hangingwalls - towards the rapidly subsiding basin centres [e.g. minor streams in central overlap, Figs. 4.20 and 7.6].

Stream courses are most strongly deflected by closely-spaced faults [e.g. downstream reaches of northern stream, Fig. 5.2]. Fault propagation and linkage can lead to stream deflection [e.g. main stream in central overlap, Figs. 4.20; 7.6; rerouting of axial and F1/F0 overlap streams in F0 basin, Figs. 5.26; 7.8]. In other cases, stream abandonment and major reorganisations may occur [e.g. following the incision of main central stream; termination of the supply down the road stream, both due to growth of Fault 2, Figs. 5.46; 7.6; beheading of fumarole-axial stream, Figs. 5.46; 5.47]. Increasing slip rates led to ponding of the central stream supply in the subsiding hangingwall basin of Fault 2 [inferred from profile of road stream, Fig. 5.46].

The influence of faults is in places aided by variations in the welding or jointing of the tuff [e.g. Figs. 4.20 and 5.1]. However, evidence suggests that jointing has influenced some parts of the fault pattern, and hence the coordination of some lithological and fault effects on stream growth may not be coincidental.

Despite the magnitude of these changes, the effect of faulting is localised. Both upstream and downstream of the fault influence, stream courses are controlled simply by the regional slope, although in places tempered by variations in the welding and jointing of the tuff.

Stream gradient: The spatial variation in displacement around a fault exerts a varying influence on the gradient of nearby streams. Most of the surveyed streams are dominated by faults at high angles to their initial flow direction. An initial decrease in gradient is experienced in the uplifting footwall, and in the subsiding hangingwall [e.g. Ouchi (1985); Holbrook and Schumm (1999); section 2.3.3]. If the stream is not

forced to change its course, increased sinuosity, aggradation and braiding of alluvial reaches on either side of the fault [e.g. Fig. 4.21] give way to incision in the footwall as the base level drop is transmitted upstream. Steepening of the footwall reach increases towards the fault [section 7.1.3], demonstrating the upstream transmission of the base level change [e.g. Howard et al. (1994)], and is associated with narrowing of the channel and an increase in the aspect ratio [e.g. Fig. 4.34]. The steepest reaches in each stream occur at the actual fault scarps [e.g. Tables 4.3; 4.6; 5.1 and 5.3], although these present gradients are a function not only of the amount of displacement but also the ability of the stream to adjust to it. Bedrock incision occurs for several hundred metres upstream of the largest faults [e.g. Figs. 4.32; 5.13 and 5.19]. Plungepools at the base of many faults [e.g. Fig. 4.29c,d] demonstrate the erosive power of falling water, but reduced gradient in the hangingwall generally causes aggradation [e.g. Fig. 5.22] over an increasing area as the basin grows [e.g. Fig. 4.20].

The along-strike variation in fault displacement imposes a lateral gradient on streams which flow across faults, and may result in deflection, or lateral migration, as described above. The current overall gradient of the streams in the central overlap [Tables 4.3 and 4.6] has largely been dictated by the along-strike variation in slip on Fault 2: the main stream has been rejuvenated repeatedly, but the minor streams have experienced virtually no displacement at Fault 2 [section 7.2]. The gradients of fault-parallel streams also reflect the along-strike displacement variation. High displacement gradients on the interacting F1 and F0 tips have steepened the overlap stream [Figs. 4.5 and 5.42], and also caused incision and braiding of the axial stream in the starved F1 basin [Fig. 5.25].

Gradient changes affect the stream power: increased velocity in steep reaches allows the stream to entrain more sediment and provides more impetus to incise the channel bed [section 2.3]. All the fault-steepened reaches have locally high SL indices [Tables 4.3; 4.6; 5.1 and 5.3], reflecting increased stream power. Similarly, high aspect ratios in the immediate footwall demonstrate active downcutting to reduce the perturbation. Repeated fault activity results in increased profile-steepening, driving greater incision into the footwall, and high aspect ratios [see also the stream/bank profiles]. The largest faults, which have accumulated the most displacement, drive the deepest incision over the longest distances, as reflected by the largest changes in aspect ratio relative to the unfaulted reaches [section 7.1.3].

Where streams have incised the most, their gradients are lowest, despite the magnitude of the fault activity [e.g. canyon through the northern tip of the array, 5.1; compare gradients of different reaches in the central overlap, Table 4.3]. This demonstrates the negative feedback of the stream. For a given discharge, the amplitude and wavelength of the response appears roughly proportional to the displacement on the fault: the amplitude of the perturbation of the stream. The northern stream upstream of the array shows the largest and longest response to the greatest perturbation: [Fig. 5.11]. A large fault has driven incision of up to 14m and over 112m from the scarp [Fig. 5.13], while a small fault [throw$\geq$1m] causes a tiny step in the profile, and affects the morphology for only a few metres [xc 10, 10a in Fig. 5.12]. Similarly, Fault 1 has the largest effect on the main stream in the central overlap [Fig. 4.37, and section 7.1.3.2].

In contrast, other low gradient reaches show little incision, and generally have aggradational morphologies [e.g. 'wide' reach of northern stream, Fig. 5.9; axial stream

in southern Fault 1 basin, Fig. 5.34]. Away from the faults, streams have an almost uniformly low gradient and hence generally occupy shallow, winding channels, which can be hard to trace. This demonstrates again the local influence of faults: although stream gradients may reach 40° through a fault scarp, and have driven deep vertical incision, they may return to a fraction of a degree only a few hundred metres away. The rapid stream gradient changes as faults are approached [e.g. Figs. 5.25; 5.20] demonstrate that almost all the gradient variations are fault-induced. In contrast, where evident, changes in gradient due to lithology are less pronounced, and occur over smaller distances. The evidence demonstrates that the Tableland streams have responded rapidly and dramatically to fault movements, interaction and linkage, and that the stream patterns are extremely sensitive markers of even subtle tectonic activity.

Distribution of bedrock and alluvial reaches: Bedrock incision occurs in the immediate footwalls of transverse faults and where plungepools are scoured in the immediate hangingwalls by water cascading over the knickpoint. Incision is deepest and transmitted furthest upstream from the largest faults [e.g. Fault 1], and in the most powerful streams [e.g. northern tip stream]. Alluvial deposition, sometimes developing a discrete fan [e.g. base of Fault 2] occurs in the rest of the hangingwall. Streams parallel to faults occupy low gradient alluvial channels, with the exception of the steep reach in the northern part of the Fault 1 basin, where the axial channel incises bedrock [Fig. 5.29]. Away from the influence of the faults, streams are consistently alluvial, and occupy shallow winding channels. A few exceptions to this rule reflect lithological heterogeneities [e.g. indurated fumarole regions, Fig. 5.2; variations in jointing, Fig. 5.14e]. Hence lithology tempers stream responses, but faulting has the first-order control on the distribution of bedrock and alluvial reaches.

Potholes and scours from abrasion, and the removal of jointed blocks by plucking are evident throughout the surveyed bedrock reaches [e.g. Figs. 4.26; 4.29 and 5.14]. Potholes are particularly well-developed immediately upstream of some knickpoints in the central overlap, indicating focused erosion and possibly a role in the process of knickpoint retreat [e.g. Bishop and Goldrick (1992); Wohl (1993)]. Plucking of joint-bounded blocks is widespread in pervasively-jointed reaches, and the shapes of the knickpoints at Fault 1 and further upstream [e.g. Fig. 4.27] may indicate that it is central to the mechanism of knickpoint retreat in this reach [section 7.2.2.4].

The relative efficiency of incision by plucking and by abrasion (Hancock et al., 1998; Whipple et al., 2000a) implies that incision may be faster in the jointed reaches of Tableland streams than where joints are fewer. However, the lower reaches of the central footwall stream are littered with large angular joint-bounded blocks [~2-3m diam.] that have been stripped, or have collapsed, from the channel walls [e.g. Fig. 4.26e]. These blocks can only be moved by rare high discharges, and hence probably reduce the rate of incision of the underlying channel floor until weathering makes the blocks transportable [e.g. Seidl et al. (1994); Granger et al. (2001a)]. Seidl et al. (1994) reported similar 'armouring' of Hawaiian stream beds, emphasising the importance of knickpoint propagation under the blocks in lowering the otherwise protected bed.

Stream processes and hence the evolution of bedrock and alluvial reaches differ considerably [section 2.3.1]. Bedrock is incised where the stream's capacity to carry sediment exceeds the available supply, and the excess energy is expended on the rock

walls. The consistent correlation of bedrock exposure with fault-steepened reaches demonstrates that faulting is the principal control on the stream power of the Tableland rivers.

Resistant walls make bedrock stream morphology more constant than that of alluvial reaches, adjusted only relatively slowly, and usually in response to large or sustained discharges [section 2.3.3.3]. Hence the long-term fault movements which determine the distribution of bedrock and alluvial reaches also dictate the ability of a given reach to respond to subsequent tectonic activity, and the mechanisms by which the adjustments are made.

Alluvial reaches in Tableland streams have responded to fault-induced gradient changes by changes in sinuosity and braiding [e.g. main stream at faults in ramp, Fig. 4.21] as well as through incision or aggradation [compare different reaches in downstream northern stream, Figs. 5.2 and 5.8]. Bedrock reaches respond to increased gradient purely by incision, at times coupled with narrowing, resulting in steeply V-ed cross-sections, and inner channels [e.g. Fig. 4.34; xcs 30,30a in Figs. 5.12 and Fig. 5.14e]. Aggradation in bedrock reaches in response to lowered gradients is erased during subsequent increases in gradient, but the sinuosity in the immediate footwall of Fault 1 [Fig. 4.21] must have been preserved from the early, and probably alluvial, stages of the stream's development, before the deep incision of the stream. This implies that while alluvial reaches may record *small* changes in fault growth patterns, bedrock reaches may be more likely to actually *preserve* the evidence of larger, more fundamental changes in fault activity.

The higher transport efficiency of steep bedrock reaches also has important consequences for the relative value of upstream channels vs. basin deposits as records of fault activity. The effects of erosion may be quickly seen in footwall streams, but subsequently take a long time to appear in depositional patterns further downstream. Hence where they are able to incise rapidly enough to keep pace with fault movements, footwall bedrock streams will provide relatively sensitive records of small, or relatively rapid changes in fault activity. In contrast, the sediment record is more ambiguous, as it averages the smaller wavelength or amplitude changes, and fluctuations in the volume or location of deposits can be caused by changes in a number of factors in the upstream catchment.

Other external influences: The surveyed streams have responded rapidly and dramatically to fault movements, interaction and linkage. However, the response to faulting is tempered by other factors, including the stream power. Streams with greater or more prolonged discharge are able to incise through even rapidly uplifting scarps, while smaller streams would be defeated [section 2.3.3.2; Burnett and Schumm (1983); Ouchi (1985); Merritts and Vincent (1989)]. The influence of high discharge is demonstrated by the incision of a deep canyon through the northern tip of the fault array. The canyon reaches almost 11m depth, yet has a low, almost uniform gradient, indicating that the differential uplift has been completely accommodated by the incising stream [Figs. 5.3 and 5.4]. In contrast, the upstream tributaries preserve steep gradients and steps in their profiles in response to similar size faults [e.g. Figs. 5.19 and 5.22].

The impact of lithological variation is evident in the sudden focused incision of the upstream northern river where faulting has exposed a pervasively-jointed section of tuff [Fig. 5.14a-e]. Softer, less consolidated tuff is partly responsible for the excavation of a

large canyon in the footwall of a large fault further upstream. Regions of indurated tuff around fumaroles are responsible for at least some of the 'guiding' of the downstream northern channel through a series of almost right-angled bends [Fig. 5.2]. Immediately upstream of the Telegraph Road, tributary confluences appear to be influenced by the density of fumaroles [Fig. 5.11]. Fumaroles confine streams which are then forced to incise when they cannot migrate laterally [e.g. 'narrow' section of downstream northern channel; fumarole-axial stream; axial stream in F1 basin].

The influence of climatic cycles is hard to determine definitively from the available data on the Tableland streams. Pinter and Keller (1995) proposed that the stream occupation was limited to the two major glaciations after the emplacement of the tuff, arguing that runoff was only adequate to support streams during these periods. However, the cosmogenic isotope data [Chapter 6 and section 7.2.2] imply that stream initiation and occupation may not have been governed purely by the glacial periods, and hence that climatic influences on the stream evolution may be less pronounced than those of the faults. Clearly the availability of water is a pre-requisite for the stream development, but the cosmogenic data implies that the wetter climate of the Late Pleistocene (Smith et al., 1997) may have been able to support streams on the Tableland even during interglacials [see sections 7.2.2 and 7.4].

7.1.2 Faults

The faults on the surface of the Tableland show many of the features described in section 2.1, as previously demonstrated by Dawers et al. (1993); Scholz et al. (1993); Dawers and Anders (1995) and more recently by McFadzean (2002). This study has demonstrated interaction and feedback between neighbouring faults, linkage and variations in the rate and style of displacement accumulation on some of the faults within the array. Some of these features are clear in the cutoff and displacement profiles presented in section 4.1; others are implied by the responses of the developing streams [section 7.1.1 above], demonstrating the value of the streams as indicators of tectonic motion, and the benefit of using *both* stream and fault data to investigate an evolving extensional area.

Fault interaction: 'Skewed' displacement profiles are the clearest evidence of interaction between neighbouring faults; the maximum displacement located closer to the tip of the interacting structure [e.g. Fig. 2.4]. Asymmetrical displacement is evident on virtually all the surveyed faults [section 4.1], demonstrating that the faults grew synchronously, and influenced each other. Interaction is evident on a series of different scales from small segments that link to form larger faults [e.g. Fault 1 and fault k; segments in the southern part of the linking fault], to major faults [e.g. Fault 1 and Fault 0].

Tip gradients are linear on all the surveyed faults [section 4.1], which is consistent with the observations of Dawers et al. (1993) and Dawers and Anders (1995), and implies that slip has occurred on small slip patches, as suggested by Cowie and Shipton (1998). The gradients are considerably steeper at interacting fault tips [section 4.1]. The different tip gradients are also evident from the contrasting responses of streams draining fault overlaps, as steep tip gradients favour stream deflection rather than incision. This is one factor responsible for the contrasting development of the

streams which drain the two ends of Fault 1. A low tip gradient at the southern fault tip [F1/F2 overlap] allowed the main stream to incise through a region of low displacement in the Fault 1 scarp [Fig. 4.10]. High displacement and the steep northern tip gradient prevented scarp incision, deflecting the stream draining the northern tip [F1/F0 overlap] through the overlap parallel to Fault 1 [Figs. 5.26 and 5.42]. Other factors contributing to the different stream geometries include the fault separation and rates of displacement [see section 7.5]. The along-strike displacement variation on Fault 1, caused by interaction, is responsible for the varying morphology of the axial stream, which is braided and incised in the steep northern basin, but meanders in a sandy channel further south in the basin, where the along-strike displacement variation is lower.

Interaction has warped and fractured the rock between fault segments. This is most evident in the development of the central overlap, ruptured by many small faults [Fig. 4.20]; more ductile deformation characterises the overlap between Faults 1 and 0 [Figs. 4.11 and 5.28]. The difference is evident from the profiles of the overlap streams: the F1/F2 overlap streams have a series of steep knickpoints, very varying gradients, and deeply-incised reaches [section 4.2]; the F1/F0 stream has a smoother profile, no sharp steps, and rarely incises bedrock [section 5.2.4.1].

The asymmetrical D/L profiles constrain some of the relative timing of fault growth. Interaction between Faults 1 and 2 is evident from the structures and streams in the overlap, but both main fault profiles are skewed towards their *distal* tips, demonstrating later interaction with other faults in the array [Fig. 4.5 and 4.16]. This places the formation of the F1-F2 overlap relatively early in the development of the array [as implied by the evolution of the main stream; section 7.2.1 and Fig. 7.6]. However, the later growth of Fault 1 has been heavily influenced by Fault 0 to the north; Fault 2 has become hard-linked to faults to the south.

The streams provide more detailed information on the relative timing of fault activity. The extent of the accommodation of fault activity by the central overlap streams implies that Fault 1 was active long before Fault 2, which predated the linking fault. The response of the main central stream to Fault 2 constrains the extent of the linkage of the Fault 1 segments prior to its interaction with Fault 2. The central streams also shed light on the evolution of the fault which hard-links the two main faults [section 7.2.1.1].

Segment linkage: Segmentation of the Tableland faults is evident on a variety of scales from 50 to over 400m [section 4.1]. The smaller scale of segmentation may be partially dependent on the spacing and length of joints in the tuff, along which at least some of the faults have nucleated and propagated [see below]. The growth of long faults by the linkage of small segments is demonstrated by the lobed shape of the fault displacement profiles, while the preservation of small displacement lows at palaeo-segment boundaries [red boxes in profiles in section 4.1] demonstrates that not all the displacement anomalies have been equilibrated after linkage. This probably reflects that segment linkage was relatively recent [c.f. McLeod et al. (2000)], but also the accommodation of some of the extensional strain by ductile and brittle deformation between the main structures [e.g. Fig. 3.6; Dawers and Anders (1995)].

Abandoned footwall and hangingwall splays are evident on each of the surveyed faults [e.g. fault k, Fig. 4.7; southern parts of linking and Fault 2, Figs. 4.16; 4.18]. The

orientation and shape of these splays, their displacement profiles and the correlation with displacement lows in the main faults, all indicate that the splays are the remnant tips of small segments, which have joined to become part of the through-going structure [e.g. Fig. 2.5; Trudgill and Cartwright (1994); McLeod et al. (2000)]. The displacement profile of the linking fault displays a hierarchy of segments, which suggests the fault grew by the gradual linkage of segments of increasing size [section 7.2.1.1 and Fig. 7.4].

Stream patterns also highlight the original segmentation of the faults, as there are many examples of drainage exploiting local displacement lows. The main stream in the central overlap drains through a palaeo-segment boundary in Fault 1 and also through a low displacement region in the linking fault [Figs. 4.6 and 4.18 and section 7.2.1.2]. The axial stream incises through a fault overstep, and hence probably exploited an old displacement low in Fault 0 [Fig. 5.24]. Tributary 4 of the northern stream is deflected between two overlapping faults [Fig. 5.22]. The extent of the Fault 1 fan deposits [sections 4.2.3 and 7.2.1.3] indicates the state of linkage of Fault 1 prior to the propagation of Fault 2 [section 7.2].

However, the effect of segment linkage depends on the size of the stream. Small abandoned talus piles indicate the original route of small streams that drained through early displacement lows in the F2 scarp. Supply by these streams appears to have been terminated when the segments linked to form a through-going fault [Fig. 4.16]. In contrast, linkage of segments within Fault 1 and the hard-linkage of Faults 1 and 2 have not defeated the main stream, which has continued to drain from the footwall of Fault 1 into the hangingwall of Fault 2. Linkage of segments in the northern part of Fault 1 may have defeated and deflected any cross-scarp streams which contributed to the talus piles at the base of the scarp [Fig. 4.1.1]. All drainage from the Fault 1 footwall drains either south into the central overlap stream through incised joints [e.g. Fig. 4.26h], or northwards into the F1/F0 overlap stream.

Development of the through-going axial stream [sections 5.2 and 7.3] required connection of all the southern hangingwall basins, and hence was probably impossible until around the time of the array linkage [see Dawers and Anders's displacement profile, Fig. 3.6]. The scale of the topographic changes in the southern part of the array around the time of this linkage is demonstrated by the scale of the drainage reorganisation [section 5.2 and 7.3]. Development of the axial channel has overprinted the earlier stream patterns and reworked much of the sediment [e.g. Fig. 4.1]. Although the faults are not hard-linked at the surface, the connection of the Fault 1 and Fault 0 basins occurred due to filling of the F0 basin, allowing supply from the F1 footwall to finally reach the starved F1 basin from the north. Sediment from the main central stream has been reworked from the F2 basin towards the south [section 7.2].

Distribution of displacement: In the centre of the array, displacement is focused on large faults with tens of metres throw. At the northern tip of the array, a plethora of small faults with displacements up to only ~20m accommodate extension [Fig. 4.1]. This distribution of deformation is similar to that seen in other fault arrays [e.g. Wasatch Fault, Machette et al. (1991)], and reproduced by numerical modelling [e.g. Cowie (1998)]. It is also demonstrated by the contrasting courses of the main stream through the central overlap, and that which incises through the northern tip of the array [Figs. 4.20 and 5.1]. While the straighter course of the northern stream

may partially reflect a higher discharge [section 7.4], it also demonstrates the lesser influence of small faults.

A series of distinct phases have occurred in the growth and development of Fault 1, each associated with a different pattern of displacement accommodation along strike. The distribution of the rounded clast deposits in the immediate hangingwall of Fault 1 [Fig. 4.47] implies that the contemporary controlling fault was only a few hundred metres long [section 7.2.1.3]. Similarly, the drainage direction of the main stream [towards the northeast; Fig. 4.20] implies that it was influenced by a small fault with relatively low displacement: a significantly larger fault would have caused more northerly drainage patterns [section 7.2.1.3]. The skewing of the Fault 1 profile implies sequential interaction, first with F2 and later with F0. The present D_{max} of Fault 1 is significantly higher than expected for its length, due to the fact that it scales with the length of the entire array, which today acts as a single fault [Fig. 3.6; Dawers and Anders (1995)].

Increases in displacement rate follow the increase in fault length after segment linkage. Thus the phases of the development of Fault 1 are probably also associated with increasing slip rate as well as the increasing displacement on the fault. Evidence for the increasing slip comes from the comparison of the streams in the area. While the early development of the main central overlap stream was influenced by a small Fault 1, the stream draining the F1/F0 overlap has responded to a steep displacement gradient. There is no significant evidence of a cross-scarp stream supplying the talus at the centre of Fault 1, and the catchments of the north and south overlap streams meet at a drainage divide close to the centre of Fault 1. Thus a single long fault may have been established relatively early, as the southern segments linked prior to interaction with Fault 0.

Development of the axial stream was dependent on the connection of the F1 and F0 basins [section 7.3]. The IBH between the basins was overcome by sedimentation in the F0 basin, supplied predominantly from the F1/F0 stream [section 5.2]. An increase in displacement rate on Fault 1 following the linkage of the array [e.g. Nicol et al. (1997); Cowie (1998); Gupta et al. (1998); Cowie et al. (2000)] may have increased the supply from the overlap stream, and hence been responsible for finally connecting the two hangingwall basins.

Influence of lithology: Many of the small faults on the Tableland are associated with joints. The consistent spacing and orientation of the footwall splays of both the linking fault and Fault 2 [sections 4.1.2 and 4.1.3] imply that these segments nucleated, or at least propagated, on joint planes. A similar conclusion seems appropriate for many of the small faults around Fault 1, and several at the northern tip of the array, which have steep planar surfaces [$\geq 75°$], and a stepped trace, with steps parallel to local joints [e.g. fault j, Fig. 4.9]. Many of the faults also die into joints at one or both tips. Similar relationships have been described for normal faults nucleated along columnar joint planes in basaltic lava flows in Iceland (Gudmundsson, 1992; Acocella et al., 2000)], although there is no evidence in the Tableland for the formation of open fissures.

The joint distribution on the Tableland is not uniform [section 3.2]. Sheridan (1970) described two generations of joints. Long conjugate shear joints, which penetrate up to 120m into the tuff, formed soon after the tuff's emplacement, and follow similar

orientations to those of major joints in the Sierras (Bateman, 1965). They are clearly visible on aerial photos in some parts of the Tableland [e.g. southern tip of Fault 1, Fig. 4.2], but less evident elsewhere. More pervasive unaltered cooling joints outline polygonal columns 1-4m across, and penetrate only the upper 9-15m of the tuff affected by the escaping gases (Sheridan, 1970). Faults appear to be associated predominantly with the long major joints, although they may also step laterally along cooling joints which intersect them [Fig. 4.1]. The stepping may help accommodate extension oblique to the major joint orientations.

The influence of the joints may be significant only in some parts of the Tableland. The small faults at the southern tip of Fault 1 differ from those at its northern tip, where joints are less visible, and most displacement has been accommodated by ductile deformation [section 4.1.1.3]. Since large faults grow from the linkage of smaller segments, the influence of joints on the nucleation of small faults also affects the pattern of larger scale faulting. There is a clear bend in the trace of Fault 1 [Fig. 4.4], which brings the southern part of the fault sub-parallel to one of the principal joint orientations. This may be the result of the linkage of southern segments, nucleated along joints like fault j, with segments further north, whose orientation was purely perpendicular to the regional extension. The larger number of faults, and steep warping at the southern tip of Fault 1 may also be the result of the slight difference in the orientations of the joints and of the regional extension [see fault and joint orientations in Fig. 4.2].

Fault 2 splits into two splays at a large fumarole mound, the two tip splays then extending along the lines of fumaroles to the north [Fig. 4.15]. Northern faults are also commonly associated with fumaroles, both by the major canyon [Fig. 5.5] and further downstream [Fig. 5.8]. Sheridan (1970) described volatiles escaping along the long conjugate joints in the tuff, and hence the initial pattern of these long joints also determines the distribution and alignment of the fumaroles. The minerals which were contained in the escaping gases altered the rock which they encountered, resulting in the increased welding of the tuff around fumarolic mounds and ridges. Some larger areas of indurated tuff are evident, particularly to the east of the array, between the axial and fumarole-axial channels [Figs. 5.24 and 5.26]. Thus in some cases, the gases affected a much larger area around the vent mounds, as demonstrated by the drainage patterns [e.g. course of the fumarole-axial stream and the downstream part of the northern stream, Fig. 5.24]. Influence of the fumaroles on the propagation of faults is therefore unsurprising, since the mounds represent rheological heterogeneities within the tuff. However, as with the joints, their distribution is not uniform [e.g. see Fig. 3.4b], and hence the influence of the fumaroles on fault propagation and growth also varies considerably across the Tableland.

Hence analysis of the faults themselves [section 4.1] provides a lot of information about the mechanism of fault growth, and on fault scaling. However, the streams record additional information about fault development, and constrain the relative timings of fault movements more sensitively. Large-scale reorganisations of the stream networks are linked to changes in the fault pattern, and hence record major events in the evolution of the fault array, that are not all evident from analysis of the faults alone.

7.1.3 Stream power and cross-sectional morphology

The previous section discussed the observations of downstream variations in morphology, course and profile of the surveyed streams, and concluded that faults have been the main external influence on their evolution. The aim of this section is to investigate the numerical evidence for this, and hence provide quantitative, not just qualitative, estimations of the impact of the different faults. Since the two parameters used here can be easily measured elsewhere, this approach is also applicable to the investigation of other extending regions.

Two different parameters were considered in Chapters 4 and 5: the SL index, a proxy for stream power [Eqn. 2.7; Hack (1973)]; and the aspect ratio, AR, which is a simple measure of the cumulative evolution of the stream cross-section [section 3.3, Fig. 3.8]. In the following section, I discuss the observed patterns in both SL and AR, and their implications for the evolution of the Tableland streams. The relative values of the two different parameters as tools to assess the Tableland stream development and the influence of faulting are also discussed.

7.1.3.1 Stream power

The stream-gradient, or SL, index is a proxy for the local stream power [Eqn. 2.7; Hack (1973)]. Abnormally high local SL values, within the normal downstream increase in SL, highlight steep reaches, and hence increased stream velocity and erosivity [section 2.3.2]. Variations in cross-sectional shape are not included in the calculation. Since the SL index is based on the profile of an equilibrium stream, *absolute* values cannot be compared directly between the actively-incising [and hence non-equilibrium] Tableland streams. However, the variation of SL within each stream demonstrates the changing stream power, and the *shape* of the downstream variation can be usefully compared between streams.

SL indices are reported with stream gradients for reaches in the central overlap, northern tip and axial streams [Tables 4.3, 4.6, 5.1 and 5.3]. In cross-scarp streams, the highest local SL values distinguish the scarps. SL indices increase towards the scarp in the footwall, and drop sharply in the immediate hangingwalls, before increasing again away from the fault. Despite the size of the contributing drainage area, SL indices are extremely low throughout the fault-parallel reaches of the axial stream, reflecting the very low gradient [Table 5.3]. The steep reach in the northern F1 basin is an exception: SL indices are almost as high as in some of the faulted reaches.

SL indices correlate with the present bed gradient [Eqn. 2.7], and hence the downstream SL variation described above is expected from the stream long profiles [Figs. 4.24; 4.39; 5.2; 5.11 and 5.25]. The SL indices provide confirmation that the faults are the main influences on stream gradient, and that the upstream transmission of base level drops at faults is responsible for increased erosive power in the immediate footwalls. No large changes in SL index occur away from the faults, which is consistent with the observed low gradients [section 7.1.1] and the relatively small variations in substrate erodability on the Tableland.

The channels in the central overlap are supplied from the same footwall stream, and hence a very similar drainage area, A. Despite this, there is considerable variation

in incision along all of the streams [section 4.2]. Since the downstream variation in erosivity is not due to variations in discharge, the patterns of incision demonstrate the impact of fault-induced changes in gradient [S] on the stream power [$\varepsilon = KA^mS^n$; Eqn. 2.10], as implied by the correlation of the SL highs with incised reaches.

In situ cosmogenic isotopes provide maximum estimates of long-term average erosion rates at the six sampled locations [section 7.2.2]. An attempt was made to constrain n in the stream power law using the simplified formulation [Eqn. 2.11; after Burbank et al. (1996a) and Whipple et al. (2000b)], and using values for the local slope and stream width at the sampled sites. Due to complex exposure of VT8, this sample was not included. However, no correlation was obtained with the calculated erosion rates. This simplified stream power law [Eqn. 2.11] assumes that the contributing drainage area is constant for the sampled reaches. However, no correlations was observed [R^2=0.14] even using only the samples within the main stream in the ramp [VT2, VT4, VT6] for which the contributing area was truly identical [some discharge from the VT14 reach flowed down the northern streams for some period].

Sample	Erosion rate, ε (mMy^{-1})		SL index	S/w (m^{-1})		Aspect
	^{10}Be	^{26}Al	(grad. m)	Bank	Latest	ratio, AR
VT2	3.02±0.32	2.66±0.21	-88.19	0.00384	0.0164	0.0669
VT6	5.52±0.60	5.20±0.48	-374.47	0.00176	0.0285	0.0846
VT11	2.27±0.24	1.81±0.09	-89.08†	0.00519	0.0431	0.0418
VT4	6.94±0.79	5.59±0.58	-36.24‡	0.00859	0.0125	0.121
VT8	1.77±0.19§	2.02±0.15§	-69.29	0.00360	0.0100	0.0918
VT14	8.15±0.85	9.06±1.62	-17.95	0.00242	0.0513	0.191

Table 7.1: *Comparison between averaged erosion rates, stream power estimates and aspect ratios for central overlap streams. Averaged erosion rates are maxima: calculated from the* in situ *cosmogenic isotope content using Eqn. 2.25, and corrected for shielding. SL indices and aspect ratios are reach averages [see Chapter 4].*
Slope / width [S/w] values are calculated from the cross-sectional profiles used for the AR calculations. Upper and lower bounds on the true width of flow are used: 'bank' width is that between the tops of the banks, as used for the AR; 'latest' refers to the width of the lowest estimate of water depth preserved in the channel.
† *VT11 in the minor stream 1: considerably lower discharge than the main stream.*
‡ *VT4 in southern fork of main stream: value of SL not reported in Chapter 4.*
§ *VT8 has undergone complex exposure, and hence the erosion rate is overestimated. Calculated exposure ages [Table 6.7] imply burial for the order of 10^5 years.*
No correlation was obtained on a log/log plot between S/w and cosmogenic erosion rates [R^2=0.14 using samples VT2, VT4, VT6: see text].
Poor correlation between SL and long-term erosion rate [averaged ^{26}Al / ^{10}Be]: R^2=.
Good correlation between AR and long-term erosion rate [averaged ^{26}Al / ^{10}Be]: R^2=0.76.

This lack of correlation implies that the stream power law cannot be used to investigate the evolution of these channels. This failure may be partly due to the fact that stream incision has been dominated by the propagation of fault-induced knickpoints [section 7.2.2.3]. Several workers have reported the failure of the stream power law to predict incision patterns in knickpoint-dominated streams [e.g. Seidl and Dietrich (1992); Weissel and Seidl (1998); Wohl and Ikeda (1998); Stock and Montgomery (1999); Wohl and Merritt (2001)], and the added complication of the spatial variation in the imposed topography around the faults is likely to have added to the mismatch. A small amount

of recent fault motion may have steepened parts of the profiles, but this is unlikely to be a large effect.

At VT14, the high long-term erosion rate demonstrates considerable stream response to induced base level drops, reducing the imposed slope, and hence also the SL index. The SL index is useful as a marker of the *present* slope and hence the energy distribution within the Tableland streams. However, the present stream power distribution [from SL and Eqn. 2.11] cannot be used to predict the *long-term* patterns of erosion, as recorded by the TCN erosion rates [Table 7.1: $\mathbf{R^2}$=]. Thus the lack of correlation between long-term erosion rates and SL or slope/width values [Eqn. 2.11] demonstrates contrasting extents of stream accommodation of faulting in different reaches, and that the stream power variation has not remained constant through time. In contrast, the aspect ratio [section 7.1.3.2 below] provides a picture of the *cumulative* patterns of erosion through time, and hence correlates well with the TCN erosion rates [R^2=0.76].

7.1.3.2 Aspect ratio

The aspect ratio as defined in this thesis [section 3.3; Fig. 3.8] is a measure of the long-term cumulative incision of the stream, based on the dimensions of the entire channel: AR is the ratio of the bank-channel bed depth to the bank-bank crest width. As discussed, this has limitations, as it does not record the variation in the *active* part of a given channel through time [e.g. formation of an inner channel], and hence cannot distinguish between a stream which narrows as it incises and one which maintains a constant width [Fig. 3.8]. Attempts were made to calculate aspect ratios using the latest indication of water depth in the cross-sections, but this could not be done consistently and reliably in all the measured sections in the surveyed streams.

Nonetheless, as used, the AR does provide an integrated picture of the *long-term* evolution of a stream's cross-sectional morphology. Where bedrock is incised, the morphological change is one-directional: the rock cannot be replaced [section 2.3.1.2], and hence a record is preserved of the incision. Thus a high aspect ratio reflects repeated focused incision while a very low aspect ratio implies that low energy has been maintained for much of the reach's history, and hence that it has been dominated by deposition. Aspect ratios between these extremes may record a range of histories, from periodic incision to periodic flooding and deposition. Thus the endmembers are the most useful indicators of stream evolution, but information can also be gleaned from intermediate aspect ratios.

Downstream variation in AR: The aspect ratio plots in Chapters 4 and 5 show consistent patterns of variation in aspect ratio. Streams which cross fault scarps show a direct correlation of AR variation with fault pattern. Aspect ratios increase in the footwall towards a maximum at the fault scarp, and are lower in the immediate hangingwall of faults [e.g. Figs. 4.37; 5.12 and 5.20]. Away from the influence of faults, the aspect ratio is low and almost constant. AR variations in streams which drain parallel to faults demonstrate the local balance between subsidence and sediment supply. The northern part of the F1 basin has a steep gradient and produces relatively high ARs, reflecting the preservation of the steep displacement profile in the basin floor topography, due to low rates of deposition [Fig. 5.35]. In contrast, low aspect ratios in the fault-parallel sections of the northern stream and the southern reaches of the axial

channel [Fig. 5.38] reflect a sediment supply sufficient to even out the local subsidence variation, even though the basins have not been completely filled [Fig. 5.9].

The aspect ratio records long-term cumulative changes of the stream cross-section. The consistently high aspect ratios in the immediate footwalls demonstrate repeated incision, and adjustment of the cross-section in response to the perturbation of the profile by fault motion. Similarly, the low hangingwall aspect ratios reflect little or no incision, and in some cases deposition. The fact that the aspect ratios are low and almost uniform away from faults is consistent with the other evidence [e.g. stream course, profiles, incision patterns, distribution of alluvial/bedrock reaches; section 7.1.1] and implies that faulting has been the dominant influence on stream evolution. The aspect ratio variation in the F1 basin demonstrates that sediment supply tempers the influence of faults.

Correlation of AR with displacement: Footwall AR values are highest immediately upstream of the largest faults [compare the values in F1 and the upstream northern channel with e.g. those due to the linking fault, Figs. 4.36 and 4.45]. This is consistent with the growth of large faults from smaller faults, as the accumulation of greater displacement causes more perturbations of the stream profiles. As the slip in any event also scales with fault size, the driving force for incision is likely to be higher for the most recent events on the larger faults. If a stream has sufficient discharge to avoid defeat, the incisional response to the displacement accumulation should be preserved in the aspect ratio.

This pattern has been tested in the central overlap streams, where the fault throws are known from the surveying [section 4.1]. Aspect ratios were not measured within the main stream in the Fault 2 scarp, but comparisons are possible between the incision of the main stream into Fault 1 and in the two branches at the linking fault [Fig. 7.1]. Comparison with the incision of the minor stream branches yields an interesting pattern: the incision into the two branches of Fault 2 fits the trend of the main stream data [solid line is best fit of the combined data: R^2=0.91 - $AR = 0.0177SD + 0.0338$]. However, the incision of the minor streams into the linking fault is considerably lower than that predicted from the displacement [Fig. 7.1]. Inclusion of these data considerably reduces the correlation of the AR values and local displacements [R^2=0.53].

Two points arise from this data:

- Faulting drives incision, and streams are able to respond to repeated fault activity by long-term incision: AR$\propto$D. The accommodation of the fault movement by the main stream has been similar at both the linking fault and Fault 1.
- Much of the motion on the linking fault probably occurred considerably later than that on Fault 2 [see also AR:slope correlation below, and section 7.2.3]. Although the minor streams have ~fully accommodated the displacement on Fault 2, there is little adjustment to movement on the linking fault. This implies that their discharge was reduced, or zero, before much of the linking fault motion.

AR values also show that the wavelength of response scales with the displacement. Fault growth causes increasing stream incision and deposition through time, over a widening area [see profiles in Chapters 4 and 5]. However, this also leads to superposition of responses to neighbouring faults. Deep incision and profile adjustment

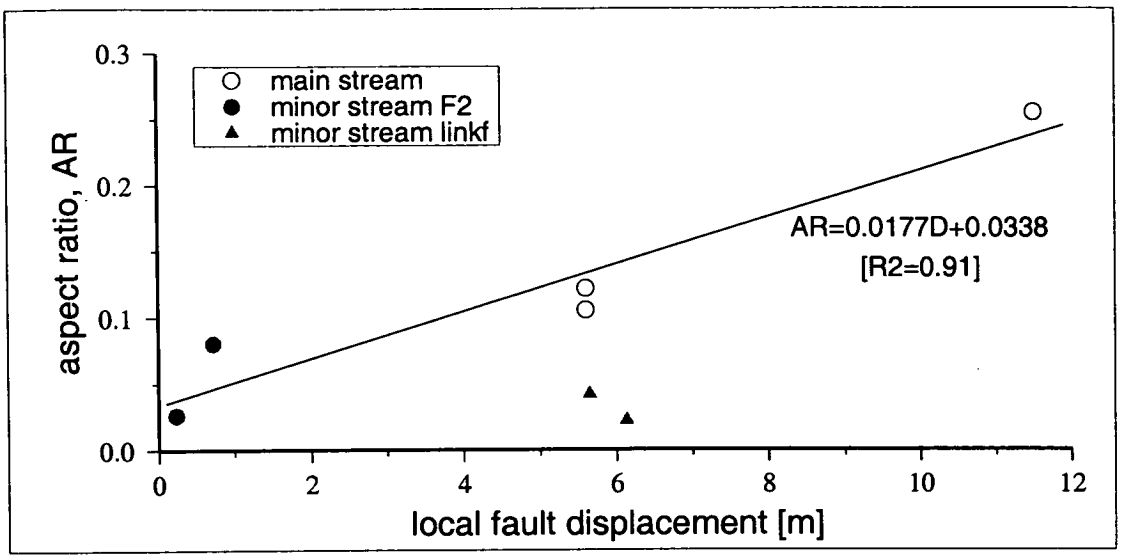

Figure 7.1: *Correlation of aspect ratio with fault displacement in the central overlap. Values for the main stream in hollow circles; for minor stream are filled. Black line is the best-fit linear regression line for the main stream and the minor stream incision into Fault 2 [circles]:* R^2*=0.91 [*$AR = 0.0177D + 0.0338$*].*
Inclusion of the significantly lower incision of the minor streams into the linking fault [triangles] reduces the correlation dramatically: R^2*=0.53 [*$AR = 0.0156D + 0.0142$*].*

is evident for several hundred metres in the footwall of Fault 1, and also in the footwalls of large faults in the northern stream and its tributaries. However, xc1 in the central ramp, measured only 11m upstream of Fault 2, has an unexpectedly low aspect ratio [0.0718, Fig. 4.37]. This probably reflects the response to Fault 2 superimposed onto the broad region of subsidence in the hangingwall of Fault 1, so that incision is less marked than might be expected. This superposition of fault influences is probably responsible for the 'spikiness' of the aspect ratios in the ramp, in comparison with the smoothly-varying AR profile in the footwall [Fig. 4.37].

The data implies that where discharge is relatively constant [i.e. no large tributaries join: see assumptions for simplified SPL, Eqn. 2.11], aspect ratio may be useful as a proxy for relative fault displacements along a stream. It is likely to be a better measure of displacement for isolated faults, where the fault separation along the stream course is wider than the region affected by neighbouring faults. This is probably the case for Fault 1, and also for the largest faults in the upstream northern channel [Fig. 5.13], and tributary 4 [Fig. 5.22]. The exact relationship between AR and D is dependent on the rock properties, but a similar relationship may be evident for other regions. However, more measurements of local fault displacements are clearly required to adequately constrain the equation for the Tableland streams, and to assess the effect of discharge on the stream response.

AR distribution: The distribution of aspect ratios within each channel [Fig. 7.2] provides a simple comparison of the surveyed streams. The distributions are clearly very different, and reflect the overall differences in the evolution of the streams. The broad distribution of AR in the northern stream [Fig. 7.2b] reflects the combination of deeply-incised fault-normal and shallow fault-parallel reaches. Lower discharges

in the tributary streams [Fig. 7.2c] give a distribution skewed towards low aspect ratios, though localised incision in response to large faults is evident. The central overlap streams [Fig. 7.2d,e] have lower discharges than the northern trunk stream but have responded to long-lived focused faulting. Low gradients in the fault-parallel axial channel [Fig. 7.2a] skew the profile towards low aspect ratios, despite the large contributing drainage area. This emphasises the importance of faulting to drive incision. However, due to the incomplete surveying of this stream [no cross-sections in scarps of F0, FA or in the F0 basin], the contribution of high aspect ratios to this distribution is underestimated, and the distribution is dominated by the channel shape in fault-parallel reaches.

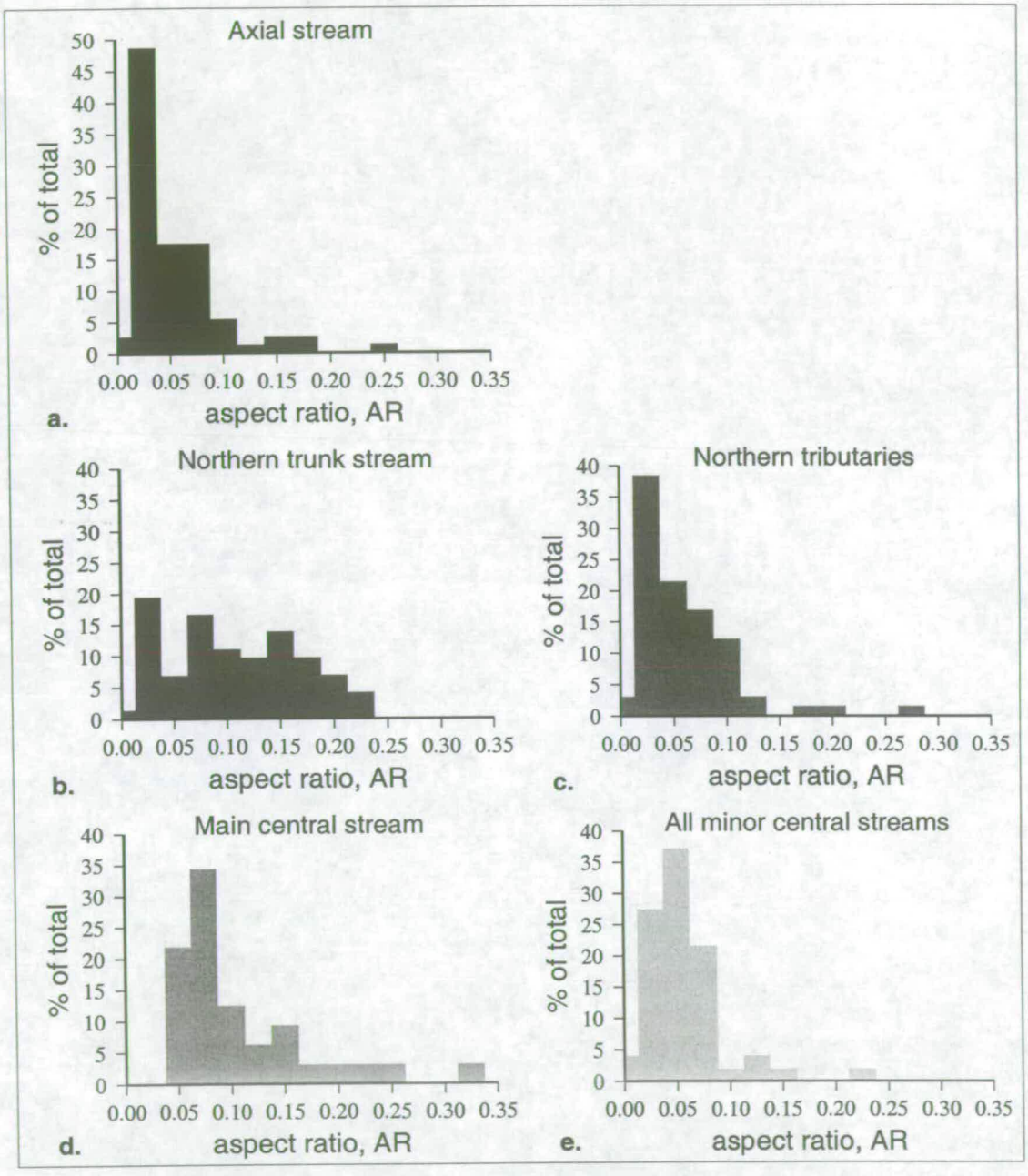

Figure 7.2: *Distribution of aspect ratios in surveyed streams.*
Measured aspect ratios have been grouped into 0.025-wide bins.
No cross-sections were measured in the scarps of F0, FA or in the F0 basin. The contribution of high aspect ratios to the axial stream distribution is therefore underestimated, and a more bimodal distribution should perhaps be expected.

Correlation of AR with slope: AR profiles imply a close link between aspect ratio and local bed slope, S, which is expected since the high aspect ratios reflect deep incision in response to increased slopes following fault activity. However, attempts to correlate AR with slope along a whole stream are fruitless: efficient reaches remove high slopes by deep incision [high AR; low S], but less efficient reaches take time to adjust, and hence may preserve high slopes for longer despite a long history of incision [high AR; high S]. Hence the scatter in AR:S values is the effect of sampling a continuously-varying dynamic system, much as fault D-L data displays an inherent scatter [section 2.1.2; Cartwright et al. (1995); Cowie et al. (2000)]. In the case of the Tableland streams, this scenario is exacerbated, as the streams have been abandoned, while the faults are probably still active. Thus a small part of the measured slope may reflect the imposition of fault topography that was not experienced by the active streams [see section 7.1.3.1]. However, comparisons of the downstream variation in slope and aspect ratio are useful in assessing locations of recent fault activity, and also the most efficient stream reaches [Fig. 7.3].

Figure 7.3 plots AR and local slope at each cross-section site in the surveyed streams. Bed gradient has been averaged over 3-5m around each cross-section site, to remove the effects of very local bed topography [e.g. small erosional features], and the profile assessed to ensure that the slope was representative of the bed. Local slope is here reported as *positive* dimensionless numbers [m/m]. [NB: reach-averaged gradients in Chapters 4 and 5 were reported as negative values in degrees.]

The contrasting aspect ratio and slope variations within each stream highlight the varying responses of the different reaches. The plots also highlight the differences in the evolution of the different streams, due to discharge, timing of faulting and also possibly varying lengths of occupation. Absolute AR:S values are not considered [see above] but the four different possible relationships at each cross-section are interpreted as:

- high AR, high S - long-term incision, but currently steep ⇒ repeated fault activity but some recent motion, or relatively low discharge.
- high AR, low S - long-term incision, currently low gradient ⇒ full response to all faulting; high discharge or long occupation.
- low AR, high S - little/no overall incision, currently steep ⇒ recent onset of faulting, or low discharge.
- low AR, low S - little/no overall incision, currently low gradient ⇒ little fault activity, or xc measured in hangingwall; possible equilibrium with tectonics, or deposition.

The main points which arise from Fig. 7.3 are:

- *Fault 1 was active before the linking fault and Fault 2: from absolute AR and AR:S ratio [~constant discharge].*
  High aspect ratios and low slopes in the footwall of Fault 1 [Fig. 7.3a] demonstrate a high level of accommodation of the fault motion by incision. The pattern of AR and S variation in the ramp is completely different: the accommodation of faulting is far less advanced. High ARs [0.1-0.33] in steep reaches at all the faults is testament to repeated incision, but also shows that some fault activity remains to be accommodated at each fault.

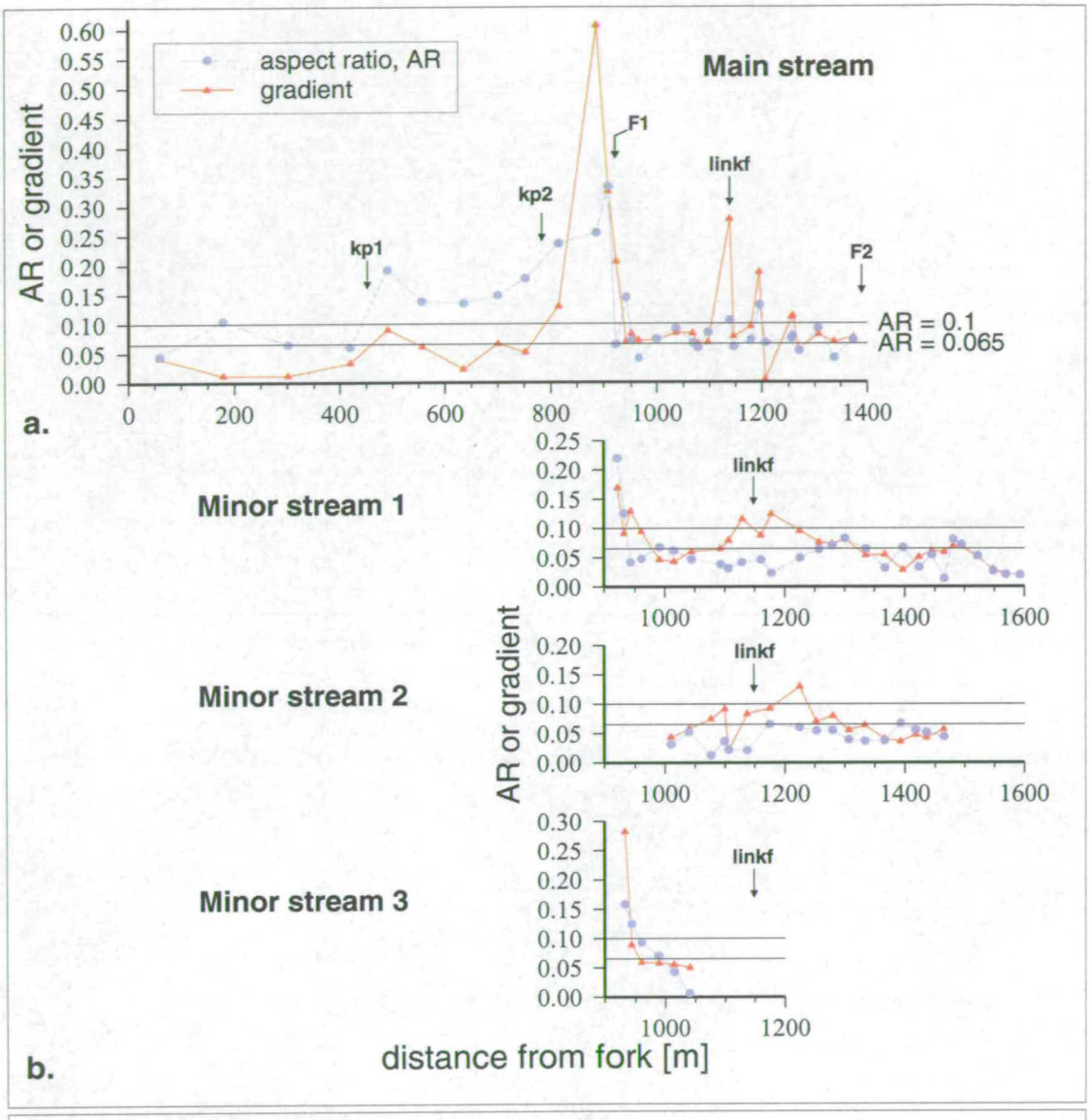
aspect ratio, AR
gradient
Main stream
AR or gradient
kp1
kp2
F1
linkf
F2
AR = 0.1
AR = 0.065
a.
Minor stream 1
Minor stream 2
Minor stream 3
AR or gradient
distance from fork [m]
b.

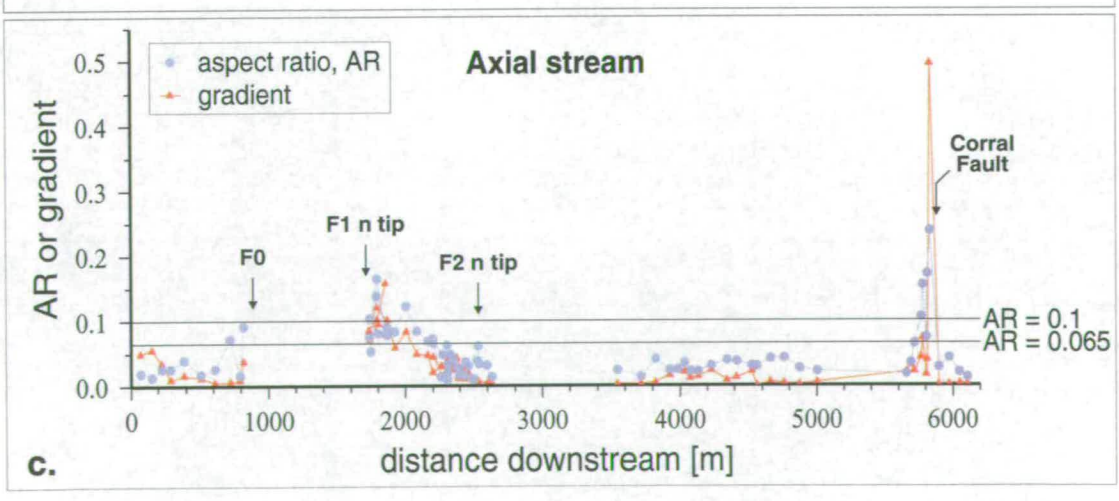
aspect ratio, AR
gradient
Axial stream
AR or gradient
F0
F1 n tip
F2 n tip
Corral Fault
AR = 0.1
AR = 0.065
distance downstream [m]
c.

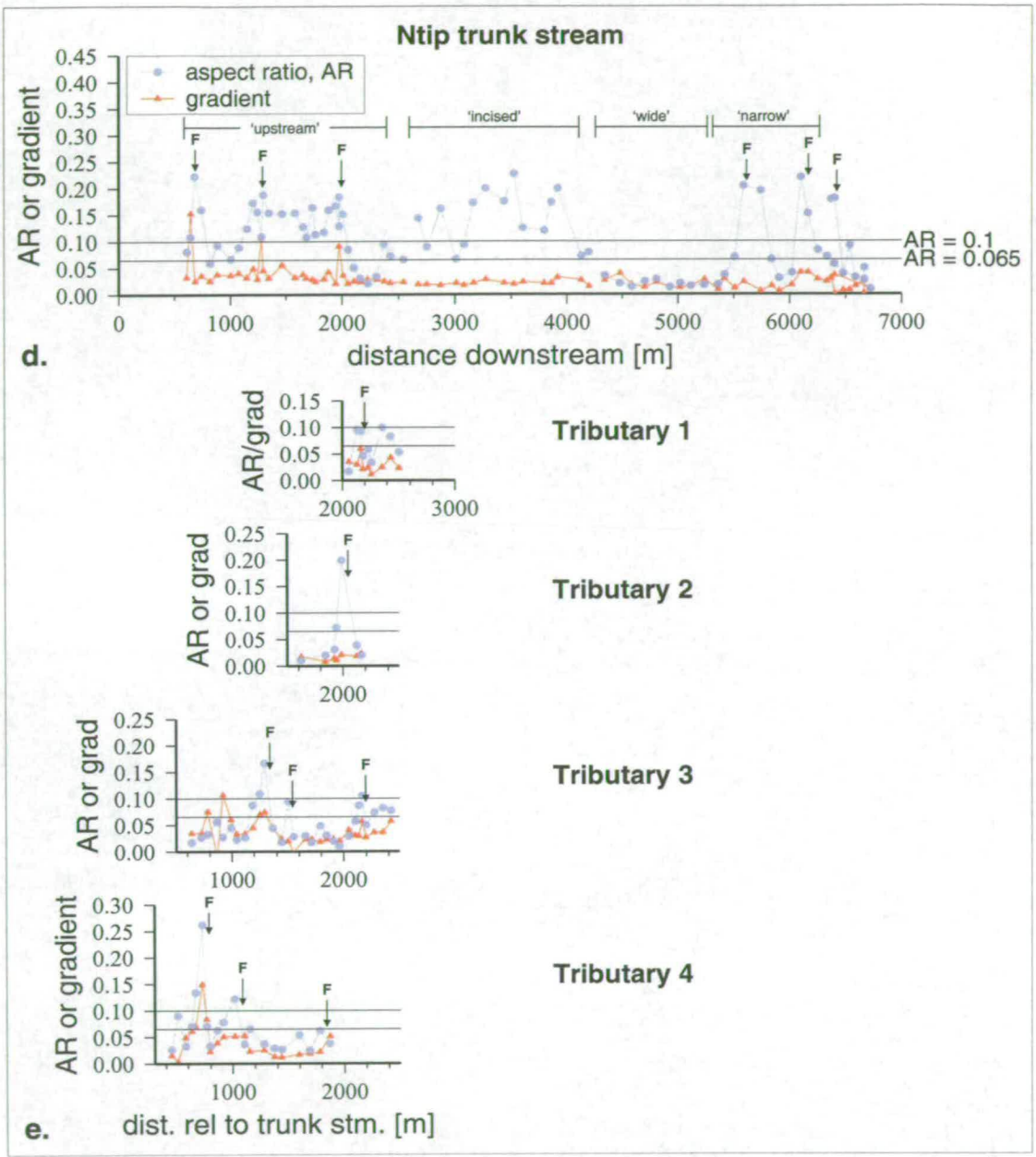

Figure 7.3: *Downstream variations in aspect ratio and local channel bed slope.*
a. Main and b. minor streams through central overlap.
c. Axial stream.
d. Trunk stream and e. tributaries from northern tip of array.
Local slope averaged over 3-5m around cross-section site, and here reported as positive to simplify the comparison, although reported as true negative values [height decreases with increasing distance] in Chapters 4 and 5. Major faults are marked.
Horizontal lines at AR=0.065 and AR=0.1 allow comparison of different streams. AR>0.065 appears to correlate broadly with bedrock reaches: overall incision into the tuff; AR≪0.065 correlates with overall deposition in alluvial reaches - see text.

- *Late development of axial stream: from good correlation between AR and S.*
  High aspect ratios correlate with steep gradients in the fault-normal reach near the Corral fault, demonstrating very little profile adjustment to the fault motion, in contrast to the low gradient, low AR reach immediately upstream. AR also correlates closely with gradient in the F1 basin [Fig. 7.3c].
- *Different evolution of fault-parallel and fault-normal reaches: from AR:S.*
  The bed gradient is low throughout the surveyed northern trunk stream: despite the faulting, only three locations have slopes of over 0.06 [3.4°; Fig. 7.3d]. In the fault-parallel reaches, low AR [$\ll$0.06] correlates with low S [e.g. 'wide' reach in section 5.1.1]. The low gradient in the fault-normal reaches has been achieved by intense incision, particularly in the canyon through the main array [section 5.1.1.1], giving almost uniformly high aspect ratios [AR>0.06, and often AR$\gg$0.1].
- *Effect of discharge: from absolute AR and AR:S.*
  The northern stream has accommodated virtually all fault activity in the upstream 5.5km by incision [Fig. 7.3d]. A knickpoint formed in response to a fault [~900m from survey start] has migrated over 110m upstream [Fig. 5.13]; high aspect ratios in the incised gorge correlate with very low bed slopes [Fig. 7.3d]. The upstream decrease in aspect ratio coincides with the high slope of the current knickpoint: the step is preserved due to lower incision. Locally high slopes at smaller faults [~1300 and 1900m from survey start] imply much more recent fault activity. The slope through the gorge is uniformly low [$\leq$1.5°, Fig. 7.3d] despite the very high AR. In contrast, high AR at the faults in the downstream reaches occur at slightly raised slopes, which may be the result of small increments of recent activity, or reflect a less complete accommodation of earlier movement [Figs. 5.9 and 7.3d].
  AR values in the tributary streams [Fig. 7.3e] rarely exceed 0.1, implying far less profile adjustment. High AR values almost always correlate with locally high slopes, demonstrating little accommodation of fault motion, although in some cases the displacement is quite small. These features imply that discharge has been consistently lower than in the trunk stream [Fig. 7.3d], consistent with the far smaller catchments [Fig. 5.1]. Similarly, in the central overlap [Fig. 7.3a and b], a high AR in the main stream, but relatively low aspect ratios in the smaller streams is consistent with their different gradients at the linking fault. This confirms the conclusion from the AR/D plot [Fig. 7.1] that discharge in the minor stream was too low to adjust to much of the motion on the linking fault.
- *Distribution of deformation: from absolute AR and wavelength of AR variation.*
  AR and S values in the footwall of Fault 1 [Fig. 7.3a] are similar to those in the incised canyon of the northern stream [Fig. 7.3d], implying that both have adjusted well to imposed slope. However, the AR peaks in the central stream are far more localised, demonstrating a response to more focused deformation.

Overall, the paired profiles indicate the ability of a given reach to respond to fault motion, and in some cases constrain the relative timing of fault activity. A stream's ability to respond to fault motion by incision is a function of its discharge, and also the length of time it was occupied. The profile of the main northern stream [Fig. 7.3d] indicates either a very powerful discharge, or a very long occupation relative to the other streams, which allowed it to develop a very low gradient despite crossing many faults. The anomalous high local slopes at small upstream faults implies that they must have moved more recently than other faults crossed by this stream. The distinct

footwall and ramp profiles of the central stream [Fig. 7.3a] imply that Fault 1 began to influence it far earlier than the downstream faults.

'Threshold' AR: Long-term differences in stream processes are implied by the dramatic differences in style between fault-normal reaches, dominated by extremely variable, but often high aspect ratios, and fault-parallel reaches where aspect ratios are consistently much lower [Fig. 7.3c,d]. Correlation of the AR profiles with field observations suggests that consistent values of aspect ratio define reaches characterised by long-term incision and those where incision has rarely or never occurred. Values of AR>0.06-0.065 correlate with bedrock-incising reaches, while AR$\ll$0.065 in reaches that show no evidence of bedrock incision, but have been dominated by alluvial deposition. Fault-proximal incision is generally associated with AR>0.1.

The correlation of cross-sectional morphology with incision or deposition is hardly surprising. However, the aspect ratio as measured in this thesis, is an indication of *long-term* morphological change, and hence is a measure of the *cumulative* evolution of the stream at that point. The fact that such consistent values of AR occur in streams with a wide range of discharges and occupation durations demonstrates that the streams have all been subject to similar external forces.

Faulting is the dominant external control on patterns of stream incision and deposition on the Tableland. Once nucleated, each fault exerts a similar pattern of subsidence and uplift, although over different length scales. Episodic fault motion imparts gradient changes repeatedly to the same reaches, so that footwall reaches consistently incise, while deposition occurs in hangingwall reaches. Thus repeated fault activity preserves and accentuates differences in stream power, and hence morphology, between reaches. However, as the fault population evolves, strain is localised gradually onto a few faults, resulting in the death of others and hence the overprinting of the patterns of stream incision and deposition. Thus in these Tableland streams, the consistent relationship between cross-sectional morphology and process is probably the result of the specific timescale over which the streams have evolved, relative to the evolution of the controlling faults.

The shape of a channel is also related to the resistance of the eroding material. The Tableland streams all drain the same lithology, and hence all encounter a similar rock resistance. In this case, the uniform AR probably also reflects the fact that the streams all erode a $\sim$uniform lithology, and are dominated by growth of the same fault population.

7.1.3.3 Comparison of stream power and aspect ratio

Both the aspect ratio and the stream-gradient index, SL, provide useful quantitative data which constrain aspects of the evolution of the Tableland streams. SL values show the *present* pattern of stream energy, and highlight that faulting exerts a first order control on stream erosivities, largely through imposed changes in bed gradient. Variations in SL demonstrate that base level drops at faults are transmitted upstream, and also reveal the scale over which the influence of faulting is felt by the streams.

In this particular case, where the streams have been abandoned, possibly for around 50ky (Pinter and Keller, 1995; Phillips et al., 1996; and Chapter 6 data), the *current* variation in stream power gives only a small insight into the pattern of

stream development. Faulting since the stream abandonment may have made a small contribution to the measured slopes, in which case, the current SL and stream power are unrepresentative of even the time of their last occupation. More detailed investigation of the exposed scarps is required to see if any significant recent faulting has occurred, but scoured lips and well-developed plungepools at fault scarps imply that any contribution is likely to be small.

However, fault populations are dynamic, and the surveyed streams have developed in response to a continually-changing fault pattern. The SL index shows only a snapshot of a continuously-evolving stream network, which is the product of a whole series of different fault patterns. This is demonstrated by the lack of correlation between the SL indices and the calculated long-term average erosion rates at the 6 sampled sites [Table 7.1].

In contrast, the aspect ratio provides a measure of the *total* impact of all the cumulative stages of fault growth on the stream development. As used in this thesis, it cannot provide a detailed picture of each major fault geometry. Nonetheless, it provides useful information about the overall stream evolution. The aspect ratio allows some assessment of how long-term patterns of incision and deposition compare with those predicted by the present variation in stream power, recorded in the SL index. That the aspect ratio is robust as a long-term indicator of incision patterns is demonstrated by the high correlation between measured AR and the calculated long-term average erosion rates [R^2=0.76; Table 7.1].

The comparison between local slope and AR [Fig. 7.3] is a crude comparison between the present stream power variation and the locations of long-term focused energy. The common correlation of high AR and high local slope [or SL] in the immediate vicinity of faults demonstrates that they have been the dominant effect on stream evolution, and that activity has been focused on faults close to the present locations for most of the stream evolution, although the distribution of the deformation has clearly varied considerably.

Both the SL index and the aspect ratio as used in this study should be directly measurable from digital topographic data in high-resolution DEMs, although with lower resolution than has been obtained here. Hence the approach used here to quantity the temporal variations in the impact of the extensional faults on stream evolution could be remotely assessed by comparing the aspect ratio and stream-gradient index in streams within digital datasets.

7.2 The central overlap: Interaction and linkage of two overlapping faults

This section discusses the evolution of the central overlap, pulling together information from section 4.2 and from the surrounding streams [e.g. section 5.2]. Section 7.2.1 discusses the main observations from the field that provide clues to the evolution of the overlap, and hence interaction between the faults that bound it, beginning with the development of the linking fault, and then discussing the evidence for the changing stream patterns. Section 7.2.2 details the additional constraints on the timing of events and rates of processes that can be supplied from the cosmogenic sampling in the relay [Chapter 6]. These ideas are all brought together into a simple model of the evolution of the overlap in section 7.2.3 [Fig. 7.6]. The evolution of this relay is compared with the 'classic' stream geometry [Fig. 2.14] in section 7.5.

7.2.1 Constraints on fault and drainage evolution from surveying

7.2.1.1 Linking fault evolution

The northern ~400m of the linking fault profile is very different from the southern part [Fig. 4.18]. The northern part of the linking fault has significantly lower elevations and displacements [Fig. 4.18]. The two parts of the fault also show different patterns of segmentation, which imply different mechanisms of fault growth, caused by different controls on fault nucleation and propagation. The splay which joins the northern part of the fault also has a much higher displacement than the rest of the north part of the fault. Together, these observations imply a different pattern of strain accommodation in the two parts of the relay.

Numerous footwall splays, all oriented sub-parallel to a major joint set [004-010°] are spaced every ~150m in the southern part of the fault. The map and displacement profiles of the splays and the main fault are very similar to published examples of abandoned footwall splays [e.g. Trudgill and Cartwright (1994); McLeod et al. (2000)]. When their contributions are included, the 150m-spaced highs in the raw linking fault displacement profile subside, revealing two segments around 350-400m long, with displacement maxima skewed towards each other [Fig. 4.18c]. This suggests that the southern linking fault grew from a series of small segments which nucleated, or at least propagated, along joint planes. These small faults linked together, initially forming two segments, which themselves interacted before linking to form a much longer through-going fault. The control of joints on fault development is consistent with the observations from Fault 1 [sections 4.1.1 and 7.1.2].

North of the main displacement low, the linking fault consists of a western fault, and an eastern splay [Fig. 4.2], in both of which two discrete segments can be distinguished [e.g. Fig. 4.17]. Despite its length, the splay has the highest displacement on the linking fault [Fig. 4.18b]. Displacement maxima on both the western fault and the splay are skewed towards the north, implying that their evolution was dominated by interaction with Fault 1. Comparison with the distribution of small faults around the master faults observed by Ackermann and Schlische (1997) [Fig. 2.9] suggests that these faults may have nucleated at an early segment boundary in Fault 1, where their growth would

have been enhanced by displacement accommodation on the larger fault. The two parts of the northern linking fault probably developed as *en echelon* segments, which propagated towards each other as they grew [Fig. 7.4]. Two small footwall splays where the splay joins the main fault [Fig. 4.17] imply that linkage may have been facilitated by joints. Relatively huge displacement on the eastern splay suggests that is preferentially accommodated most of the early displacement although the western structure was more favourably located to link later with the growing fault to the south [Fig. 7.4].

The striking difference between the northern and southern parts of the fault, and the mechanisms of their respective developments, may be related to variations in the tuff. Joints are pronounced in the southern part of the ramp [Fig. 4.2], where footwall splays occur in both the linking fault and Fault 2. Thus joints control extension accommodation by the southern linking fault, while less segmented *en echelon* faults grew in the northern part of the overlap. The pronounced north/south differences in the linking fault may also reflect differences in the displacement variation along Faults 1 and 2. The southern tip of Fault 1 aligns roughly with the change in style of the two parts of the linking fault. The northern splay fault aligns roughly with the splitting of the tip of Fault 2 [Fig. 4.2]. Thus the different styles of accommodation on the linking fault probably also reflect grossly different distributions of strain within the overlap.

Between the north and south parts of the linking fault lies a prominent displacement low [Fig. 4.18c]. The size of the displacement drop implies that linkage of the two parts of the fault occurred relatively recently, when strain in the ramp due to the interaction of the bounding faults [1 and 2] was very high. This is supported by the preservation of marked differences between the two parts of the faults, and the observation that the main stream draining the overlap crosses this part of the fault [Fig. 4.18 and 4.19]. The stream is likely to have initially exploited any displacement low in the scarp, and hence implies that this location had low displacement at the time of the stream incision into the ramp.

The two separate parts of the linking fault each grew at opposite ends of the overlap, near the bounding faults. Their initiation may thus have been linked to the growth of the segments which comprise the major faults, possibly reflecting regions of enhanced fault growth around old segment tips [e.g. Ackermann and Schlische (1997); Cowie (1998)]. Propagation and linkage of the two parts of the linking fault probably occurred in response to the increasing interaction of the bounding faults [1 and 2], as Fault 2 propagated northwards. Most of the growth of the central linking fault therefore may have occurred during and since the incision of the main stream into the footwall of Fault 1, and hence can be at least loosely constrained by correlation with the cosmogenic exposure ages [section 7.2.2].

These observations are brought together in a model of the evolution of the linking fault [Fig. 7.4].

7.2.1.2 Footwall stream response to faulting

Pinter and Keller (1995) estimated that the Tableland streams initially responded to a regional tilt towards 121-125°. However, the present course of the footwall stream has been modified by the influences of local faulting and the prevailing joint pattern. The stream was not deflected southwards by propagation of the Fault 1 tip [e.g. Fig. 2.14],

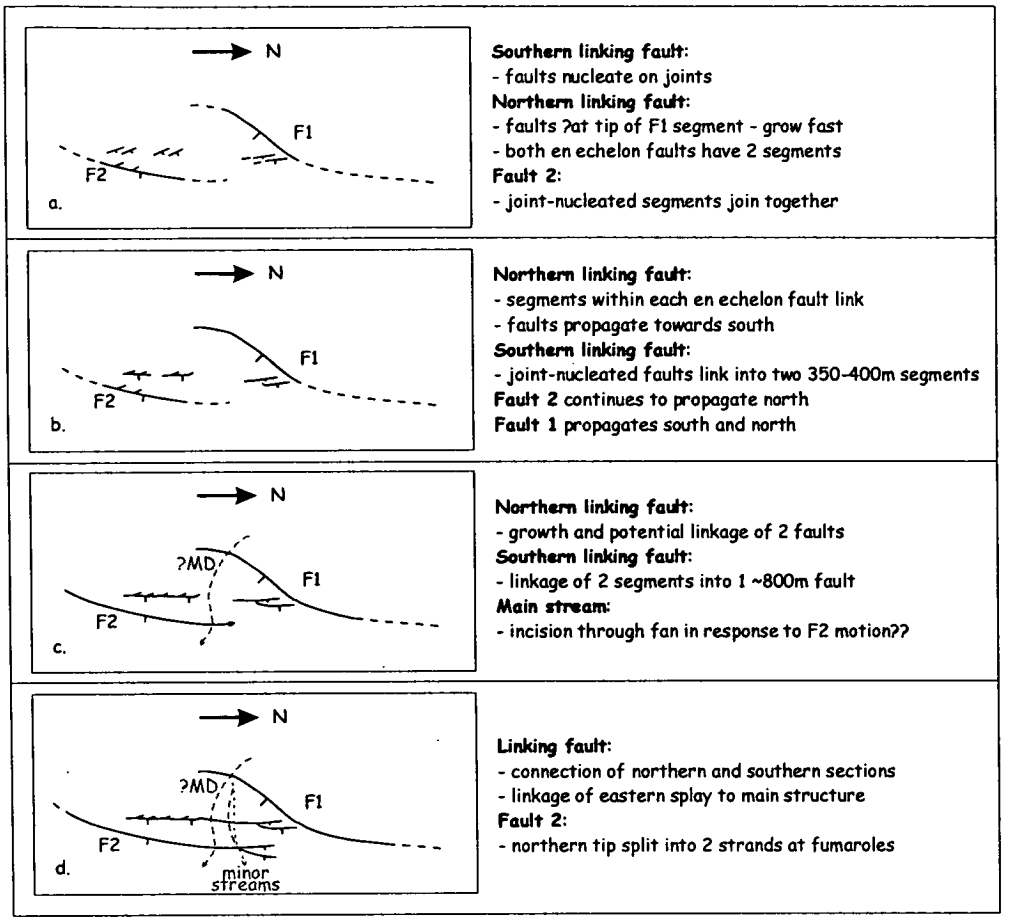

Figure 7.4: *Simple model of linking fault evolution, based on evidence from the linking fault profiles and stream morphologies in the central overlap.*

but instead bends northeast in the immediate footwall *towards* the fault scarp [compare Fig. 4.20]. Increased sinuosity is evident in the immediate hangingwall of Fault 1, and also preserved by the pattern of incision in the 'dogleg' in the footwall [Fig. 4.22]. Braiding and increased sinuosity are typical stream responses to small vertical motions [e.g. Fig. 2.25, and Holbrook and Schumm (1999); their Fig. 8], and in this case probably reflect the response to *early* fault activity. The stream course and the presence of high sinuosity also imply fault modification of an *existing* stream, as a stream developed *after* the onset of significant faulting would simply follow the steepest local gradient.

The dramatic increase in aspect ratio in the footwall of Fault 1 [Figs. 4.34c and 7.3d] reflects not only an increase in incision depth, but also a decrease in width as the fault is approached. As 'width' in the aspect ratio refers to the distance between the top of the banks, this reflects that *at the onset of incision*, the stream narrowed downstream towards the fault, as typically seen where a knickpoint is approached [e.g. Gardner (1983); Jorgensen (1990)]. The incised stream bends, and the decrease in *original* channel width towards the fault, indicate that incision occurred in response to motion

on Fault 1: the stream was not significantly incised before it felt the fault movements. This is consistent with the fact that no earlier stream courses are preserved in the footwall.

The stream course, both through the bends of the 'dogleg' and in the long straight reach further upstream, has clearly been dictated by joints [Fig. 4.20]. The stream may have migrated over the surface of the tuff until it found a weak line down which it was able to incise rapidly in response to the fault motion. The Fault 1 displacement profile, and the presence of splay fault 'k' at the point of the main stream incision, imply that the river exploited a topographic low at a palaeo-segment boundary [Figs. 4.5; 4.6 and 4.10]. This may partly explain why the stream was not deflected around the southern tip of the fault. However, it also implies that the stream course was fixed relatively early in the fault's evolution, before the tip segments had linked, and the Fault 1 profile adjusted. Once fixed by incision along joint planes, the stream was not able to respond to fault activity by deflection, but only by incision [see also section 7.5].

In summary, the shape of the main stream's course in the footwall of Fault 1 reflects the response of a pre-existing stream to fault slip, and the exploitation of weaknesses in the rock. The initial occupation of the stream therefore predates the onset of significant motion on at least this part of the fault. Further constraints can be placed on the stream evolution by the cosmogenic exposure ages and incision rates [section 7.2.2].

7.2.1.3 Development of alluvial fan in Fault 1 basin

In contrast to the rest of the Tableland, most of the overlap is covered with rounded clasts of Bishop Tuff, ranging from millimetres to over 3m in diameter [Figs. 4.46 and 4.47]. The main stream and the upper reaches of the small streams are incised into these rounded deposits, the size and distribution of which are not consistent with overbank or bar deposition from the current streams [section 4.2.3]. The size, roundness and distribution of the rounded clasts instead indicate alluvial fan deposition, emanating from a point source at the mouth of the main footwall stream [Fig. 4.47].

Deposition of alluvial material in this region would have followed the onset of faulting on Fault 1, as subsidence of the immediate hangingwall created space for deposition of material eroded by the incising stream in the footwall. The main ramp stream has been incised deeply into the alluvial deposits, indicating a later downcutting event which resulted in bypass of this early depositional area. The numerous small streams visible on the aerial photographs [e.g. Fig. 4.20] may be the migrating distributary channels which supplied the developing fan. The fact that few can be easily traced on the ground indicates a shorter occupation than the surveyed streams, and little subsequent incision.

The alluvial deposits cover only the northern part of the ramp, extending only a short distance to the south of the main stream [Figs. 4.46c and 4.47]. Similarly, most of the small streams in the overlap drain the northern part of the ramp. This northward 'skewing' of the fan deposits may be an artefact of erosional winnowing of the southern fan margin, but given the low rates of erosion on the Tableland [e.g. Table 7.3], it seems more likely to reflect asymmetry at the time of deposition, as implied by the geometry of the non-incised [?contemporary] stream pattern. The depositional pattern implies

a strong topographic slope towards the north or northeast, possibly aided by a barrier near the sediment source, which prevented deposition to the south.

The primary control on the depositional pattern was the contemporary geometry of the Fault 1 basin. The northward deposition of material from the footwall stream points to the location of the maximum displacement on the contemporary fault. Without detailed assessment of the varying thickness of the fan material, the contemporary D_{max} cannot be located accurately, but the fan material suggests deposition occurred over only a few hundred metres to the north of the sediment input [Figs. 4.20; 4.47 and 7.6]. This argues against complete connection of the Fault 1 segments by the end of the fan development, and hence that much of the displacement on Fault 1 accumulated later. This is consistent with the evidence from the course of the main stream [section 7.1.1], the skewing of the F1 profile towards the north and F0 [Fig. 4.5], and the probable increase in displacement rates following array linkage, much later.

A second influence on the depositional pattern of the fan was the development of Fault 2. The overlap currently slopes towards the NNE, reflecting the along-strike variation in displacement on both Faults 1 and 2 [see also slope in Fig. 2.14]. As Fault 2 propagated northwards, the overlap experienced an increasing tilt towards the NNE; similar to that inferred from the stream and fan deposits. Thus the northward propagation of Fault 2 is likely to have pushed the fan towards the north, beyond the propagating tip.

The small fault 'k' joins the main Fault 1 scarp where the footwall stream incises the scarp [Fig. 4.6 and4.7]. If active, and particularly if linked to the main scarp before or during deposition of the fan, fault k may have hindered southward deposition of alluvium. The coincidence of the stream's incision with the segment boundary does seem consistent with this relative timing of activity and linkage of these segments.

All three of these influences act in the same direction, forcing fan deposition towards the north. While the influence of fault k is likely to have been only local, it is hard to use only the surficial geometry of the fan material to distinguish the relative magnitudes of the other two effects, as it may well record only the latest stage of the fan's development. The shape of the fan provides some constraints on the linkage of the Fault 1 segments, but also records the effect of increasing interaction with Fault 2. The influences are also recorded in the shape of the main stream, which drains towards the northeast before it incises through the scarp of Fault 2 [Figs. 4.20; 4.21 and section 7.2.1.4].

The volume of the fan deposits is quite high. A conservative estimate of an average thickness of 10cm over a surface area of perhaps 270 000m^2 implies a volume of 27 000m^3 rock eroded from the footwall. The deep incision in the immediate footwall of Fault 1 is easily sufficient to supply this volume of tuff without invoking deep erosion of a large catchment, but given the long-term erosion rates in the footwall stream [section 7.2.2], the volume of fan deposition implies a relatively long-lived, stable depositional system, lasting over the order of 10^5 years.

In summary, the distribution of rounded clasts on the surface of the overlap indicates deposition of an alluvial fan in a subsiding basin in the hangingwall of the young Fault 1, over a period of the order of 10^5 years. The asymmetry of the deposits and the distributary streams indicate that the maximum displacement on the contemporary Fault 1 was located to the north of the input, but that the basin, and hence the controlling fault, was probably less than 1km long by the end of fan deposition. The asymmetry probably also reflects the gradual northward propagation of Fault 2.

7.2.1.4 Connection of main stream to E/SE

Prior to the onset of activity on Fault 1, the main stream probably flowed towards the SE, following the regional tilt of the Tableland surface [121-125°: Pinter and Keller (1995)]. No record of this course across the ramp can be traced today, implying that the stream was not significantly incised before it responded to fault motion. However, it may have flowed along a course similar to that of the southern part of the surveyed axial channel, around the southern margin of the fumarole high [near current Corral fault, Figs. 4.1; 4.20 and 5.26]. Within the overlap, the main stream currently drains towards the northeast, reflecting the pattern of subsidence in the Fault 1 basin, which governed its early evolution [section 7.2.1.2]. However, it must have also responded to the enhanced NNE-tilt resulting from the propagation of the Fault 2 tip.

The incision of the main stream into the rounded fan deposits [e.g. Figs. 4.46 and 4.48] probably occurred in response to a base level drop caused by motion on Fault 2. The fact that the main stream does not flow along a more northerly route also demonstrates that the contemporary Fault 1 did not exert an overwhelming effect on this area. To have incised the Fault 2 scarp, the stream must already have flowed NNE beyond the present location of Fault 2. Hence either the fan extended beyond the present line of Fault 2, or the main stream overspilled the basin margin. The distribution of rounded clasts in Fig. 4.47 implies that at least latterly, the F1 basin extended beyond this point. However, the connection of the main stream with a channel to the east [Figs. 4.20 and 5.46] also suggests at least an intermittent overspilling, carrying sediment beyond the F1 hangingwall basin. The pattern of fumaroles to the east of the overlap [Fig. 4.1] probably controlled its downstream course, channelling the main stream between the indurated highs, roughly along the course of the 'road stream' [red in Figs. 5.26 and 5.46], rather than allowing it to follow a direct southeasterly route.

The location of deposits eroded from the footwall is dictated by a balance between the sediment supply and the slip rate of the controlling fault. Supply may outpace subsidence during the early stages of fault development, but the balance tips to production of unfilled hangingwall space as the fault grows [e.g. Schlische (1991); Davies et al. (2000); McLeod et al. (2000); section 2.2.2]. The size of the fan [section 7.2.1.3] suggests that it formed during an early stage in the fault evolution, when pulses in sediment supply following pulses of fault motion may have supplied sufficient sediment to fill the small basin. Thus intermittent flow beyond the basin, broadly following the regional tilt, may well have occurred.

Incision of this stream in preference to the smaller channels is the result of the northward propagation of Fault 2: this stream was the first to have experienced a base level drop due to movements on the growing fault. Incision, rather than defeat, of the stream implies that its discharge was sufficient to keep pace with the movement on the contemporary Fault 2. However, once incised into the fan surface, the main stream would have provided a more appealing route for water from the footwall, resulting in the gradual starvation of the more northerly streams, and the abandonment of the Fault 1 fan. Later incision of the minor streams at the north of the overlap was minimal due to the small displacement at the northern tip of Fault 2. However, some incision in the upper part of these streams [Fig. 4.39] demonstrates a partial adjustment to motion on the linking fault.

Supply from the main stream beyond the F1 basin towards the east or southeast was probably highest immediately after its incision into the fan surface, during which time it carried virtually all of the discharge from the footwall. Pale sand deposits are evident along the 'road stream' in Fig. 4.1, highlighting the connection with the stream incised through the central overlap. However, as Fault 2 grew, subsidence and rotation of the hangingwall increased, until the supply to the east through the road stream was completely cut off [Figs. 5.40 and 5.46]. Sediment from the main stream was subsequently ponded in a hangingwall fan at the base of Fault 2. Since this time, local topography has been dominated by the subsidence pattern. Supply has been insufficient to reconnect the main stream and road stream, as shown by the southerly flow of the stream in the F2 basin, and the westerly tilt of the road stream profile [Figs. 4.1; 5.40 and 5.46]. However, the story is complicated by the development of the axial stream, which has reworked sediment towards the south, following the subsidence of the proximal Fault 2 basin [Fig. 4.1 and section 7.3].

7.2.1.5 Relative occupation of main and minor streams

The main stream through the overlap clearly carried a considerable discharge, as demonstrated by the size of some of the clasts in the channel [Fig. 4.29], and the volume of sediment deposited in the hangingwall, and redistributed down the road and axial streams [Fig. 4.20]. Considerable braiding is evident around all of the faults, demonstrating the response to early fault movements [Fig. 4.21]. The entire stream course in the overlap is incised into the ramp surface, and deep incision is evident into the footwalls of each fault, increasing in depth towards the scarps [3-4m into linking fault; 2-3m at F2; 1-3m at small faults; Figs. 4.24; 6.6 and 6.7]. Aspect ratios confirm that the stream has responded to each fault by repeated footwall incision [Figs. 7.1 and 7.3]. The gradient of the stream is high, but almost constant between the faults in the ramp, implying that it is the result of episodic rejuvenation by Fault 2: the stream has a drastically lower gradient in the F2 basin [Table 4.3]. This rejuvenation is probably also responsible for the lack of significant sediment storage in the ramp reaches.

In contrast, the minor streams have a smaller cross-section, and no large clasts line the channels [Figs. 4.40 and 4.45]. Any sediment carried into the hangingwall was probably sand-sized or smaller, though a distinct sediment pile is not preserved. The profile is more graded than that of the main stream, with marked alluviation in the lower reaches, implying little rejuvenation by Fault 2 [Fig. 4.39]. This is confirmed by the extremely small displacement where Fault 2 is crossed [Fig. 4.16]. Incision of this stream into the rounded deposits on the ramp surface reaches only 0.5-1m in the immediate footwall of the linking fault [Fig. 6.9], and steep steps are preserved at the scarp. Aspect ratios confirm that the streams have not responded as fully to the linking fault [Figs. 7.1 and 7.3]. The minor stream course shows no deflection at the linking fault, but does not coincide with a current displacement low [Fig. 4.18]. Together, this suggests that much of the displacement was accumulated when the minor streams were no longer capable of adjusting to it.

This dramatic contrast between the streams indicates a significant difference in their development. All the evidence suggests that the main stream had a significantly higher discharge, and possibly also a longer occupation, than the minor streams. However, the minor streams probably drained down a steeper gradient during construction of

the fan, and hence would be expected to have carried more material. The fact that the main stream morphology records a larger discharge than those in the smaller streams demonstrates that they were all predominantly determined by later discharges.

Once transmitted upstream, the incision of the main stream into the fan would have reduced the flow down the minor channels, even as the northerly slope of the ramp increased with ongoing development of Fault 1. Thus incision of the main stream probably immediately preceded a significant drop in the discharge through the northern channels. Very little incision of the minor streams was driven by Fault 2 movements due to the sharp decrease in displacement towards its northern tip, and the distribution of displacement onto two fault strands [Fig. 4.16]. By the time Fault 2 had propagated sufficiently to affect these northern streams, they may anyway have already been effectively starved by the incision of the main stream.

This scenario is supported by the presence of a large pile of angular debris at the mouth of the footwall stream [Fig. 4.48]. The pile is likely to have formed through the progressive removal of jointed blocks from the footwall canyon which were too large to be transported further downstream [section 7.2.2.4]. That the blocks dam the course into the *minor* streams implies the material was piled at the margins of the active main stream, while discharge through the northerly channels was relatively tiny. Certainly today, any flow would be funnelled down the main channel, and only extremely high discharges could drain over the boulder pile into the northern channels.

Thus as the main stream incised into the ramp, the northern streams were progressively abandoned, and an increasing proportion of the footwall discharge was carried down the main channel. Deposition on the fan stopped as the incised channel bypassed it, carrying sediment into the developing hangingwall basin of Fault 2, and beyond [section 7.2.1.4]. Using the age of VT2, ~200m upstream of Fault 2, the incision into the ramp occurred $\leq$200ka [section 7.2.2]. Given that the youngest ages imply that streams were abandoned after the Tahoe stage [~49ka, Phillips et al. (1996)], the main stream may have been occupied for as much as 150ky longer than the minor streams, which, along with considerably larger discharges, could account for the significant differences in the channel morphology.

7.2.2 Constraints from the cosmogenic isotope data

This section discusses the implications of the CRN data for the development of the Tableland streams. Sections 7.2.2.1 to 7.2.2.4 consider the constraints that are provided by the exposure ages, on the relative influences of faults and climate, fault/stream interaction, and the mechanism of stream incision. Section 7.2.2.5 uses the CRN data to calculate long-term average erosion rates, and considers the additional constraints these values place on stream evolution on the Tableland.

Minimum apparent exposure ages for the six Tableland samples are given in Table 6.7, and repeated in Table 7.2 on the next page for simplicity. Ages in the following section have been reported as ^{10}Be$\pm$error/^{26}Al$\pm$error, and two rates are given for processes based on the two values, respectively. However, the errors in the ^{10}Be data are always lower than those in the ^{26}Al analysis, and the ^{10}Be data [first given] should be considered the most reliable in each case.

Apparent exposure ages		
Sample	**Corrected exposure age** (x 10^3 years)	
	^{10}Be	**^{26}Al**
VT2	**196.32**±10.10	**200.21**±16.16
VT6	**97.00** ± 5.83	**96.57** ± 9.14
VT11	**251.92**±11.99	**268.53**±14.03
VT4	**83.48** ± 5.87	**97.05** ±10.29
VT8 †	**311.51**±15.96	**246.58**±18.72
VT14	**73.44** ± 3.24	**64.08** ±11.60

Table 7.2: *^{26}Al and ^{10}Be exposure ages, corrected for sample thickness and topographic shielding. These ages are as reported in Table 6.7, but included here for simplicity.*

These ages were calculated from the disintegration rates of Lal (1991) using the scaling factors of Nishiizumi et al. (1996), and include corrections for shielding of the sample sites [section 6.3]. Exposure ages calculated using several other scaling factors are given in Table 6.8, and demonstrate how the choice of scaling factor affects the final interpretation of the data. However, as noted in Chapter 6, the lack of correlation with regional glacial cycles is not an artefact of the choice of scaling factor made in this thesis. Nonetheless, it is important to appreciate that the absolute values of constraints placed on processes in the following section are dependent on the calculation of exposure ages and incision rates from the Nishiizumi et al. (1996) and Lal (1991) data. Slightly different results would be obtained with different production rate scaling, although the same overall patterns would be evident.

7.2.2.1 Correlation with regional climate cycles

The exposure ages calculated in section 6.4 represent the last significant incision at the sampled location in the surveyed streams. These ages are minima [see Eqn. 2.23]. All exposure ages are >60ka, and hence imply that there has been no significant occupation of the streams since that date. The old ages and low average erosion rates [section 7.2.2.5] are consistent with low rates of recent subaerial erosion during suggested by the widespread preservation of fine fluvial textures [e.g. Fig. 5.14d] and also of petroglyphs that are ≥4000yrs old.

However, the grouping of the apparent exposure ages does not fit the expected pattern for streams dominated by regional glacial cycles, as proposed by Pinter and Keller (1995). To fit their model, the exposure ages should reflect stream formation in a pre-Tahoe stage [206-131ka, Pinter and Keller (1995), though see also Table 3.1], and possibly reoccupation in the subsequent Tahoe stage [79-56ka, Pinter and Keller (1995)]. As argued in section 6.5, exposure ages older than the onset of the pre-Tahoe stage belie a formation by increased runoff during this stage. Similarly, exposure ages of VT4 and VT6 imply that significant incision occurred *between* the two glacial stages described by Pinter and Keller (1995), and hence that the streams were not abandoned between the glacial periods. However, the lack of ages younger than 73±3/64±12ka [VT14] is consistent with final abandonment after the Tahoe stage.

Pinter and Keller's interpretation of the stream evolution was based on the correlation

of terraces of the Owens River at the southern margin of the Tableland with Sierran moraines in Pine Creek (Pinter et al., 1994; Fig. 7.10). Terraces were correlated with the pre-Tahoe, Tahoe and Tioga moraines of Berry (1994). Streams draining the Tableland surface grade to the Q3 [Tahoe] terrace, implying that they were subsequently unoccupied (Pinter and Keller, 1995), which is consistent with the data in this thesis. However, assuming that the exposure ages presented in this thesis can be relied upon [see below], the lack of other correlation with the glacial periods defined by Pinter and Keller implies either an error in the assignment of the glacial stages, or that regional climate was not the main control on Tableland channel evolution.

The early ages of incisions at samples VT2, VT11 and particularly the inferred antiquity of VT8 [section 6.5] point to channel initiation well before the onset of the pre-Tahoe stage. Although there is no evidence of glaciation in the Sierran canyons between this stage and the pre-Bishop Tuff Sherwin glacial [Table 3.1], the sediment record in OL-92 in Owens Lake hints at three [four?] earlier glacials at 300, 360 [455??] and 670ka (Smith et al., 1997). Owens Lake is supplied by Owens River, and hence if these periods were significant enough to initiate streams on the Tableland surface, a record of them would be expected within the river that supplies the lake. To my knowledge, no terraces along Owens River have been attributed to earlier glaciations, which implies that either the record of any contemporary incision has been lost, or that these cold periods could have had only minor impacts on the Tableland streams.

Although Pinter and Keller (1995) described the Tableland stream evolution in terms of their Q4 and Q3 periods, glacial advances along the Sierran margin were probably not completely synchronous [section 3.1.1]. Table 3.1 demonstrates the variations in the postulated advances of the small alpine glaciers within the Sierran canyons near to the Tableland. Advances in Bishop Creek, Little McGee Creek and Bloody Canyon have been placed between 120 and 100ka, and hence may possibly imply sufficient runoff during this period to allow incision at VT6 and VT4 in response to fault motion. Thus some of the discrepancy between the data in this thesis and Pinter and Keller's model may be due to their specific assignment of ages to the glacial periods.

Incision in parts of the surveyed streams from ?$\geq$450ka to 73$\pm$3/64$\pm$12ka [section 6.5] implies that the streams were supplied with quite large volumes of water at least intermittently throughout this period. If no direct correlation with glacial periods can be established, then a considerably wetter climate than the present arid conditions is required. Continual supply of water to Searles Lake by overflow of Owens Lake for long periods of the late Pleistocene is consistent with a wetter climate, particularly from 350-10ka, and 810-645ka (Smith et al., 1997; section 3.1.2). Searles Lake was completely isolated and desiccated at the onset of the Holocene. Thus stream incision on the Tableland may have been enhanced during glacial periods, but a minimal supply may have been maintained for much of the intervening period.

The distribution of the exposure ages in the surveyed streams implies a strong control on the incision patterns by the local faults [Fig. 6.16]. All the surveyed streams on the Tableland demonstrate the dominant influence of faulting, with both the amplitude and wavelength of incision controlled by the variation in displacement on the nearby faults, both perpendicular and parallel to the streams [section 7.1.3]. The youngest ages of the analysed samples are found at fault scarps [VT6], or downstream of

prominent knickpoints [VT14, VT4], while old ages occur upstream of tectonically-driven knickpoints [VT2, VT11]. Thus incision has been driven not purely by increased runoff, but dictated by the local patterns of uplift and subsidence. Increases in runoff volumes would undoubtedly have allowed streams to respond more rapidly to tectonic forcing, but as long as some water was available, the glacial signal would not necessarily dominate the exposure age pattern.

An alternative explanation for the lack of correlation between the exposure ages calculated here and the stream evolution proposed by Pinter and Keller (1995) is the introduction of an error in the CRN calculations in Chapter 6. Samples VT2 and VT11 are relatively shallowly incised into the tuff surface [depths 1m and 0.5m, respectively] and hence there is some potential for inheritance of CRN buildup from previous exposure [section 2.5.3]. However, the other samples are all deeply-incised, and hence inheritance is very unlikely. These four ages are therefore likely to be robust.

Calculations imply that inheritance in VT2 and VT11 may be as high as 22%, resulting in adjusted exposure ages of 160±8/163±13ka and 206±10/220±11ka for the two samples, respectively. However, the exact contribution of inheritance cannot be assessed directly from this data without additional sampling in the field area. The reduced ages if inheritance is significant have important implications for the evolution of the central overlap, particularly as they significantly reduce the time available for propagation of the F2 knickpoint, imply later motion on the northern linking fault, and also later incision and abandonment of the ramp streams [see section 7.2.2.2 below].

The discrepancy between the ^{10}Be and ^{26}Al ages of VT8, however, implies burial for the order of 10^5 years [section 6.5], and hence even with a conservative estimate of ages, VT8 records incision before the onset of the pre-Tahoe glaciation. Since the field relations imply that the streams were active *before* incising in response to fault activity, the CRN data still refutes Pinter and Keller (1995): VT8 demonstrates incision before the pre-Tahoe glaciation, and VT4 and VT6 demonstrate incision during interglacials. Further sampling is required to properly constrain the potential inheritance of samples VT2 and VT11. Hence the calculated ages reported in Table 6.7 [and Table 7.2] have been used throughout the following section to constrain process rates and the timing of events in the overlap evolution. However, it should be noted that calculations dependent on VT2 and VT11 ages may *under*estimate the true rate of stream processes and ramp development if inheritance is significant.

In summary, the timing of glacial events in the area [Table 3.1, and Pinter and Keller (1995)] cannot be correlated convincingly with the cosmogenic data collected here to provide clear evidence of dominant climatic control on the initial formation of the Tableland streams. Exposure ages are, however, consistent with abandonment of the streams following the Tahoe glacial, as proposed by Pinter and Keller (1995). With the small number of samples, and the potential for inheritance in two of them, this thesis cannot refute the glacial signal completely. However, incision patterns do show a close correlation with the local fault pattern, implying that faults have had a larger effect on the stream's development. Thus although glacial periods may have allowed established streams to respond more rapidly to tectonic forcing, the lack of clear correlation between incision ages and glacial periods implies that these streams were occupied, at least intermittently, during interglacials. Sediment records from lakes supplied ultimately by the Owens River demonstrate that the late Pleistocene climate

was considerably wetter than the Holocene [e.g. Smith et al. (1997)], and hence may have been able to support small streams on the surface of the Tableland outwith glacial periods.

7.2.2.2 Fault and drainage evolution

The apparent exposure ages can be used to constrain the timing of some of the events within the central ramp.

Main stream incision/minor stream abandonment: As discussed above [section 7.2.1.4], incision of the main stream, driven by propagation of Fault 2, led to the starvation and eventual abandonment of the northern ramp streams. The last significant incision in the minor stream at VT11 occurred at 252±12/269±14ka, although incision in the main stream is documented as recently as 73±3/64±12ka [VT14] and 83±6 to 97±10ka in the ramp [both VT4 and VT6]. The lack of more recent incision may partly reflect the lack of rejuvenation of the northern stream by motion on Fault 2 [section 4.2.2]. The exposure age of VT2, the furthest downstream sample in the main stream, records the latest significant incision at this point at 196±10/200±16ka. If the incision of the main stream into the cobble deposits was driven by motion on Fault 2, as implied by the field relations [sections 4.2.1 and 4.2.3], then the age of VT2 constrains the onset of this incision within the main stream. The exposure ages of VT11 and VT2 are consistent with virtual abandonment of the minor streams sometime after 250-270ka, caused by a wave of incision in the main stream which began around 200ka. However, if inheritance is significant in VT2 and VT11, this may have occurred more recently, possibly around 160ka [see above].

Fan development: VT8, between the linking fault and Fault 1 [Fig. 6.16], shows evidence of significant burial. The length of burial is of the order of 10^5yrs [Bierman et al. (1999); section 6.5], implying an initial exposure age of $\geq$?450ka. However, the initial exposure age is subject to errors of at least 10^5yrs, as the method assumes rapid and complete burial below the production zone, and rapid exhumation [see section 2.5.2.1 and Granger and Muzikar (2001)]. The total burial period may also have been punctuated by a series of exhumations.

The location of VT8 near the mouth of the footwall stream makes a three-stage history quite feasible, with initial incision of the stream in response to motion on the young Fault 1; a subsequent period of possibly multiple burials and exhumations during the development of a fan in the hangingwall basin; and final exhumation during incision of the main channel following growth of Fault 2. If an initial exposure age of ?450ka is used for VT8, then the timing of the incision of the main stream calculated from VT2 implies that $\geq$?250ky elapsed between the initial exposure of VT8 and the final incision of the main stream. This is sufficient to have allowed burial of VT8 for the order of 10^5yrs, and gives a broad constraint on the period of fan building. The rough calculation of the fan construction duration based on sediment volumes [section 7.2.1.3], produced an estimate of the same order of magnitude.

Linking fault activity: The samples in both the northern and southern branches of the main stream at the linking fault show virtually identical exposure ages [Table 6.7: VT4: 83±6/97±10ka; VT6: 97±6/97±9ka]. The synchroneity of the last significant incision in the branches of the main stream demonstrates that both forks were probably

active at the same time. It also demonstrates that at least this part of the linking fault was active around 83-97ka. In contrast, VT11, taken from a corresponding location in the minor stream has an exposure age of 250±10/269±14ka[1]. Warping and fracturing of the overlap reflects interaction between the two main faults long before Fault 2 had propagated to cause incision of the main stream. While the linking fault may not have completely breached the relay until later [Fig. 7.4], the incision in the minor stream implies that some displacement had accrued by around 250-270ka. However, a large proportion of the uplift recorded by the knickpoint in the minor stream was probably created later [see section 7.1.3].

Growth of the linking fault has been quite slow. The main stream incision into the ramp is unlikely to have occurred much before 200ka [from VT2] but the lack of deviation indicates that local displacements on the linking fault were low. Around 5.6m displacement was accrued at samples VT4 and VT6 by 83±6 to 97±10ka. This suggests slip rates on this central part of the linking fault may be as low as 0.047±0.003mmyr^{-1} [Be] or 0.054±0.007mmyr^{-1} [Al]. Similarly, slip rates on the eastern splay fault may lie in the range 0.02-0.06mmyr^{-1} [for 760-250ky activity]. However, if inheritance is significant in VT2 and VT11, these slip rates will increase correspondingly.

Fault 2 uplift and propagation rates: Incision of the main stream may have occurred when the tip of Fault 2 reached the downstream part of the main stream. The main stream incises through the Fault 2 scarp 484m from the current position of its northern tip. Thus, VT2 gives a long-term [~200ky] averaged propagation rate for this tip of 2.47±0.13 [Be], or 2.42±0.18mmyr^{-1} [Al]. Published estimates for fault tip propagation rates vary from 1-2mmyr^{-1} (Jackson et al., 2002) to 12.1-16.7mmyr^{-1} (Morewood and Roberts, 1999, 2002).

Jackson and Leeder (1994) describe incision of streams *in front* of the advancing tip of a propagating fault in Pleasant Valley, Nevada. If the base level fall was transmitted to the main stream in advance of the F2 tip, the calculated propagation rate is an underestimate. Northward deflection of the main stream [e.g. Figs. 4.20 and 4.21] may have occurred due to increasing subsidence on Fault 1, or in response to the propagation of the Fault 2 tip, in which case incision may have occurred *after* the Fault 2 tip had passed. In this case, the calculated average propagation rate is an overestimate. Tip propagation was also more probably episodic, and potentially occurred at varying rates, due to interaction with Fault 1, and lithological heterogeneities such as the fumaroles and joints within the tuff.

If no slip had been accrued on Fault 2 prior to the incision of VT2, the measured fault displacement of 9.11m [Fig. 4.16] gives a long-term average slip rate of 0.46±0.02 [0.46±0.04] mmyr^{-1}. However, including an estimate of 4-8m sediment deposited in the hangingwall [Fig. 5.40], the averaged slip rate estimate becomes 0.65-0.88mmyr^{-1}. This estimate is ~800m from the D_{max} on the fault, but is reasonable for a fault of this size in this region.

Both these estimates assume that incision occurred at Fault 2 scarp at the same time that it was recorded in VT2, 139m upstream of the scarp. The time elapsed between incision at F2 and at VT2 can be loosely constrained using the propagation rate of the F1 knickpoint [see section 7.2.2.3 below], the ages of VT4 and VT6, and the

[1] with no correction for inheritance

maximum time taken for the transmission of the VT2 incision to the base of Fault 1 [196±10/200±16-49ky: the approximate end of stream occupation, Phillips et al. (1996)]. These alternative approaches yield values for the Fault 2 propagation rate of 1.2-2mmyr^{-1} and for the slip rate of 0.03-0.09mmyr^{-1}.

7.2.2.3 Knickpoint propagation rates

Neither of the two steps in the stream profile in the footwall of Fault 1 [kp1 and kp2, Fig. 4.24] are associated with a change in lithology, an change in the extent of jointing, fumaroles or faults. They form sharp boundaries between morphologically distinct reaches, which show a gradual change in a number of properties towards Fault 1 [section 4.2.1.2]. The simplest explanation for this pattern is that the steps are knickpoints which have migrated upstream since their formation in response to tectonic movements at Fault 1 [see also section 2.3.3.1]. The field observations are also consistent with the prediction of "patchy alluvial cover, or short alternating sections of alluvial and bedrock channels" in bedrock streams undergoing uplift (Howard et al., 1994).

VT14, taken from between steps kp1 and kp2 [Figs. 4.24 and 4.32], can be used to estimate the rate at which the knickpoints have migrated through the footwall of Fault 1. I have assumed that the exposure age of VT14 represents the time at which kp1 reached the sample position, and hence that it has migrated upstream from VT14 to its present position since 73±3/64±12ka. Since only VT14 was analysed within the footwall stream, and VT8, closest to the base of Fault 1, shows complex exposure, assumptions must be made in the calculation of the knickpoint propagation rate.

Using the distance from VT14 to the current position of kp1 [69.28m], the ^{10}Be and ^{26}Al exposure ages give a lower boundary of 0.95±0.04/1.08±0.25mmyr^{-1} for the average upstream knickpoint propagation rate. However, VT14 is the youngest exposure age, and since the Tableland streams grade to the Tahoe [Q3] terraces of the Owens River (Pinter and Keller, 1995), it is probable that they were abandoned after the Tahoe glacial. Taking 49ka as the end of the Tahoe stage (Phillips et al., 1996; Table 3.1), and hence the abandonment of the stream, gives an upper boundary of 2.89±0.33 [Be] or 4.62-2.1+18.4mmyr^{-1} [Al] for the average knickpoint propagation rate of kp1 during the latter part of the Tahoe glacial.

An alternative approach is to use the distance that the knickpoint has travelled from Fault 1 to VT14 [364.12m], and estimates of the timing of the initial formation of the knickpoint. The lowest possible boundary on the knickpoint propagation rate comes from the crystallisation age of the Bishop Tuff [758.9±1.8ka, Sarna-Wojcicki et al. (2000)], which gives 0.52±0.015mmyr^{-1}. Incision in the footwall of Fault 1 is unlikely to have begun after the incision recorded by the samples in the ramp. Using the uncertain initial exposure age of VT8 [≥?450ka] produces a propagation rate of 0.91-0.97mmyr^{-1}; using the timing of incision at VT2 [196±10/200±16ka], which almost certainly postdates the footwall incision by a considerable margin, gives an estimate of 2.22-3.31mmyr^{-1}. These estimates are of the same order of magnitude as those based on the current location of kp1, but all lower. The most likely range of this data is a long-term average rate of 0.7-1.5mmyr^{-1}. However, it is perfectly feasible that the knickpoint migrated considerably faster during the wetter period of the Tahoe glacial, as implied by the estimate based on its current location.

Published estimates of knickpoint propagation rates from *in situ* cosmogenic isotope dating are similar. Seidl et al. (1997) calculated an upstream migration rate of 0.4mmyr^{-1} in basalt for knickpoints in Hawaiian streams, which compared well with their initial estimates of 0.2mmyr^{-1} based on observations and modelling (Seidl et al., 1994). Weissel and Seidl (1998) estimated long-term average upstream propagation of 2mmyr^{-1} in tributaries of the Macleay River, SE Australia, where pervasive jointing has allowed extremely rapid downwearing of the gorge head. I would expect the long-term average rates in the Tableland to be higher than those in harder basalt, but lower than in the Australian example, as the Tableland streams had lower discharges, and jointing is less pervasive. However, it is feasible that increased discharges during particularly the heavy Tahoe glacial, could have resulted in periods of faster propagation.

Fault displacement rates have not remained constant through time. As Fault 1 grew, and as it interacted with nearby faults, the rate of displacement at the fault increased considerably. Thus the base level drops experienced by this stream will have increased through time, resulting in greater steepening of the profile, and probably an increase in stream power [section 2.3.2]. Thus later rates of knickpoint propagation are likely to have been higher, even without any added impetus from periodically increased discharges.

The estimates of knickpoint propagation rate constrain the rate and timing of the onset of incision at Fault 1. If kp1 migrated at a constant average rate of 0.7-1.5mmyr^{-1}, then it would have been formed, at Fault 1, 520-243ky before the incision at VT14, i.e. at 589-311ka, which is consistent with the timing of incision in the ramp samples. Since that time, the footwall stream bed at the Fault 1 scarp has incised *at least* the depth of the two knickpoints kp1 and kp2 [4.5m total], and hence a minimum long-term average incision rate of the footwall stream at the Fault 1 scarp [until 49ka] is 0.0083-0.017mky^{-1}. If significant flattening of these steps has occurred on migration upstream [e.g. Fig. 2.22], this rate may be considerably underestimated. Averaged maximum erosion rates at the sampled sites in the Tableland have been calculated in section 7.2.2.5 for comparison.

These incision rates are ~ten times lower than the long-term [1.22My] average incision rates of 0.12-0.29mky^{-1} into the Bandelier Tuff calculated by Reneau (2000) along Frijoles Canyon. Incision along Frijoles Canyon was also affected by knickpoint propagation, and varied drastically though time, reaching a peak of up to 4mky^{-1} during the Mid-Late Holocene - over ten times the long-term rate. However, the Tableland estimates assume continuous occupation until 49ka, which may not be realistic, and hence the real incision rates may be significantly higher. It is also probable that much of the incision occurred in discrete events [section 7.2.2.4]. Discharge in the Bandelier example may also have been higher than on the Tableland. However, the calculated erosion rates, which are in the range of published estimates, require early formation of the footwall stream on the Volcanic Tableland, certainly before the pre-Tahoe stage proposed to have initiated the Tableland streams (Pinter and Keller, 1995).

Incision of the footwall stream has occurred in response to fault movements. Most of this incision reflects motion on Fault 1, but a small part may reflect some upstream transmission of the base level drops at Fault 2 and the smaller faults in the ramp. Steepening of the entire stream profile through the ramp [Fig. 4.24 and Table 4.3] implies that some of the base level drop from Fault 2 has been transmitted to the

base of Fault 1, even if not further upstream. If the footwall stream is in dynamic equilibrium with the fault [e.g. Burbank et al. (1996a)], then the estimated incision rates also constrain the long-term average displacement rates on this part of the Fault 1. It is likely that the rate of incision of the footwall stream has increased through time with the fault displacement, and also that it has been highly variable, reflecting climatic influences on the runoff rates. Measurement of more samples from the incised gorge of the footwall stream are required to constrain the rate and pattern of incision more closely.

7.2.2.4 Knickpoint propagation mechanism

The steep gradients of the knickpoints kp1 and kp2 imply that little flattening has occurred during upstream migration. Howard et al. (1994) demonstrated that the form of the migrating knickpoint in *homo*geneous bedrock depends on the formulation of the stream power law [see Fig. 2.22], the step remaining steep where incision rate is proportional to stream power [high values of the exponents m and n; Eqn. 2.10]. They also noted that knickpoints were rounded away more rapidly where steep intervening alluvial reaches were maintained. These results imply that knickpoints in the steep reaches of the ramp may be rounded and decrease in gradient more rapidly than those in the shallower footwall reaches. However, evolution of at least the footwall reach knickpoints is probably heavily influenced by the pervasive jointing of the tuff, and hence the steep knickpoint faces may well not be useful in constraining the stream power law exponents. [See the model in Fig. 7.5.]

The profile of the main stream through the Fault 1 scarp consists of a series of steps, each 1-2.5m high: equivalent to the horizontal joint spacing [Figs. 4.25 and 4.27b]. Similar steps are evident in the Fault 0 knickpoint in the axial stream [section 5.2.1]. The southern part of Fault 1 lies subparallel to one of the principal joint directions [see Fig. 4.2 and section 4.1.1], and nucleation or propagation of faults along joint planes is evident throughout the overlap region [e.g. sections 4.1.1.3 and 7.1.2]. Exploitation of joints parallel to Fault 1 by small rills and channels within the footwall of Fault 1 is also common, supplying water from the surface of the footwall into the main stream [e.g. Fig. 4.26f]. The widespread extensional opening of joints parallel to the main fault has allowed infiltration of water which erodes and widens the joint planes.

This mechanism is probably also responsible for the stepped nature of the knickpoint through Fault 1, and of the Fault 0 knickpoint in the axial stream. Extensional opening of fault-parallel joint planes is likely to be most pronounced in the immediate footwall of the fault, where some of the joint surfaces may also have accommodated extension by dip-slip motion, as along fault j [section 4.1.1.3]. Infiltration of water and hydraulic wedging by debris carried within the flow widened the joint cracks. Once water reached the horizontal planes under joint blocks, they could be plucked or quarried out [Fig. 2.17; Hancock et al. (1998); Whipple et al. (2000a)]. This process was also facilitated by the steep gradient of the stream through the scarp, and the removal of downstream blocks, allowing toppling [Fig. 7.5]. Repeated movement on Fault 1 continually steepened the reach, increasing the erosional power of the stream. The number of large [c.1-3m diameter] angular blocks in the main stream in this faulted reach, forming the debris pile at the base of the scarp [Figs. 4.27b], and seen in the axial channel at Fault 0 [section 5.2.1] is consistent with this mechanism of removal. Toppling

and quarrying of jointed blocks has been described in tributaries of the Macleay River as an extremely efficient mechanism of knickpoint downwearing (Weissel and Seidl, 1997, 1998).

The discrete steps in the footwall stream profile may reflect earthquake clustering, as it is unlikely that single events on the juvenile fault [≤1km long] would have resulted in 2-2.5m stream incision. Alternatively, they may simply reflect the mechanism of erosion. Hancock et al. (1998) and Whipple et al. (2000a) demonstrated that rates of erosion by plucking are higher than those by abrasion alone. Incision at the scarp probably proceeded relatively slowly by abrasion [Fig. 7.5b], until the base of a joint was exposed [Fig. 7.5c]. Subsequent rapid upstream migration of the knickpoint by quarrying then produced regular upstream steps [Fig. 7.5d,e]. The difference in height between the knickpoint at Fault 1 [~10.5m: 4-11x joint spacing] and the upstream steps [2-2.5m: 1-2x joint spacing] could reflect the increased slip rate on Fault 1, forcing relatively rapid downcutting of several metres. In this case, a series of jointed blocks exposed in larger or more closely-spaced slip events may be eroded simultaneously, resulting in a higher knickpoint.

Variation in the density of jointing, welding of the tuff, or discharge may also account for variations in the style and rate of knickpoint propagation. Jointing of the tuff is not uniform throughout the Tableland [sections 3.2 and 7.1.2]. Prominent long joint planes occur near the southern end of Fault 1 [e.g. Fig. 4.1], but are less evident further north. The variation in joint density clearly affects the development of faults [e.g. sections 4.1.1.3 and 7.2.1.1], and stream courses. However, as well as determining the *location* of incision, the jointing density evidently also affects the *style* of incision [e.g. upstream northern channel, Fig. 5.14b]. The horizontal and vertical joint spacing has a major influence on knickpoint migration and hence the incision pattern. Similar results have been reported from streams which erode jointed lithologies [e.g. Miller (1991); Wohl and Ikeda (1998)]. In the Tableland, knickpoint height appears to be intimately controlled by the horizontal spacing of the joints.

While knickpoints in the footwall of Fault 1 have propagated several hundred metres upstream and retain steep high faces, knickpoint propagation may be less pronounced or absent in less pervasively-jointed reaches. Thus within the central overlap, downstream of Fault 1, and particularly in the northern tip stream, knickpoints formed by fault activity could be rounded and degraded more quickly, so that long-distance migration of steep faces has not been recognised [e.g. Howard et al. (1994)]. Erosion in joint-rich reaches may proceed more rapidly than where joints are absent, and plucking reduced [e.g. Hancock et al. (1998); Whipple et al. (2000a)]. The accommodation of fault motion in less pervasively-jointed reaches on the Tableland may therefore require a considerably higher discharge or longer occupation than in the central footwall stream.

Potholes abound throughout the bedrock reaches of the streams in the central overlap, and are particularly common immediately upstream of knickpoints [e.g. at the linking fault; Fig. 4.29b]. In the central ramp, where the bases of jointed blocks are less commonly exposed, knickpoint propagation may be aided by the coalescence of potholes, as proposed by Wohl (1993) and Bishop and Goldrick (1992).

7.2.2.5 Erosion rates

Maximum long-term average erosion rates have been calculated at the sample sites using Eqn. 2.25 [section 2.5.1]: Table 7.3.

Sample	ε (mMy^{-1})	
	^{10}Be	^{26}Al
VT2	3.02±0.32	2.66±0.21
VT6	5.52±0.60	5.20±0.48
VT11	2.27±0.24	1.81±0.09
VT4	6.94±0.79	5.59±0.58
VT8	*1.77±0.19*§	*2.02±0.15*§
VT14	8.15±0.85	9.06±1.62

Table 7.3: *Maximum long-term averaged erosion rates at sample sites.*
Averaged erosion rates are maxima: calculated from the in situ *cosmogenic isotope content using Eqn. 2.25 with* Λ*=150gcm*$^{-2}$*, and* ρ*=2.3gcm*$^{-3}$*; and corrected for shielding of the samples.*
§ *VT8 has undergone complex exposure, and hence the erosion rate is drastically overestimated, as the true length of exposure of this sample is underestimated by the order of* 10^5 *years [section 6.5].*

Although a rate has been calculated for VT8, this sample has experienced significant burial [of the order of 10^5yrs] and hence the erosion rate is fairly meaningless. However, with this exception, the erosion rates calculated above do follow the expected pattern, with the highest rates of erosion [VT14] within the footwall stream, which has experienced the greatest base level falls. High rates of erosion have occurred in the immediate footwall of the linking fault within the main stream [VT4 and VT6], but a considerably lower rate characterises the minor stream sample, VT11. The erosion rate calculated for VT14 is of a similar order of magnitude to the long-term averaged incision rate estimated for the crest of Fault 1, from the knickpoint propagation rates in section 7.2.2.3: 8.3-17mMy^{-1}.

The absolute erosion rates are very low. The rates are similar to the downwearing rates calculated by Weissel and Seidl (1998) for reaches of the Macleay River tributaries in the plateau and *upstream* of the knickpoints [3.5-8.4mMy^{-1}], but far lower than those estimated at the knickpoint lip [19-20mMy^{-1}] or the rapidly-eroded gorge head [>50mMy^{-1}]. This is consistent with the lower discharge of the Tableland streams. However, the Tableland rates are long-term averages, and hence assume continuous stream occupation. It is likely that most of the erosion occurred in large events, and hence that the periodic erosion rates were considerably higher. While unoccupied, the stream bed would erode at a lower subaerial rate. As a comparison, the erosion rates of bedrock summit tors calculated by Small et al. (1997) are similar to the erosion rates calculated here: 7.6±3.9mMy^{-1}.

Since footwall stream incision has been dominated by the upstream migration of knickpoints from Fault 1, controlled in turn by joint spacing, errors may be introduced into the erosion rate calculation for VT14 by the assumption that erosion occurred by continuous removal of a thin coating of the rock. In the model presented in section 7.2.2.4, erosion may occur by the periodic removal of joint-bounded blocks around a metre across. Small et al. (1997) propose a method to assess the error introduced into cosmogenic erosion rate calculations by periodic removal of chips of rock [see also

section 2.5.3]. Using their equation [7], I estimate that erosion occurring by removal of 1m thick blocks would introduce an error of -40/+195% into the calculation of the erosion rate at VT14. Errors in the other calculated rates are probably considerably lower, as there is little evidence at the other sampled sites for removal of anything like this size of block [see also Small et al. (1997): their Fig. 5].

This potential underestimation of the long-term erosion rate at VT14 is consistent with crude estimates of incision rate ranges based on the depth of the channel, and either the crystallisation age of the Bishop Tuff, or the combined lengths of the pre-Tahoe and Tahoe glacial periods [94ky, after Pinter and Keller (1995)]. These simple calculations place VT14 erosion rates in the range 5.2-42.6mMy^{-1}, and rates at the Fault 1 scarp approximately twice as high.

The erosion rates can also be used to constrain the development of the stream draining the northern tip of the array [section 5.1]. Comparison of the aspect ratio and slope profiles of the streams [Fig. 7.3 showed that the northern stream has adjusted far more to the local faulting than other surveyed streams. This is particularly clear in the canyon incised through the northern tip of the fault array [section 5.1.1.1], and implies either a higher discharge or a longer occupation. If the stream incised at the rate calculated for the fastest long-term average incision in the central stream, [VT14: 8.15±0.85/9.06±1.62mMy^{-1}], then it would require over 1160ky to incise the canyon to the observed depth of 10m. Thus incision must have occurred far more rapidly, probably due to higher discharge. Conservative boundaries of 13.1-106.4mMy^{-1} can be placed on the actual long-term average incision rate from the crystallisation age of the tuff, and the combined lengths of the pre-Tahoe and Tahoe glacial periods [94ky, after Pinter and Keller (1995)]. The upper boundary of these values approximates the lower boundary of the Bandelier measurements (Reneau, 2000).

7.2.3 Model of the evolution of the central overlap

The evidence from the central overlap can be combined into a simple model of the stream and fault evolution [Fig. 7.6]. Major stages in the incision and re-organisation of the stream network are all triggered by tectonic activity, and changes in the interaction between neighbouring faults. Increased runoff during particularly the broad Tahoe glaciation may have allowed the streams to respond more fully or more rapidly to changes in the fault activity, but cannot be directly linked to specific changes in the stream evolution from the available data. However, the final stream abandonment probably occurred after the end of the Tahoe glaciation.

- *Small streams drained towards the SE [121-125°] following the local slope of the Tableland surface* [Fig. 7.6a]. These streams may have been initiated soon after the cooling of the tuff, and before significant fault activity. Fumaroles and joints, developed during degassing, exerted a local influence on stream patterns. Streams were probably supplied only from the surface of the Tableland [possible connection of some streams to Sierras - section 7.4], and hence barely incised. Occupation may have been ephemeral.
- *Onset of more significant motion on Fault 1.* Initial braiding and increased sinuosity in response to initial faulting [Fig. 7.6b]. Increased fault activity drove upstream incision of main stream into the developing footwall, exploiting weaker parts of the

tuff, and infiltrating joint planes in the footwall [Fig. 7.6c]. Later fault motions were accommodated by upstream propagation of knickpoints, aided by the geometry of cooling joints [Fig. 7.5].

- *Development of an alluvial fan in the growing hangingwall basin of Fault 1, sourced from footwall stream* [Fig. 7.6d]. Sediment deposited by migrating streams: distribution of rounded clasts [Fig. 4.47] implies drainage preferentially towards the NNE, and the contemporary D_{max}. Fan expanded in volume as more material eroded from incising footwall stream, and size of Fault 1 basin increased. Growth and linkage of fault 1 segments pushed deposition increasingly towards the north. Pulses of activity on Fault 1, and possibly climatic impacts on discharge from the footwall stream, allowed periodic overspilling of the basin and connection of the southernmost stream with a channel between fumarole highs to the E [Figs. 5.26 and 5.46].
- *Fault 2 propagated northwards, intersecting the southern stream, and driving incision into the fan* [Fig. 7.6e]. Faults nucleated along joints to the SE of the tip of Fault 1 linked and propagated northwards as extension increased [Fig. 7.4]. Intersection by Fault 2 caused a base level drop in the main stream, and initial braiding and increased sinuosity. Finally, a wave of incision passed upstream, cutting the main stream into the fan deposits, and fixing its location through the ramp. Transmission of this incision to the base of Fault 1 resulted in the ?gradual abandonment of the northern streams, as water was preferentially carried down the incised channel [Fig. 7.6e]. Deposition on the fan effectively stopped as material was carried into the Fault 2 basin and out towards the east, bypassing the fan, and leading to gradual starvation of the Fault 1 basin.
- *Continued growth of Fault 2 cut off supply to the E/SE and led to breaching of the ramp* [Fig. 7.6f]. Rotation of the F2 hangingwall ponded sediment at the base of the growing Fault 2, and towards D_{max} to the south. Pulses of motion on Fault 2 periodically rejuvenated the stream through the developing ramp, causing pulses of increased input to the hangingwall basin. Strain in the ramp increased as Faults 1 and 2 grew, finally leading to the development of a through-going linking fault [Fig. 7.4]. Slip on the linking fault increased as the segments linked, causing braiding and pulses of incision in the ramp streams [Fig. 4.30]. The main stream was not defeated [section 7.5.1].
- *Development of an axial system.* Continued growth of Faults 1 and 2 led to interaction with faults further from the overlap: Fault 1 with Fault 0 to the north; Fault 2 with faults to the south, changing the distribution of slip [section 4.1]. Interaction finally resulted in a fully-linked array (Dawers and Anders, 1995), and slip rates increased dramatically, particularly on the central faults. A through-going axial system developed proximal to the faults, linking the hangingwall basins, and reworking sediment originally ponded at the base of the Fault 2 scarp towards the south [section 7.3].

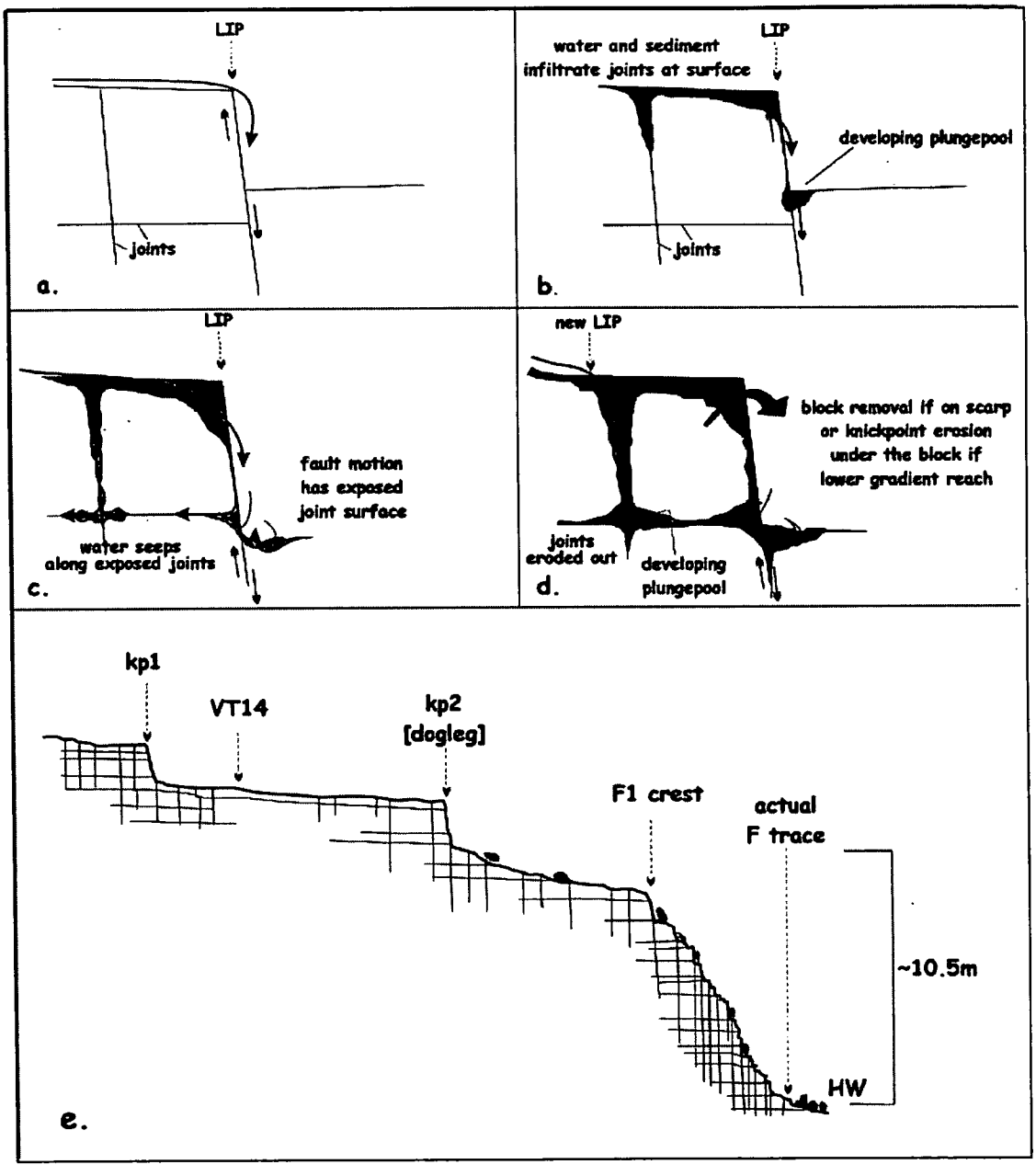

Figure 7.5: *Sketch of proposed mechanism of downwearing of the Fault 1 knickpoint by quarrying of jointed blocks. See also the cartoon of plucking [Fig. 2.17; Whipple et al. (2000a)].*

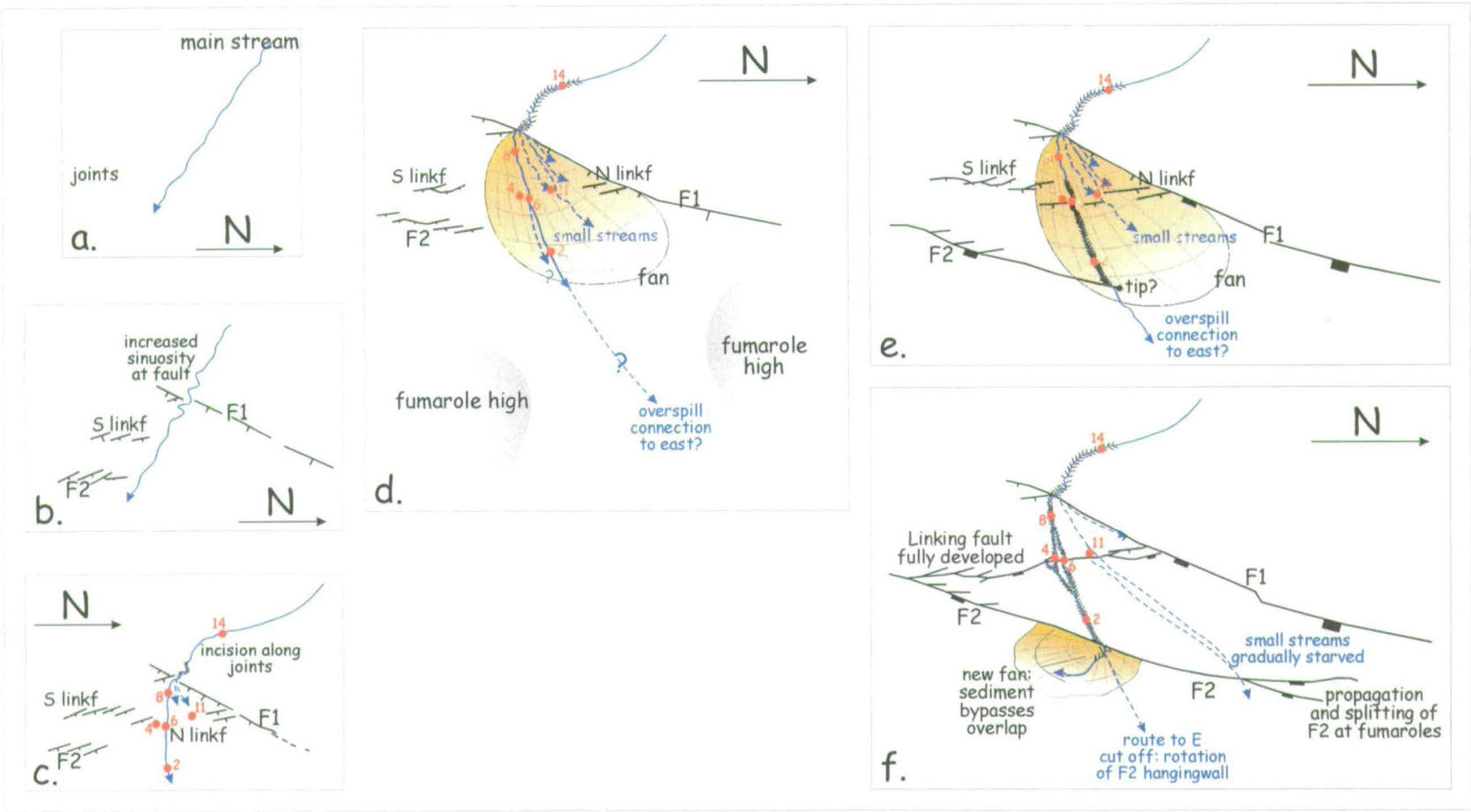

Figure 7.6: *Palaeogeographic evolution of the central overlap.*

7.3 Axial stream: Evolution and linkage of the array

This section considers some of the features of the axial stream network, and the small streams around it [section 5.2]. A model of the evolution of the evolution of these streams is presented on page 321, in terms of the state of linkage of the surrounding faults [Fig. 7.8].

7.3.1 Early drainage from the F0 footwall

The axial stream rises in the footwall of Fault 0 [Fig. 5.26]. The stream has a reasonably large catchment, squeezed between those of the main stream through the central overlap, and the large network which drains the northern tip of the array [Fig. 5.24]. The axial stream drops over 40m at Fault 0, and a further 4m across Fault A into the basin. This ability to incise suggests the stream developed relatively early in the evolution of these controlling faults, and was already supplied from much of its present catchment. The upstream reaches of the axial stream may thus have developed around the same time as the central footwall stream, its course controlled, prior to the development of the faults, by the regional slope of the Tableland surface [towards 121-125°, Pinter and Keller (1995)]. A clear step in the trace of Fault 0 at the incision of the axial stream [Figs. 5.24 and 5.27a], which coincides with a diverging fault in the footwall, implies further that this stream, like the footwall stream to the south [section 7.2.1.2], exploited a displacement low between initially discrete fault segments.

The development of an axial stream connecting the southern basins must have occurred relatively late in the evolution of the fault array [sections 2.2.1, 5.2 and 7.3.4]. A stream following the proposed regional slope [towards 121-125°; Pinter and Keller (1995)] from its incision in Fault 0 would connect the axial stream with the present course of the 'road stream' [purple in Fig. 5.26] between the fumarole highs west of Casa Diablo Road. Prior to fault growth, the main local control on the stream course would have been the fumarole mounds. Thus the road stream, funnelled between the two large indurated regions, may lie along the route of an early stream from the Fault 0 footwall deflected around the fumarole highs east of the current faults [Fig. 7.8a]. In this case, the road stream course, followed by the main stream spilling from the early F1 basin [section 7.2], may have been established quite early. This early stream course could also explain the broad region of deposition evident between the two fumarole highs [Fig. 5.24].

7.3.2 Sediment supply to the F1 basin

Despite having the highest footwall uplift in the array, Fault 1 has very little sediment in its hangingwall basin, indicating a long period of relative starvation [Fig. 5.40]. The northern part of the hangingwall basin preserves the tectonic subsidence profile, as demonstrated by the gradient of the axial stream [Fig. 5.35b], and the hangingwall profiles [Fig. 5.40]. This preservation of the basin topography is the result of the growth history of the fault, and its consequent influence on the footwall drainage patterns.

Much of the footwall of Fault 1 is drained through the central overlap [Fig. 4.1]. The course of this stream was determined quite early, as it exploited a displacement low

near the southern tip of Fault 1 [section 7.2]. Although some sediment from the stream was captured in the developing hangingwall [fan deposits on ramp, Fig. 4.47], the contemporary fault was only short, and hence the deposits only line the southern part of the present fault. The propagation of Fault 2 cut off supply to the F1 basin by incision of the main stream through the fan [section 7.2.1.3]. Virtually all the material eroded from the catchment of the main stream subsequently bypassed the Fault 1 basin, draining either away to the east, or ponding in the Fault 2 basin [Fig. 7.6f].

Large talus aprons line parts of Fault 1 [Figs. 4.3]. These have been partially supplied by slope wash, but may also indicate early drainage from the developing footwall of Fault 1. Although there is no well-developed stream which can be definitively connected with these deposits, many near-vertical joints in the upper footwall of the fault have been exploited by water [as seen in Fig. 4.26f]; in some cases forming small channels which can be traced for tens of metres. Thus some form of cross-scarp drainage occurred in this region. The largest pile of talus is associated with a large step in the fault scarp [Fig. 4.1], hinting at the possibility of an early supply directly from the footwall. However, the volume of this material is small, and any significant supply is likely to have been cut off by the connection of the fault segments.

The other prominent stream from the footwall of Fault 1 drains through the overlap at its northern tip, into the Fault 0 basin [Fig. 5.24; green in Fig. 5.26]. The steep displacement gradient and extremely high displacement at the northern tip, together promote the deflection, rather than incision of a stream from this part of the footwall [section 7.1.1]. Thus even if a precursor to this stream drained across the scarp directly into the Fault 1 basin, interaction with Fault 0 would probably have forced it to drain northwards, down the steep slope. Due to fault activity on both margins, the Fault 0 basin probably subsided rapidly, and hence all the sediment supplied from the F1/F0 overlap was deposited within this small basin, until very recently [section 7.3.4].

Thus although carried in two big stream systems, very little of the sediment generated from the Fault 1 footwall entered its hangingwall basin, until the development of a through-going axial stream. By this point, the F1 basin was virtually isolated. This was the result of the pattern of fault growth and the relative timing of segment linkage and interaction with the surrounding faults. The preservation of steep hangingwall topography has been further enhanced by the accumulation of additional displacement on the fault, following the linkage of the array. Much of the very high displacement on this fault may have been accrued during the late stages of the array development [e.g. Gupta et al. (1998); Cowie et al. (2000); McLeod et al. (2000)], developing both footwall and hangingwall topography that would have swamped any pre-existing drainage pattern.

7.3.3 Controls on development of the axial stream

Development of a through-going axial stream system relies on linkage of the individual hangingwall basins along the array [section 2.2.1]. This therefore requires that intrabasin highs [IBHs; e.g. Anders and Schlische (1994)] are overcome, either by filling the basins to the top of the highs, incision through them by aggressive streams, or their subsidence following linkage of the controlling fault segments [section 2.2.2]. The present fault-proximal axial stream connects the basins of Faults 0, 1, 2, and 3 [Fig. 4.1

and 5.24], and hence its development is dependent on the evolution of the overlapping regions between these faults.

F0/F1 basins: The Fault 0 basin is very narrow, constricted by a west-dipping fault [margin of a small horst block], and a series of fumarole mounds on its eastern margin, as well as by the major faults on the west [Figs. 5.24 and 5.28]. However, fault activity on both margins probably resulted in rapid and deep subsidence of the basin floor. Thus connection of the Fault 0 and Fault 1 basins was impossible until the lip between the two basins, at the northern tip of Fault 1, was overcome [Fig. 7.7].

A considerable amount of sediment entered the F0 basin, from both the Fault 1 footwall, via the heavily-loaded F1/F0 overlap stream [Fig. 5.27b], and the Fault 0 footwall, as the axial precursor stream was captured in the subsiding basin. The limiting step for connection of the fault basins was the balance between sediment supply and the subsidence rate of the basin. Incision in the stream draining the F0 footwall is very low, and hence supply to the basin may have been dominated by the F1/F0 overlap stream, as implied by the pile of sediment at the base of the ramp [Fig. 5.27b]. This, in turn, was probably heavily influenced by displacement on Fault 1, which affected the stream gradient, and fracturing of the ramp. Increased slip rates on Fault 1, possibly following the linkage of the array, may have been ultimately responsible for pushing the balance in favour of sedimentation, allowing the Fault 0 basin to fill, and connecting it to the Fault 1 basin further south.

F1/F2 basins: Deformation at the northern tip of Fault 2 is distributed onto two small splays, each with displacements $\leq$1m [Fig. 4.16]. These splays extend towards the centre of Fault 1, where displacements currently reach 80m [Fig. 4.5]. Coalescence of the Fault 1 and Fault 2 basins probably followed the linkage of the southern and northern segments of Fault 1, and the later accumulation of tens of metres of displacement, allowing the fault to influence a wider area. Recent subsidence in this region has been thus been dominated by the later accumulation of displacement on Fault 1, while the tip of Fault 2, and the isolated fumarole mounds, only have a local influence on stream courses [Fig. 5.40].

Rounded clast deposits demonstrate that sediment was deposited over the northern part of the central overlap, and beyond the current tips of Fault 2, during the early development of Fault 1 [Fig. 4.47 and section 7.2.1.3]. The propagation of Fault 2 cut off much of this supply, which was re-routed into the developing Fault 2 basin, through the incised main stream over 400m from its northern tip. This material initially overspilled the Fault 2 basin into the road stream, but was later ponded as the basin grew, and has gradually infilled the developing space. Thus since the linkage of the Fault 1 segments, there has probably been very little topography between the central Fault 1 basin and the Fault 2 basin which would prevent axial stream flow between them.

F2/F3 basins: The southern tip of Fault 2 is hard-linked to another large fault ['Fault 3'] [Fig. 4.1]. The region between the two faults is broken by a series of large faults, forming an almost solid fault 'wall' along the array. The sand distribution [pale area on the aerial photograph; Fig. 4.1] demonstrates that supply from this overlap has spread over a wide area to both the north and south along the array. There is no significant topography in the hangingwall today, implying that this supply has been sufficient to fill both basins, to the north and south of the initial overlap, to the level of the original intervening high.

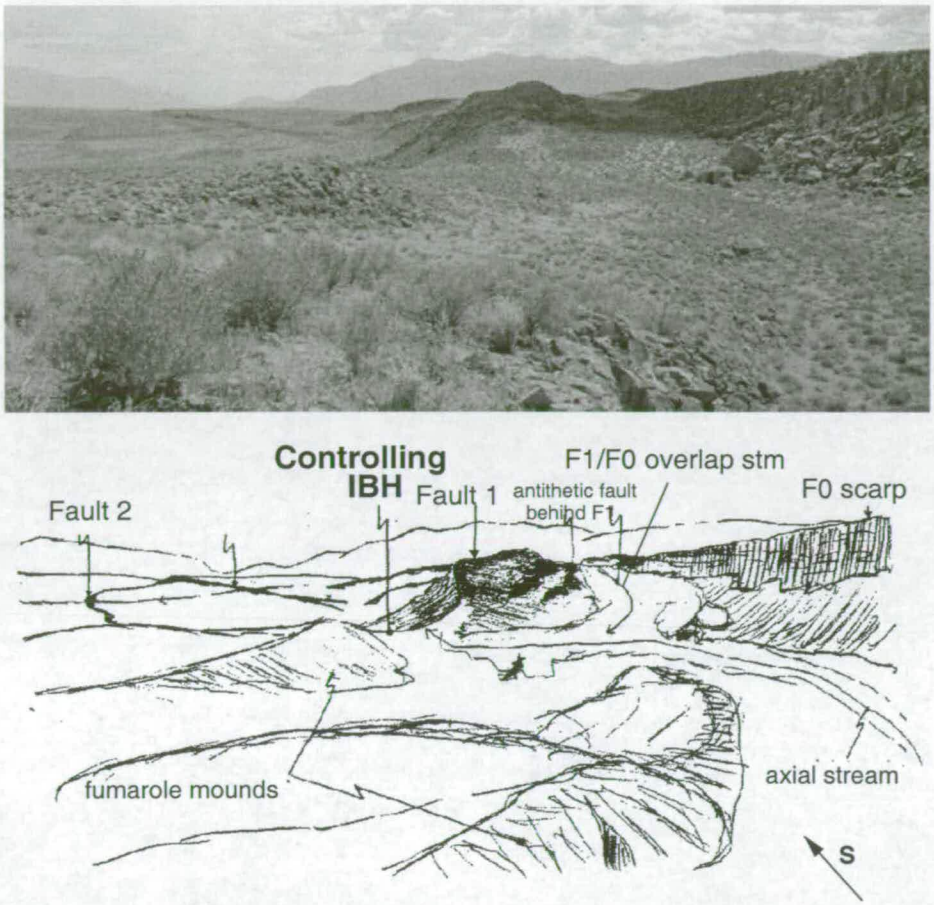

Figure 7.7: *View of southern Fault 0 basin, and lip at tip of Fault 1 controlling the drainage into the F1 basin.*

The displacement profile of Fault 2 is skewed towards the south [survey in Fig. 4.16 terminated at the F2/F3 linkage; see also profile in Fig. 3.6; Dawers and Anders (1995)]. As discussed, this indicates that the later development of Fault 2 was dominated by interaction with Fault 3 to the south, which has swamped evidence in the displacement profile of the earlier interaction with Fault 1 during the formation of the central overlap. Linkage of the F2 and F3 hangingwall basins may thus have occurred any time after the northward propagation of Fault 2 which led to the incision of the main stream [$\leq$200ka from VT2 age], and probably before the connection of the F0/F1 basins further north.

7.3.4 Establishment of the axial stream

The limiting step in the development of the axial stream was probably the connection of the Fault 1 and Fault 0 basins, as all the basins to the south may well have been connected much earlier in the evolution of the array [see above]. Once the axial stream spilled over the lip of the northern F1 basin, the steep slope preserved due to the high displacement gradient at the northern tip of Fault 1 caused braiding and incision [Fig. 5.29]. This was enhanced by the confinement of the stream between the fault and an indurated fumarole high to the east [Fig. 5.28]. Upstream transmission of this

incision lowered the constraining sill, ensuring that the basins remain connected, and probably also stripped sediment from the higher F0 basin. Sediment from the F1/F0 overlap therefore bypassed the Fault 0 basin after the incision of the axial stream, as can be seen looking south from the horst block [Fig. 7.7].

The axial stream brought the first significant sediment supply to the Fault 1 basin from the north. Once connected, however, this stream was also able to drain into the fault basins to the south, which were probably no longer isolated by this stage [section 7.3.3]. Thus sediment has been reworked from the central overlap stream towards the south [Fig. 5.24], into the F3 basin, and from there finally into the Corral fault basin. Initially, the axial stream probably flowed into the centre of the graben, although modern irrigation of a corral has removed any evidence of this connection [section 5.2].

Although confined close to the base of Fault 1 at the northern part of its route, the axial stream course is more distal from the southern faults, running almost along the margin of the indurated fumarole region [Fig. 5.24]. This may reflect the influence of the regional tilt of the Tableland surface, pulling the stream towards a more SSE course [which has gradually rotated towards 113°, Pinter and Keller (1995)], rather than one directly parallel to the faults. The fact that this SSE course is followed in the *southern* basins demonstrates that the hangingwall topography there has been sufficiently filled to allow the stream to flow further from these faults. In contrast, the northern basins of Fault 0 and Fault 1 are confined by the proximity of the fumarole high to the east. The distant axial course may also indicate that there was little contemporary activity on the southern faults, as active faulting would tend to cause an axial stream to migrate or avulse towards the scarps [e.g. Peakall (1998); Peakall et al. (2000)].

It is also possible that the southern part of the axial stream lies along a pre-existing stream course. Prior to the onset of faulting, a stream draining down the contemporary regional slope towards 121° from the point of incision of the main central overlap stream through Fault 1 would drain roughly along the present axial course through the Corral Fault scarp [Fig. 7.8a]. Activity on this fault may well be later than that on the southern faults, in which case it may have caused some deflection of the axial stream away from the main fault scarps, and possibly into an earlier abandoned stream course. However, this scenario is hard to determine without additional evidence.

7.3.5 Fumarole-axial stream

The course of the 'fumarole-axial' stream [red in Fig. 5.45] along the southern margin of the fumarole high implies that it was initially controlled by the patterns of welding within the tuff. The stream has been beheaded by the incision of the downstream reaches of the northern tip stream, which now runs along the central axis of the graben [Fig. 5.47]. The profile of the 'fumarole-axial' stream has a very low gradient, consistent with its wide channel, and implying a relatively mature, long-lived supply from a large upstream catchment [section 5.2.5.1]. It may therefore be an early downstream route of the northern stream at a time before significant faulting, when welding variations were the principal control on drainage patterns. The abandonment of this course through the preferential incision of the current more easterly route may have occurred due to tilting and subsidence following motion on the W-dipping array to the east, which has had a major impact on the development of streams in the region [Fig. 7.8c]. The small

faults near Casa Diablo Road may have also played a part in the stream rearrangement [Fig. 5.1].

The presence of the fumarole-axial stream implies that the northern tip system established a route to the southeast relatively early, and probably never flowed closer to the southern faults of the main array. Thus the northern stream system and the streams which have later been captured by the southern axial system have been separated during most of the development of the faults, only meeting far downstream, where the southern streams drained into the centre of the graben [Fig. 7.8]. The current isolation of the southern basins is the result of small faults and basin highs to the north of the Fault 0 basin [Fig. 4.1]. However earlier isolation, implied by the fumarole-axial stream, demonstrates that the northern stream had the power to maintain a course to the SE, presumably initiated in response to the regional slope, despite the subsequent development of the N-S faults. The early route has been modified, but never substantially redirected, by the fault activity. This is consistent with the AR profiles [section 7.1.3.2] which indicate a powerful, long-lived stream, and is additional support for a relatively early initiation of the northern system, relative to other streams in the area [see also section 7.4].

The fumarole-axial stream is isolated from the hangingwall basins immediately to the west by the indurated fumarole region on its western flank [Fig. 4.1]. The development of hangingwall basins between the faults and the fumaroles cut off any supply from the west which originally entered this stream [e.g. through the stream which now drains east from the fumarole high, Fig. 5.46], continuing the isolation of the two main systems [northern stream and southern axial]. While its course may have been unaffected by subsidence during early fault growth, the fumarole-axial stream was probably tilted towards the west as the region affected by the faults widened during their later development. However, it was unable to migrate laterally towards the faults due to the resistance of the indurated tuff. Thus the fumarole high has ensured the isolation of the northern supply from the runoff from the southern footwalls. Lateral migration of the fumarole-axial channel may in any case have been virtually impossible if beheading occurred before significant motion on Faults 0 and 1.

The shape of the confluence between the fumarole-axial channel and the road stream [Fig. 5.45] implies that the two streams were active simultaneously. This places some constraints on the abandonment of the fumarole-axial stream, which may therefore postdate at least the incision of the central overlap stream [$\geq$200ka], and possibly the termination of the supply from the central overlap as displacement on Fault 2 increased. However, if the road-stream was established as a route by an early stream draining the F0 footwall [section 7.3.1], then the beheading of the fumarole-axial channel may have occurred significantly earlier.

7.3.6 Reorganisation of the array stream patterns

The development of a through-going axial system marks the final stage in a large-scale reorganisation of the drainage routes in this part of the Tableland [Fig. 7.8]. Prior to the onset of faulting, drainage followed the regional slope of the Tableland surface, towards the southeast [121-125°; Pinter and Keller (1995); Fig. 7.8a]. The growth and linkage of the main E-dipping fault array gradually altered the local topography, and hence

modified the streams by deflection, capturing the sediment in growing hangingwall basins [Fig. 7.8b]. Due to their high sediment volumes and high stream power, some large streams were able to maintain a supply beyond these new basins. However their courses were severely modified, as seen in the northern stream, which is forced to bend through almost 90° several times in response to small faults [Fig. 5.2]. The main central overlap supply was not carried towards the southeast, but routed through the road stream towards the east [section 7.2.1.4], possibly partly due to the position of strongly-welded fumarolic regions.

Continued growth of the faults led to the connection of the southern hangingwall basins, and the final overprinting of drainage patterns established on the pre-existing SE slope. Supply from the uplifted footwalls was all forced to drain towards the south, parallel to the faults, and finally into the main stream flowing down the centre of the graben [Fig. 7.8c]. This is also partly governed by the growth of a major W-dipping fault array to the east, which has helped focus drainage down the centre of the graben [e.g. possible effect on the fumarole-axial stream: section 7.3.5; Fig. 7.8c], and cut off the exit to the east or southeast. The influence of the initial southeasterly regional slope remains evident in the powerful northern tip system, whose course implies early development [section 7.4]; and the more SSE-ly flow of the axial stream where it is unconfined in the southern basins. However, the initial regional slope has otherwise been overwhelmed by the effect of faulting in this graben [e.g. Fig. 7.8: compare [a] and [d]].

The cosmogenic samples in the central overlap provide some constraints on the rate of the stream re-orientations. Incision of the main stream through the overlap, due to the propagation of Fault 2, occurred $\geq$200ka. Following this incision, supply from the main stream drained east through the road stream, before being ponded at the base of Fault 2, and infilling much of the developing basin topography. Interaction of Faults 1 and 2 was followed by interaction with faults to the north and south of the overlap, finally resulting in the connection of the sub-basins, and the development of the axial stream, which reworked material from the central overlap towards the south. All these reorganisations, and the controlling changes in fault geometry, must have occurred in the $\sim$150ky between the incision of the stream by Fault 2 development and the final abandonment of the Tableland streams after the Tahoe glaciation. If sample VT2 has significant inheritance from prior exposure, its true age is younger than 200ka, and hence the changes in the fault array which caused reorganisation of the stream pattern must have been considerably faster.

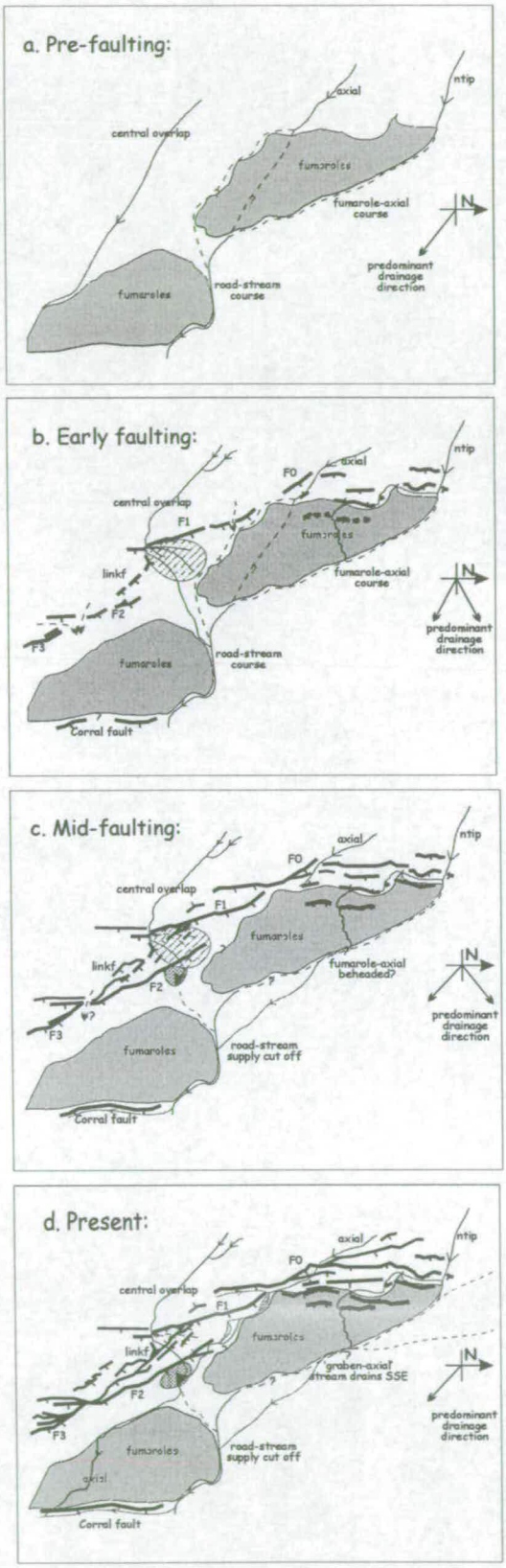

Figure 7.8: *Palaeogeographic evolution of the axial stream.*

7.4 Non-tuff clasts: Early drainage evolution

The non-tuff clasts [section 5.1.4] represent over ten different lithologies, from acidic to mafic igneous material, as well as a smaller percentage of metamorphic clasts [Fig. 5.23]. The clasts are generally well rounded and quite highly weathered, implying considerable transport in a powerful drainage system, and thus that a much earlier initial erosion than the more common Bishop Tuff deposits, which show signs of relatively little weathering, despite being considerably softer. The non-tuff material shows little sign of sorting in the upper parts of the northern tip stream, either by lithology or size [Fig. 5.23]. In Chapter 5, I thus suggested the material had been reworked after original erosion from an extremely heterolithic catchment. This section considers possible origins of the non-tuff material, and hence constrains the early development of the Tableland streams.

Non-tuff clasts have been observed only in the drainage system which flows through the northern tip of the array, and a large stream in the SW corner of the Tableland [N. Dawers, pers. comm.]. All the other streams which I have seen on the surface of the Tableland contain only Bishop Tuff clasts, implying a catchment solely on the surface of the Volcanic Tableland. The presence of these alien clasts implies a similarity between these two streams, and also a significant difference between their evolution and that of all the other streams in the area.

The northern tip drainage system [section 5.1] is considerably larger than the network which drains the central overlap of the array [section 4.2.1]. Bedforms throughout the system are testament to a larger discharge, even in the upstream surveyed reaches. In contrast to the deflection of streams within the central overlap, the deep canyon incised through the northern faults shows an apparent disregard for the neighbouring faults: the stream course is barely deflected [section 5.1.1.1]. Apart from a step at the most-easterly fault, the canyon floor has a uniform low gradient more typical of unfaulted reaches oriented parallel to fault strike in other parts of the Tableland [e.g. compare Tables 5.1 and 5.3].

While this stream has a considerably larger catchment, the virtually complete accommodation of faulting in this incised reach, compared to the steep gradient of the central overlap, may also reflect a longer period of adjustment. In section 7.2.3, I proposed that the incision of the central stream into the footwall of Fault 1 was driven by the gradual accumulation of displacement on the fault, and that prior to the onset of faulting, the channel was relatively shallow. Although the northern stream flows through a whole series of faults along the canyon, the throws are smaller than on Fault 1, and the slip rates are likely to have been consistently lower than in the central overlap, where the faults would have been repeatedly loaded by motion on surrounding structures [e.g. Cowie (1998)]. Hence it may follow that even with the higher discharge, the northern faults alone would not have been capable of driving incision to the extent seen in the northern canyon [$\sim$11m] in the same time as $\sim$8m incision occurred within the central overlap stream. In this case, the depth of incision, and particularly the uniform low gradient, may demonstrate a commitment to this route before the onset of significant faulting in this region.

The southwestern stream was not described in the previous chapters, but was examined in the field. The stream occupies a large channel which originally drained towards the

southeast, presumably following the initial slope of the Tableland surface [e.g. Bateman (1965); Pinter and Keller (1995)], but has been subsequently dissected by the N-S faults in the area. There is some evidence of continued activity of the stream after the onset of faulting [e.g. deviation of the stream course along the base of west-dipping faults, Pinter and Keller (1995) their Fig. 6]. However, the stream has clearly been offset by fault activity, and alternate reaches of the stream have been uplifted and downthrown, making the initial route unviable. The relatively early death of this system is confirmed by subsequent south-flowing streams, parallel to the faults, which overprint its course, and in places rework the sediment deposited by the original channel. Assuming that the onset of faulting was roughly synchronous across the Tableland, which seems reasonable given the regional scale of the stress causing it, then this southwestern stream was abandoned *before* most of the development of the other surveyed streams, which all show evidence of significant syn-tectonic evolution [e.g. sections 7.2.3 and 7.3], and may therefore be more synchronous with the N-S streams which overprint this ancestral drainage.

Both the northern network and the SW stream originally drained towards the SE, which is consistent with the initial slope of the Tableland surface [e.g. Bateman (1965); Pinter and Keller (1995)]. Although non-tuff material has been observed immediately to the NNE of the northern stream [section 5.1.4], a source from the area of the Benton Range [see Figs. 3.5 and 3.4b] would not supply non-tuff material to the upper reaches of the surveyed northern stream. Since no non-tuff clasts have been seen between the northern stream and the SW stream, a single Benton area source would also not be adequate to explain the observed distribution of the clasts. A source of non-tuff clasts from the NW is more likely to have supplied the two streams. The most obvious source area for this material is clearly the eastern margin of the Sierra Nevada, where all the observed lithologies outcrop [see maps in Bateman (1965), and section 3.1].

Although most of the alluvial fans from the Sierras lie against the range front, some older Quaternary alluvial material outcrops on the western margin of the Tableland, the closest outcrops of which are 6.5-7km due west of the non-tuff material seen in the northern stream. This material is the Pleistocene older fan, 'Q_{of}', unit of Bateman (1965), which he describes as *'scattered remnants of fanglomerate'* which are *'thin, and probably nowhere more than 50 feet thick'*, deposited by systems from the north. The location and the direction of the supply of these deposits make correlation with the non-tuff material in the two Tableland streams tempting, particularly as the fans are very likely to be heterolithic, and contain predominantly igneous material, like the younger fans along the Sierras. Descriptions of the weathering of clasts on terraces of the Owens River to the south of the Tableland (Pinter et al., 1994), demonstrates that quite thick weathering rinds can develop on the valley floor in the order of 10^5 years. Hence the age of the Q_{of} deposits is sufficient to have generated the weathering observed on the non-tuff clasts on the Tableland. However, I have not seen the Q_{of} outcrops personally yet, and hence the correlation can only be tentative at present.

7.4.1 Proposed model of large-scale Tableland drainage evolution

The Bishop Tuff originally filled the entire of the northern Owens Valley (Bateman, 1965; Sheridan, 1970; Wilson and Hildreth, 1997), although only the Tableland and a few scattered remnants are left at the surface today. Once the tuff had cooled

sufficiently, it is likely that streams began to drain from the Sierras across the surface of the tuff into the Owens River, near their pre-ignimbrite courses, although the position of the Owens River was drastically altered. Core OL-92 in southern Owens Lake shows a nearly-constant deposition rate was maintained throughout the 800ky record (Bischoff et al., 1997). Since runoff from the eastern Sierras dominates the supply to Owens River and hence to Owens Lake, the core implies that the supply was not significantly interrupted by the emplacement of the tuff. Sarna-Wojcicki et al. (1997) describe ~9m of reworked Bishop Tuff in the OL-92 core, above the initial ashfall layer, demonstrating that tephra shrouding the tributary catchments was rapidly removed by active streams. Sarna-Wojcicki et al. (1997) estimate a maximum time elapsed before a return to the normal erosional pattern as 13ky, although they believed the true period was more likely to be 100-1000yrs. The high activity of Sierran streams in this period is also consistent with the evidence from Owens and Searles Lake cores of considerably wetter climates around the time of the Long Valley eruption (Smith et al., 1997).

Streams drained across the ignimbrite surface to the south or southeast into an Owens River. These streams built fans onto the surface of the ignimbrite, the remains of which are Bateman's Q_{of} deposits, now preserved only on the western margin of the Tableland. As motion on the range-bounding faults increased, the ignimbrite began to warp slowly into an arch (Bateman, 1965; Pinter, 1995), and the Sierran streams were directed more towards the southeast [potentially towards 121-125°, as proposed by Pinter and Keller (1995)]. Thus the dissected SW stream, and an ancestor of the northern stream, may be downstream remnants of the Sierran streams which carried non-tuff clasts further onto the Tableland, as they drained down the developing regional tilt [Fig. 7.9a].

As the Sierran faults grew, warping of the Tableland increased, developing N-S-oriented normal faults in the tuff sheet itself, which in turn affected the evolution of the surface streams. The SW stream shows some evidence of deviation along the margin of W-dipping faults, but was eventually dissected by the developing structures, and subsequently overprinted by south-flowing streams. In contrast, a large stream network developed at the north of the array studied here, which was able to keep pace with the developing faults [Fig. 7.9b].

Warping of the tuff enhanced the SE-tilt of the eastern part of the sheet, but also tilted the western limb of the arch towards the southwest. Bateman (1965) states that the *later* Pleistocene alluvial material [his Q_{al}] lies on top of the Bishop Tuff in Round Valley [Fig. 3.1], which is consistent with the gradual downwarping of this margin of the tuff. While the *older* fans, depositing the Q_{of}, extended as far as the western margin of the present Tableland, '*structural depression of Round Valley has caused dissection of these older fans and the building of new ones west of the Volcanic Tableland.*' (Bateman, 1965) [Fig. 7.9b]. The Q_{of} deposits at Paradise [Fig. 3.1] have been preserved above the level of the Round Valley fill due to uplift on the footwall of a small fault along the margin of the present Tableland.

The contrasting evolution of the two non-tuff-bearing streams is largely the result of their different locations. The SW stream was tilted southwest through time, as the western limb of the arch rotated towards the Sierras, possibly reversing the stream course, but certainly making it unable to compete with the growing faults (Bateman, 1965; and Fig. 7.9b). In contrast, the northern stream lies on the eastern limb, and

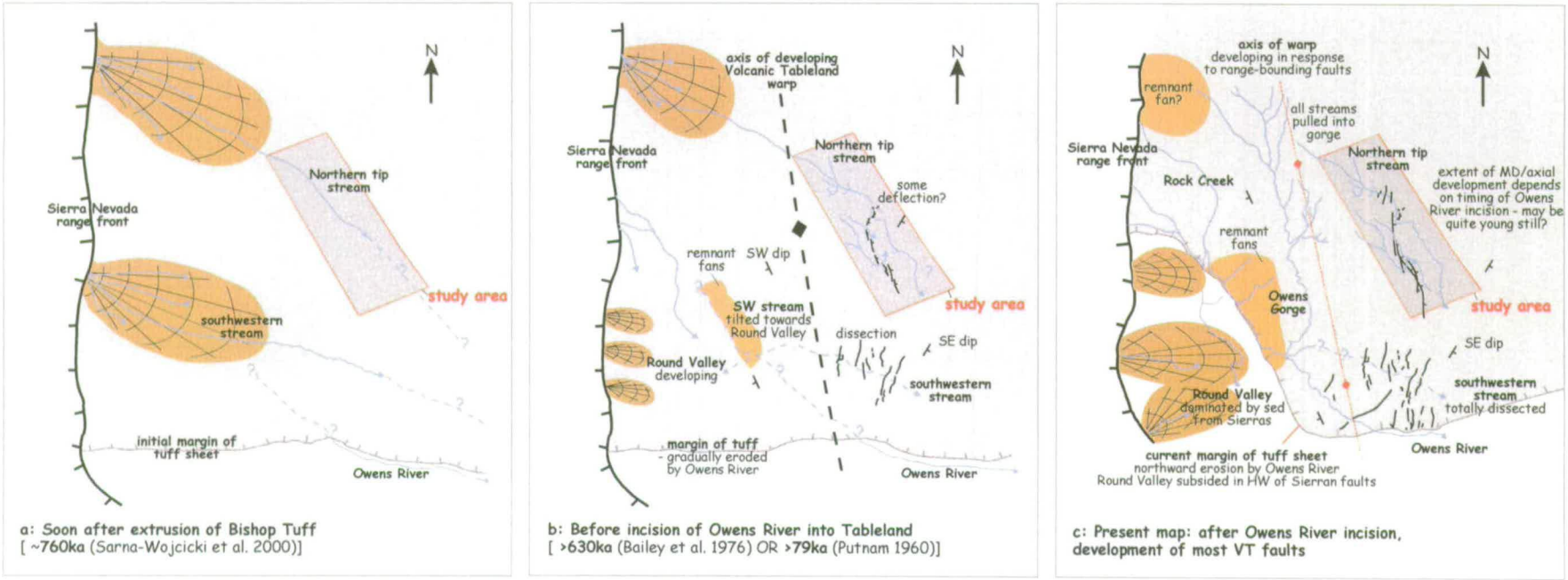

Figure 7.9: *Proposed model of drainage evolution on the Volcanic Tableland.*
a. Streams drain from the eastern Sierras across the surface of the Tableland into an ancestral Owens River. Hence streams carry non-tuff clasts derived from Sierran catchments onto the surface of the Tableland.
b. Increasing slip on the range-bounding faults warps the Tableland about a N-S hinge. SW Tableland stream tilted towards the SW and unable to keep pace with the growing faults: supply cut off. Northern stream experiences predominantly SE-tilt, so stream power enhanced, and river incises through all the developing faults. Continued slip on the Sierran faults causes local subsidence of Round Valley, forming a depocentre for Sierran sediment at the foot of the range. Several hundred metres of Q_{al} sediment overlie the downwarped Bishop Tuff in Round Valley (Bateman, 1965).
c. Incision of the Owens River into the Tableland completely cuts off northern stream from the Sierran supply. Most nearby streams forced into the growing gorge. A W-dipping fault preserves old Q_{of} deposits above the level of Round Valley, and isolates the northern Tableland from the subsidence of Round Valley. All subsequent Tableland drainage evolution sourced from the Tableland surface alone.

experienced an increasing SE-tilt through time. Warping of the Tableland *enhanced* its power, allowing it to incise through the developing faults [Fig. 7.9b]. Uplift on the fault at the western margin of the Tableland may also have helped separate this part of the Tableland from the subsidence of Round Valley.

Thus gradually, the subsidence of Round Valley and the increased warping and fracturing of the tuff sheet isolated the Tableland from the Sierran drainages. Most of the Pleistocene deposition from this part of the eastern Sierras has been dumped in Round Valley, or been carried into Owens River, e.g. by Horton Creek [see Fig. 3.1]. As a result, the subsequent evolution of the Tableland drainages must have been dependent only on runoff from the surface of the Tableland itself [Fig. 7.9c], which is consistent with the monolithic deposits in all the rest of the surveyed streams, and the evidence for significantly lower discharge than that in the northern system. However, the loss of the Sierran supply would probably have resulted in a considerable drop in the discharge through the northern stream. The downstream-winnowing of the non-tuff material in this stream is consistent with gradual reworking of material initially deposited further west by an earlier stream.

However, this scenario also requires a wetter climate, to support rapidly-incising streams from catchments solely upon the surface of the Tableland. Although Owens Lake records imply that the Pleistocene climate was considerably wetter than the Holocene (Smith et al., 1997), it is perhaps surprising to suggest that precipitation on the surface of the Tableland alone was sufficient to support streams which incised over 8m into the tuff surface. Nonetheless, the cosmogenic data from the central overlap channel demonstrate that the streams did not develop solely during the two glacial stages suggested by Pinter and Keller (1995), and imply a longer occupation, at least before the Tahoe stage [sections 6.5 and 7.2.3]. It is possible that streams such as the network which drains the central overlap were established with some runoff from the Sierras, before the isolation of the Tableland by the subsidence of Round Valley. However, the lack of non-tuff material and the shallow upstream channels belie a significant discharge from the range.

7.4.2 Correlation with Owens River incision

The Owens River currently occupies a deep gorge incised over 150m into the Tableland surface [e.g. Fig. 3.4b]. Incision of the Owens River would have prevented Sierran streams supplying the surveyed Tableland streams, which all lie to the east of the Owens Gorge. Similarly, supply from the western part of the Tableland would be forced into the gorge. Hence, if the non-tuff bearing Tableland streams received a significant supply from the west before they were cut off by the subsidence of Round Valley and movement on the western Tableland margin fault, some constraints can be placed on the longevity of this western supply by considering the timing of the incision of the Owens River.

Mayo (1934) and Putnam (1960) invoked headward incision of the Owens River northwards through the ignimbrite until it breached the restraining tuff barrier of the Long Valley Lake, which then catastrophically drained, incising the deep gorge into the Tableland [Fig. 3.7]. Putnam (1960) suggested that the headward incision was driven by increased runoff in the Tahoe glacial, which correlated with an estimate of the lake's

highstand. Bailey et al. (1976) used volcanic outcrops to plot the varying lake levels through time [their Fig. 6], showing that the lake level rose quickly after extrusion of the tuff, then rapidly fell over 60m before 630ka. Thus, they suggested that the gorge was cut from the north, by the lake spilling over the tuff barrier, and draining mostly down a path originally occupied by the Owens River before emplacement of the tuff [e.g. Sheridan (1970); Wilson and Hildreth (1997); Holt and Taylor (1998)].

Wilson and Hildreth (1997) proposed that the ignimbrite was originally deposited over 15km further south than the present outcrop of the Tableland. Lateral incision by the Owens River, displaced to the south, gradually cut into the southern margin of the tuff sheet, eroding a steep bluff [Fig. 3.4a]. This northward erosion can be seen from the pattern of the terraces at the southern margin of the tuff, which have been correlated with 'pre-Tahoe', Tahoe and Tioga moraines (Pinter et al., 1994; Fig. 7.10 and Fig. 3.4b), thus implying that the Owens River incision was dominated by increased runoff in three glacial periods. The level of the Q4 ['pre-Tahoe'] terrace ~30m *below* the surface of the Tableland implies that incision into at least the southern margin of the Tableland occurred by or during this stage [206-131ka in Pinter and Keller (1995), but see Table 3.1]. The preservation of Q3 [Tahoe] deposits in the gorge (Pinter et al., 1994) demonstrates that the gorge had been incised at least to ~60m into the tuff at the *southern* margin by the Tahoe [79-56ka in Pinter and Keller (1995); see Table 3.1], but that subsequent incision of a further ~45m has occurred.

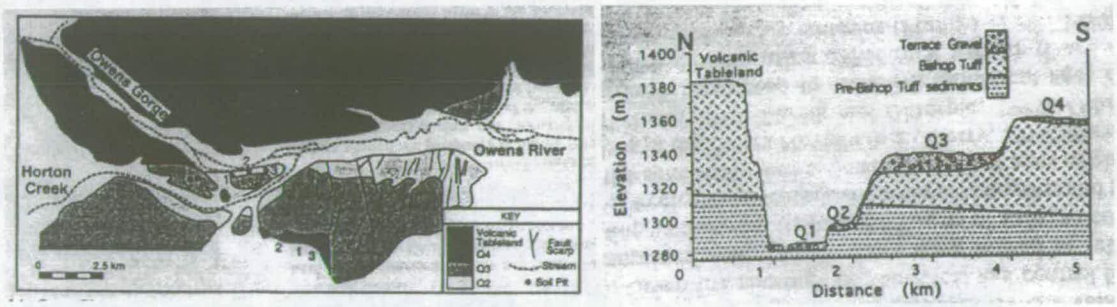

Figure 7.10: *a. Map and b. cross-section of terraces at the southern margin of the Tableland, from Pinter et al. (1994).*
Q4 correlated with 'pre-Tahoe'; Q3 correlated with Tahoe; Q2 correlated with Tioga. Q1 present river banks.
Gradual northward incision into the tuff, creating a steep escarpment at the southern margin of the Tableland. The highest preserved terrace, Q4 ['pre-Tahoe'] is below the surface of the Tableland, implying that the stream lay below the tuff by this time. Q3 [Tahoe] deposits are the most widespread, and also found within the gorge, as remnants of an ancestral gorge floor.

Together, the terraces imply that

- if incision was headwards [Mayo; Putnam], it began at the southern margin before or during the pre-Tahoe glaciation. The lower terrace levels reflect periodic incisions in at least the glacial periods. Connection to the Long Valley lake is not constrained by these terraces, although the Tahoe stage has left the most widespread deposits.
- if incision was by overspilling [Bailey et al.], the Long Valley lake must have been connected to the Owens River before or during the pre-Tahoe glaciation. However, it

probably did not incise through the entire tuff sheet in one event. Unless aggradation of tens of metres occurred periodically through the Pleistocene, the terrace levels imply that the river incised in a series of events, linked to increased runoff during glacial periods.

Thus the terrace data are consistent with Bailey et al.'s 1976 model, but require that a gorge created by headward incision began to form earlier than suggested by Putnam (1960). Bailey et al. proposed that the incision was only initiated by the overflow, and the gorge level probably stabilised when the harder tuff was reached, consistent with the periodic lowering implied by the terrace levels. Incision of the Owens River would prevent Sierran streams supplying the surveyed Tableland streams, which all lie to the east of the Owens Gorge [Fig. 3.4b]. If Long Valley lake rose to a point where it overflowed over the Tableland (Bailey et al., 1976), then a gorge would have been cut by 630ka, and been at least ~30m deep before the pre-Tahoe glaciation. Thus the surveyed streams must have been supplied from only Tableland surface runoff for virtually their entire evolution. If there was any connection to the west, this model requires *very* early development of the northern and SW stream precursors. However, if the Owens Gorge was formed by headward incision of the Owens River, then supply from the west may have continued for much longer, possibly through much of the occupation of the Tableland streams, which were probably abandoned after the Tahoe glaciation [section 7.2.2].

Overspilling of the lake (Bailey et al., 1976) would probably cause widespread erosion on the northern part of the Tableland, before the overflow incised a channel down which it funnelled the later, largest part of its discharge. Hence the northern Tableland should provide evidence to allow better differentiation of the likely direction of the Owens River incision through the tuff sheet. The diffuse non-tuff deposits to the NNE of the northern stream network [section 5.1.4] may have been deposited by an early more sheet-like system which drained into this area from the north, possibly reworking the non-tuff material from other parts of the Tableland. This could be related to the southern fringe of an overflow from the Long Valley lake. Alternatively, the material may simply be the remnants of an early drainage system sourced from the Benton-Casa Diablo Mountain high ground [see Figs. 3.5 and 3.4b], where granitic and some metamorphic rocks are exposed. Closer analysis of the non-tuff clasts and more detailed mapping of their distribution is required to distinguish the two possible causes.

7.5 Comparison with the 'classic' overlap stream geometry

The course of the main central overlap stream [Fig. 4.21] presents a sharp contrast with the 'classic' model of relay drainage [Fig. 2.14]. This stream geometry was initially described from a series of large overlap zones in the Gulf of Corinth, and the authors have described several examples of relays which do not conform to same pattern [e.g. Jackson et al. (1982); Leeder and Jackson (1993)]. However, the stream geometry in Fig. 2.14 is often assumed to be the natural route of a stream draining a synthetic overlap, and to predict the location of deposition in the hangingwall. The obvious failure of this model to explain the evolution of the Tableland overlap, and also of other synthetic overlaps [e.g. Armstrong (1997); Goldsworthy and Jackson (2000)], leads us to question the unhesitating application of the Gawthorpe et al./Jackson and Leeder model to all extensional environments, and to investigate the conditions under which different stream geometries may arise.

This section brings together the evidence for the main factors that have governed the evolution of the central overlap streams. This information is then used to constrain the conditions under which the 'classic' stream geometry may arise. Far from being a universal model, the 'classic' pattern is shown to be, like other potential stream geometries, the product of a specific set of external conditions, including the local tectonic system, and also the local lithology and climate. Thus the accurate prediction of stream geometries, even in a relatively simple fault overlap, relies on an understanding of the interplay between the many different external controls, which can produce a wide range of contrasting outcomes.

7.5.1 Controls on the development of the Tableland overlap geometry

The central overlap stream has not been deflected around the tips of the two main faults [1 and 2], but instead incises through both scarps. It has also not been defeated by the hard-linkage of these faults, and the dissection of the ramp. The factors that probably exerted the most control on these events are outlined below.

At Fault 1, incision was favoured by:

- *Segmentation of the fault.* The stream incised through a topographic low at a palaeo-segment boundary [Figs. 4.5 and 4.6]. This reflects incision occurring relatively early in the fault's growth, before segments were linked, or at least before the displacement profile adjusted to linkage.
- *Timing of stream occupation.* The stream was probably occupied before the growth of F1, but certainly very early in its development. The stream already drained this area, and was also able to take advantage of a relatively small fault displacement.
- *Distribution of deformation.* Slip at the southern tip of the fault is distributed onto a series of small faults, often nucleated along joints, rather than focused on a single large structure [Fig. 4.10]. The displacement and slip rate on the main fault was consequently reduced.
- *A shallow tip displacement gradient.* Although the displacement on the main fault is much higher to the north, there is a very slow decrease in displacement towards the

southern tip [Fig. 4.5]. This reduces the topographic imperative to deflect: there was probably little slope towards the tip.

- *Jointing of the tuff.* As well as allowing distribution of the extension, joints have been exploited by the downcutting stream [Fig. 4.20]. The relative ease of incision along joint planes allowed the stream to accommodate early fault motions without significant deflection. Once incised, the stream was very unlikely to have been deflected laterally by later fault activity.
- *Pre-existing slope.* Drainage towards the SE was favoured before the onset of faulting. The stream only gradually responded to the growing fault as it modified the existing slope.
- *Relatively high stream power.* Due to encountering the fault early, the stream was relatively powerful. Incision may have occurred during a glacial pluvial period, and hence been more rapid due to an increased discharge. Certainly the late Pleistocene was wetter than the Holocene (Smith et al., 1997), hence providing more stream power than would be available today.

As Fault 2 propagated towards the north, it first influenced the main stream, causing incision through the F1 basin deposits, and the virtual starvation of the more northerly streams. If Fault 2 had encountered these minor streams first, the central overlap may have been drained predominantly down the steepest slope, more like the classic geometry in [Fig. 2.14]. Thus the incision over 400m south of the Fault 2 tip was largely determined by the intersected stream's course *before* the propagation of Fault 2, and thus was favoured by:

- *The size and geometry of the Fault 1 basin deposits.* The fanning of the distributary channels from the input stream [Fig. 4.20] demonstrates that the basin must have been virtually filled, or the streams courses would lie closer to the fault, in the most rapidly subsiding part of the basin [e.g. axial stream in northern F1 basin]. In this case, the propagating Fault 2 would have intercepted a stream closer to its northern tip. The fan and stream geometries are a function of:
  - — *Propagation of Fault 2 relatively early in the development of Fault 1.* At the onset of F2 propagation, F1 was comparatively small [section 7.2.1.3], and hence its hangingwall basin could be relatively easily filled by the footwall supply [section 2.2.1; e.g. Schlische (1991); Davies et al. (2000)]. Later propagation might have encountered a starved basin, and thus driven incision nearer the F2 tip.
  - — *Relatively high supply from the footwall.* High supply was a function of relatively soft tuff, pervasive jointing and a glacially-enhanced discharge. Supply kept pace with accommodation generation, filling the F1 basin, and allowing stream migration and probably intermittent overspill [sections 7.2.1.3; 7.2.1.4 and Fig. 7.6].
  - — *The location of the sediment supply relative to D_{max} on the contemporary Fault 1.* The short F1 and incision north of the fault tip brought supply from close to the D_{max}. Not all the distributary streams were forced to drain towards the north.
  - — *The pre-existing SE slope of the Tableland.* The relatively youthful F1 had a very local effect on topography. Overspilling of the basin and supply to the E/SE was favoured by the existing slope.
- *The separation of the two faults.* F2 propagated quite close to Fault 1, intersecting the main stream and the distal margin of even the young F1 basin [Fig. 4.47].

Base level fall at F2 caused incision of the intersected stream and starvation of the northern streams before the streams draining the steepest part of the ramp were intersected.

- *Jointing of the tuff.* This influenced the location and possibly the rate of Fault 2 propagation [section 4.1.2], the rate of sediment supply from the F1 footwall, and probably facilitated incision of the intersected stream.
- *High stream power of the intersected stream.* A weaker stream would have been deflected northwards by the propagation of F2 and not incised the scarp. In this case, incision may have occurred further north as the deflected stream combined with the discharge of the streams draining the northern overlap [e.g. Fig. 2.13; Jackson et al. (1996); Burbank et al. (1996b)].
- *Slip rate and propagation rate of Fault 2*: A faster uplift rate, or slower propagation might have defeated the stream and forced deflection.

Preferential incision of the northern streams into the overlap, and deflection around the F2 tip, which would have given a stream geometry closer to the classic pattern, did not occur in this case because:

- *Incision of the southern [main] stream starved the northern streams.* Propagation of F2 caused incision of the main stream before intersecting the northern streams. By the time F2 tip reached the minor streams, they were unable to respond to any base level drops.
- *Displacement at the F2 tip was too low.* Displacement on F2 totals less than 2m at the minor stream channel [Fig. 4.16]. This is unlikely to have driven headward incision into the ramp, or to have forced deflection around the fault tip in the classic shape.
- *Displacement was distributed onto 2 strands.* F2 splits into two small strands, possibly due to interaction with joints and welded tuff at the fumaroles. This further reduces the driving force for stream incision to monopolise the F1 supply, and deflection around the F2 tip.
- *The drainage route was already fixed between fumarolic highs.* The downstream course may have been fixed by the hard fumarole highs [Fig. 4.40a] before the propagation of the Fault 2 tip, preventing lateral deflection of the streams around the F2 tip.

Truncation of the sediment supply following hard-linkage of the faults has been suggested by some authors [e.g. Gawthorpe and Hurst (1993); Gawthorpe et al. (1994)?]. This does not occur in the case of the Tableland overlap as:

- *The main stream was relatively powerful.* The stream was able to keep pace with the growth of the linking fault. Repeated steepening of the stream gradient by motion on F2, the relatively soft tuff and the relatively large upstream catchment provided sufficient stream power.
- *The main stream course was already fixed by incision in response to F2 growth.* Once incised, the stream was very unlikely to be deflected or defeated.
- *The linking fault had relatively low displacement.* Although braiding occurs at the fault scarp, there is no significant deflection of the stream course to imply the influence of a large scarp [Fig. 4.21].

- *Breaching of the relay occurred too late.* The linking fault profile indicates that the fault nucleated at the two ends of the ramp, which linked relatively late in the development of the ramp [Fig. 4.18; section 7.2.1.1]. The lack of stream deflection may imply that linkage had not occurred, or displacement at the fault centre was very small when the main stream initially incised into the ramp.

7.5.2 Controls on the development of the 'classic' overlap geometry

The 'classic' model [Fig. 2.14] is relatively simplistic. Although it describes well the geometry of many streams draining fault steps in the Gulf of Corinth, Gulf of Suez and the Basin and Range [e.g. Leeder and Jackson (1993); Gawthorpe and Hurst (1993); Jackson and Leeder (1994); Gawthorpe et al. (1994), it does not adequately predict the influence of other factors such as lithological heterogeneity, stream power and variation in fault uplift and propagation rates. By comparison with the stream pattern in this overlap on the Tableland, it is possible to assess the factors which favour the development of the 'classic' geometry. The expected stream geometry may be favoured by:

- rivers with relatively low stream power [low precipitation, shallow slopes, hard rocks, small catchments..]
- hard and relatively homogeneous rocks, which prevent rapid incision, and hence favour stream deflection.
- relatively synchronous fault growth, so that the stream cannot fix its course in respect to one fault, but is simultaneously influenced by the displacement profiles of *both* faults. OR propagation of the second [front] fault after the first fault basin has become relatively starved.
- a high displacement rate relative to propagation rate.
- a steep tip gradient.
- stream development relatively late in the evolution of at least the first [back] fault. Thus the stream encounters a higher, more continuous scarp, with a higher slip rate, favouring deflection towards the tip rather than incision. If segments are already linked, there are no local displacement lows which could be exploited.
- little jointing, or existing fracturing, which may distribute deformation, and increase the power of the stream relative to the faults.
- no, or only a shallow, pre-existing slope. The fault topography therefore dominates the drainage orientation almost immediately.
- little pre-existing topography. The stream patterns are not influenced by local non-fault topographic highs or lows.

The 'classic' model relies on displacement accumulation occurring fast enough on both faults to drive lateral deflection of a transverse stream, forcing it to bend around the propagating fault tips. In any case where the displacement rate is not sufficient to drive lateral deflection, the geometry of the classic stream will not be observed. Similarly, if a stream is able to take advantage of local displacement lows within the fault scarp, it is unlikely to deflect laterally towards the tip. The effect of fault motion on a transverse stream is a result of the balance of the fault displacement rate and the erosive power of the stream. This is dictated by the strength and homogeneity of the footwall lithology,

the power of the stream, and the rate and pattern of growth of the faults themselves. Examples of streams which do not follow the classic stream pattern around both fault tips due to lithological control have been described from Central Greece [e.g. Jackson et al. (1982); Leeder and Jackson (1993); Goldsworthy and Jackson (2000)], the Gulf of Suez (Armstrong, 1997) and also the Basin and Range [e.g. Leeder and Jackson (1993)]. The stream pattern in this Tableland relay is the result of lithological influences and is possibly aided by increased stream power from higher discharges during glacials. However, it also reflects the pattern of fault growth [section 7.5.1].

Hence, far from being a 'catch-all' model, which explains the evolution of the majority of streams draining synthetic fault overlaps, the model shown in Fig. 2.14 relies on a very specific set of conditions, by which a stream draining the footwall of the first fault is continually deflected around a propagating tip, follows the steepest slope of the ramp, and is again repeatedly deflected by the second fault. While the stream geometry observed in the central overlap of the Tableland array is dependent on the specific properties of the stream, the rock heterogeneity, the pattern of fault growth, and the pre-existing topography, it hints that the 'classic' stream pattern, though widely expected, may not be any more likely than any other stream pattern in a developing synthetic overlap.

The stream pattern is the cumulative product of a continually-changing fault pattern, and hence records a series of events dictated by the contemporary balance between the power of the stream and of the faults. Any number of small events may prevent the stream following what later becomes the steepest local slope, and hence the expected ['classic'] drainage route. In this sense, the current fault pattern, and gradient of the overlap, are of limited use to interpret the stream evolution. The interpretation or prediction of stream or depositional geometries in an extensional fault step instead requires an understanding of the factors which control the evolving stream/fault balance.

7.6 Overview

Analysis of aerial photographs and surveying of fault scarps provides a great deal of information about a fault pattern. In particular, it highlights the distribution of deformation onto different structures, the variation of displacement along strike, the scales and extent of segmentation, and interaction through profile asymmetry. In this case, it also highlights the potential for the nucleation or propagation of faults along pre-existing joints. Analysis of the profiles illustrates the scaling of faults, and hence indicates the mechanism of growth [e.g. Dawers et al. (1993); Dawers and Anders (1995)]. The patterns and hierarchy of segmentation can be used in some cases to model potential mechanisms of fault linkage [e.g. for the linking fault, Fig. 7.4]. Fault profiles also highlight interaction between faults, and can demonstrate overall patterns of displacement accommodation [e.g. Dawers and Anders (1995)].

Fault analysis also explains some features of the drainage pattern. The contrasting distribution of deformation between the northern tip of the array and the central faults explains the different courses of the large streams in each area. The smaller northern faults would be expected to cause less perturbation in the profiles and courses of nearby streams, as observed. However, the value of the stream analysis is in the provision of *additional* information about changes in the contemporary fault patterns, and particularly the relative timing of events, and the spatial extent over which they occurred.

Some features of the stream patterns and morphologies are easily predicted, but as such, they serve as confirmation that the streams are valuable indicators of the local tectonic motion. Where stream patterns do not show a close correlation with fault data, they may arise from streams too powerful to be controlled by the faults, or too weak to respond. The streams around the Tableland array record patterns of fault segmentation, interaction and linkage that fit well with the fault data, demonstrating an evolution intimately linked to that of the faults, as well as constraining the timing of some of the fault development.

Stream patterns provide information about the *contemporary* fault pattern. Although displacement-length profiles hint at previous fault geometries, from the patterns of segmentation and asymmetry [e.g. Dawers and Underhill (2000); Davies et al. (2000); McLeod et al. (2000)], much detail is lost as the profiles begin to equilibrate after linkage. In contrast, stream patterns may elucidate the size of the controlling faults, from the distance over which the river was influenced, and the size of depositional packages [e.g. the rounded clasts on the central overlap, Fig. 4.47]. Similarly, changes in the connection of different streams demonstrate the relative influences of neighbouring faults. Continued motion on Fault 2 is demonstrated by the increased gradient of the main stream through the central overlap, and the subsequent truncation of the supply from that stream to the east [section 7.2.1.4]. Large scale stream rearrangements point to major changes in the controlling fault geometries.

Some parts of the stream profiles and aspect ratio plots demonstrate a surprising sensitivity to relatively subtle fault motions. The pattern of incision in the northern tip canyon pinpoints the axis of the array [Fig. 5.4], while the effect of faults with only tens of centimetres of displacement can be picked out by steps in the profile, or small

changes in the cross-sectional morphology, due to the accelerating effect of the gradient increase on the stream velocity [e.g. Eqn. 2.3].

The stream-gradient index [SL] and long profile indicate the *present* gradient and erosive power of stream reaches. The aspect ratio [AR; section 3.3] gives an indication of the cumulative incision at a specific site. Hence the different parameters can be combined to show the extent of fault influences, even where a stream has had sufficient discharge or time to completely accommodate the tectonic perturbations [e.g. incised northern canyon: section 5.1.1.1; Fig. 7.3]. The overall correlation of the aspect ratio with slope demonstrates stream adjustment to perturbations by incision, aggradation, and width changes. It also indicates that local faulting has had the dominant influence on stream evolution [Fig. 7.1; Fig. 7.3].

The Tableland streams have responded relatively quickly to fault motion, and hence evidence of discrete stages in the development and interconnection of the streams is preserved. Different patterns of incision and deposition, changes in stream course and major reorganisations of stream networks have occurred in response to each specific fault geometry. Thus the stream analysis provides a series of snapshots of stages in the fault evolution. The exact timing and length of occupation of the streams remains uncertain [sections 7.2.2 and 7.4], but it is likely that all the recorded erosion, deposition and stream reorganisations occurred in only a few hundred thousand years, and potentially in barely more than 100ky (Pinter and Keller, 1995). Detailed pictures of fault reorganisation on this timescale are hard to obtain using alternative methods.

The stream patterns constrain the *relative* timing of stages in the fault evolution, which cannot be easily extracted from fault data alone. The central overlap streams constrain the relative timing of movement on faults in the overlap, and through correlation with the axial stream, relative to the interaction and linkage of faults further north [sections 7.2 and 7.3]. Changes in the ultimate destination of material from the footwall of Fault 1 demonstrate large scale changes in the topography of the region, and the increasing dominance of the local fault topography over the pre-existing regional slope [section 7.3]. The non-tuff material in the northern stream indicates a unique connection between this stream and a dissected channel to the SW. These streams point to the possibility of a very early establishment of streams on the Tableland, and allows their development to be placed more accurately into the framework of the regional drainage evolution [section 7.4].

Thus the stream analysis provides a better picture of the sequence, and also the magnitude, of events within the development of the fault array. However, the reliability of the streams as indicators of tectonic motion is dependent on their magnitude relative to the faults, the presence of sufficient time for the systems to respond between events, and also the availability of water. This last may be important in the evolution of the Tableland streams if they were abandoned for long periods of time [e.g. Pinter and Keller (1995)]. The streams were almost certainly also abandoned after the Tahoe glaciation [~49ka: Phillips et al. (1996); Table 3.1]. Stream responses lag the triggering event, and may also be complicated by the effects of lithological variation. However, the Tableland consists of a single lithology, and heterogeneity within it is associated with joints and fumaroles in specific orientations, which can be clearly isolated from the data.

The combination of stream and fault data with cosmogenic exposure dating adds

another dimension to the work, as it provides constraints on the *absolute* timing and rates of fluvial responses. Exposure ages constrain the timing and extent of occupation of the streams, the rates of knickpoint propagation and also tectonic slip and propagation rates [section 7.2.2]. Evidence of complex exposure [VT8] demonstrates the changing patterns of deposition and also provides coarse indications of the duration of depositional events [section 7.2.2]. Erosion rate estimates constrain long-term downwearing rates in different reaches, and also maximum rates of subaerial erosion [section 7.2.2.5]. The small study carried out here has limitations, due primarily to the difficulty of assessing inheritance in the older samples, and to the small number of samples [section 7.2.2.1]. However, it provides valuable constraints on the rates of stream responses to external controls, and the processes by which those responses have occurred, which can be directly compared with the evolution of other areas. Analysis of the fault scarp samples [section 6.1.1] would have been useful in constraining slip rates, and possibly the recurrence interval of tectonic events [e.g. Fig. 2.34]. However, by dating the streams within the overlap, where the 3D stream analysis provides a detailed picture of the relative timing of events, more information has been provided about the rates of the landscape evolution, and the sensitivity of the streams to changes in the governing fault pattern.

Chapter 8

Numerical modelling approach: CASCADE

The fieldwork outlined in Chapters 4 to 7 has demonstrated that stream evolution on the Volcanic Tableland is intimately linked to that of the faults. The streams are incredibly sensitive to the changes in fault geometry, and thus give a detailed picture of the mechanisms and patterns of fault growth. Numerical modelling provides a powerful alternative mechanism to investigate stream/fault evolution, as features of both the fault and surface process systems can be changed at will, allowing the varying landscape response to be assessed [section 2.4]. It is also useful as a mechanism to quantify some aspects of the temporal evolution of a system, where often only relative timings can be established from field examples.

However, no-one has yet introduced realistic dynamic, interacting faults into a surface process model - 'interacting' in this chapter being used to mean stress feedback between growing faults, as discussed in section 2.1.2. Stress perturbations due to slip on one fault affect the stress concentrations, and hence slip rates, on neighbouring faults, even where there is no physical linkage between them. *Zscape* has incorporated the most sophisticated fault model to date [e.g. Ellis et al. (1999); section 2.4], but these faults have been simple elastic fractures, and importantly do not interact. In contrast, this study provides an opportunity to assess the impact of interaction on the development of surface processes in the surrounding landscape.

This chapter outlines some of the findings of a preliminary study using the surface process model *CASCADE* [section 2.4]. It shows some early results from the incorporation of a dynamic, interacting fault population [from Patience Cowie's model; e.g. Cowie et al. (1993); Cowie (1998); Gupta et al. (1998); Cowie et al. (2000)]. This fault evolution model specifically calculates the positive feedback between rupturing elements and hence is a much closer analogue to natural systems than the simpler faults modelled in other surface process models. The comparison with results obtained by other workers clearly demonstrates the impact of fault interaction and linkage on evolving stream networks, and hence the importance of including feedback between faults if natural systems are to be accurately modelled.

The Tableland fieldwork demonstrates that the present stream pattern is a direct product of:

- fault growth by segment linkage:
  - — streams exploit local displacement lows, particularly at segment boundaries
  - — major changes in stream patterns occur as segments link
  - — pronounced changes in stream organisation mark large increases in displacement rates or total slip
- interaction between faults and the linkage of the array
- consequent changes in the pattern of fault activity through time

However, the exact response of any stream is a balance between a its ability to incise, and the faults' abilities to deflect it. Streams may incise, be deflected or defeated by growing faults, depending on the local fault pattern, and the eroding landscape. Thus stream evolution is not only a function of the fault displacement, slip rate, tip propagation rate and interaction with neighbouring structures, it is also a function of

- the stream power - discharge, slope
- the resistance of the eroding rock
- sediment supply

The Tableland faults are small [whole array $\leq$7km long], and hence represent an early stage in fault development [relative to typical Basin and Range faults with $\geq$25km long segments]. However, many of the main stream courses are already deeply incised, and were established very early in the development of the existing fault array. This implies that they will probably remain in their current channels into the future, and hence that the *early* fault development and fault/stream interaction controls the mature stream patterns. Thus at least some of the stream patterns seen around major fault arrays may have been determined very early in the evolution of the fault population, and may be only relatively slightly modified by the later fault growth.

The aim of this chapter is to investigate some of these conclusions of the field study, by incorporating dynamic faults within the surface process model CASCADE. In particular, I demonstrate how changing aspects of the fault growth patterns, and also of the eroding landscape, affects the resultant evolution of the surrounding streams.

The main advantage of CASCADE over other surface process models is its ability to model any regular or irregular arrangement of elements or 'nodes' (Braun and Sambridge, 1997). This unique triangulation method allows CASCADE to deal with complex uplift functions, with a high degree of variability in all dimensions. It also avoids biasing the orientations of sediment transport pathways, which in regular grids must follow one of eight directions between regularly positioned 'nodes' [Fig. 2.30]. Fluvial transport follows the method of Beaumont et al. (1992), where deposition or erosion occurs at each node according to the local transport capacity [2.4.1]. Hillslope processes are modelled as simple diffusion. The runs discussed here allow both hillslope and fluvial processes to occur in each node, but CASCADE does have the scope to define a threshold, such that only certain nodes contain rivers [e.g. Willgoose et al. (1991)]. A stochastic landsliding algorithm (Champel et al., 2002), similar to that of Densmore et al. (1998) [section 2.4.1.1], was developed while my studies were in progress. The experiments described in this chapter include a prototype landsliding

algorithm, but problems were experienced with its function in this model environment, as discussed in the text which follows.

8.1 Incorporation of dynamic interacting faults

8.1.1 Fault model

The fault model developed by Patience Cowie and others [e.g. Cowie et al. (1993); Cowie (1998); Cowie et al. (2000)] consists of a diamond lattice of 180x180 elements, oriented at 45° to the boundaries of a square grid. Cyclic boundary conditions are applied at the x-edges to reduce edge effects. A constant velocity is applied to the y=180 boundary, while the y=0 boundary is kept fixed, thus producing a uniform shear of the thin elastic-brittle plate. The elements remain fixed in x and y through time, but change their elevations.

The elements have a randomly varying stress threshold. When the applied stress exceeds the threshold of any element, it ruptures, causing a 100% stress drop, and then instantaneously heals, so that it can rupture again. The rupture of any one element changes the stress pattern in the surrounding region, and can thus lead to the rupture of other neighbouring elements, if their critical stress is exceeded. Events gradually become clustered in time, and also in space. Thus positive stress feedback occurs between the elements, and strain is gradually localised onto a few large through-going structures through time [Cowie (1998); Gupta et al. (1998); Cowie et al. (2000) and Fig. 8.2. This localisation is not due to any strain-weakening, but is purely the result of the preferential pattern of loading of elements due to the rupture of their neighbours [see section 2.1.3].

The model output is converted to a tilted fault block topography by applying a simple rigid body rotation, as shown in Fig. 8.1. In the work presented here, the elements have been scaled to represent 2km nodes, allowing the investigation of faults from 2-360km length. These faults create topography of up to ±180m as the faults grow [Fig. 8.2].

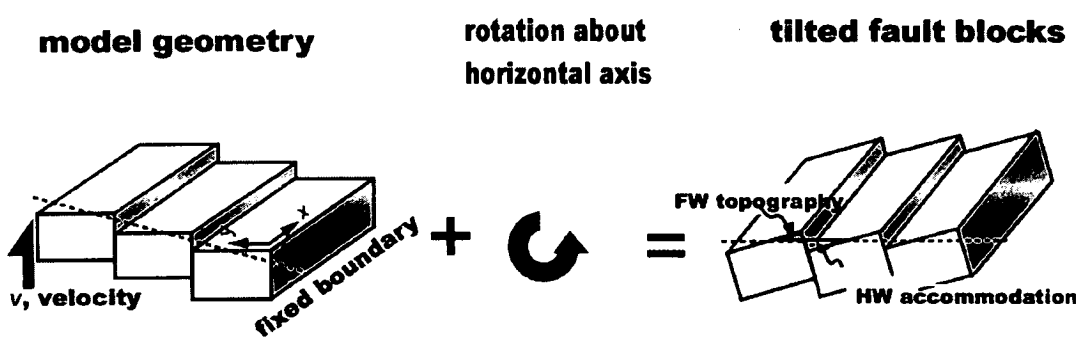

Figure 8.1: *Calculation of topography from the positive feedback model; from Cowie et al. (2000). Cartoon illustrates the antiplane geometry of the model, and the imposed constant strain rate boundary condition. Topography is created by a rigid body rotation of the model output, simulating natural tilting fault blocks.*

8.1.1.1 Incorporation into CASCADE

The fault topography generated by this fault model was interpolated to produce regular points separated by 2km in both x and y [from initial diamond lattice]. This is similar to the scale used by previous workers with CASCADE [e.g. van der Beek and Braun (1998, 1999); van der Beek et al. (2002)].

The fault topography was sampled at specific times, and the elevation change between steps added to the contemporary topography of CASCADE as a tectonic *dh* at each node. Thus, as in the previous examples, the landscape in CASCADE responds not to a continuously varying fault, but to abrupt changes in fault topography [see section 8.1.4 for further discussion]. The differences in elevation at each element in the fault model were calculated between each of the snapshots considered, and the relevant elevation change, *dh*, at each node added to the contemporary land surface. Thus the pre-existing variations in local topography, such as channels, were preserved.

The runs described in detail here [section 8.1.3] start with the topography in Fig. 8.2a, and update the fault topography in three steps, corresponding to the latter stages in Fig. 8.2. The changes in topography between these stages are large, although they are widely-spaced in time. This makes the changes in the landscape simpler to interpret, but may also swamp some of the transport systems. This is different from natural systems, where faults move in smaller, though more frequent, events. Some experiments have therefore been carried out to assess this issue, by comparing the results where topography is updated in a series of smaller, more closely-spaced events [see section 8.1.4].

8.1.2 Model parameters

8.1.2.1 Model scale and resolution

Runs were carried out on a square grid of 180x180nodes, representing 360x360km and hence a horizontal spatial resolution of 2km, for 1-2My. . Surface processes were updated every 100y [50y in section 8.1.3.3]; faulting events were widely and irregularly spaced, though some runs considered more frequent, smaller events [section 8.1.4].

8.1.2.2 Surface processes

Fluvial transport: Incision or deposition is calculated at each node according to the local transport capacity of the stream (Beaumont et al., 1992; Eqn. 2.16). Unless otherwise described, all runs discussed here use erosional length scales of 100km for bedrock, and 10km for alluvium; and the fluvial constant, κ_F=1.e^{-5} [see below]. The model space is closed: no sediment enters from outside the grid, and sediment carried to the boundaries is deposited there. Streams and hillslope processes both occur in each cell, which is reasonable given the resolution of the model (van der Beek and Braun, 1999).

Streams would not develop initially on an utterly flat plateau [before fault growth] and hence all runs described here were begun at a time when the fault model has begun to

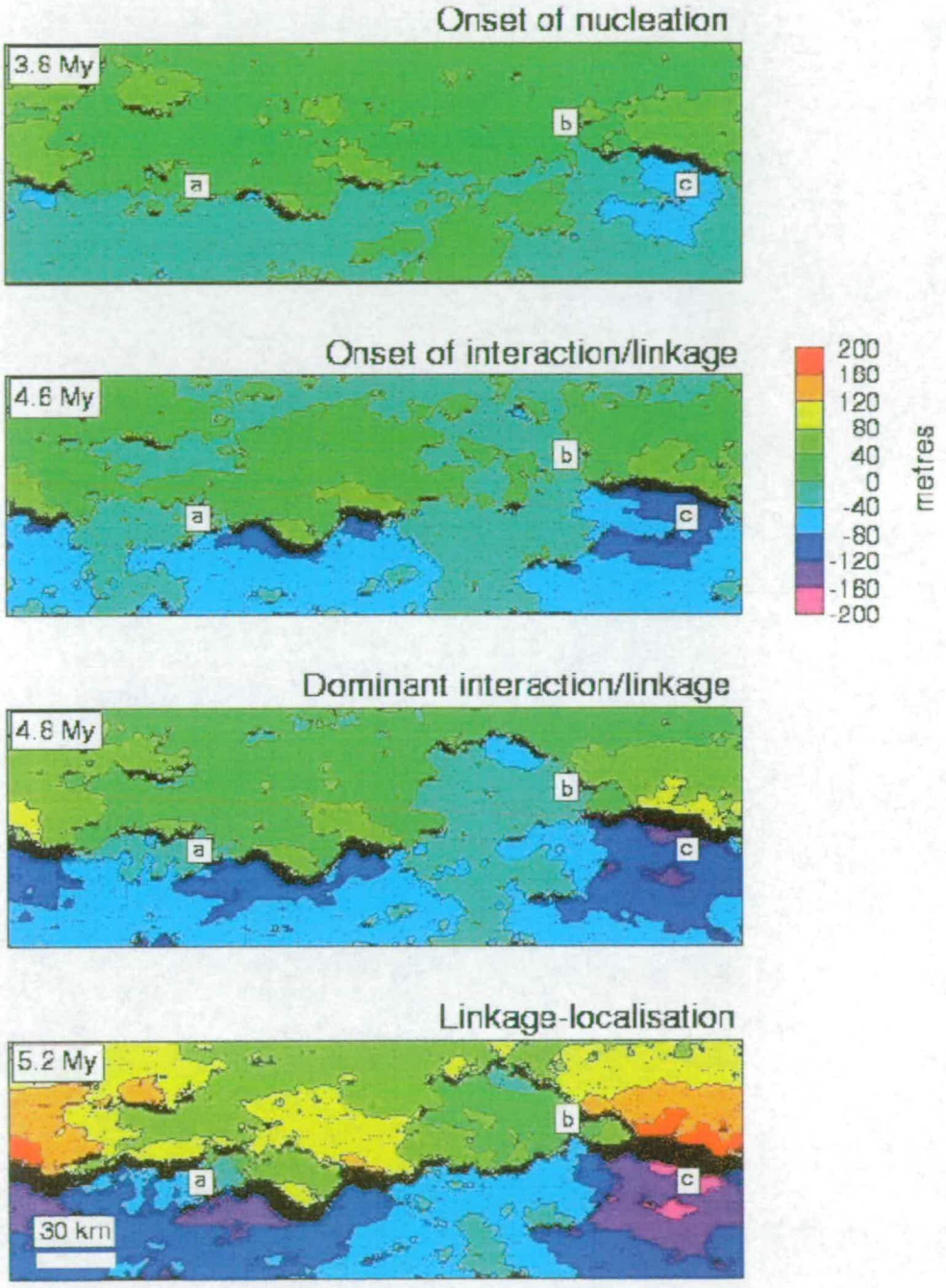

Figure 8.2: *Evolution of faulting and topography created by positive feedback fault model, from Cowie et al. (2000).*
The four panels represent the fault displacement and topography at 4 distinct stages in the evolution of the fault population: 3.8, 4.6, 4.8 and 5.2My through the simulation. Only the central part of the model space is shown, for $0 \leq x \leq 180$; $55 \leq y \leq 115$ *[compare with Fig. 8.3]. Displacement at each element is shown by a black square centred on the element, its size proportional to the magnitude of the displacement. Topography is calculated as described in Fig. 8.1. The white bar represents 30km.*

generate small topography, but with significant spatial variations [Fig. 8.2]. The effect of varying these starting conditions is discussed in section 8.1.4.

Landsliding: A stochastic landsliding algorithm, following Densmore et al. (1998), was being developed for CASCADE by Bénédicte Champel at Grenoble University while the studies described here were underway [e.g. Champel et al. (2002)]. The importance of including landsliding in these model runs is obvious [e.g. Densmore et al. (1998); Hovius (1998)], particularly as active tectonic landscapes are also periodically shaken by fault movements [e.g. Keefer (1984a,b); Pearce and Watson (1986); Stewart and Hancock (1988)]. However, for some reason, the prototype landslide algorithm used in this preliminary work erroneously did not erode sediment from the developing landscape at all. The real contribution of landslides to erosion and sediment transport from this type of environment is likely to be large, and so this is a significant concern [see section 8.1.5].

Hillslope processes: All other hillslope processes are governed by a simple diffusional equation. Various values of diffusional constant, κ_D, were tested, and compared with different values of the fluvial erosional constant, κ_F, to obtain the most realistic topography over this model scale [see also van der Beek and Braun (1998)]. For all the following runs described in this section, values of κ_D=1.e^{-6} and hence R=0.1 [see section 2.4.1] were used.

8.1.3 Results

A few of the early results are outlined below. Section 8.1.4 describes some of the implications of different features, such as the size and frequency of the faulting events, and the importance of early fault geometries. The value of this study in comparison with existing surface process model approaches to tectonic landscapes is discussed in section 8.2, along with some goals for future work using this model.

8.1.3.1 Experiment 1: Evolution of streams around a growing fault population

The first experiment considered here shows the evolution of streams within CASCADE around the evolving fault population. Model conditions for this run are:

- initial topography is 'stage 1' fault topography from Fig. 8.2a.
- three major faulting events:
  - — faults updated to stage 2 [Fig. 8.2b] at 199.9ky
  - — faults updated to stage 3 [Fig. 8.2c] at 499.9ky
  - — faults updated to stage 4 [Fig. 8.2d] at 699.9ky
- final fault topography allowed to erode for a further 300ky: total run time is 1My.

Figure 8.3 shows the surface topography initially [t=0], immediately after each faulting event [200ky, 500ky, 700ky], and at the end of the run [1My]. Superimposed on this are the major drainage divides in red - the large streams are clear from the topography, while the smaller streams are too complex to consider here. Letters on the displacement profiles and maps refer to streams [lower case] and faults/basins [capitals] mentioned in the text, as examples of key features.

At each stage, a huge number of faults are active within the fault population. Faults nucleate throughout the run, although there is a gradual localisation of the fault activity onto a few large faults in the centre of the population through time. Transparent overlays [**in folder at back**] show the broken elements at each stage of the population development [topog1 for t=0; topog2 for 200ky; topog3 for 500ky; topog4 for 700ky]. Most faults are oriented E-W, and the largest structures, whose profiles are shown in Fig. 8.3, all dip north.

The regional topography is dominated by the evolution of four large faults [A, B, C, Splay] which develop in the central part of the model space [see also Fig. 8.2]. Displacement profiles for these major faults are shown in Fig. 8.3 for the fault patterns at t=0, 200ky, 500ky and 700ky, which match the four stages shown in Fig. 8.2 [see also the transparent overlays]. The last fault event is at 699.9ky, and hence the final fault topography has the same fault pattern [D/L profile shown from 700ky], by then eroded for 300ky. The horizontal axis of each displacement profile is marked in km corresponding with the x-axis of the maps. These displacement profiles are extracted directly from the fault model, and hence are true displacements, not eroded topography, and therefore not the product of stream incision or erosion.

Blue arrows on the profiles mark the points at which streams incise the scarps. The streams have been classified from 'minor' - draining only the immediate footwall - to 'major' - having a significant catchment in the hinterland. The stream evolution can be followed by comparing the magnitude of the incising streams at each time snapshot in Fig. 8.3, as the faults grow. [**NB**: *no streams* are established at t=0, and hence the streams on the first D/L profile are superimposed from their *200ky* courses, to show how they have been influenced by the distribution of displacement in the early stages of fault growth.]

The arrows demonstrate the broad changes in the stream pattern during the model run. Some streams remain in their initial courses throughout, and often increase their catchment and discharge: evident from increasing arrow size at a given point through time. The points of incision of some streams migrate as the fault grows [lateral shift of arrow], while others are defeated entirely. Significant changes in the stream geometries result in major changes in drainage area, and the reorganisation of the catchments [bounded in red on the topography in Fig. 8.3, and also shown in Fig. 8.4].

The model results are very complex. However, the experiment clearly demonstrates that stream evolution is intimately linked to that of the faults: fault development is a first order control on stream evolution.

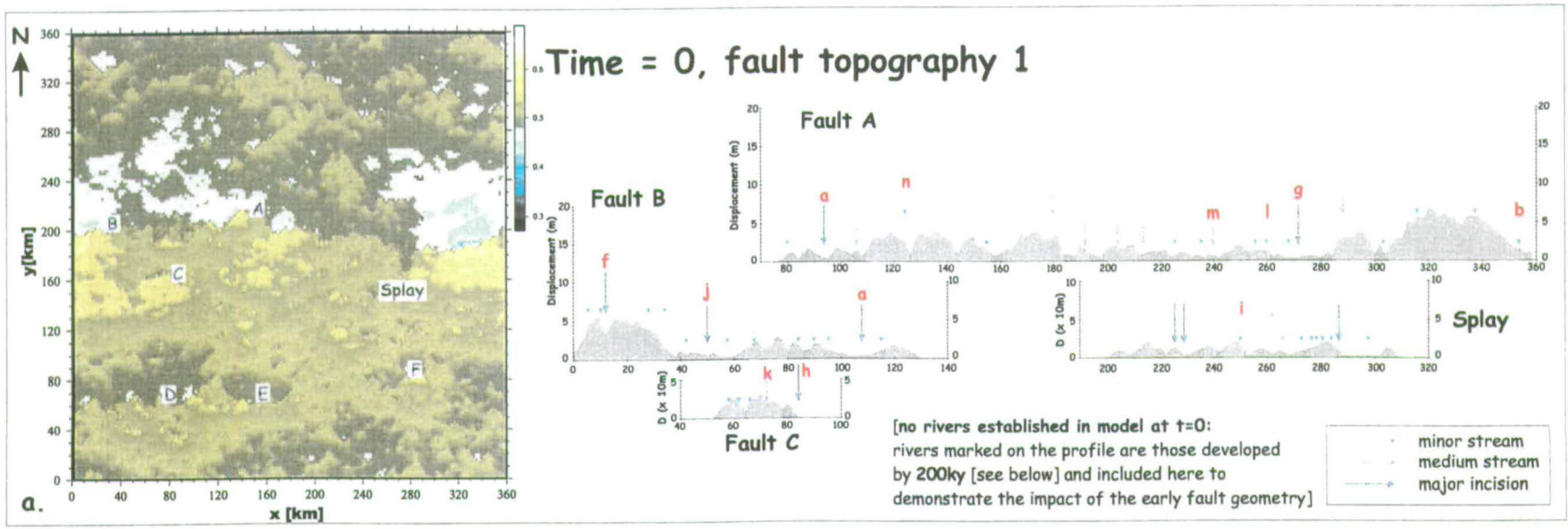

Figure 8.3: *a.-e: Evolution of stream patterns and topography around a developing fault population [see also next two pages]. Topography from model at t=0, 200ky, 500ky, 700ky and 1My, with major drainage divides in red. Fault displacement profiles for the main four faults at each stage [compare with Figs. 8.2 and 8.6]. Shaded area in each plot is increase in displacement since the last stage [white]. Faulting occurs at 199.9ky, 499.9ky, 699.9ky. Final topography [e] eroded from 700ky fault pattern - no more faulting has occurred. Transparent overlays [**back envelope**] show the broken elements in each fault event [topog1 for t=0; topog2 for 200ky; topog3 for 500ky; topog4 for 700ky].*
Arrows mark the location of stream incisions through each of the four main central faults, A, B, C and Splay. Larger, darker arrows mark larger streams. Streams typically incise through local displacement lows, though some stream courses are maintained from earlier incisions. No streams were established at t=0 [a], and hence there are no drainage divides on the topography. 200ky streams are superimposed on the initial fault profile to demonstrate the correlation of the 200ky stream with the initial displacement pattern.
Letters highlight the streams [lower case] and faults/basins [capitals] referred to in the text.
Catchments and main stream patterns are highlighted in Fig. 8.6a.

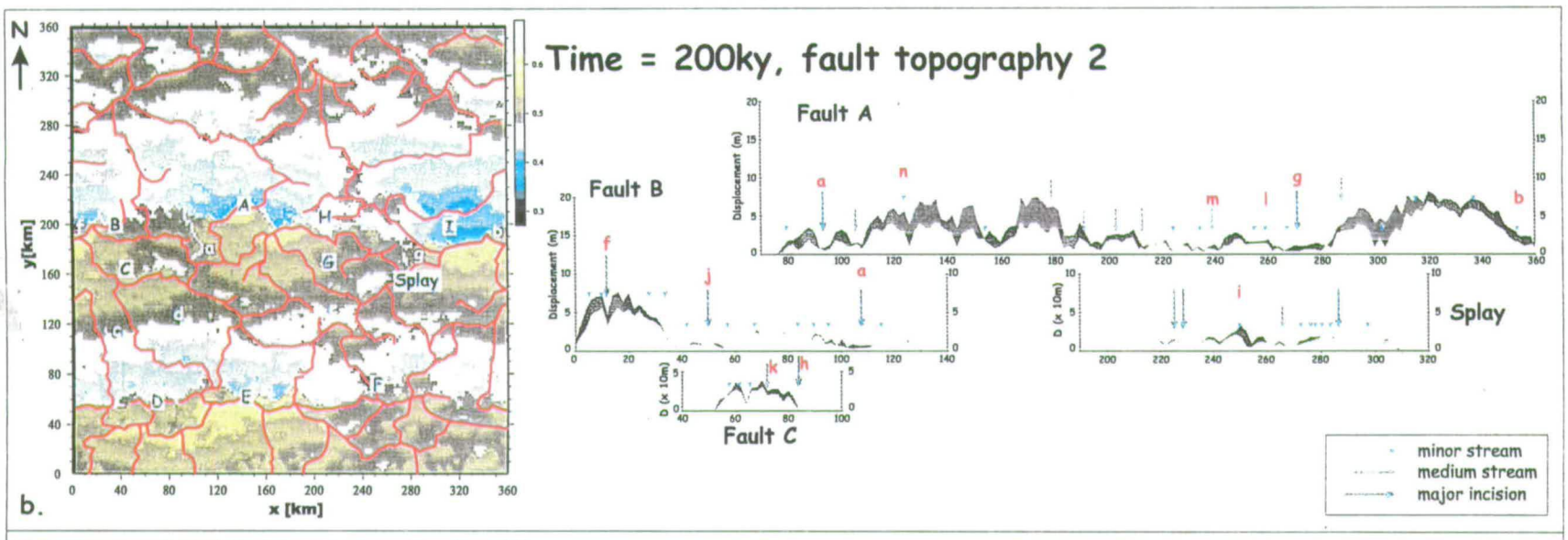
Time = 200ky, fault topography 2
Fault A
Fault B
Fault C
Splay
Displacement (m)
D (x 10m)
x [km]
y[km]
N
b.
minor stream
medium stream
major incision

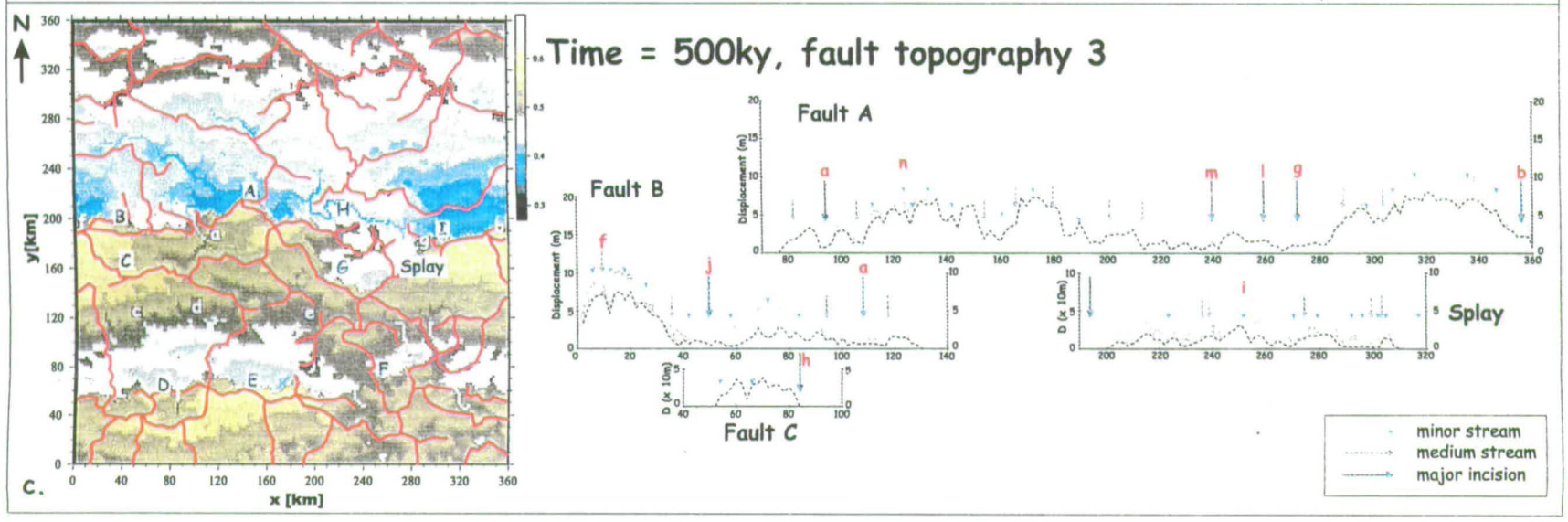
Time = 500ky, fault topography 3
Fault A
Fault B
Fault C
Splay
Displacement (m)
D (x 10m)
x [km]
y[km]
N
c.
minor stream
medium stream
major incision

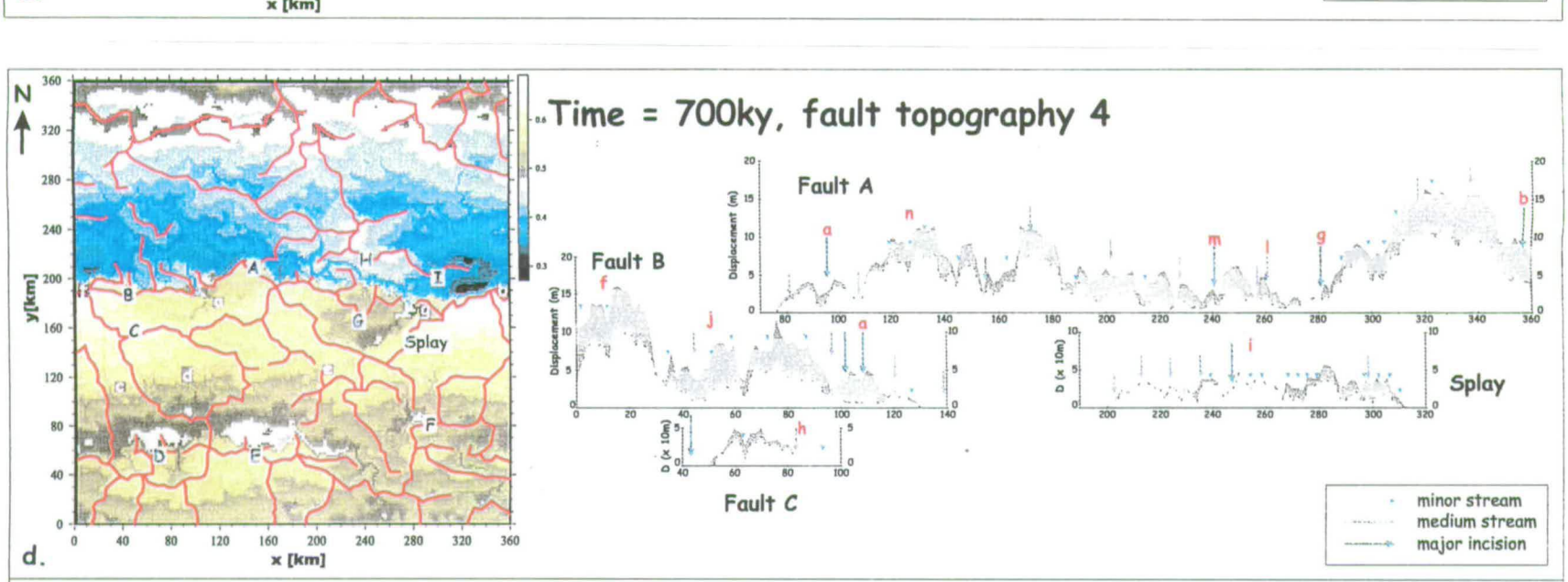
Time = 700ky, fault topography 4
Fault A
Fault B
Fault C
Splay
Displacement (m)
D (x 10m)
x [km]
y[km]
N
d.
minor stream
medium stream
major incision

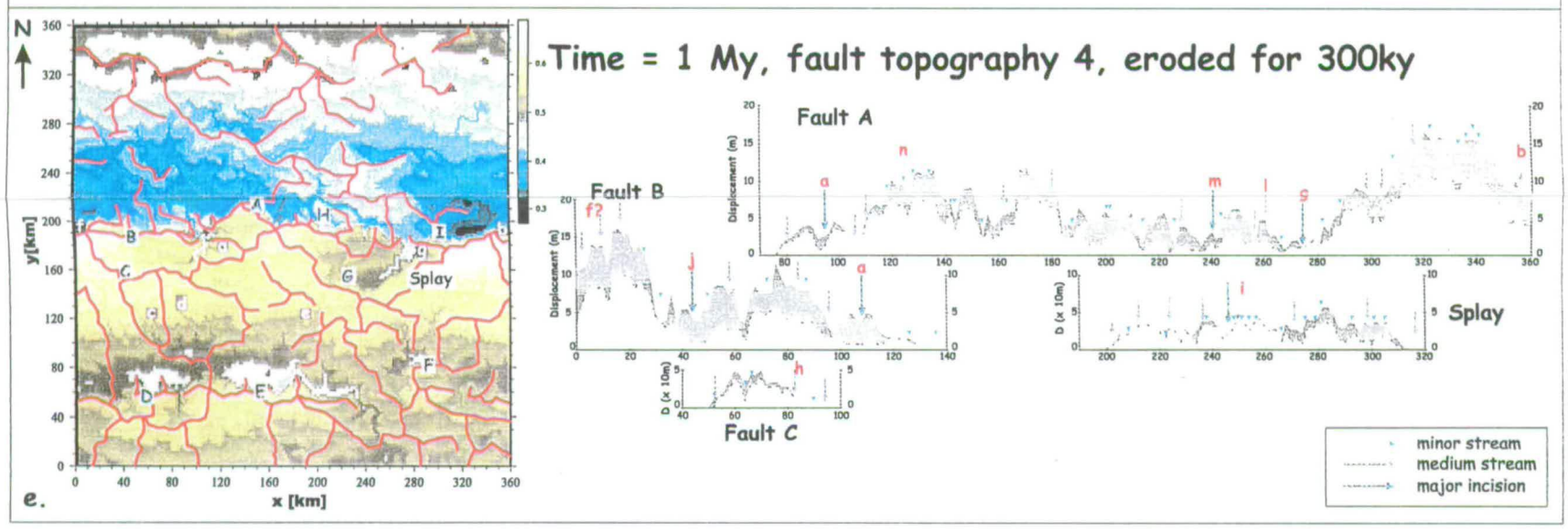
Time = 1 My, fault topography 4, eroded for 300ky
Fault A
Fault B
Fault C
Splay
Displacement (m)
D (x 10m)
x [km]
y[km]
N
e.
minor stream
medium stream
major incision

- Streams drain into the basins created in the subsiding hangingwalls of active faults. Most streams flow predominantly transverse to the faults [i.e. N⇌S], either draining directly across/through/round the scarp [e.g. **a**, **b**] or directed back down the footwall into a different hangingwall basin [e.g. **c**, **d**, **e**].
- Stream patterns and basin geometries are not static, but evolve in response to changes in the distribution of deformation through time.
- Streams generally incise through local displacement lows in the fault scarps [e.g. **a**, **f**, **g**] or are directed towards the fault tips [e.g. **b**, **h**], although some streams do cut through higher displacement regions [e.g. **n**].
- Stream courses are subsequently
  - — *maintained*, if the local displacement does not increase significantly [e.g. **a** and **g** in Fault A] or if the stream has sufficient discharge to incise through the scarp [e.g. **i** in Splay, **j** in Fault B].
  - — *deflected*, if the displacement at that point increases, but a favourable local low is present nearby [e.g. **b** in Fault A, deflected towards the fault tip].
  - — *defeated*, if the fault displacement increases dramatically [e.g. **f** in Fault B], or the stream is too weak to keep up [e.g. **k** in Fault C]. Some streams that show a sharp reduction in discharge at a given point are probably on the verge of being defeated or at least deflected [e.g. **l** in Fault A].
- The largest faults have the most wide-reaching effect on the stream and landscape development [e.g. compare central faults with smaller faults [**D**, **E** and **F**] to the south].
- Streams often incise through recesses or 'nicks' in the fault trace [e.g. **f**, **g**, **j**].
- Variations in the pattern of fault activity result in major reorganisations of stream patterns, and hence catchment size through time. The most striking example is at **G**:
  - — 200ky [b]: displacement highs widely spaced → internally drained basin with low topography
  - — 500ky [c]: major activity on Splay, little growth of Fault A → increased basin topography, streams directed to base of Splay fault; reduced incision through the Splay fault scarp
  - — 700ky [d]: major activity on Fault A, little motion on Splay, uplifts Splay basin → headward incision by **g** capturing the Splay fault catchment, draining it northwards into the Fault A basin.
- Strain localisation onto a few large faults results in coalescence to form a few large catchments [e.g. 700ky [d]] from an originally much larger number [e.g. t=0[a]. See also Fig. 8.6.] The increase in displacement drives an increase in stream power of successful streams, leading to headward erosion and capture of the drainage area of weaker neighbouring streams [e.g. **a**, **e**, **g**].
- However, some features of the stream pattern are inherited from the initial distribution of displacement in the early stages of fault growth. The courses of a number of major streams [e.g. **a**, **h**, **j**, **m**] are maintained throughout the evolution of the population. Some of the stream courses [e.g. **a**, **f** and **j** in Fault B, **n** in Fault A], would never be predicted from the final fault pattern, but have remained in courses initially developed in response to the early distribution of displacement on the faults [Fig. 8.3a].

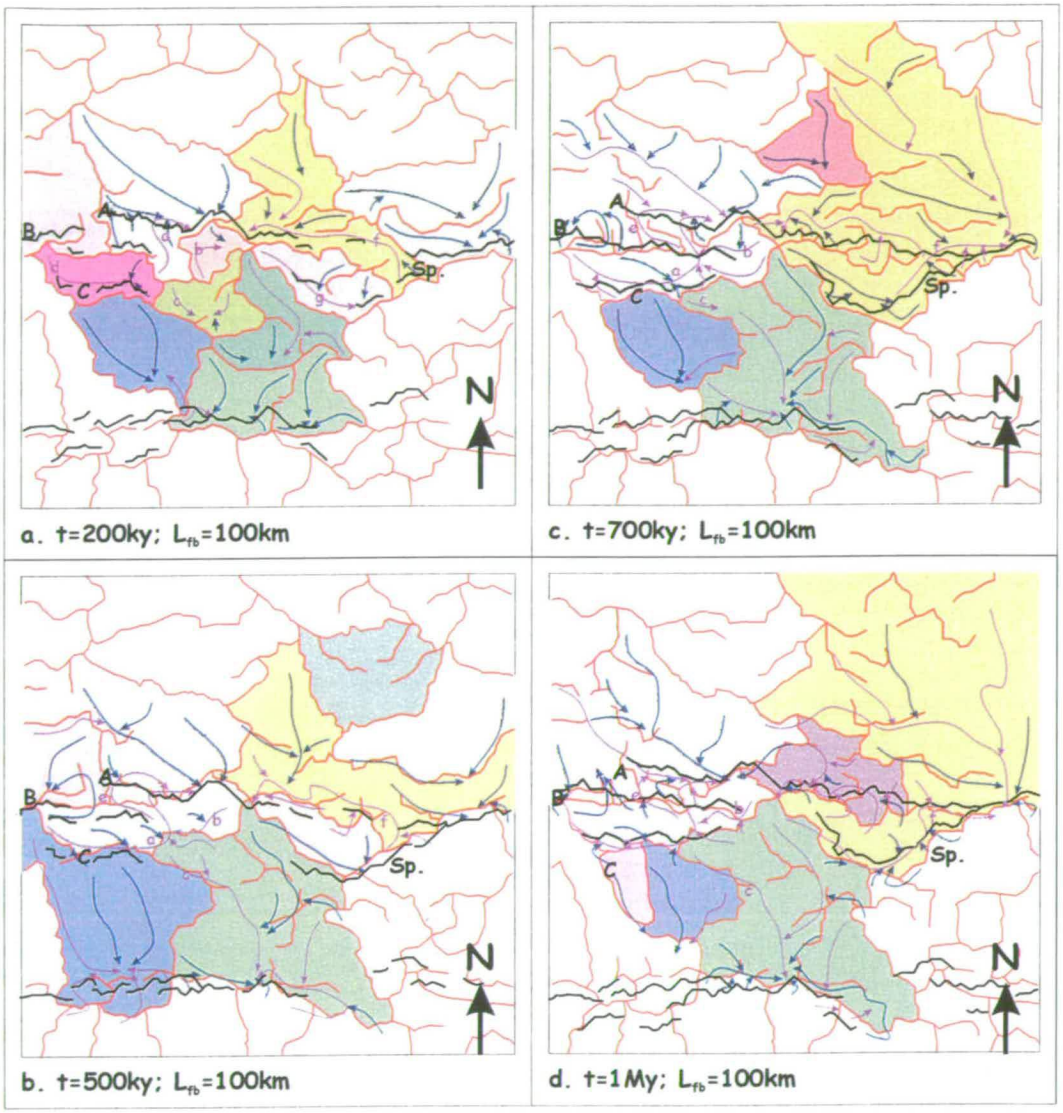

Figure 8.4: *Catchments and summarised streams at four stages through model run. Drainage basin pattern from model output [red lines] immediately after the faulting events, at a. 200ky, b. 500ky, c. 700ky and d. 1My. The central basins are coloured to show their evolution and coalescence through time. Thick black lines mark the major faults which dominate the landscape evolution towards the later part of the runs [displacement profiles shown in Fig. 8.3]; all dip north. The principal differences in the stream patterns of the two runs at each stage are summarised by the purple arrows. Other major streams are coloured navy. Small letters refer to the streams discussed in the text, capitals label the four principal faults [A,B,C and S].*

Thus the stream pattern closely reflects the pattern of displacement accommodation through time. Streams highlight the complexity in the distribution of displacement: displacement variations along fault strike, nicks in the fault trace and changes in the distribution and relative amounts of displacement on different faults through time. The stream response to deformation distributed onto a series of small faults [e.g. whole population at t=0; southern faults [**D**, **E**, **F**] at 700ky] is very different from the response to the localisation of high displacements onto a few major faults [e.g. the four central faults **A**, **B**, **C**, **Splay** by 700ky, Fig. 8.3d]. However, once established, some parts of the transport systems which form during the early stages of fault growth can be maintained throughout the subsequent fault development. Thus stream/fault interaction in the early stages of fault growth has a profound effect on the development of the later distribution routes.

The patterns of incision through the fault scarps provide a marked contrast with the results of experiments with simpler [i.e. non-interacting] faults. The drainage divide development is very complex and extremely variable along-strike, while non-interacting faults often promote drainage divide development at the fault crest. The faults used in other surface process models [e.g. Ellis et al. (1999)] have smoothly varying displacement along strike, and a straight fault trace. Thus they do not show the more natural variability along strike seen in the field [section 4.1] and which, as shown with this dynamic model, fosters a significant complexity in stream evolution. In contrast, smoothly-varying displacement profiles favour stream deflection or defeat, as only powerful rivers are able to maintain courses from the hinterland through the growing fault scarps.

Many of these observations from the modelling work agree with studies of natural systems, including the Volcanic Tableland, discussed in Chapters 4 to 7. The central overlap streams on the Tableland exploited displacement lows in all of the faults [Figs. 4.5, 4.16 and 4.18]. The current geometry of the largest stream draining that overlap is explicitly dependent on the presence of a contemporary displacement low at a segment boundary in Fault 1 [section 7.5.1], and the specific state of linkage of the Fault 1 segments during its early evolution. A stream developing later would have encountered a higher, more continuous scarp, and been more likely to have adopted the 'classic' stream geometry [Fig. 2.14]. Very similar conclusions can be drawn for the stream [**a**] draining across the Fault A/Fault B overlap in this model run [Fig. 8.3] - its development exploits the distribution of local displacement lows in the early faults.

Abandoned talus fans in the Fault 2 basin on the Tableland [Fig. 4.16] are testament to the less successful incisions of earlier weaker streams, supplied from significantly smaller catchments. Correlative examples of the defeat of scarp-draining streams are widespread in this model run [Fig. 8.3]. Many examples of the contrasting responses of streams with different discharges, demonstrated by the northern trunk and tributary streams on the Tableland [section 5.1] can be found: deep incision and minimal deflection [Fig. 5.3] occurs in streams with high discharge [e.g. **a**, **g** in Fig. 8.3]; the smaller streams are more prone to deflection [e.g. **b** in Fault A], or incise more slowly [section 5.1.3].

An axial system develops in the model run at **H** [Fig. 8.3], in response to the connection of small hangingwall basins between t=0 and 200ky. The system links to the deepest basin [**I**] by 500ky into the run. The gradual linkage of hangingwall basins is very

apparent in the Volcanic Tableland, although the final development of the through-going stream was delayed by the late connection of the upstream basins [F1 and F0, section 7.3].

8.1.3.2 Experiment 2: Lithological resistance

The Tableland study concluded that one of the factors which allowed the main central overlap stream to adopt its current geometry through the overlapping faults was the relative weakness of the rock [section 7.5.1]. In more resistant rock, the stream may not have been able to incise fast enough to keep pace with the growing Fault 1. Leeder et al. (1991); Leeder and Jackson (1993) and Goldsworthy and Jackson (2000) have described the different stream geometries and topography that can develop around normal faults in different strength rocks. The effect of lithological resistance can be investigated within CASCADE by varying the erosional length scale of the bedrock, L_{fb}, which affects the bedrock resistance to both fluvial and hillslope processes. Without introducing any lithological heterogeneity, Figs. 8.5 and 8.6 demonstrate the effect of increasing the bedrock resistance to erosion. The model conditions are identical to those in Experiment 1 [Fig. 8.3], but the bedrock resistance has been increased five-fold: L_{fb}=500km.

Figure 8.5 shows the model topography at the same four stages as in Fig. 8.3: immediately after the major faulting events at 200ky, 500ky and 700ky and at the end of the run, after 1My. The initial topography is identical to Fig. 8.3a.

Although subject to the same faulting pattern, the landscape evolves differently, and parts of the stream patterns are markedly different from those developed in the softer rock [Fig. 8.3]. Figure 8.6 compares the evolution of the model landscape between the two runs. The main central drainage basins are coloured to demonstrate their evolution and coalescence through time. Contemporary major faults [see also transparent overlay to Fig. 8.3] are marked in black: all dip north. The principal stream patterns between the two runs at each stage are summarised by the purple arrows in each case [other streams not marked for simplicity: compare with the fuller description of stream patterns in Fig. 8.4].

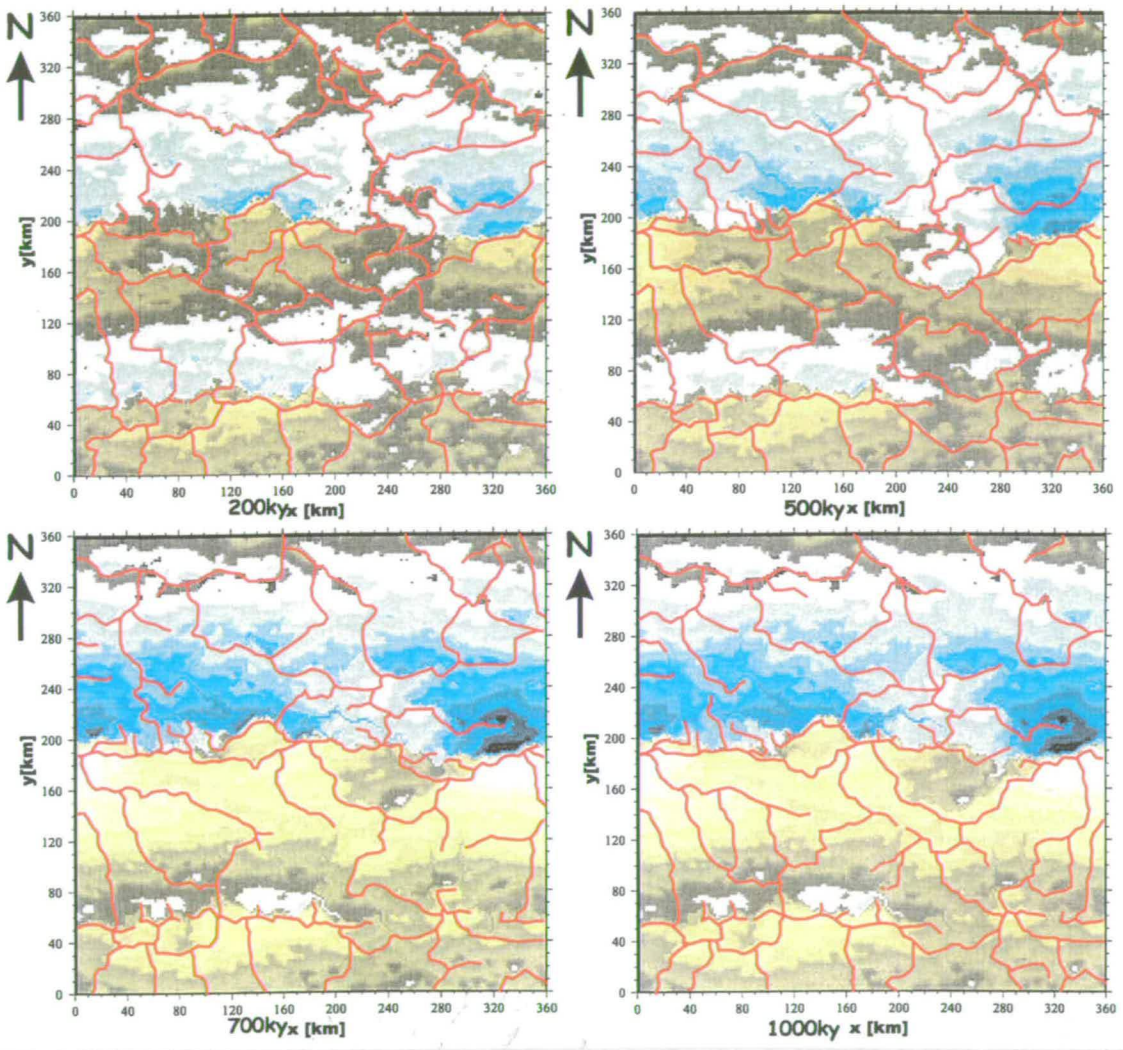

Figure 8.5: *Effect of increased lithological resistance: model topography with L_{fb}=500km. Model topography and superimposed drainage divides [red] at a. 200ky, b. 500ky, c. 700ky, d. 1My. The initial topography is identical to that in the previous example: Fig. 8.3a. Compare with the model topography with weaker rock [L_{fb}=100km] in Fig. 8.3. Catchments and the principal differences in stream patterns are summarised for the two runs in Fig. 8.6.*

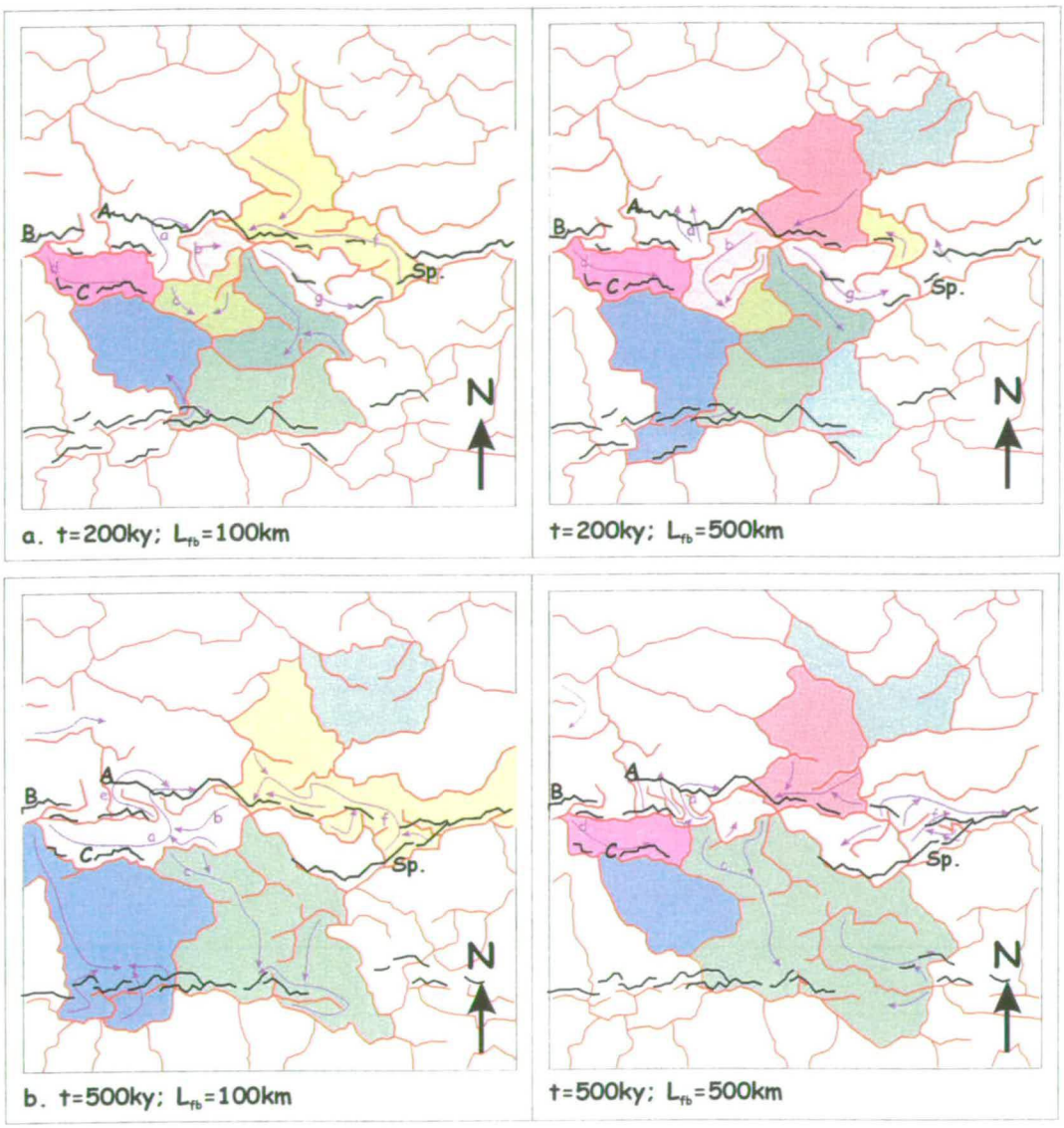
A
B
C
Sp.
N
a. t=200ky; L_{fb}=100km
t=200ky; L_{fb}=500km
b. t=500ky; L_{fb}=100km
t=500ky; L_{fb}=500km

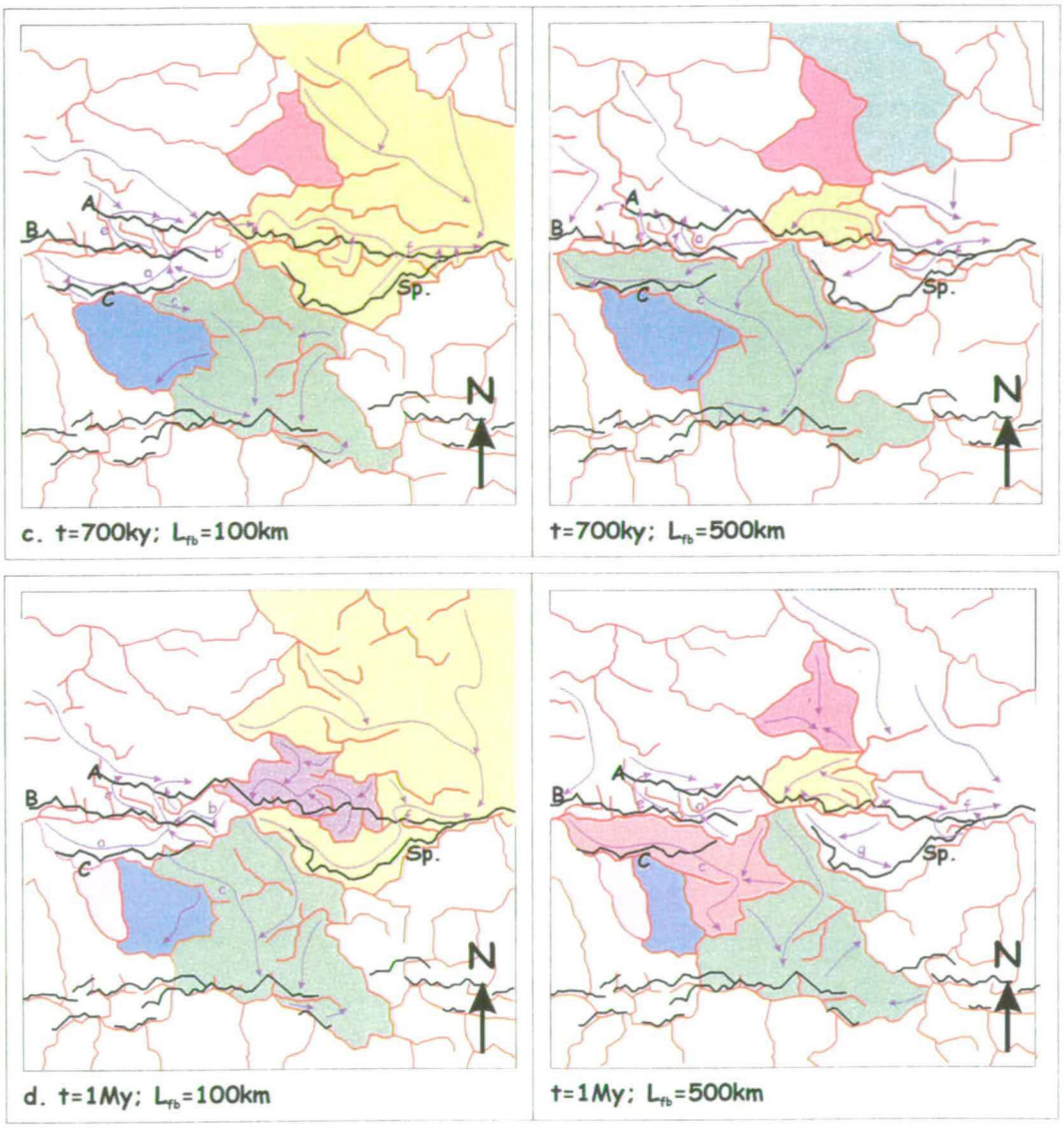

Figure 8.6: *Comparison of drainage basins and stream patterns developed around faults in soft [left panel, L_{fb}=100km] and hard rock [right panel, L_{fb}=500km].*
Drainage basin pattern from model output [red lines] at the four stages shown in Figs. 8.3 and 8.5: a. 200ky, b. 500ky, c. 700ky and d. 1My. The central basins are coloured to show their evolution and coalescence through time, and to highlight the differences between the two runs. Thick black lines mark the major faults which dominate the landscape evolution towards the later part of the runs [displacement profiles shown in Fig. 8.3]; all dip north. The principal differences in the stream patterns of the two runs at each stage are summarised by the purple arrows. Small letters refer to the streams discussed in the text, capitals label the four principal faults [A,B,C and Splay].

The differences in stream development and the resultant topography in the two runs are striking: the eroding rock exerts a major control on a stream's ability to respond to fault growth. Harder rock effectively tips the fault/stream balance in favour of the faults: its principal effect is to reduce, or slow, stream incision. Through reducing the rates of hillslope erosion, sediment loads are lower, and the steep fault topography is maintained for longer, also increasing the fault control on the streams. The reduced incision has a number of different implications for the evolution of the regional drainage:

- A greater proportion of the streams are deflected southwards away from the growing major faults [especially Fault A and B: compare with Fig. 8.3]: streams are more easily deflected from shallower channels. Few footwall streams can generate sufficient drainage area to maintain their courses as the faults grow. Catchments draining north into the hangingwall basins of Faults A and B are smaller throughout. Note particularly the size of the pale blue basin [east/central Fault A] and the slowed development of the northward supply from the Splay/Fault A overlap [purple/yellow/grey catchments].
- Reduced headward erosion and hence less stream capture, causing
  - — slower coalescence of catchments in response to the strain localisation: purple Splay basin is captured by stream **f** significantly later in hard rock; a single [pale blue] basin has formed by 500ky at the Fault A/Fault B overlap in soft rock [left], but 3 sub-basins remain in the hard rock case [right]; the northern brown catchment remains isolated at 1My in the hard rock case.
  - — generally smaller catchments for a given stream at any one time; at each stage, the available space is more compartmentalised: e.g. there are 5 coloured catchments at 700ky in the soft rock [left], but 9 in the hard rock case [right], with a slightly smaller area.
- Longer stream response time to external forcing: despite the change in fault activity between 500ky and 700ky [see D/L profiles in Fig. 8.3], the purple Splay basin remains isolated until almost 300ky later than in the soft rock case. The response of stream **g** to incise headward into the uplifted Splay fault catchment is limited by the high bedrock resistance.

The variation in lithological resistance emphasises the fine balance which dictates the stream response to faulting. Streams respond differently to changes in the pattern of fault activity in particular parts of the model. The largest changes are in the regions where major faults interact, demonstrating the importance of a few key points in controlling the stream evolution.

- where the Splay fault and Fault A overlap, the switch of activity from the Splay to Fault A [700ky in fault model] is recorded at different times:
  - — in soft rock [left], stream **f** rapidly cuts headward, capturing the Splay fault drainage area [purple]: the 700ky stream pattern is dominated by the evolution of Fault A
  - — in hard rock [right], slower headward incision of stream **f** means that the effect of Fault A is not recorded till later; stream **g** is still dominated by the Splay fault at 1My
- where Faults A, B and C overlap, the differences in stream evolution occur earlier:
  - — in soft rock [left], stream **a** rapidly cuts through the growing Fault A and captures **d**, draining the Fault C basin *north*wards, into the Fault A basin. Only the footwall

of Fault C drains southward: the drainage divide is established at the Fault C crest by 500ky [b]. A single large stream, **e**, drains round the tip of Fault A.

— in hard rock [right], the slower headward incision of stream **a** allows Fault A to dominate the evolution of the streams: very little of the footwall drains northwards, even after the capture of stream **b** [pale blue basin]. Most of the footwall is drained *south*wards, following the tilt of the Fault A footwall. Stream **c** captures **d** by 700ky [c], draining *BACKwards* through the Fault C scarp towards the south.

The two stream patterns demonstrate a very different sensitivity to the growing faults, due to the increased response time in the harder rock. Lithological resistance affects the ability of a stream to record changes in fault activity, as deflection or defeat is favoured if streams cannot grow fast enough to maintain their initial courses. Interpretation of the two patterns of evolution could give very different impressions of the fault development. In both cases, the different stream geometries caused by the change in the hardness of the rock are long-lived [compare 1My patterns]. Thus, as inferred from the comparison between the Tableland stream and the 'classic' relay geometry in section 7.5.1, changes in *any* of the factors which control stream evolution can result in dramatically different ultimate stream patterns.

8.1.3.3 Experiment 3: Event size

Faulting clearly dominates the stream evolution in both the experiments shown above. However, both experiments updated the fault topography in only three large events, widely-spaced in time. The dominant nature of the faults could be an artefact of the magnitude of the steps in this coarse tectonic model: streams are more likely to be defeated by faults which grow in large events, while they might keep pace with displacement accrued in smaller steps.

The potential impact of this effect can be investigated by comparing stream patterns which develop in response to tectonic topography generated in a number of smaller events, more closely approximating natural systems. Using a finer temporal resolution for the tectonic model also reflects more accurately the spatial variation in displacement accommodation through time: the three large events each sum the topographic effect of a series of smaller events on each fault, and hence conceal some of the spatial variability at intermediate stages.

Figure 8.7 shows an example of the differences in topography and stream patterns developed during two runs identical but for the size of the steps in which the tectonic topography was generated. The timings of the tectonic events in these runs were taken directly from events in the fault model, relative to the generation of the 'stage 1' topography used as the initial conditions as above. Model conditions were identical to those in experiments 1 and 2, but:

- timestep=50yr: erosional landscape recalculated every 50y [c.f.100y above] to allow accurate spacing of the tectonic events
- Lfb=100km, as in Experiment 1
- models run for 2My [c.f.1My above]
- more frequent, smaller tectonic events:

— a: *6 events*, irregularly spaced between 216.5 and 1365.6ky; [the topography at 3 of these events corresponds to the stages considered in Experiments 1 and 2]
— b: *48 events*, irregularly spaced between 216.5 and 1365.6ky [again, 3 stages are the key topographies considered in Experiments 1 and 2]

Figure 8.7 shows a snapshot of the model topography and catchment connectivity in each run, taken after 800ky: equivalent to the fault topography of stage 2 in the previous examples [Fig. 8.2b]. This was achieved in the left panel [Fig. 8.7a] in 4 large events; in 34 smaller events in the right panel [b]. As with Fig. 8.6, purple arrows summarise the largest differences in the stream patterns between the two cases.

Broadly the topography is the same in the two runs, but some major differences can be seen even at this early stage in the fault development. As in Fig. 8.6, the most pronounced difference is evident near the overlap between Faults A, B and C, centred at (100,180) [blue basins]. In the case of the large, infrequent events [Fig. 8.6a], the Fault C basin is drained by stream **c** towards the south, around the Fault C scarp. Where faulting occurred in smaller events, this basin is drained by stream **a**, *north*wards through Faults A and B, as is the rest of the Fault A footwall further east [pale blue basin]

This particular difference is almost identical to that which occurred when the streams encountered differing bedrock resistances. Hard bedrock and large fault events both favoured drainage of the Fault C basin to the south; soft rock and small fault steps both allow stream **a** to incise headward through Faults A and B to capture the drainage area of the Fault C hangingwall. In one case, Fault C acts as a drainage divide; in the other it is overwhelmed by the tilt of the larger faults to the north.

Similar examples of basin geometries that differ between the two runs are evident elsewhere in the grid, as shown by the different compartmentalisation of the southern drainage area, supplying the basins of faults D, E and F. Three basins occur in a. [dark blue, green, eastern uncoloured]; four basins with very different shapes have developed in b. [dark blue, green, uncoloured at both east and west].

Major differences in the stream patterns are maintained throughout the runs. Although the basins gradually coalesce, the drainage direction of the Fault C basin [S or N] is maintained throughout, with consequently considerably less incision through the Fault A/Fault B overlap in the case of the infrequent tectonic events [a]. This implies that

- stream response is different where tectonic topography is generated in small, frequent events rather than large, though less common, events.
- small changes in the elevation of key points affect the large scale stream patterns, as seen in section 8.1.3.2. The capture of the Fault C basin by stream **a** must have arisen following an intermediate faulting event which is not adequately represented by the summed growth of the coarser model, resulting in capture instead by the south-flowing stream **c**.
- some aspects of early stream patterns are maintained throughout the subsequent development of the landscape.

This experiment has important consequences for modelling landscape responses to tectonic growth. Many existing fault models are extremely coarse, updating the topography only infrequently, as in the initial examples. Natural landscapes are the result of a series of varying magnitude, but relatively frequent, events. The

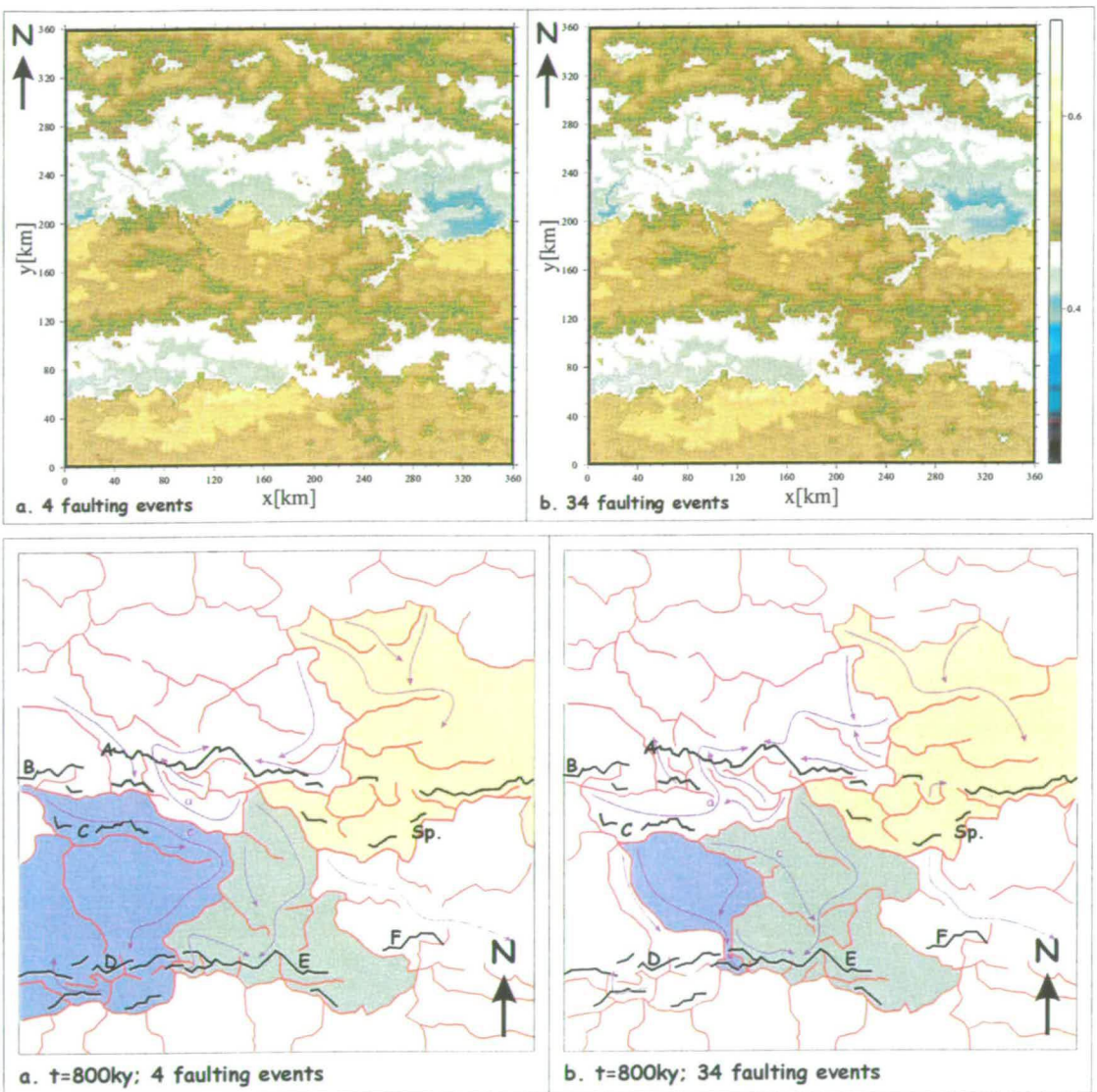

Figure 8.7: *Effect of tectonic event magnitude: model topography and stream development after 800ky, with fault topography created in a. 4 large events; b. 34 small events.*
Model topography and summarised drainage basin/stream pattern after 800ky, fault topography equivalent to 'stage 2' [200ky] in the previous model runs, created in a. 4 large events; b. 34 small events.
Red lines are the major drainage divides, thick black lines are the contemporary traces of the four faults which dominate the displacement accommodation in the later stages [A, B, C and Splay]. Central basins are coloured as in Fig. 8.6. The principal differences between the streams in the two runs are highlighted by the purple arrows. Capital letters refer to faults; lower case letters refer to streams mentioned in the text.

results of Experiment 3 imply that coarse tectonic models are unlikely to adequately reproduce natural landscapes, or accurately predict the factors that control natural stream responses to external forcing. Coarse models may overpredict tectonic control, favouring deflection and defeat over incision, as the large events can overwhelm streams. This result must therefore also be taken into account in further studies with this model.

8.1.4 Other considerations: Initial topography

CASCADE and the dynamic fault model have also been used to investigate the impact of the shape / variability of the initial topography which is being eroded. One of the major external factors which contributed to the development of the Tableland streams was the presence of a pre-existing regional slope towards the SE, which caused early streams to initiate draining from the footwalls to the hangingwalls of the developing faults [sections 7.2 and 7.4]. Had this slope been absent, or directed streams in a different direction prior to faulting, the present stream pattern, particularly through the central overlap, would probably not have developed.

1. ***Pre-existing slope***: A series of experiments were carried out where streams were allowed to erode a simple south→north slope for varying periods of time before the onset of faulting [i.e. before updating to the 'stage 1' fault topography [Fig. 8.2a] used as the initial conditions in the above runs].

   The pre-existing south→north slope favoured the subsequent development of streams flowing across the faults *from* the south [e.g. across the western overlap zone between Faults A and B, as **a** in Fig. 8.3], and retarded the development of streams which drained *towards* the south off the footwalls of the developing north-dipping faults [e.g. **c**, **d**, **e**]. In this case, faults must do more 'work' to overwhelm and redirect streams which have developed courses down the pre-existing slope. A clear correlation was seen between the amount of northward drainage and the length of time over which streams had drained the south→north slope before the onset of faulting. Where streams had 1My to incise courses prior to faulting, incision in the south-flowing streams was considerably reduced. However, in each case, the catchments developed very similar general patterns, demonstrating the dominance of the faulting, and its ability to eventually overprint the pre-existing stream patterns, as seen in the field.

2. ***Early fault growth***: The field observations and several of the examples discussed above have pointed to the importance of the early fault topography in determining some major aspects of the stream pattern, which may be maintained throughout the subsequent fault development. The 'stage 1' topography [Fig. 8.2a] was chosen as a starting point for the above experiments to ensure that there was sufficient topographic variation to allow stream patterns to develop [CASCADE cannot erode a completely flat topography]. However, 'stage 1' is the result of an earlier 63 small events in the tectonic model. Some of the impact of the initial conditions can therefore be investigated by allowing CASCADE to begin working on progressively earlier stages in the fault topography [e.g. event 53 topography, event 43 topography etc.].

   Initial results demonstrate significant differences between the stream patterns generated in the runs which start with different fault topographies. In some cases,

the differences were small enough that they were swamped by the development of the later fault topography. However, other examples again demonstrate the importance of a few key locations in determining the stream patterns which later dominate the evolving landscape.

Hence both these experiments point in the same direction, implying a significant level of control by the early topography on the subsequent development of the landscape, and the sediment transport systems. These results are preliminary, and need to be investigated further, but appear to lend some weight to the conclusions about early fault growth from the Volcanic Tableland work. The observations are particularly significant in modelling terms as the initial conditions are the hardest to determine reliably, and hence the most prone to error. Assumptions made at the outset of a given run may determine to some extent the conclusions that it provides.

8.1.5 Limitations of the dynamic model

Although much more successful than other existing models at reproducing the complexity of natural stream systems, these dynamic fault experiments have some important drawbacks. The failure of the landsliding algorithm is particularly significant, as shown by the impact on fault topography of landslides in other published results [e.g. Hovius (1998); Allen and Densmore (2000)]. With the rapid reduction of the steep fault topography by landsliding, and a considerably larger sediment supply to the proximal basins, the stream patterns would no doubt be considerably modified. The effect is likely to be even more marked in the comparison between the different lithological resistances [section 8.1.3.2], with the harder rock leading to reduced erosion of the scarps by landsliding. However, this shortcoming of these experiments should be relatively simply to address, as a correctly working algorithm has now been developed [e.g. Champel et al. (2002)].

Another important concern is the effect of the tectonic model element arrangement on the stream orientations. Although the diamond lattice of the fault model was interpolated onto a regular grid [section 8.1.1.1], the fault pattern retains a distinct geometry, with structures preferentially oriented along lines at 45° to the model boundaries [see transparent overlays to Fig. 8.3]. Stream segments which develop in response to this fault topography are severely biased, and appear considerably more regular [and hence less 'natural'] than those which develop on the irregular grid used in other work with CASCADE.

Attempts were made to minimise this effect by incorporating a random 'shake', in both x and y, to the node positions before interpolation, so that a regular nodal arrangement was not retained in the final grid. While this was successful in generating more 'random' [and hence more 'natural'] stream patterns, the exact location of a few key elements proved vital in determining the stream patterns. Hence very different stream patterns were generated from the same faulting patterns, as an artefact of the artificial perturbation of the data. I felt that this manipulation of the topography was impossible to justify, as the resultant stream patterns were not inherently dependent on the true output of the tectonic model alone. As a result, despite the biasing of the stream patterns, the original data has been used throughout. Many existing fault models generate relatively regular stream segment orientations, as an artefact

of their regular gridding algorithms [CASCADE was the first to generate significantly less biased stream orientations: Fig. 2.30], and hence these results are in many ways no less pre-determined than other published results. However, its impact should be carefully considered as this model is developed in the future.

8.2 Discussion of the model results

The modelling work outlined here demonstrates that relatively complex faults can be successfully incorporated into a surface process model, and hence used to gain more insight into fault/stream interactions.

Results show that

1. both fault growth [slip rate, fault tip propagation, magnitude and frequency of tectonic events and the impact of early fault geometries] *and* landscape features [e.g. pre-existing slope longevity and lithological resistance] have an impact on the development of the sediment transport patterns.

2. the dynamic fault in this model produce an incredibly complex landscape, particularly in comparison with the results of non-interacting fault algorithms. Streams exploit local variations in fault displacement both along and perpendicular to strike, and temporally as well as spatially. Figure 8.3 demonstrates examples of gradual increases and decreases in incising stream discharge, and major changes in upstream catchments, caused directly by variations in the distribution of deformation.

3. stream development in extensional regions is the result of a complex balance between stream power and perturbations by growing faults, which act to incise, deflect or defeat the developing river. The sensitivity of this balance is highlighted by the observation that the most fundamental changes in stream development are determined by relatively subtle changes in a few key locations. The important factor appears not to be the *magnitude* of the absolute differences in topography, but the *locations* at which they occur. In each case, topography in the regions of complex fault interactions [e.g. between faults **A**, **B** and **C**; between **A** and **Splay**] was crucial in controlling the regional drainage patterns.

The variability in the landscape in each experiment is purely due to tectonic movements: the rainfall in each run is uniform over the model space, and the eroding rock is completely homogeneous. The variability in the tectonic landscape is a direct result of the mechanism of fault growth, where stress feedback allows neighbouring faults to interact. Slip on one fault affects the stress distribution in the surrounding rock and hence triggers, or retards, slip on neighbouring structures. Therefore the separation, size and slip rate of one structure has important effects on the development of the surrounding landscape. Stress feedback causes a variability in

- displacement along and perpendicular to strike.
- displacement rate.
- tip propagation rate.
- fault activity through both space and time.
- along-strike orientation of the fault trace.

and the resulting localisation of displacement onto a few structures through time. A large variation in the slip distribution occurs over a very small area [e.g. Cowie (1998); Cowie et al. (2000)].

Comparison with natural examples: This complexity or variability is similarly an important feature of natural systems, with many examples on the Tableland of streams exploiting local variations in displacement, lithological strength, fault orientation and so on [Chapters 4 to 7]. Major reorganisations of the stream patterns are all linked to changes in the distribution of deformation, and the gradual localisation of fault activity onto a few key structures [e.g. sections 7.2 and 7.3]. Growth of fault segments resulted in changes in the courses of some streams draining from the footwall area [e.g. northern tributaries, section 5.1.3] and in some cases cut off the supply from footwall streams [e.g. small abandoned channels in the central overlap, section 4.1.2].

Many of the observations from the dynamic modelling are consistent with those made from the Volcanic Tableland. The correlation of stream incisions with displacement lows in the model results is strikingly similar to observations of the surveyed faults in the central overlap [compare Fig. 8.3 with Figs. 4.5, 4.16 and 4.18]. Examples of incision, deflection and stream abandonment in CASCADE can be related to similar circumstances as those demonstrated on the Tableland [Chapters 4 and 5]. Thus the modelling results do appear to mirror several of the traits of natural drainage systems responding to interacting faults, as observed in the field.

Comparison with other models: However, other existing fault models [e.g. Ellis et al. (1999)], do not incorporate any stress feedback between model faults. Their approaches have considered faults with uniform, or smoothly varying, displacement along strike, and straight traces. There is none of the more natural variability along strike seen in the field [section 4.1] and reproduced in this dynamic model. Smoothly-varying displacement profiles favour deflection or defeat, as only powerful streams can maintain courses through the growing faults, and hence scarp streams often drain only the immediate footwall. In contrast to the complex patterns of footwall drainage and scarp incision in Fig. 8.3, simpler, more continuous continuous drainage divides generally develop at the crest of fault scarps.

Other similar comparisons can be drawn between the monotonic growth of simple fault models and the highly complex development of the dynamic fault population in this study, which demonstrate the closer approximation of the dynamic models to reality. Most published fault models allow slip in each event to occur along the entire fault length, and on all faults at the same time. However, the evolution of the main central overlap stream on the Tableland would have been totally different had all the faults moved simultaneously [section 7.5]. Model results reiterate this: the dramatic effect of the change in tectonic event size and frequency shown in section 8.1.3.3 demonstrates how sensitive streams are to variability in the distribution of fault movements, both in space and in time.

Non-interacting fault algorithms incorporate many features of natural faults, and hence also successfully reproduce some of the features of natural stream responses to growing faults, e.g. deflection, defeat and incision of footwall streams as faults grow. However, the comparison with the results of this study demonstrates that faults cannot be considered in isolation. The stress perturbations following slip on each fault not only

influence the development of nearby faults, but have a major impact on the styles and patterns of stream responses over a broad region.

As discussed in section 7.5, streams are the product of a specific set of external controls. Changes in any of these controls can have drastic, and long-lived, effects on the landscape, as shown particularly by the drainage of the Fault C basin in the examples in Figs. 8.3 to 8.6. Models that do not capture this complexity will similarly fail to capture the true sensitivity of streams to growing faults.

Thus although the overall topographic shape of the landscape is the same, simple tectonic models tend to influence drainage patterns on a broader, more regional scale, reflecting the scale of variation in the tectonic topography. However, the sudden changes in incision and morphology in the Tableland streams demonstrate their extreme sensitivity to *local* changes in topography and vertical ground movements. The complex small-scale variations in topography caused by fault interaction mean that the stream/fault balance can tip suddenly over a small distance. Hence the dynamic model used in this study shows a remarkable sensitivity to small fluctuations in elevation in the areas where faults overlap, and hence their interactions are greatest. This mirrors the effects seen in fault overlap regions on the Tableland.

Impact of early fault topography: Many of the experiments described here have demonstrated that the early topography exerts a significant level of control on the subsequent landscape development. This is consistent with observations made by Davies et al. (2000) and also McLeod et al. (2000), based on sediment distributions in extensional basins in the northern North Sea. They concluded that sedimentation patterns can only be understood in the context of the *contemporary* fault pattern that governed their development, and that later fault patterns shed little light on early sediment distributions. Jackson and Leeder (1994) used the shape of Bushee Canyon in Pleasant Valley, Nevada, to infer the fault tip propagation that gave rise to the present stream geometries.

Thus at least some stream geometries in major fault arrays were probably determined very early in the evolution of the fault population, as implied by the establishment of major streams through the small Tableland faults, and may have been relatively impervious to later fault growth. This has important implications for modelling these systems, as small variations in the initial conditions may have dramatic impacts on the patterns of landscape evolution. Since the initial conditions are the hardest to constrain in the field, they are the most likely to be erroneously modelled in numerical studies. However, the results of this small study imply that in some cases, the initial assumptions may largely control on the outcome of model runs. An analogy may possibly be the indirect control of joints on the development of major faults in some regions, in as much as the joints control the initial orientation of fractures which later develop into fault segments.

Summary: This study, although preliminary, has demonstrated the impact of stress feedback between extensional faults on the development of the surrounding landscape. This work, which incorporates the output from a realistic, dynamic fault model, shows that the inclusion of feedback between growing faults imparts a natural complexity, in both time and space, into the tectonic system, and hence into the evolution of nearby streams. Landscape evolution around normal faults is inherently complex, as it is

closely controlled by complex variations in the distribution of deformation within the growing fault population.

Simple models, with regular patterns of fault growth, fail to reproduce natural systems accurately as the true spatial/temporal variation in tectonic activity is not adequately modelled. Thus many streams may be artificially forced to deflect or are reversed, losing much of the complexity and sensitivity of natural stream systems. Attempts to model landscape evolution beginning with large fault topography or using coarse tectonic steps are also unlikely to adequately predict the factors that determine stream evolution in extensional regions.

Model results are consistent with the observations from many natural examples [e.g. section 7.5] that changes in *any* of the external controls can upset the fault/stream balance, and change the local stream pattern. Model and field results demonstrate that the landscape is most delicately balanced where the fault pattern if particularly complex. Thus relatively subtle changes in an external control at certain locations in a fault overlap can result in dramatic and long-lived differences not only in the local, but in the more regional, patterns of water and sediment distribution.

Future work should examine in more detail the impact of the early fault topography on later stream development, and conditions under which its effect is sustained or overwhelmed by the subsequent fault growth. The impact of spatial heterogeneity in lithological resistance would also make a valuable comparison with natural environments. Further work is required incorporating landsliding, and testing the relative impacts of different transport mechanisms.

Chapter 9

Synthesis

The conclusions of each part of this thesis have been brought together at the end of each chapter. This section considers the main findings of the project as a whole, and compares my approach to that of previous work. Some suggestions for how this work could be extended to give more insights into the interplay between fault and stream growth are outlined at the end.

This project developed from the premiss that streams hold a vast amount of information about the evolution of local tectonic systems, which, if used in conjunction with the evidence contained in the fault systems themselves, can add significantly to our understanding of how faults grow and interact. This thesis explores whether this information can be successfully extracted from the stream record. In particular, it has considered two factors central to the extraction of the information:

- inadequate understanding of the processes by which streams respond to tectonic impacts, and the rates and scales over which they occur
- the ability to isolate the impact of tectonic evolution from other influences on stream evolution

The approach used in this project is novel as it combines information from both the tectonic and geomorphic communities. Previous studies have considered only one of these aspects. Fault-driven studies of landscape morphology [e.g. Jackson and Leeder (1994); Gawthorpe et al. (1994); Jackson et al. (1996); Goldsworthy and Jackson (2000)] have predominantly focused on drainage routes, to investigate the volumes and locations of sediment removal and deposition within a drainage basin. These studies have often been qualitative, and considered large systems, where major faults dominate the landscape evolution, e.g. Central Greece, Gulf of Suez, large Basin and Range systems. Fluvial studies have used stream morphology to develop a detailed understanding of the processes by which streams respond to external controls. However, tectonic forcing has been considered mostly at a regional scale [e.g. Burnett and Schumm (1983); Merritts and Vincent (1989); Seidl and Dietrich (1992)]. Some studies have investigated stream responses to a single fault [e.g. Jorgensen (1990)]. This work is perhaps closest to the starting point of this thesis, but these studies focused on

single large faults, with no significant change in tectonic activity during the period of investigation.

In contrast to these approaches, this project combines tectonic information about fault growth and interaction with geomorphic insights into fluvial processes and the responses to external controls. It also investigates far more complex tectonic problems, where the distribution of faults and the loci of tectonic activity change drastically during the evolution of the streams.

Two different methods have been used to tackle this problem:

- fieldwork in a young system in the Volcanic Tableland, Owens Valley, California [Chapters 4 to 7]
- modelling synthetic extensional landscapes in a surface process model, CASCADE [Chapter 8]

9.1 Fieldwork

Fieldwork was carried out on the Volcanic Tableland, Owens Valley, California [see Chapter 3]. This area is uniquely valuable as a location to investigate stream/fault interaction as:

- the system is young [faults and streams drain ~760ka Bishop Tuff]:
  - — the fault patterns have changed significantly during the period of stream evolution
  - — the streams are the correct size [not too small or too large] to respond over a timescale compatible with the fault evolution, providing a sensitive record of tectonic activity
  - — the system is small enough to survey in detail
  - — it has not been overprinted/buried by more recent tectonic/climatic activity
  - — surface exposure dating [cosmogenic $^{10}Be/^{26}Al$] can be used with good resolution
- previous work (Dawers et al., 1993; Dawers and Anders, 1995) has provided a detailed understanding of the tectonic framework, documenting fault interaction in the array
- exposure is excellent: low erosion rates have hardly degraded fault scarps, nor filled the basins
- the streams are currently unoccupied, and hence easy to survey at high resolution
- other external influences can be quantified:
  - — the streams and faults are contained in a single lithology, the ~760ka Bishop Tuff
  - — the regional climatic variation since deposition of the Bishop Tuff is well documented [Table 3.1]
  - — pre-faulting topography is minimal, and can be constrained

---

Detailed GPS surveying of both streams and faults provides high resolution records of both stream morphology and the distribution of tectonic strain within parts of

the array. Cosmogenic analysis of samples from stream beds within the central fault overlap zone constrains the occupation of the streams, and hence rates and scales of the stream response to changes in the fault pattern. Results show that indeed streams *can* be used to gain additional information about the patterns and rates of fault evolution, and supply some answers to the questions posed at the beginning of this thesis:

- How do fluvial systems respond to changes in the distribution of displacement, and in particular to changes in the uplift rate, propagation rate, and in the location of activity within a fault population?

Previous studies have documented changes in stream course as faults evolve. This study also demonstrates changes in stream gradient, recorded in the long profile; and in the cross-sectional morphology, highlighted particularly by the aspect ratio, AR. Incision has occurred by both plucking and abrasion; base level changes are translated upstream by the migration of steep knickpoints. Major changes in the loci of tectonic activity caused large-scale reorganisations of stream patterns, and the incision/overprinting/reworking of previous deposits [Chapters 4 and 5]. Each significant change in the stream pattern can be linked to a major change in tectonic activity.

- How fast do these changes occur?

$^{10}Be/^{26}Al$ cosmogenic exposure dating of stream beds have data pinpoints the *absolute* timing of major waves of fluvial incision caused by motion on particular faults, and hence constrains the length of stream occupation. The dates have been used to calculate rates of erosion, incision and knickpoint migration in a major fault overlap [section 7.2.2]. Stream morphology and changes in depositional patterns outline the *relative* timing of stages within the evolution of the fault population. Correlation of these observations with the cosmogenic data constrains tectonic slip and propagation rates, and the timing of larger-scale stream reorganisations in response to changes in fault activity.

- How does the magnitude of the tectonic trigger affect the fluvial response?

Aspect ratios and local slope variations in the Tableland streams demonstrate that the fluvial response is dependent on the magnitude of the displacement [Fig. 7.1 implies that $AR \propto D$], and also on the distribution of deformation between faults [section 7.1.3]. Large faults lead to larger amplitude and longer wavelength perturbations in nearby streams, and can overprint the effect of smaller faults. Major reorganisations of the stream pattern, often leading to the reversal or abandonment of channels, occur in response to increases in displacement following linkage of fault segments [section 7.3].

- Can the response to a tectonic trigger be reliably isolated from the other factors which affect stream development?

Isolation of the tectonic signal requires an understanding of the various factors that have controlled stream evolution. The Volcanic Tableland system is ideal to assess this question, as it is relatively simple, with streams draining a single lithology and minimal, but quantifiable pre-faulting topography. The main controls on stream evolution are therefore regional climate and the changing tectonic pattern, both of which have been studied in detail [Table 3.1; Dawers and Anders (1995)].

The timings of major incisions in the surveyed streams, dated by cosmogenic analysis, show no correlation with glacial cycles [Fig. 6.17]. In contrast, incision patterns, burial

histories and knickpoint migration rates are consistent with a high level of control by the local fault population [sections 6.5 and 7.2.2].

This simple system also demonstrates how other factors modulate stream responses to tectonic growth. Variations in fracturing and welding even within the single lithology of the Bishop Tuff affect stream incision styles [e.g. plucking vs. abrasion], rates and patterns. The evolution of the central overlap demonstrates the impact of pre-existing topography [regional slope] on stream response to fault growth and linkage [section 7.5].

The information extracted from the Volcanic Tableland fluvial system has been combined with tectonic evidence to develop evolutionary models at a variety of scales, from a single fault [Fig. 7.4] to an overlap zone [Fig. 7.6], a fault array [Fig. 7.8] and also the regional drainage patterns [Fig. 7.9]. The fault array investigated on the Tableland is only 7km long, and hence demonstrates that significant changes occur during the early stages of landscape development [compare with more mature 25km long faults investigated in the Basin and Range, Central Greece, North Sea and Gulf of Suez].

9.2 Modelling

Surface process modelling provides a mechanism to investigate explicitly the impact of fault parameters relative to other controls on drainage evolution, and the sensitivity of streams to various changes in fault development. The main contribution of this aspect of the PhD project has been to introduce a far more realistic fault system into a surface process model, so that model results can be compared more directly with natural examples. Until now, surface process models have used simple uplift models, or at best single faults with little displacement variation along strike, and where events occur at the same time throughout the model space [e.g. Ellis et al. (1999)]. The main differences of the approach in this thesis are:

- an entire population is considered, rather than a single fault, or regional uplift
- faults interact: positive stress feedback between faults causes each fault to affect the growth of others nearby
- patterns of fault activity are irregular, due to fault interaction - events are irregularly spaced through time, not every fault ruptures in each event and only parts of each fault break in each event
- fault displacement varies both along- and perpendicular to strike

Thus this project considers a far more complicated tectonic environment than any previously incorporated into a surface process model, but one which more closely approximates reality, and which can therefore be compared more directly with natural examples.

Chapter 8 demonstrates that fault populations of this complexity can be successfully introduced into a surface process model. Experiments produce stream geometries that are far more complex than those produced by simplified tectonic models [e.g. Ellis et al.

(1999)]. However, the model landscapes show a surprising similarity to many features of natural examples, such as the Volcanic Tableland [section 8.1.3].

This work with CASCADE demonstrates that natural landscape complexity is an inherent result of the mechanism of fault growth. In the model, it occurs even where lithology and climate are constant and uniform throughout. Fault interaction results in short wavelength but high amplitude variations in tectonic displacement. Thus the impact of tectonic growth relative to the other controls on stream evolution varies considerably over small scales, as seen in the Tableland. With simplified tectonic models [e.g. Ellis et al. (1999)], landscapes are simpler, as tectonic displacement varies more smoothly over longer wavelengths.

Changing parameters in the model [sections 8.1.3.2 and 8.1.3.3] demonstrates the delicate balance of the stream/fault relationship. Increasing the lithological 'hardness' results in major changes in catchment boundaries, from relatively subtle elevation changes at a few key locations. Similarly, changing the size or frequency of tectonic events affects the stream's ability to respond rapidly enough to record the changing topography. This sensitivity to the tectonic influence correlates well with observations from the Tableland, but is not reproduced with simpler tectonic models.

Thus modelling results show that it is the *contemporary* balance between fault movements and stream erosivity that controls stream development - present stream and fault geometries may not always be an adequate key to the past evolution patterns. Many features of a stream may be determined during the early stages of its evolution.

9.3 Holistic Approach

Although initiated from a tectonic standpoint, this thesis demonstrates above all that a more holistic approach to investigating landscape evolution is needed. The landscape *can* be unravelled to produce a wealth of additional information about e.g. tectonic evolution, but only by considering *all* of the various factors that have influenced it, and which have affected the landscape's ability to accurately record external changes.

The unique characteristics of the Tableland make it an ideal location to investigate the interplay between climatic, tectonic and lithological controls on stream evolution. However, the results discussed in this thesis are not limited to that area, but have a much wider application to the study of tectonic landscapes. This study demonstrates that the influences of different controls can be successfully isolated from a stream record, and investigates ways that lithology and pre-existing topography modulate fluvial responses to changing fault patterns. It also provides much-needed quantitative data about the processes, rates and scales of these stream responses. Both the field and modelling work imply that the early stages of landscape development may be the most important in defining its later shape. The fieldwork also highlights two important parameters, aspect ratio and local slope variation, which are particularly valuable in analysing tectonically-influenced streams. Both parameters can be easily measured in other datasets, including those collected remotely, such as DEMs.

Section 7.5 applies a wider approach, based on the Tableland observations, to the generic question of stream evolution within fault overlap zones. It demonstrates that fault growth is only one of a series of fundamental controls on stream development. The

evidence of this study argues that there is no favoured stream geometry in extensional fault overlaps. Instead of applying a universal model, it is more valuable to approach each example independently, and to consider the relative contributions of each external influence. This argument is emphasised by the modelling work in Chapter 8 which demonstrates how delicately balanced the landscape actually is in regions of complex fault activity. Relatively subtle elevation changes at a few key locations can have widespread effects on the landscape evolution.

9.4 Future work

There is a currently a dearth of quantitative data on stream/fault development, and the rates of surface processes. Both the field and modelling work in this thesis imply that the early stages of landscape development are vital in determining its later morphology. More combined stream/fault studies in both young and more mature fault populations would be valuable to assess whether streams preserve evidence of the early fault development, or whether it is overwhelmed by subsequent increased slip rates and strain localisation.

The cosmogenic isotope study has been extremely powerful in constraining the occupation of the streams on the Tableland, and also aspects of the stream response to faulting. However, the limited number of samples was not sufficient to assess whether inheritance is significant in any of the samples, and hence the data were not able to conclusively establish the role of climate in the evolution of these streams. Since this study has proved the potential of the technique in this area, and for tackling this type of problem, more detailed sampling on the Volcanic Tableland could well provide important constraints on the development of the streams, and the relative influences of tectonics and climate.

The preliminary work with CASCADE and the dynamic fault model implies that this modelling approach will yield valuable information about the scales and rates of stream responses to fault evolution. However, the influence of the diagonal trend of the elements needs to be quantified, to be certain that streams are not being unreasonably pre-determined by the model structure. Landslides must also be properly incorporated. Early results are very encouraging, as the model appears to reproduce natural geometries and complexity more faithfully than other existing models. More work is needed to compare the model topography with field studies to build on this. Further work should also aim to quantify the contribution of early fault growth to determining stream geometries, and the conditions under which they may be overwhelmed by later fault growth, or other factors.

Appendix A

In situ cosmogenic isotope analysis theory

This appendix explains in more detail the theory behind the analysis of *in situ* cosmogenic isotopes to investigate the evolution of geomorphic surfaces. Equations used in section 2.5 are derived fully, and the theory behind calculations of sample shielding [section 6.3] is also explained.

Terrestrial cosmogenic isotopes [TCN] are produced by the interaction of cosmic rays with nuclei in the atmosphere or on the earth's surface. Specific target atoms produce specific cosmogenic isotopes [Table 2.1], some stable, and others radiogenic. This project considers specifically *in situ* cosmogenic isotopes: those nuclides produced in rocks at the earth's surface. Due to the reduced flux and energy of the cosmic radiation by this point, typically only of the order of 10^{-14}atoms are produced per gram of target rock at the surface per year. Due to these vanishingly small concentrations, targets for analysis must be produced extremely carefully, and can only be analysed in high-resolution accelerator mass spectrometers, AMS. An AMS incorporates a tandem accelerator, which accelerates ions to speeds of up to 10^7m.p.h, according to their charge/mass ratio, separating ions more efficiently, and hence allowing detection down to concentrations of 10^{-15} atoms.

A.1 Production of cosmogenic isotopes

The high-energy primary cosmic radiation consists largely of protons, which have enough energy to cause nuclear disintegrations in the upper atmosphere, in turn producing a cascade of secondary cosmic particles with energies of over 100MeV. This secondary radiation is largest at intermediate atmospheric levels, and then decreases as the number of interactions with target atoms increases lower down in the atmosphere. The flux of cosmic radiation is modulated by the geomagnetic field of the Earth, and hence varies with latitude. Although hard to model exactly [section A.3.1], the cosmic ray flux at any point may be considered proportional to the horizontal component of the Earth's magnetic field [e.g. Compton (1933), cited in Gosse and Phillips (2001)], and thus reaches a maximum near the poles. A debate surrounds the best way to calculate production rates [section A.3.1].

As the cosmic radiation passes through the atmosphere, it becomes composed predominantly of neutrons, which, being neutral, are not significantly slowed by ionization reactions with other atoms. A smaller proportion of the radiation consists of short-lived muons. Both the neutrons and muons form TCNs as they interact with nuclei in the atmosphere and the surface rocks. These reactions may be summarised as spallation [high-energy neutrons], thermal-capture [very low energy neutrons] and [predominantly negative-]muon capture.

In **spallation**, a high-energy neutron breaks a series of lighter particles off a target nucleus, leaving behind a lighter nucleus, the TCN. Typically the splitting is asymmetrical, favouring the production of a large fragment, with most of the target mass, and a series of small fragments [protons, neutrons]. This results in a higher production rate for ^{26}Al than for ^{10}Be in quartz, although ^{10}Be is produced from both ^{28}Si and ^{16}O targets. The production of TCN by spallation decreases exponentially as the cosmic radiation passes into the target rock [Fig. A.1a]. However, attenuation depends on the number of atoms hit, and hence is proportional to the *density* of the target, and not its thickness, or composition [Fig. A.1c], although there is some debate about the TCN production in the initial few centimetres (Masarik and Reedy, 1995; Gosse and Phillips, 2001). Production typically drops to virtually zero by a depth of 1.5 - 2m from the surface.

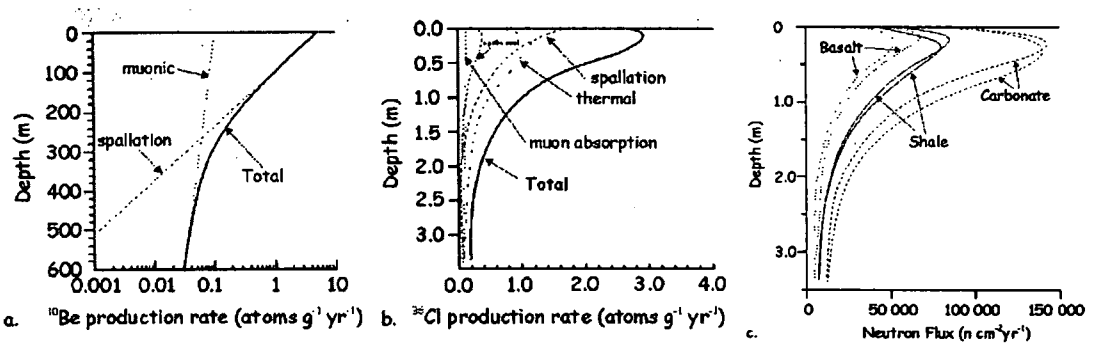

Figure A.1: *Variation of TCN production rate with depth in a target, modified from Gosse and Phillips (2001).*
a. Variation in production of ^{10}Be with depth: production dominated by spallation.
b. Variation in production of ^{36}Cl with depth: production by spallation, thermal capture and muon capture. Note the 'bulge' in the thermal production near the surface.
c. Decrease in production rate of ^{10}Be [spallation] with depth in samples of varying density. The attenuation depends on the number of atoms hit, i.e. the density *of the target, and hence the rate at which the production rate decreases varies for rocks with differing density, ρ.*

As the cosmic neutrons collide with target nuclei, they become too slow to cause spallations. At very low **'thermal'** energies, TCN production occurs by capture of the neutrons by target nuclei, e.g. ^{14}C from ^{14}Ne atoms in the atmosphere; *in situ* ^{36}Cl and ^{41}Ca production. Unlike spallation, production rates initially *in*crease below the surface to a maximum and then decrease with depth deeper in the rock [Fig. A.1b].

Muons account for less than half the cosmic flux at the earth's surface. They have a low reactivity, and hence longer attenuation lengths, as they do not lose energy as quickly on passing through a target [Fig. A.1b]. TCN production occurs predominantly

by capture of negative muons by positively charged nuclei, but some production also occurs by coulombic interactions of target nuclei with faster muons (Gosse and Phillips, 2001). Reactions release TCNs, along with electrons and neutrinos, or in some cases thermal neutrons, which may themselves be absorbed by other targets to produce ^{36}Cl. Muon TCN production at the surface is hard to gauge [section A.3.1]. Early estimates suggested that the muon contribution could be as high as 10% [e.g. Middleton and Klein (1987)], although this has been reduced to 1-3% of surface *in situ* TCN production [e.g. Brown et al. (1992); Heisinger et al. (1997); Stone (2000)], and hence some production rate scaling factors have been revised downwards [e.g. Nishiizumi et al. (1996); Schaller et al. (2001)].

The low attenuation causes a greater penetration of muons, and hence TCN production at depths below the limit of production by spallation and thermal neutron capture. Therefore certain TCNs [e.g. ^{36}Cl], are useful for measuring deep profiles. However, muons can also introduce *inheritance* problems. Removal of a thick overburden [e.g. 2m rock] might be expected to remove any previously-produced TCNs, and hence 'reset' the cosmogenic clock in a sample. The exposure age [section A.5] calculated from a surficial sample after this time should record the time of exhumation. However, where muon production is high at depth, some TCNs may be retained or 'inherited' in the exhumed rock. The apparent exposure age would then suggest too old an exhumation date. Inheritance problems are reduced for isotopes that do not have a significant muon production [e.g. ^{10}Be], and for short-lived isotopes [Table A.1].

A.2 Advantages and disadvantages of *in situ* cosmogenic analysis

Six cosmogenic isotopes are commonly used for geomorphic studies [Table A.1 and section 2.5.3]. They have a variety of half-lives [including two stable isotopes], making them useful over timescales from 10^3 - 10^6yrs. Resolution is typically high, particularly where more than one isotope is used [section 2.5.2]. The main disadvantage of TCNs is their extremely low: typically 10^{-14} atoms g^{-1}target mineral.

Thus although many isotopes are produced cosmogenically, only six TCNs are commonly used for geomorphic purposes: ^{3}He, ^{10}Be, ^{14}C, ^{21}Ne, ^{26}Al and ^{36}Cl. Other isotopes cannot be used due to:

- the existence of an alternative non-cosmogenic [e.g. primordial or radiogenic] source, against which the cosmogenic component cannot be quantified explicitly - e.g. ^{7}Li.
- having a short half-life, so that the concentration of the TCN drops to zero too quickly for use - e.g. ^{24}Na [$t_{1/2}$ = 15hours].
- having a production rate too low for detection in an AMS - e.g. TCNs with atomic numbers >56: the targets have very low abundancies in natural rocks.
- there being a high abundance of the stable [non-cosmogenic] isotopes in the target rock, so that the ratio of isotopes measured in the AMS is below detection - e.g. ^{41}Ca in plagioclase. This can also be a limitation of the use of ^{26}Al in some rocks.

Nuclide	Advantages	Disadvantages
^{3}He	highest production rate: useful for young surfaces	diffusion from qz and fine groundmass in aphanitic rocks too rapid (Brook and Kurz, 1993)
	low detection limit in standard MS: useful for young surfaces	need to correct for radiogenic / nucleogenic / magmatic ^{3}He
	stable: can be used for v old samples	stable: inheritance from previous exposures highly probable
	prodn rate better constrained than ^{21}Ne	interference from $^{1}H^{2}H$ molecules in AMS
^{10}Be	simple stoichiometry of target	hard to remove ^{10}B isobar
	qz: resistant to weathering; ubiquitous	major contamination with atmospheric nuclide
	mostly produced by spallation and muon reactions on Si, O	lowest production rate in qz: hard to use for young surfaces
	easily prepared with ^{26}Al, ^{14}C, ^{21}Ne in qz	
	olivine also good target: resistant and common	production rate in olivine solid series not well understood
	long half-life: useful for old samples	
	not a gas: relatively immobile	
^{14}C	short half-life: good for young samples	no use for >30 kyr samples
	insensitive to low erosion rates	qz is only reliable target
	low probability of inheritance	high probability of contamination
	higher production rate than ^{10}Be	hard preparation and analysis
^{21}Ne	stable: useful for v long exposures	stable: inheritance from previous exposures highly probable
	slower diffusion than ^{3}He through qz (Brook and Kurz, 1993)	need to correct for radiogenic / nucleogenic ^{21}Ne
	higher production rate than ^{10}Be	interference in AMS with isotopes from $H_2{}^{18}O^{+}$, $^{40}Ar^{2+}$
^{26}Al	simple stoichiometry of target	mostly restricted to qz
	low stable Al abundancies [<1%]	AMS required to separate from ^{26}Mg isobar
	higher production rate than ^{10}Be	difficult to measure $^{26}Al/^{27}Al$ in qz with high Al content
^{36}Cl	multiple sources: can be used alone for erosion and burial studies	multiple sources: hard to decipher production rates from one source
	low background atmospheric TCN production: can use whole rock, more lithologies	radiogenic and nucleogenic sources limit low-level applications
	higher AMS sensitivity than ^{10}Be and ^{26}Al	complicated system unless pathways isolated for low (non 0) erosion
	production rates higher than ^{10}Be	no use for exposures >1Myr
		significant thermal leakage in variable moisture conditions, snow cover
		AMS required

Table A.1: *Advantages and disadvantages of the six commonly-used TCNs [modified from Gosse and Phillips (2001)].*

A.3 Production rates

Production rates of *in situ* TCNs vary considerably across the planet, due to variations in the geomagnetic field which modulates the incoming cosmic radiation. Most importantly, production rates vary drastically with both latitude and elevation. Scaling equations modify the production rates, which are modelled at sea level and high latitude (SLHL), for production at the specific sampled site. However, the exact values of the scaling factors at SLHL are debated.

A.3.1 Scaling coefficients for production rates

Reference	Exposure time (kyr)	Production rate atom $g^{-1}SiO_2yr^{-1}$	
		^{10}Be	^{26}Al
Lal (1991)	calculated	6.5	27.5
Nishiizumi et al. (1989)†	12.2	6.03	36.8
Brown et al. (1991)	2 500	6.4	-
Nishiizumi et al. (1991)	7 000	6.13	37
Clark et al. (1995)	14	4.74	28.9
Masarik and Reedy (1995)	calculated	5.97	36.1
Bierman et al. (1996)	21.5	5.17±0.15	-
Nishiizumi et al. (1996)	4 solar cycles	5.32±0.27	-
Nishiizumi et al. (1996)†	11	5.80	35.03
Gosse and Klein (1996)	12.9 17.6	5.5 ± 0.7 5.4 ± 0.6	- -
Kubik et al. (1998) ‡	10.0	5.75±0.24	37.4 ±1.9
Stone (2000)	-	5.1 ± 0.3	31.1 ±1.9
Barrows et al. (2001)	up to 61.7	5.02±0.27	30.62±1.6
Schaller et al. (2001)‡	10.0	5.37±0.22	35.01±1.9

Table A.2: *Production rate scaling factors for ^{10}Be and ^{26}Al in quartz, modified from Gosse and Phillips (2001).*
†*The scaling factors quoted for Nishiizumi et al. (1989) have now been altered downwards after recalibration of the ages of the sampled surfaces [see Clark et al. (1995)].* ‡*Schaller et al. (2001) recalculated the Kubik et al. (1998) values, following re-estimation of the muon contribution.*

The calculation of production rates remains problematic, as the Earth's geomagnetic field is complicated, and has not remained constant through time. Many authors have modelled a simplified magnetic field, due to a dipole [e.g. Lal (1991)], but this introduces large inaccuracies into the prediction of cosmic flux (Dunai, 2000). Errors are also introduced from the models used to calculate the flux of secondary particles. The most commonly-used standard for atmospheric nuclear disintegration rates, (Lal, 1991), is based on the data of Lal and Peters (1967), and includes an uncertainty of at least 10%. Dunai (2000) suggests using inclination as an alternative to latitude to calculate the secondary flux variation. The uncertainty in his method is around 2% at sea-level, but increases at higher altitudes. Although this model gives greater sensitivity near the poles, it fails to accurately represent variations in palaeo-longitude. The model also includes recent [up to 10^2 years] variations in the magnetic field, which may not be representative of variations during the lifetimes of collected samples. Long-term pressure deviations observed in certain parts of the world could alone account for a variation of up to 3-4% in the calculated production rates Stone (2000). Although this

is within the Lal's error, differences of 25-30% are predicted between sites in Antarctica and those at similar latitudes in the Arctic (Stone, 2000).

Although not wholly representative of the known temporal field variations, most workers still use the Lal's 1991 model to calculate nuclear disintegration rates at the specific sample site, and then calculate *in situ* production rates using scaling factors, which are quoted at sea level and high latitude [SLHL]. Independent scaling coefficients are generated by measuring the nuclide concentration in rocks with known exposure histories, where the age of the sample can be determined by an independent technique, such as Ar / Ar or radiocarbon dating [e.g. Nishiizumi et al. (1994, 1996); Kubik et al. (1998); Stone (2000); Barrows et al. (2001); Schaller et al. (2001); Table A.2]. Other scaling factors [e.g. Masarik and Reedy (1995)], are based on numerical simulations. Despite many studies, there remains a variation of up to 40% in published scaling factors for ^{10}Be [Table A.2]. This partly reflects the different locations of the calibration studies, but is also the result of recent lower estimates of the muon contribution [e.g. Nishiizumi et al. (1989): 7% at altitude; 20% at SL; Lal (1991): 15.6%]; Stone (2000): 3%]. In contrast, Dunai (2000) calculated nuclear disintegration rates based on two recent datasets, recording the high-altitude and sea-level geomagnetic field over a huge range of latitudes in place of the 1950's observations used by Lal (1991) [section A.3.2].

A.3.2 Calculation of production rates at a sample location

Lal (1991) used Eqn. A.1 [from Lal and Peters (1967)] to scale nuclear disintegration rates to a given altitude and latitude. The coefficients in Table A.3 [from his Table (2)], scale linearly with latitude between 0° and 60°; interpolation of these values may be used to calculate the disintegration rates at a given site. A scaling factor [e.g. Nishiizumi et al. (1996); Barrows et al. (2001); Schaller et al. (2001)] is used to convert these to production rates for the individual isotopes at the sample location.

$$s = a_1 + a_2 y + a_3 y^2 + a_4 y^3 \tag{A.1}$$

where s is the nuclear disintegration rate in the atmosphere at altitude y km, in g^{-1} yr^{-1}
the coefficients a_1, a_2, a_3, a_4 change with geomagnetic latitude, as shown in Table A.3.

In contrast, Dunai (2000) considered a varying geomagnetic field, and explicitly looked at the contribution from the *non*-dipole field. He also questioned whether the high altitude data of Lal (1991) can be successfully extrapolated to sea level (Dunai, 2000). For nuclides where muon production is insignificant [e.g. ^{10}Be], Dunai's methodology simplifies to:

$$N(z, I) = N_{1030}(I).\exp\frac{z(h)}{\Lambda(I)} \tag{A.2}$$

where $N(z, I)$ is the scaling factor for the sampling site
$N_{1030}(I)$ is the neutron flux at sea-level and high-latitude (SLHL), in neutrons cm^{-2}

Nuclear disintegration rates - Lal (1991)				
Geomagnetic latitude (°)	Polynomial coefficients			
	a_1 x 10^2	a_2 x 10^2	a_3 x 10^2	a_4 x 10^1
0	3.307	2.559	0.9843	2.050
10	3.379	2.521	1.110	2.073
20	3.821	2.721	1.325	2.483
30	4.693	3.946	0.9776	4.720
40	5.256	5.054	1.420	5.887
50	5.711	5.881	1.709	7.612
60-90	5.634	6.218	1.773	7.891

Table A.3: *Nuclear disintegration rates in the atmosphere, from Lal (1991). Polynomial coefficients estimated by Lal and Peters (1967) for solving Eqn. A.1. Resultant nuclear disintegration rates are calculated in atoms g^{-1} yr^{-1} for altitudes in km.* In situ *production rates for individual cosmogenic isotopes at the sampled site are calculated using published scaling factors. See text for discussion, and section 6.6.*

yr^{-1}

$z(h)$ is the difference in atmospheric depths, in gcm^{-2}

$\Lambda(I)$ is the mean absorption free pathlength at the given inclination, in cm.

Nuclide production rates are then calculated for the required sample latitude and elevation by scaling published SLHL values:

$$P_{nuclide}(z, I) = P_{nuclide} \cdot N(z, I) \tag{A.3}$$

where $P_{nuclide}$ is the quoted SLHL production rate for the nuclide in question, in atoms g^{-1}target yr^{-1}

$P_{nuclide}(z, I)$ is the nuclide production rate at the sample site, in atoms g^{-1}target yr^{-1}.

In the presence of this plethora of scaling variations, it is hard to choose the most reliable and appropriate method to scale production for collected samples. This project uses the nuclear disintegration rates from Lal (1991), scaled using Nishiizumi et al. (1996) values, as these were derived from samples collected near my study area, in the Sierra Nevada, California. However, Nishiizumi et al.'s samples were collected from considerably higher altitudes, and in the light of the scaling debate, I have compared them with production rates calculated from alternative scaling factors, and from the Dunai (2000) disintegration rates [Table 6.8].

A.4 Modification of production rates: sample shielding

The production rates discussed above are based on four main assumptions:

1. The sample has been taken from an infinitely thin layer at the surface of the outcrop [i.e. it has zero thickness].

2. The sample has been exposed to cosmic radiation from the entire of the sky - from the full 90° from horizontal to vertical inclination, and through the full 360° azimuth range.

3. The sample has been taken from a horizontal surface.

4. The sample has not been covered [e.g. by sediment or snow etc.] during its exposure.

However, in reality, these assumptions are not all valid, and errors are introduced into the calculated production rates. To obtain true exposure ages, corrections must be made for these factors.

A.4.1 Sample thickness

As the spallation production rate decreases exponentially below the surface, an error is introduced since all samples have a finite [non-zero] thickness. Thus measured nuclide abundancies [e.g. N_{26} and N_{10}*: section 6.2.2], record an *average* of the varying nuclide concentration in the sampled rock [Figs. A.1 and A.2]. Attempts should be made to limit this error by collecting very thin samples [e.g. section 6.1.1]. However, a correction should still be made to allow for the reduction in production rate.

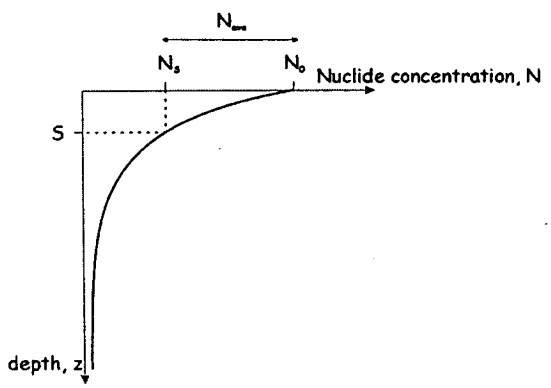

Figure A.2: *Sketch of variation in nuclide abundancy with depth.*
The nuclide concentration decreases exponentially with depth, z, through the rock, from N_0 *at the surface.* N_S *is the concentration at the bottom of the sample.* N_{ave} *is the averaged nuclide concentration through this sampled thickness,* S*. S should be very small compared with the distance over which the nuclide concentration drops to zero. [≪ 3 cm for the Tableland samples: Chapter 6].*

The measured nuclide concentration, N_{ave} is:

$$N_{ave} = \frac{1}{S-0} N_0 \int_S^0 e^{-z/z*} \mathrm{d}z \qquad \text{(A.4)}$$

where N_{ave} is the measured nuclide concentration - an average over the sample thickness, in atoms g^{-1} SiO_2
S is the sample thickness, in cm
N_0 is the actual nuclide concentration at the surface of the outcrop, in atoms g^{-1} SiO_2
z is thickness, in cm
$z*$ is the attenuation length of the sample, in cm, where $z* = \Lambda/\rho$.

Thus the measured nuclide concentration can be scaled to obtain the actual *surface* value, N_0, by:

$$N_0 = \frac{S}{\int_S^0 e^{-z/z*}\mathrm{d}z} N_{ave} = \frac{S}{z* - (z* . e^{-S/z*})} N_{ave} \qquad \text{(A.5)}$$

A.4.2 Topographic shielding

Calculated production rates assume that the samples are exposed to cosmic radiation from the entire sky. However, in reality, samples are shielded by topographic obstructions, such as mountains, fault scarps and channel banks [Fig. A.3].

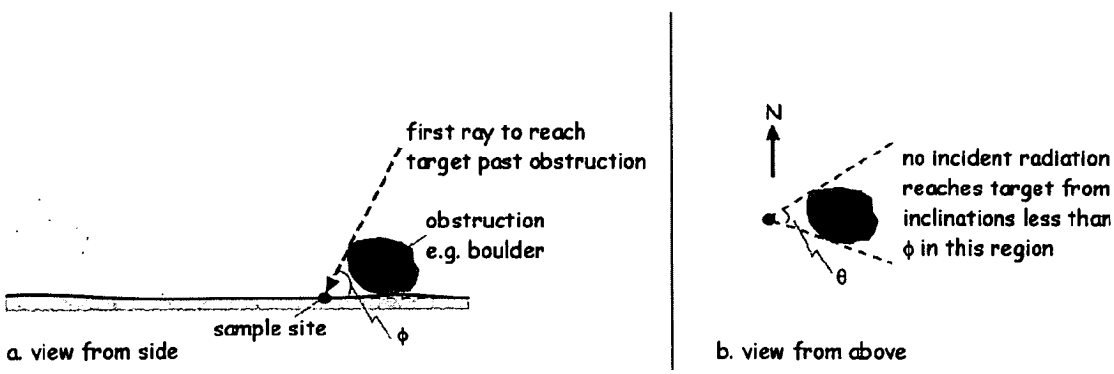

Figure A.3: *Sketch of topographic shielding for a sample.*
a. Side view: obstacle blocks the sample from all radiation incident at less than ϕ.
b. Map view: obstacle blocks the sample from radiation with azimuths within θ.

Obstructions reduce the effective cosmic flux reaching the samples, and thus in turn reduce the effective TCN production rates. A correction for this shielding may be calculated if the proportion of the sky that is obstructed is known. Hence the inclination of the horizon from the Tableland sample sites was measured in sixteen sectors around each sample [e.g. Fig. 6.13]. The part of each sector that is blocked by the obstruction is:

$$\text{blocked sky} = \text{fraction of azimuth} \,.\, \text{fraction of inclination}$$

$$\text{blocked sky} = \frac{16}{360°} \cdot \frac{\text{inclination to horizon}}{90°} \qquad \text{(A.6)}$$

The total amount of sky that is shielded is the sum of the blocked part of each sector. I have used the equation (6) of Dunne et al. (1999) for rectangular obstructions to relate the shielding of the sky to the effect on the production rates at the sample:

$$S_P = 1 - \frac{1}{360°} \sum_{i=1}^{n} \Delta\phi_i \sin^{m+1} \theta_i \tag{A.7}$$

where S_P is the total shielding factor due to all obstacles [my subscript denotes the change in production rate]
n is the total number of obstacles [16 sectors for the Tableland samples]
$\Delta\phi_i$ is the fraction of the azimuth that is blocked by each obstacle, i, in degrees [= 22.5° for each sector in Tableland samples: section 6.1.1]
θ_i is the inclination of the horizon from the sample, in degrees [i.e. the lower part of the sky blocked by sample i]
m is an experimentally determined constant; here m =2.3
NB the 'sin' term here and in Eqn. A.9 takes into account foreshortening effects due to low angle radiation [see Dunne et al. (1999)].

The reduced production rate at the sample, P_0', is:

$$P_0' = \frac{1}{S_P} . P_0 \tag{A.8}$$

where P_0 is the original production rate, calculated from Eqn. A.1 or A.3.

A second important implication of topographic shielding is its effect on the incident angle of the radiation which strikes the sample. Topographic obstructions block the lower part of the sky, and thus much of the low angle radiation, thus increasing the proportion of high-angle radiation hitting the target. This results in a longer effective attenuation length, as near-normal incident rays pass through a lower volume of rock to reach a target atom than low angle incident rays [Fig. A.4]. The longer attenuation length also reduces the production rates: higher angle rays interact with fewer atoms in the upper part of the rock as they pass through the sample. Thus a correction for this change in the attenuation length must also be made.

The relevant equation from Dunne et al. (1999) is:

$$\frac{\Lambda^*}{\Lambda} = \left[\frac{1 - \sum_{i=1}^{n} \frac{\Delta\phi_i}{360°} \sin^{m+2} \theta_i}{1 - \sum_{i=1}^{n} \frac{\Delta\phi_i}{360°} \sin^{m+1} \theta_i} \right] \tag{A.9}$$

where Λ^* and Λ are the effective and unshielded attenuation lengths, respectively, in cm.

NB Dunne et al. (1999) used Λ and Λ^* as *lengths*, whereas in this thesis, [e.g. Eqn. 2.26], Λ is the *coefficient* of attenuation, related to the attenuation length, $z*$, by $z* = \Lambda/\rho$. However, since the density of the Tableland samples can be assumed to be constant, then $z* \propto \Lambda$, and hence the *ratio* of attenuation lengths considered above is identical, whichever notation is used.

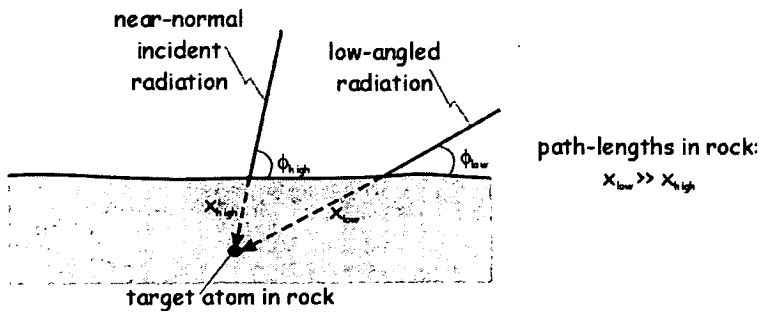

Figure A.4: *The effect of shielding: sketch of path lengths for near normal and low angle incident radiation.*
A topographic obstruction blocks some of the low-angle radiation [Fig. A.3a]. TCNs are produced predominantly by near-normal incident radiation. Low angle rays have a longer path to a target atom than rays with near-normal incidence. Hence attenuation is lower for near-normal rays, and the attenuation length is increased.

A.4.3 Sloping surfaces

The third assumption in the calculation of production rates is that the sampled surface was horizontal. If a sample lies on a steeply sloping surface, then up to half of the incident radiation is blocked from reaching the target. This is due to a combination of two factors:

- A considerable part of the incident radiation is blocked by the part of the slope above the sample [Fig. A.5a]. This is an extreme case of topographic shielding [section A.4.2], resulting in a larger proportion of near-vertical incident radiation. In the case of a vertical cliff, the incident radiation is reduced by half, as *all* sub-vertical rays coming from 'behind' the cliff are obstructed.
- Few rays strike the sample from azimuths parallel to the cliff-face, as the sample has very little surface area in that direction due to the slope of the surface [Fig. A.5b]. In the case of a vertical cliff, the surface area of the target is zero to rays striking parallel to the cliff with **any** inclination.

A.4.4 Surface coverage

Gosse and Phillips (2001) describe a technique for calculating the cover due to snow; a similar approach should be used for other materials, e.g. sand, peat. The period and depth of cover must be quantified. In the case of snow, this may be estimated by extrapolation of snow records, although the variation in density and water content of the snow also drastically affects the shielding of the rock underneath. The shielding is calculated by integrating for the variation in thickness [and water content etc.] of the cover. Gosse and Phillips (2001) show that snow may account for significant shielding: up to 15% variation in the calculated exposure age may arise for reasonably dense snow up to 3m thick [their Fig. 17].

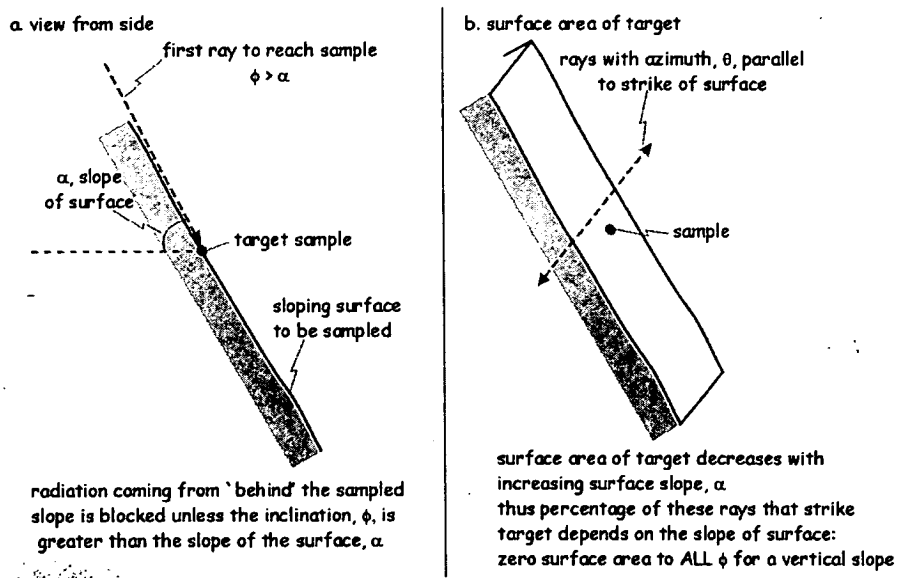

Figure A.5: *Sketch of shielding of a sample on a sloping surface.*
a. Only rays with ϕ greater than the slope of the cliff are not obstructed.
b. Few rays travelling parallel to the cliff face contribute to in situ *cosmogenic production at the sample site.*

A.5 Calculation of exposure ages and erosion rates

The concentration of any cosmogenic nuclide increases through time as long as the sample remains in the productive zone near the surface [Fig. A.1]. For a sample that remains at the surface, the rate of increase is the surficial production rate at the specific sample latitude and elevation [section A.3]. The concentration radiogenic TCNs, e.g. ^{10}Be and ^{26}Al, also *de*creases exponentially with time, as the nuclide decays. For very old samples [exposure age $\geq$ nuclide half-life], the rate of decay will equal the rate of production, and the concentration of the TCN remains constant: 'secular equilibrium'. However, for younger samples, an apparent 'exposure age' can be calculated: the amount of time that the sample has been exposed at the surface. For stable TCNs, e.g. ^{3}He, this is the measured TCN concentration divided by the production rate. For radiogenic isotopes, radioactive decay must also be considered.

AMS measures the ratio of the cosmogenically-produced to stable isotope, R_{TCN}, in a sample:

$$R_{TCN} = \frac{N_{TCN}}{N_{stable}} \quad \left[\text{e.g. } = \frac{N^{26}Al}{N^{27}Al}\right] \tag{A.10}$$

where N_{TCN} and N_{stable} are the abundancies of the cosmogenically-produced and stable isotopes, respectively, in atoms g^{-1} target.

The concentration of the element is measured independently, e.g. by ICP, and an assumption made about the ratio of stable to TCN isotope. For elements with a low natural abundance, e.g. ^{10}Be, a carrier is added. The production rate [P_{TCN}] is

calculated [section A.3], and corrections made for shielding of the sample site [section A.4]. The rate of change of TCN concentration [after Lal (1991)] is the rate of radioactive decay added to the rate of production:

$$\frac{\mathrm{d}N(x,t)}{\mathrm{d}t} = -N(x,t)\lambda + P(x,t) \tag{A.11}$$

$$P(x,t) = P(0,t)\exp -\mu x(t) \tag{A.12}$$

where $N(x,t)$ is the number of atoms of the cosmogenically-produced isotope at a depth x [cm], and time, t [yrs]
$P(x,t)$ is the production rate of the TCN, in atoms g^{-1} target
μ is the absorption coefficient of the rock, in cm^{-1}: $\mu = 1/z*$: $\mu = \rho/\Lambda$.

This assumes that the TCN is produced by spallation, and hence that the production rate decreases exponentially below the surface. If muon-production is significant, e.g. for ^{36}Cl, then additional calculations must be made [e.g. Lal (1991); Gosse and Phillips (2001)]. Since the equations above depend on the depth at which the sample is taken, then the erosion rate, $\epsilon(t)$, must be considered:

$$x(t) = \int_0^t \epsilon(t)\mathrm{d}t + constant \tag{A.13}$$

where $x(t)$ is the depth [cm] at a time, t [yrs].

For the simplest case of constant erosion: $\epsilon(t) = \varepsilon$, and constant surface production rate, P_0, the abundance of the TCN, $N(x,t)$, at a depth, x, is given [after Lal (1991); Brown et al. (1991)] by:

$$N(x,t) = N_0 \mathrm{e}^{-\lambda t} + \frac{P_0}{\lambda + \mu\varepsilon}\,\mathrm{e}^{-\mu x}\left(1 - \mathrm{e}^{-[\lambda+\mu\varepsilon]t}\right) \tag{A.14}$$

where N_0 is the initial number of cosmogenically-produced atoms at a depth, x [cm], in atoms g^{-1} target
λ is the radiogenic decay constant [$= 1/t_{1/2}$], in yr^{-1}.

If the depth-dependence in N is removed by normalising to the value for TCN production solely at the surface, then Eqn. A.14 becomes:

$$N(t) = \frac{P_0}{\lambda + \mu\varepsilon}\left(1 - \mathrm{e}^{-[\lambda+\mu\varepsilon]t}\right) \tag{A.15}$$

If erosion is negligible, $\varepsilon \to 0$, and the sample can be assumed to have remained at the surface throughout:

$$N(t) = \frac{P_0}{\lambda}\left(1 - e^{-\lambda t}\right) \tag{A.16}$$

The **apparent exposure age** of a sample exposed continuously at the surface may be calculated by rearranging Eqn. A.16 as described in Chapter 2 to give:

$$\boxed{t_{exp} = -\frac{1}{\lambda} ln\left[1 - \frac{N(t)\lambda}{P_0}\right]} \tag{A.17}$$

If the length of the exposure is known, then Eqn. A.15 can be used to estimate the long-term average erosion rate during the exposure. For samples that have been irradiated for a long time [$t \gg 1\,(\lambda + \mu\varepsilon)$], then Eqn. A.14 simplifies [Lal (1991)] to:

$$N(x,t) = e^{-\mu x}\,\frac{P_0}{\lambda + \mu\varepsilon} \tag{A.18}$$

This is the steady-state case, and hence after long term irradiation, samples will attain secular equilibrium. Rearranging Eqn. A.18 gives the steady-state maximum **erosion rate**:

$$\boxed{\varepsilon = \frac{1}{\mu}\left[\frac{P_0}{N} - \lambda\right]} \tag{A.19}$$

Comparison of more than one isotope allows more detailed information about a sample's history to be ascertained, as explained in section 2.5.2, and demonstrated with the Volcanic Tableland samples in section 6.5.1.

Appendix B

Methodology

This appendix outlines the methodology used for collection of the field data, and also the labwork involved in preparing the targets for AMS analysis of the cosmogenic isotope samples.

B.1 Collection of field data using differential GPS

B.1.1 GPS Theory

The Global Positioning System [GPS] uses a network of 24 satellites orbiting the earth to precisely locate a position on the earth's surface. A receiver on the earth's surface can find its position effectively by a sort of 'triangulating', using the satellites. Each satellite sends out a continuous radio transmission, of a specific pseudo-random code [PRC]: a very complex long signal, modulating a carrier signal of a set frequency. The receiver calculates the distance between itself and each satellite by calculating the time taken for the signal to reach it; evident in the phase difference between a signal from the satellite and an identical one produced by the receiver itself.

The GPS satellite system was established such that at least 5 satellites are visible from any point on the earth's surface at any time. This ensures that a receiver can always locate itself, since 4 satellites are needed for a unique solution in three dimensions. However, obtaining a unique solution of 3D position also requires that the receiver clock is exactly synchronised with the satellites' timing. By using three satellites, a receiver may obtain an apparent position, which should be confirmed by comparison with a fourth satellite. However, if a unique solution is not be obtained when the fourth satellite is checked, then the receiver computer is alerted that an error in the timing must have been made. Thus the receiver calculates what single timing correction can be made to produce a unique solution based on the known satellite locations. By checking its location every one or two seconds, the receiver is able to ensure that it remains exactly synchronised with the satellites' clocks.

Errors are introduced into the distance calculations due to perturbations of the signals in the atmosphere. The largest error comes from ionised particles, although differences in the water content, temperature and pressure also affect the signal. Military GPS can correct for atmospheric perturbations by comparing the refraction of two different

frequency signals, but the second frequency is not available for civilian use. The best locations are calculated using well-spaced satellites, where the overlap of the solutions is small. However, if the satellites used for the solution are close to each other, then the correlations are all relatively shallow-angle, and hence a wider region of error is introduced into the location solution: 'geometric dilution of precision'. Multipath errors, much like 'ghosts' on television pictures, are caused by the signal reflecting off objects near the receiver. Although the first signal to arrive travels directly to the receiver, it may be swamped by a series of large 'echoes' that arrive shortly afterwards. Satellites transmit a navigation message, constantly updating receivers with their status, so that slight 'ephemeris' [orbital] errors may be adjusted for. Recent removal of the Selective Availability [SA] error, originally introduced by the US Defence Dept., has improved the resolution of single GPS receivers.

With one GPS receiver, it is now possible to obtain a location accurate to within approximately 10-30 m. However, if two receivers are used, *'differential' GPS*, then locations can be calculated to fractions of a centimetre. One receiver is set at a fixed location, the 'base station', and the second 'rover' receiver may be moved relative to this fixed location. The distance between the two receivers [up to a few hundred kilometres] is tiny relative to the distance between the satellites and the receivers on the surface [17 440km orbit]. Hence the signal from any one satellite to each of the two receivers may be considered to be travelling along virtually exactly the same path, and comparison of the two received signals will give an accurate distance between the two receivers. Since their two paths are effectively identical, errors introduced due to the signals passing through the atmosphere are virtually cancelled out, as are the satellite orbital errors.

Effectively, the stationary receiver solves an inverse problem: knowing its position, it is able to calculate all the errors in the calculation of distances to the satellites, and can pass this information to the mobile receiver, whose position is consequently much better constrained. Hence the stationary receiver constantly records the location, orbit and velocity of each satellite, calculates the changing errors, and the rate of change of errors, in timing and orbit. The mobile receiver can interpolate between updates, and calculate its position very accurately.

Differential GPS can remove or reduce errors due to atmospheric perturbations, and satellites, but receiver noise and multipath interference remain. Multipath errors depend considerably on the area in which the receivers are being used: inner city surveying results in high interference, due to the number of nearby obstacles. Errors introduced before May 2000 by Selective Availability [SA] could also be removed by differential GPS, as comparing the signals allowed the deliberate interference [the same for both receivers] to be eliminated. The stationary receiver may also further reduce errors by using *'carrier-phase'* data. Although the complexity of the pseudo-random code [PRC] makes it easy to match the right *part* of the signal, its long wavelength can introduce errors of up to one or two metres in the solution. More sophisticated receivers use the PRC to get a reasonable approximation to the time lag in the satellite signal, then constrain the solution by matching the much shorter carrier waves. This allows location calculation to within a few millimetres [for 1-2% error].

Differential GPS may be carried out in two ways. *Real Time Kinetic [RTK]* systems solve the differential in real time, and hence a radio link is required between the

mobile and stationary receivers. The mobile receiver is constantly updated with the satellite information calculated by the base station, and hence it can compute a location relative to the base station in real time, allowing state-of-the-art navigation. However, this limits the range over which solutions can be found to that of the radio. It may often also effectively require line-of-sight surveying, as the radiowaves can suffer serious interference from large objects or topography between the receivers.

Where a real time solution is not required, e.g. for mapping, the solutions may be calculated by *post-processing* the mobile data against the base station data. In this case, the base station is set up to constantly record all the satellite data throughout the surveying time. The rover records its position and the exact time of each measurement. The differential position can be calculated by comparing the two sets of data after collection. This is very useful over longer distances, as the GPS is not limited to the range of a radio link, and topography between the base station and the mobile receiver is not a problem. However, it is much more time consuming, as downloading and processing of the data can take almost as long as the initial data collection.

B.1.2 Data collection on the Volcanic Tableland

The data discussed in this project was collected in two field seasons: during the summer of 1999, and the early summer of 2001. Two different GPS kits were used, but both gave subcentimeter resolution in all dimensions.

The GPS kit used in the first season was a Magellan Promark-X-CM. Differentials were calculated by post-processing the mobile data against a carrier-phase stationary file, at the end of each day. This allowed us to establish a single base station for the entire project at a surveyed position at the University of California's White Mountain Research Station [WMRS] in Bishop. In some instances, data was also processed against a community base station in Mammoth Lakes, about 50miles north, when the base station batteries failed.

The receiver was a flat circular disc mounted on a 2m aluminium pole, and attached to a small computer carried in a rucksack. The pole was carried vertically such that its base was kept a set distance [~5cm] above the ground surface. A correction was then made for this offset. Data was collected every second throughout the survey. Specific features [e.g. fault/river intersections, locations of cross-sections, tributary confluences etc.] were marked with 'attributes' in the data during the survey.

In the 2001 fieldseason, I was loaned a Ashtech Z-Xtreme GPS kit from my supervisor, Nancye Dawers at Tulane University. This system calculated real-time differential locations for the surveys, using a VHF radio link between the base station and the mobile receiver. Since solutions were calculated in real time, no post-processing was required, and a small map of the collected data could be immediately seen in the field. In this case, the base station had to be established on the Tableland, due to the limiting range of the VHF radio link.

The receiver is a circular disc mounted on an aluminium pole, which can be either fixed to a tripod [for the base station, or stationary readings], or carried in a rucksack, as for the Tableland surveying. The small computer storing the positional data can also be carried in the rucksack [Fig. B.1b.], and a correction made for the vertical offset from the ground. Datapoints were collected every two seconds in the field [equivalent

to 0.5-2 m walking slowly, depending on the terrain]. A handheld data collector allows the user to control the surveying. The base station VHF radio transmitter is powered by a vehicle battery [Fig. B.1a.], and picked up by a small antenna on the mobile receiver. Due to the scale of the field area, and the steep topography in places, no one base station location could be used for the entire fieldseason. Three separate positions were used, and hence some points had to be resurveyed, to allow comparison of the mobile data from different parts of the field area.

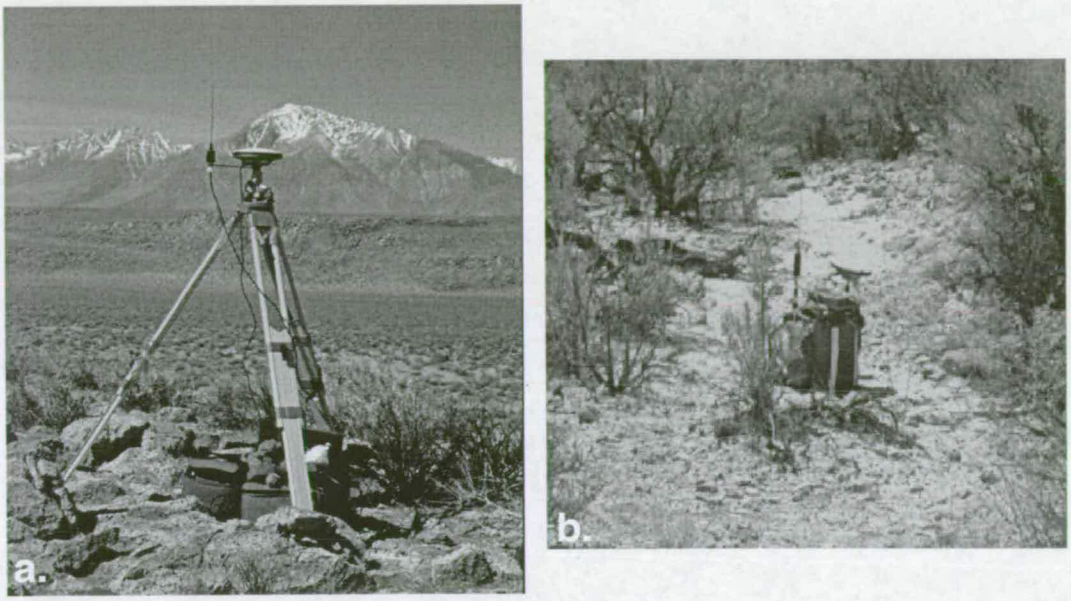

Figure B.1: *The Z-Xtreme kit in the field.*
a. Base station. [Bear and pig operators for scale.] The GPS receiver is the disc mounted at the top of the central pole, held in place by the tripod. Computer storing positional and satellite data is the small blue-black box under the tripod, powered by an internal battery. The VHF radio transmitter [stubby aerial on the receiver] allows real-time communication with the mobile receiver. Vehicle battery powers the radio transmitter.
b. Mobile receiver pack. The mobile receiver is virtually identical to the base station [without the tripod], but can be mounted on a short [50cm] pole, which fits onto a special rucksack, in which the computer, and a radio receiver aerial are carried. The vertical offset of the receiver disc from the ground is measured, and the data corrected accordingly.

Collecting the fault data involved walking out the footwall and hangingwall cutoffs of the faults, from which the displacement profiles are constructed. The footwall cutoff was walked out along the top edge of the fault scarp. The hangingwall cutoff was surveyed by walking around the bottom of the exposed scarp. The dip of each fault scarp was measured where possible, and it was assumed that the faults continued as planar structures to depth. Since erosion of the footwalls and deposition in the hangingwalls is minimal, the fault scarp topography may be considered a reasonable proxy for the fault displacement (Dawers et al., 1993; Dawers and Anders, 1995). Fault displacements were therefore calculated from the vertical separation of the cutoffs. Where a significant talus slope was evident, on the largest faults, the base of the talus was also surveyed, and the dip of both scarp and talus fan used to calculate the additional part of the scarp that was effectively hidden by the talus apron. The fault

profiles discussed in this project were all collected in 1999, with a datapoint collected every second, roughly equivalent to 0.5-2 m separation depending on the terrain.

The river channels on the Tableland are dry [section 3.2], and hence can be easily surveyed. Long profiles were walked out down the centre of each channel, with a datapoint collected every 1 (1999) or 2 (2001) seconds, roughly equivalent to 0.5-2 m separation depending on the gradient of the stream. Streams were walked out as far upstream as a channel could be reliably traced on the ground. All significant tributaries were marked and also walked out. Cross-sectional profiles [bank-bank, perpendicular to the flow] were measured every 50 to 100 m along each channel, depending on the complexity of the structure: profiles were more widely spaced in shallow meandering channels than in deeply incised gorges. Thus the changes in gradient of the channel bed, particularly those relating to fault motion, are picked out in the long profiles. Cross-sectional profiles show the changing channel morphology: width, incision patterns and bank asymmetry. Notes, sketches and photographs were taken at many points in each channel, recording the variations in channel morphology, bedforms and also, where applicable, bedload along the stream.

B.1.3 Data analysis and plotting

Fault displacement profiles have been calculated from the vertical separation of the top and bottom of the exposed scarps (vertical difference between footwall and hangingwall cutoff). Where a significant talus slope was evident, the total displacement was calculated as the sum of the displacement on the exposed scarp and that hidden by the talus deposits. The cutoffs were calculated as a variation in elevation with distance from one tip of the fault, along a 'spine', which allowed for bends in the fault trace. The Generic Mapping Tools [GMT] were used to interpolate and sample the data at regular intervals, from which the vertical separation of the top and base of the exposed scarp was calculated. The throw on each fault was calculated using the average of the dip measurements taken in the field. In the case of the largest fault, Fault 1, the footwall surveys did not match correctly, leaving gaps which were interpolated using GMT [see Chapter 4].

The channel data was plotted as elevation change with increasing distance downstream along the river bed: the *river* long profile. Thus the profiles plotted in Chapters 4 and 5 include all the bends in the channel, and are not *valley* profiles, which are calculated with distance along the valley [i.e. cancelling out the meanders and bends]. Variations in channel bed gradient can then be investigated, and also used to calculate the variation in stream power and SL index along the surveyed streams [see section 2.3.2].

Cross-sectional profiles [Fig. 3.8], perpendicular to the local flow direction, were used to investigate the changing morphology of the channels in various parts of their courses. They also enabled me to measure the bank-bank width, and the bank-base depth of the channels accurately. This data was used to calculate the aspect ratio, AR [=total depth/total width] as discussed in Chapter 3 [section 3.3].

B.2 Cosmogenic isotope target preparation

Chapter 6 describes the collection of samples for *in situ* TCN analysis from streams in the central overlap of the fault array. This section outlines the production of targets for AMS analysis of ^{26}Al and ^{10}Be from the whole-rock samples collected in the Volcanic Tableland, which was carried out at the Geography department in Edinburgh University, after the method of Kohl and Nishiizumi (1992).

The AMS analyses the ratios of ^{10}Be:^{9}Be and ^{26}Al:^{27}Al in pure quartz. Thus the first step of the target preparation is to isolate quartz from the whole-rock samples. The separated quartz crystals are etched in hydrofluoric acid [HF] to remove the outer part of the crystal, and hence any meteoric ^{10}Be that might contaminate the samples. Once the quartz crystals have been separated and cleaned, the Be and Al within the quartz can be separated in a series of steps, beginning with the dissolution of the quartz in HF. Impurities are removed by fuming with a sequence of acids, then the two metals Al and Be are separated using first an anion and then a cation column. Ammonium solution is used to generate the hydroxides which are then oxidised to produce the targets, Al_2O_3 and BeO.

AMS measures concentrations of ^{10}Be and ^{26}Al to 10^{-15} atoms $g^{-1}SiO_2$, and hence it is essential to avoid contamination of the samples, particularly with meteoric ^{10}Be, which is present in normal water and hence also in the air. After the initial crushing and mineral separation, all the subsequent chemistry was carried out in an ultra-clean laboratory, with scrubbed internal air circulation, and using ultra-pure [18MΩ] water, to avoid contamination with meteoric ^{10}Be. Targets were prepared in teflon beakers, and using reagents from plastic bottles, to reduce the possibility of contamination with boron [^{10}B], a natural isobar of Be, and which is present in most glassware.

B.2.1 Preparation of quartz concentrates

Crushing: Samples were prepared from sand-sized grains, in this case 500-125μm. The initial part of the preparation involves crushing and repeated sieving and washing of the whole rock samples [500-900g] to obtain the clean fraction required. Any traces of organic material [e.g. lichen] were first removed from the field samples.

Mineral separation: The cosmogenic nuclides ^{10}Be and ^{26}Al are produced *in situ* from bombardment of Si and O atoms in quartz. Thus only quartz grains are required for target production. Quartz was separated from the whole-rock samples by density separation. Separation was carried out using lithium meta-tungstate ['LMT': Li_2WO_4], a heavy liquid [$\rho \sim 2.8 gcm^{-3}$] in which quartz naturally floats. Thus if the whole-rock sample is shaken in LMT, heavy minerals will sink and can be removed. If water is added carefully to LMT, its density may be reduced to a point where quartz sinks slowly through the fluid column. Thus less dense minerals may be easily separated from the quartz.

The largest contaminants in the Tableland samples were sanidine and glass. Glass was simply removed, as its density [$\rho > 2.5 gcm^{-3}$] is significantly lower than that of quartz [$\rho = 2.65 gcm^{-3}$]. Similarly, heavy minerals, such as biotite [$\rho \sim 3.10 gcm^{-3}$] and opaques [$\rho > 3.1 gcm^{-3}$] were easily removed. However, sanidine [$\rho = 2.56 - 2.62 gcm^{-3}$] was a more significant problem, as its density is similar to that of quartz, and incomplete

separation of some of the samples was apparent under a dissecting microscope. Since sanidine contains aluminium, it was important to ensure that it was completely removed before dissolution of the samples [section B.2.2; high Al content makes the ^{26}Al:^{27}Al ratio below detection in the AMS]. In some cases, where the contamination was significant [>5%], the quartz separates were shaken in a mixture of 1:1 HCl:ultrapure water overnight at room temperature, to remove as much of the feldspar as possible. In most cases, however, since the contamination was relatively small, and sanidine should be dissolved in hydrofluoric acid [HF], the separates were etched [see below] without prior washing in HCl.

Etching: All traces of meteorically-produced ^{10}Be must be completely removed if the smaller concentrations of *in situ*-produced ^{10}Be are to be analysed. Thus the outer part of all quartz grains must be removed to ensure that all the ^{10}Be measured in the AMS was produced *in situ*. This was done by leaching the quartz separates in hydrofluoric acid [HF] for several days. The HF digests quartz, breaking down the Si-O bonds, and by using only dilute HF and a short reaction time, this process can be controlled to attack only the outer part of the grains; the stoichiometry of this procedure is calculated to remove up to 30% of the outer part of the quartz grains, in order to reliably remove all meteoric ^{10}Be [e.g. Kohl and Nishiizumi (1992); Gosse and Phillips (2001)]. The Tableland samples were etched four times for 18-24 hours each, and then the resultant quartz concentrates dried completely.

Picking: Due to the difficulties of separating sanidine from these samples, all the concentrates were examined carefully under the dissecting microscope, which revealed traces of light mineral contamination. Examination of backscattered light in the SEM confirmed that many of the contaminants were feldspars, and predominantly sanidine. This was unexpected, as all feldspathic material should be removed during etching. The SEM also revealed some Fe-rich and Cr-rich opaques in the samples which contained no significant Al. In the case of VT2 [see Chapter 6 for location], the contamination was of the order of 10% and hence the concentrate was etched a second time [over 5 days]. In all the other cases, the contamination was less than 2%, but still presented a problem due to the high Al content of the feldspars. Thus all contaminating non-quartz crystals were removed by hand picking from the concentrates [12 to 48 hours per sample]. The second etching of VT2 considerably reduced its sanidine content, and the remaining small traces were removed by hand. No contaminating sanidines were observed under the SEM in any of the samples after picking. Final concentrates contained 10-18g quartz.

B.2.2 Preparation of target oxides

Targets were prepared in two batches of three [1: VT2, VT6, VT11; 2: VT4, VT8, VT14], with one blank prepared for each of the two batches. The blank allows corrections to be made for any trace Al added to the samples from the reagents during the target production. Total Al in the samples is measured independently by ICP analysis of a small aliquot of the samples after dissolution, so that the ratio of ^{26}Al / ^{27}Al measured in the AMS can be used to calculate an abundancy of ^{26}Al in the samples. Since Be is naturally rare in quartz, a known quantity of Be is added to all samples in a carrier to allow the respective calculation to be made.

Dissolution: The quartz is initially digested in hydrofluoric acid, HF, which breaks the strong Si-O bonds, releasing ions from within the quartz lattice. Once finally dissolved, the samples contain the various metal ions: Be, Al, Fe, Mg, Na, K, Ca etc., generally as fluorides, and SiF_4:

$$SiO_2 + 4HF \Longrightarrow SiF_4 + 2H_2O \tag{B.1}$$

Each sample was placed into a clean teflon beaker, weighed, and then a Be carrier added to each. The carrier is specifically prepared from beryl extracted from a deep mine [and thus predominantly ^{9}Be: see Kohl and Nishiizumi (1992)], to avoid swamping the *in situ*-produced isotope. An Al carrier was added to the blank only. Pipettes used for these additions were carefully calibrated before use. Digestion was carried out in a 2:1 mixture of HF and HNO_3, and took 5-14 days, depending on the size of the sample.

Fuming: The final product of the digestion was fumed three times with each of three acids: HNO_3, HCl and $HClO_4$ (perchloric acid). This process gradually cleans the dissolved solid, by making first the NO_3^- and then Cl^- salt of the various metal ions in each sample, and removing the fluoride [as HF]. The perchloric acid fume evaporates off the remaining SiF_4, and removes any traces of boron [^{10}B] which would interfere with the AMS analysis of ^{10}Be. In each case, the solid in the teflon was taken up in a very small volume of acid [< 3ml] and then left to fume at a high temperature until all the acid had reacted, and the teflon was dry. This was repeated three times with each acid to ensure complete reaction of all the sample.

Al aliquot: At this stage, an aliquot of each sample was taken and analysed by ICP-AES, to provide an independent measurement of the total Al [predominantly ^{27}Al] in the sample. This allows the ratio of ^{26}Al / ^{27}Al measured in the AMS to be used to calculate the actual amount of the cosmogenic ^{26}Al present in the sample. ICP analysis relative to the blank also allows a correction to be made for any Al added to the samples in the reagents. The expected ICP Be concentration can be calculated from the volume of carrier added, since Be concentrations in quartz are vanishingly small [really only the cosmogenically produced ^{10}Be: of the order of 10^{-14} atoms $g^{-1}SiO_2$], and hence virtually all of the Be in the samples was added in the carrier at the beginning of the dissolution. The aliquot used in this procedure is a diluted fraction of ~2% of the total sample.

Anion column: The samples at this stage contain a series of other metal ions [Fe, Mg, Ca, Ti, Na and K], which must be removed to ensure proper separation of Al and Be in the subsequent stages. Fe and Ti were removed using an anion column, eluted with various concentrations of HCl. In *strong* HCl, the Fe, and much of the Ti, form strong bonds with Cl^- and bind to the column [as $FeCl_4^-$, $FeCl_5^-$ and $FeCl_6^-$, and $TiCl_6^{2-}$], while the Al and Be [and some Ti] run out of the column. After removal of all the Al and Be, the column was eluted with *dilute* HCl, which washed off the Fe and Ti from the resin into a separate container.

Ammonium precipitation I: Although the Fe and Ti were removed on the anion column, traces of other metal cations, particularly Mg and Ca, may still remain. These were removed by precipitating the Al and Be hydroxides at pH8 with ammonia solution:

the Mg and Ca ions remain in solution at this pH. This precipitation also removes any remaining traces of the interfering ^{10}B left in the samples (Ivy-Ochs, 1996).

Cation column: The two cations were separated using a cation column eluted with different strengths of HCl. This stage also removes any minute traces of other metal ions [Na and K, and trace Ti]. Be can be removed from the column using weak [1M] HCl, while Al remains bound to the column until removed with stronger [4.5M] acid. If the samples are large, the column will not adequately bind all the Al ions even with the weak acid [completely saturated resin] and hence the initial 'Be' fraction will contain some Al, and must be re-separated using a second [and possibly third] cation column. In the case of the Tableland samples [10-18g], only one cation column stage was required.

Ammonium precipitation II: Hydoxides were again made from both the Al and Be separates as after the anion column, for each metal. The two hydroxides, however, form at different pHs: Be at pH10-11 and Al at pH8.

Oxidation: The metal hydroxides were oxidised in quartz vials using a small propane-butane jet burner, to produce the targets: Al_2O_3 and BeO. The Volcanic Tableland targets were then sent to Dr Keith Fifield at the Australian National University [ANU] in Canberra, for analysis, in April-June 2001. The AMS returned the ratios of ^{26}Al / ^{27}Al and ^{10}Be / ^{9}Be in the samples. Calculation of the exposure ages and an interpretation of the results can be found in Chapter 6.

References

R.V. Ackermann and R.W. Schlische. Anticlustering of small normal faults around larger faults. *Geology*, 25(12):1127–30, 1997.

V. Acocella, A. Gudmundsson, and R. Funiciello. Interaction and linkage of extension fractures and normal faults: examples from the rift zone of Iceland. *Journal of Structural Geology*, 22:1233–46, 2000.

P.A. Allen and A.L. Densmore. Sediment flux from an uplifting fault block. *Basin Research*, 12(3/4):367–80, 2000.

P.A. Allen and N. Hovius. Sediment supply from landslide-dominated catchments: implications for basin-margin fans. *Basin Research*, 10:19–35, 1998.

M.H. Anders and R.W. Schlische. Overlapping faults, intrabasin highs and the growth of normal faults. *Journal of Geology*, 102:165–80, 1994.

M.H. Anders, M. Spiegelman, D.W. Rodgers, and J.T. Hagstrum. The growth of fault-bounded tilt blocks. *Tectonics*, 12:1451–9, 1993.

R.S. Anderson. Evolution of the Santa Cruz Mountains, California, through tectonic growth and geomorphological decay. *Journal of Geophysical Research*, 99(B10): 20161–79, 1994.

R.S. Anderson, A.L. Densmore, and M.A. Ellis. The generation and degradation of marine terraces. *Basin Research*, 11(1):7–20, 1999.

R.S. Anderson, J.L. Repka, and G.S. Dick. Explicit treatment of inheritance in dating depositional surfaces using in situ ^{10}Be and ^{26}Al. *Geology*, 24(1):47–51, 1996.

B. Armstrong. The temporal and spatial evolution of clastic syn-tectonic sedimentation on and adjacent to a developing relay ramp: An example from the Suez rift. unpublished MRes thesis, University of Edinburgh, 1997.

B.F. Atwater, D.P. Adam, J.P. Bradbury, R.M. Forester, R.K. Mark, W.R. Lettis, G.R. Fisher, K.W. Gobalet, and S.W. Robinson. A fan dam for Tulare lake, California, and implications for the Wisconsin glacial history of the Sierra Nevada. *Geological Society of America Bulletin*, 97:97–109, 1986.

A. Aydin and R.A. Schultz. Effect of mechanical interaction on the development of strike-slip faults with echelon patterns. *Journal of Structural Geology*, 12:123–9, 1990.

S.B. Bachman. Pliocene-Pleistocene break-up of the Sierra Nevada-White-Inyo Mountains block and formation of Owens Valley. *Geology*, 6:461–3, 1978.

R.A. Bailey, G.B. Dalrymple, and M.A. Lanphere. Volcanism, structure, and geochronology of Long Valley caldera, Mono County, California. *Journal of Geophysical Research*, 81:725–44, 1976.

T.T. Barrows, J.O. Stone, L.K. Fifield, and R.G. Cresswell. Late Pleistocene Glaciation of the Kosciuszko massif, Snowy Mountains, Australia. *Quaternary Research*, 55: 179–189, 2001.

P.C. Bateman. Geology and tungsten mineralisation of the Bishop district, California. *USGS Professional Paper*, 470:208pp, 1965.

P.C. Bateman and Wahrhaftig. Geology of the Sierra Nevada. In E.H. Bailey, editor, *Geology of Northern California*, California Division of Mines and Geology Bulletin 190, pages 107–72, 1966.

S. Beanland and M.M. Clark. The Owens Valley fault zone, eastern California, and surface faulting associated with the 1872 earthquake. *USGS Bulletin*, 1982:29pp, 1994.

C. Beaumont, P. Fullsack, and J. Hamilton. Erosional control of active compressional orogens. In K.R. McClay, editor, *Thrust Tectonics*, pages 1–18. Chapman and Hall, London, 1992.

L.V. Benson, J.W. Burdett, M. Kashgarian, S.P. Lund, F.M. Phillips, and R.O. Rye. Climatic and hydrologic oscillations in the Owens Lake Basin and adjacent Sierra Nevada, California. *Science*, 274(5288):746–9, 1996.

P. Bentham, R.E.Ll. Collier, R.L. Gawthorpe, M.L. Leeder, S. Prosser, and C. Stark. Tectono-sedimentary development of a sedimentary basin: the Neogene Megara basin, Greece. *Journal of the Geological Society of London*, 148:923–41, 1991.

M.E. Berry. Soil-geomorphic analysis of Late-Pleistocene glacial sequences in the McGee, Pine and Bishop Creek drainages, east-central Sierra Nevada, California. *Quaternary Research*, 41:160–75, 1994.

M.E. Berry. Geomorphic analysis of Late Quaternary faulting on Hilton Creek, Round Valley and Coyote Warp faults, east-central Sierra Nevada, California, USA. *Geomorphology*, 20:177–95, 1997.

P. Bierman and A. Gillespie. Accuracy of rock-varnish chemical analyses: Implications for cation-ratio dating. *Geology*, 19:196–9, 1991a.

P. Bierman and A. Gillespie. Range fires: A significant factor in exposure-age determination and geomorphic surface evolution. *Geology*, 19:641–4, 1991b.

P. Bierman and A. Gillespie. Replies to comments on 'Accuracy of rock-varnish chemical analyses: Implications for cation-ratio dating'. *Geology*, 20:470–2, 1992.

P.R. Bierman. Using in situ produced cosmogenic isotopes to estimate rates of landscape evolution: A review from the geomorphic perspective. *Journal of Geophysical Research*, 99(B7):13 885–96, 1994.

P.R. Bierman, A.R. Gillespie, and M.W. Caffee. Cosmogenic ages for earthquake recurrence intervals and debris flow fan deposition, Owens Valley, California. *Science*, 270(5235):447–50, 1995a.

P.R. Bierman, P. Larsen, E. Clapp, and D. Clark. Estimating erosion rates and exposure ages with ^{36}Cl produced by neutron activation. *Geochimica et Cosmochimica Acta*, 59:3779–98, 1996.

P.R. Bierman, K.A. Marsella, C. Patterson, P.T. Davis, and M. Caffee. Mid-Pleistocene cosmogenic minimum-age limits for pre-Wisconsinan glacial surfaces in southwestern Minnesota and southern Baffin Island: a multiple nuclide approach. *Geomorphology*, 27:25–39, 1999.

P.W. Birkeland, M.E. Berry, and D.K. Swanson. Use of soil catena field data for estimating relative ages of moraines. *Geomorphology*, 19:281–3, 1991.

J.L. Bischoff, J.P. Fitts, and J.A. Fitzpatrick. Responses of sediment geochemistry to climate change in Owens Lake sediment: An 800-ky record of saline/fresh cycles in core OL-92. In G.I. Smith and J.L. Bischoff, editors, *An 800 000-year paleoclimatic record from Core OL-92, Owens Lake, Southeast California*, Special Paper 317, pages 37–48. Geological Society of America, Boulder, Colorado, 1997.

P. Bishop and G. Goldrick. Morphology, processes and evolution of two waterfalls near Cowra, New South Wales. *Australian Geographer*, 23(2):116–121, 1992.

P. Bishop, R.W. Young, and L. McDougall. Stream profile change and longterm landscape evolution: Early Miocene and modern rivers of the East Australian highland crest, central New South Wales, Australia. *Journal of Geology*, 93:455–74, 1985.

E. Blackwelder. Pleistocene glaciation in the Sierra Nevada and Basin Ranges. *Geological Society of America Bulletin*, 42:865–922, 1931.

T.C. Blair and J.G. MacPherson. Historical adjustments by Walker River to lake-level fall over a tectonically tilted half-graben floor, Walker Lake Basin, Nevada. *Sedimentary Geology*, 92:7–16, 1994.

J.P. Bradbury. A diatom-based paleohydrologic record of climate change for the past 800 ky from Owens Lake, California. In G.I. Smith and J.L. Bischoff, editors, *An 800 000-year paleoclimatic record from Core OL-92, Owens Lake, Southeast California*, Special Paper 317, pages 99–112. Geological Society of America, Boulder, Colorado, 1997.

J. Braun and M. Sambridge. Modelling landscape evolution on geological timescales: a new method based on irregular spatial discretization. *Basin Research*, 9:27–52, 1997.

E.J. Brook, E.T. Brown, M.D. Kurz, R.P. Ackert Jr., G.M. Raisbeck, and F. Yiou. Constraints on age, erosion and uplift of Neogene glacial deposits in the Transantarctic

Mountains, determined from in situ cosmogenic ^{10}Be and ^{26}Al. *Geology*, 23(12): 1063–6, 1993.

E.J. Brook and M.D. Kurz. Surface exposure chronology using ^{3}He in Antarctic quartz sandstone boulders. *Quaternary Research*, 39:1–10, 1993.

E.T. Brown, D.L. Bourlès, B.C. Burchfiel, D. Qidong, L. Jun, P. Molnar, G.M. Raisbeck, and F. Yiou. Estimation of slip rates in the southern Tien Shan using cosmic ray exposure dates of abandoned alluvial fans. *Geological Society of America Bulletin*, 110(3):377–86, 1998.

E.T. Brown, E.J. Brook, G.M. Raisbeck, F. Yiou, and M.D. Kurz. Effective attenuation lengths of cosmic rays producing ^{10}Be and ^{26}Al in quartz. *Geophysical Research Letters*, 19:369–72, 1992.

E.T. Brown, J.M. Edmund, G.M. Raisbeck, M.D. Kurz, and E.J. Brook. Examination of surface exposure ages of Antarctic moraines using in situ produced ^{10}Be and ^{26}Al. *Geochimica et Cosmochimica Acta*, 55:2269–83, 1991.

E.T. Brown, R.F. Stallard, M.C. Larsen, G.M. Raisbeck, and F. Yiou. Denudation rates determined from the accumulation of in situ-produced ^{10}Be in the Luquillo Experimental Forest, Puerto Rico. *Earth and Planetary Science Letters*, 129:193–202, 1995.

D.W. Burbank and R.S. Anderson. *Tectonic Geomorphology.* Blackwell Science, Malden, Massachusetts, 2001. 274pp.

D.W. Burbank, J. Leland, E. Fielding, N. Anderson, R.S.and Brozović, M.R. Reid, and C. Duncan. Bedrock incision, rock uplift and threshold hillslopes in the northwestern Himalayas. *Nature*, 379:505–10, 1996a.

D.W. Burbank, A. Meigs, and N. Brosović. Interactions of growing folds and coeval depositional systems. *Basin Research*, 8(3):199–224, 1996b.

R. Burgmann, D.D. Pollard, and S.J. Martel. Slip distributions on faults: effects of stress gradients, inelastic deformation, heterogeneous host-rock stiffness, and fault interaction. *Journal of Structural Geology*, 16(12):1675–90, 1994.

R.M. Burke and P.W. Birkeland. Reevaluation of multiparameter relative dating techniques and their application to the glacial sequence along the eastern escarpment of the Sierra Nevada, California. *Quaternary Research*, 11:21–51, 1979.

A.W. Burnett and S.A. Schumm. Alluvial river response to neotectonic deformation in Louisiana and Mississippi. *Science*, 222:49–50, 1983.

M.I. Bursik and A.R. Gillespie. Late Pleistocene glaciation of Mono Basin, California. *Quaternary Research*, 39:24–35, 1993.

J.A. Cartwright and C.S. Mansfield. Lateral displacement variation and lateral tip geometry of normal faults in the Canyonlands National Park, Utah. *Journal of Structural Geology*, 20(1):3–19, 1998.

J.A. Cartwright, B.D. Trudgill, and C.S. Mansfield. Fault growth by segment linkage: an explanation for scatter in maximum displacement and trace length data from the Canyonlands Grabens of SE Utah. *Journal of Structural Geology*, 17(9):1319–26, 1995.

T.E. Cerling, R.H. Webb, R.J. Poreda, A.D. Rigby, and T.S.. Melis. Cosmogenic ^{3}He ages and frequency of late Holocene debris flows from Prospect Canyon, Grand Canyon, USA. *Geomorphology*, 27:93–111, 1999.

B. Champel, P. van der Beek, J-L. Mugnier, and P. leTurmy. Growth and lateral propagation of fault-related folds in the Siwaliks of western Nepal: Rates, mechanisms and geomorphic signature. *Journal of Geophysical Research*, 107:*in press*, 2002.

C. Childs, J. Watterson, and J.J. Walsh. Fault overlap zones within developing normal fault systems. *Journal of the Geological Society of London*, 152:535–49, 1995.

D.H. Clark, P.R. Bierman, and P. Larsen. Improving in situ cosmogenic chronometers. *Quaternary Research*, 44(3):366–76, 1995.

D.H. Clark and A.R. Gillespie. Timing and significance of late-glacial and Holocene cirque glaciation in the Sierra Nevada, California. *Quaternary International*, 38/39: 21–38, 1995.

A.H. Compton. A geographic study of physical rays. *Physical Review*, 43(6):387–403, 1933.

J. Contreras, M.H. Anders, and C.H. Scholz. Growth of a normal fault system: observations from the Lake Malawi basin of the East African Rift. *Journal of Structural Geology*, 22:159–68, 2000.

J. Contreras and C.H. Scholz. A model of rift basin evolution constrained by first-order stratigraphic observations. *Journal of Geophysical Research*, 102(B4):7673–90, 1997.

S. Corfield and I.R. Sharp. Structural style and stratigraphic architecture of fault-propagation folding in extensional settings: a seismic example from the Smørbukk area, Halten Terrace, Mid-Norway. *Basin Research*, 12(3/4):329–342, 2000.

P.A. Cowie. A healing-reloading feedback control on the growth rate of seismogenic faults. *Journal of Structural Geology*, 20(8):1075–87, 1998.

P.A. Cowie, S. Gupta, and N.H. Dawers. Implications of fault array evolution for synrift depocentre development: Insights from a numerical fault growth model. *Basin Research*, 12:241–61, 2000.

P.A. Cowie and C.H. Scholz. Physical explanation for the displacement-length relationship of faults using a post-yield fracture mechanics model. *Journal of Structural Geology*, 14(10):1133–48, 1992a.

P.A. Cowie and C.H. Scholz. Growth of faults by accumulation of seismic slip. *Journal of Geophysical Research*, 97(B7):11085–95, 1992b.

P.A. Cowie and C.H. Scholz. Displacement-length scaling relationship for faults: data synthesis and discussion. *Journal of Structural Geology*, 14(10):1149–56, 1992c.

P.A. Cowie and Z.K. Shipton. Fault-tip displacement gradients and process zone dimensions. *Journal of Structural Geology*, 20(8):983–97, 1998.

P.A. Cowie, C. Vanneste, and D. Sornette. Statistical physics model for the spatiotemporal evolution of faults. *Journal of Geophysical Research*, 98(B12):21809–21, 1993.

A.J. Crone and K.M. Haller. Segmentation and the coseismic behavior of Basin and Range normal faults: examples from east-central Idaho and southwestern Montana, U.S.A. *Journal of Structural Geology*, 13(2):151–64, 1991.

R. Crossley. Controls of sedimentation in the Malawi Rift Valley, Central Africa. In L.F. Jansa, P.F. Burollet, and A.C. Grant, editors, *Basin Analysis: Principles and Applications*, volume 40, pages 33–50. Sedimentary Geology, 1984.

R.R. Curry. *Glacial and Pleistocene history of the Mammoth Lakes Sierra, California-A geologic guidebook.* Geological Serial Publication 11. University of Montana Department of Geology, Missoula, 1971.

G.B. Dalrymple, R.M. Burke, and P.W. Birkeland. Concerning K-Ar dating of a basalt flow from the Tahoe-Tioga interglaciation, Sawmill Canyon, southeastern Sierra Nevada, California. *Quaternary Research*, 17:120–22, 1982.

S.J. Davies, N.H. Dawers, A.E. McLeod, and J.R. Underhill. The structural and sedimentological evolution of early synrift successions: the Middle Jurassic Tarbert Formation, North Sea. *Basin Research*, 12:343–65, 2000.

N.H. Dawers and M.H. Anders. Displacement-length scaling and fault linkage. *Journal of Structural Geology*, 17:607–14, 1995.

N.H. Dawers, M.H. Anders, and C.H. Scholz. Growth of normal faults: displacement-length scaling. *Geology*, 21:1107–10, 1993.

N.H. Dawers and J.R. Underhill. The rôle of fault interaction and linkage in controlling syn-rift stratigraphic sequences: Statfjord East area, northern North Sea. *Bulletin of the American Association of Petroleum Geologists*, 84(1):45–64, 2000.

A.L. Densmore, R.S. Anderson, B.G. McAdoo, and M.A. Ellis. Hillslope evolution by bedrock landslides. *Science*, 275:369–72, 1997.

A.L. Densmore, N.H. Dawers, S. Gupta, P.A. Allen, and Gilpin. R.E. Landscape evolution and catchment development at extensional relay zones. *Journal of Geophysical Research*, 107:submitted, 2002.

A.L. Densmore, M.A. Ellis, and R.L. Anderson. Landsliding and the evolution of normal fault-bounded mountains. *Journal of Geophysical Research*, 103(B7):15203 –19, 1998.

C.M. DePolo and J.G. Anderson. Estimating the slip rates of normal faults in the Great Basin, USA. *Basin Research*, 12(3/4):227–240, 2000.

C.M. DePolo, D.G. Clark, D.B. Slemmons, and A.R. Ramelli. Historical surface faulting in the Basin and Range province, western North America: implications for fault segmentation. *Journal of Structural Geology*, 13(2):123–36, 1991.

C.M. DePolo and A.R. Ramelli. Preliminary report on surface fractures along the White Mountains Fault Zone associated with the July 1986 Chalfant Valley earthquake sequence. *Bulletin of the Seismological Society of America*, 77:290–6, 1987.

W.E. Dietrich, C.J. Wilson, D.R. Montgomery, J. McKean, and R. Bauer. Erosion thresholds and land surface morphology. *Geology*, 20:675–9, 1992.

R.I. Dorn. Radiocarbon dating of glacial moraines using the aeolian biome: Test results at Bishop Creek, Sierra Nevada, California. *Physical Geography*, 17(2):157–79, 1996.

R.I. Dorn, T.A. Cahill, R.A. Eldred, T.E. Gill, B.H. Kusko, A.J. Bach, and D.L. Elliott-Fisk. Dating rock varnishes by the cation ratio method with PIXE, ICP and the electron microprobe. *International Journal of PIXE*, 1:157–95, 1990.

R.I. Dorn, B.D. Turin, A.J.T. Jull, T.W. Linick, and D.J. Donahue. Radiocarbon and cation-ratio ages for rock varnish on Tioga and Tahoe morainal boulders of Pine Creek, eastern Sierra Nevada. *Quaternary Research*, 28:38–49, 1987.

R.J. Dorsey, P.J. Umhoefer, and P.D. Falk. Earthquake clustering inferred from Pliocene Gilbert-type fan deltas in the Loreto basin, Baja California Sur, Mexico. *Geology*, 25(8):679–82, 1997.

T.J. Dunai. Scaling factors for production rates of in situ produced cosmogenic nuclides: a critical reevaluation. *Earth and Planetary Science Letters*, 176:157–169, 2000.

J. Dunne, D. Elmore, and P. Muzikar. Scaling factors for the rates of production of cosmogenic nuclides for geometric shielding and attenuation at depth on sloped surfaces. *Geomorphology*, 27:3–11, 1999.

M.A. Ellis, A.L. Densmore, and R.S. Anderson. Development of mountainous topography in the Basin Ranges, USA. *Basin Research*, 11(1):21–42, 1999.

A. Fleming, M.A. Summerfield, J.O. Stone, L.K. Fifield, and R.G. Cresswell. Denudation rates for the southern Drakensberg escarpment, SE Africa, derived from *in-situ*-produced cosmogenic ^{36}Cl: initial results. *Journal of the Geological Society of London*, 156:209–12, 1999.

T.W. Gardner. Experimental study of knickpoint and longitudinal profile evolution in cohesive, homogeneous material. *Geological Society of America Bulletin*, 94:664–72, 1983.

R.L. Gawthorpe, A.J. Fraser, and R.E.Ll. Collier. Sequence stratigraphy in active extensional basins: implications for the interpretations of ancient basin fills. *Marine and Petroleum Geology*, 11(6):642–58, 1994.

R.L. Gawthorpe and J.M. Hurst. Transfer zones in extensional basins: their structural style and influence on drainage development and stratigraphy. *Journal of the Geological Society of London*, 150:1137–52, 1993.

R.L. Gawthorpe, J.M. Hurst, and C.P. Sladen. Evolution of Miocene footwall-derived coarse-grained deltas, Gulf of Suez, Egypt: Implications for exploration. *Bulletin of the American Association of Petroleum Geologists*, 74(7):1077–86, 1990.

R.L. Gawthorpe and M.R. Leeder. Tectono-sedimentary evolution of active extensional basins. *Basin Research*, 12(3/4):195–218, 2000.

R.L. Gawthorpe, I. Sharp, J.R. Underhill, and S. Gupta. Linked sequence stratigraphic and structural evolution of propagating normal faults. *Geology*, 25(9):795–8, 1997.

G.K. Gilbert. Niagara Falls and their History. *National Geographic Society Monograph*, 1(7):203–36, 1895. cited in many papers, incl. Young (1985) and Howard *et al.* (1994).

A.R. Gilchrist, H. Kooi, and C. Beaumont. The post-Gondwana geomorphic evolution of south-western Africa: Implications for the controls on landscape development from observations and numerical experiments. *Journal of Geophysical Research*, 99: 12 211–28, 1994.

A.R. Gillespie. Evidence for both Wisconsin and Illinoian ages for the Tahoe glaciation, Sierra Nevada, California. *Geological Society of America Abstracts with programs*, 16(6):519, 1984. (abstract).

A.R. Gillespie. Letter to the editor in response to article by Dorn *et al.* *Quaternary Research*, 30:102–3, 1988.

P.A. Gillespie, J.J. Walsh, and J. Watterson. Limitations of dimension and displacement data from single faults and the consequences for data analysis and interpretation. *Journal of Structural Geology*, 14(10):1157–72, 1992.

R.E. Gilpin. Controls on structural geometries and sediment dispersal in dissected relay ramps: Evolution of the Baba Fault, eastern Gulf of Suez. unpublished MRes thesis, University of Edinburgh, 1998. 211pp.

G. Goldrick and P. Bishop. Differentiating the roles of lithology and uplift in the steepening of bedrock river profiles: An example from southeastern Australia. *Journal of Geology*, 103:227–31, 1995.

M. Goldsworthy and J. Jackson. Active normal fault evolution in Greece revealed by geomorphology and drainage patterns. *Journal of the Geological Society of London*, 157:967–81, 2000.

J. Gomberg and M. Ellis. Topography and tectonics of the Central New Madrid Seismic Zone-results of numerical experiments using a three-dimensional boundary element program. *Journal of Geophysical Research*, 99:20 299–310, 1994.

B. Gomez and D.C. Marron. Neotectonic effects on sinuosity and channel migration, Belle Fourche River, western South Dakota. *Earth Surface Processes and Landforms*, 16:227–35, 1991.

I. Gordon and P.L. Heller. Evaluating major controls on basinal stratigraphy, Pine Valley, Nevada: Implications for syntectonic deposition. *Geological Society of America Bulletin*, 105:47–55, 1993.

J.C. Gosse and J. Klein. Production rate of in situ cosmogenic ^{10}Be in quartz at high altitude and mid-latitude. *Radiocarbon*, 38(1):154–5, 1996.

J.C. Gosse, J. Klein, E.B. Evenson, B. Lawn, and R. Middleton. Beryllium-10 dating of the duration and retreat of the last Pinedale glacial sequence. *Science*, 268(5215): 1329–33, 1995.

J.C. Gosse and F.M. Phillips. Terrestrial in situ cosmogenic nuclides: theory and applications. *Quaternary Science Reviews*, 20:1475–1560, 2001.

D.E. Granger, D. Fabel, and A.N. Palmer. Pliocene-Pleistocene incision of the Green River, Kentucky, determined from radioactive decay of cosmogenic ^{26}Al and ^{10}Be in Mammoth Cave sediments. *Geological Society of America Bulletin*, 113(7):825–36, 2001b.

D.E. Granger, J.W. Kirchner, and R.C. Finkel. Quaternary downcutting rate of the New River, Virginia, measured from differential decay of cosmogenic ^{26}Al and ^{10}Be in cave-deposited alluvium. *Geology*, 25(2):107–110, 1997.

D.E. Granger and P.F. Muzikar. Dating sediment burial with in situ-produced cosmogenic nuclides: theory, techniques and limitations. *Earth and Planetary Science Letters*, 188:269–81, 2001.

D.E. Granger, C.S. Riebe, J.W. Kirchner, and R.C. Finkel. Modulation of erosion on steep granitic slopes by boulder armoring, as revealed by cosmogenic ^{26}Al and ^{10}Be. *Earth and Planetary Science Letters*, 186:269–81, 2001a.

A. Gudmundsson. Tectonics of the Thingvellir fissure swarm, SW Iceland. *Journal of Structural Geology*, 9(1):61–9, 1987a.

A. Gudmundsson. Geometry, formation and development of tectonic features on the Reykjanes Peninsula, southwest Iceland. *Tectonophysics*, 139:295–308, 1987b.

A. Gudmundsson. Formation and growth of normal faults at the divergent plate boundary in Iceland. *Terra Nova*, 4:464–71, 1992.

A. Gupta and C.H. Scholz. A model of normal fault interaction based on observations and theory. *Journal of Structural Geology*, 22:865–79, 2000.

S. Gupta and P. Cowie. Processes and controls in the stratigraphic development of extensional basins. *Basin Research*, 12(3/4):185–94, 2000.

S. Gupta, P.A. Cowie, N.H. Dawers, and J.R. Underhill. A mechanism to explain rift-basin subsidence and stratigraphic patterns through fault-array evolution. *Geology*, 26(7):595–8, 1998.

S. Gupta, J.R. Underhill, I.R. Sharp, and R.L. Gawthorpe. Role of fault interaction in controlling synrift dispersal patterns: Miocene Abu Alaqa Group, Suez Rift, Sinai, Eqypt. *Basin Research*, 11:167–89, 1999.

J.T. Hack. Stream-profile analysis and stream-gradient index. *US Geological Survey Journal of Research*, 1:421–9, 1973.

B. Hallet and J. Putkonen. Surface dating of dynamic landforms: young boulders on aging moraines. *Science*, 265:937–40, 1994.

G.S. Hancock, R.S. Anderson, O.A. Chadwick, and R.C. Finkel. Dating fluvial terraces with ^{10}Be and ^{26}Al profiles: application to the Wind River, Wyoming. *Geomorphology*, 27:41–60, 1999.

G.S. Hancock, R.S. Anderson, and K.X. Whipple. Beyond power: Bedrock incision form and process. In K. Tinkler and E. Wohl, editors, *Rivers over Rock*, Geophysical Monograph 107, pages 35–60. American Geophysical Union, 1998.

D.J. Harbor. Landscape evolution at the margin of the Basin and Range. *Geology*, 25(12):1111–4, 1997.

D.J. Harbor. Dynamic equilibrium between an active uplift and the Sevier River, UT. *Geological Society of America Bulletin*, 106:181–94, 1998.

N.J. Hayward and C.J. Ebinger. Variations in the along-axis segmentation of the Afar Rift system. *Tectonics*, 15(2):244–57, 1996.

S. Hecker, H.D. Stenner, D.P. Schwartz, and J.C. Hamilton. Palaeoseismic results from the central part of the 1959 Hebgen Fault Rupture, Montana. *EOS*, AGU 2000 Fall Meeting Abstract:T72C–27, 2000.

A.M. Heimsath, W.E. Dietrich, K. Nishiizumi, and R.C. Finkel. Cosmogenic nuclides, topography, and the spatial variation of soil depth. *Geomorphology*, 27:151–72, 1999.

B. Heisinger, M. Niedermayer, J.F. Hartmann, G. Korshinek, E. Nolte, G. Morteani, S. Neumaier, C. Petitjean, P. Kubik, A. Synal, and S. Ivy-Ochs. In-situ production of radionuclides at great depths. *Nuclear Instruments and Methods in Physics Research*, B 123:267–76, 1997.

J. Holbrook and S.A. Schumm. Geomorphic and sedimentary response of rivers to tectonic deformation: a brief review and critique of a tool for recognizing subtle epeirogenic deformation in modern and ancient settings. *Tectonophysics*, 305:287–306, 1999.

E.W. Holt and H.P. Taylor. $^{18}O/^{16}O$ mapping and hydrogeology of a short-lived (approximate to 10 years) fumarolic ($> 500°C$) meteoric-hydrothermal event in the upper part of the 0.76 Ma Bishop Tuff outflow sheet, California. *Journal of Volcanology and Hydrothermal Research*, 83(1-2):115–39, 1998.

N. Hovius. Controls on sediment supply by large rivers. In K.W. Shanley and P.J. McCabe, editors, *Relative Role of Eustacy, Climate and Tectonics in Continental Rifts*, volume 59. Society of Economic Palaeontology and Mineralogy Special Publication, 1998.

N. Hovius and M. Leeder. Clastic supply to basins: Invited editorial. *Basin Research*, 10:1–5, 1998.

N. Hovius, C.P. Stark, and P.A. Allen. Sediment flux from a mountain belt derived by landslide mapping. *Geology*, 25(3):231–4, 1997.

N. Hovius, C.P. Stark, H.-T. Chu, and J.-C. Lin. Supply and removal of sediment in a landslide-dominated mountain belt: Central Range, Taiwan. *Journal of Geology*, 108(1):73–89, 2000.

A.D. Howard. Equilibrium and time scales in geomorphology: Application to sand-bed alluvial streams. *Earth Surface Processes and Landforms*, 7:303–25, 1982.

A.D. Howard. A detachment-limited model of drainage basin evolution. *Water Resources Research*, 30:2261–85, 1994.

A.D. Howard. Long profile development of bedrock channels: Interaction of weathering, mass wasting, bed erosion and sediment transport. In K. Tinkler and E. Wohl, editors, *Rivers over Rock*, Geophysical Monograph 107, pages 297–320. American Geophysical Union, 1998.

A.D. Howard, W.E. Dietrich, and M.A Seidl. Modeling fluvial erosion on regional to continental scales. *Journal of Geophysical Research*, 99(B7):13 971–86, 1994.

A.D. Howard and G. Kerby. Channel changes in badlands. *Geological Society of America Bulletin*, 94:739–52, 1983.

P. Huggins, J. Watterson, J.J. Walsh, and C. Childs. Relay zone geometry and displacement transfer between normal faults recorded in coal-mine plans. *Journal of Structural Geology*, 17(12):1741–55, 1995.

N.F. Humphrey and S.K. Konrad. River incision or diversion in response to bedrock uplift. *Geology*, 28(1):43–6, 2000.

S. Ivy-Ochs. *The dating of rock surfaces using in situ-produced ^{10}Be, ^{26}Al and ^{36}Cl, with examples from Antarctica and the Swiss Alps.* unpublished Ph.D. thesis, Swiss Federal Institute of Technology, 1996.

S. Ivy-Ochs, R. Weuest, P. Kubik, H. Muller-Beck, and C. Scluchter. Can we use cosmogenic isotopes to date stone artefacts? *Radiocarbon*, 43:759–64, 2001.

J. Jackson. Fault death: a perspective from actively deforming regions. *Journal of Structural Geology*, 21:1003–10, 1999.

J. Jackson and T. Blenkinsop. The Bilila-Mtakataka fault in Malawi: an active, 100km long, normal fault segment in thick seismogenic crust. *Tectonics*, 16:137–50, 1997.

J. Jackson, R. Norris, and J. Youngson. Structural evolution of active fault and fold systems in central Otago, New Zealand: Evidence revealed by drainage patterns. *Journal of Structural Geology*, 18:217–34, 1996.

J. Jackson, J.-F. Ritz, L. Siame, G. Raisbeck, F. Yiou, R. Norris, J. Youngson, and E. Bennett. Fault growth and landscape development rates in Otago, New Zealand, using in situ cosmogenic ^{10}Be. *Earth and Planetary Science Letters*, 195:185–93, 2002.

J.A. Jackson, J. Gagnepain, G. Houseman, G.C.P. King, P. Papadimitrou, C. Soufleris, and J. Virieux. Seismicity, normal fault and geomorphological development of the Gulf of Corinth: the Corinth earthquakes of February and March 1981. *Earth and Planetary Science Letters*, 57:377–97, 1982.

J.A. Jackson and M.R. Leeder. Drainage systems and the development of normal faults: an example from Pleasant Valley, Nevada. *Journal of Structural Geology*, 16: 1041–59, 1994.

J.A. Jackson and D.. McKenzie. The geometrical evolution of normal fault systems. *Journal of Structural Geology*, 5:471–82, 1983.

J.A. Jackson and N.J. White. Normal faulting in the upper continental crust: observations from regions of active extension. *Journal of Structural Geology*, 11(1/2): 15–36, 1989.

S.J. Jones, L.E. Frostick, and T.R. Astin. Climatic and tectonic controls on fluvial incision and aggradation in the Spanish Pyrenées. *Journal of the Geological Society of London*, 156:761–9, 1999.

D.W. Jorgensen. *Adjustment of alluvial river morphology and process to localized active tectonics.* Unpublished Ph.D. thesis, Colorado State University, 1990. 240pp [referenced in Schumm *et al.* (2000)].

D.K. Keefer. Rock avalanches caused by earthquakes: source characteristics. *Science*, 223:1288–90, 1984a.

D.K. Keefer. Landslides caused by earthquakes. *Geological Society of America Bulletin*, 95:406–21, 1984b.

E.A. Keller, L. Gurrola, and T.E. Tierney. Geomorphic criteria to determine direction of lateral propagation of reverse faulting and folding. *Geology*, 27(6):515–8, 1999.

G.C.P. King, R.S. Stein, and J. Lin. Static stress changes and the triggering of earthquakes. *Bulletin of the Seismological Society of America*, 84:935–53, 1994.

C.P. Kohl and K. Nishiizumi. Chemical isolation of quartz for measurement of *in-situ*-produced cosmogenic nuclides. *Geochimica et Cosmochimica Acta*, 56:3583–7, 1992.

H. Kooi and C Beaumont. Escarpment development on high-elevation rifted margins; insights derived from a surface processes model that combines diffusion, advection and reaction. *Journal of Geophysical Research*, 99:12191–210, 1994.

H. Kooi and C. Beaumont. Large-scale geomorphology: Classical concepts reconciled and integrated with contemporary ideas via a surface processes model. *Journal of Geophysical Research*, 101(B2):3361–86, 1996.

P.O. Koons. The topographic evolution of collisional mountain belts: A numerical look at the Southern Alps, New Zealand. *American Journal of Science*, 289:1041–69, 1989.

P.W. Kubik, S. Ivy-Ochs, J. Masarik, M. Frank, and C. Schluchter. ^{10}Be and ^{26}Al production rates deduced from an instantaneous event within the dendro-calibration curve, the landslide of Köfels, Ötz Valley, Austria. *Earth and Planetary Science Letters*, 161:231–41, 1998.

D. Lal. Cosmic ray labeling of erosion surfaces: *in situ* nuclide production rates and erosion models. *Earth and Planetary Science Letters*, 104:424–439, 1991.

D. Lal and B. Peters. Cosmic ray produced radioactivity on the earth. In *Handbuch der Physik*, volume XLVI/2, pages 551–612. Springer, Berlin, 1967.

P.-H. Larsen. Relay structures in a Lower Permian basement-involved extension system, East Greenland. *Journal of Structural Geology*, 10(1):3–8, 1988.

M.R. Leeder and J. Alexander. The origin and tectonic significance of asymmetrical meander-belts. *Sedimentology*, 34:217–26, 1987.

M.R. Leeder and R.L. Gawthorpe. Sedimentary models for extensional tilt-block / half-graben basins. In *Continental Extensional Tectonics*, Special Issue 28, pages 139–52. Journal of the Geological Society of London, 1987.

M.R. Leeder and J.A. Jackson. The interaction between normal faulting and drainage in active extensional basins, with examples from the western United States and central Greece. *Basin Research*, 5:79–102, 1993.

M.R. Leeder, G.H. Mack, and S.L. Salyards. Axial-transverse fluvial interactions in half-graben: Plio-Pleistocene Palomas Basin, southern Rio Grande Rift, New Mexico, USA. *Basin Research*, 8(3):225–42, 1996.

M.R. Leeder, M.J. Seger, and C.P. Stark. Sedimentation and tectonic geomorphology adjacent to major active and inactive normal faults: Southern Greece. *Journal of the Geological Society of London*, 148:331–43, 1991.

F. Legros, K. Kelfoun, and J. Marti. The influence of conduit geometry on the dynamics of caldera-forming eruptions. *Earth and Planetary Science Letters*, 179:53–61, 2000.

J. Leland, M.R. Reid, D.W. Burbank, R. Finkel, and M. Caffee. Incision and differential uplift along the Indus River near Nanga Parbat, Pakistan Himalaya, from ^{10}Be and ^{26}Al exposure age dating of bedrock straths. *Earth and Planetary Science Letters*, 154:93–107, 1998.

J.J. Lienkaemper, S.K. Pezzopane, M.M. Clark, and M.J. Rymer. Fault fractures formed in association with the 1986 Chalfant Valley, California, earthquake sequence-Preliminary report. *Bulletin of the Seismological Society of America*, 77:297–305, 1987.

R.J. Litwin, D.P. Adam, N.O. Frederiksen, and W.B. Woolfenden. An 800,000 year pollen record from Owens Lake. In G.I. Smith and J.L. Bischoff, editors, *An 800 000-year paleoclimatic record from Core OL-92, Owens Lake, Southeast California*, Special Paper 317, pages 143–60. Geological Society of America, Boulder, Colorado, 1997.

L.K.C. Lubetkin and M.M. Clark. Late Quaternary activity along the Lone Pine fault, eastern California. *Geological Society of America Bulletin*, 100:755–66, 1988.

S.B. Lueddecke, N. Pinter, and P. Gans. Plio-Pleistocene ash falls, sedimentation, and range-front faulting along the White-Inyo Mountains front, California. *Journal of Geology*, 106:511–22, 1998.

M.N. Machette, S.F. Personius, A.R. Nelson, D.P Schwartz, and W.R. Lund. The Wasatch fault zone, Utah: Segmentation and history of Holocene earthquakes. *Journal of Structural Geology*, 13(2):137–49, 1991.

J.H. Mackin. Concept of the graded river. *Geological Society of America Bulletin*, 59: 463–512, 1948.

J.G. Marr, J.B. Swenson, C. Paola, and V.R. Voller. A two-diffusion model of fluvial stratigraphy in closed depositional basins. *Basin Research*, 12(3/4):381–98, 2000.

R. Marrett and R.W. Allmendinger. Estimates of strain due to brittle faulting: sampling of fault populations. *Journal of Structural Geology*, 13(6):735–8, 1991.

D.G. Martinson, N.G. Pisias, J.D. Hays, J. Imbrie, T.C. Moore Jnr., and N.J. Shackleton. Age dating and the orbital theory of the Ice Ages: Development of a high-resolution 0 to 300,000-year chronostratigraphy. *Quaternary Research*, 27: 1–29, 1987.

J. Masarik and R.C. Reedy. Terrestrial cosmogenic-nuclide production systematics calculated from numerical simulations. *Earth and Planetary Science Letters*, 136(3-4):381–95, 1995.

E.B. Mayo. Pleistocene Long Valley Lake in eastern California. *Science*, 80:95–6, 1934.

P.J. McFadzean. *Normal fault growth and interaction, displacement profiles, and tanning studies on the Volcanic Tableland, Owens Valley, California.* Unpublished Ph.D. thesis, Edinburgh University, 2002. many pages.

A.E. McLeod. The propagation and linkage of normal faults: stuff. Unpublished m.res. thesis, University of Edinburgh, 1996. pp.

A.E. McLeod, N.H. Dawers, and J.R. Underhill. The propagation and linkage of normal faults: Insights from the Strathspey-Brent-Statfjord fault array, northern North Sea. *Basin Research*, 12:263–84, 2000.

A.E. McLeod and J.R. Underhill. Processes and products of footwall degradation, northern Brent Field, Northern North Sea. In A.J. Fleet and S.A.R. Boldy, editors, *Petroleum Geology of Northwest Europe: Proceedings of the 5th conference*, pages 91–106. Geological Society of London, 1999.

D. Merritts and T. Hesterberg. Stream networks and long-term surface uplift in the New Madrid Seismic Zone. *Science*, 265:1 081–4, 1994.

D. Merritts and K.R. Vincent. Geomorphic response of coastal streams to low, intermediate and high rates of uplift, Mendocino triple junction region, northern California. *Geological Society of America Bulletin*, 101:1373–88, 1989.

R. Middleton and J. Klein. ^{26}Al: measurement and applications. *Philosophical Transactions of the Royal Society of London*, R323:121–143, 1987.

J.R. Miller. The influence of bedrock geology on knickpoint development and channel-bed degradation along downcutting streams in south-central Indiana. *Journal of Geology*, 99:591–605, 1991.

D. Montgomery and W.E. Dietrich. Where do channels begin? *Nature*, 336:232–4, 1988.

D.R. Montgomery. Valley incision and the uplift of mountain peaks. *Journal of Geophysical Research*, 99(B7):13 913–21, 1994.

D.R. Montgomery and J.M. Buffington. Channel-reach morphology in mountain drainage basins. *Geological Society of America Bulletin*, 109(5):596–611, 1997.

D.R. Montgomery and W.E. Dietrich. Channel initiation and the problem of landscape scale. *Science*, 255:826–30, 1992.

J.M. Moore and R.A. Schultz. Processes of faulting in jointed rocks of the Canyonlands National Park, Utah. *Geological Society of America Bulletin*, 111(6):808–22, 1999.

N.C. Morewood and G.P. Roberts. Lateral propagation of the surface trace of the South Alkyonides normal fault segment, Central Greece: its impact on models of fault growth and displacement-length relationships. *Journal of Structural Geology*, 21:635–52, 1999.

N.C. Morewood and G.P. Roberts. Surface observations of active normal fault propagation: implications for growth. *Journal of the Geological Society of London*, 159:263–72, 2002.

C.K. Morley. Patterns of displacement along large normal faults: Implications for basin evolution and fault propagation, based on examples from East Africa. *Bulletin of the American Association of Petroleum Geologists*, 83(4):613–34, 1999.

C.K. Morley, R.A. Nelson, T.L. Patton, and S.G. Munn. Transfer zones in the East African Rift system and their relevance to hydrocarbon exploration in rifts. *Bulletin of the American Association of Petroleum Geologists*, 74(8):1234–53, 1990.

C.K. Morley and N. Wonganon. Normal fault displacement characteristics, with particular reference to synthetic transfer zones, Mae Moh Mine, northern Thailand. *Basin Research*, 12(3/4):307–28, 2000.

H. Muraoka and H. Kamata. Displacement distribution along minor fault traces. *Journal of Structural Geology*, 5:483–95, 1983.

G.C. Nanson. A regional trend to meander migration. *Journal of Geology*, 88:100–08, 1980.

A. Nicol, J.J. Walsh, J. Watterson, and C. Childs. The shapes, major axis orientations and displacement patterns of fault surfaces. *Journal of Structural Geology*, 18(2/3): 235–48, 1996.

A. Nicol, J.J. Walsh, J. Watterson, and J.R. Underhill. Displacement rates of normal faults. *Nature*, 390:157–9, 1997.

K. Nishiizumi, R.C. Finkel, M.W. Caffee, J.R. Southon, C.P. Kohl, J.R. Arnold, C.T. Olinger, and J. Poths, J.and Klein. Cosmogenic production of ^{10}Be and ^{26}Al on the surface of the earth and underground. U.S.G.S. Circular 1107, Eighth International

Conference on Cosmochronology and Isotope Geochronology, Berkeley, California, 1994. 234pp.

K. Nishiizumi, R.C. Finkel, J. Klein, and C.P. Kohl. Cosmogenic production of ^{7}Be and ^{10}Be in water targets. *Journal of Geophysical Research*, 101:22 225–32, 1996.

K. Nishiizumi, C.P. Kohl, J.R. Arnold, J. Klein, D. Fink, and R. Middleton. Cosmic ray produced ^{10}Be and ^{26}Al in Antarctic rocks: exposure and erosion history. *Earth and Planetary Science Letters*, 104(2/4):440–54, 1991.

K. Nishiizumi, C.P. Kohl, E.M. Shoemaker, J.R. Arnold, J. Klein, D. Fink, and R. Middleton. *In situ* ^{10}Be and ^{26}Al exposure ages at Meteor Crater, Arizona. *Geochimica et Cosmochimica Acta*, 55:2699–703, 1991b.

K. Nishiizumi, E.L. Winterer, C.P. Kohl, J. Klein, R. Middleton, D. Lal, and J.R. Arnold. Cosmic ray production rates of ^{10}Be and ^{26}Al in quartz from glacially polished rocks. *Journal of Geophysical Research*, 94(B12):17 907–15, 1989.

S. Ouchi. Response of alluvial rivers to slow active tectonic movement. *Geological Society of America Bulletin*, 96:504–15, 1985.

C. Paola, P.L. Heller, and C.L. Angevine. The large-scale dynamics of grain-size variation in alluvial basins, 1: Theory. *Basin Research*, 4:73–90, 1992.

D.C.P. Peacock and D.J. Sanderson. Displacements, segment linkage and relay ramps in normal fault zones. *Journal of Structural Geology*, 19(6):721–33, 1991.

D.C.P. Peacock and D.J. Sanderson. Geometry and development of relay ramps in normal fault systems. *Bulletin of the American Association of Petroleum Geologists*, 78(2):147–65, 1994.

D.C.P. Peacock and D.J. Sanderson. Effects of propagation rate on displacement variations along faults. *Journal of Structural Geology*, 18(2/3):311–20, 1996.

J. Peakall. Axial river evolution in response to half-graben faulting: Carson River, Nevada. *Bulletin of the American Association of Petroleum Geologists*, 68:788–99, 1998.

J. Peakall, M. Leeder, J. Best, and P. Ashworth. River response to lateral ground tilting: a synthesis and some implications for the modelling of alluvial architecture in extensional basins. *Basin Research*, 12:413–24, 2000.

A.J. Pearce and A.J. Watson. Effects of earthquake-induced landslides on sediment budget and transport over a 50-year period. *Geology*, 14:52–55, 1986.

F.M. Phillips, M.G. Zreda, L.V. Benson, M.A. Plummer, D. Elmore, and P. Sharma. Chronology for fluctuations in late Pleistocene Sierra Nevada glaciers and lakes. *Science*, 274(5288):749–51, 1996.

F.M. Phillips, M.G. Zreda, J.C. Gosse, J. Klein, E.B. Evenson, R.D. Hall, O.A. Chadwick, and P. Sharma. Cosmogenic ^{36}Cl and ^{10}Be ages of Quaternary glacial and fluvial deposits in the Wind River Range, Wyoming. *Geological Society of America Bulletin*, 109(11):1453–63, 1997.

F.M. Phillips, M.G. Zreda, S.S. Smith, D. Elmore, P.W. Kubik, R.I. Dorn, and D.J. Roddy. Age and geomorphic history of Meteor Crater, Arizona, from cosmogenic ^{36}Cl and ^{14}C in rock varnish. *Geochimica et Cosmochimica Acta*, 55:2695–8, 1991.

F.M. Phillips, M.G. Zreda, S.S. Smith, D. Elmore, P.W. Kubik, and P. Sharma. Cosmogenic chlorine-36 chronology for glacial deposits at Bloody Canyon, eastern Sierra Nevada. *Science*, 248(4962):1529–32, 1990.

W.M. Phillips, E.V. McDonald, S.L. Reneau, and J. Poths. Dating soils and alluvium with cosmogenic ^{21}Ne depth profiles: case studies from the Pajarito Plateau, New Mexico, USA. *Earth and Planetary Science Letters*, 160:209–23, 1998.

N. Pinter. Faulting on the Volcanic Tableland, Owens Valley, California. *Journal of Geology*, 103:73–83, 1995.

N. Pinter and E.A. Keller. Geomorphological analysis of neotectonic deformation, Northern Owens Valley, California. *Geologische Rundschau*, 84:200–212, 1995.

N. Pinter, E.A. Keller, and R.B. West. Relative dating of terraces of the Owens River, Northern Owens Valley, California, and correlation with moraines of the Sierra Nevada. *Quaternary Research*, 42:266–76, 1994.

S. Prosser. Rift-related linked depositional systems and their seismic expression. In G.D. Williams and A. Dobb, editors, *Tectonics and Seismic Sequence Stratigraphy*, Special Publication 71, pages 35–66. Geological Society of London, 1993.

W.C. Putnam. Origin of Rock Creek and Owens River gorges, Mono County, California. *University of California Geological Sciences Publications*, 34:221–278, 1960.

R. Ravnås and R.S. Steel. Architecture of Marine Rift-Basin Successions. *Bulletin of the American Association of Petroleum Geologists*, 82(1):110–46, 1998.

J.B. Reid. The Owens River as a tiltmeter for Long Valley Caldera, California. *Journal of Geology*, 100:353–63, 1992.

S.L Reneau. Stream incision and terrace development in Frijoles Canyon, Bandelier National Monument, New Mexico, and the influence of lithology and climate. *Geomorphology*, 32:171–93, 2000.

J.L. Repka, R.S. Anderson, and R.C. Finkel. Cosmogenic dating of fluvial terraces, Fremont River, Utah. *Earth and Planetary Science Letters*, 152:59–73, 1997.

J.F. Ritz, E.T. Brown, D.L. Bourlès, H. Philip, A. Schlupp, G.M. Raisbeck, F. Yiou, and B. Enkhtuvshin. Slip rates along active faults estimated with cosmic-ray-exposure dates: Application to the Bogd fault, Gobi-Altai, Mongolia. *Geology*, 23(11):1019–22, 1995.

N.A. Rosenbloom and R.S. Anderson. Hillslope and channel evolution in a marine terraced landscape, Santa Cruz, California. *Journal of Geophysical Research*, 99(B7): 14 013–29, 1994.

A.M. Sarna-Wojcicki, C.E. Meyer, and E. Wan. Age and correlation of tephra layers, position of the Matayama-Brunhes chron boundary, and effects of Bishop ash eruption on Owens Lake, as determined from drill hole OL-92, southeast California. In G.I. Smith and J.L. Bischoff, editors, *An 800 000-year paleoclimatic record from Core OL-92, Owens Lake, Southeast California*, Special Paper 317, pages 79–90. Geological Society of America, Boulder, Colorado, 1997.

A.M. Sarna-Wojcicki, M.S. Pringle, and J. Wijbrans. New $^{40}Ar/^{39}Ar$ age of the Bishop Tuff from multiple sites and sediment rate calibration for the Matuyama-Brunhes boundary. *Journal of Geophysical Research*, 105(B9):21 431–43, 2000.

J.C. Savage, M. Lisowski, W.H. Prescott, and N.E. King. Strain accumulation near the epicenters of the 1978 Bishop and 1980 Mammoth Lakes, California, earthquakes. *Bulletin of the Seismological Society of America*, 71:465–76, 1981.

M. Schaller, F. von Blankenburg, N. Hovius, and P.W. Kubik. Large-scale erosion rates from in situ-produced cosmogenic nuclides from European river sediments. *Earth and Planetary Science Letters*, 188:441–58, 2001.

R.W. Schlische. Half-graben basin filling models: new constraints on continental extensional basin development. *Basin Research*, 3:123–41, 1991.

R.W. Schlische. Geometry and origin of fault-related folds in extensional settings. *Bulletin of the American Association of Petroleum Geologists*, 79(11):1661–78, 1995.

R.W. Schlische and M.H. Anders. Stratigraphic effects and tectonic implications of the growth of normal faults and extensional basins. In K.K. Beratan, editor, *Reconstructing the History of Basin and Range Extension Using Sedimentology and Stratigraphy*, Special Paper 103, pages 183–203. Geological Society of America, Boulder, Colorado, 1996.

R.W. Schlische, S.S. Young, R.V. Ackermann, and A. Gupta. Geometry and scaling relationships of a number of very small rift-related normal faults. *Geology*, 24(8): 683–6, 1996.

C.H. Scholz and J.C. Contreras. Mechanics of continental rift architecture. *Geology*, 26(11):967–70, 1998.

C.H. Scholz and P.A. Cowie. Determination of total strain from faulting using slip measurements. *Nature*, 346:837–9, 1990.

C.H. Scholz, N.H. Dawers, J-Z. Yu, M.H. Anders, and P.A. Cowie. Fault growth and fault scaling laws: Preliminary results. *Journal of Geophysical Research*, 98(B12):21 951–61, 1993.

R.A. Schultz and H. Fossen. Displacement-length scaling in three dimensions: the importance of aspect ratio and application to deformation bands. *Journal of Structural Geology*, 24(9):1389–1411, 2002.

S.A. Schumm. Fluvial Paleochannels. *Society of Economic Paleontologists and Mineralogists*, Special Publication 13:98–107, 1972.

S.A. Schumm. *The Fluvial System.* John Wiley and Sons, New York, 1977. 338pp.

S.A. Schumm. Evolution and response of the fluvial system: sedimentologic implications. *Society of Economic Paleontologists and Mineralogists*, Special Publication 31: 19–29, 1981.

S.A. Schumm, J.F. Dumont, and J.M. Holbrook. *Active tectonics and alluvial rivers.* Cambridge University Press, Cambridge, 2000. 276pp.

S.A. Schumm and H.R. Kahn. Experimental study of channel patterns. *Geological Society of America Bulletin*, 83:1755–70, 1972.

L. Seeber and V. Gornitz. River profiles along the Himalayan arc as indicators of active tectonics. *Tectonophysics*, 92:335–67, 1983.

M.A. Seidl and W.E. Dietrich. The problem of channel erosion into bedrock. *CATENA Supplement*, 23:101–24, 1992.

M.A. Seidl, W.E. Dietrich, and J.W. Kirchner. Longitudinal profile development into bedrock: An analysis of Hawaiian channels. *Journal of Geology*, 102:457–74, 1994.

M.A. Seidl, R.C. Finkel, M.W. Caffee, G.B. Hudson, and W.E. Dietrich. Cosmogenic isotope analyses applied to river longitudinal profile evolution: Problems and interpretations. *Earth Surface Processes and Landforms*, 22(3):195–209, 1997.

I.R. Sharp, R.L. Gawthorpe, B. Armstrong, and J.R. Underhill. Propagation history and passive rotation of mesoscale normal faults: implications for synrift stratigraphic development. *Basin Research*, 12(3/4):285–306, 2000.

I.R. Sharp, R.L. Gawthorpe, J.R. Underhill, and S. Gupta. Syn-rift structure and stratigraphy of the El-Qaa half-graben, Suez rift, Egypt. AAPG Hedberg Conference Field Guide, Cairo, 1998.

R.P. Sharp and J.H. Birman. Additions to classical sequence of Pleistocene glaciations, Sierra Nevada, California. *Geological Society of America Bulletin*, 74:1079–86, 1963.

R.P. Sharp and A.F. Glazner. *Geology underfoot in Death Valley and Owens Valley.* Mountain Press, Missoula, Montana, 1997. 319pp.

M.F. Sheridan. Fumarolic mounds and ridges of the Bishop Tuff, California. *Geological Society of America Bulletin*, 81:851–68, 1970.

L.L. Siamé, D.L. Bourlès, M. Sébrier, O. Bellier, J.C. Castano, M. Araujo, M. Perez, G.M. Raisbeck, and F. Yiou. Cosmogenic dating ranging from 20 to 700ka of a series of alluvial fan surfaces affected by the El Tigre fault, Argentina. *Geology*, 25(11): 975–8, 1997.

L. Sklar and W.E. Dietrich. River longitudinal profiles and bedrock incision models: Stream power and the influence of sediment supply. In K. Tinkler and E. Wohl, editors, *Rivers over Rock*, Geophysical Monograph 107, pages 237–60. American Geophysical Union, 1998.

E.E. Small and R.S. Anderson. Geomorphically driven late Cenozoic uplift in the Sierra Nevada, California. *Science*, 270:277–80, 1995.

E.E. Small, R.S. Anderson, and G.S. Hancock. Estimates of the rate of regolith production using ^{10}Be and ^{26}Al from an alpine hillslope. *Geomorphology*, 27:131–50, 1999.

E.E. Small, R.S. Anderson, J.L. Repka, and R. Finkel. Erosion rates of alpine bedrock summit surfaces deduced from in situ ^{10}Be and ^{26}Al. *Earth and Planetary Science Letters*, 150:413–25, 1997.

G.I. Smith and J.L. Bischoff. Core OL-92 from Owens Lake: Project rationale, geologic setting, drilling procedures and summary. In G.I. Smith and J.L. Bischoff, editors, *An 800 000-year paleoclimatic record from Core OL-92, Owens Lake, Southeast California*, Special Paper 317, page 18. Geological Society of America, Boulder, Colorado, 1997.

G.I. Smith, J.L. Bischoff, and J.P. Bradbury. Synthesis of the paleoclimatic record from Owens Lake core OL-92. In G.I. Smith and J.L. Bischoff, editors, *An 800 000-year paleoclimatic record from Core OL-92, Owens Lake, Southeast California*, Special Paper 317, pages 143–60. Geological Society of America, Boulder, Colorado, 1997.

N.P. Snyder, K.X. Whipple, G.E. Tucker, and D.J. Merritts. Landscape response to tectonic forcing: Digital elevation model analysis of stream profiles in the Mendocino triple junction region, northern California. *Geological Society of America Bulletin*, 112(8):1250–63, 2000.

M.S. Steckler, F. Berthelot, N. Lyberis, and X. lePichon. Subsidence in the Gulf of Suez: Implications for rifting and plate kinematics. *Tectonophysics*, 153:249–70, 1988.

R.S. Stein and S.E. Barrientos. Planar high-angle faulting in the basin and range: Geodetic analysis of the 1983 Borah Peak, Idaho, earthquake. *Journal of Geophysical Research*, 90(B1/3):11355–66, 1985.

I.S. Stewart and P.L. Hancock. Normal fault zone evolution and fault scarp degradation in the Aegean region. *Basin Research*, 1:139–53, 1988.

M.D. Stewart. *The effect of fault growth and fault geometry change on drainage development and sediment flux in the active, extensional Basin and Range Province, USA*. Unpublished Ph.D. thesis, Leeds University, 1995. 316pp.

J.D. Stock and D.R. Montgomery. Geologic constraints on bedrock river incision using the stream power law. *Journal of Geophysical Research*, 104(B3):4983–93, 1999.

J.O. Stone. Air pressure and cosmogenic isotope production. *Journal of Geophysical Research*, 105(B10):23 753–9, 2000.

J.O. Stone, C.K. Ballantyne, and L.K. Fifield. Exposure dating and validation of periglacial weathering limits, northwest Scotland. *Geology*, 26:587–90, 1998.

M.A. Summerfield, F.M. Stuart, H.A.P. Cockburn, D.E. Sugden, G.H. Denton, T. Dunai, and D.R. Marchant. Long-term rates of denudation in the Dry Valleys, Transantarctic Mountains, southern Victoria Land, Antarctica, based on in-situ-produced cosmogenic ^{21}Ne. *Geomorphology*, 27:113–29, 1999.

P.J. Talling and M.J. Sowter. Erosion, deposition and basin-wide variations in stream power and bed shear stress. *Basin Research*, 10:87–108, 1998.

L.A. Tebbens, A. Veldkamp, J.J. van Dijke, and J.M. Schoorl. Modeling longitudinal-profile development in response to Late Quaternary tectonics, climate and sea-level changes: the River Meuse. *Global and Planetary Change*, 27:165–86, 2000.

D. Thompson and E. Wohl. Flume experimentation and simulation of bedrock channel processes. In K. Tinkler and E. Wohl, editors, *Rivers over Rock*, Geophysical Monograph 107, pages 279–96. American Geophysical Union, 1998.

K. Tinkler and E. Wohl, editors. *Rivers over Rock.* Geophysical Monograph 107. American Geophysical Union, 1998. 261-78.

K. Tinkler and E. Wohl. A primer on bedrock channels. In K. Tinkler and E. Wohl, editors, *Rivers over Rock*, Geophysical Monograph 107, pages 1–18. American Geophysical Union, 1998a.

K. Tinkler and E. Wohl. Field studies of bedrock channels. In K. Tinkler and E. Wohl, editors, *Rivers over Rock*, Geophysical Monograph 107, pages 261–78. American Geophysical Union, 1998b.

K.J.. Tinkler. Fluvially sculpted rock bedforms in Twenty Mile Creek, Niagara Peninsula, Ontario. *Canadian Journal of Earth Science*, 30:945–53, 1993.

J.H. Tomkin and J. Braun. Simple models of drainage reorganisation on a tectonically active ridge system. *New Zealand Journal of Geology and Geophysics*, 42(1):1–10, 1999.

B.D. Trudgill and J.A. Cartwright. Relay-ramp forms and normal fault linkages, Canyonlands National Park, Utah. *Geological Society of America Bulletin*, 106: 1143–57, 1994.

T.W. Trull, E.T. Brown, B. Marty, G.M. Raisbeck, and F. Yiou. Cosmogenic ^{10}Be and ^{3}He accumulation in Pleistocene beach terraces in Death Valley, California, USA: Implications for cosmic-ray exposure dating of young surfaces in hot climates. *Chemical Geology*, 119:191–207, 1995.

G.E. Tucker and R.L. Slingerland. Erosional dynamics, flexural isostasy and long-lived escarpments: A numerical modeling study. *Journal of Geophysical Research*, 99(B6): 12229–43, 1994.

G.E. Tucker and R.L. Slingerland. Predicting sediment flux from fold and thrust belts. *Basin Research*, 8:329–49, 1996.

J.R. Unruh. The uplift of the Sierra Nevada and implications for late Cenozoic epeirogeny in the western Cordillera. *Geological Society of America Bulletin*, 103: 1395–1404, 1991.

P. van der Beek and J. Braun. Numerical modelling of landscape evolution on geological time-scales: a parameter analysis and comparison with the south-eastern Highlands of Australia. *Basin Research*, 10:49–68, 1998.

P. van der Beek and J. Braun. Controls on post-mid-Cretaceous landscape evolution in the southeastern Highlands of Australia: Insights from numerical surface process models. *Journal of Geophysical Research*, 104(B3):4945–66, 1999.

P. van der Beek, B. Champel, and J-L. Mugnier. Control of detachment dip on drainage development in regions of active fault-propagation folding. *Geology*, 30/5:471–4, 2002.

P. van der Beek, A. Pulford, and J. Braun. Cenozoic landscape development in the Blue Mountains [SE Australia]: Lithological and tectonic controls on rifted margin morphology. *Journal of Geology*, 109:35–56, 2001.

J. van der Woerd, F.J. Ryerson, P. Tapponinier, Y. Gaudemer, R. Finkel, A.S. Meriaux, M. Caffee, Z. Gouguang, and H. Qunlu. Holocene left-slip rate determined by cosmogenic surface dating on the Xidatan segment of the Kunlun fault (Qinghai, China). *Geology*, 26(8):695–8, 1998.

J. Vandenberghe. Timescales, climate and river development. *Quaternary Science Reviews*, 14:631–8, 1995.

Vening-Meinesz. . 1950.

J.J. Walsh and J. Watterson. Analysis of the relationship between displacements and dimensions of faults. *Journal of Structural Geology*, 10:239–247, 1988.

J.J. Walsh and J. Watterson. Displacement gradients on fault surfaces. *Journal of Structural Geology*, 11(3):307–16, 1989.

J.J. Walsh and J. Watterson. *Geometric and kinematic coherence and scale effects in normal fault systems*, pages 193–203. Special Publication 56. Geological Society of London, 1991.

J. Watterson. Fault dimensions, displacements and growth. *Pure Applications of Geophysics*, 124:365–363, 1986.

J.K. Weissel and G.D. Karner. Flexural uplift of rift flanks due to mechanical unloading of the lithosphere during extension. *Journal of Geophysical Research*, 94:13919–50, 1989.

J.K. Weissel and M.A. Seidl. Influence of rock strength properties on escarpment retreat across passive continental margins. *Geology*, 25:631–4, 1997.

J.K. Weissel and M.A. Seidl. Inland propagation of erosional escarpments and river profile evolution across the southeast Australian passive margin. In K. Tinkler and E. Wohl, editors, *Rivers over Rock*, Geophysical Monograph 107, pages 189–206. American Geophysical Union, 1998.

K.X. Whipple, G.S. Hancock, and R.S. Anderson. River incision into bedrock: Mechanics and relative efficiency of plucking, abrasion and cavitation. *Geological Society of America Bulletin*, 112:490–503, 2000a.

K.X. Whipple, N.P. Snyder, and K. Dollenmayer. Rates and processes of bedrock incision by the Upper Ukak River since the 1912 Novarupta ash flow in the Valley of Ten Thousand Smokes, Alaska. *Geology*, 28(9):835–8, 2000b.

K.X. Whipple and C.R. Trayler. Tectonic control of fan size: the importance of spatially variable subsidence rates. *Basin Research*, 8(3):351–66, 1996.

K.X. Whipple and G.E. Tucker. Dynamics of the stream-power incision model: Implications for height limits of mountain ranges, landscape response timescales and research needs. *Journal of Geophysical Research*, 104:17 661–74, 1999.

S.J. Wilkins and M.R. Gross. Normal fault growth in layered rocks at Split Mountain, Utah: influence of mechanical stratigraphy on dip linkage, fault restriction and fault scaling. *Journal of Structural Geology*, 24(9):1413–29, 2002.

E.J.M. Willemse, D.D. Pollard, and A. Aydin. 3D analyses of slip distributions on normal fault arrays, with consequences for fault scaling. *Journal of Structural Geology*, 18:295–309, 1996.

S. Willett, C. Beaumont, and P. Fullsack. Mechanical model for the tectonics of doubly-vergent compressional orogens. *Geology*, 21:371–4, 1993.

G. Willgoose, R.L. Bras, and I. Rodriguez-Iturbe. Results from a new model of river basin evolution. *Earth Surface Processes and Landforms*, 16:237–54, 1991.

C.J.N. Wilson and W. Hildreth. The Bishop Tuff: New insights from eruptive stratigraphy. *Journal of Geology*, 105:407–39, 1997.

C.J.N. Wilson and W. Hildreth. Hybrid fall deposits in the Bishop Tuff, California: A novel pyroclastic depositional mechanism. *Geology*, 26(1):7–10, 1998.

E. Wohl. Bedrock channel morphology in relation to erosional processes. In K. Tinkler and E. Wohl, editors, *Rivers over Rock*, Geophysical Monograph 107, pages 133–52. American Geophysical Union, 1998.

E.E. Wohl. Gradient irregularity in the Herbert Gorge of northeastern Australia. *Earth Surface Processes and Landforms*, 17:69–84, 1992.

E.E. Wohl. Bedrock channel incision along Piccaninny Creek, Australia. *Journal of Geology*, 101:749–61, 1993.

E.E. Wohl. Substrate influences on step-pool sequences in the Christopher Creek Drainage, Arizona. *Journal of Geology*, 108:121–9, 2000.

E.E. Wohl, N. Greenbaum, A.P. Schick, and V.R. Baker. Controls on bedrock channel incision along Nahal Paran, Israel. *Earth Surface Processes and Landforms*, 19:1–13, 1994.

E.E. Wohl and H. Ikeda. Patterns of bedrock channel erosion on the Boso Peninsula, Japan. *Journal of Geology*, 106:331–45, 1998.

E.E. Wohl and D.M. Merritt. Bedrock channel morphology. *Geological Society of America Bulletin*, 113(9):1205–12, 2001.

E.E. Wohl, D.M. Thompson, and D.J. Miller. Canyons with undulating walls. *Geological Society of America Bulletin*, 111(7):949–59, 1998.

R.W. Young. Waterfalls: Form and process. *Zeitschrift fur Geomorphologie, NF*, Supplement Band 55:81–95, 1985.

R.W. Young and I. McDougall. Long-term landscape evolution: early Miocene and modern rivers in southern New South Wales, Australia. *Journal of Geology*, 101: 35–49, 1993.

P.H. Zehfuss, P.R. Bierman, A.R. Gillespie, R.M. Burke, and M.W. Caffee. Slip rates on the Fish Springs fault, Owens Valley, California, deduced from cosmogenic ^{10}Be and ^{26}Al and soil development on fan surfaces. *Geological Society of America Bulletin*, 113(2):241–55, 2001.

M. Zreda and J. Noller. Ages of prehistoric earthquakes revealed by cosmogenic ^{36}Cl in a bedrock fault scarp at Hebgen Lake. *Science*, 282:1097–9, 1998.

M. Zreda and F.M. Phillips. Insights into alpine moraine development from cosmogenic ^{36}Cl buildup dating. *Geomorphology*, 14:149–56, 1995.